NEURAL CIRCUITS REVEALED

EDITED BY: Mariano Soiza-Reilly, Peter Saggau and Benjamin R. Arenkiel

PUBLISHED IN: Frontiers in Neural Circuits

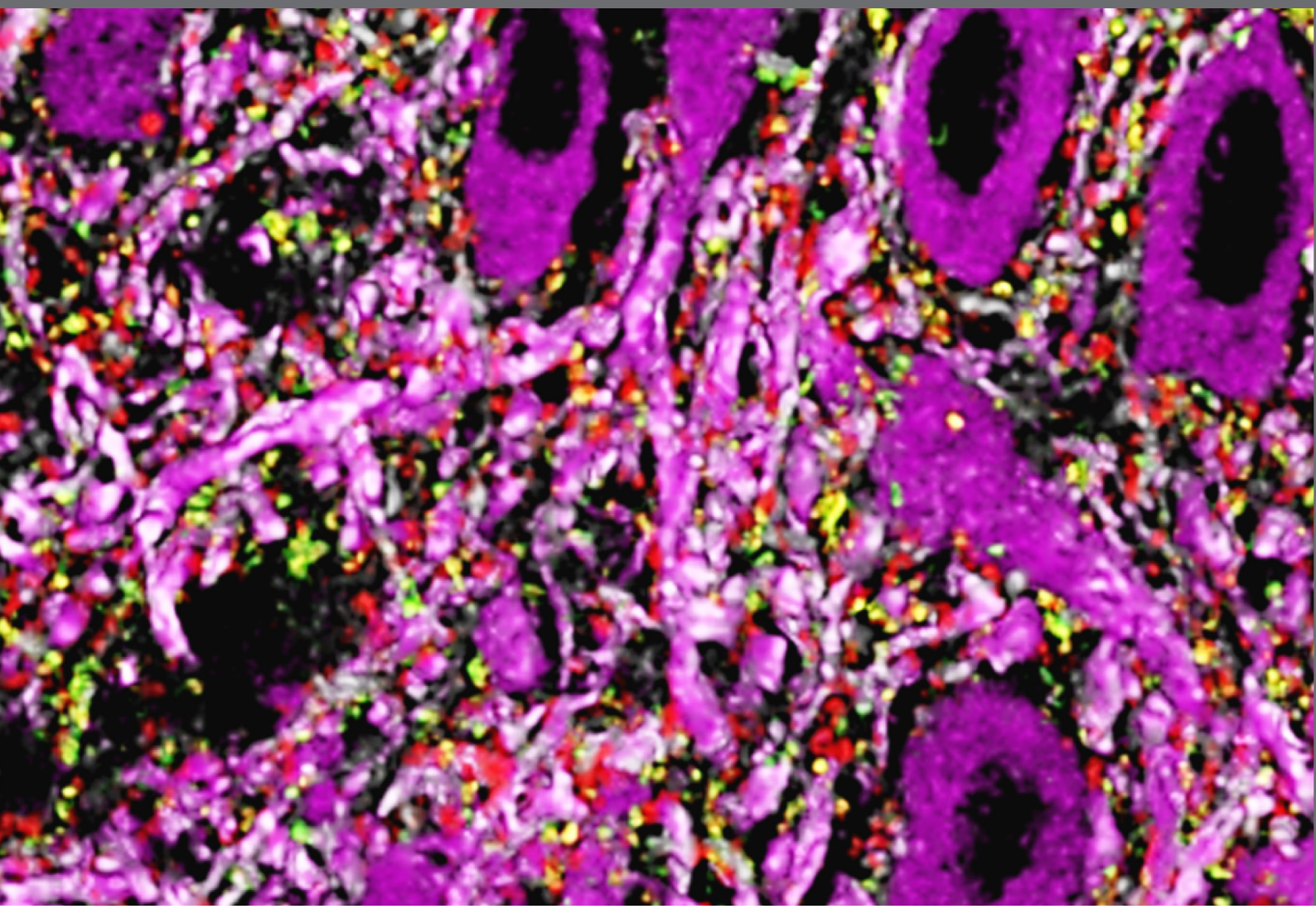

frontiers Research Topics

frontiers

ISSN 1664-8714
ISBN 978-2-88919-561-9
DOI 10.3389/978-2-88919-561-9

About Frontiers

Frontiers is more than just an open-access publisher of scholarly articles: it is a pioneering approach to the world of academia, radically improving the way scholarly research is managed. The grand vision of Frontiers is a world where all people have an equal opportunity to seek, share and generate knowledge. Frontiers provides immediate and permanent online open access to all its publications, but this alone is not enough to realize our grand goals.

Frontiers Journal Series

The Frontiers Journal Series is a multi-tier and interdisciplinary set of open-access, online journals, promising a paradigm shift from the current review, selection and dissemination processes in academic publishing. All Frontiers journals are driven by researchers for researchers; therefore, they constitute a service to the scholarly community. At the same time, the Frontiers Journal Series operates on a revolutionary invention, the tiered publishing system, initially addressing specific communities of scholars, and gradually climbing up to broader public understanding, thus serving the interests of the lay society, too.

Dedication to Quality

Each Frontiers article is a landmark of the highest quality, thanks to genuinely collaborative interactions between authors and review editors, who include some of the world's best academicians. Research must be certified by peers before entering a stream of knowledge that may eventually reach the public - and shape society; therefore, Frontiers only applies the most rigorous and unbiased reviews.
Frontiers revolutionizes research publishing by freely delivering the most outstanding research, evaluated with no bias from both the academic and social point of view.
By applying the most advanced information technologies, Frontiers is catapulting scholarly publishing into a new generation.

What are Frontiers Research Topics?

Frontiers Research Topics are very popular trademarks of the Frontiers Journals Series: they are collections of at least ten articles, all centered on a particular subject. With their unique mix of varied contributions from Original Research to Review Articles, Frontiers Research Topics unify the most influential researchers, the latest key findings and historical advances in a hot research area! Find out more on how to host your own Frontiers Research Topic or contribute to one as an author by contacting the Frontiers Editorial Office: **researchtopics@frontiersin.org**

NEURAL CIRCUITS REVEALED

Topic Editors:
Mariano Soiza-Reilly, Institut du Fer à Moulin (U839), INSERM - Université Pierre et Marie Curie, France
Peter Saggau, Allen Institute for Brain Science, USA
Benjamin R. Arenkiel, Baylor College of Medicine, USA

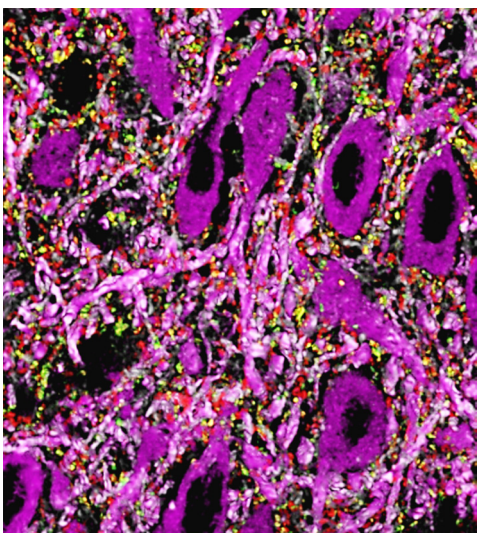

The cover image shows a high-resolution immunolabeling of the mouse dorsal raphe nucleus using array tomography taken from "Unraveling the architecture of the dorsal raphe synaptic neuropil using high-resolution neuroanatomy. Front. Neural Circuits doi: 10.3389/fncir.2014.00105", in this eBook. The complexity of serotonin neuron's (magenta) dendritic trees is evidenced by tubulin labeling to delineate microtubule bundles (light magenta). GABAergic synaptic boutons in the neuropil typically contain synapsin (red) and the enzyme glutamate decarboxylase 65 (GAD2, green).

Deciphering anatomical and functional maps in the nervous system is a main challenge for both clinical and basic neuroscience. Modern approaches to mark and manipulate neurons are bringing us closer than ever to better understand nervous system wiring diagrams. Here we present both original research and review material on current work in this area. Together, this eBook aims to provide a comprehensive snapshot of some of the tools and technologies currently available to investigate brain wiring and function, as well as discuss ongoing challenges the field will be confronted with in the future.

Citation: Soiza-Reilly, M., Saggau, P., Arenkiel, B. R., eds. (2015). Neural Circuits Revealed. Lausanne: Frontiers Media. doi: 10.3389/978-2-88919-561-9

Table of Contents

CHAPTER 3: Methods and tools for data acquisition and analysis

frontiers in Neural Circuits

EDITORIAL
published: 28 July 2015
doi: 10.3389/fncir.2015.00035

Neural circuits revealed

Mariano Soiza-Reilly[1]*, *Peter Saggau*[2] *and Benjamin R. Arenkiel*[3]*

[1] *Institut du Fer à Moulin (U839), INSERM/Université Pierre et Marie Curie, Paris, France,* [2] *Allen Institute for Brain Science, Seattle, WA, USA,* [3] *Department of Molecular and Human Genetics, Baylor College of Medicine, Houston, TX, USA*

Keywords: neuronal tracing, ultrastructure, connectome, optogenetics, networks, electrophysiology, behavior, neurological and psychiatric disorders

The appropriate function of the nervous system relies on precise patterns of connectivity among hundreds to billions of neurons across different biological systems. Evolutionarily conserved patterns of neural circuit organization and connectivity between morphologically and functionally diverse sets of neurons emerge from a remarkably robust set of genetic blueprints, uniquely defining circuits responsible for planning and execution of behavioral repertoires (Arenkiel et al., 2004; Dasen, 2009; Pecho-Vrieseling et al., 2009; Sürmeli et al., 2011; White and Sillitoe, 2013; Inamata and Shirasaki, 2014). Although it is well-established that individual neurons represent the elemental building blocks of the brain, understanding the architecture of neural circuits and how neurons functionally "wire up" through synapses, remains one of biology's major challenges. Our current understanding of how interconnected neuronal populations produce perception, memory, and behavior remains nascent. To unravel the details of complex nervous system function, we must consider not only the morphological and physiological properties of individual neurons, but also the structure and function of connections formed between different cell types. In the last decade much effort has been focused on trying to fully characterize "the brain connectome" and to understand how patterns of synaptic connectivity between neurons might help to better inform the underlying defects associated with neurological and psychiatric disorders (Sporns et al., 2005; Lichtman and Sanes, 2008). More recently there is a growing interest in mapping, and eventually classifying, all synapses in the brain to construct a complete "synaptome" (DeFelipe, 2010; O'Rourke et al., 2012). The very nature of these studies, which rely on multidisciplinary research efforts, have thus catalyzed the development of new research tools and technologies. For instance, advances in molecular genetics, viral engineering, and imaging technologies now allow precise labeling, manipulation, and mapping of complex neural circuits, together revealing previously unattainable details about the cellular morphologies and subcellular structures that are unique to the different types of neurons that make up the brain. Such technological advances could not be possible without successful co-evolution of novel computational tools and analytical methods that allow acquisition, management, and interpretation of gigantic and complex datasets. In fact, this last point perhaps represents the main challenge for the future of "connectomics" (Lichtman et al., 2014).

This Research Topic comprises a wide variety of articles contributing to current views and understanding of different neural circuits, how they are organized in neural networks, and what are the functional outputs of this organization. Additionally, pioneering researchers in the field review novel high-throughput tools and analytical approaches, further describing how these methods have evolved to better explore neural circuits at different levels, covering a wide spectrum of analyses that range from the study of big volumes of brain tissue, to the functional properties of a given network.

The Research Topic eBook is organized into three chapters that cover different aspects of our current knowledge of neural circuits. In chapter 1 the reader will find articles related to the architecture and structural definition of neural circuits. In this chapter Li et al. (2014) use a combination of classical immunofluorescence techniques and immuno-Electron Microscopy (EM) to understand the neuronal connectivity of a pain-related circuitry. With a similar aim,

OPEN ACCESS

Edited by:
Patrick O. Kanold, University of Maryland, USA

Reviewed by:
Ariel Agmon, West Virginia University, USA

***Correspondence:**
Mariano Soiza-Reilly, mariano.soiza-reilly@inserm.fr; Benjamin R. Arenkiel, arenkiel@bcm.edu

Received: *21 April 2015*
Accepted: *01 July 2015*
Published: *28 July 2015*

Citation:
Soiza-Reilly M, Saggau P and Arenkiel BR (2015) Neural circuits revealed. Front. Neural Circuits 9:35. doi: 10.3389/fncir.2015.00035

Serrano-Velez et al. (2014) apply fluorescent retrograde labeling together with freeze-fracture replica immunogold labeling (FRIL) to understand the synaptic organization of the mosquitofish spinal cord. Marc et al. (2014) fully characterized the complete connectome of a retinal cell population using a combination of serial-EM and immunolabeling of small molecules. Soiza-Reilly and Commons (2014) discuss recent evidence about the complex architecture of the dorsal raphe's synaptic neuropil using the novel high-resolution imaging technique called array tomography. Nagayama et al. (2014) review the wiring diagram of the olfactory bulb integrating anatomical and functional aspects. In chapter 2, authors describe and discuss genetic and chemical manipulations of neuronal populations to understand their functionality and their role in neural networks. Thus, Harris et al. (2014) present a high-throughput characterization of numerous new mouse lines that express Cre recombinase selectively in different neuronal populations, allowing dissection and manipulation of neuronal population-specific circuits. Burgalossi et al. (2014) explore the complex neural coding of the medial entorhinal cortex under different environmental conditions. Rothermel and Wachowiak (2014) use novel genetically-encoded calcium sensors (GCaMPs) to explore the cortical feedback to the olfactory bulb. Kawashima et al. (2014) review recently characterized activity-dependent promoters and enhancer elements particularly useful for monitoring the activity of neural networks. Additionally, Murphey et al. (2014) discuss how genetically encoded fluorescent proteins, viral tracing methods, opto- and chemical genetics, and biosensors can be used in the study of inhibitory interneurons. Finally, in chapter 3, new methods and tools for data acquisition and analysis are introduced and discussed. Mazurek et al. (2014) describe new analytical tools to extract quantitative data from orientation and direction selectivity studies in the visual cortex. Hayworth et al. (2014) introduce a novel approach for mapping and imaging large libraries of ultrathin sections. In addition, Lütcke et al. (2013) present a novel method to assess the quality of spike dynamics and network topology inferred from calcium imaging data.

Together, this Research Topic brings to the readers not only new neurobiological data and novel analytical tools, but also offers new perspectives about the way we think about neural circuits and networks, giving rise to important insights to be considered when exploring structural and functional features of micro- and macrocircuits.

Acknowledgments

This was supported by NIH NINDS (NS078294), the Klarman Family Foundation, and the Klingenstein-Simons Fund to Benjamin R. Arenkiel.

References

Arenkiel, B. R., Tvrdik, P., Gaufo, G. O., and Capecchi, M. R. (2004). Hoxb1 functions in both motoneurons and in tissues of the periphery to establish and maintain the proper neuronal circuitry. *Genes Dev.* 18, 1539–1552. doi: 10.1101/gad.1207204

Burgalossi, A., von Heimendahl, M., and Brecht, M. (2014). Deep layer neurons in the rat medial entorhinal cortex fire sparsely irrespective of spatial novelty. *Front. Neural Circuits* 8:74. doi: 10.3389/fncir.2014.00074

Dasen, J. S. (2009). Transcriptional networks in the early development of sensory-motor circuits. *Curr. Top. Dev. Biol.* 87, 119–148. doi: 10.1016/S0070-2153(09)01204-6

DeFelipe, J. (2010). From the connectome to the synaptome: an epic love story. *Science* 330, 1198–1201. doi: 10.1126/science.1193378

Harris, J. A., Hirokawa, K. E., Sorensen, S. A., Gu, H., Mills, M., Ng, L. L., et al. (2014). Anatomical characterization of Cre driver mice for neural circuit mapping and manipulation. *Front. Neural Circuits* 8:76. doi: 10.3389/fncir.2014.00076

Hayworth, K. J., Morgan, J. L., Schalek, R., Berger, D. R., Hildebrand, D. G. C., and Lichtman, J. W. (2014). Imaging ATUM ultrathin section libraries with WaferMapper: a multi-scale approach to EM reconstruction of neural circuits. *Front. Neural Circuits* 8:68. doi: 10.3389/fncir.2014.00068

Inamata, Y., and Shirasaki, R. (2014). Dbx1 triggers crucial molecular programs required for midline crossing by midbrain commissural axons. *Development* 141, 1260–1271. doi: 10.1242/dev.102327

Kawashima, T., Okuno, H., and Bito, H. (2014). A new era for functional labeling of neurons: activity-dependent promoters have come of age. *Front. Neural Circuits* 8:37. doi: 10.3389/fncir.2014.00037

Lichtman, J. W., Pfister, H., and Shavit, N. (2014). The big data challenges of connectomics. *Nat. Neurosci.* 17, 1448–1454. doi: 10.1038/nn.3837

Lichtman, J. W., and Sanes, J. R. (2008). Ome sweet ome: what can the genome tell us about the connectome? *Curr. Opin. Neurobiol.* 18, 346–353. doi: 10.1016/j.conb.2008.08.010

Li, M.-Y., Wu, Z.-Y., Lu, Y.-C., Yin, J.-B., Wang, J., Zhang, T., et al. (2014). Connections between EM2-containing terminals and GABA/μ-opioid receptor co-expressing neurons in the rat spinal trigeminal caudal nucleus. *Front. Neural Circuits* 8:125. doi: 10.3389/fncir.2014.00125

Lütcke, H., Gerhard, F., Zenke, F., Gerstner, W., and Helmchen, F. (2013). Inference of neuronal network spike dynamics and topology from calcium imaging data. *Front. Neural Circuits* 7:201. doi: 10.3389/fncir.2013.00201

Marc, R. E., Anderson, J. R., Jones, B. W., Sigulinsky, C. L., and Lauritzen, J. S. (2014). The AII amacrine cell connectome: a dense network hub. *Front. Neural Circuits* 8:104. doi: 10.3389/fncir.2014.00104

Mazurek, M., Kager, M., and Van Hooser, S. D. (2014). Robust quantification of orientation selectivity and direction selectivity. *Front. Neural Circuits* 8:92. doi: 10.3389/fncir.2014.00092

Murphey, D. K., Herman, A. M., and Arenkiel, B. R. (2014). Dissecting inhibitory brain circuits with genetically-targeted technologies. *Front. Neural Circuits* 8:124. doi: 10.3389/fncir.2014.00124

Nagayama, S., Homma, R., and Imamura, F. (2014). Neuronal organization of olfactory bulb circuits. *Front. Neural Circuits* 8:98. doi: 10.3389/fncir.2014.00098

O'Rourke, N. A., Weiler, N. C., Micheva, K. D., and Smith, S. J. (2012). Deep molecular diversity of mammalian synapses: why it matters and how to measure it. *Nat. Rev. Neurosci.* 13, 365–379. doi: 10.1038/nrn3170

Pecho-Vrieseling, E., Sigrist, M., Yoshida, Y., Jessell, T. M., and Arber, S. (2009). Specificity of sensory-motor connections encoded by Sema3e-Plxnd1 recognition. *Nature* 459, 842–846. doi: 10.1038/nature08000

Rothermel, M., and Wachowiak, M. (2014). Functional imaging of cortical feedback projections to the olfactory bulb. *Front. Neural Circuits* 8:73. doi: 10.3389/fncir.2014.00073

Serrano-Velez, J. L., Rodriguez-Alvarado, M., Torres-Vazquez, I. I., Fraser, S. E., Yasumura, T., Vanderpool, K. G., et al. (2014). Abundance of gap junctions at glutamatergic mixed synapses in adult Mosquitofish spinal cord neurons. *Front. Neural Circuits* 8:66. doi: 10.3389/fncir.2014.00066

Soiza-Reilly, M., and Commons, K. G. (2014). Unraveling the architecture of the dorsal raphe synaptic neuropil using high-resolution neuroanatomy. *Front. Neural Circuits* 8:105. doi: 10.3389/fncir.2014.00105

Sporns, O., Tononi, G., and Kötter, R. (2005). The human connectome: a structural description of the human brain. *PLoS Comput. Biol.* 1:e42. doi: 10.1371/journal.pcbi.0010042

Sürmeli, G., Akay, T., Ippolito, G. C., Tucker, P. W., and Jessell, T. M. (2011). Patterns of spinal sensory-motor connectivity prescribed by a dorsoventral positional template. *Cell* 147, 653–665. doi: 10.1016/j.cell.2011.10.012

White, J. J., and Sillitoe, R. V. (2013). Development of the cerebellum: from gene expression patterns to circuit maps. *Wiley Interdiscip. Rev. Dev. Biol.* 2, 149–164. doi: 10.1002/wdev.65

Conflict of Interest Statement: The authors declare that the research was conducted in the absence of any commercial or financial relationships that could be construed as a potential conflict of interest.

frontiers in
NEURAL CIRCUITS

ORIGINAL RESEARCH ARTICLE
published: 24 October 2014
doi: 10.3389/fncir.2014.00125

Connections between EM2-containing terminals and GABA/μ-opioid receptor co-expressing neurons in the rat spinal trigeminal caudal nucleus

Meng-Ying Li[1†], Zhen-Yu Wu[2†], Ya-Cheng Lu[2], Jun-Bin Yin[2], Jian Wang[2], Ting Zhang[2], Yu-Lin Dong[2]* and Feng Wang[1]*

[1] *Department of Nutrition and Food Hygiene, The Fourth Military Medical University, Xi'an, China*
[2] *Department of Anatomy, Histology and Embryology, K.K. Leung Brain Research Centre, The Fourth Military Medical University, Xi'an, China*

Edited by:
Benjamin R. Arenkiel, Baylor College of Medicine, USA

Reviewed by:
Andres Couve, University of Chile, Chile
Nicholas Justice, University of Texas at Houston, USA

***Correspondence:**
Yu-Lin Dong, Department of Anatomy, Histology and Embryology, K.K. Leung Brain Research Centre, The Fourth Military Medical University, No. 169, West Changle Road, Xi'an 710032, China
e-mail: donganat@fmmu.edu.cn;
Feng Wang, Department of Nutrition and Food Hygiene, The Fourth Military Medical University, No. 169, West Changle Road, Xi'an 710032, China
e-mail: wfeng@fmmu.edu.cn

† *These authors have contributed equally to this work.*

Endomorphin-2 (EM2) demonstrates a potent antinociceptive effect via the μ-opioid receptor (MOR). To provide morphological evidence for the pain control effect of EM2, the synaptic connections between EM2-immunoreactive (IR) axonal terminals and γ-amino butyric acid (GABA)/MOR co-expressing neurons in lamina II of the spinal trigeminal caudal nucleus (Vc) were investigated in the rat. Dense EM2-, MOR- and GABA-IR fibers and terminals were mainly observed in lamina II of the Vc. Within lamina II, GABA- and MOR-neuronal cell bodies were also encountered. The results of immunofluorescent histochemical triple-staining showed that approximately 14.2 or 18.9% of GABA-IR or MOR-IR neurons also showed MOR- or GABA-immunopositive staining in lamina II; approximately 45.2 and 36.1% of the GABA-IR and MOR-IR neurons, respectively, expressed FOS protein in their nuclei induced by injecting formalin into the left lower lip of the mouth. Most of the GABA/MOR, GABA/FOS, and MOR/FOS double-labeled neurons made close contacts with EM2-IR fibers and terminals. Immuno-electron microscopy confirmed that the EM2-IR terminals formed synapses with GABA-IR or MOR-IR dendritic processes and neuronal cell bodies in lamina II of the Vc. These results suggest that EM2 might participate in pain transmission and modulation by binding to MOR-IR and GABAergic inhibitory interneuron in lamina II of the Vc to exert inhibitory effect on the excitatory interneuron in lamina II and projection neurons in laminae I and III.

Keywords: endomorphin 2, γ-amino butyric acid, μ-opioid receptor, inhibitory interneuron, synapse, spinal trigeminal caudal nucleus

INTRODUCTION

The superficial laminae (lamina I and lamina II) of the spinal trigeminal caudal nucleus (Vc), which is morphologically and functionally identical to the superficial laminae of the spinal dorsal horn and also named medullary dorsal horn, play a critical role in the transmission and modulation of oro-facial nociceptive information conveyed via primary afferents in the trigeminal nerve (Dubner and Bennett, 1983; Todd, 2010; Wu et al., 2010). Primary afferent fibers either contact projection neurons in lamina I directly or indirectly via interneurons in lamina II, through which they affect the activity of the interneurons and projection neurons (Dubner and Bennett, 1983; Wang et al., 2000, 2001; Todd, 2010; Wu et al., 2010). It has been reported that approximately 30% of lamina II interneurons show γ-amino butyric acid (GABA)-immunoreactivity in the Vc or spinal dorsal horn and GABAergic interneurons could be activated to regulate the nociceptive information transmission in the superficial laminae of the Vc (Todd et al., 1994; Wang et al., 2000, 2001; Yasaka et al., 2010). The results of our previous investigations have demonstrated that inflammatory nociceptive stimulation induced by subcutaneous injection of formalin into the lip could activate GABAergic neurons within the Vc exhibiting by expression functional marker FOS protein in the nuclei of the related neurons (Wang et al., 2000). Moreover, substance P (SP)-containing primary afferent terminals make asymmetric synapses with GABAergic interneurons in lamina II of the Vc (Wang et al., 2000) and GABAergic terminals originating from lamina II interneurons form symmetric synapses with projection neurons in lamina I and lamina III (Wang et al., 2001). These results suggest that inhibitory interneuronsplay an important role in regulating the excitatory neuronal activities in the Vc or spinal dorsal horn by releasing GABA (Dubner and Bennett, 1983; Todd et al., 1994; Wang et al., 2000, 2001; Todd, 2010; Wu et al., 2010; Yasaka et al., 2010).

Previous investigations have also demonstrated that endomorphins (EMs; including EM1 and EM2) are the specific endogenous ligands with the highest affinity to the μ-opioid receptor (MOR) (Zadina et al., 1997), and EM1- and EM2-immunopositive neuronal cell bodies are principally located in the hypothalamus and solitary tract nucleus in the central nerve system (CNS) (Martin-Schild et al., 1999). It has been reported that EM2 is more effective and potent in suppressing nociceptive information transmission than EM1, including pain relief

in acute, inflammatory and neuropathic pain (Tseng, 2002). Administration or delivery of EM2, EM2 derivatives, EM2 analogues and EM2 gene recombination virus vectors have provided an analgesic effect in different pain models, which could be blocked by intrathecal delivery of the MOR antagonist, suggesting that EM2 might be used for the treatment of chronic pain (Przewlocka et al., 1999; Tseng, 2002; Fichna et al., 2013; Makuch et al., 2013; Varamini and Toth, 2013; Mizoguchi et al., 2014). EM2-immunoreactive (IR) fibers and terminals have been densely observed in the superficial laminae, particularly lamina II of the Vc (Martin-Schild et al., 1999). Most of the laminae are terminals of the primary afferent fibers originating from the EM2-containing neuronal cell bodies within the trigeminal ganglion (TG) (Zhu et al., 2011). Activities of the neurons in the superficial laminae are inhibited when EM2 was applied onto the spinal dorsal horn (Przewlocka et al., 1999; Tseng, 2002; Fichna et al., 2013; Makuch et al., 2013; Varamini and Toth, 2013; Mizoguchi et al., 2014). EM2-IR terminals have been found to make synaptic connections with the projection neurons in lamina I of the Vc (Aicher et al., 2003). Recently, it has been observed that EM2 and SP co-localized primary afferent terminals might regulate pain transmission in the spinal dorsal horn through co-releasing EM2 and SP to affect the activity of GABAergic interneurons in lamina II (Luo et al., 2014). There are MOR-IR neurons in lamina II of the Vc (Ding et al., 1996); however, morphological evidence to show that EM2 might modulate nociceptive information transmission through binding to MOR-expressing GABAergic interneuron in lamina II is still lacking. Based on these previous results, we proposed the hypothesis that EM2 might participate in oro-facial antinociception by releasing EM2 to act on GABA/MOR co-expression interneuron to regulate the activity of the projection neuron and interneuron, especially the excitatory interneuron, in lamina II of the Vc. To provide morphological evidence for the hypothesis, the connections between EM2-IR fibers and terminals and GABA/MOR co-localized neurons or nociceptive stimulation activated GABA- or MOR-IR neurons in lamina II of the Vc were investigated.

MATERIALS AND METHODS

ANIMALS

Twenty one adult male Wistar rats (weighing 250–300 g) were used in the present study. The experimental procedures in this study were carried out in accordance with the National Institutes of Health Guide for the Care and Use of Laboratory Animals (NIH Publication No. 80-23) revised 1996 and IASP's guidelines for pain research in conscious animals (Zimmermann, 1983) and were approved by The Committee of Animal Use for Research and Education in The Fourth Military Medical University (Xi'an, China). All efforts were made to minimize animal suffering as well as the number of animals used.

The rats were divided into 3 groups ($n = 6$ for group 1 and 3, $n = 9$ for group 2). Group 1 was used for mapping the distribution pattern of EM2-, GABA- and MOR-IR neuronal structures, co-localization of GABA- and MOR-IR neurons in lamina II neurons and the close contacts between EM2-IR fibers and terminals and GABA/MOR co-localized neurons. Group 2 was used for subcutaneous injection of 5% formalin solution (100 μl) into the left lower lip of the mouth 2 h before the perfusion (Wang et al., 2000) and the connections between EM2-IR fibers and terminals and GABA/FOS or MOR/FOS double-immunopositive neurons in lamina II of the Vc. Group 3 was used for electron-microscopic immunohistochemical double-staining to observe the synaptic connections between EM2-IR terminals and GABA- or MOR-IR neuronal cell bodies and dendritic processes.

IMMUNOHISTOCHEMISTRY AND IMMUNOFLUORESCENT HISTOCHEMISTRY

The rats from group 2 were anesthetized with diethyl ether inhalation and were then used for quick subcutaneous injection of 5% formalin solution (100 μl) into the left lower lip of the mouth (Wang et al., 2000). The same volume of saline was injected as control experiment. Two hours later, the rats from group 1 and group 2 were anesthetized with sodium pentobarbital (50 mg/kg) and then perfused transcardially with 100 ml of 0.9% saline, followed by 500 ml of 0.1 M phosphate buffer (PB, pH 7.4) containing 4% (w/v) paraformaldehyde and 0.2% (w/v) picric acid. The lower part of the brainstem, containing the medulla oblongata, were removed and postfixed in the same fixative for 4 h and then transferred to 30% sucrose in 0.1 M PB for cryoprotection at 4°C. The brainstem was transversely cut into 30 μm thick sections on a freezing microtome (Kryostat 1720; Leitz, Mannheim, Germany). The sections were divided into 6 serial sets and stored into 6 dishes containing 0.01 M phosphate-buffered saline (PBS, pH 7.4). Each dish contained a complete set of sections. Then, all sections were washed with 0.01 M PBS.

The immunohistochemical and immunofluorescent histochemical staining protocols used in the present study were the same as those in our previous study (Wang et al., 2000, 2001; Zhu et al., 2011; Kou et al., 2014; Luo et al., 2014); 4 sets of the sections from the first to fourth dishes from group 1 and one set of sections from the first dish from group 2 were incubated at room temperature sequentially with primary antibodies. All the antisera used in each group are shown in **Table 1**.

Briefly, the sections from group 1 were incubated with primary antibodies (1) rabbit anti-EM2 IgG (1:200, Abcam); (2) guinea pig anti-MOR IgG (1:500, Millipore); (3) mouse anti-GABA IgG (1:200, Sigma) and (4) the mixture of rabbit anti-EM2 IgG (1:200), guinea pig anti-MOR (1:500) and mouse anti-GABA (1:200) for 72 h in PBS containing 0.3% (v/v) Triton X-100, 0.25% (w/v) λ-carrageenan and 5% (v/v) donkey serum (PBS-XCD). Secondary antibodies included biotinylated donkey anti-rabbit IgG (1:500, Millipore), biotinylated donkey anti-guinea pig IgG (1:500, Millipore), biotinylated donkey anti-mouse IgG (1:500, Millipore) or a mixture of biotinylated donkey anti-rabbit IgG (1:500), Alexa Fluor 647-conjugated donkey anti-guinea pig IgG (1:500, Molecular Probes) and Alexa Fluor 488-conjugated donkey anti-mouse IgG (1:500, Molecular Probes) in PBS containing 0.3% (v/v) Triton X-100 for 4 h, followed by incubation with avidin-biotin-horseradish peroxides (HRP) complex or fluorophore-conjugated avidin, Alexa Fluor 594-conjugated avidin (1;1000, Molecular Probes), for 1 h. To demonstrate the HRP conjugation to the

Table 1 | Antisera used in each group.

Group	Purposes	Primary antisera	Secondary antisera	Horseradish peroxides (HRP)- or fluorophore-conjugated *avidin*
Immuno-fluorescence	EM2	Rabbit anti-EM2 IgG(1:200, Abcam)	Biotinylated donkey anti-rabbit IgG (1:500, Millipore)	ABC Elite kit (1:100, Vector Labs)
	MOR	Guinea pig anti-MOR IgG(1:500, Millipore)	Biotinylated donkey anti-guinea pig IgG (1:500, Millipore)	ABC Elite kit (1:100, Vector Labs)
	GABA	Mouse anti-GABA IgG (1:200, Sigma)	Biotinylated donkey anti-mouse IgG (1:500, Millipore)	ABC Elite kit (1:100, Vector Labs)
	EM2/MOR/GABA	Rabbit anti-EM2IgG(1:200, Abcam)	Biotinylated donkey anti-rabbit IgG (1:500, Millipore)	Alexa 594-labeled avidin (1:1000, Molecular Probes)
		Guinea pig anti-MOR IgG (1:500, Millipore)	Alexa 647 donkey anti- guinea pig IgG (1:500, Molecular Probes)	
		Mouse anti-GABA IgG (1:200, Sigma)	Alexa 488 donkey anti-mouse IgG (1:500, Molecular Probes)	
	EM2/MOR/FOS	Rabbit anti-EM2 IgG(1:200, Abcam)	Biotinylated donkey anti-rabbit IgG (1:500**,** Millipore)	Alexa 594-labeled avidin (1:1000, Molecular Probes)
		Guinea pig anti-MOR IgG(1:500, Millipore)	Alexa 488 donkey anti- guinea pig IgG (1:500, Molecular Probes)	
		Goat anti-FOS IgG (1:200,Abcam)	Alexa 647 donkey anti-goat IgG (1:500, Molecular Probes)	
	EM2/GABA/FOS	Rabbit anti-EM2 IgG(1:200, Abcam)	Biotinylated donkey anti-rabbit IgG (1:500**,** Millipore)	Alexa 594-labeled avidin (1:1000, Molecular Probes)
		Mouse anti-GABA IgG (1:200,Sigma)	Alexa 488 donkey anti- mouse IgG (1:500, Molecular Probes)	
		Goat anti-FOS IgG (1:200, Abcam)	Alexa 647 donkey anti-goat IgG (1:500, Molecular Probes)	
Electron-microscopy	EM2/GABA	Rabbit anti-EM2 IgG (1:100, Abcam)	Biotinylated anti-rabbit IgG (1:200, Millpore)	ABC Elite kit (1:100, Vector Labs)
		Mouse anti-GABA IgG(1:100, Sigma)	Goat anti-mouse IgG antibody conjugated to 1.4 nm gold particles (1:100 Nanoprobes)	
	EM2/MOR	Rabbit anti-EM2 IgG(1:100, Abcam)	Biotinylated anti-rabbit IgG (1:200, Millpore)	ABC Elite kit (1:100, Vector Labs)
		guinea pig anti-MOR IgG(1:300, Millipore)	Goat anti-guinea pig IgG antibody conjugated to 1.4 nm gold particles (1:100, Nanoprobes)	

avidin-biotin complex, the sections from the first to third dishes from group 1 were treated with 0.05 M of Tris-HCl buffer (pH 7.6) containing 0.04% diaminobenzidinetetrahydrochloride (DAB) (Dojin, Kumamoto, Japan) and 0.003% H_2O_2 for 30 min.

The sections from group 2 were incubated with a mixture of primary antibodies as (1) rabbit anti-EM2 IgG (1:200), guinea pig anti-MOR IgG (1:500) and goat anti-FOS IgG (1:200, Abcam); (2) rabbit anti-EM2 IgG (1:200), mouse anti-GABA IgG (1:200) and goat anti-FOS IgG (1:200) in PBS-XCD for 72 h. Secondary antibodies were a mixture of (1) biotinylated donkey anti-rabbit IgG (1:500), Alexa Fluor 488-conjugated donkey anti-guinea pig IgG (1:500), and Alexa Fluor 647-conjugated donkey anti-goat IgG (1:500, Millipore) or (2) biotinylated donkey anti-rabbit IgG (1:500), Alexa Fluor 488-conjugated donkey anti-mouse IgG (1:500, Molecular Probes) and Alexa Fluor 647-conjugated donkey anti-goat IgG (1:500) in PBS containing 0.3% (v/v) Triton X-100 for 4 h, followed by incubation with fluorophore-conjugated avidin, Alexa Fluor 594-conjugated avidin (1;1000), for 1 h.

The specificities of the staining were tested on the sections in the fifth to seventh dishes from both group 1 and group 2 by omitting the specific primary antibodies. Neither immunopositive product nor immunoreactive labeling was found on these sections. The sections in the eighth dish from group 1 and group 2 were used for Nissl's staining.

Both incubated sections and reacted or stained sections were mounted onto gelatin-coated glass slides, air-dryed, dehydrated, and coverslipped. The sections were observed under a common light microscope (AHBT3; Olympus, Tokyo, Japan) for the DBA reacted sections or under a confocal laser-scanning microscope (Fluoview 1000, Olympus) for the immunofluorescent histochemically stained sections. Under the confocal laser-scanning microscope, all the sections were observed with appropriate laser beams and filter sets for Alexa 488 (excitation, 490 nm, emission, 525 nm), Alexa 594 (excitation, 590 nm, emission,

617 nm) or Alexa 647 (excitation, 650 nm, emission, ≥650 nm). Digital images were captured using Fluoview software (version 1.6; Olympus).

In each rat, the numbers of immuno-stained neurons in the Vc were counted through five randomly selected sections from each set and the ratios of different types of neurons were calculated. A careful review of the thickness of the selected sections determined that the immunolabeling had penetrated the entire thickness of the sections and only the neuronal cell bodies with obvious light emission were counted. The light from some positive neurons might be too weak to detect; therefore, the numbers of MOR-IR neurons and/or GABA-IR neurons in **Tables 2–4** should be regarded as representing the minimum of the real positive neurons in the sections.

IMMUNO-ELECTRON MICROSCOPY

For the electron microscopic study, rats in group 3 were deeply anesthetized and perfused transcardially with 100 ml of 0.9% saline followed by 500 ml of 0.1 M PB containing 4% paraformaldehyde, 0.05% glutaraldehyde and 0.2% picric acid. The lower brainstems were removed and postfixed in the same fixative without glutaraldehyde for 4 h at 4°C. The brainstem was transversely cut into 50 μm thick sections on a vibratome (Microslicer DTK-100; Dosaka, Kyoto, Japan). The sections were divided into two sets and collected into two dishes. To enhance the penetration of antibody, the sections were freeze-thawed in liquid nitrogen after cryoprotection. Details of these immuno-electron microscopy procedures were described in our previous studies (Wang et al., 2000; Li et al., 2002; Yasaka et al., 2010; Luo et al., 2014). Briefly, the sections were incubated with 0.05 M Tris-buffered saline (TBS; pH 7.4) containing 20% normal goat serum for 1 h to block non-specific immunoreactivity, and then collected in two dishes. The sections in each dish were incubated for 24 h at 4°C with a mixture of primary antibodies as (1) rabbit anti-EM2 IgG (1;100, Abcam) and guinea pig anti-MOR IgG (1:300, Millipore) (set 1) and (2) rabbit anti-EM2 IgG (1:100, Abcam) and mouse anti-GABA IgG (1:100, sigma) (set 2) (**Table 1**), respectively in 50 mM TBS containing 2% (v/v) normal goat serum (TBS-NGS). Then, a mixture of biotinylated donkey anti-rabbit IgG (1:200, Millipore) and goat anti-mouse IgG or goat anti-guinea pig IgG conjugated with 1.4 nm gold particles for GABA (1;100, Nanoprobes) or MOR (1:100, Nanoprobes) (**Table 1**) were incubated in TBS-NGS overnight at room temperature. Subsequently, the sections were processed with the following steps: (1) postfixation with 1% glutaraldehyde in 0.1 mol/L PB for 10 min; (2) silver enhancement with HQ Silver Kit (Nanoprobes); (3) incubation with ABC kit (Vector); (4) reaction with DAB and H_2O_2; (5) osmification; (6) counterstaining with uranylacetate. Ultrathin sections at 70 nm thickness were cut from lamina II of the Vc, mounted on single-slot grids, and examined with an electron microscope (JEM1440, Tokyo, Japan).

Table 2 | Numbers of MOR-IR neuron, GABA-IR neuron and MOR/GABA co-expressing neuron.

Rat	MOR-IR neurons	GABA-IR neurons	MOR/GABA neurons	%[a]	%[b]
R1-1	767	978	134	17.5	13.7
R1-3	806	1203	157	19.5	13.1
R1-5	738	894	145	19.6	16.2
Total	2311	3075	436	18.9	14.2

[a] *The percentage of MOR/GABA double-labeled neurons to the total number of MOR-IR neurons;*

[b] *The percentage of MOR/GABA double-labeled neurons to the total number of GABA-IR neurons.*

RESULTS

In the Vc, dense EM2-, MOR- and GABA- IR short-filate-like fibers and terminals punctiform in shape were found to be concentrated in the superficial laminae (lamina I and lamina II), especially in lamina II of the Vc (**Figure 1**). In lamina III of the Vc, only sparsely distributed EM2-, MOR- and GABA-IR fibers and terminals were found (**Figure 1**). A few MOR- and GABA-IR neuronal cell bodies were also located in laminae I- III, especially in lamina II (**Figures 1B′,C′**), but none of EM2-IR neuronal cell bodies were seen in the Vc (**Figure 1A′**). In lamina I and lamina III only a small number of sparsely distributed MOR- and GABA-IR neurons were encountered. MOR- and GABA-IR neuronal cell bodies were spherical, ovoid, fusiform or triangular in shape, and the diameters of cell bodies of these neurons ranged from 15 to 30 μm (**Figures 1B′,C′**).

Table 3 | Numbers of MOR-IR neuron, GABA-IR neuron and FOS/MOR or FOS/GABA co-expressing neuron.

Rat	FOS-IR neurons	MOR-IR neurons	GABA-IR neurons	MOR/FOS neurons	GABA/FOS neurons	%[a]	%[b]	%[c]	%[d]	%[e]	%[f]
R2-1	1279	723	915	323	407	56.5	71.5	25.3	44.7	31.8	44.5
R2-3	1206	694	1045	381	476	57.5	86.7	31.6	54.9	39.5	45.6
R2-5	1178	706	962	308	438	59.9	81.7	26.1	43.6	37.2	45.5
Total	3663	2123	2922	1012	1321	58.0	79.8	27.6	47.7	36.1	45.2

[a] *The percentage of MOR-IR neurons to the total number of FOS-IR neurons;*

[b] *The percentage of GABA-IR neurons to the total number of FOS-IR neurons;*

[c] *The percentage of MOR/FOS co-expressing neurons to the total number of FOS-IR neurons;*

[d] *The percentage of MOR/FOS co-expressing neurons to the total number of MOR-IR neurons;*

[e] *The percentage of GABA/FOS co-expressing neurons to the total number of FOS-IR neurons;*

[f] *The percentage of GABA/FOS co-expressing neurons to the total number of GABA-IR neurons.*

Table 4 | Synaptic types between EM2-IR terminals and MOR-IR or GABA-IR sotamic profiles and dendritic processes.

	Symmetric synapses	Asymmetric synapses	Symmetric synapses	Asymmetric synapses	Symmetric synapses	Asymmetric synapses
	MOR-IR somatic profiles		MOR-IR dendritic processes		Total	
EM2-IR terminal	1 (0.7%)	12 (7.9%)	2 (1.3%)	138 (90.1%)	3 (2.0%)	150 (98.0%)
	GABA-IR somatic profiles		GABA-IR dendritic processes		Total	
EM2-IR terminal	0 (0%)	15 (8.3%)	1 (0.5%)	165 (91.2%)	1 (0.5%)	181 (99.5%)

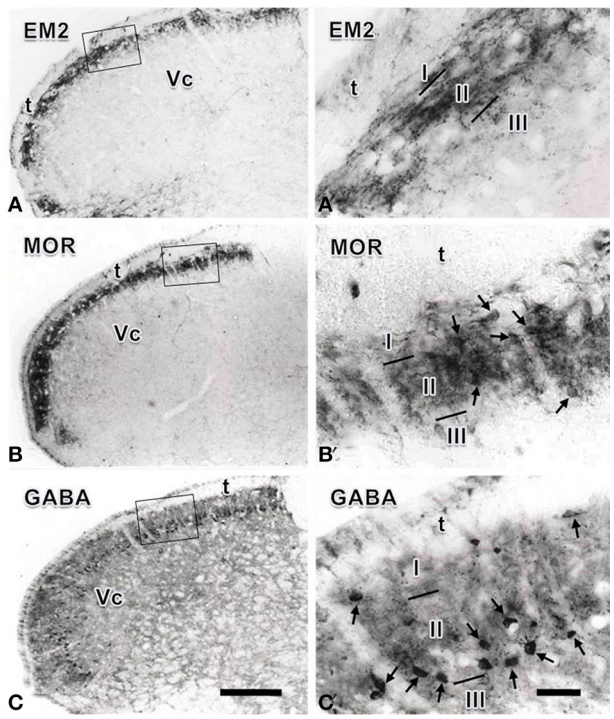

FIGURE 1 | Immunohistochemical staining showing the distributions of endomorphin-2 (EM2, A), μ-opioid receptor (MOR, B) and GABA (C) immunoreactive (IR) neuronal cell bodies and/or fibers and terminals in the spinal trigeminal caudal nucleus (Vc). The rectangle areas in **(A–C)** are enlarged in **(A′–C′)**, respectively. Arrows in **(B′,C′)** point to MOR- and GABA-IR neuronal cell bodies, respectively. I, lamina I; II, lamina II; III, lamina III; t, spinal trigeminal tract. Scale bars = 320 μm (in **C** and also for **A** and **B**) and 60 μm (in **C′** and also for **A′** and**B′**).

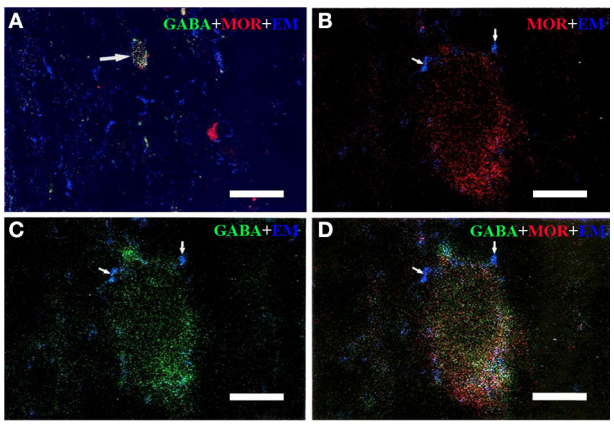

FIGURE 2 | Immunofluorescent histochemical triple-staining showing the connections between EM2-immunoreactive (IR) terminals (A–D, blue) and neuronal cell bodies exhibiting both MOR-IR (B, red) and GABA-IR (C, green) positive staining in lamina II of the Vc. The merged image in **(D)** reveals close contacts between EM2-IR axon terminals and MOR/GABA co-localized neuronal cell bodies (yellow). The arrow in **(A)** showed a MOR/GABA co-localized neuron connecting with EM2-IR axonal terminals. The arrows in **(B–D)** showed connections between EM2-IR axonal terminals and MOR or GABA-IR neuronal cell body. Scale bars = 45 μm **(A)**, 6 μm (in **B–D**).

Triple-immunofluorescent histochemical staining revealed that a small number of neurons contained both MOR- and GABA-immunopositive reaction products. Quantitative analysis showed that approximately 18.9% of MOR-IR neuronal cell bodies contained both MOR- and GABA-immunoreactivity and approximately 14.2% of GABA-IR neuronal cell bodies were immunoreactive for both MOR and GABA (**Table 2**). MOR/GABA co-localized neuronal cell bodies share the same morphological features of the MOR-IR or GABA-IR neurons. Then, we observed that some of these MOR- and GABA-IR co-localized neuronal cell bodies and their processes were in close contacted with EM2-IR fibers and terminals in the Vc (**Figure 2**, Supplementary Figure 1). In the formalin lip injected rats, triple-immunofluorescent histochemical staining also revealed that approximately 58% of the MOR-IR neurons or 79.8% of the GABA-IR neurons expressed FOS protein principally in lamina II of the Vc (**Table 3**); 27.6% and 47.7% of the FOS-IR and MOR-IR neurons co-expressed MOR and FOS (**Table 3**); and 36.1 and 45.2% of the FOS-IR and GABA-IR neurons co-localized GABA and FOS (**Table 3**). EM2-IR fibers and terminals were also observed to be in close contacts with the MOR/FOS or GABA/FOS double-labeled neurons in the Vc (**Figure 3**). Only a few FOS immunoreactivities were observed in the Vc in saline injected group (Supplementary Figure 2).

To provide convincing morphological evidence for these connections observed under light microscopy, electron microscopy was performed subsequently to demonstrate the synaptic connections between the EM2-IR fibers and terminals and MOR-IR or GABA-IR neurons. Under the electron microscope, EM2-IR axonal terminals, usually filled with synaptic vesicles, were characterized by the presence of electron dense DAB reaction products adhering to the outer surface of cell organelles such as mitochondria and synaptic vesicles and the inner surface of the plasma membrane (**Figure 4**). MOR-immunoreactivity was

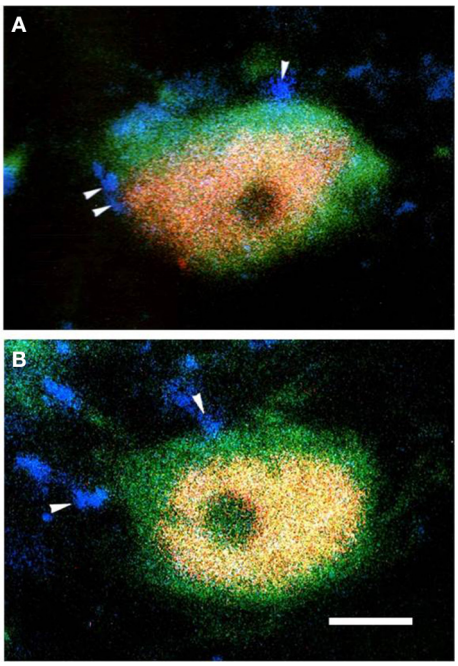

FIGURE 3 | The fluorescence photomicrographic images of triple-labeling showing the connections between EM2-IR terminals and GABA/FOS or MOR/FOS double-labeled neurons in lamina II of the Vc ipsilateral to the formalin injecting into the lower lip of the mouth. Some of the EM2-IR terminals (**A**,**B**; blue, arrowheads) were in close contacts with GABA (green) and FOS (red) double-labeled neurons **(A)** and with MOR (green) and FOS (red) double-labeled neurons **(B)**. Scale bar = 8 μm.

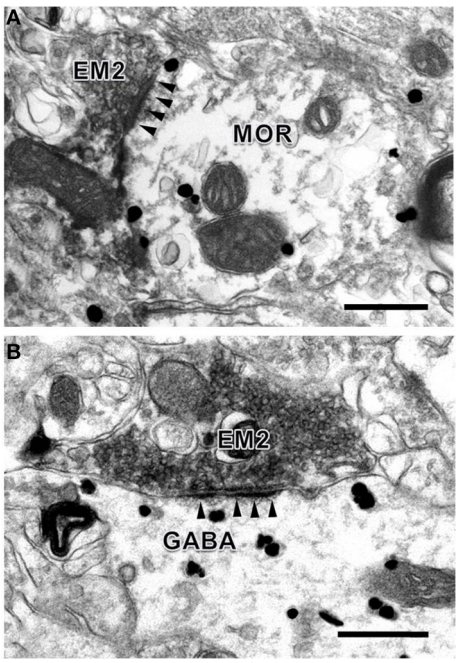

FIGURE 4 | Synaptic connections between EM2-IR axon terminals and MOR-IR and GABA-IR structures in lamina II of the Vc. EM2-IR pre-synaptic axon terminals **(A**,**B**; EM2; filled with DAB reaction products) made asymmetric synapses with a post-synaptic MOR-IR **(A)** or GABA-IR **(B)** dendritic process, both of which were labeled with immune-gold particles. Arrowheads indicate post-synaptic membranes. Scale bars = 300 nm **(A)**, 400 nm (in **B**).

determined by the presence of the immunogold-silver grains distributed in the cytoplasm of the neuronal cell bodies, dendrites, and axonal fibers and terminals of the MOR-IR neurons. These gold particles trended to be localized beneath the membrane of the neuronal cell bodies, dendrites, and axons (**Figure 4A**). GABA-IR staining was exhibited by the presence of the immunogold-silver particles localized homogenously in both cytoplasm of the neuronal cell bodies and their processes (**Figure 4B**) of the GABA-IR neurons. For the sections from the first dish, a total of 153 EM2-IR axon terminals were found to mainly make asymmetric axo-dendritic and axo-somatic synapses with MOR-IR dendritic processes (**Figure 4A**) and MOR-IR neuronal cell bodies (**Table 4**). For the sections from the second dish, 181 EM2-IR axon terminals were also observed to form asymmetric axo-dendritic and axo-somatic synapses with GABA-IR dendritic processes (**Figure 4B**) and GABA-IR somatic profiles (**Table 4**).

DISCUSSION

The superficial laminae (lamina I and lamina II) of the spinal trigeminal caudal nucleus (Vc, also named medullary dorsal horn) are critical for oro-facial nociceptive information transmission and regulation (Dubner and Bennett, 1983). There are many inhibitory interneurons located in lamina II (substantia gelatinosa) of the Vc and they are fundamental for nociceptive modulation (Dubner and Bennett, 1983; Todd et al., 1994; Wang et al., 2000, 2001; Todd, 2010; Wu et al., 2010; Yasaka et al., 2010). Therefore, in the present study, morphological methods were used to investigate the connections between the primary afferent EM2-containing fibers and terminals and MOR-expressing and GABA-containing inhibitory interneurons related to oro-facial nociceptive information transmission and/or modulation in the superficial laminae of the Vc. Our previous results have shown that SP released from the primary afferent fibers may activate GABAergic inhibitory neurons in lamina II (Wang et al., 2000). GABAergic inhibitory neurons may inhibit the activity of ascending projection neurons in lamina I of the Vc (Wang et al., 2001). These results suggest that GABAergic interneurons might play an important role in regulating the transmission of oro-facial nociceptive information to the medullary dorsal horn.

Here, we found that EM2-IR fibers and terminals make close contacts with the MOR/GABA co-localized neurons and GABAergic or MOR-IR neurons in the superficial laminae of the Vc, especially in lamina II were activated by peripheral noxious stimulation. Additionally, EM2-IR fibers and terminals were also observed to form asymmetric synapses with GABAergic neurons or MOR-IR neurons in the present study.

It has been demonstrated that EM2, a MOR agonist, is released from the presynaptic site, i.e., the primary afferent terminals coming from the primary sensory neurons in trigeminal ganglion (TG). The released EM2 might bind to the MOR autoreceptor

located on the primary afferent terminals, to further inhibit SP release attenuating the sensation of pain and alleviating neuropathic pain (Li et al., 1998; Greenwell et al., 2007; Luo et al., 2014). Therefore, the interaction between EM2 and SP may affect the modulation of nociceptive information transmitted from the peripheral to the CNS. Previous studies focused on the co-localization of EM2-containing primary afferents and presynaptic pain control mechanism of the EM2 (Li et al., 1998; Greenwell et al., 2007; Luo et al., 2014), but less on the postsynaptic mechanism, especially for the EM2-IR targeted interneurons in lamina II containing both MOR and inhibitory transmitters, such as GABA. GABA is believed to be involved in both pre-synaptic and post-synaptic inhibition in the superficial laminae of the spinal and medullary dorsal horns (Heinke et al., 2004). GABAergic inhibitory interneurons in the spinal and medullary dorsal horns can be activated by subcutaneous injection of formalin into the hind paw or lip of mouth in the rat, and these GABAergic neurons can also express FOS after noxious stimulation (Todd et al., 1994; Wang et al., 2000). The present results provide a morphological evidence for our hypothesized connections between direct connections between EM2-IR fibers and terminals and MOR/GABA co-localized neurons mainly in lamina II of the Vc. However, because of the limitation of methods, it is difficult to make triple-labeling for EM2, GABA, and MOR simultaneously on the same section under electron microscope. It is well worth observation of synaptic connection between EM2-IR axonal terminals and the GABA/MOR double labeling neuronal profiles after new pre-embedding method coming.

As mentioned above, these results suggest that there are potential modulatory interactions between EM2-IR primary afferent fibers and terminals and lamina II interneurons through both pre-synaptic and post-synaptic mechanisms, especially through MOR-expressing GABAergic inhibitory interneurons, in nociceptive information transmission and modulation in both spinal and medullar dorsal horns. The present results also indicate that connections between EM2-IR fibers and terminals and MOR/GABA co-localized neurons in the superficial laminae of the Vc might be very important for the regulation of the peripheral oro-faical nociceptive transmission.

AUTHOR CONTRIBUTIONS

Study concept and design: Yu-Lin Dong and Feng Wang. Light microscopic study: Meng-Ying Li and Zhen-Yu Wu. Electron microscopic study: Ya-Cheng Lu and Yu-Lin Dong. Data analysis: Jun-Bin Yin and Jian Wang. Technical support: Ting Zhang. Manuscript writing: Meng-Ying Li, Zhen-Yu Wu, Yu-Lin Dong, and Feng Wang.

ACKNOWLEDGMENTS

This work was supported by the grants from National Natural Science Foundation of China (Nos. 434119512, 81171050, and 81371239).

SUPPLEMENTARY MATERIAL

The Supplementary Material for this article can be found online at: http://www.frontiersin.org/journal/10.3389/fncir.2014.00125/abstract

REFERENCES

Aicher, S. A., Mitchell, J. L., Swanson, K. C., and Zadina, J. E. (2003). Endomorphin-2 axon terminals contact mu-opioid receptor-containing dendrites in trigeminal dorsal horn. *Brain Res.* 977, 190–198. doi: 10.1016/S0006-8993(03)02678-7

Ding, Y. Q., Kaneko, T., Nomura, S., and Mizuno, N. (1996). Immunohistochemical localization of mu-opioid receptors in the central nervous system of the rat. *J. Comp. Neurol.* 367, 375–402.

Dubner, R., and Bennett, G. J. (1983). Spinal and trigeminal mechanisms of nociception. *Annu. Rev. Neurosci.* 6, 381–418. doi: 10.1146/annurev.ne.06.030183.002121

Fichna, J., Mazur, M., Grzywacz, D., Kamysz, W., Perlikowska, R., Piekielna, J., et al. (2013). Novel glycosylated endomorphin-2 analog produces potent centrally-mediated antinociception in mice after peripheral administration. *Bioorg. Med. Chem. Lett.* 23, 6673–6676. doi: 10.1016/j.bmcl.2013.10.041

Greenwell, T. N., Martin-Schild, S., Inglis, F. M., and Zadina, J. E. (2007). Colocalization and shared distribution of endomorphins with substance P, calcitonin gene-related peptide, gamma-aminobutyric acid, and the mu opioid receptor. *J. Comp. Neurol.* 503, 319–333. doi: 10.1002/cne.21374

Heinke, B., Ruscheweyh, R., Forsthuber, L., Wunderbaldinger, G., and Sandkuhler, J. (2004). Physiological, neurochemical and morphological properties of a subgroup of GABAergic spinal lamina II neurones identified by expression of green fluorescent protein in mice. *J. Physiol.* 560, 249–266. doi: 10.1113/jphysiol.2004.070540

Kou, Z. Z., Li, C. Y., Hu, J. C., Yin, J. B., Zhang, D. L., Liao, Y. H., et al. (2014). Alterations in the neural circuits from peripheral afferents to the spinal cord: possible implications for diabetic polyneuropathy in streptozotocin-induced type 1 diabetic rats. *Front. Neural Circuits* 8:6. doi: 10.3389/fncir.2014.00006

Li, J. L., Ding, Y. Q., Li, Y. Q., Li, J. S., Nomura, S., Kaneko, T., et al. (1998). Immunocytochemical localization of mu-opioid receptor in primary afferent neurons containing substance P or calcitonin gene-related peptide. A light and electron microscope study in the rat. *Brain Res.* 794, 347–352. doi: 10.1016/S0006-8993(98)00332-1

Li, Y. Q., Tao, F. S., Okamoto, K., Nomura, S., Kaneko, T., and Mizuno, N. (2002). The supratrigeminal region of the rat sends GABA/glycine-cocontaining axon terminals to the motor trigeminal nucleus on the contralateral side. *Neurosci. Lett.* 330, 13–16. doi: 10.1016/S0304-3940(02)00711-5

Luo, D. S., Huang, J., Dong, Y. L., Wu, Z. Y., Wei, Y. Y., Lu, Y. C., et al. (2014). Connections between EM2- and SP-containing terminals and GABAergic neurons in the mouse spinal dorsal horn. *Neurol. Sci.* 35, 1421–1427. doi: 10.1007/s10072-014-1774-9

Makuch, W., Mika, J., Rojewska, E., Zychowska, M., and Przewlocka, B. (2013). Effects of selective and non-selective inhibitors of nitric oxide synthase on morphine- and endomorphin-1-induced analgesia in acute and neuropathic pain in rats. *Neuropharmacology* 75, 445–457. doi: 10.1016/j.neuropharm.2013.08.031

Martin-Schild, S., Gerall, A. A., Kastin, A. J., and Zadina, J. E. (1999). Differential distribution of endomorphin 1- and endomorphin 2-like immunoreactivities in the CNS of the rodent. *J. Comp. Neurol.* 405, 450–471.

Mizoguchi, H., Takagi, H., Watanabe, C., Yonezawa, A., Sato, T., Sakurada, T., et al. (2014). Involvement of multiple micro-opioid receptor subtypes on the presynaptic or postsynaptic inhibition of spinal pain transmission. *Peptides* 51, 15–25. doi: 10.1016/j.peptides.2013.10.012

Przewlocka, B., Mika, J., Labuz, D., Toth, G., and Przewlocki, R. (1999). Spinal analgesic action of endomorphins in acute, inflammatory and neuropathic pain in rats. *Eur. J. Pharmacol.* 367, 189–196. doi: 10.1016/S0014-2999(98)00956-X

Todd, A. J. (2010). Neuronal circuitry for pain processing in the dorsal horn. *Nat. Rev. Neurosci.* 11, 823–836. doi: 10.1038/nrn2947

Todd, A. J., Spike, R. C., Brodbelt, A. R., Price, R. F., and Shehab, S. A. (1994). Some inhibitory neurons in the spinal cord develop c-fos-immunoreactivity after noxious stimulation. *Neuroscience* 63, 805–816. doi: 10.1016/0306-4522(94)90525-8

Tseng, L. F. (2002). The antinociceptive properties of endomorphin-1 and endomorphin-2 in the mouse. *Jpn. J. Pharmacol.* 89, 216–220. doi: 10.1254/jjp.89.216

Varamini, P., and Toth, I. (2013). Lipid- and sugar-modified endomorphins: novel targets for the treatment of neuropathic pain. *Front. Pharmacol.* 4:155. doi: 10.3389/fphar.2013.00155

Wang, D., Li, Y. Q., Li, J. L., Kaneko, T., Nomura, S., and Mizuno, N. (2000). gamma-aminobutyric acid- and glycine-immunoreactive neurons postsynaptic to substance P-immunoreactive axon terminals in the superficial layers of the rat medullary dorsal horn. *Neurosci. Lett.* 288, 187–190. doi: 10.1016/S0304-3940(00)01226-X

Wang, D., Wu, J. H., Dong, Y. X., and Li, Y. Q. (2001). Synaptic connections between trigemino-parabrachial projection neurons and gamma-aminobutyric acid- and glycine-immunoreactive terminals in the rat. *Brain Res.* 921, 133–137. doi: 10.1016/S0006-8993(01)03109-2

Wu, S. X., Wang, W., Li, H., Wang, Y. Y., Feng, Y. P., and Li, Y. Q. (2010). The synaptic connectivity that underlies the noxious transmission and modulation within the superficial dorsal horn of the spinal cord. *Prog. Neurobiol.* 91, 38–54. doi: 10.1016/j.pneurobio.2010.01.005

Yasaka, T., Tiong, S. Y., Hughes, D. I., Riddell, J. S., and Todd, A. J. (2010). Populations of inhibitory and excitatory interneurons in lamina II of the adult rat spinal dorsal horn revealed by a combined electrophysiological and anatomical approach. *Pain* 151, 475–488. doi: 10.1016/j.pain.2010.08.008

Zadina, J. E., Hackler, L., Ge, L. J., and Kastin, A. J. (1997). A potent and selective endogenous agonist for the mu-opiate receptor. *Nature* 386, 499–502. doi: 10.1038/386499a0

Zhu, C., Hui, R., Chen, T., Zuo, Z. F., Wang, W., Gao, C. J., et al. (2011). Origins of endomorphin-2 immunopositive fibers and terminals in the rat medullary dorsal horn. *Brain Res.* 1410, 38–47. doi: 10.1016/j.brainres.2011.06.067

Zimmermann, M. (1983). Ethical guidelines for investigations of experimental pain in conscious animals. *Pain* 16, 109–110. doi: 10.1016/0304-3959(83)90201-4

Conflict of Interest Statement: The authors declare that the research was conducted in the absence of any commercial or financial relationships that could be construed as a potential conflict of interest.

Received: 25 June 2014; accepted: 29 September 2014; published online: 24 October 2014.

*Citation: Li M-Y, Wu Z-Y, Lu Y-C, Yin J-B, Wang J, Zhang T, Dong Y-L and Wang F (2014) Connections between EM2-containing terminals and GABA/**μ**-opioid receptor co-expressing neurons in the rat spinal trigeminal caudal nucleus. Front. Neural Circuits **8**:125. doi: 10.3389/fncir.2014.00125*

This article was submitted to the journal Frontiers in Neural Circuits.

frontiers in
NEURAL CIRCUITS

ORIGINAL RESEARCH ARTICLE
published: 26 June 2014
doi: 10.3389/fncir.2014.00066

Abundance of gap junctions at glutamatergic mixed synapses in adult Mosquitofish spinal cord neurons

Jose L. Serrano-Velez[1], Melanie Rodriguez-Alvarado[1], Irma I. Torres-Vazquez[1], Scott E. Fraser[2], Thomas Yasumura[3], Kimberly G. Vanderpool[3], John E. Rash[3,4] and Eduardo Rosa-Molinar[1,5]*

[1] *Biological Imaging Group, University of Puerto Rico, San Juan, PR, USA*
[2] *Molecular and Computational Biology Section, University of Southern California, Los Angeles, CA, USA*
[3] *Department of Biomedical Sciences, Colorado State University, Fort Collins, CO, USA*
[4] *Program in Molecular, Cellular and Integrative Neurosciences, Colorado State University, Fort Collins, CO, USA*
[5] *Institute of Neurobiology, School of Medicine, University of Puerto Rico, San Juan, PR, USA*

Edited by:
Benjamin R. Arenkiel, Baylor College of Medicine, USA

Reviewed by:
Audrey Mercer, University College London, UK
Brian Burrell, University of South Dakota, USA

****Correspondence:***
Eduardo Rosa-Molinar, Biological Imaging Group, University of Puerto Rico, P.O. Box 21809 UPR Station, San Juan, PR 00931-1809, USA
e-mail: ed@hpcf.upr.edu

"Dye-coupling", whole-mount immunohistochemistry for gap junction channel protein connexin 35 (Cx35), and freeze-fracture replica immunogold labeling (FRIL) reveal an abundance of electrical synapses/gap junctions at glutamatergic mixed synapses in the 14th spinal segment that innervates the adult male gonopodium of Western Mosquitofish, *Gambusia affinis* (Mosquitofish). To study gap junctions' role in fast motor behavior, we used a minimally-invasive neural-tract-tracing technique to introduce gap junction-permeant or -impermeant dyes into deep muscles controlling the gonopodium of the adult male Mosquitofish, a teleost fish that rapidly transfers (complete in <20 mS) spermatozeugmata into the female reproductive tract. Dye-coupling in the 14th spinal segment controlling the gonopodium reveals coupling between motor neurons and a commissural primary ascending interneuron (CoPA IN) and shows that the 14th segment has an extensive and elaborate dendritic arbor and more gap junctions than do other segments. Whole-mount immunohistochemistry for Cx35 results confirm dye-coupling and show it occurs via gap junctions. Finally, FRIL shows that gap junctions are at mixed synapses and reveals that >50 of the 62 gap junctions at mixed synapses are in the 14th spinal segment. Our results support and extend studies showing gap junctions at mixed synapses in spinal cord segments involved in control of genital reflexes in rodents, and they suggest a link between mixed synapses and fast motor behavior. The findings provide a basis for studies of specific roles of spinal neurons in the generation/regulation of sex-specific behavior and for studies of gap junctions' role in regulating fast motor behavior. Finally, the CoPA IN provides a novel candidate neuron for future studies of gap junctions and neural control of fast motor behaviors.

Keywords: connexin 35/36, connexins, dye-coupling, freeze-fracture replica immunogold labeling, gap junctions, mixed synapses, neurons, spinal cord

INTRODUCTION

Electrical synapses, hereafter, gap junctions, are abundant, are evidenced by widespread coupling at birth, and until the central nervous system (CNS) matures, play a role in shaping and patterning neuronal connectivity in the invertebrate[1] and vertebrate[2] CNS ([1]Furshpan and Potter, 1959; Bennett et al., 1963; Robertson et al., 1963; Furshpan, 1964; Sotelo and Korn, 1978; Fulton et al., 1980; Vaney, 1991; Walton and Navarrete, 1991; Dermietzel and Spray, 1993; Peinado et al., 1993a,b; Kalb, 1994; Kandler and Katz, 1995; Wolszon, 1995; Laird, 1996; Rash et al., 1996; Bennett, 1997, 2000; Dermietzel, 1998; Edwards et al., 1999; Personius et al., 2001; Cohen-Cory, 2002; Herberholz et al., 2002; Mentis et al., 2002; Lewis and Eisen, 2003; Pereda et al., 2003; Scheiffele, 2003; Bennett and Zukin, 2004; Connors and Long, 2004; Montoro and Yuste, 2004; Szabo et al., 2004; Fan et al., 2005; Marin-Burgin et al., 2005, 2006, 2008; Phelan, 2005; Waites et al., 2005, [2]Arumugam et al., 2005; Kamasawa et al., 2006; Chen et al., 2007; Chuang et al., 2007; McAllister, 2007; Norman and Maricq, 2007; Szabo and Zoran, 2007; Todd et al., 2010; Whelan, 2010; Hoge et al., 2011; Park et al., 2011; Hamzei-Sichani et al., 2012; Lynn et al., 2012; Sugimoto et al., 2013; Bautista and Nagy, 2014). As the CNS matures, gap junction uncoupling occurs as the initial

Abbreviations: AFB-594, Alexa Fluor®-594 Biocytin; Mini-Emerald, Dextran, Fluorescein and Biotin, 10,000 MW, Anionic, Lysine Fixable; MNs, motor neurons; CoPA IN, commissural primary ascending interneuron; CNS, central nervous system; Cx35/36, connexin 35/connexin 36; FRIL, freeze-fracture replica immunogold labeling; GFAP, glial fibrillary acid protein; IMP, intramembrane particle; LE, labeling efficiency; sCM, spinning-disk confocal microscopy; $LMC^{lateral}$, lateral lateral motor column; LMC^{medial}, medial lateral motor column; MLF, medial longitudinal fasciculus; MMC, medial motor column; DV, dorso-ventral; PBS, phosphate buffered saline; PBSS, phosphate buffered saline with saponin; RT, room temperature.

electrical synapses switch to chemical synapses and the former concomitantly decrease in number in the adult.

Axo-axonal or dendrodendritic gap junctions are probably best known for coupling parvalbumin-containing γ-aminobutyric acid (GABA)ergic interneurons (Ins)to facilitate the synchronization of rhythmic oscillatory activity for neuronal communication in the adult neocortex (Galarreta and Hestrin, 1999, 2001a,b; Gibson et al., 1999; Fukuda and Kosaka, 2000, 2003; Bartos et al., 2002; Muller et al., 2005, 2006). Gap junction coupling has been identified in numerous neural microcircuits and has been linked to motor behavior; however, the extent to which gap junctions are linked to fast motor behavior has not been fully explored (Saint-Amant and Drapeau, 2000, 2001; Tresch and Kiehn, 2000; Bonnot et al., 2002; Drapeau et al., 2002; Kiehn and Tresch, 2002; Hervé et al., 2004; Rash et al., 2004, 2013; Söhl et al., 2005; Goodenough and Paul, 2009; Vervaeke et al., 2010; Pereda et al., 2013).

To assist in understanding gap junctions' role in fast motor behavior, we used a minimally-invasive neural-tract-tracing/labeling technique to introduce either gap junction-permeant or -impermeant dyes into deep muscles controlling the gonopodium (a sexually dimorphic sperm transferring organ) of a "reference species", the adult male Western Mosquitofish, *Gambusia affinis* (Mosquitofish) a small, sexually dimorphic teleost fish whose radical remodeling and shifting of the axial and appendicular musculoskeletal support facilitates an extremely rapid movement of the gonopodium to transfer encapsulated sperm bundles, spermatozeugmata, into the adult female reproductive tract (Rosa-Molinar et al., 1994, 1996, 1998; Rosa-Molinar, 2005; Rivera-Rivera et al., 2010).

To transfer spermatozeugmata, the male Mosquitofish body bends into an "S-shaped fast-start" curvature defined as "torque" (**Figure 1**); simultaneously the gonopodium makes an extremely rapid directional movement defined as "thrust" (**Figure 1**; Weihs, 1973; Webb, 1976; Harper and Blake, 1990, 1991; Johnston et al., 1995; Rosa-Molinar et al., 1996; Domenici and Blake, 1997; Spierts and Leeuwen, 1999; Hale, 2002; Rosa-Molinar, 2005; Rivera-Rivera et al., 2010). The speed of the "torque/thrust" maneuver (complete in <20 mS), particularly of the "thrust" component, suggests that electrical and not chemical synapses are involved in controlling the finer aspects of Mosquitofish rapid motor behavior.

A simple dye-coupling assay combined with spinning disk confocal microscopy shows spinal motor neurons are dye-coupled to

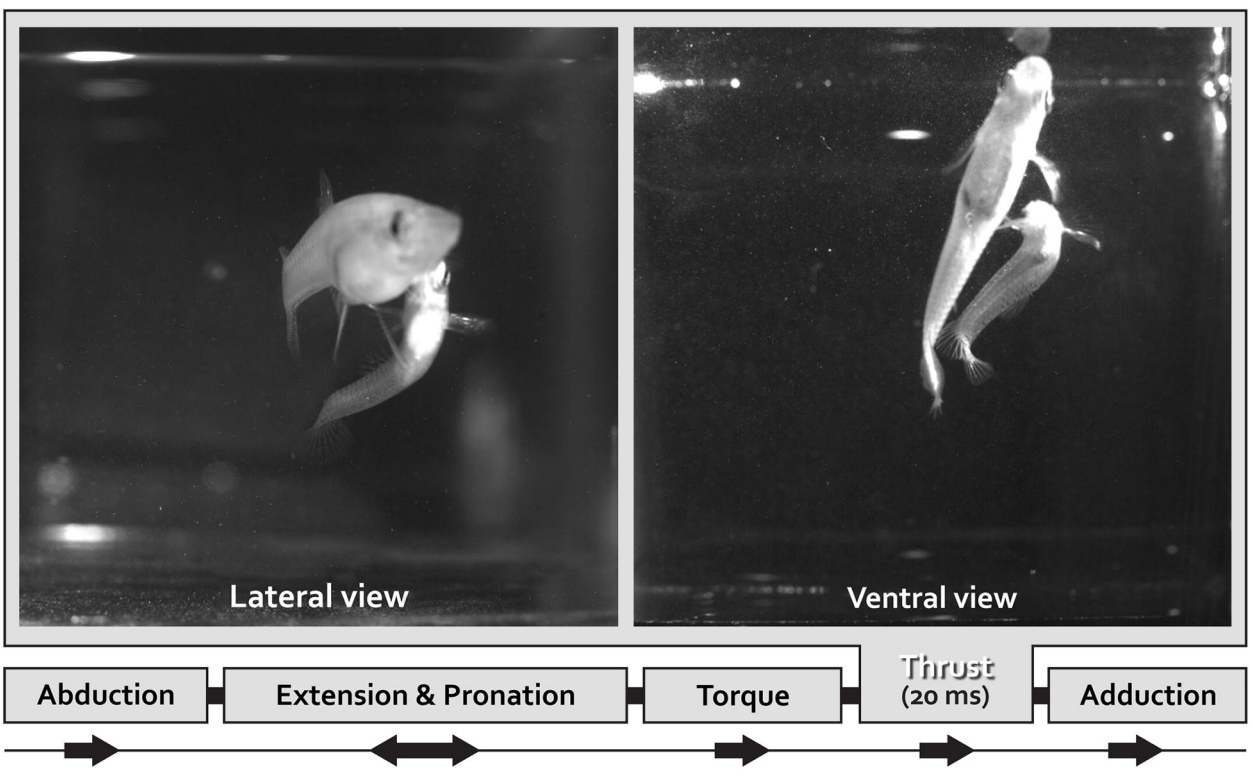

FIGURE 1 | One lateral and one ventral view of coital behavioral sequences filmed using high speed video at 500●frames●s–1.frames for a male Mosquitofish show the rapid movement portion of the circumduction of the gonopodium. With the gonopodium abducted, the male approaches the female from behind and directly underneath her and then adducts the gonopodium. Just prior to circumducting, the gonopodium is extended and pronated to a point that is nearly parallel with the body. To transfer spermatozeugmata, the male Mosquitofish bends his body into an S-shape-type fast-start-like movement (see lateral and ventral view) during the torque-thrust motion of the circumduction of the gonopodium. The sequence ends with the gonopodium adducted. We analyzed the speed of the circumduction of the gonopodium (the specific movements were: abduction, extension and pronation, torque, thrust, and adduction), specifically the fastest portion of the sequence, the "thrust" movement (20 ms).

interneurons and reveals their unique arborization patterns and morphologies. Whole-mount immunohistochemistry combined with spinning disk confocal microscopy shows the dye-coupling to be via Cx35/36 puncta (i.e., gap junctions). Freeze-facture replica immunogold labeling (FRIL) confirms the immunohistochemistry results and reveals that the Cx35/36 puncta are, in fact, gap junctions at mixed synapses. Our results demonstrate the occurrence and abundance of axo-dendritic gap junctions at glutamatergic synapses between dye-coupled spinal motor neurons and interneurons in the adult Mosquitofish, particularly in a spinal region controlling an innate fast coital behavior of the adult male. The fundamental data and insights reported in this paper provide a basis for on-going work to unambiguously determine the connexin composition in apposed axo-dendritic gap junctions' hemiplaques at glutamatergic synapses and to differentially map connexin distribution within the arbors of dye-coupled spinal motor neurons and interneurons in the adult Mosquitofish. The results also move us closer to attaining a clear understanding of the fundamental role of gap junctions in sculpting complex arborization patterns, morphologies, and synaptic connectivity of neurons during development and maturation of the CNS.

MATERIALS AND METHODS

Eighty wild-type adult (female n = 40; male n = 40) Western Mosquitofish, *Gambusia affinis* (hereafter Mosquitofish) were used. All experimental procedures and care were approved and conducted according to Principles of Laboratory Animal Care (NIH publication No. 86–23, Rev. 1985 (Rosario-Ortiz et al., 2008)) and the University of Puerto Rico-Rio Piedras Institutional Animal Care and Use Committee guidelines. All fish were collected and maintained under permits issued by the Puerto Rico Department of Natural Resources.

DYE-COUPLING ASSAY

The 80 adult Mosquitofish were anesthetized by immersion in pasteurized tank water plus dilute benzocaine (1:2000). Filter paper fibers saturated with a gap junction-permeant dye (0.32 kDa Alexa Flour®-594 Biocytin; hereafter AFB-594) or with a mixture of a gap junction-permeant dye, 0.32 kDa AFB-594 and a gap junction-nonpermeant dye (10 kDa Dextran, Fluorescein and Biotin, Anionic, Lysine Fixable; hereafter Mini-Emerald) were surgically implanted directly into nerves innervating the deep muscles (*musculus erector analis major*, *musculus erector analis*, and *musculus depressor analis*) of the adult male gonopodium, the sexually dimorphic genitalia, and into the deep muscles of the adult female anal fin; Mosquitofish were revived and the dye was allowed to transport 6.0 h, which is sufficient to obtain Golgi-like filling of spinal motor neurons (MNs) and INs. Mosquitofish were euthanized by immersion in pasteurized tank water containing benzocaine (1:4000) and intracardially perfused with teleost buffer pH 7.4, followed with 2.0% formaldehyde made from an 8% aqueous depolymerized paraformaldehyde (PFA) diluted in teleost buffer pH 7.4. The spinal cord associated with vertebral segments 7–17 was removed, dissected-free, and post-fixed overnight with 2% PFA in teleost buffer pH 7.4. Spinal cords were covered with mounting medium (Vectashield® Vector Laboratories, Burlingame, CA) and cover-slipped. Spinal cord whole-mount preparations were viewed and digitally photographed using a Nikon CFI Super Fluor 20X objective (N.A. 0.50; W.D. 2.10) and a Nikon CFI Plan Fluor 60X 0.11–0.23 correction collar spring load objective (N.A. 0.85; W.D. 0.30) in a Nikon Eclipse 800 epi-fluorescence microscope with the appropriate single pass epi-fluorescence filters and a fluorescence illumination system (XCite™120) to attain optimal fluorescence detection efficiency. High-resolution images taken using a Qimaging Retiga Exi 12-bit CCD camera with a HRF50L1 High Resolution 0.5x coupler captured large areas and neurocytological details of MNs and interneurons (INs), specifically, commissural primary ascending interneurons (CoPA INs). The Nikon E800's peripheral components were controlled by NIS Elements Advance Research software. Spinal cord whole-mount preparations were also viewed with a Nikon C1 Laser Scanning Confocal Microscope (LSCM) using a Nikon CFI Super Fluor 20X objective (N.A. 0.50; W.D. 2.10) and a Nikon CFI-PLAN APO 60X objective with correction collar and spring load (N.A. 0.85; W.D. 0.30). The light path consisted of 543 nm excitation, with collection using a long pass 560 nm filter or a 633 nm excitation, with collection using a long pass 650 nm filter. A PerkinElmer UltraView™ Spinning Disk Confocal scan head mounted on a Zeiss Axiovert Microscope was also used to view spinal cord whole-mount preparations.

A simple dye-coupling assay was used to validate the gap junctional dye-coupling reported in this paper. In 100% of adult male and female Mosquitofish, retrograde labeling using either a low-molecular gap junction-permeant dye, 0.32 kDa AFB-594 (red fluorescence channel only; **Figure 2A**), a high-molecular weight gap junction-nonpermeant dye, 10 kDa Mini-Emerald (green fluorescence channel only; **Figure 2B**), or a mixture of a low-molecular gap junction-permeant dye, 0.32 kDa AFB-594 (red and green fluorescence channel overlay; **Figure 2C**), and a high-molecular weight gap junction-nonpermeant dye, 10 kDa Mini-Emerald (red and green fluorescence channel overlay; **Figure 2C**), revealed "dye-coupling" (red fluorescence in coupled spinal neurons; **Figure 2C**), defined as the movement of a gap junction-permeant dye (i.e., 0.32 kDa AFB-594 [red, **Figure 2C**]) from spinal neuron to spinal neuron.

It is important to note that the overlay channel seen in **Figure 2C** differs from the co-localization channel seen in **Figure 2D**. The overlay channel seen in **Figure 2C** shows all of the pixel information within a selected region of interest (ROI), including pixel information that appears in the same spatial location within the retrogradely-filled spinal neurons. The co-localization channel seen in **Figure 2D** shows only pixel information that appears in the same spatial location within the retrogradely-filled spinal neurons that can be seen in both the green and red fluorescence channels as seen in **Figures 2B,C**, respectively. We set the lower threshold limit to 900 and set the upper threshold limit based on the highest intensity level of pixels within the soma of the MN's in a ROI. Note that this threshold was applied equally to the red and green fluorescence channels for all of the images used in our co-localization analysis. Note, too, that the excitation and emission spectra (**Figure 2E**) were carefully selected to avoid cross-talk and bleed-through of the gap junction-permeant and gap junction-non-permeant dyes.

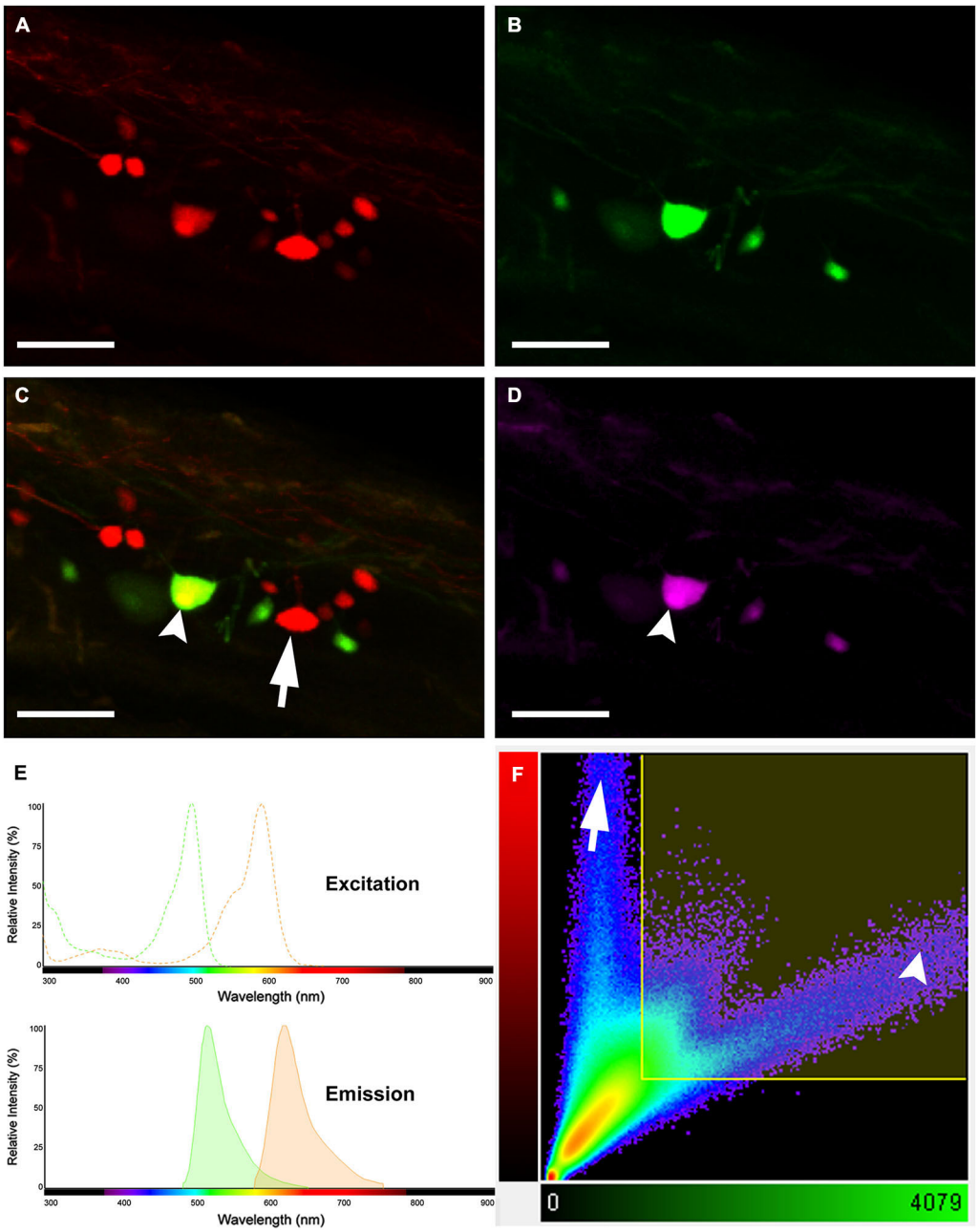

FIGURE 2 | Images showing double labeling AFB-594 (red) and Mini-Emerald (green) revealing dye-coupling between spinal motor neurons. AFB-594 **(A)** and Mini-Emerald **(B)** retrogradely labeling revealed motor neurons from the 14th ventral root. We merge red and green channels **(C)** to demonstrate that Mini-Emerald retrograde labeling was restrict to fewer cells, presumably to motor neurons projecting to the periphery. A three-dimensional threshold co-localization analysis confirmed, as seen in the co-localization channel **(D)**, that AFB-594 retrogradely labeling diffuse to neighbor cells (arrow) in contrast to Mini-Emerald (arrow head). **(E)** Excitation and Emission spectra were carefully selected to avoid cross-talk and bleed-through of the dyes. Finally, **F** shows the co-localization scatter plot, the selected region was thresholded based on the average intensity of the somas (900) on each channel. Pearson's coefficient in the co-localized volume for this analysis was 0.5172. Calibration bar equals 50 μm.

The scatterplot (**Figure 2F**) reveals the intensity contribution of both the red fluorescence channel (vertical axis) and the green fluorescence channel (horizontal axis) in the pixel values of the analyzed images. Note that pure signal from each single channel tends to be close to the corresponding axis. In **Figure 2C**, the dye-coupled spinal neuron contained "pure signal" from the AFB-594 (red fluorescence channel) and is represented in the scatterplot by the pixels outside the threshold box and close to the vertical axis (see **Figure 2F**). In contrast, since the spinal neurons labeled with Mini-Emerald also are labeled with AFB-594, the scatterplot reveals the co-localized pixels corresponding to those spinal neurons distributed far from the horizontal axis (green

fluorescence channel), thus, confirming the positive correlation between the two dyes (see **Figure 2F**). We used the Pearson's correlation coefficient as a measure of the correlation of the intensity distribution between each channel. Pearson's correlation coefficient in the co-localized volume for this analysis was 0.5172.

WESTERN BLOTS

Western blots (WB) of tissue extracts from vertebrae 8–16 of intact adult Mosquitofish spinal cords, brains, and livers were used to detect female/male differences in gap junction protein expression. The spinal cords, brains, and livers of adult females (N = 28; groups n = 4) and males (N = 28, groups n = 4) were dissected out. Sample tissues were immediately frozen in dry ice and homogenized or were kept at −80°C until use. WB protocol was performed as previously described, with few minor modifications (Vega et al., 2005, 2008). Tissues were pooled, weighed, and homogenized in radioimmunoprecipitation (RIPA) buffer (1X) [Cell Signaling Technology, Beverly, MA, USA] containing 1% protease inhibitor cocktail (PIC; Sigma Aldrich, St. Louis, MO) and 1 mM phenylmethylsulfonyl fluoride (PMSF; Sigma Aldrich, St. Louis, MO). Insoluble materials were removed by centrifugation at 14,000 rpm for 5 min at 4°C. The Bradford assay (BioRad, Hercules, CA, USA) was used to estimate the approximate protein concentration of the supernatants by detecting change in absorbance using a spectrophotometer (DU730 Beckman Coulter, Brea, CA, USA). Then, samples were diluted in loading buffer (60 mM Tris–HCl [pH 6.8], 5% 2-metacaptoethanol, 2% sodium dodecyl sulfate (SDS), 10% glycerol, 0.025% Bromophenol Blue) in the appropriate volume to load 40 μg of protein per well. The supernatants, loading control, and the molecular weight marker (Precision Plus Protein Standards, Bio-Rad, Hercules, CA, USA) were electrophoresed on SDS-polyacrylamide gel (SDS-PAGE 12%). For immunoblotting, the separated proteins were transferred onto pure nitrocellulose membrane (0.45 μm, Bio-Rad, Hercules, CA, USA) for 1 hr at 4°C at a constant voltage of 100 V. Membranes were then stained with Ponceau S to corroborate transfer of proteins; then they were blocked with 5% skim milk in tris (hydroxymethyl) aminomethane [Tris] Buffered Saline with Tween® 20 (polyoxyethylene sorbitane monolaureate) [TBST] Buffer (1xTBS: 25 mM Tris Base, 150 mM NaCl, 30 mM KCl; and 0.1% Tween-20; hereafter, blocking buffer) for 1 hr. Following the blocking step, membranes were incubated overnight at 4°C with either a mouse anti-Connexin (Cx)35/36 monoclonal antibody; clone: 9D7.2 (1:250 [Cat. # MAB3043, Chemicon]; EMD Millipore, Billerica, MA, USA) or a mouse anti-Cx35/36 monoclonal antibody, clone 8F6.2 (1:250; Cat. # MAB3045, Chemicon; EMD Millipore, Billerica, MA, USA) diluted in blocking buffer. Membranes were washed several times to remove unbound Cx35/36 antibody and incubated with Goat anti-Mouse Poly-horseradish peroxidase (HRP; 1:2000; Cat. # 2230, Thermo Fisher Scientific, Suwanee, GA, USA) for 1 hr at room temperature (RT). The recognized immunoreactive bands were detected using enhanced chemiluminescence reactions according to manufacturer's instructions (SuperSignal West Femto Maximum Sensitive Substrate [Cat.# 34095]; or SuperSignal West Dura Extended Duration Substrate [Cat. # 34075] Thermo Fisher Scientific, Suwanee, GA, USA). Then, the membranes were exposed in the ChemiDoc™ XRS+ System with Image Lab™ software (Bio-Rad, Hercules, CA, USA). For spinal cord and liver samples, membranes were stripped and reprobed for loading with anti-glyceraldehyde 3-phosphate dehydrogenase (GAPDH)-HRP conjugated (1:1000; Cat. # ab105428, Abcam, Cambridge, MA, USA). For brain samples, monoclonal anti-acetylated tubulin (1:1000; Cat. # T6793, Sigma Aldrich, St. Louis, MO, USA) was used. Then, membranes were visualized as described above. Optical density (OD) was expressed as a ratio of Cx35/36 and GAPDH or acetylated α-tubulin (Loading Control proteins [LC]) by using a densitometer and the Image Lab™ software (Bio-Rad, Hercules, CA, USA). Statistical analysis was performed with Prism 6.0 software (GraphPad Software, Inc., San Diego, CA, USA) and Office Excel 2007 (Microsoft Redmond, WA, USA). Results are reported as mean ± SEM; all the p-values were calculated by Student's t-test (* $p < 0.05$). Western blots (**Figures 3A,C**) and band density (**Figures 3B,D**) of the mouse anti-Cx35/36 monoclonal antibodies (MAB3045 and MAB3043) show that both antibodies detect differences in Cx35/36 expression (see **Figures 3A–D**). Note that only mouse anti-Cx35/36 monoclonal antibody (MAB3043) revealed significant sex differences in Cx35/36 expression in spinal cord tissue homogenates (see **Figures 3C,D**).

CONNEXIN 35/36 WHOLE-MOUNT IMMUNOHISTOCHEMISTRY

We used the primary anti-Cx35/36 antibody anti-Cx35 MAB3043 (Millipore, Billerica, MA). Spinal cord whole-mounts were rinsed with phosphate buffered saline (PBS) [3 × 10 min each at RT] to remove fixative and permeabilized in a solution of PBS and 0.1% Saponin (PBSS) for 4 h at RT. Spinal cord whole-mounts were incubated with blocking buffer (3% Normal Goat Serum/PBSS) for 1 h at RT then incubated overnight at 4°C with the anti-Cx35/36 MAB3043. Following several rinses at RT with PBS [6 × 10 min each], the spinal cord whole-mounts were incubated with secondary antibody (Alexa Fluor® 488 Goat anti-Mouse [Invitrogen, Carlsbad, CA]) for 3 h at RT. Unbound antibody was removed by rinsing tissues with PBS at RT [6 × 10 min each]. The spinal cord whole-mounts were incubated with blocking buffer for 30 min at RT and were incubated with second primary antibodies or nuclear stained and mounted, as described below. All second primary antibodies were diluted in blocking buffer and incubated overnight at 4°C. Then, the spinal cord whole-mounts were rinsed several times with PBS to remove unbound second primary antibody, and the appropriate secondary antibody was added. As controls for the whole-mount immunohistochemical procedures, eye (positive control) and liver tissue (negative control) were incubated in blocking solution without primary or secondary antibody (i.e., NGS/PBSS only) followed by the standard protocol to validate the specificity of the antibody. Spinal cord, eye, and liver whole-mounts were covered with mounting medium (Vectashield® Vector Laboratories, Burlingame, CA) and cover-slipped. Spinal cord, eye, and liver whole-mounts were then viewed and digitally photographed using a Nikon CFI Super Fluor 20X

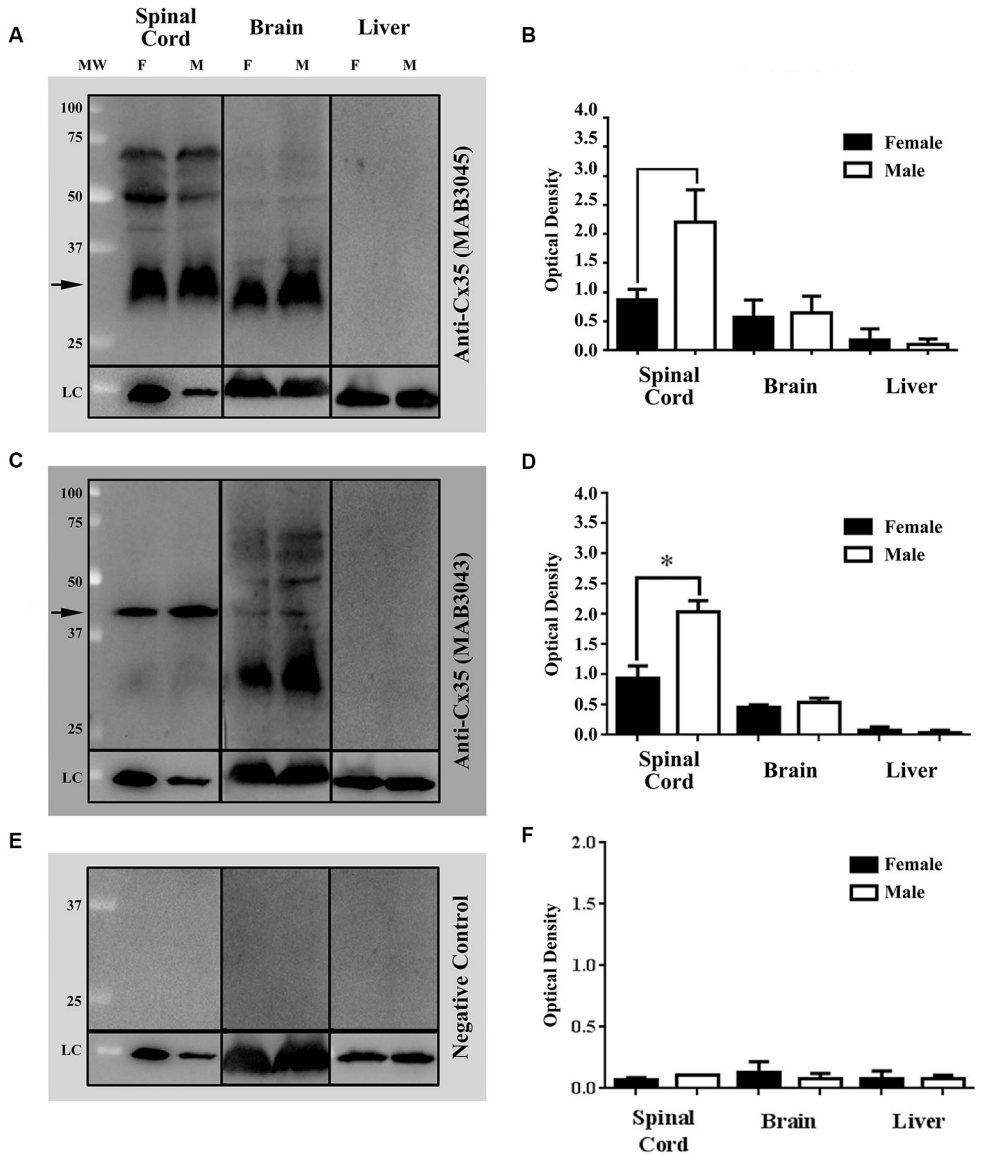

FIGURE 3 | Western blots (WB) and densitometric analysis demonstrate the specificity of two commercially available mouse anti-Cx35/36 monoclonal antibodies, MAB3045 [1:250] and (MAB3043 [1:250]) (See Figures 1A–D, respectively). Both mouse anti- Cx35/36 monoclonal antibodies recognized single bands in both male and female spinal cords at the expected molecular weight of 35 kDa, several bands in brain tissue homogenates, and no bands (as expected) in liver tissue homogenates (see **Figures 1A,C**). In male and female Mosquitofish, anti-Cx35/36 monoclonal antibodies recognized single bands in spinal cord tissue homogenates, several bands in brain tissues homogenates, and no bands in liver tissue homogenates (see **Figures 1A,C**). WB (**Figure 1C**) and band density analysis (**Figure 1D**) of mouse anti-Cx35/36 monoclonal antibody (MAB3043 [1:250]) revealed a sex difference in Cx35/36 expression in the spinal cord tissues homogenates. In one WB (see **Figure 1E**), mouse anti-Cx35/36 monoclonal antibodies were omitted and the WB was incubated with only the goat anti-mouse Poly-HRP antibody. The WB and densitometric analysis (see **Figures 1E,F**) of this negative control validates the results of the commercially available mouse anti-Cx35/36 monoclonal antibodies by demonstrating that the specific bands recognized are not associated with a non-specific binding from the secondary antibody. OD at each protein concentration was averaged (3 blots), showing differences determined by using each potential loading control (anti-GAPDH or anti-acetylated-tubulin). Statistical differences were determined with student *t*-test analysis (* $p < 0.05$). Each lane contains 40 μg of the extracted proteins from selected tissues homogenates of adult female and male Mosquitofish. The difference in the band intensity in the loading controls (LC) of the spinal cord tissue homogenate of male and female Mosquitofish could be interpreted as an issue in the total protein loaded in the WB (see **Figures 1A,C,E**). However, the densitometric analysis (see **Figures 1B,D,F**) demonstrates a difference between males and females.

objective (N.A. 0.50; W.D. 2.10) and a Nikon CFI Plan Fluor 60X 0.11–0.23 correction collar spring load objective (N.A. 0.85; W.D. 0.30) in a Nikon Eclipse 800 epi-fluorescence microscope with the appropriate single pass epi-fluorescence filters and a fluorescence illumination system (XCite™120) to attain optimal fluorescence detection efficiency. High resolution images

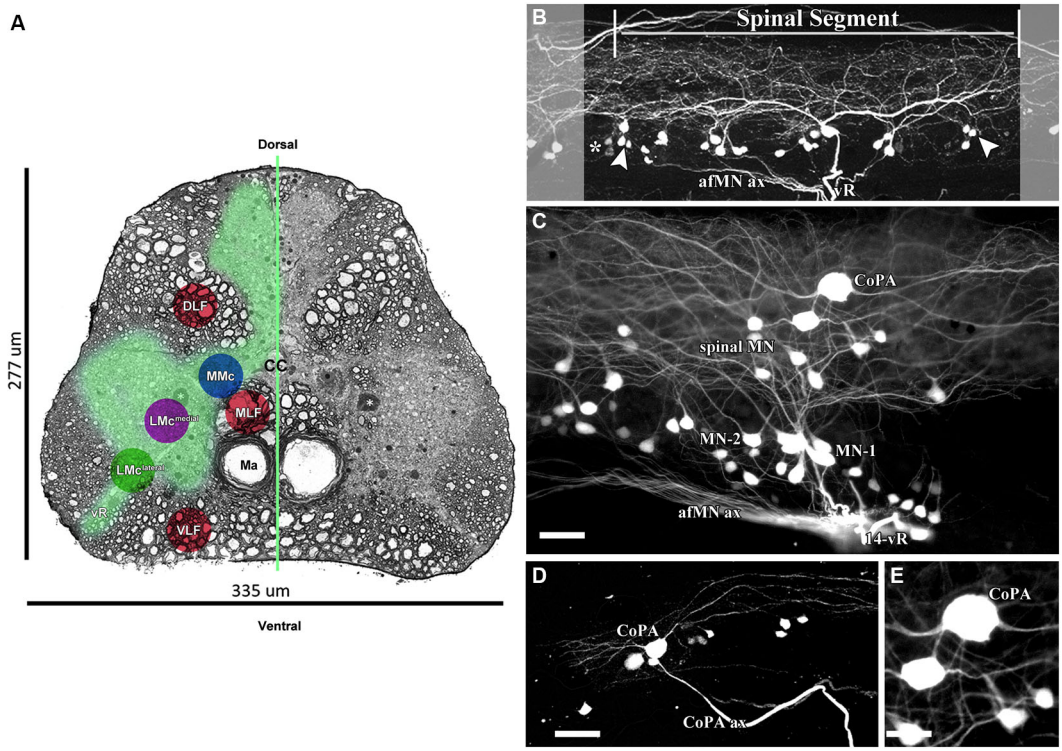

FIGURE 4 | 0.32 kDa AFB-594 revealing dye-coupling between spinal motor neurons (MN) and a CoPA interneuron (IN). (A) Serial block-face scanning electron micrograph showing a cross-sectional view of the spinal cord at the 14th ventral root. The AFB-594 motor neurons were visualized with Avidin-Biotin-Peroxidase/DAB reaction and are located in the Medial Lateral Motor Column (LMC^{medial}). **(B)** Extensive dye-coupling spanned across three (14th–16th) spinal segments. **(C)** 0.32 kDa AFB-594 retrograde labeling reveal presumptive dye-coupling between MNs and an IN of the commissural primary ascending (CoPA) class. **D** and **E** higher magnification views show CoPA INs are located dorsally to the MNs in the spinal cord, have a bi-polar T-shaped dendritic arbor with fine dendrites extending rostrally and caudally from the soma into the dorsal longitudinal fasciculus, and a long axon [CoPA ax] projects ventrally. Calibration bar equals **(C and D)** 50 μm and **(E)** 30 μm.

taken using a Qimaging Retiga Exi 12-bit CCD camera with a HRF50L1 High Resolution 0.5x coupler captured large areas and neurocytological details of MNs and interneurons INs, specifically, CoPA INs.

FRIL

The FRIL protocol has been described in detail (Rash and Yasumura, 1999; Pereda et al., 2003). The labeled spinal cord region associated with vertebral segments 7–17 (n = 12 females; n = 12 males; see labeling section above for details) was placed in a 3% low melting agarose, then transferred and embedded in 6% agarose, followed by refrigeration until fully gelled. Coronal sections (100 μm-thick) and longitudinal sections were cut using a Lancer Vibrotome 3000 (Technical Products, Inc., St. Louis, MO, USA) that maintained the tissue sections at 4°C. Spinal cord sections were infiltrated with 30% glycerol, mounted on aluminum planchettes, and frozen by contact with a liquid nitrogen-cooled metal mirror (i.e., Ultra-Freeze MF 7000; RMC Products, Tucson, AZ, USA). Frozen samples were fractured and replicated in a JEOL/RMC 9010 freeze-fracture device, then bonded to gold "index" grids by using 2.0% Lexan (GE Plastics, Pittsfield, MA, USA) dissolved in dichloroethane. After solvent evaporation at −25°C, the Lexan-stabilized samples were thawed, viewed, and digitally photographed using a 5X (0.15 N.A. Fluar) or 10X (0.5 N.A.; Plan Neofluar) objective in a Zeiss 510 Meta Laser Scanning Confocal Microscope (Carl Zeiss MicroImaging, Thornwood, NY, USA). Replicas were washed in 2.5% SDS detergent in 0.16% Tris-HCl buffer (pH 8.9) for 29 h at 48.5°C. After the initial wash in 2.5% SDS (4.0 h), the samples were digested 1.25 h in 4.0% collagenase D in 0.15 M Sorensen's phosphate buffer (pH 7.4), followed by an additional 18–24 h in SDS solution. The replicas were rinsed in "labeling-blocking buffer" (1mg/mL LBB), then incubated for 1–1.5 hrs at 22–24°C in 1:100 dilution of anti-Cx35/36 antibody in LBB, which consists of 1.5% fish gelatin plus 10% heat-inactivated goat serum in Sorensen's phosphate buffer (Dinchuk et al., 1987). The antibodies used for FRIL were polyclonal anti-Cx36 (36-4600) or monoclonal anti-Cx36 (39-4200 or 37-4600) from Invitrogen, polyclonal anti-Cx35 P-Ser276 from John O'Brien (Li et al., 2009), monoclonal anti-Glutamate Receptor NMDAR1 (556308, BD Biosciences), monoclonal anti-Glutamate Receptor 2 (GluR2, MAB397, Milllipore), and three anti-pannexin 1 antibodies (no specific labeling detected; therefore antibodies not separately listed). The replicas were labeled for 12–16 hrs with species-specific secondary antibodies (goat anti-rabbit or goat anti-mouse) coupled to 6-nm, 12-nm, or 18-nm gold nanoparticles

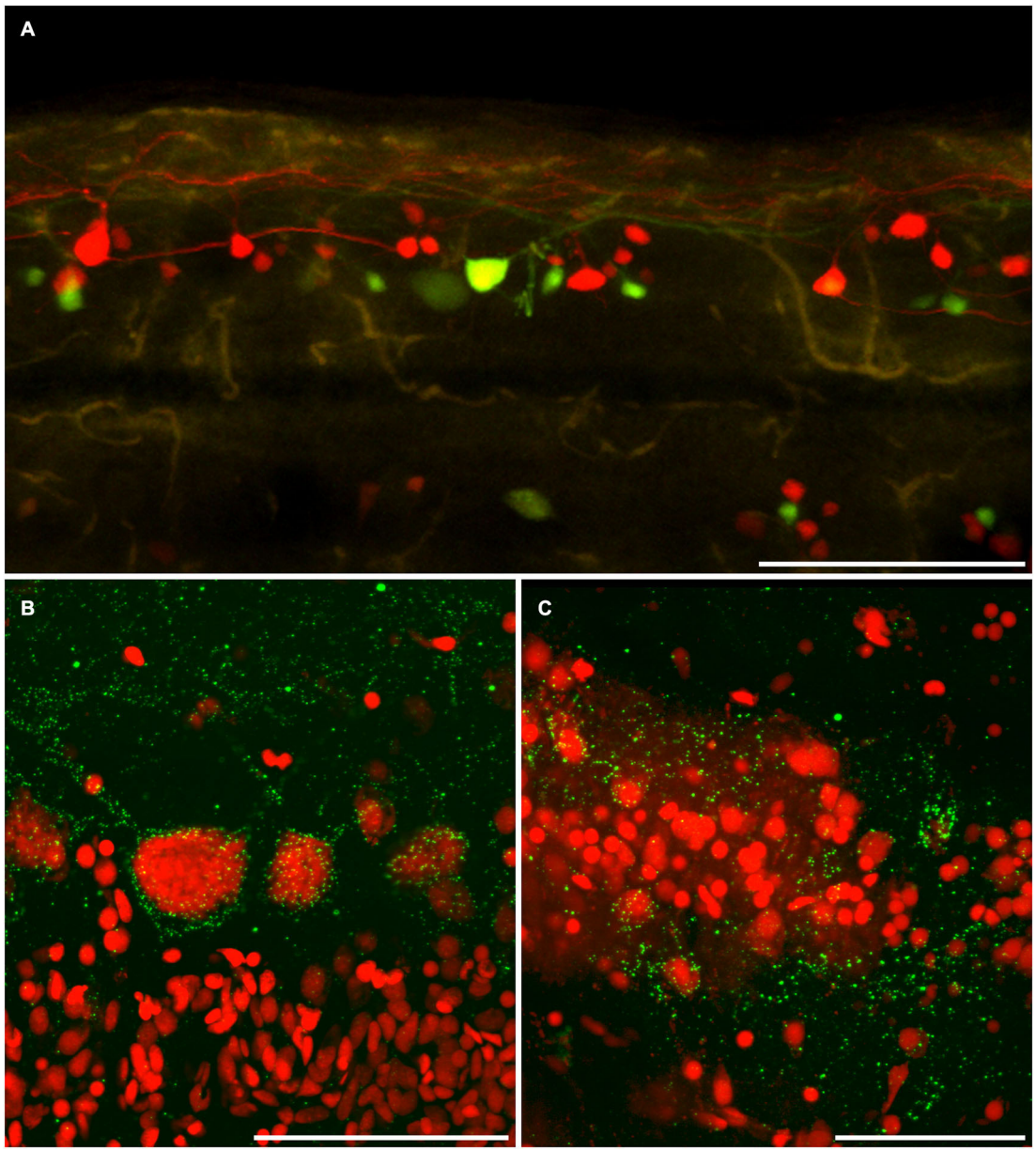

FIGURE 5 | Dye coupling is confirmed by anti-connexin 35/36 immuno-labeling. (A) AFB-594 and Mini-Emerald retrograde labeling revealed motor neurons from the 14th ventral root, and showed the extensive labeling of presumably coupled neurons. Whole-mount immunohistochemistry with anti-Cx35 antibody confirms the widespread presence of connexins (green puncta) in both male **(B)** and female **(C)** Mosquitofish. Calibration bars equals **(A)** 200 um, **(B,C)** 50 um.

(Jackson ImmunoResearch, Westgrove, PA, USA), or 30-nm gold nanoparticles (BBI). All FRIL replicas were viewed with a JEOL 2000 EX-II transmission electron microscope operated at 100 kV. Stereoscopic images (8° included angle) allowed assessment of the "sidedness" of the gold nanoparticles and the level of background immunogold labeling. Cell-specific ultrastructural markers were used to confirm cell identifications (Matsumoto et al., 1989; Rash et al., 1997), including GFAP filaments in astrocytes, spherical synaptic vesicles in axon terminals, and 10-nm E-face IMPs in glutamatergic "asymmetric" synapses *vs.* pleomorphic synaptic vesicles and 9-nm P-face IMPs in GABAergic "symmetric" synapses (Harris and Landis, 1986; DeFelipe et al., 1988; Peters et al., 1991), and labeling for NMDA and AMPA receptors in glutamatergic mixed synapses (Rash et al., 2005; also see DeFelipe et al., 1988). FRIL images were correlated with confocal microscopic images that had been obtained before SDS washing to determine specific locations of Cx35/36 gap junction puncta.

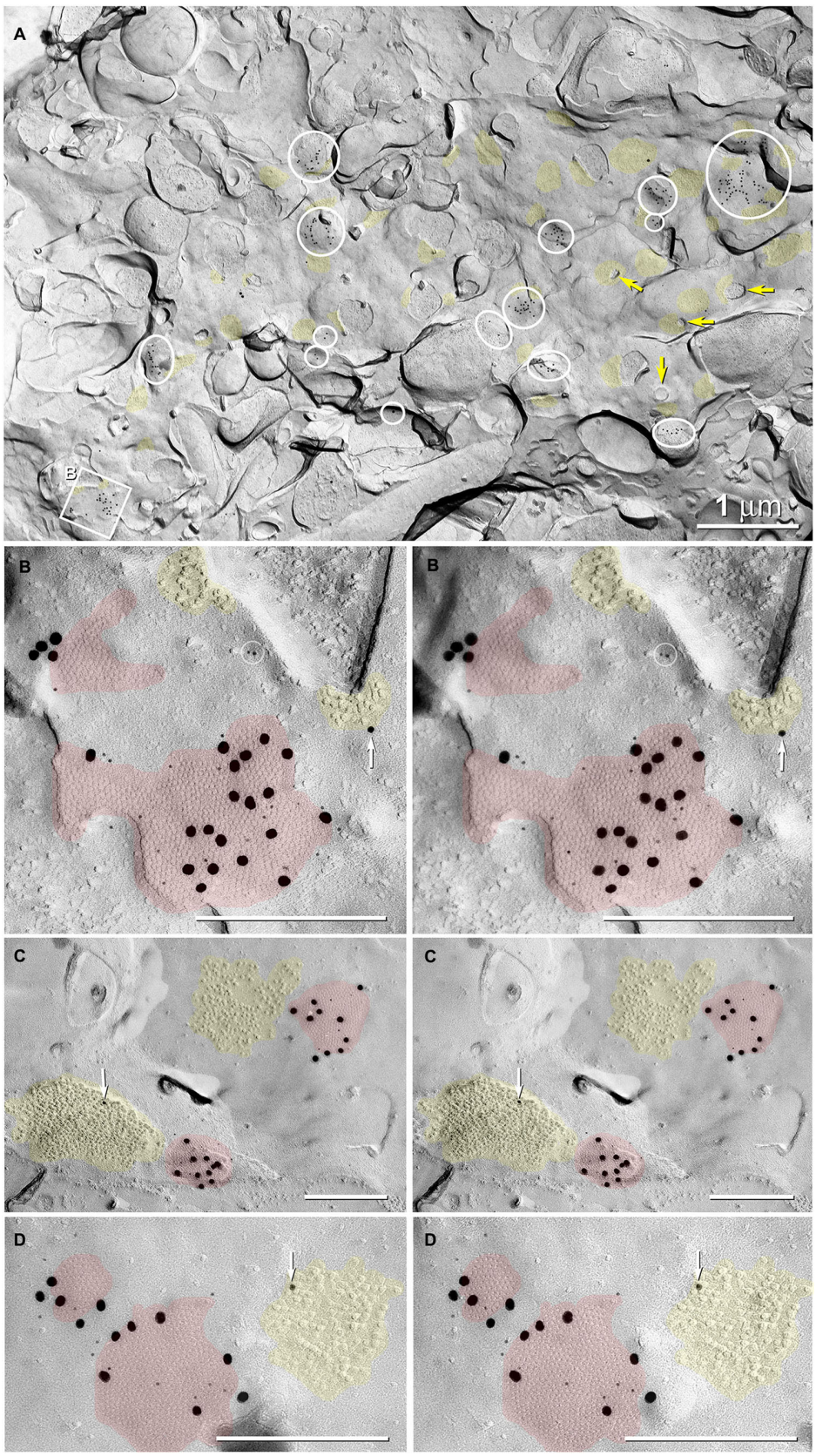

FIGURE 6 | (*Continued*)

FIGURE 6 | Continued
Abundance of glutamatergic mixed synapses in adult male Mosquitofish shown at low magnification, with selected synaptic contacts shown in higher magnification stereoscopic images. (A) The E-face of a dendrite having few spines (*yellow arrows* = cross-fractured necks of dendritic spines) is labeled extensively for Cx35 by 6-nm and 18-nm gold beads. All gap junctions are at axo-dendritic synapses (*inscribed circles* and *inscribed square B* mark 20 gap junctions in this field of view); distinctive clusters of 10-nm IMPs are weakly labeled for NMDAR1 (12- and 30-nm gold nanoparticles, *yellow overlays*; 46 PSDs in this field of view). Some cross-fractured axon terminals contain spherical synaptic vesicles. **(B)** High-magnification stereoscopic view of the inscribed square "B" in **(A)** shows two E-face gap junctions (*red overlays*) labeled for Cx35 (6-nm and 18-nm gold beads) and two postsynaptic clusters of E-face IMPs identified as glutamate receptors (*yellow overlays*) based on weak but positive labeling for NMDAR1 (12-nm gold bead, *white arrow*). Two 6-nm gold beads on top of the replica are circled to identify them as non-specific "noise". **(C)** High-magnification stereoscopic view of two E-face gap junctions (*red overlays*) labeled for Cx35 (6-nm and 18-nm gold beads). Each gap junction has a postsynaptic cluster of IMPs (*yellow overlay*) immediately adjacent to it (i.e., within 50 nm). One IMP cluster is labeled for NMDAR1 (12-nm gold bead, *white arrow*). **(D)** High-magnification stereoscopic view of two E-face gap junctions (*red overlays*) labeled for Cx35 (6-nm and 18-nm gold beads); one postsynaptic cluster of IMPs (*yellow overlays*) is labeled for NMDAR1 (12-nm gold bead, *white arrow*). Unless otherwise indicated, calibration bars in all FRIL images are 0.25 μm, which corresponds to the limit of resolution of light microscopy in blue and green wavelengths.

RESULTS

AFB-594 retrograde labeling reveals extensive dye-coupling between MNs located in the lateral motor column (LMC) and INs located in the medial longitudinal fasciculus (MLF) of the spinal cord (**Figures 4A,B**). Note that this extensive dye-coupling spans three (14th–16th) spinal segments (**Figure 4B**), but only one spinal segment, the 14th, is shown in **Figure 4B**. Each spinal segment contains 44 neurons.

The 14th spinal segment, a region controlling adult male fast coital behavior, shows a more extensive and elaborate dendritic arbor (**Figure 4C**) than do other spinal segments. Of the 44 neurons seen in the 14th spinal segment of 12 male Mosquitofish, 28 neurons are MN-1, 7 are MN-2, and 9 are spinal MN. Of the 44 neurons seen in the 14th spinal segment in 12 female Mosquitofish, 29 were MN-1, 9 were MN-2, and 6 were spinal MN. The two phenotypes of motor neurons (MN-1 and MN-2) were identified based on the presence of basal and apical dendrites (see **Figure 4C**). The spinal neurons seen in **Figure 4C** are located within the medial motor column (MMC; **Figure 4A**) and the medial lateral motor column (LMC^{medial}; **Figure 4A**). These neurons are being characterized and identified for a subsequent report. The number of MNs was assessed by counting all of the entering axons through each of the spinal segment ventral roots and correlating them with the total number of retrogradely-filled MNs. Each of the spinal segments was confirmed by the presence of "boundary neurons" (**Figure 4B**).

It is clear from these results that the rapid, minimally-invasive method is selective because the only spinal neurons that send axonal processes to muscles are MNs; thus, the neuronal somas and their axonal and dendritic processes extensively filled with AFB-594 are clearly distinguishable as MNs. Dye-coupling also reveals a spinal interneuron that we identify as a commissural primary ascending interneuron (CoPA IN) based on the dorso-ventral (DV) position of its soma within the MLF, and on its large slightly elongated spherical shape (see **Figure 4A**, and **Figures 4C–E**).

In keeping with the results of Hale et al. (2001), our results show that two distinct dendrites emerge from the rostral and caudal poles of the soma (**Figure 4C**) and run longitudinally across three spinal segments within the dorsal longitudinal fasciculus. Two dendrites (**Figure 4E**), together with the ventrally emerging axon, give the CoPA IN its characteristic T-shape (see **Figures 4C–E**). Note that dye-coupling revealed no more than one CoPA IN per spinal segment.

The AFB-594 dye-coupling between MNs and INs in adult female and adult male Mosquitofish as seen in **Figure 5A** was confirmed by performing Cx35/36 whole-mount fluorescence immunohistochemistry. **Figure 5B** shows the high density of Cx35/36 immuno-positive gap junction puncta covering the soma and outlining the basal, apical, and proximal dendrites of MNs in male Mosquitofish; in female Mosquitofish (see **Figure 5C**), the density of Cx35/36 immuno-positive gap junction puncta, especially large puncta, seems greater than it does in males.

To confirm that dye-coupling between MNs and CoPA INs was mediated by Cx35-containing-gap junctions at mixed synapses, we employed FRIL and four Cx35/36 antibodies. P-Ser276 abundantly labeled pre-synaptic hemiplaques within the neuronal gap junctions (**Figures 6**, **7B**), as was previously reported in giant club endings on Mauthner cells (Rash et al., 2013). In 6 replicas (3 males; 3 females), FRIL reveals >115 gap junctions are immunogold labeled for Cx35/36; 97 gap junctions are found in males and 18 in females. The immunogold labeling efficiency [LE; defined as the number of gold beads *vs.* the number of connexons counted in each gap junction (Rash and Yasumura, 1999)] ranged from 1:5 to 1:50, comparable to those of previous gap junction FRIL studies (Fujimoto, 1995; Rash et al., 2001; Pereda et al., 2003).

In 5 replicas (2 in adult males and 2 in adult females, each containing 6–9 spinal cord cross sections; plus 1 replica in male containing 2 longitudinal sections), we identified 35 Cx35/36 immuno-positive gap junctions in 30 appositions between neurons in the ventral horns of segment 14 in the adult Mosquitofish spinal cord (**Figures 6–8**); we found no gold beads on astrocyte or oligodendrocyte gap junctions (absence of labeling of glial gap junctions not shown). In one of two sagital section replicas of adult male Mosquitofish, we found 62 Cx35/36 immuno-positive gap junctions in segments containing the 8th–16th ventral roots, with >50 of those gap junctions in neurons innervating the 14th spinal segment ventral root (**Figures 6–7**).

Gap junctions at these glutamatergic mixed synapses are extraordinarily abundant in the 14th spinal segment (**Figures 6–7**), the main spinal segment that innervates the male sexually dimorphic genitalia, the gonopodium (Rosa-Molinar, 2005; Rivera-Rivera et al., 2010). Gap junctions are much less abundant in the 16th spinal segment and in the more rostral (1–7) spinal segments and in the more caudal (17–33) spinal segments of the adult (male and female) Mosquitofish spinal cord (data not shown).

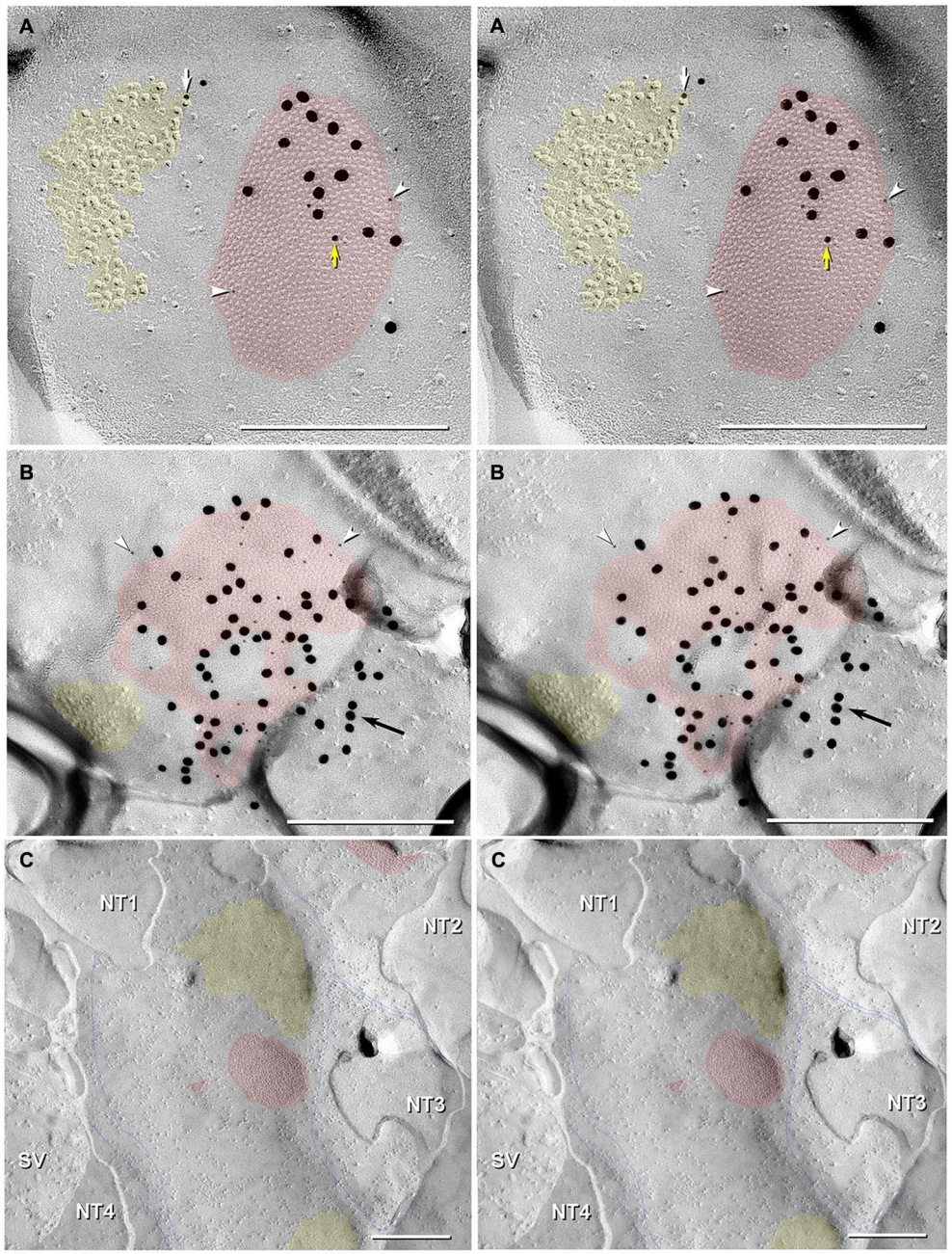

FIGURE 7 | Stereoscopic images of large plaque and reticular gap junctions in adult male Mosquitofish. (A) Large plaque gap junction (*red overlay*) on a neuronal postsynaptic E-face labeled with antibodies against mouse/human Cx36 (36–4600, 6-nm [*white arrowheads*] and much more electron-dense 18-nm gold beads) and for GluR2 AMPA receptors (12-nm gold beads, *white arrow*) (*Yellow arrow* indicates either a 12-nm gold bead as "noise" on the Cx36-labeled gap junction or an anomalously small "18-nm" gold bead for Cx36). **(B)** High-magnification stereoscopic image of E-face of a neuronal reticular gap junction (*red overlay*) labeled for Cx35 (P-Ser276) by 6-nm (*white arrowheads*) and 18-nm gold beads. The *black arrow* points to "cryptic" labeling of connexins in an extended portion of the gap junction beneath the cross-fractured neuronal cytoplasm. Immediately adjacent to the gap junction is a cluster of E-face IMPs (*yellow overlay*, not labeled) similar to other immunogold-labeled glutamate receptor channels. **(C)** P-face image showing three of more than a dozen unlabeled postsynaptic hemiplaques (*red overlays*) in the same replica as **Figures 4**, **5B**, where presynaptic hemiplaques are heavily labeled for Cx35 (P-Ser276). This absence of labeling in C is consistent with our demonstration in goldfish giant club ending/Mauthner cell mixed synapses that Cx35 is exclusively presynaptic and that Cx34.7 is exclusively postsynaptic (Rash et al., 2013). The postsynaptic P-face reveals distinct clusters of faintly resolvable pits (*yellow overlays*) where glutamate receptors had been removed during membrane splitting. Thin blue lines indicate probable margins of axon terminals impressed into the dendritic or somatic plasma membrane (NT1-NT4). SV = synaptic vesicles. Calibration bars are 0.25 μm.

Gap junctions at mixed synapses between coupled MNs and CoPA INs usually are large (>400 connexons) and are immunogold labeled by a variety of Cx35/36 antibodies. In ultrastructurally-identified mixed synapses, FRIL analysis reveals Cx35/36-labeled gap junctions adjacent to postsynaptic glutamate receptor E-face IMPs (see Pereda et al., 2003) in 43 out of 74 E-face images of mixed synapses (**Figure 7**, *red vs. yellow overlays*). These distinctive clusters of 10-nm E-face particles are weakly labeled for NMDA (**Figure 6**) or for GluR2 (**Figure 7A**) glutamate receptors, thereby demonstrating that both NMDA and AMPA glutamate receptors are present and intermixed in the glutamate receptor clusters. These glutamatergic mixed synapses occur primarily on dendritic shafts (**Figure 6A**) and are only infrequently seen on dendritic spines (not shown). The antibodies used for identifying glutamate receptors were made to mammalian amino acid sequences that vary from the sequence in fish. As a result, the glutamate-receptor antibodies are only weakly cross-reactive with fish glutamate receptors, thus yielding a low but positive level of labeling. Pereda et al. (2003) previously documented the properties of these antibodies. In any case, the number, size, and clustering of the E-face IMPs in the glutamate receptor-labeled PSDs appear identical in mammals and fish.

In addition to typical "plaques", two large "reticular" gap junctions immunogold labeled for Cx35/36 were found in adult male Mosquitofish (**Figure 7B**); no reticular gap junctions have yet been found in female Mosquitofish. Reticular gap junctions are characterized by the presence of one or more oval areas that are devoid of connexon P-face IMPs / E-face pits (Kamasawa et al., 2006; Rash et al., 2007). Occasionally, the fracture plane stepped from the E-face to the P-face within the perimeter of a gap junction (**Figure 8A** from adult female Mosquitofish), thereby revealing the characteristic narrowing of the extracellular space (**Figure 8A**, blue overlay) at the contact area of gap junction coupling. Reverse stereoscopic imaging of Cx35/36 immunogold-labeled neuronal gap junctions (**Figure 8**; right pair of each triplet) facilitates discrimination of 6-nm gold beads from the equally electron-opaque 6–9 nm platinum-shadowed IMPs (**Figure 8A**).

Finally, gold beads specifically labeling Cx35 but not Cx34.7 (antibody P-Ser276; Rash et al., 2013) are restricted to presynaptic hemiplaques of neuronal gap junctions (**Figures 6**, **7B**) and do not label nearby postsynaptic hemiplaques in the same replica (**Figure 7C**). We previously showed the following: two anti-Cx36 antibodies cross-react with teleost Cx35 and Cx34.7 (Mouse anti-Connexin 36 [39–4200; **Figure 8A**] and Ab298 [not used here]); two cross react with Cx35 but not Cx34.7 (37–4600 [**Figure 8A**] and Invitrogen 51–6300; not used here); two cross-react with Cx34.7 but not Cx35 (Cx34.7 IL and Cx34.7 CT; not used here);

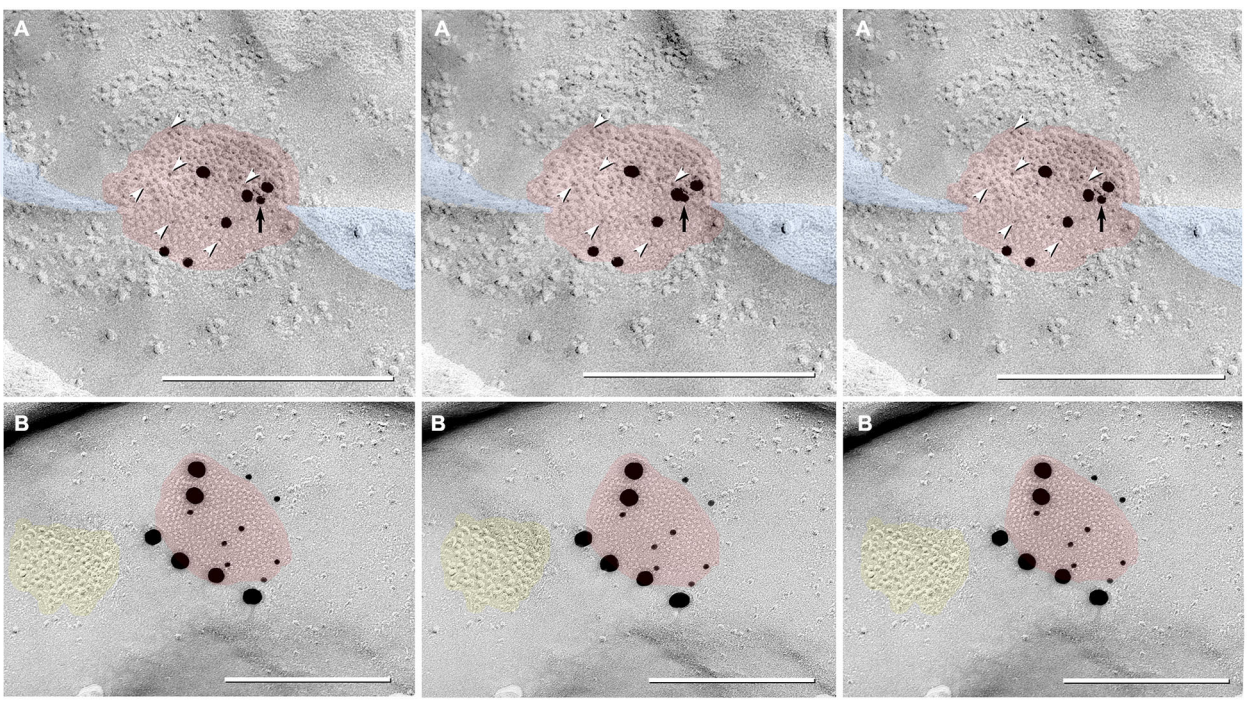

FIGURE 8 | Triplet images showing stereoscopic (left two of three images) and reverse stereoscopic images (right two images) of medium-size gap junction in adult female Mosquitofish. (A) Classical gap junction plaque (*red overlays*) labeled by 14 6-nm gold beads (six indicated by *white arrowheads*) and six 18-nm gold beads representing Cx36 (39–4200 and 37–4600). A single 12-nm gold nanoparticle (*black arrow*), ostensibly for anti-pannexin 1 (see Section Materials and Methods), represents non-specific labeling because it is on the non-biological side (upper surface) of the replica where labeling is not possible. Note the narrowing of the extracellular space (*blue overlay*) at the point of closest membrane approach within the gap junction. **(B)** E-face image of gap junction plaque (*red overlay*) labeled for Cx36 (36–4600) by eight 12-nm gold beads and six 30-nm gold beads. Because of greatly different amino acid sequences in fish *vs.* mammalian glutamate receptors (see text), the immediately adjacent cluster of glutamate receptor-like E-face IMPs (*yellow overlay*) does not exhibit labeling for GluR2 (6-nm and 18-nm gold beads, none present). Calibration bars are 0.25 μm.

and one cross-reacts with Cx35 but has unknown cross-reactivity with Cx34.7 (36–4600 [**Figures 7A**, **8B**]) (For antibody specificities, see Table S1 in Rash et al., 2013). In addition, phospho-specific P-Ser276 labels Cx35/Cx36 but not Cx34.7 (**Figures 6**, **7B,C**).

Thus, the current data provide independent verification for Cx35/36 antibody specificity for labeling neuronal gap junctions but not glial gap junctions. In particular, current data confirm specificity of labeling for Cx35/Cx36 only in presynaptic hemiplaques but not in postsynaptic hemiplaques. Thus, as in goldfish, a second connexin homolog of Cx36 (likely Cx34.7; Rash et al., 2013) occurs in the otherwise unlabeled postsynaptic hemiplaques (**Figure 7C**). If so, these data from Mosquitofish imply that asymmetry of connexin distribution/heterotypic coupling may be widespread in teleost neuronal gap junctions.

DISCUSSION

The results support other studies that report gap junctions in the adult spinal cord as well as those that link gap junctions to motor behavior. Moreover, our results suggest mixed synapses have a role in the fast coital behavior of the adult male Mosquitofish, and, thus, extend prior studies (Gogan et al., 1974, 1977; Lewis, 1994; Laird, 1996; van der Want et al., 1998; Tresch and Kiehn, 2000; Kiehn and Tresch, 2002; Mentis et al., 2002; Arumugam et al., 2005; Park et al., 2011). Our findings show extensive dye-coupling between MNs and CoPA INs throughout the Mosquitofish spinal cord and permit the identification of two phenotypes of motor neurons, MN-1 and MN-2. Labeling reveals 44 neurons in the 14th spinal segment that controls the fast coital movement of the male, and it also shows that the 14th spinal segment has the most extensive and elaborate dendritic arbor. The dye-coupling study shows that the number of mixed synapses falls off precipitously in more rostral (1–13) and in more caudal (17–33) spinal cord segments in both adult male and female Mosquitofish (data not shown). The latter three findings are consistent with a fast-responding role for mixed synapses in the adult male Mosquitofish spinal cord region linked to a male-specific coital behavior.

The labeling also shows abundant anti-Cx35/36 puncta surrounding the primary basal dendrite and the soma of Mosquitofish spinal neurons. The anti-Cx35/36-labeled puncta are widely distributed throughout the Mosquitofish spinal cord. The latter finding suggests that gap junctions may link a wide constellation of spinal neurons.

Because it is well accepted that anti-Cx35/36-labeled puncta are indicative of the occurrence of gap junctions between neurons, to confirm that dye-coupling between MNs and CoPA INs was mediated by Cx35-containing-gap junctions at mixed synapses, we employed FRIL and four Cx35/36 antibodies to define the ultrastructural details of the gap junctions. Results show 62 Cx35/36 immuno-positive gap junctions in segments 8–16. In the 16th spinal segment, the more rostral (1–7) spinal segments, and the more caudal (17–33) spinal segments of the adult male and female Mosquitofish, gap junctions are not as abundant as they are in the 14th spinal segment where >50 are shown.

Thus, in the main spinal segment ventral root (14th spinal segment) that innervates the male sexually dimorphic gonopodium, gap junctions at glutamatergic mixed synapses are extraordinarily abundant, reinforcing the suggestion that they have a role in fast behavior.

Although our findings contrast with those of Matsumoto et al. (1988, 1989) who found gap junction plaques only between MNs of the spinal nucleus of the bulbocavernosus (SNB) and the dorsolateral nucleus (DLN), they are in keeping with those of others. Coleman and Sengelaub (2002) reported dye-coupling between MNs and INs associated with the rodent SNB and the DLN, both of which are sexually dimorphic motor nuclei in the lumbosacral spinal cord involved in controlling genital reflexes. Although the Coleman and Sengelaub results should be replicated in response to the Bautista and Nagy (2014) questions regarding methodological issues and the observation that dye-coupling normally occurs between neurons of the same phenotype, the dye-coupling we observed between MNs and CoPA INs in the Mosquitofish spinal cord region associated with the sexually dimorphic ano-urogenital region supports and extends the Coleman and Sengelaub (2002) results. In addition, our results are in keeping with those of Rash and coworkers who first described gap junctions at neuronal mixed synapses throughout the spinal cord of adult rat (Rash et al., 1996, 1997, 1998, 2000, 2001; Rash and Yasumura, 1999).

In short, the independent use of "dye-coupling", whole-mount immunofluorescence for gap junction channel protein connexin 35 (Cx35), and freeze-fracture replica labeling, show the abundance and persistence of gap junctions at glutamatergic mixed synapses in adult male and female Mosquitofish and provide a means for future studies to assign specific roles to spinal neurons in the generation/regulation of a sex-specific behavior.

The results establish a base for future studies to elucidate the idea that gap junctions have a major role in regulating neuronal aborization and morphology that directly affect spinal motor activity, particularly fast motor behavior, such as the male Mosquitofish "torque/thrust" maneuver. In addition, the gap junctions found at mixed synapses between MNs and CoPA INs suggest the CoPA IN may be a novel candidate neuron for future studies of an extended role for gap junctions in coordinating fast motor behavior.

ACKNOWLEDGMENTS

We thank John O'Brien for Cx35-specific antibody P-Ser276. We also thank N. L. Rivera-Rivera for characterizing the Cx35-specific antibody P-Ser276 and the mouse anti- Cx35/36 monoclonal antibodies, A. Pereda, M. Morita R. Diaz-De Leon, and E. Sierra-Lopez for their helpful comments throughout the study, and J. Taylor for her editorial comments. This research was partially supported by grants to Eduardo Rosa-Molinar and Scott E. Fraser from NIH (NS 39405), NSF-1039620 (Eduardo Rosa-Molinar), NSF-0964114 (Eduardo Rosa-Molinar), Puerto Rico Science, Technology and Research Trust (Eduardo Rosa-Molinar Agreement 2013-000034); and NIH NS44395 (John E. Rash). Melanie Rodriguez-Alvarado was supported by a training grant from NIH (GM 007821).

REFERENCES

Arumugam, H., Liu, X., Colombo, P. J., Corriveau, R. A., and Belousov, A. B. (2005). NMDA receptors regulate developmental gap junction uncoupling via CREB signaling. *Nat. Neurosci.* 8, 1720–1726. doi: 10.1038/nn1588

Bartos, M., Vida, I., Frotscher, M., Meyer, A., Monyer, H., Geiger, J. R., et al. (2002). Fast synaptic inhibition promotes synchronized gamma oscillations in hippocampal interneuron networks. *Proc. Natl. Acad. Sci. U S A* 99, 13222–13227. doi: 10.1073/pnas.192233099

Bautista, W., and Nagy, J. I. (2014). Connexin36 in gap junctions forming electrical synapses between motoneurons in sexually dimorphic motor nuclei in spinal cord of rat and mouse. *Eur. J. Neurosci.* 39, 771–787. doi: 10.1111/ejn.12439

Bennett, M. V. (1997). Gap junctions as electrical synapses. *J. Neurocytol.* 26, 349–366. doi: 10.1023/A:1018560803261

Bennett, M. V. (2000). Electrical synapses, a personal perspective (or history). *Brain Res. Brain Res. Rev.* 32, 16–28. doi: 10.1016/s0165-0173(99)00065-x

Bennett, M. V., Aljure, E., Nakajima, Y., and Pappas, G. D. (1963). Electrotonic junctions between teleost spinal neurons: electrophysiology and ultrastructure. *Science* 141, 262–264. doi: 10.1126/science.141.3577.262

Bennett, M. V., and Zukin, R. S. (2004). Electrical coupling and neuronal synchronization in the Mammalian brain. *Neuron* 41, 495–511. doi: 10.1016/s0896-6273(04)00043-1

Bonnot, A., Whelan, P. J., Mentis, G. Z., and O'donovan, M. J. (2002). Spatiotemporal pattern of motoneuron activation in the rostral lumbar and the sacral segments during locomotor-like activity in the neonatal mouse spinal cord. *J. Neurosci.* 22:RC203. doi: 10.3410/f.1003953.42704

Chen, B., Liu, Q., Ge, Q., Xie, J., and Wang, Z. W. (2007). UNC-1 regulates gap junctions important to locomotion in C. elegans. *Curr. Biol.* 17, 1334–1339. doi: 10.1016/j.cub.2007.06.060

Chuang, C. F., Vanhoven, M. K., Fetter, R. D., Verselis, V. K., and Bargmann, C. I. (2007). An innexin-dependent cell network establishes left-right neuronal asymmetry in C. elegans. *Cell* 129, 787–799. doi: 10.1016/j.cell.2007.02.052

Cohen-Cory, S. (2002). The developing synapse: construction and modulation of synaptic structures and circuits. *Science* 298, 770–776. doi: 10.1126/science.1075510

Coleman, A. M., and Sengelaub, D. R. (2002). Patterns of dye coupling in lumbar motor nuclei of the rat. *J. Comp. Neurol.* 454, 34–41. doi: 10.1002/cne.10438

Connors, B. W., and Long, M. A. (2004). Electrical synapses in the mammalian brain. *Annu. Rev. Neurosci.* 27, 393–418. doi: 10.1146/annurev.neuro.26.041002.131128

Costes, S. V., Daelemans, D., Cho, E. H., Dobbin, Z., Pavlakis, G., and Lockett, S. (2004). Automatic and quantitative measurement of protein-protein colocalization in live cells. *Biophys. J.* 86, 3993–4003. doi: 10.1529/biophysj.103.038422

DeFelipe, J., Conti, F., Van Eyck, S. L., and Manzoni, T. (1988). Demonstration of glutamate-positive axon terminals forming asymmetric synapses in cat neocortex. *Brain Res.* 455, 162–165. doi: 10.1016/0006-8993(88)90127-8

Dermietzel, R. (1998). Gap junction wiring: a 'new' principle in cell-to-cell communication in the nervous system? *Brain Res. Brain Res. Rev.* 26, 176–183. doi: 10.1016/s0165-0173(97)00031-3

Dermietzel, R., and Spray, D. C. (1993). Gap junctions in the brain: where, what type, how many and why? *Trends Neurosci.* 16, 186–192. doi: 10.1016/0166-2236(93)90151-b

Dinchuk, J. E., Johnson, T. J., and Rash, J. E. (1987). Postreplication labeling of E-leaflet molecules: membrane immunoglobulins localized in sectioned, labeled replicas examined by TEM and HVEM. *J. Electron Microsc. Tech.* 7, 1–16. doi: 10.1002/jemt.1060070102

Domenici, P., and Blake, R. (1997). The kinematics and performance of fish fast-start swimming. *J. Exp. Biol.* 200, 1165–1178.

Drapeau, P., Saint-Amant, L., Buss, R. R., Chong, M., Mcdearmid, J. R., and Brustein, E. (2002). Development of the locomotor network in zebrafish. *Prog. Neurobiol.* 68, 85–111. doi: 10.1016/s0301-0082(02)00075-8

Edwards, D. H., Heitler, W. J., and Krasne, F. B. (1999). Fifty years of a command neuron: the neurobiology of escape behavior in the crayfish. *Trends Neurosci.* 22, 153–161. doi: 10.1016/s0166-2236(98)01340-x

Fan, S. Y., Ke, Y. N., Zeng, Y. J., Wang, Y., Cheng, W. L., and Yang, J. R. (2005). [Effects and the mechanism of carvedilol on gap junctional intercellular communication in rat myocardium]. *Zhonghua Xin Xue Guan Bing Za Zhi* 33, 1141–1145.

Fujimoto, K. (1995). Freeze-fracture replica electron microscopy combined with SDS digestion for cytochemical labeling of integral membrane proteins. Application to the immunogold labeling of intercellular junctional complexes. *J. Cell Sci.* 108(Pt. 11), 3443–3449.

Fukuda, T., and Kosaka, T. (2000). Gap junctions linking the dendritic network of GABAergic interneurons in the hippocampus. *J. Neurosci.* 20, 1519–1528.

Fukuda, T., and Kosaka, T. (2003). Ultrastructural study of gap junctions between dendrites of parvalbumin-containing GABAergic neurons in various neocortical areas of the adult rat. *Neuroscience* 120, 5–20. doi: 10.1016/s0306-4522(03)00328-2

Fulton, B. P., Miledi, R., and Takahashi, T. (1980). Electrical synapses between motoneurons in the spinal cord of the newborn rat. *Proc. R. Soc. Lond. B Biol. Sci.* 208, 115–120. doi: 10.1098/rspb.1980.0045

Furshpan, E. J. (1964). "Electrical transmission" at an excitatory synapse in a vertebrate brain. *Science* 144, 878–880. doi: 10.1126/science.144.3620.878

Furshpan, E. J., and Potter, D. D. (1959). Transmission at the giant motor synapses of the crayfish. *J. Physiol.* 145, 289–325.

Galarreta, M., and Hestrin, S. (1999). A network of fast-spiking cells in the neocortex connected by electrical synapses. *Nature* 402, 72–75. doi: 10.1038/47029

Galarreta, M., and Hestrin, S. (2001a). Electrical synapses between GABA-releasing interneurons. *Nat. Rev. Neurosci.* 2, 425–433. doi: 10.1038/35077566

Galarreta, M., and Hestrin, S. (2001b). Spike transmission and synchrony detection in networks of GABAergic interneurons. *Science* 292, 2295–2299. doi: 10.1126/science.1061395

Gibson, J. R., Beierlein, M., and Connors, B. W. (1999). Two networks of electrically coupled inhibitory neurons in neocortex. *Nature* 402, 75–79. doi: 10.1038/47035

Gogan, P., Gueritaud, J. P., Horcholle-Bossavit, G., and Tyc-Dumont, S. (1974). Electronic coupling between motoneurones in the abducens nucleus of the cat. *Exp. Brain Res.* 21, 139–154. doi: 10.1007/bf00234386

Gogan, P., Gueritaud, J. P., Horcholle-Bossavit, G., and Tyc-Dumont, S. (1977). Direct excitatory interactions between spinal motoneurones of the cat. *J. Physiol.* 272, 755–767.

Goodenough, D. A., and Paul, D. L. (2009). Gap junctions. *Cold Spring Harb. Perspect. Biol.* 1:a002576. doi: 10.1101/cshperspect.a002576

Hale, M. E. (2002). S- and C-start escape responses of the muskellunge (Esox masquinongy) require alternative neuromotor mechanisms. *J. Exp. Biol.* 205, 2005–2016.

Hale, M. E., Ritter, D. A., and Fetcho, J. R. (2001). A confocal study of spinal interneurons in living larval zebrafish. *J. Comp. Neurol.* 437, 1–16. doi: 10.1002/cne.1266

Hamzei-Sichani, F., Davidson, K. G., Yasumura, T., Janssen, W. G., Wearne, S. L., Hof, P. R., et al. (2012). Mixed electrical-chemical synapses in adult rat hippocampus are primarily glutamatergic and coupled by connexin-36. *Front. Neuroanat.* 6:13. doi: 10.3389/fnana.2012.00013

Harper, D. G., and Blake, R. W. (1990). Fast-start performance of rainbow-trout Salmo-Gairdneri and Northern Pike Esox-Lucius. *J. Exp. Biol.* 150, 321–342.

Harper, D. G., and Blake, R. W. (1991). Prey capture and the fast-start performance of Northern Pike Esox-Lucius. *J. Exp. Biol.* 155, 175–192.

Harris, K. M., and Landis, D. M. (1986). Membrane structure at synaptic junctions in area CA1 of the rat hippocampus. *Neuroscience* 19, 857–872. doi: 10.1016/0306-4522(86)90304-0

Herberholz, J., Antonsen, B. L., and Edwards, D. H. (2002). A lateral excitatory network in the escape circuit of crayfish. *J. Neurosci.* 22, 9078–9085.

Hervé, J. C., Bourmeyster, N., and Sarrouilhe, D. (2004). Diversity in protein-protein interactions of connexins: emerging roles. *Biochim. Biophys. Acta* 1662, 22–41. doi: 10.1016/j.bbamem.2003.10.022

Hoge, G. J., Davidson, K. G., Yasumura, T., Castillo, P. E., Rash, J. E., and Pereda, A. E. (2011). The extent and strength of electrical coupling between inferior olivary neurons is heterogeneous. *J. Neurophysiol.* 105, 1089–1101. doi: 10.1152/jn.00789.2010

Johnston, I. I., Leeuwen, J., Davies, M., and Beddow, T. (1995). How fish power predation fast-starts. *J. Exp. Biol.* 198, 1851–1861.

Kalb, R. G. (1994). Regulation of motor neuron dendrite growth by NMDA receptor activation. *Development* 120, 3063–3071.

Kamasawa, N., Furman, C. S., Davidson, K. G., Sampson, J. A., Magnie, A. R., Gebhardt, B. R., et al. (2006). Abundance and ultrastructural diversity of

neuronal gap junctions in the OFF and ON sublaminae of the inner plexiform layer of rat and mouse retina. *Neuroscience* 142, 1093–1117. doi: 10.1016/j.neuroscience.2006.08.020

Kandler, K., and Katz, L. C. (1995). Neuronal coupling and uncoupling in the developing nervous system. *Curr. Opin. Neurobiol.* 5, 98–105. doi: 10.1016/0959-4388(95)80093-x

Kiehn, O., and Tresch, M. C. (2002). Gap junctions and motor behavior. *Trends Neurosci.* 25, 108–115. doi: 10.1016/s0166-2236(02)02038-6

Laird, D. W. (1996). The life cycle of a connexin: gap junction formation, removal and degradation. *J. Bioenerg. Biomembr.* 28, 311–318. doi: 10.1007/bf02110107

Lewis, D. I. (1994). Dye-coupling between vagal motoneurones within the compact region of the adult rat nucleus ambiguus, in-vitro. *J. Auton. Nerv. Syst.* 47, 53–58. doi: 10.1016/0165-1838(94)90065-5

Lewis, K. E., and Eisen, J. S. (2003). From cells to circuits: development of the zebrafish spinal cord. *Prog. Neurobiol.* 69, 419–449. doi: 10.1016/s0301-0082(03)00052-2

Li, H., Chuang, A. Z., and O'brien, J. (2009). Photoreceptor coupling is controlled by connexin 35 phosphorylation in zebrafish retina. *J. Neurosci.* 29, 15178–15186. doi: 10.1523/JNEUROSCI.3517-09.2009

Lynn, B. D., Li, X., and Nagy, J. I. (2012). Under construction: building the macromolecular superstructure and signaling components of an electrical synapse. *J. Membr. Biol.* 245, 303–317. doi: 10.1007/s00232-012-9451-5

Marin-Burgin, A., Eisenhart, F. J., Baca, S. M., Kristan, W. B. Jr., and French, K. A. (2005). Sequential development of electrical and chemical synaptic connections generates a specific behavioral circuit in the leech. *J. Neurosci.* 25, 2478–2489. doi: 10.1523/jneurosci.4787-04.2005

Marin-Burgin, A., Eisenhart, F. J., Kristan, W. B. Jr., and French, K. A. (2006). Embryonic electrical connections appear to pre-figure a behavioral circuit in the leech CNS. *J. Comp. Physiol. A Neuroethol. Sens. Neural. Behav. Physiol.* 192, 123–133. doi: 10.1007/s00359-005-0055-8

Marin-Burgin, A., Kristan, W. B. Jr., and French, K. A. (2008). From synapses to behavior: development of a sensory-motor circuit in the leech. *Dev. Neurobiol.* 68, 779–787. doi: 10.1002/dneu.20551

Matsumoto, A., Arnold, A. P., and Micevych, P. E. (1989). Gap junctions between lateral spinal motoneurons in the rat. *Brain Res.* 495, 362–366. doi: 10.1016/0006-8993(89)90229-1

Matsumoto, A., Arnold, A. P., Zampighi, G. A., and Micevych, P. E. (1988). Androgenic regulation of gap junctions between motoneurons in the rat spinal cord. *J. Neurosci.* 8, 4177–4183.

McAllister, A. K. (2007). Dynamic aspects of CNS synapse formation. *Annu. Rev. Neurosci.* 30, 425–450. doi: 10.1146/annurev.neuro.29.051605.112830

Mentis, G. Z., Diaz, E., Moran, L. B., and Navarrete, R. (2002). Increased incidence of gap junctional coupling between spinal motoneurones following transient blockade of NMDA receptors in neonatal rats. *J. Physiol.* 544, 757–764. doi: 10.1113/jphysiol.2002.028159

Montoro, R. J., and Yuste, R. (2004). Gap junctions in developing neocortex: a review. *Brain Res. Brain Res. Rev.* 47, 216–226. doi: 10.1016/j.brainresrev.2004.06.009

Muller, J. F., Mascagni, F., and Mcdonald, A. J. (2005). Coupled networks of parvalbumin-immunoreactive interneurons in the rat basolateral amygdala. *J. Neurosci.* 25, 7366–7376. doi: 10.1523/jneurosci.0899-05.2005

Muller, J. F., Mascagni, F., and Mcdonald, A. J. (2006). Pyramidal cells of the rat basolateral amygdala: synaptology and innervation by parvalbumin-immunoreactive interneurons. *J. Comp. Neurol.* 494, 635–650. doi: 10.1002/cne.20832

Norman, K. R., and Maricq, A. V. (2007). Innexin function: minding the gap junction. *Curr. Biol.* 17, R812–R814. doi: 10.1016/j.cub.2007.07.043

Park, W. M., Wang, Y., Park, S., Denisova, J. V., Fontes, J. D., and Belousov, A. B. (2011). Interplay of chemical neurotransmitters regulates developmental increase in electrical synapses. *J. Neurosci.* 31, 5909–5920. doi: 10.1523/JNEUROSCI.6787-10.2011

Peinado, A., Yuste, R., and Katz, L. C. (1993a). Extensive dye coupling between rat neocortical neurons during the period of circuit formation. *Neuron* 10, 103–114. doi: 10.1016/0896-6273(93)90246-n

Peinado, A., Yuste, R., and Katz, L. C. (1993b). Gap junctional communication and the development of local circuits in neocortex. *Cereb. Cortex* 3, 488–498. doi: 10.1093/cercor/3.5.488

Pereda, A., O'brien, J., Nagy, J. I., Bukauskas, F., Davidson, K. G., Kamasawa, N., et al. (2003). Connexin35 mediates electrical transmission at mixed synapses on Mauthner cells. *J. Neurosci.* 23, 7489–7503.

Pereda, A. E., Curti, S., Hoge, G., Cachope, R., Flores, C. E., and Rash, J. E. (2013). Gap junction-mediated electrical transmission: regulatory mechanisms and plasticity. *Biochim. Biophys. Acta* 1828, 134–146. doi: 10.1016/j.bbamem.2012.05.026

Personius, K., Chang, Q., Bittman, K., Panzer, J., and Balice-Gordon, R. (2001). Gap junctional communication among motor and other neurons shapes patterns of neural activity and synaptic connectivity during development. *Cell Commun. Adhes.* 8, 329–333. doi: 10.3109/15419060109080748

Peters, A., Palay, S. L., and Webster, H. D. (1991). *The Fine Structure of the Nervous System. Neurons and Their Supporting Cells*. New York: Oxford University Press.

Phelan, P. (2005). Innexins: members of an evolutionarily conserved family of gap-junction proteins. *Biochim. Biophys. Acta* 1711, 225–245. doi: 10.1016/j.bbamem.2004.10.004

Rash, J. E., Curti, S., Vanderpool, K. G., Kamasawa, N., Nannapaneni, S., Palacios-Prado, N., et al. (2013). Molecular and functional asymmetry at a vertebrate electrical synapse. *Neuron* 79, 957–969. doi: 10.1016/j.neuron.2013.06.037

Rash, J. E., Davidson, K. G., Kamasawa, N., Yasumura, T., Kamasawa, M., Zhang, C., et al. (2005). Ultrastructural localization of connexins (Cx36, Cx43, Cx45), glutamate receptors and aquaporin-4 in rodent olfactory mucosa, olfactory nerve and olfactory bulb. *J. Neurocytol.* 34, 307–341. doi: 10.1007/s11068-005-8360-2

Rash, J. E., Dillman, R. K., Bilhartz, B. L., Duffy, H. S., Whalen, L. R., and Yasumura, T. (1996). Mixed synapses discovered and mapped throughout mammalian spinal cord. *Proc. Natl. Acad. Sci. U S A* 93, 4235–4239. doi: 10.1073/pnas.93.9.4235

Rash, J. E., Duffy, H. S., Dudek, F. E., Bilhartz, B. L., Whalen, L. R., and Yasumura, T. (1997). Grid-mapped freeze-fracture analysis of gap junctions in gray and white matter of adult rat central nervous system, with evidence for a "panglial syncytium" that is not coupled to neurons. *J. Comp. Neurol.* 388, 265–292. doi: 10.1002/(sici)1096-9861(19971117)388:2<265::aid-cne6>3.0.co;2-#

Rash, J. E., Olson, C. O., Davidson, K. G., Yasumura, T., Kamasawa, N., and Nagy, J. I. (2007). Identification of connexin36 in gap junctions between neurons in rodent locus coeruleus. *Neuroscience* 147, 938–956. doi: 10.1016/j.neuroscience.2007.04.061

Rash, J. E., Pereda, A., Kamasawa, N., Furman, C. S., Yasumura, T., Davidson, K. G., et al. (2004). High-resolution proteomic mapping in the vertebrate central nervous system: close proximity of connexin35 to NMDA glutamate receptor clusters and co-localization of connexin36 with immunoreactivity for zonula occludens protein-1 (ZO-1). *J. Neurocytol.* 33, 131–151. doi: 10.1023/B:NEUR.0000029653.34094.0b

Rash, J. E., Staines, W. A., Yasumura, T., Patel, D., Furman, C. S., Stelmack, G. L., et al. (2000). Immunogold evidence that neuronal gap junctions in adult rat brain and spinal cord contain connexin-36 but not connexin-32 or connexin-43. *Proc. Natl. Acad. Sci. U S A* 97, 7573–7578. doi: 10.1073/pnas.97.13.7573

Rash, J. E., Yasumura, T., and Dudek, F. E. (1998). Ultrastructure, histological distribution and freeze-fracture immunocytochemistry of gap junctions in rat brain and spinal cord. *Cell Biol. Int.* 22, 731–749. doi: 10.1006/cbir.1998.0392

Rash, J. E., Yasumura, T., Davidson, K. G., Furman, C. S., Dudek, F. E., and Nagy, J. I. (2001). Identification of cells expressing Cx43, Cx30, Cx26, Cx32 and Cx36 in gap junctions of rat brain and spinal cord. *Cell Commun. Adhes.* 8, 315–320. doi: 10.3109/15419060109080745

Rash, J. E., and Yasumura, T. (1999). Direct immunogold labeling of connexins and aquaporin-4 in freeze-fracture replicas of liver, brain and spinal cord: factors limiting quantitative analysis. *Cell Tissue Res.* 296, 307–321. doi: 10.1007/s004410051291

Rivera-Rivera, N. L., Martinez-Rivera, N., Torres-Vazquez, I., Serrano-Velez, J. L., Lauder, G. V., and Rosa-Molinar, E. (2010). A male poecillid's sexually dimorphic body plan, behavior and nervous system. *Integr. Comp. Biol.* 50, 1081–1090. doi: 10.1093/icb/icq147

Robertson, J. D., Bodenheimer, T. S., and Stage, D. E. (1963). The ultrastructure of mauthner cell synapses and nodes in goldfish brains. *J. Cell Biol.* 19, 159–199. doi: 10.1083/jcb.19.1.159

Rosa-Molinar, E. (2005). "Edwin S. Goodrich's theory of transposition revisited: the shift to a sexually dimorphic axial formulae and nervous system in a

poeciliine fish," in *First International Symposium on Livebearing Fishes*, eds M. C. Uribe and H. J. Grier (Homestead, Florida: New Life Publications, Inc.), 1–12.

Rosa-Molinar, E., Fritzsch, B., and Hendricks, S. E. (1996). Organizational-activational concept revisited: sexual differentiation in an atherinomorph teleost. *Horm. Behav.* 30, 563–575. doi: 10.1006/hbeh.1996.0059

Rosa-Molinar, E., Hendricks, S. E., Rodriguez-Sierra, J. F., and Fritzsch, B. (1994). Development of the anal fin appendicular support in the western mosquitofish, Gambusia affinis affinis (Baird and Girard, 1854): a reinvestigation and reinterpretation. *Acta Anat. (Basel)* 151, 20–35. doi: 10.1159/000147639

Rosa-Molinar, E., Proskocil, B. J., Hendricks, S. E., and Fritzsch, B. (1998). A mechanism for anterior transposition of the anal fin and its appendicular support in the western mosquitofish, gambusia affinis affinis. *Acta Anat. (Basel)* 163, 75–91. doi: 10.1159/000046487

Rosario-Ortiz, L., Rivera-Pabon, S., Torres-Vazquez, I., Ortiz-Perez, E. G., Diaz-Perez, L., Pesquera-Diaz, L., et al. (2008). The Western Mosquitofish (Gambusia affinis affinis): a new laboratory animal resource for the study of sexual dimorphism in neural circuits. *Lab. Anim. (NY)* 37, 263–269. doi: 10.1038/laban0608-263

Saint-Amant, L., and Drapeau, P. (2000). Motoneuron activity patterns related to the earliest behavior of the zebrafish embryo. *J. Neurosci.* 20, 3964–3972.

Saint-Amant, L., and Drapeau, P. (2001). Synchronization of an embryonic network of identified spinal interneurons solely by electrical coupling. *Neuron* 31, 1035–1046. doi: 10.1016/s0896-6273(01)00416-0

Scheiffele, P. (2003). Cell-cell signaling during synapse formation in the CNS. *Annu. Rev. Neurosci.* 26, 485–508. doi: 10.1146/annurev.neuro.26.043002.094940

Söhl, G., Maxeiner, S., and Willecke, K. (2005). Expression and functions of neuronal gap junctions. *Nat. Rev. Neurosci.* 6, 191–200. doi: 10.1038/nrn1627

Sotelo, C., and Korn, H. (1978). Morphological correlates of electrical and other interactions through low-resistance pathways between neurons of the vertebrate central nervous system. *Int. Rev. Cytol.* 55, 67–107. doi: 10.1016/s0074-7696(08)61887-2

Spierts, I. L., and Leeuwen, J. L. (1999). Kinematics and muscle dynamics of C- and S-starts of carp (Cyprinus carpio L.). *J. Exp. Biol.* 202, 393–406.

Sugimoto, M., Sasaki, S., Gotoh, Y., Nakamura, Y., Aoyagi, Y., Kawahara, T., et al. (2013). Genetic variants related to gap junctions and hormone secretion influence conception rates in cows. *Proc. Natl. Acad. Sci. U S A* 110, 19495–19500. doi: 10.1073/pnas.1309307110

Szabo, T. M., and Zoran, M. J. (2007). Transient electrical coupling regulates formation of neuronal networks. *Brain Res.* 1129, 63–71. doi: 10.1016/j.brainres.2006.09.112

Szabo, T. M., Faber, D. S., and Zoran, M. J. (2004). Transient electrical coupling delays the onset of chemical neurotransmission at developing synapses. *J. Neurosci.* 24, 112–120. doi: 10.1523/jneurosci.4336-03.2004

Todd, K. L., Kristan, W. B. Jr., and French, K. A. (2010). Gap junction expression is required for normal chemical synapse formation. *J. Neurosci.* 30, 15277–15285. doi: 10.1523/jneurosci.2331-10.2010

Tresch, M. C., and Kiehn, O. (2000). Motor coordination without action potentials in the mammalian spinal cord. *Nat. Neurosci.* 3, 593–599. doi: 10.1038/75768

van der Want, J. J., Gramsbergen, A., Ijkema-Paassen, J., De Weerd, H., and Liem, R. S. (1998). Dendro-dendritic connections between motoneurons in the rat spinal cord: an electron microscopic investigation. *Brain Res.* 779, 342–345. doi: 10.1016/s0006-8993(97)01238-9

Vaney, D. I. (1991). Many diverse types of retinal neurons show tracer coupling when injected with biocytin or neurobiotin. *Neurosci. Lett.* 125, 187–190. doi: 10.1016/0304-3940(91)90024-n

Vega, I. E., Cui, L., Propst, J. A., Hutton, M. L., Lee, G., and Yen, S. H. (2005). Increase in tau tyrosine phosphorylation correlates with the formation of tau aggregates. *Brain Res. Mol. Brain Res.* 138, 135–144. doi: 10.1016/j.molbrainres.2005.04.015

Vega, I. E., Traverso, E. E., Ferrer-Acosta, Y., Matos, E., Colon, M., Gonzalez, J., et al. (2008). A novel calcium-binding protein is associated with tau proteins in tauopathy. *J. Neurochem.* 106, 96–106. doi: 10.1111/j.1471-4159.2008.05339.x

Vervaeke, K., Lorincz, A., Gleeson, P., Farinella, M., Nusser, Z., and Silver, R. A. (2010). Rapid desynchronization of an electrically coupled interneuron network with sparse excitatory synaptic input. *Neuron* 67, 435–451. doi: 10.1016/j.neuron.2010.06.028

Waites, C. L., Craig, A. M., and Garner, C. C. (2005). Mechanisms of vertebrate synaptogenesis. *Annu. Rev. Neurosci.* 28, 251–274. doi: 10.1146/annurev.neuro.27.070203.144336

Walton, K. D., and Navarrete, R. (1991). Postnatal changes in motoneurone electrotonic coupling studied in the in vitro rat lumbar spinal cord. *J. Physiol.* 433, 283–305.

Webb, P. W. (1976). The effect of size on the fast-start performance of rainbow trout Salmo cairdneri and a consideration of piscivorous predator-prey interactions. *J. Exp. Biol.* 65, 157–177.

Weihs, D. (1973). The mechanism of rapid starting of slender fish. *Biorheology* 10, 343–350.

Whelan, P. J. (2010). Shining light into the black box of spinal locomotor networks. *Philos. Trans. R Soc. Lond. B Biol. Sci.* 365, 2383–2395. doi: 10.1098/rstb.2009.0322

Wolszon, L. (1995). Cell-cell interactions define the innervation patterns of central leech neurons during development. *J. Neurobiol.* 27, 335–352. doi: 10.1002/neu.480270307

Conflict of Interest Statement: The authors declare that the research was conducted in the absence of any commercial or financial relationships that could be construed as a potential conflict of interest.

Received: 16 February 2014; accepted: 28 May 2014; published online: 26 June 2014.
Citation: Serrano-Velez JL, Rodriguez-Alvarado M, Torres-Vazquez II, Fraser SE, Yasumura T, Vanderpool KG, Rash JE and Rosa-Molinar E (2014) Abundance of gap junctions at glutamatergic mixed synapses in adult Mosquitofish spinal cord neurons. Front. Neural Circuits ***8****:66. doi: 10.3389/fncir.2014.00066*
This article was submitted to the journal Frontiers in Neural Circuits.

frontiers in
NEURAL CIRCUITS

ORIGINAL RESEARCH ARTICLE
published: 04 September 2014
doi: 10.3389/fncir.2014.00104

The AII amacrine cell connectome: a dense network hub

Robert E. Marc*, James R. Anderson, Bryan W. Jones, Crystal L. Sigulinsky and James S. Lauritzen

Department of Ophthalmology and Visual Sciences, John A. Moran Eye Center, University of Utah School of Medicine, Salt Lake City, UT, USA

Edited by:
Mariano Soiza-Reilly, Institut du Fer à Moulin (U839), INSERM, France

Reviewed by:
Narayanan Kasthuri, Harvard University, USA
Yoshihiko Tsukamoto, Hyogo College of Medicine, Japan

****Correspondence:***
Robert E. Marc, Department of Ophthalmology and Visual Sciences, John A. Moran Eye Center, University of Utah School of Medicine, 65 Mario Capecchi Dr., Salt Lake City, Utah 84132, USA
e-mail: robert.marc@hsc.utah.edu

The mammalian AII retinal amacrine cell is a narrow-field, multistratified glycinergic neuron best known for its role in collecting scotopic signals from rod bipolar cells and distributing them to ON and OFF cone pathways in a crossover network via a combination of inhibitory synapses and heterocellular AII::ON cone bipolar cell gap junctions. Long considered a simple cell, a full connectomics analysis shows that AII cells possess the most complex interaction repertoire of any known vertebrate neuron, contacting at least 28 different cell classes, including every class of retinal bipolar cell. Beyond its basic role in distributing rod signals to cone pathways, the AII cell may also mediate narrow-field feedback and feedforward inhibition for the photopic OFF channel, photopic ON-OFF inhibitory crossover signaling, and serves as a nexus for a collection of inhibitory networks arising from cone pathways that likely negotiate fast switching between cone and rod vision. Further analysis of the complete synaptic counts for five AII cells shows that (1) synaptic sampling is normalized for anatomic target encounter rates; (2) qualitative targeting is specific and apparently errorless; and (3) that AII cells strongly differentiate partner cohorts by synaptic and/or coupling weights. The AII network is a dense hub connecting all primary retinal excitatory channels via precisely weighted drive and specific polarities. Homologs of AII amacrine cells have yet to be identified in non-mammalians, but we propose that such homologs should be narrow-field glycinergic amacrine cells driving photopic ON-OFF crossover via heterocellular coupling with ON cone bipolar cells and glycinergic synapses on OFF cone bipolar cells. The specific evolutionary event creating the mammalian AII scotopic-photopic hub would then simply be the emergence of large numbers of pure rod bipolar cells.

Keywords: connectomics, retina, networks, hub, bipolar cells, amacrine cells, synapses, gap junctions

INTRODUCTION

The network spanning photoreceptor input and ganglion cell output in the mammalian retina was detailed by Kolb and Famiglietti (1974) using serial section transmission electron microscope (TEM) imaging. Unlike non-mammalian retinal networks (Famiglietti et al., 1975; Naka et al., 1975), mammalian photoreceptor networks were parsed into discrete cone and rod bipolar cell pathways and, remarkably, rod-driven bipolar cells did not synapse on ganglion cells. So how would scotopic signals reach the brain? The solution was a unique interneuron, the AII amacrine cell (**Figures 1A,B**), which captured rod bipolar cell input and redistributed it to cone bipolar cells (**Figure 1C**), using the synaptic endings of cone bipolar cells as adaptors. This motif was unprecedented in any CNS network: a stage in an afferent amplification chain acting as the entire signal output for a qualitative channel to a prior parallel stage, effecting divergence of one signal into channels primarily used by another signal, with additional amplification. While reentrant CNS motifs are well-known, e.g., layer 6 corticothalamic projections (Da Costa and Martin, 2009), the outflow pattern of the AII cell is unique in its scope and nature. Reconstruction and tabulation of synaptic flow in a single AII amacrine cell was achieved by Strettoi et al. (1992). These TEM studies of AII amacrine cells described an architecture and synaptic partnerships that still cannot be explained by or predicted from physiological data. Conversely, while some features of AII cell connectivity broadly predict its physiological responses, no complete model emerges from these anatomical data. On balance and despite its extensive analysis, the evolution, functional scope and connectivity of the AII amacrine cell remains unclear.

Why do we care about the AII cell at all if alternative paths bypass rod bipolar cells? Put simply, AII paths dominate scotopic vision and appear to set the scotopic threshold. Alternative paths access cone bipolar cells via presumably weaker paths, e.g., small gap junctions between rods and cones (Massey, 2008) or sparse direct contacts with OFF cone bipolar cells (Devries and Baylor, 1995; Soucy et al., 1998; Tsukamoto et al., 2001; Pang et al., 2010, 2012) or ON cone bipolar cells (Tsukamoto et al., 2007; Pang et al., 2010). AII and rod bipolar cells comprise a great fraction of their cognate groups and vastly outnumber those OFF bipolar cells thought to receive rod input (Pang et al., 2012). The AII network has a unique mechanism for achieving the high sensitivity characteristic of mammalian scotopic vision (e.g., Saszik et al., 2002; Frishman, 2006). Finally, threshold scotopic OFF responses of retinal ganglion cells are blocked by strychnine, implying a dominant glycinergic drive, consistent with the key role of AII

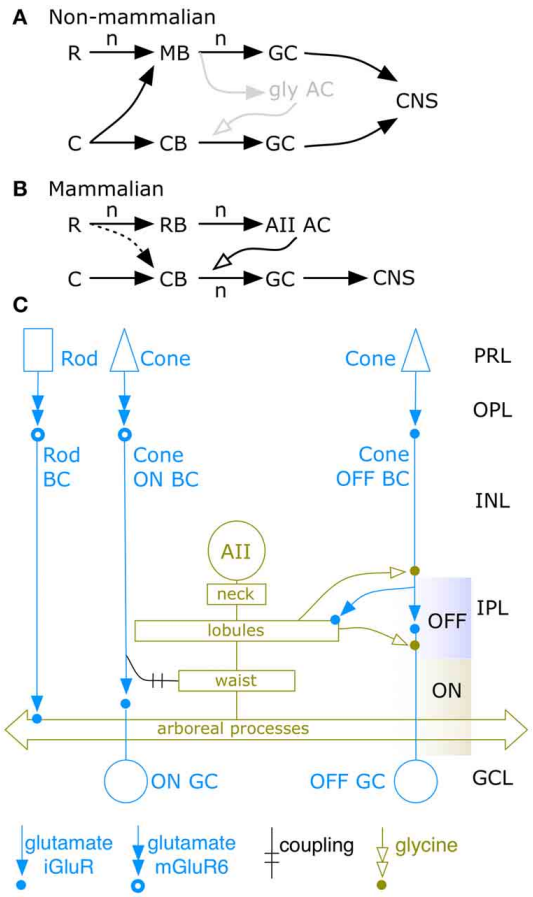

FIGURE 1 | Basic AII cell networks. Vertebrate rod R and cone C signal convergence patterns onto bipolar cells, amacrine or ganglion cells, and CNS targets. **(A)** Non-mammalian networks display two channel types: pure cone bipolar cell (CB) and mixed rod-cone bipolar cell (MB) channels that drive sets of retinal ganglion cells (GC) projecting to CNS targets via high gain (n) glutamate signaling (black arrows). The non-mammalian rod to GC chain has a net gain of n^2. **(B)** Mammalian networks display separate CB and rod bipolar cell (RB) channels. Only CB channels drive GCs. RB channels drive only amacrine cells (ACs), in particular the AII AC that provides low gain coupling or glycinergic signaling (open arrow) from the third stage back to stage two in the CB chain. The mammalian rod to GC chain has a net gain of n^3. There is evidence for sparse rod signal leakage into the CB chain. The gray glycinergic (gly) motif in **(A)** is the hypothetical evolutionary precursor of the mammalian AII AC. **(C)** The classic AII amacrine cell network, *circa* 1992. The rod input is collected by rod bipolar cells (Rod BC) which drive AII cells by ionotropic glutamate receptors (iGluRs). Cone input is collected by OFF cone bipolar cells (OFF BC) that also sparsely drive AII cells by iGluRs. The AII network is extensively coupled to ON cone bipolar cells. Glycinergic output from the AII network targets OFF BCs and OFF ganglion cells (OFF GC).

cells in the network (Muller et al., 1988; Arman and Sampath, 2012).

The rod::cone coupling pathway is nominally shared across vertebrates (e.g., Attwell et al., 1984) but there is no evidence that it accounts for the high scotopic sensitivities of mammals. Further, rod convergence onto bipolar cells in mammals is not homologous to the mixed rod-cone bipolar cell cohorts of non-mammalians. The mammalian retina is rod dominated but rod contacts with OFF bipolar cells (**Figure 1B**) are sparse (Tsukamoto et al., 2001) and can even be missing within target OFF bipolar cell classes (Li et al., 2010). Rod input to OFF cone bipolar cells in mammals also appears restricted to a one class of bipolar cell in mouse (Pang et al., 2012) and appears constrained to flow to only a subset of target ganglion cells (Devries and Baylor, 1995; Wang, 2006). In contrast, ectotherms exhibit multiple classes of rod-dominated bipolar cells (**Figure 1A**) that have precise amounts of cone input (Scholes and Morris, 1973; Scholes, 1975; Ishida et al., 1980). Further, the mixed rod-cone ON pathway in teleost fishes uses different transduction mechanisms for rods and cones (Grant and Dowling, 1996) with distinct positive cationic and negative anionic reversal potentials for rods and cones respectively (Saito et al., 1979). No such weighting or specific transduction appears in mammals. Thus, is it unlikely that the alternative mammalian pathways approach the sensitivity of the AII system. Mammals show high scotopic sensitivity and the sensitive STR (scotopic threshold response) waves of the mammalian electroretinogram are APB-sensitive and kinetically slow, implying the STR depends on rod bipolar cells and, likely, AII cells (Saszik et al., 2002; Frishman, 2006). The unique AII cell and its connectivity thus remains of central interest in the evolution of mammalian rod vision.

Our approach to this problem is based on automated TEM (ATEM) connectomics. ATEM connectomics enables the acquisition of rich synaptic maps by characterizing all partners and structural weights for all synapses and synapse types using connectome volume RC1. Connectome volume RC1 is a synaptic resolution ATEM dataset from rabbit retina spanning the inner nuclear, inner plexiform and ganglion cell layers of a sample field 0.243 mm in diameter. It currently contains ≈890,000 annotations; ≈600 identified neurons; 6500 conventional and 13,700 ribbon synapses; 26,000 identified postsynaptic sites, over 3800 gap junction pairs, and 2280 adherens junctions; all assembled into 8600 identified presynaptic/postsynaptic partnerships. Volume RC1 specifically contains 39 verified AII amacrine cells, 104 rod bipolar cells, ≈300 cone bipolar cells, and ≈200 amacrine cells, with processes from many more amacrine cells entering the margins of the volume (Anderson et al., 2011b; Marc et al., 2013). This provides us with the opportunity to characterize the complete AII amacrine cell morphology, synaptology, network motifs and synaptic weighting. We have reconstructed 5 cells to statistical completion with large portions of all 39 mapped. This has permitted definitions of all AII partner classes and establishes key synaptic weights for a more comprehensive model of AII cells.

MATERIALS AND METHODS

The methods for connectome RC1 have been extensively detailed by Anderson et al. (2009, 2011a,b). The RC1 dataset is freely available at connectomics.utah.edu. The associated software is available as free (SerialEM) or open-source applications (Nornir build manager, nornir.github.io/nornir-buildmanager), or via a free license (Viking and Viz web-services tools) for educational use through the University of Utah. The raw RC1 dataset is available on user-provided storage media.

TISSUE HARVEST AND PROCESSING

The retinal sample for ATEM image volume RC1 was acquired from a euthanized light-adapted female Dutch Belted rabbit (Oregon Rabbitry, OR). All protocols were in accord with Institutional Animal Care and Use protocols of the University of Utah, the ARVO Statement for the Use of Animals in Ophthalmic and Visual Research, and the Policies on the Use of Animals and Humans in Neuroscience Research of the Society for Neuroscience. At euthanasia, the eye was injected with 0.1 ml fixative with 18 gauge needle pressure relief, enucleated, hemisected, and fixed 24 h in 1% formaldehyde, 2.5% glutaraldehyde, 3% sucrose, 1 mM $MgSO_4$, in 0.1 M cacodylate buffer, pH 7.4. Dissected, isolated retinal pieces were immersed in 0.5% OsO4 in 0.1 M cacodylate buffer for 60 min, processed in maleate buffer for *en bloc* staining with uranyl acetate, and processed for resin embedding (Marc and Liu, 2000; Anderson et al., 2009). Retinal blocs were serially sectioned in the horizontal plane at 70–90 nm on a Leica UC6 ultramicrotome onto carbon-coated Formvar® films supported by gold slot grids. Optical 70–90 nm sections were captured and processed for computational molecular phenotyping (CMP) as defined previously (Marc et al., 1995; Marc and Jones, 2002) by probing with anti-hapten IgGs targeting small molecules: GABA, glycine, glutamate, glutamine, or taurine (Signature Immunologics Inc, Salt Lake City, UT). Small molecule signals were visualized with silver-intensification of 1.4 nm gold granule-conjugated goat anti-rabbit IgGs (Nanoprobes, Yaphank, NY). Optical (8-bit 1388 pixel × 1036 line frames) images were captured, mosaicked, aligned, and processed for classification (e.g., Marc and Jones, 2002; Anderson et al., 2009). Volume RC1 was bracketed by 10-section optical CMP series and intercalated every 30 sections with one CMP section. This inserted definitive molecular signals into every retinal neuron. The final dataset spanned 401 sections.

VOLUME ASSEMBLY

RC1 was created as previously described (Anderson et al., 2009, 2011b; Lauritzen et al., 2012). Briefly, the desired field on each grid was captured by SerialEM (Mastronarde, 2005; Anderson et al., 2009) using a Gatan US4000 phosphorimaging camera. Each capture field is an array of ≈1000 tiles captured at 2.18 nm resolution. Mosaics and 3D volumes were originally generated using the NCR Toolset (http://www.sci.utah.edu/download/ncrtoolset). This code has now been superseded by Nornir (nornir.github.io/nornir-buildmanager/). CMP-to-TEM registrations are operator-guided with ir-tweak software from the NCR toolset. Re-imaging for optimized resolution and section tilt is performed using using high resolution (20,000–60,000×) goniometric tilt series.

IMAGE VIEWING, ANNOTATION, AND ANALYSIS

Volume RC1 was visualized and annotated with the Viking viewer (Anderson et al., 2011a). The annotations trace 3D cell architectures as well as locations and dimensions of presynaptic, postsynaptic, adherens, and gap junction motifs as well as non-junctional touches are logged in the Viking database and visualized using VikingPlot, a compiled Matlab application that queries structure information from the annotation database and renders surfaces for display. VikingPlot exports formats for rendering of 3D data in a variety of free (e.g., Blender, blender.org) and commercial applications. The annotation database permits standard SQL queries.

IMAGE PREPARATION

Publication figure preparation followed Anderson et al. (2009, 2011b). Raw optical image data are available upon request and RC1 is public-access. Multi-modal registered optical images were max-min contrast stretched and sharpened using unsharp masking at a kernel extent of ≈540 nm. While ATEM images after NCRToolset and Nornir processing tend to have high contrast, none of the Viking ATEM data shown here except for **Figures 9B–D** have been processed. Overlay methods for combining optical and TEM images generally computed HSB values for a new image using the TEM gray scale brightness (B) and hue and saturation from (H,S) from the rgb optical image. Occasionally, fourth or fifth channels were added using alpha blending. Renderings of structures in VikingPlot were created in Matlab 2009a as described in Anderson et al. (2011b).

DATASET ANALYSIS

Every cell annotation in RC1 is a 2D disc that is the largest inscribed circle contained by the close shape of the cell's margins (typically a star domain) in a given slice. Internal structures such as gap junctions, presynaptic specializations, postsynaptic densities (PSDs), etc., are linked to a cell via child annotations: 2D discs representing the child structure's Feret diameter. These annotations, summed over slices, enable quantitative assessments of features (e.g., gap junction and PSD areas) and 3D representations of cells and child structures. These data are accessed via Viking Viz (Anderson et al., 2011a) or Microsoft SQL queries. Large queries were exported as delimited text files. We used AnalystSoft, StatPlus:mac (www.analystsoft.com) for statistics and histogramming.

RESULTS

BASIC ATTRIBUTES OF AII CELLS

The analysis of AII cells in RC1 includes (1) mapping all AII somas and domains, (2) complete 3D reconstruction of five specific AII neighboring cells (cells 410, 476, 514, 2610, and 3679), (3) classification of contacts with AII cells, and (4) mapping all synapses and gap junctions made by discrete AII cells. Volume RC1 contains 39 AII cells (**Figure 2A**) corresponding to a density of 841 cells/mm^2 with a center-to-center tile spacing of 34 μm. The nearest-neighbor soma-to-soma spacing is 30 ± 8 μm (mean ± 1 standard deviation, $n = 39$ pairs), consistent with the fact that somas are rarely positioned over the center of a Voronoi tile (e.g., **Figure 3B**) and the average jitter is about 10%. Five AII cells were selected for detailed analysis (**Figure 2B**).

AII cells in RC1 have distinctive features that enable unambiguous classification. They are narrow field glycinergic amacrine cells with somas of ≈8–10 μm in breadth and thick necks ≈5–8 μm in diameter that extend deeply into the inner plexiform layer (**Figure 3C**). The neck is a target of four to six large synapses from TH1 dopamine/glutamate neurons (Anderson et al., 2011b) and also extends five or six thin stalks

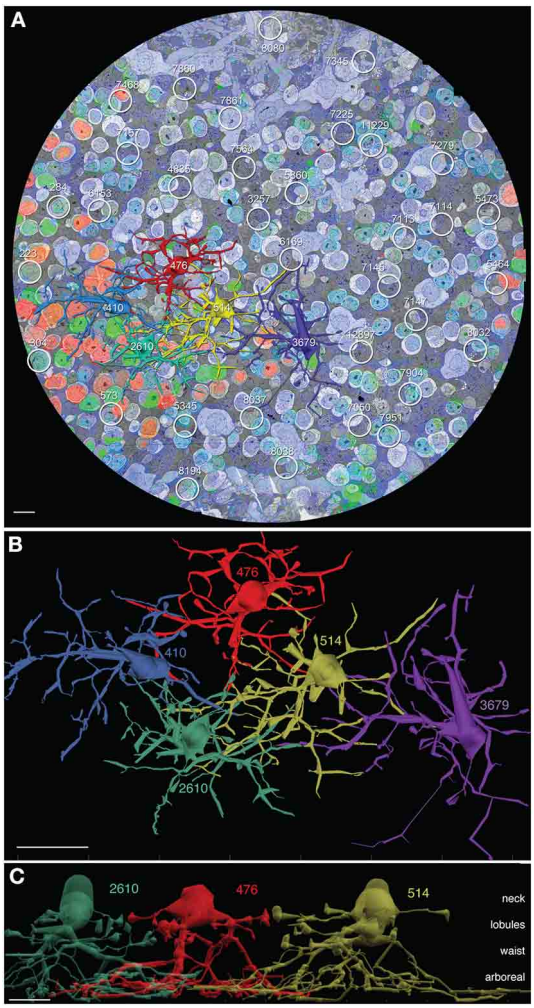

FIGURE 2 | AII cells in connectome RC1. (A) Slice z001 with 5 channel molecular overlay (see Anderson et al., 2011b), 5 rendered AII cells (410 blue, 476 red, 514 gold, 2610 green, 3679 purple) and 34 other AII loci indicated by circles. **(B)** Top view (XY plane) of VikingPlot rendered AII amacrine cells. **(C)** Side view of AII amacrine cells 2610, 476, and 514 laterally displaced to reveal the neck, lobule, waist, and arboreal zones. Scales **(A,C)** 10 μm; **(B)** 20 μm.

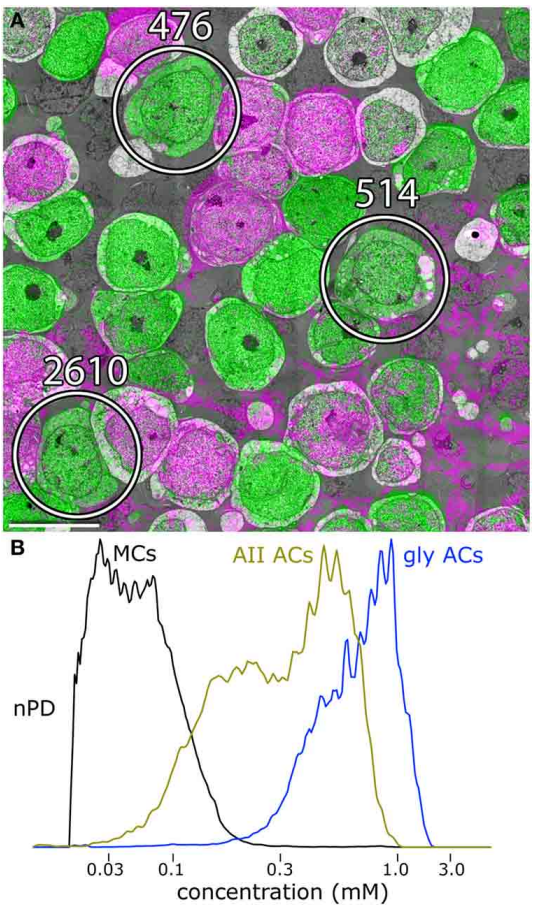

FIGURE 3 | Glycine and GABA signals in amacrine cells. (A) Slice 030, volume RC1. Three of the AII amacrine cells are marked. The gray space in between cells is filled with glial Müller cell processes. The pale gray cells are bipolar cells. Scale 10 μm. **(B)** Glycine content histograms distinguish AII cells from other retinal cells. The glycine content of AII cells (AII AC, gold trace) is about 2-fold lower than all other glycinergic amacrine cells combined (gly ACs, blue trace), but over 20-fold higher than signals in glial Müller cell (MCs). The histograms each represent aggregate signals from 25 cells calibrated as described in Marc and Jones (2002) and displayed as normalized probability density (nPD) vs. pixel value scaled as concentration.

that extend about 10–20 μm laterally and form irregular synaptic vesicle-rich lobules, often prolate in shape with a major axis of ≈3 μm and a minor axis ≈2 μm. At the base of the neck, four or five thick arboreal dendrites emerge and can branch once or twice, forming a conical waist about 30 μm in diameter as they descend obliquely the inner plexiform layer to the proximal margin where rod bipolar cells provide direct synaptic input over a field ≈60 μm wide. Each of these zones, the neck, lobules, waist, and arboreal terminal branches, have distinctive connectivities that are zone-specific, not merely encounter-specific. We will discuss this more extensively below. But, as an example, rod bipolar cell axons touch AII lobules in passage yet never form the connections that are found between AII arboreal processes and rod axons or axon terminals.

AII cells are glycinergic, maintaining ≈0.6 mM cytoplasmic glycine. Volume RC1 is supported by capstone and intercalated ultrathin optical sections with an array of molecular markers. **Figure 3A** shows a small section of slice 030 of the inner nuclear layer displaying glycine (green) and GABA signals (magenta) in adjacent amacrine cells. Every AII cell was validated for glycine content by population histograms (**Figure 3B**). High contrast optical maps of small molecule signals are compliant with ATEM connectomics and significantly assist in tracking neural features (Marc and Liu, 2000; Jones et al., 2003; Anderson et al., 2011b; Lauritzen et al., 2012). Annotation of individual processes often intersects one of the intercalated molecular channels, enabling confirmation of identity, even at the limits of optical resolution. **Figure 4** is a set of direct Viking images of serial sections through

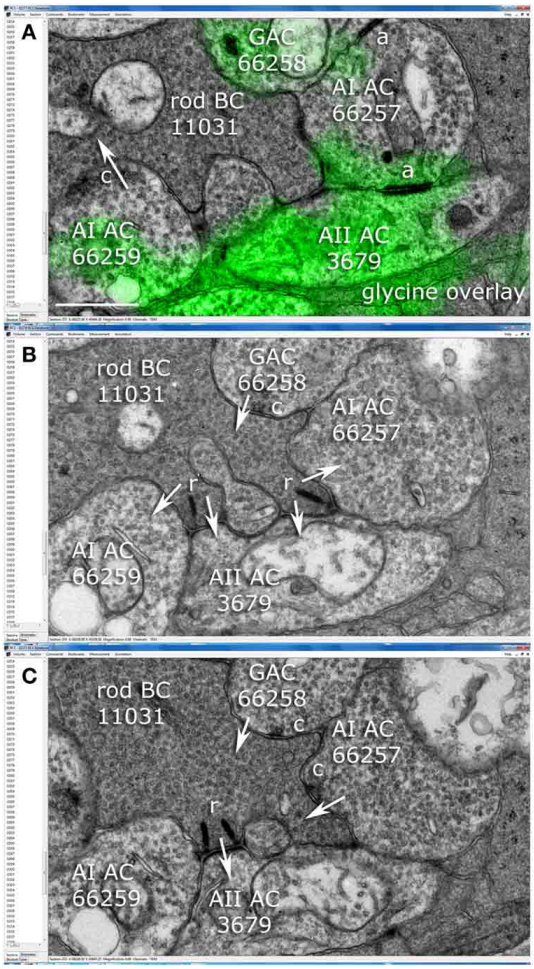

FIGURE 4 | Synaptic relationships among amacrine and rod bipolar cells in the Viking connectome viewer. (A) Slice z277: overlay of glycine channel and TEM. AI cell 66257 forms adherens junctions (a) with AII cell 3679 and glycinergic amacrine cell (GAC) 66258. AI cell 66259 forms a conventional synapse (c) onto postsynaptic target (arrow) rod bipolar cell (rod BC) 11031. **(B)** Slice z274: Rod BC forms two synaptic ribbons (r) onto postsynaptic targets AII 3679, AI 66257 and AI 66259.GAC 66258 is presynaptic to rod BC 11031. **(C)** Slice z272: rod BC forms a third ribbon with AII 3679 and AI 66257 forms a feedback synapse. Scale **(A)**, 500 nm.

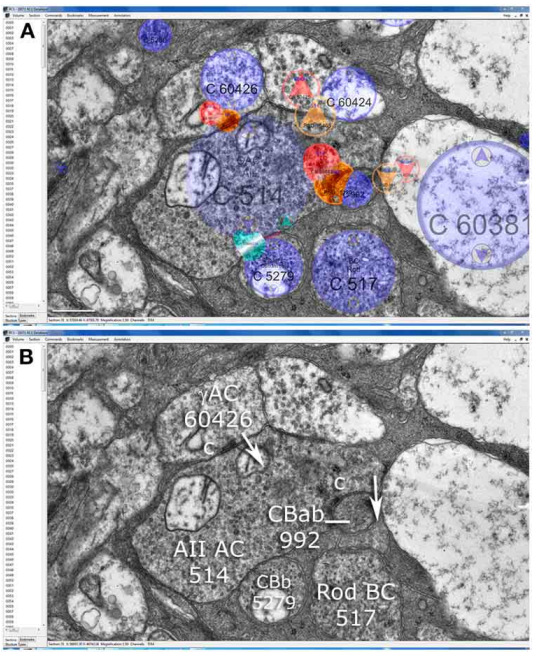

FIGURE 5 | Synaptic patterns of AII cell lobules in the Viking connectome viewer. (A) Slice z71 showing annotation overlays for cells (blue), presynaptic elements (red), postsynaptic elements (orange) and touches (cyan). **(B)** A lobule from AII cell 514 is presynaptic to OFF cone bipolar cell CBab 992, postsynaptic to GABAergic amacrine cell (γAC) 60426, and touches ON cone bipolar cell CBb 5279 without making any other specialization. Scale **(A)**, 500 nm.

an AII cell arboreal dendrite as at traverses the surface of a rod bipolar cell. In slice z277 (**Figure 4A**), a strongly glycine positive arboreal dendrite of AII amacrine cell 3679 approaches one of its target rod bipolar cells (rod BC 11031), as well as a cluster of other amacrine cells. Notably, every AII cell makes large adherens junctions with AI amacrine cells (e.g., AI AC 66257), despite their structural and molecular diversities. As AII 3679 passes rod bipolar cell 11031, it makes three ribbon synapses in a span of 200–250 nm (z274 **Figure 4B**, z272 **Figure 4C**). This ribbon cluster also targets two AI cells, one of which is presynaptic to the rod bipolar cell in a classic reciprocal feedback motif. Nearby, a cone-driven glycinergic amacrine cell GAC 66258, part a major cone → rod crossover motif, is presynaptic to the rod bipolar cell.

AII cells display their only synaptic output at the level of the synaptic lobules (**Figure 5**), which maintain vesicle densities as high as retinal bipolar cells (1488 ± 171 vesicles/um^3, mean ± 1 standard deviation, $n = 7$ lobule sections excluding organelle volumes). The dominant targets of lobules are OFF cone bipolar cells, although AII cells also target specific OFF driven amacrine and ganglion cells (summarized below). AII lobules are complete integration sites as they are postsynaptic to OFF cone bipolar cells and several classes of GABAergic and glycinergic amacrine cells (Anderson et al., 2011b). However, as shown below, the amacrine cell input dominates by far and a typical AII cell can have has few as 3 OFF bipolar cell inputs or as many as 10. Finally, a distinctive feature of AII cells is their extensive homocellular and heterocellular coupling through large gap junctions made by their arboreal processes. Visualization of gap junctions requires at least 2 nm resolution. **Figure 6** displays a triple gap junction complex formed by three of the mapped AII cells in this study. Coupling sites are always accompanied by distinctive adherens complexes. Heterocellular gap junctions are made between AII cells and a range of ON cone bipolar cells (Kolb and Famiglietti, 1974; McGuire et al., 1984; Strettoi et al., 1992; Anderson et al., 2011b; Marc et al., 2013).

LARGE SCALE PARTNERSHIP MAPPING

Mapping complete synaptic contacts is straightforward and the five AII cells contact between 9 and 17 rod bipolar cells (11.8 ± 3.3

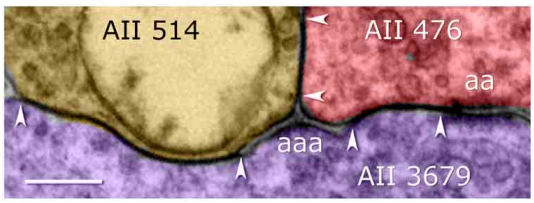

FIGURE 6 | Coupling among arboreal processes of AII cells in the Viking connectome viewer. Contiguous gap junctions between arrowheads range 200–500 nm in extent. All gap junctions are accompanied by dual (aa) or triple (aaa) adherens junctions. Scale, 200 nm.

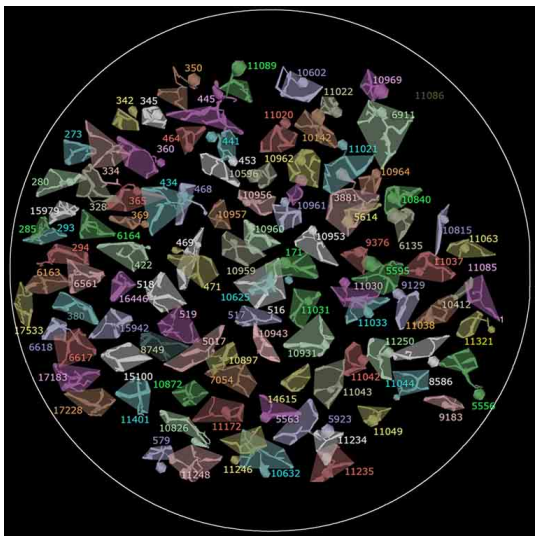

FIGURE 7 | The array of all 104 rod bipolar cell axonal fields in RC1. The shaded polygon represents the convex hull for each cell. In some cases the soma and axon extend at an angle away from the axonal field and are not included in the hull. Circle scale, 0.25 mm.

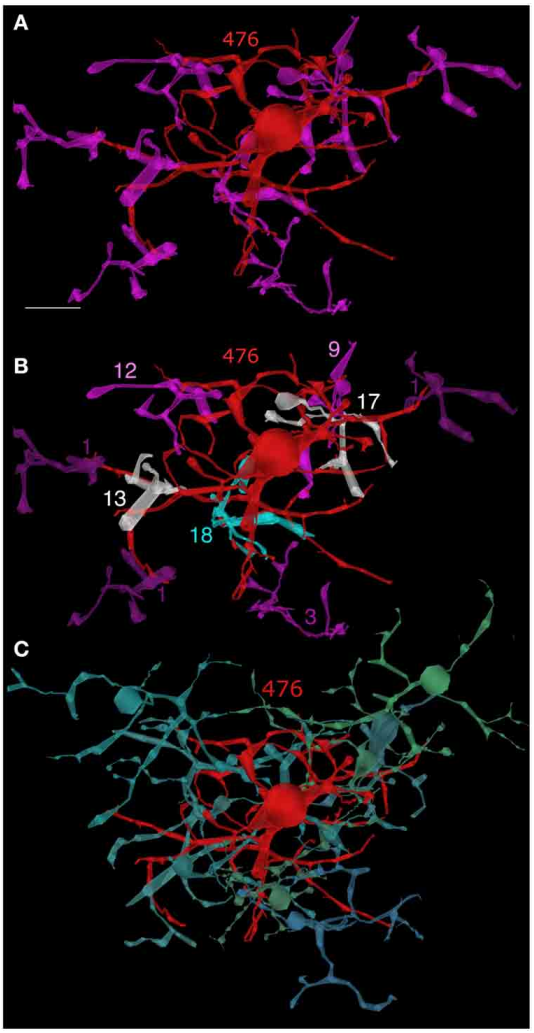

FIGURE 8 | AII cell 476—bipolar cell clusters. (A) AII cell 476 (red) contacting nine rod bipolar cells (magenta). **(B)** Contact weights: 1 ribbon (dark purple), 3 ribbons (purple), 9–12 ribbons (magenta), 13–17 ribbons (white), 18 ribbons (cyan). **(C)** AII cell 476—ON cone bipolar cell clusters. Eight ON cone bipolar cells representing five of the eight known classes make multiple gap junctions with AII 476. Scale, 10 μm.

SD, 0.28 coefficient of variation, CV). Their ribbon sampling is 7-fold more precise, however, averaging 75.6 ± 3 ribbons per AII cell with a CV of 0.04. Rod bipolar cells (**Figure 7**) are also precise in ribbon expression, with 31 ± 3.9 synaptic ribbons/bipolar cell ($n = 27$). The variation in rod bipolar cell contact seems to be completely geometric, representing the overlap of AII arboreal dendrites with rod bipolar cell axonal domains (**Figures 8A,B**). This difference in precision between cell sampling and synapse sampling is powerful. For a sixth AII cell to increase the synaptic CV to match the cell sampling CV, it would have to have a ribbon sampling rate 20 SDs larger. Conversely, for AII cell sampling to be as precise as synaptic sampling, the next 20 ACs counted would have to have SDs of zero. This argues that AII cells count synapses, not cells.

When AII amacrine cells encounter other cell classes, they make or decline connections by clearly stereotyped rules in their different compartments. The 39 AII amacrine cells in RC1 encounter each of 104 rod bipolar cells in multiple instances at multiple levels of the inner plexiform layer. Their arboreal dendrites are always postsynaptic to rod bipolar cells and never presynaptic, in 777 verified encounters from 1246 ribbons. And when lobules encounter rod bipolar cell axons in transit (in 6 validated instances) no ribbon contacts are formed, despite the fact that both rod bipolar cells do make axonal ribbons and will make synapses with AII arboreal dendrites high in the ON layer (Lauritzen et al., 2012). More importantly, AII cells can always distinguish between rod and ON cone bipolar cells by never making gap junctions with rod bipolar cells in the same encounters, and making gap junctions with every validated ON cone bipolar cell ($n = 172$ validated AII-CBb encounters). Similarly, AII lobular dendrites have their own rules. In contacts with 180 different OFF cone bipolar cells, they are presynaptic, postsynaptic, or both, but never form gap junctions, despite the fact that AII and CBa cells both express connexins. And while AII cell arboreal

processes make extensive gap junctions with each other at every encounter ($n = 525$), rare instances of direct lobule-lobule contact ($n = 6$) do not show coupling, suggesting that AII connexins are excluded from lobules. Declined connections are more difficult to track, as they require first documenting a "touch" and then tracing both processes to ensure that a contact is not made elsewhere. By tracking the arboreal dendrites of AII cells in validated 11 touches with ganglion cells spanning many microns each, AII cells made no specializations (adherens, gap junctions, or synapses). In contrast, we have tracked an OFF α ganglion cell dendrite as it traversed the entire RC1 volume, encountering 23 separate AII lobules from 12 validated AII cells in its path. AII lobules also make abundant synapses onto verified GABAergic amacrine cells. Every lobule was presynaptic to the OFF α ganglion cell. But when lobules encounter AI GABAergic amacrine cell processes in the OFF layer (12 validated instances so far), they never make synapses, even though AI and AII amacrine cells make large adherens junctions at the arboreal level (**Figure 5A**). If we define AII contact errors as making gap junctions with rod or CBa bipolar cells, receiving ribbon from a CBb cell (with the exception of the CBb7 cell, described below), failing to accept ribbons from rod bipolar cells, or any variation of other detailed associations, we have documented 1773 proper connections (fully identifying both AII cells and the target cell) and 0 improper connections. We have also annotated and additional 3067 contacts between AII cells and targets not yet fully traced. In no case have we documented an obviously aberrant connection. These data suggest that AII cells are effectively errorless in executing their connectivity rules.

The interactions between AII cells and all other classes of neurons are too extensive to detail cell-by-cell, but can be tabulated (**Table S1**) and graphically summarized. There are 17 sign-conserving input partners to AII cells: nine glutamatergic and eight coupling. Volume RC1 contains at least six distinct classes of OFF cone bipolar cells and seven classes of ON cone bipolar cells (Marc et al., 2013, 2014) and all of them display partnerships with AII cells. All classes of OFF cone bipolar cells are both presynaptic and postsynaptic to AII cells, with postsynaptic events dominating by over 5-fold. Importantly, a single AII cell rejects input from most OFF bipolar cells and only a few ribbon inputs are permitted (see below).

All classes of ON cone bipolar cells are coupling partners with AII cells, but only in the waist or arboreal zone. **Figure 8C** displays the eight ON cone bipolar cell partners of AII 476, each of which forms multiple gap junctions with the AII at 28 sites: CBb3 6155 (1 gap junction), CBb3 4569 (9), CBb4w 170 (2), CBb4w 324 (1), CBb5w 483 (2), CBb4-5i 6156 (2), CBb5-6i 419 (8), CBb5-6i 4570 (3). While rod bipolar cells dominate the ON polarity input, wide-field, probable blue-sensitive (see Famiglietti, 2008) CBb7 bipolar cells are also presynaptic to AII cells and are unique in also being coupled via gap junctions (**Figures 9A–D**), which puts them in a position of being sparse amplifiers. We have partly analyzed seven CBb7 cells from a cohort of a dozen candidate cells that arborize close to the rod bipolar cells and are not part of the CBb3, 4, or 5 sheets. Every cell makes 1–3 three ribbon synapses and 2–7 gap junctions with neighboring AII cells (CBb 180 → AII As depolarizing rod signals invade CBb7 cells through gap junctions, they can immediately reinforce the signal with synaptic glutamate release. The significance of this small sample is nevertheless high: over 200 mapped non-CBb7 cone bipolar cells never make ribbon inputs AII cells despite making extensive numbers of gap junctions. Conversely all 7 CBb7 cells do make ribbons inputs (Komolgorov–Smirnov, $\alpha = 0.01$, $p = 5 \times 10^{-7}$).

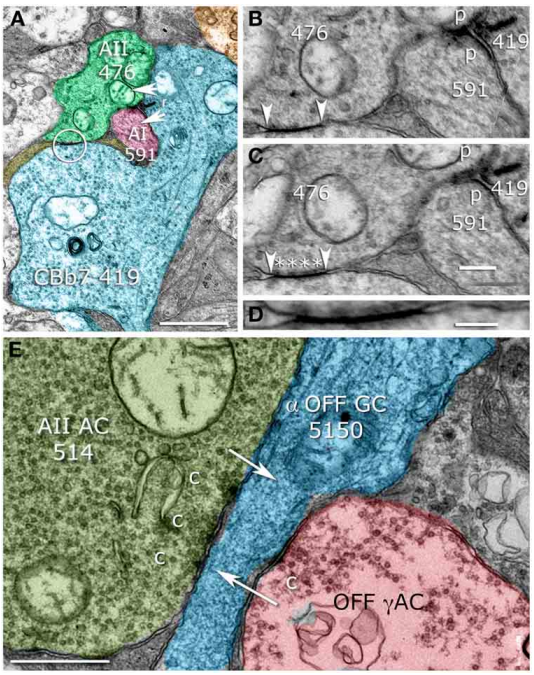

FIGURE 9 | Sparse AII cell contacts. (A) CBb7 419 forming both ribbon synapses (r) and a gap junction (circle) with AII cell 476. CBb7 419 also contacts AI cell 591. **(B,C)** Serial sections through the ribbon synapse and its postsynaptic targets (p) and the gap junction (arrowheads) with characteristic AII cell cytoplasmic densities (Anderson et al., 2011b), asterisks. **(D)** Maximal resolution image of the gap junction showing apparent membrane fusion. **(E)** AII cell 514 making a multi-projection conventional presynaptic specialization (c) targeting OFF ganglion cell 5150 (arrow). Scales **(A,E)** 500 nm; **(C)** 250 nm, **(D)** 100 nm. **(B–D)** Were contrast adjusted to $\gamma = 1.5$ to discriminate gap junction membranes and cytoplasm.

Finally, the dominant dopaminergic neuron of the mammalian retina is the TH1 (tyrosine hydroxylase positive type 1) axonal cell. It is also a glutamate neuron that is presynaptic to the neck region of AII amacrine cells (Anderson et al., 2011b) through very large synapses. The TH1 inputs are significantly larger than the aggregate OFF cone BC inputs and may dominate the photopic ON response of AII cells. This collection of sign-conserving inputs makes the AII cell a formal network hub, but the key to its function lies in synaptic weighting.

Inhibitory input to AII cells spans the retina and includes GABAergic amacrine cells of both OFF and ON varieties, and glycinergic ON and possible glycinergic ON-OFF amacrine cells. At least two classes of GABAergic OFF cells target AII lobules. While it is possible that some of the GABAergic input is also from ON-OFF cells, we have identified several classes of GABAergic ON-OFF amacrine cells that touch but explicitly fail to make any synaptic partnerships with AII cells. So, on balance, it appears that

the GABAergic drive largely comes from monophasic cone-driven ON or OFF ACs. We have not dissected the weighting analyses of these subgroups, which will take at least another year of annotation, but they outnumber OFF bipolar cell ribbon synapses by >5-fold and outweigh them in synaptic area by >10-fold. Arboreal dendrites are targeted by GABAergic ON cells driven by cone bipolar cells as well as GABAergic AI amacrine cells in a feed-forward motif. There are also narrow-field glycinergic amacrine cell inputs to arboreal dendrites from cone-driven ON and possible ON-OFF amacrine cells. Collectively, the inhibitory drive of the arboreal dendrites represents a cone → rod path inhibitory crossover; part of a collection of networks enabling cone signals that may suppress rod signals in the mesopic transition (Marc et al., 2013).

The synaptic outputs of AII cells are completely restricted to the lobules and target all OFF cone bipolar cell classes; GABAergic and glycinergic OFF amacrine cells that are also presynaptic to AI amacrine cells at large inhibitory sites on the proximal AI dendrites (Anderson et al., 2011b); and the dendrites of selected classes of retinal ganglion cells: specifically OFF α and δ ganglion cells (e.g., **Figure 9E**). These ganglion cell dendrites are very sparse and not every lobule encounters one. In contrast, every lobule encountered by these specific ganglion cells makes a synapse.

Even with this diversity, we can develop a summarization of signal flow in the AII system. One approach involves mapping all the synapses associated with AII cells into five categories: rod bipolar cell input, off bipolar cell input, amacrine cell synaptic input, coupling and AII synaptic output. **Figure 10** summarizes these partnerships for AII cell 2610 in dimensionally correct 3D positioning throughout the inner plexiform layer. Combining such partnership maps for all five cells generates a comprehensive view of the major signal flow architecture for the AII system. By aligning and superimposing all partnerships in the lateral XZ view (Z spans the IPL), the combined stratification profiles can be visualized (**Figure 11A**) and extracted into separate components on the same scale: outputs and coupling (**Figure 11B**), inputs (**Figure 11C**), and a summary of lateral spread (**Figure 11D**). The simultaneous visualization of outputs (blue) and coupling (yellow) demonstrates that the differential trafficking and functional assembly of presynaptic proteins for vesicle release into lobules and connexins for coupling into the waist and arboreal dendrites is errorless and defines the border between OFF (blue) and ON (yellow) layers of the inner plexiform layer, as first proposed by Kolb and Famiglietti (1974). And what we mean by errorless is that every CBb cell (>200 CBb cells making >1000 gap junctions) is always coupled to the AII cells it contacts, whereas no rod bipolar or CBa cell (>100 each) ever makes a gap junction. Similar counts can be had for all other classes of contacts. These inputs can be stratified into three simple zones (**Figures 11B,C**): excitatory ON inputs from TH1 cells (cyan), inhibitory OFF inputs (green), inhibitory ON inputs (red), and excitatory rod bipolar cell inputs (magenta). These can be further refined into finer classes but, for now, this analysis demonstrates

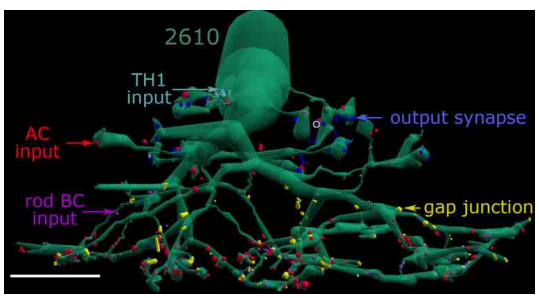

FIGURE 10 | AII cell partnerships. AII cell 2610 with its rod bipolar cell input (magenta), amacrine cell input synaptic input (red), coupling sites (yellow), TH1 cell input (cyan), and glycinergic synaptic output (blue) dimensionally mapped onto its surface. Small white dots are adherens junctions. A single visible OFF cone BC ribbon is marked with a white circle. Scale, 10 μm.

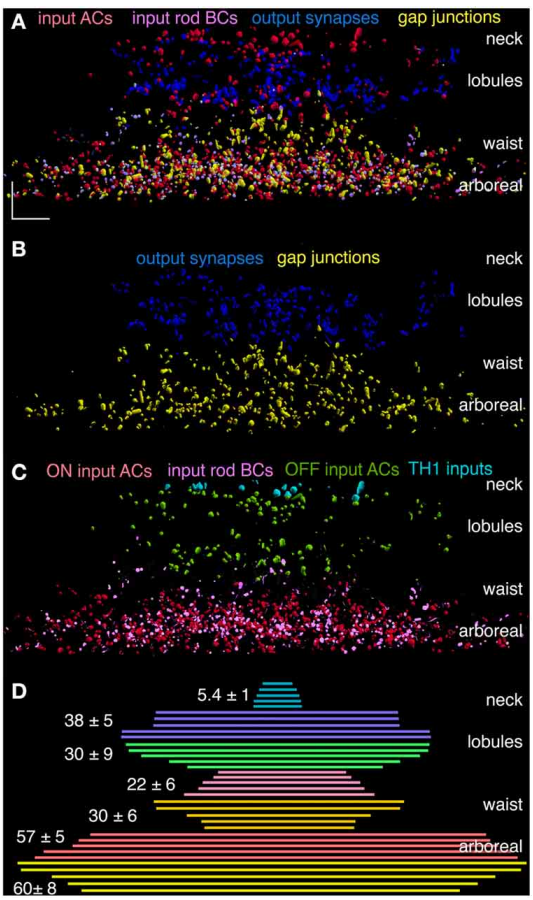

FIGURE 11 | Combined partner distributions for AII cells 410, 476, 514, 2610, and 3679. (A) Superimposed AC synaptic input (red), rod BC ribbon input (magenta), coupling (yellow) and synaptic output (blue) mapped onto its surface with stratified anatomical features. **(B)** Outputs and coupling are completely segregated. **(C)** Inputs can be parsed into TH1 cell ON (cyan), OFF inhibition (green) and ON excitation (magenta) and ON inhibition (red). OFF excitation is so minimal that it is not visible in the plots. **(D)** The lateral extents of key stratified zones for each cell are centered and superimposed with the mean ± 1 SD width at left. The larger spread for the neck in C is caused by the misalignment of cell bodies with the center of the dendritic arbor. XY Scale, 10 μm.

how we can weight synaptic data from connectomics to build neuronal models. Weighting may require spatial rules as well, and by summarizing the lateral spread of each component we see that the interaction zones of the lobules and the waist are much narrower than the arboreal system. In fact, the lobular radius is only half the distance between cells, resulting in coverage of synaptic space without redundancy. Thus, the distal portion of the AII cell tiles retinal space and its lobules form a sampling grid with an approximate 10–15 μm spacing. The waist and neck subtile the space and their partnership patterns reflect the aggregation of wide-field TH1 cell signals, and the coupled ON cone bipolar cell network (Lauritzen et al., 2013). Finally the arboreal dendrites represent a center-to-center spatial covering, rather than a tile, with an ideal coverage factor of 4 (arboreal area/single cell area), which predicts that every AII cell should be 8-connected in a 2D grid. The measured homocellular coupling for eight AII cells whose arboreal dendrites have been completely mapped is 7.6 ± 0.9 partners.

These data can be summarized as synaptic area weightings (**Figure 12**). Partnership patterns were converted to binary images, capturing the location, number, and sizes of contacts, and profiled across the inner plexiform layer by averaging with over the width of the image. This computes the area of an input, coupling or output site and provides the spatial weights for modeling such connections. Based on prior descriptions of AII cells, we were surprised at first to find that inhibitory synapses (mostly ON GABAergic input) dominate the drive, but this is consistent with patterns of signal flow bipolar cells as well (Marc and Liu, 2000). The area of ON amacrine cell input is ≈8-fold higher that rod bipolar cell ribbon input. The integrated AII::AII coupling is approximately 6–7 μm^2 while AII-CBb coupling represents ≈1 μm^2. The lobular domain is dominated by output synapse areas, with minor OFF amacrine cell input and negligible OFF bipolar cell input. Finally the neck region is an approximate 1:1 mix of OFF amacrine cell and TH1 presumed ON synapses. Thus, the TH1 ON excitation is ≈1/3 the ON coupling excitation area.

We can also parse the strengths of individual gap junctions for homocellular AII::AII and heterocellular AII::CBb coupling. The RC1 database includes includes 525 AII::AII and 172 AII::CBb coupling instances (**Figure 13**), with a mean ± 1 SD gap junction diameter of 267 ± 95 nm for AII::AII and 238 ± 95 nm for AII::CBb pairings. The mean for heterocellular coupling is only about 11% smaller, but due to the large sample size is still highly significant (2 tailed homoscedastic t-test, $p = 0.00052$). More to the point, however, the largest gap junctions made by AII::AII

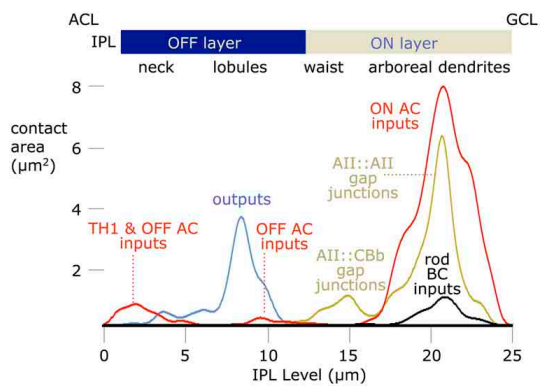

FIGURE 12 | Contact area profiles. Contact areas were computed at every level of the inner plexiform layer (IPL), where 0 is the amacrine cell layer (ACL), and 25 is the ganglion cell layer (GCL). The ordinate scales presynaptic (outputs), postsynaptic (inputs) or gap junction contact areas for a typical AII cell. The abscissa is the depth of the inner plexiform layer. were computed for a lateral traverse through every level of the inner plexiform layer (IPL), where 0 is the amacrine cell layer and 25 is the ganglion cell layer.

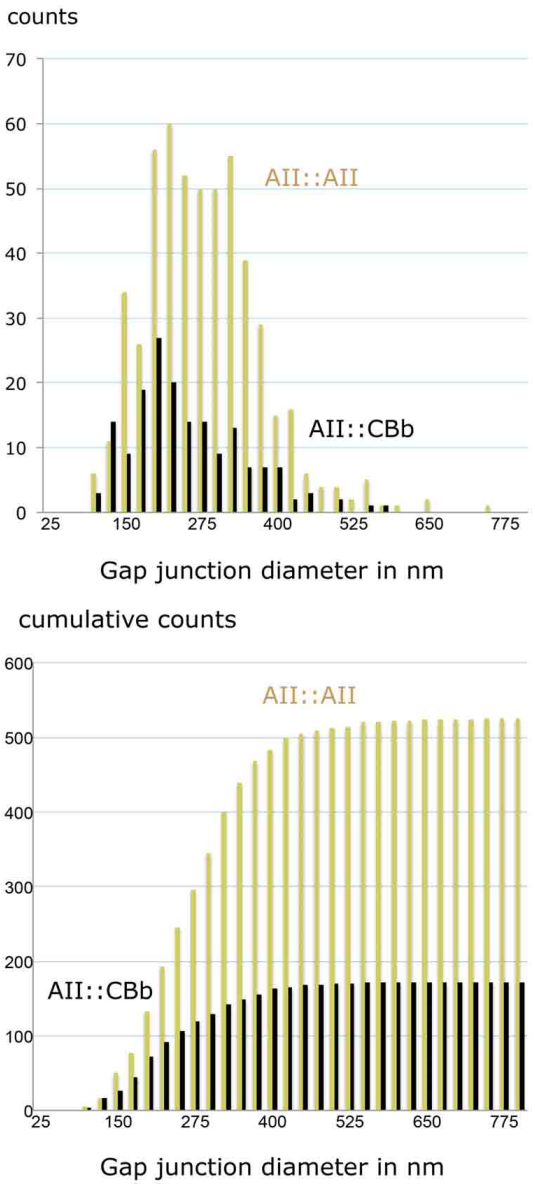

FIGURE 13 | Gap junction partnerships with AII cells. Top, size distribution. **Bottom**, cumulative size distribution. Both histograms are binned in 25 nm increments. The cumulative frequency histograms are significantly different (Komolgorov–Smirnov, $p = 0.0002$).

pairings (745 nm) are 20% larger than made in AII::CBb pairings (592 nm) and the cumulative frequency distributions are significantly different. This corresponds to a 60% larger area for the largest homocellular versus heterocellular AII cell gap junctions.

DISCUSSION

THE AII CELL IS A DENSE HUB

The partnerships of AII cells (**Table S1**) establish it as a network hub of high density and complexity. The AII cell contacts *every* retinal bipolar cell, which requires recognizing 15 cell classes with four differential contact rules: (1) exclusively postsynaptic for rod bipolar cells; (2) exclusively coupling for most CBb ON cone bipolar cells; (3) mixed coupling and postsynaptic for CBb7 bipolar cells; and both presynaptic and postsynaptic for all CBa OFF bipolar cells, albeit sparsely. Within the arboreal dendrite zone, AII cells can distinguish between rod and cone ON bipolar cells without error, being postsynaptic for the former and coupled to the latter. Further, the putative blue selective CBb7 makes both synapses and gap junctions, supporting the notion that unique bipolar cell surface markers facilitate synapse formation and that contact type and weight is a deterministic, not a stochastic process. This specificity, precise weighting, and consistent topology across AII is the antithesis of adjustable functional weighting of networks to compensate for variable connectivity (Prinz et al., 2004).

In detail, our conclusions regarding the numbers and variances of rod bipolar cells contacting a single AII cell are different from measurements of Tsukamoto and Omi (2013) in mouse, where their coefficients of variation (CV) are very similar for either number of rod bipolar cells or ribbon synapses contacting AII cells. This is almost certainly due to the small span of both mouse rod bipolar cell terminals and AII cells in the mouse ($\approx$10 μm), while rabbit rod bipolar cell terminals span 20–30 μm and AII cells span 70 μm or more, meaning that a single rod bipolar cell is unlikely to dominate connectivity. Thus, it is quite unlikely that randomly placed AII cell in rabbit will have low CV. This provides a robust test for synaptic precision, which in rabbit is revealed to be high (very low CV).

Further, All afferent signal flow from photoreceptors is shaped by the AII transfer function. The 28 cell classes make 36 kinds of contacts, which is greater than the contact diversity reported for any other cell type in any nervous system. It also understates the complexity of AII cells, as many other classes touch AII cells, but functional contact is rejected. Given that there are $\approx$60 classes of neurons in the mammalian retina (Masland, 2001; Rockhill et al., 2002), the network graph of the retina shows that all neurons are within two hops from an AII cell, and almost half are directly connected. The scope of this connectivity, in turn, makes the entire retina a small-world system (Barthelemy and Amaral, 1999), despite its obvious dependence on multiple, tuned output channels manifest as ganglion cell diversity (Marc and Jones, 2002; Rockhill et al., 2002).

Further, the contact selectivity is completely regional in the AII cell. ON cone bipolar cell axons that touch AII lobules in the OFF layer never appear to form gap junctions, while all such axons that contact AII arboreal dendrites on the ON layer do so. This prevails despite the fact the ON cone bipolar cells can make functional presynaptic and postsynaptic specializations in the OFF layer (Dumitrescu et al., 2009; Hoshi et al., 2009; Lauritzen et al., 2012). It is also certain that we have underestimated the diversity of wide-field GABAergic amacrine cell interactions.

THE NEW AII NETWORK

With this tabulation we can revise **Figure 2** to form a richer network description of AII cells (**Figure 14**). There are six separate type of sign-conserving inputs to AII cells. Starting with the neck region, TH1 axonal cells make sparse conventional synapses on AII cells. While these cells were first thought to be dual GABAergic/dopaminergic neurons, small molecule profiling in the rabbit retina establishes that they have the same signature as glutamatergic ganglion cells and definitely lack any inhibitory signature (Anderson et al., 2011b). TH1 axonal cells are predominantly ON cells (Zhang et al., 2007) and receive direct ribbon input from en passant ON cone bipolar cell axons (Dumitrescu et al., 2009; Hoshi et al., 2009; Lauritzen et al., 2012), and their effect on AII cells should be an ON transient signal. The path from cone $\rightarrow$ ON BC $\rightarrow$ TH1 AxC $\rightarrow$ AII cell is purely glutamatergic, and given that the nominal gain of each transfer is some value $n \gg 1$ (Marc et al., 2013), this synaptic chain has an amplification proportional to n^3 and may be the most sensitive photopic drive for AII cells. The low synapse number does not reduce this weighting significantly as the synaptic area is large. The second class of sign-conserving input is direct synaptic input from OFF cone bipolar cells (CBa cells) onto lobules. Despite the fact that every class of CBa cells makes some synapses onto AII lobules across the population, input to individual AII cells is low (2–5 synapses/cell) and the OFF ribbon synapse area weighting is approximately 20-fold lower than the third class of sign-conserving input, synaptic ribbons from rod bipolar cells. The fourth sign-conserving input is synaptic ribbon drive from CBb7 cells. We have begun mapping these cells and there are only seven validated cells so far in the entire RC1 volume (compared to 104 rod bipolar cells and over 200 CBb cells), as their arbors span well over 120 μm each. Nevertheless, their connectivities are unique and every one provides 1–3 ribbon inputs to a nearby AII cells. While this drive may be relatively weak compared to other inputs, it could dominate given the right stimulus conditions. The final two classes of sign-conserving input are heterocellular AII::CBb coupling and homocellular AII::AII coupling. Our profiling of gap junctions suggest that homocellular coupling is $\approx$7-fold stronger based on area than heterocellular coupling, assuming similar unitary connexin conductances. However, it appears that AII amacrine cell homocellular coupling is down-regulated by dopamine release and/or light adaptation (Mills and Massey, 1995; Bloomfield et al., 1997; Bloomfield, 2001) while heterocellular coupling is less strongly modulated. However, the regulation of AII::AII coupling may not be as simple as these early studies suggested (Hartveit and Veruki, 2012). In any case, AII::AII coupling may be attenuated in light adapted retinas, and the strength of AII::CBb coupling may become dominant. The notion that these gap junctions are differentially regulated is consistent with the fact that AII::AII coupling is completely dependent on connexin 36 (Cx36) expression, whereas

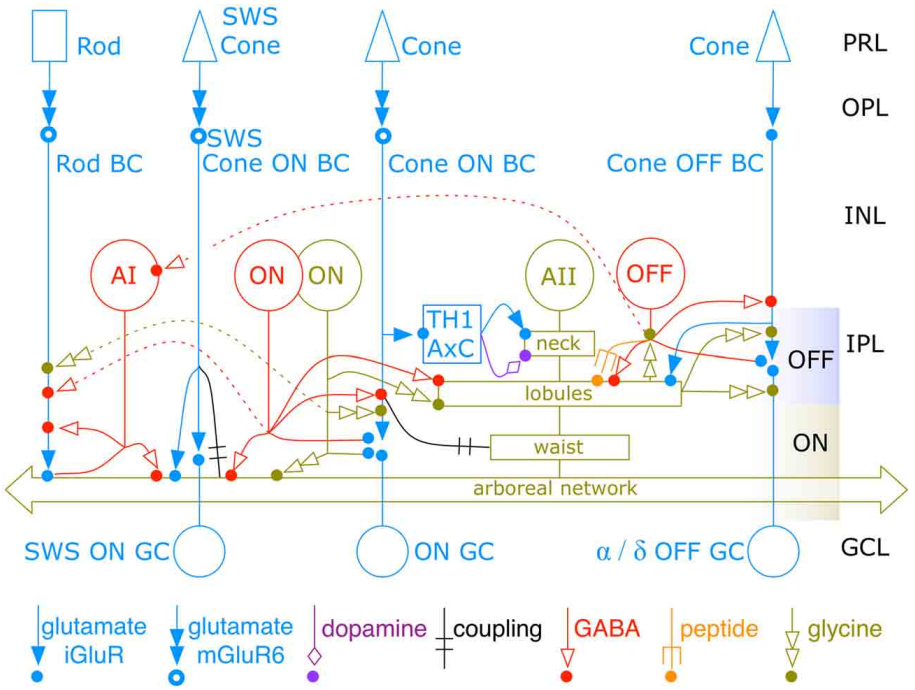

FIGURE 14 | The new AII amacrine cell network. The complete AII cell network spans 4 classes of excitatory glutamate inputs, three coupling partners, dopamine modulation, three wide-field GABAergic inputs, peptide modulation, narrow-field glycinergic input, and outputs to OFF bipolar cells, OFF inhibitory neurons and two classes of OFF ganglion cells. All classes of CBb (except CBb7) and CBa bipolar cells are lumped into single ON and OFF channels. Multiple classes of ON and OFF amacrine cells are lumped into single representative classes. Dashed lines show paths for cone → rod suppressive crossover. TH1 AxC is a dual glutamate/dopamine wide-field axonal cell. PRL, photoreceptor layer; OPL, outer plexiform layer; INL, inner nuclear layer; IPL, inner plexiform layer; GCL, ganglion cell layer. Icon key at bottom denotes connection types. The OFF band captures the AII neck and lobules, which do not overlap with neighboring AII cells. The ON band captures the waist and the heavily coupled arboreal network, which overlaps other AII cells with a coverage factor of 4. Colored dots denote postsynaptic sites for each modality.

AII::CBb coupling appears not to require Cx36 (Meyer et al., 2014).

AII::CBb coupling engages all classes of CBb ON cone bipolar cells. Thus, the physiological features of different types of CBb cells (e.g., Saszik and Devries, 2012) must readily be shared across the CBb::AII::CBb chain. How this plays out in ganglion cell drive based on targeting different bipolar cells remains to be clarified. Nevertheless, this supports a mechanistic emergence of selective connectivity patterns across cell classes, rather than a stochastic encounter-based connectivity, although whether this happens as a result of selective pruning or first intention or both remains to be resolved (Tian, 2011).

There are at least five major classes of AII interaction with inhibitory neurons. At the level of the lobules, AII cells are presynaptic and postsynaptic to two distinct classes of GABAergic feedback amacrine cells, one of which is peptidergic cell of unknown class that appears to make both conventional small vesicle and large peptide granule fusion sites on the lobules (Anderson et al., 2011b). AII lobule synaptic drive from amacrine cells is more prevalent than bipolar cell input by about 5-fold. Arboreal dndrites receive inhibition from at least three cells classes: sparse inputs from the classic AI amacrine cell and much more extensive inhibition from both wide-field cone-driven GABAergic and narrow-field glycinergic ON amacrine cells. Ultimately, each of these area weightings need to be combined with corresponding weights derived from physiological measures. The recent findings of Arman and Sampath (2012) suggest that this will be far from simple, but this is nevertheless the essential step in building a compact AII model.

We were not able to identify a unique axon-initial-segment process emerging from the AII neck as described by Cembrowski et al. (2012) using optical imaging or Tsukamoto and Omi (2013) using ultrastructure in the mouse. In rabbit AII cells, all lobular processes are long (15–20 μm), longer than the axon-initial-segment described in mouse. Every AII lobular processes displayed either large or small lobule like domains with vesicles, and both presynaptic and postsynaptic specializations. Often, one appendage was higher than most, emerging from the top of the neck, but we found no ultrastructural specialization that could be attributed to enhanced voltage-gated sodium channel expression. We noted that AII cells often display membrane densities similar to those described by Tsukamoto and Omi (2013), but have not observed that they are restricted to any compartment.

CROSSOVER

Heterocellular coupling to ON cone bipolar cells and glycinergic output to OFF cone bipolar cells appears to be a prime mechanism for redistributing amplified rod signals into cone pathways.

The threshold of OFF ganglion cells in particular appears to be set by glycine release from AII cells (Muller et al., 1988; Arman and Sampath, 2012). But these pathways (and probably others) clearly operate at photopic levels as well (Manookin et al., 2008; Münch et al., 2009). Though the ability of ON cone bipolar cells to drive lobule output from arboreal dendrite input seems probable, Arman and Sampath (2012) provide evidence in mouse against the AII → OFF BC path being a dominant control arm in the scotopic state. This is at odds with our anatomic weighting. Perhaps the scenario is different in mouse, but in rabbit, every OFF BC receives significant glycinergic input from both AII cells and other glycinergic ACs. But in mouse, OFF BC light responses show no effect of glycine blockade. OFF ganglion cells receive many fewer glycine inputs than bipolar cells, but in mouse the influence of strychnine on threshold is more potent. The explanation for this is unclear. Either glycinergic ON to OFF crossover inhibition through bipolar cells (AII → OFF BC → OFF and ON-OFF ganglion cells) or direct mechanisms (AII → OFF α ganglion cell) could be operative at the photopic level (Molnar et al., 2009; Werblin, 2010). But the addition of glycinergic drive targeting inhibitory amacrine cells (**Figure 14**) that converge on the proximal dendrites of AI amacrine cells exposes an additional role for the AII cell in cone → rod crossover suppression networks (Marc et al., 2013). This may be a mechanism for fast mesopic switching between rod and cone vision and that operates by suppressing rod bipolar cell output when cone signals are dominant. The AII is also a recipient of cone-driven inhibition at the arboreal dendrite level (**Figure 14**), which may further suppress rod output signaling.

EVOLUTION

A distinguishing feature of mammals is the prevalence of rods (in most species) and the presence of the AII amacrine cell as a device to capture and amplify rod signals by driving them through a third ribbon synapse in the two arms of the cone pathway. As far as we know, non-mammalians do not exploit this mechanism and no homolog of the AII cell has yet been found, despite the abundance of narrow-field, multistratified and likely glycinergic amacrine cells in ectotherms. Most non-mammalians use mixed rod-cone bipolar cells as a merged scotopic-photopic mechanism to drive retinal ganglion cells (Ishida et al., 1980). Volume RC1 does provide some clues to the provenance of AII cells. If one removes all the rod components from the AII connectome (**Figure 14**), the vast majority of connections remain as an ON-OFF crossover system. Further, many non-mammalians (e.g., amphibians) display glycine signals in their ON bipolar cells (Marc et al., 1995; Yang and Yazulla, 1988), suggesting the presence of gap junctions between glycinergic amacrine cells and cone bipolar cells. Thus, the emergence of rod and rod bipolar cell proliferation in mammals could be the singular event that captured this crossover system as a scotopic amplifier (Dyer et al., 2009).

ACKNOWLEDGMENTS

This work was supported by National Institutes of Health (EY02576, EY015128, and EY014800), the National Science Foundation (0941717), the Thome Foundation, and an unrestricted grant from Research to Prevent Blindness.

SUPPLEMENTARY MATERIAL

The Supplementary Material for this article can be found online at: http://www.frontiersin.org/journal/10.3389/fncir.2014.00104/abstract

Table S1 | A comprehensive list of all AII amacrine cell partnerships. sourceMarc-Frontiers-2014-Table-1.pdf.

REFERENCES

Anderson, J. R., Grimm, B., Mohammed, S., Jones, B. W., Spaltenstein, J., Koshevoy, P., et al. (2011a). The Viking viewer: scalable multiuser annotation and summarization of large connectomics datasets. *J. Microsc.* 241, 13–28. doi: 10.1111/j.1365-2818.2010.03402.x

Anderson, J. R., Jones, B. W., Watt, C. B., Shaw, M. V., Yang, J.-H., Demill, D., et al. (2011b). Exploring the retinal connectome. *Mol. Vis.* 17, 355–379. Available online at: http://www.molvis.org/molvis/v17/a41

Anderson, J. R., Jones, B. W., Yang, J.-H., Shaw, M. V., Watt, C. B., Koshevoy, P., et al. (2009). A computational framework for ultrastructural mapping of neural circuitry. *PLoS Biol.* 7:e1000074. doi: 10.1371/journal.pbio.1000074

Arman, A. C., and Sampath, A. P. (2012). Dark-adapted response threshold of OFF ganglion cells is not set by OFF bipolar cells in the mouse retina. *J. Neurophysiol.* 107, 2649–2659. doi: 10.1152/jn.01202.2011

Attwell, D., Wilson, M., and Wu, S. M. (1984). A quantitative analysis of interactions between photoreceptors in the salamander (Ambystoma) retina. *J. Physiol.* 352, 703–737.

Barthelemy, M., and Amaral, L. A. N. (1999). Small-world networks: evidence for a crossover picture. *Phys. Rev. Lett.* 82, 3180–3183.

Bloomfield, S. A. (2001). Plasticity of AII amacrine cell circuitry in the mammalian retina. *Prog. Brain Res.* 131, 185–200. doi: 10.1016/S0079-6123(01)31016-6

Bloomfield, S. A., Xin, D. Y., and Osborne, T. (1997). Light-induced modulation of coupling between AII amacrine cells in the rabbit retina. *Vis. Neurosci.* 14, 565–576.

Cembrowski, M. S., Logan, S. M., Tian, M., Jia, L., Li, W., Kath, W. L., et al. (2012). The mechanisms of repetitive spike generation in an axonless retinal interneuron. *Cell Rep.* 1, 155–166. doi: 10.1016/j.celrep.2011.12.006

Da Costa, N. M., and Martin, K. A. C. (2009). Selective targeting of the dendrites of corticothalamic cells by thalamic afferents in area 17 of the cat. *J. Neurosci.* 29, 13919–13928. doi: 10.1523/JNEUROSCI.2785-09.2009

Devries, S. H., and Baylor, D. A. (1995). An alternative pathway for signal flow from rod photoreceptors to ganglion cells in mammalian retina. *Proc. Natl. Acad. Sci. U.S.A.* 92, 10658–10662.

Dumitrescu, O. N., Pucci, F. G., Wong, K. Y., and Berson, D. M. (2009). Ectopic retinal ON bipolar cell synapses in the OFF inner plexiform layer: contacts with dopaminergic amacrine cells and melanopsin ganglion cells. *J. Comp. Neurol.* 517, 226–244. doi: 10.1002/cne.22158

Dyer, M. A., Martins, R., Da Silva Filho, M., Muniz, J. A. P. C., Silveira, L. C. L., Cepko, C. L., et al. (2009). Developmental sources of conservation and variation in the evolution of the primate eye. *Proc. Natl. Acad. Sci. U.S.A.* 106, 8963–8968. doi: 10.1073/pnas.0901484106

Famiglietti, E. V. (2008). Wide-field cone bipolar cells and the blue-ON pathway to color-coded ganglion cells in rabbit retina. *Vis. Neurosci.* 25, 53–66. doi: 10.1017/S0952523808080061

Famiglietti, E. V. Jr., Kaneko, A., and Tachibana, M. (1975). Neuronal architecture of on and off pathways to ganglion cells in carp retina. *Science (Washington, D.C.)* 198, 1267–1269.

Frishman, L. J. (2006). "The origins of the electroretinogram," in *Principles and Practice of Clinical Electroretinography of Vision, 2nd Edn.*, eds. J. R. Heckenlively and G. B. Arden (Cambridge, MA: MIT Press), 139–184.

Grant, G. B., and Dowling, J. E. (1996). On bipolar cell responses in the teleost retina are generated by two distinct mechanisms. *J. Neurophysiol.* 76, 3842–3849.

Hartveit, E., and Veruki, M. L. (2012). Electrical synapses between AII amacrine cells in the retina: function and modulation. *Brain Res.* 1487, 160–172. doi: 10.1016/j.brainres.2012.05.060

Hoshi, H., Liu, W.-L., Massey, S. C., and Mills, S. L. (2009). ON inputs to the OFF layer: bipolar cells that break the stratification rules of the retina. *J. Neurosci.* 29, 8875–8883. doi: 10.1523/jneurosci.0912-09.2009

Ishida, A. T., Stell, W. K., and Lightfoot, D. O. (1980). Rod and cone inputs to bipolar cells in goldfish retina. *J. Comp. Neurol.* 191, 315–335.

Jones, B. W., Watt, C. B., Frederick, J. M., Baehr, W., Chen, C. K., Levine, E. M., et al. (2003). Retinal remodeling triggered by photoreceptor degenerations. *J. Comp. Neurol.* 464, 1–16. doi: 10.1002/cne.10703

Kolb, H., and Famiglietti, E. V. (1974). Rod and cone pathways in the inner plexiform layer of cat retina. *Science* 186, 47–49.

Lauritzen, J. S., Anderson, J. R., Jones, B. W., Watt, C. B., Mohammed, S., Hoang, J. V., et al. (2012). ON cone bipolar cell axonal synapses in the OFF inner plexiform layer of the rabbit retina. *J. Comp. Neurol.* 521, 977–1000. doi: 10.1002/cne.23244

Lauritzen, J. S., Hoang, J. V., Sigulinsky, C., Jones, B. W., Anderson, J. R., Watt, C. B., et al. (2013). Tiered cross-class bipolar cell gap junctional coupling in the rabbit retina. *Invest. Ophthal.* 54:1754.

Li, W., Chen, S., and Devries, S. H. (2010). A fast rod photoreceptor signaling pathway in the mammalian retina. *Nat. Neurosci.* 13, 414–416. doi: 10.1038/nn.2507

Manookin, M. B., Beaudoin, D. L., Ernst, Z. R., Flagel, L. J., and Demb, J. B. (2008). Disinhibition combines with excitation to extend the operating range of the OFF visual pathway in daylight. *J. Neurosci.* 28, 4136–4150. doi: 10.1523/JNEUROSCI.4274-07.2008

Marc, R. E., Anderson, J. R., Jones, B. W., Watt, C. B., and Lauritzen, J. S. (2013). Retinal Connectomics: towards complete, accurate networks. *Prog. Retin. Eye Res.* 37, 141–162. doi: 10.1016/j.preteyeres.2013.08.002

Marc, R. E., and Jones, B. W. (2002). Molecular phenotyping of retinal ganglion cells. *J. Neurosci.* 22, 412–427.

Marc, R. E., Jones, B. W., Sigulinsky, C., Anderson, J. R., and Lauritzen, J. S. (2014). "High-Resolution Synaptic Connectomics," in *New Techniques in Neuroscience: Physical, Optical, and Quantitative Approaches*, ed D. Adams (Berlin: Springer) (in press).

Marc, R. E., and Liu, W. (2000). Fundamental GABAergic amacrine cell circuitries in the retina: nested feedback, concatenated inhibition, and axosomatic synapses. *J. Comp. Neurol.* 425, 560–582. doi: 10.1002/1096-9861(20001002)425:4<560::AID-CNE7>3.0.CO;2-D

Marc, R. E., Murry, R. F., and Basinger, S. F. (1995). Pattern recognition of amino acid signatures in retinal neurons. *J. Neurosci.* 15, 5106–5129.

Masland, R. H. (2001). Neuronal diversity in the retina. *Curr. Opin. Neurobiol.* 11, 431–436. doi: 10.1016/S0959-4388(00)00230-0

Massey, S. C. (2008). "Circuit functions of gap junctions in the mammalian retina," in *The Senses*, eds R. H. Masland and T. Albright (San Diego, CA: Academic Press), 457–472.

Mastronarde, D. N. (2005). Automated electron microscope tomography using robust prediction of specimen movements. *J. Struct. Biol.* 152, 36–51. doi: 10.1016/j.jsb.2005.07.007

McGuire, B. A., Stevens, J. K., and Sterling, P. (1984). Microcircuitry of bipolar cells in cat retina. *J. Neurosci.* 4, 2920–2938.

Meyer, A., Hilgen, G., Dorgau, B., Sammler, E. M., Weiler, R., Monyer, H., et al. (2014). AII amacrine cells discriminate between heterocellular and homocellular locations when assembling connexin36-containing gap junctions. *J. Cell Sci.* 127, 1190–1202. doi: 10.1242/jcs.133066

Mills, S. L., and Massey, S. C. (1995). Differential properties of two gap junctional pathways made by AII amacrine cells. *Nature* 377, 734–737.

Molnar, A., Hain-Ann, H., Roska, B., and Werblin, F. S. (2009). Crossover inhibition in the retina: circuitry that compensates for nonlinear rectifying synaptic transmission. *J. Comput. Neurosci.* 27, 569–590. doi: 10.1007/s10827-009-0170-6

Muller, F., Wassle, H., and Voigt, T. (1988). Pharmacological modulation of the rod pathway in the cat retina. *J. Neurophysiol.* 59, 1657–1672.

Münch, T. A., Da Silveira, R. A., Siegert, S., Viney, T. J., Awatramani, G. B., and Roska, B. (2009). Approach sensitivity in the retina processed by a multifunctional neural circuit. *Nat. Neurosci.* 12, 1308–1316. doi: 10.1038/nn.2389

Naka, K., Marmarelis, P. Z., and Chan, R. Y. (1975). Morphological and functional identifications of catfish retinal neurons. III. Functional identification. *J. Neurophysiol.* 38, 92–131.

Pang, J. J., Gao, F., Lem, J., Bramblett, D. E., Paul, D. L., and Wu, S. M. (2010). Direct rod input to cone BCs and direct cone input to rod BCs challenge the traditional view of mammalian BC circuitry. *Proc. Natl. Acad. Sci. U.S.A.* 107, 395–400. doi: 10.1073/pnas.0907178107

Pang, J. J., Gao, F., Paul, D. L., and Wu, S. M. (2012). Rod, M-cone and M/S-cone inputs to hyperpolarizing bipolar cells in the mouse retina. *J. Physiol.* 590, 845–854. doi: 10.1113/jphysiol.2011.224113

Prinz, A. A., Bucher, B., and Marder, E. (2004). Similar network activity from disparate circuit parameters. *Nat. Neurosci.* 7, 1345–1352. doi: 10.1038/nn1352

Rockhill, R. L., Daly, F. J., Macneil, M. A., Brown, S. P., and Masland, R. H. (2002). The diversity of ganglion cells in a mammalian retina. *J. Neurosci.* 22, 3831–3843.

Saito, T., Kondo, H., and Toyoda, J. I. (1979). Ionic mechanisms of two types of on-center bipolar cells in the carp retina. I. The responses to central illumination. *J. Gen. Physiol.* 73, 73–90.

Saszik, S., and Devries, S. H. (2012). A mammalian retinal bipolar cell uses both graded changes in membrane voltage and all-or-nothing Na+ spikes to encode light. *J. Neurosci.* 32, 297–307. doi: 10.1523/jneurosci.2739-08.2012

Saszik, S. M., Robson, J. G., and Frishman, L. J. (2002). The scotopic threshold response of the dark-adapted electroretinogram of the mouse. *J. Physiol.* 543(Pt 3), 899–916. doi: 10.1113/jphysiol.2002.019703

Scholes, J. H. (1975). Colour receptors, and their synaptic connexions, in the retina of a cyprinid fish. *Philos. Trans. R. Soc. Lond. B. Biol. Sci.* 270, 61–118.

Scholes, J., and Morris, J. (1973). Receptor-bipolar connectivity patterns in fish retina. *Nature* 241, 52–54.

Soucy, E., Wang, Y., Nirenberg, S., Nathans, J., and Meister, M. (1998). A novel signaling pathway from rod photoreceptors to ganglion cells in mammalian retina. *Neuron* 21, 481–493.

Strettoi, E., Raviola, E., and Dacheux, R. F. (1992). Synaptic connections of the narrow-field, bistratified rod amacrine cell (AII) in the rabbit retina. *J. Comp. Neurol.* 325, 152–168.

Tian, N. (2011). Developmental mechanisms that regulate retinal ganglion cell dendritic morphology. *Dev. Neurobiol.* 71, 1297–1309. doi: 10.1002/dneu.20900

Tsukamoto, Y., Morigiwa, K., Ishii, M., Takao, M., Iwatsuki, K., Nakanishi, S., et al. (2007). A novel connection between rods and ON cone bipolar cells revealed by ectopic metabotropic glutamate receptor 7 (mGluR7) in mGluR6-deficient mouse retinas. *J. Neurosci.* 27, 6261–6267. doi: 10.1523/JNEUROSCI.5646-06.2007

Tsukamoto, Y., Morigiwa, K., Ueda, M., and Sterling, P. (2001). Microcircuits for night vision in mouse retina. *J. Neurosci.* 21, 8616–8623.

Tsukamoto, Y., and Omi, N. (2013). Functional allocation of synaptic contacts in microcircuits from rods via rod bipolar to AII amacrine cells in the mouse retina. *J. Comp. Neurol.* 521, 3541–3555. doi: 10.1002/cne.23370

Wang, G. Y. (2006). Unique functional properties of the APB sensitive and insensitive rod pathways signaling light decrements in mouse retinal ganglion cells. *Vis. Neurosci.* 23, 127–135. doi: 10.1017/S0952523806231110

Werblin, F. S. (2010). Six different roles for crossover inhibition in the retina: correcting the nonlinearities of synaptic transmission. *Vis. Neurosci.* 27, 1–8. doi: 10.1017/S0952523810000076

Yang, C. Y., and Yazulla, S. (1988). Light microscopic localization of putative glycinergic neurons in the larval tiger salamander retina by immunocytochemical and autoradiographical methods. *J. Comp. Neurol.* 272, 343–357.

Zhang, D.-Q., Zhou, T.-R., and McMahon, D. G. (2007). Functional heterogeneity of retinal dopaminergic neurons underlying their multiple roles in vision. *J. Neurosci.* 27, 692–699. doi: 10.1523/JNEUROSCI.4478-06.2007

Conflict of Interest Statement: Robert E. Marc is a principal of Signature Immunologics, Inc., manufacturer of some of the antibodies used in this work. The authors declare that the research was conducted in the absence of any commercial or financial relationships that could be construed as a potential conflict of interest.

Received: 16 April 2014; accepted: 08 August 2014; published online: 04 September 2014.

Citation: Marc RE, Anderson JR, Jones BW, Sigulinsky CL and Lauritzen JS (2014) The AII amacrine cell connectome: a dense network hub. Front. Neural Circuits ***8****:104. doi: 10.3389/fncir.2014.00104*

This article was submitted to the journal Frontiers in Neural Circuits.

frontiers in
NEURAL CIRCUITS

MINI REVIEW ARTICLE
published: 26 August 2014
doi: 10.3389/fncir.2014.00105

Unraveling the architecture of the dorsal raphe synaptic neuropil using high-resolution neuroanatomy

Mariano Soiza-Reilly*[1,2] ***and Kathryn G. Commons*[3,4]***

[1] Institut du Fer à Moulin, INSERM, UMR-S 839, Paris, France
[2] Université Pierre et Marie Curie, Paris, France
[3] Department of Anesthesiology, Perioperative, and Pain Medicine, Boston Children's Hospital, Boston, MA, USA
[4] Department of Anaesthesia, Harvard Medical School, Boston, MA, USA

Edited by:
Benjamin R. Arenkiel, Baylor College of Medicine, USA

Reviewed by:
Harry Wilhelm Maria Steinbusch, Maastricht University, Netherlands
Christopher A. Lowry, University of Colorado Boulder, USA

****Correspondence:***
Mariano Soiza-Reilly, Institut du Fer à Moulin, INSERM, UMR-S 839, 17 Rue du Fer à Moulin, 75005 Paris, France
e-mail: mariano.soiza-reilly@inserm.fr;
Kathryn G. Commons, Department of Anesthesiology, Perioperative, and Pain Medicine, Boston Children's Hospital, 300 Longwood Ave., Boston, MA 02115, USA
e-mail: kathryn.commons@childrens.harvard.edu

The dorsal raphe nucleus (DRN), representing the main source of brain's serotonin, is implicated in the pathophysiology and therapeutics of several mental disorders that can be debilitating and life-long including depression, anxiety and autism. The activity of DRN neurons is precisely regulated, both phasically and tonically, by excitatory glutamate and inhibitory GABAergic axons arising from extra-raphe areas as well as from local sources within the nucleus. Changes in serotonin neurotransmission associated with pathophysiology may be encoded by alterations within this network of regulatory afferents. However, the complex organization of the DRN circuitry remains still poorly understood. Using a recently developed high-resolution immunofluorescence technique called array tomography (AT) we quantitatively analyzed the relative contribution of different populations of glutamate axons originating from different brain regions to the excitatory drive of the DRN. Additionally, we examined the presence of GABA axons within the DRN and their possible association with glutamate axons. In this review, we summarize our findings on the architecture of the rodent DRN synaptic neuropil using high-resolution neuroanatomy, and discuss possible functional implications for the nucleus. Understanding of the synaptic architecture of neural circuits at high resolution will pave the way to understand how neural structure and function may be perturbed in pathological states.

Keywords: vesicular glutamate transporter, glutamate decarboxylase 65, synapses, ultrathin serial-sections, axo-axonic

THE COMPLEX ARCHITECTURE OF THE DRN

The dorsal raphe nucleus (DRN) comprises the majority of cells in the brain with the capacity of synthetizing the neurotransmitter serotonin (5-hydroxytryptamine, 5-HT) (Steinbusch, 1984). These cells represent the main source of 5-HT for forebrain regions, in which 5-HT regulates the activity of local networks. In agreement with its widespread projection targets, the DRN 5-HT system is involved in a broad repertoire of physiological processes. These include the modulation of motivational states, stress, appetite, sleep, and aggression, among others (Jacobs and Azmitia, 1992; Amat et al., 2005; Nakamura et al., 2008; Monti, 2010; Takahashi et al., 2010; Bruchas et al., 2011; Rozeske et al., 2011; Warden et al., 2012). Additionally, the DRN 5-HT system has been implicated in the pathophysiology and therapeutics of mental disorders such as depression, anxiety, autism, etc. . .(Stockmeier, 1997; Arango et al., 2001; Bach-Mizrachi et al., 2006, 2008; Bruchas et al., 2011; Matthews and Harrison, 2012; Kerman et al., 2012; Veenstra-VanderWeele et al., 2012). Dysfunction of 5-HT neurotransmission associated with these disorders may reflect alterations in axonal networks and synaptic circuits within the DRN.

The activity of DRN neurons is finely modulated by the complex interaction of glutamatergic excitatory and GABAergic inhibitory neurotransmission mediated by glutamate and GABA axons arising from extra-raphe areas as well as from local sources (**Figure 1**). Glutamatergic axons originating from extra-raphe areas include the hypothalamus, lateral habenula and prefrontal cortex (Kalén et al., 1985; Lee et al., 2003; Sego et al., 2014) as well as from local sources (Jolas and Aghajanian, 1997; Commons, 2009; Hioki et al., 2010). More caudally, several medullary regions send glutamate projections to the DRN including the parabrachial nucleus and the laterodorsal tegmental nucleus, and to a lesser extent, the paragigantocellular nucleus, the prepositus hypoglossal nucleus as well as the spinal trigeminal nucleus (Lee et al., 2003; **Figure 1**). Furthermore, different populations of glutamatergic neurons sending axon projections to the DRN have a preferred expression of specific types of the vesicular glutamate transporter (VGLUT1, VGLUT2 and VGLUT3), since there is a topographic segregation of cells expressing these different types of transporters (reviewed by Soiza-Reilly and Commons, 2011a). These proteins have the capacity of filling the synaptic vesicles with glutamate and their identification represents a very useful tool to identify different types of glutamate axons. This analysis allowed us to examine the relative contribution of different populations of neurons, originating in different brain regions,

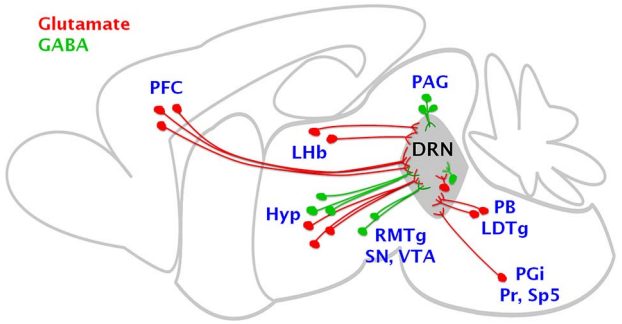

FIGURE 1 | Brain regions sending glutamate and GABA axon projections to the DRN. The cartoon summarizes the main sources of glutamate excitatory and GABAergic inhibitory inputs to the DRN. Glutamate cells (in red) are mainly located in the prefrontal cortex (PFC), lateral habenula (LHb), hypothalamus (Hyp), parabrachial nucleus (PB), laterodorsal tegmental nucleus (LDTg), paragigantocellular nucleus (PGi), prepositus hypoglossal nucleus (Pr) as well as the spinal trigeminal nucleus (Sp5), as well as in local sources including the DRN. GABAergic cells (in green) sending projections to the DRN are located mainly in the hypothalamus, substantia nigra (SN), ventral tegmental area (VTA), rostromedial tegmental nucleus (RMTg) and locally within the periaqueductal gray (PAG) and DRN.

to glutamate excitatory drive of the DRN (Soiza-Reilly and Commons, 2011b).

GABAergic axons innervating the DRN originate from extrinsic sources including the lateral and rostral hypothalamic and preoptic areas, substantia nigra, ventral tegmental area (Gervasoni et al., 2000; Kirouac et al., 2004; Taylor et al., 2014), and the rostromedial tegmental nucleus (Lavezzi et al., 2012; Sego et al., 2014; **Figure 1**). Local GABAergic neurons reside both in the DRN and laterally within the adjacent periaqueductal gray (Belin et al., 1979; Allers and Sharp, 2003; Fu et al., 2010; **Figure 1**).

There are multiple cell types within the DRN, and these often have local axon collaterals. In addition to 5-HT cells and their intra-DRN axon projections (Bang et al., 2012) there are glutamate, GABA and dopamine neurons, and these neurotransmitters as well as 5-HT may be combined with different neuropeptides (Jolas and Aghajanian, 1997; Commons, 2009; Fu et al., 2010; Hioki et al., 2010). This, together with the multiple origins of glutamate and GABA inputs converging onto DRN neurons from extrinsic sources results in a highly complex DRN circuitry that remains still poorly understood. Only when we achieve a better understanding about how this rich set of afferents is organized within the DRN, could we determine what elements of the network are vulnerable to dysfunction in pathological states.

HIGH-RESOLUTION ANALYSIS OF THE DRN NEUROPIL: GLUTAMATE EXCITATORY DRIVE

We recently applied a novel high-resolution immunofluorescence technique called Array Tomography (AT) to explore the organization of the DRN synaptic neuropil (Soiza-Reilly and Commons, 2011b; Soiza-Reilly et al., 2013). AT involves immunolabeling and imaging of ultrathin (70 nm) serial sections. Subsequently, the images can be reconstructed and rendered in 3D, and the relationships between the immunolabeled antigens can be visualized and quantitatively analyzed (Micheva and Smith, 2007; Micheva et al., 2010). One of the key features of AT is that it allows multiple rounds of immunolabeling/elution with a highly reliable preservation of antigens (Soiza-Reilly and Commons, 2011b). This results in high-resolution visualization of multiple antigens (typically 6–12) at the same time in 3D space (**Figure 2**). The physical sectioning of the tissue in AT (70 nm) provides a superb resolution especially in the *z*-axis, even beyond the theoretical limits dictated by Abbe's law (Wang and Smith, 2012). Thin sectioning also eliminates issues related to antibody penetration, obtaining a more homogeneous distribution of the antibody on the section's surface. Altogether these features allow mapping of multiple antigens in the same tissue volume, as well as the quantitative analysis of their spatial relationships to each other (**Figure 2**).

Using AT we examined the quantitative distribution of glutamate axons within the mouse DRN and determined the relative contribution of different glutamate axons arising from distinct populations of neurons to the excitatory drive of the DRN (Soiza-Reilly and Commons, 2011b). In our study, to avoid the potential inclusion of spurious immunolabeling in the quantitative analysis, we imposed a contingency such that the presence of a specific presynaptic marker for glutamate axons (e.g., VGLUT1-3) was analyzed with respect to a second and more general marker of glutamate synapses such as the postsynaptic protein PSD-95. Thus we found that synaptic boutons containing VGLUT2 provide the major glutamate input to the DRN when compared to those containing VGLUT1 or VGLUT3 (Soiza-Reilly and Commons, 2011b). Glutamate neurons in the prefrontal cortex predominantly express VGLUT1, while many subcortical regions sending axonal projections to the DRN preferentially express VGLUT2. These regions include many hypothalamic nuclei, the basal forebrain, as well as adjacent regions to the DRN such as the periaqueductal gray and parabrachial nucleus (Hisano et al., 2000; Fremeau et al., 2001; Herzog et al., 2001; Kaneko and Fujiyama, 2002; Kaneko et al., 2002; Varoqui et al., 2002). However, it still remains an open question how this balance between cortical vs. subcortical glutamate inputs influencing DRN neurons arises during development, to modulate the actions of 5-HT in the maturation of neural circuits (Gaspar et al., 2003), and whether faulty wiring of these circuits could contribute to the development of mental disorders that arise later in life such as depression or anxiety.

Additionally, in our study we did not find any preference in the cellular targets of these glutamatergic synaptic boutons and they were equally associated with both 5-HT as well as with non-5-HT neurons (Soiza-Reilly and Commons, 2011b). These findings are in agreement with previous ultrastructural studies using immunoelectron microscopy showing that glutamatergic synaptic innervations containing either VGLUT1 or VGLUT2 are not an exclusive feature of 5-HT neurons, and they are also associated with non-5-HT neurons (Commons et al., 2005). This is consistent at least with the dual influence of glutamate afferents arising from the prefrontal cortex upon 5-HT and GABA neurons within the DRN (Celada et al., 2001; Jankowski and Sesack, 2004).

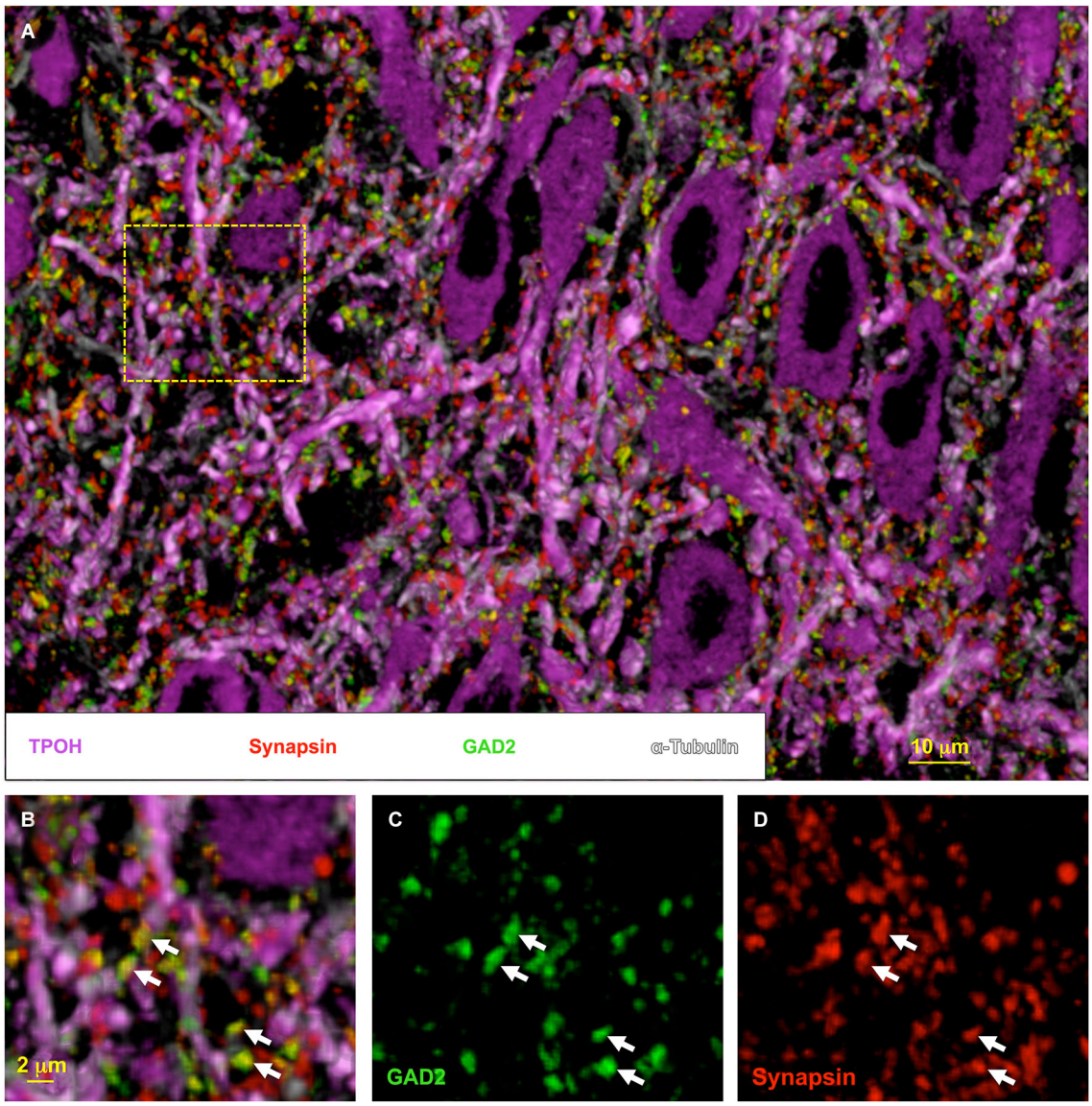

FIGURE 2 | High-resolution synaptic anatomy within the DRN using array tomography. Volumetric image of the DRN rendered from multiple rounds of immunolabeling on 16 ultrathin (70 nm) serial-sections. In **(A)**, tryptophan hydroxylase (TPOH) labeling (magenta) reveals the high abundance of 5-HT cells in the nucleus. Additionally, the co-labeling with tubulin (light magenta) to identify the microtubule bundles indicates the compact distribution of their dendritic processes within the DRN neuropil. This organization is densely invaded by synaptic boutons identified by the presence of synapsin, a protein present at the synaptic vesicles (red). A proportion of these axon boutons are co-labeled for the GABA synthetic enzyme glutamate decarboxylase 65 (GAD2) (green) (indicated by the arrows in **(B–D)**). However, a large proportion of synaptic boutons do not contain the GABAergic marker, likely representing glutamate and other axonal populations within the DRN. Individually-resolved labeled puncta visualized with AT can be subjected to semi-automatic quantitative analysis using ImageJ software, giving a distribution of multiple populations of synaptic boutons within the same volume of tissue.

However, previous studies suggested that 5-HT vs. non-5-HT neurons could be under the influence of different populations of glutamate axons or that these axons could have distinct control mechanisms. Specifically, a stress exposure appears to more selectively affect the activity of glutamatergic inputs to DRN 5-HT neurons than those associated with non-5-HT neurons (Kirby et al., 2007). Indeed, differential distribution of glutamate receptor subunits with respect to midline (5-HT-neuron rich) and lateral (GABA-neuron rich) locations in the DRN suggests different cell types may have different synaptic responses to glutamate (Soiza-Reilly and Commons, 2011a; Templin et al., 2012).

PRESYNAPTIC INTERACTION OF GLUTAMATE AND GABA TRANSMISSION IN THE DRN

There was some functional evidence indicating a possible direct interaction between glutamate and GABA transmission in the DRN, influencing the activity of 5-HT cells (Kalén et al., 1989; Tao and Auerbach, 2003). However, the fine organization of

glutamate and GABA synaptic innervations within the nucleus was poorly understood. Furthermore, the possible existence of synaptic arrangements that could underlie a direct interaction between glutamate and GABA transmission systems remained to be elucidated.

Very recently, we tackled this problem using a combined approach involving AT, electron microscopy and electrophysiological recordings to examine the organization of GABA axons within the rat DRN as well as their possible association with glutamate axons (Soiza-Reilly et al., 2013). In that study, quantitative analysis of GABA axon boutons in the DRN as well as their spatial relationships to glutamate axons were performed primarily using AT. For that, we used immunolabeling against specific markers for glutamate (VGLUT1-3) and GABA (glutamate decarboxylase 65, GAD2) axons, together with a general marker for synaptic boutons such as the protein associated with synaptic vesicles synapsin 1. Thus, only axon boutons containing both a specific marker (e.g., VGLUT1-3 or GAD2) together with the general marker for synaptic boutons (i.e., synapsin) were included in the quantitative analysis (**Figures 3A–D**).

However, the absolute density of double immunolabeled objects could also include random instances depending on the abundance of antigens and specificity of labeling. We addressed this potential caveat by performing a cross-correlation analysis of pixels, providing insights about the specificity of spatial relationships between two populations of labeled objects (van Steensel et al., 1996; Micheva et al., 2010). Using this approach we validated the specificity of immunolabeled pairs VGLUT1-3 or

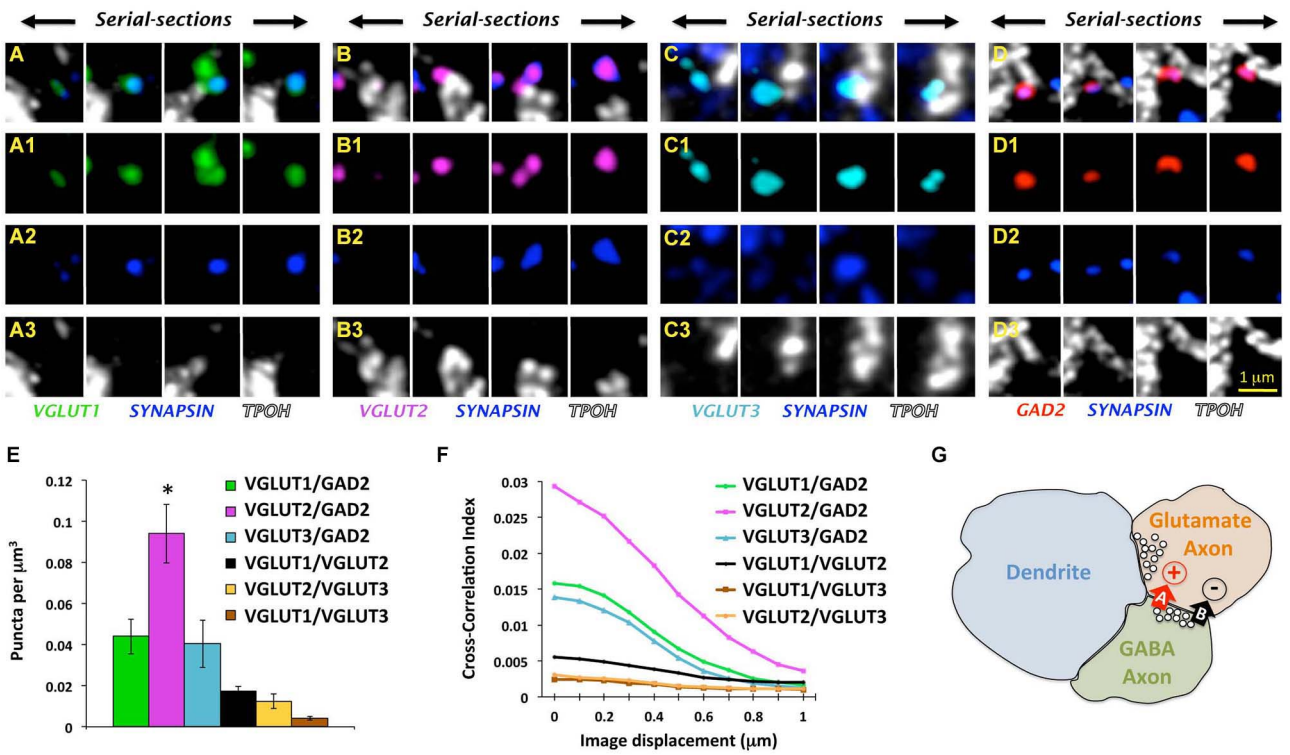

FIGURE 3 | Glutamate and GABA axon boutons in the DRN. (A–D) Array tomographic visualization across four ultrathin (70 nm) serial-sections immunolabeled against VGLUT1-3 (green, magenta, and light blue, respectively) or GAD2 (red) to identify glutamate and GABAergic boutons, respectively. These immunodetected axon boutons are often co-labeled for synapsin (blue), and in some cases associated with TPOH-labeled dendrites (white). Adapted from Soiza-Reilly et al. (2013) reprinted with permission. **(E)** Total density of axo-axonic-like arrangements of four different types of axon boutons labeled either for VGLUT1-3 or GAD2 together with synapsin. The most abundant pair of axon boutons contained VGLUT2 and GAD2 ones (*$p < 0.001$ vs. either VGLUT1 or VGLUT3). Only a small proportion of axoaxonic-like arrangements were found between different glutamatergic boutons (e.g., VGLUT1/VGLUT2, VGLUT1/VGLUT3, and VGLUT2/VGLUT3). Bars represent SEM. Adapted from Soiza-Reilly et al. (2013) reprinted with permission. **(F)** Cross-correlation analysis of pixels between four different types of axon boutons using the ImageJ plugin JACoP (Bolte and Cordelières, 2006). This analysis indicated a higher degree of colocalization of VGLUT2 axon terminals with GAD2 boutons in comparison to other glutamate axons. Specifically, when imaging channels were aligned (x = at 0 µm of displacement), the pixels co-labeled for VGLUT1-3 and synapsin showed the highest value of correlation with pixels co-labeled for GAD2 and synapsin. When imaging channels were displaced with respect to each other all of the correlation values decreased indicating the spatial proximity of all three glutamate axon types with GABA boutons (Soiza-Reilly et al., 2013). Cross-correlations between different glutamate axon types were very low. **(G)** Schematic illustration of the GABAergic presynaptic modulation of glutamate release in the synaptic triads of the DRN. Adjacent glutamate and GABA axon terminals are closely associated with a postsynaptic dendrite that receives a typical excitatory asymmetric synapse from the glutamatergic bouton. GABA boutons would have the capacity of presynaptically influencing glutamate release from terminals through a dual mechanism involving a rapid/transient GABA-A receptor-mediated facilitation, and a more delayed and sustained GABA-B receptor inhibition.

GAD2 with synapsin, and we found that among them GABAergic and VGLUT2-containing glutamate axon boutons were about three times more prevalent than other axon types in the DRN. Additionally, we found their postsynaptic cellular targets included both 5-HT and non-5-HT neurons, with no apparent preference for one population over another (Soiza-Reilly et al., 2013).

Taking advantage of the capacity of AT for quantitative analysis we examined the possible presence of axo-axonic spatial arrangements involving glutamate and GABA axons in the DRN that could underlie a direct interaction between these neurotransmission systems. Using this approach we found that all three types of glutamate axon boutons (VGLUT1-3) were spatially related to GABA boutons, and among them relationships between GABA and VGLUT2-containing boutons were the most abundant (**Figures 3E,F,** Soiza-Reilly et al., 2013). This indicated that GABA axons in the DRN would interact with all the three types of glutamate axons according to their relative abundance in the nucleus, while associations between glutamate axons to each other were more rarely found (**Figures 3E,F,** Soiza-Reilly et al., 2013).

Complementary ultrastructural studies using immuno-electron microscopy for GAD2 in the DRN showed the presence of GABA axon boutons in close apposition to unlabeled axons with the morphology compatible with glutamatergic axon boutons (Soiza-Reilly et al., 2013). Further, these findings also indicated that they organize forming synaptic triads where both presynaptic GABA and glutamate axon boutons together associate with a single postsynaptic dendrite. Moreover, in these triads glutamate axon boutons were usually found establishing asymmetric-type synapses on the postsynaptic dendrite but not on GABA boutons (Soiza-Reilly et al., 2013). This raised the possibility that GABA could presynaptically modulate glutamate release in the DRN. We explored this hypothesis by studying the effects of GABA ligands on spontaneous miniature EPSCs in putative DRN 5-HT neurons using *in vitro* electrophysiological recordings. Indeed, we found opposite modulation of DRN glutamate synaptic transmission by GABA-A and GABA-B receptors. Specifically, GABA-A receptor activation facilitated glutamate release while GABA-B receptors on the contrary mediated an inhibitory effect (Soiza-Reilly et al., 2013). We hypothesize that this coincidental excitation and inhibition at the presynaptic glutamatergic terminal could operate similarly to that observed in the cerebellum (Pugh and Jahr, 2011), where a rapid transient GABA-A facilitation and a more delayed and sustained GABA-B inhibition have the capacity to temporally gate glutamate release in the DRN (**Figure 3G**).

Synaptic triads involving GABA and glutamate axons could at least partially explain previous pharmacological studies suggesting the interaction of these neurotransmitter systems to modulate 5-HT release (Tao and Auerbach, 2003). Moreover, the presynaptic modulation of glutamate transmission by GABA is also compatible with a possible role of GABA in state-dependent modulation of 5-HT system's activity (Nitz and Siegel, 1997; Gervasoni et al., 2000). Additionally, since we found that all three types of glutamate axons can establish axo-axonic associations with GABA axons, this indicates that the presynaptic GABAergic modulation of glutamate transmission would represent a more general mechanism, influencing glutamate excitatory drives arising from multiple brain regions and converging to the DRN. Another important question that remains still open is whether glutamate and GABA synaptic inputs to the nucleus could be topographically organized to selectively modulate the activity of different subsets of DRN neurons.

From a GABA system perspective, only a proportion of GABA axon boutons were implicated in axo-axonic arrangements with glutamate axons. This raises the question of whether these GABA boutons arise from a particular subpopulation of GABAergic neurons located within or outside the DRN. Further studies combining the use of axonal tract-tracing with AT will give further insights into the selective role of GABAergic neurons in the presynaptic modulation of glutamate transmission in the DRN.

CONCLUDING REMARKS AND FUTURE PERSPECTIVES

The complete view of molecular and fine structural features of DRN synaptic circuits represents a stepping stone towards understanding of their role in normal and pathological neurotransmission, as well as if alterations in the structure of circuits could contribute to the pathophysiology of mental diseases. For this purpose, the use of recently developed high-throughput imaging techniques like AT has opened new avenues to characterize and better understand synaptic aspects of human neuropathology (Koffie et al., 2009; Hudry et al., 2013; Kay et al., 2013; Kopeikina et al., 2013). The unique ability of AT in providing high-throughput quantitative information about multiple synapse protein components co-existing in the same, unlimited in principle, volume of tissue, offers a wide spectrum of proteomic analyses of synapses. This makes possible not only to identify molecular signatures of synapses and classify them by studying the presence of neurotransmitter receptors and scaffold proteins (Micheva and Bruchez, 2012; O'Rourke et al., 2012), but also to determine the functional state of synapses by identifying channels, receptor active subunits as well as other regulatory proteins (Lacey et al., 2012). Additionally, the fact that AT allows the molecular characterization of synapses in their neuroanatomical context, it is possible to extract quantitative data about their involvement in synaptic motifs as well as their relationships to different cell types and subcellular compartments such as dendritic processes (Rah et al., 2013). Finally, AT is highly compatible with recently developed super-resolution microscopy techniques that have broken the diffraction limit (Micheva and Bruchez, 2012; Wang and Smith, 2012) such as the stimulated emission depletion microscopy (STED; Hell and Wichmann, 1994) or stochastic optical reconstruction microscopy (STORM; Rust et al., 2006). The combined use of these approaches allows the unique possibility of investigating with a superb resolution in all the optical planes (*x-y-z* axes), multiple molecular interactions within the same synapses in serially sectioned larger volumes of brain tissue. Moreover, the compatibility of AT with scanning electron microscopy allows to further locate synaptic features identified using fluorescence microscopy in their ultrastructural context (Micheva and Smith, 2007; Micheva et al., 2010). The use of these combined approaches will ultimately provide more comprehensive information about the molecular architecture of neural circuits particularly relevant in building more accurate wiring diagrams contributing to understanding of connectomes.

ACKNOWLEDGMENTS

This work was supported by the Sara Page Mayo Foundation for Pediatric Pain Research.

REFERENCES

Allers, K. A., and Sharp, T. (2003). Neurochemical and anatomical identification of fast- and slow-firing neurones in the rat dorsal raphe nucleus using juxtacellular labelling methods in vivo. *Neuroscience* 122, 193–204. doi: 10.1016/s0306-4522(03)00518-9

Amat, J., Baratta, M. V., Paul, E., Bland, S. T., Watkins, L. R., and Maier, S. F. (2005). Medial prefrontal cortex determines how stressor controllability affects behavior and dorsal raphe nucleus. *Nat. Neurosci.* 8, 365–371. doi: 10.1038/nn1399

Arango, V., Underwood, M. D., Boldrini, M., Tamir, H., Kassir, S. A., Hsiung, S., et al. (2001). Serotonin 1A receptors, serotonin transporter binding and serotonin transporter mRNA expression in the brainstem of depressed suicide victims. *Neuropsychopharmacology* 25, 892–903. doi: 10.1016/s0893-133x(01)00310-4

Bach-Mizrachi, H., Underwood, M. D., Kassir, S. A., Bakalian, M. J., Sibille, E., Tamir, H., et al. (2006). Neuronal tryptophan hydroxylase mRNA expression in the human dorsal and median raphe nuclei: major depression and suicide. *Neuropsychopharmacology* 31, 814–824. doi: 10.1038/sj.npp.1300897

Bach-Mizrachi, H., Underwood, M. D., Tin, A., Ellis, S. P., Mann, J. J., and Arango, V. (2008). Elevated expression of tryptophan hydroxylase-2 mRNA at the neuronal level in the dorsal and median raphe nuclei of depressed suicides. *Mol. Psychiatry* 13, 507–513, 465. doi: 10.1038/sj.mp.4002143

Bang, S. J., Jensen, P., Dymecki, S. M., and Commons, K. G. (2012). Projections and interconnections of genetically defined serotonin neurons in mice. *Eur. J. Neurosci.* 35, 85–96. doi: 10.1111/j.1460-9568.2011.07936.x

Belin, M. F., Aguera, M., Tappaz, M., McRae-Degueurce, A., Bobillier, P., and Pujol, J. F. (1979). GABA-accumulating neurons in the nucleus raphe dorsalis and periaqueductal gray in the rat: a biochemical and radioautographic study. *Brain Res.* 170, 279–297. doi: 10.1016/0006-8993(79)90107-0

Bolte, S., and Cordelières, F. P. (2006). A guided tour into subcellular colocalization analysis in light microscopy. *J. Microsc.* 224, 213–232. doi: 10.1111/j.1365-2818.2006.01706.x

Bruchas, M. R., Schindler, A. G., Shankar, H., Messinger, D. I., Miyatake, M., Land, B. B., et al. (2011). Selective p38α MAPK deletion in serotonergic neurons produces stress resilience in models of depression and addiction. *Neuron* 71, 498–511. doi: 10.1016/j.neuron.2011.06.011

Celada, P., Puig, M. V., Casanovas, J. M., Guillazo, G., and Artigas, F. (2001). Control of dorsal raphe serotonergic neurons by the medial prefrontal cortex: involvement of serotonin-1A, GABA(A) and glutamate receptors. *J. Neurosci.* 21, 9917–9929.

Commons, K. G. (2009). Locally collateralizing glutamate neurons in the dorsal raphe nucleus responsive to substance P contain vesicular glutamate transporter 3 (VGLUT3). *J. Chem. Neuroanat.* 38, 273–281. doi: 10.1016/j.jchemneu.2009.05.005

Commons, K. G., Beck, S. G., and Bey, V. W. (2005). Two populations of glutamatergic axons in the rat dorsal raphe nucleus defined by the vesicular glutamate transporters 1 and 2. *Eur. J. Neurosci.* 21, 1577–1586. doi: 10.1111/j.1460-9568.2005.03991.x

Fremeau, R. T. Jr., Troyer, M. D., Pahner, I., Nygaard, G. O., Tran, C. H., Reimer, R. J., et al. (2001). The expression of vesicular glutamate transporters defines two classes of excitatory synapse. *Neuron* 31, 247–260. doi: 10.1016/s0896-6273(01)00344-0

Fu, W., Le Maître, E., Fabre, V., Bernard, J.-F., David Xu, Z.-Q., and Hökfelt, T. (2010). Chemical neuroanatomy of the dorsal raphe nucleus and adjacent structures of the mouse brain. *J. Comp. Neurol.* 518, 3464–3494. doi: 10.1002/cne.22407

Gaspar, P., Cases, O., and Maroteaux, L. (2003). The developmental role of serotonin: news from mouse molecular genetics. *Nat. Rev. Neurosci.* 4, 1002–1012. doi: 10.1038/nrn1256

Gervasoni, D., Peyron, C., Rampon, C., Barbagli, B., Chouvet, G., Urbain, N., et al. (2000). Role and origin of the GABAergic innervation of dorsal raphe serotonergic neurons. *J. Neurosci.* 20, 4217–4225.

Hell, S. W., and Wichmann, J. (1994). Breaking the diffraction resolution limit by stimulated emission: stimulated-emission-depletion fluorescence microscopy. *Opt. Lett.* 19, 780–782. doi: 10.1364/ol.19.000780

Herzog, E., Bellenchi, G. C., Gras, C., Bernard, V., Ravassard, P., Bedet, C., et al. (2001). The existence of a second vesicular glutamate transporter specifies subpopulations of glutamatergic neurons. *J. Neurosci.* 21:RC181.

Hioki, H., Nakamura, H., Ma, Y.-F., Konno, M., Hayakawa, T., Nakamura, K. C., et al. (2010). Vesicular glutamate transporter 3-expressing nonserotonergic projection neurons constitute a subregion in the rat midbrain raphe nuclei. *J. Comp. Neurol.* 518, 668–686. doi: 10.1002/cne.22237

Hisano, S., Hoshi, K., Ikeda, Y., Maruyama, D., Kanemoto, M., Ichijo, H., et al. (2000). Regional expression of a gene encoding a neuron-specific Na(+)-dependent inorganic phosphate cotransporter (DNPI) in the rat forebrain. *Brain Res. Mol. Brain Res.* 83, 34–43. doi: 10.1016/s0169-328x(00)00194-7

Hudry, E., Dashkoff, J., Roe, A. D., Takeda, S., Koffie, R. M., Hashimoto, T., et al. (2013). Gene transfer of human Apoe isoforms results in differential modulation of amyloid deposition and neurotoxicity in mouse brain. *Sci. Transl. Med.* 5:212ra161. doi: 10.1126/scitranslmed.3007000

Jacobs, B. L., and Azmitia, E. C. (1992). Structure and function of the brain serotonin system. *Physiol. Rev.* 72, 165–229.

Jankowski, M. P., and Sesack, S. R. (2004). Prefrontal cortical projections to the rat dorsal raphe nucleus: ultrastructural features and associations with serotonin and gamma-aminobutyric acid neurons. *J. Comp. Neurol.* 468, 518–529. doi: 10.1002/cne.10976

Jolas, T., and Aghajanian, G. K. (1997). Opioids suppress spontaneous and NMDA-induced inhibitory postsynaptic currents in the dorsal raphe nucleus of the rat in vitro. *Brain Res.* 755, 229–245. doi: 10.1016/s0006-8993(97)00103-0

Kalén, P., Karlson, M., and Wiklund, L. (1985). Possible excitatory amino acid afferents to nucleus raphe dorsalis of the rat investigated with retrograde wheat germ agglutinin and D-[3H]aspartate tracing. *Brain Res.* 360, 285–297. doi: 10.1016/0006-8993(85)91244-2

Kalén, P., Strecker, R. E., Rosengren, E., and Björklund, A. (1989). Regulation of striatal serotonin release by the lateral habenula-dorsal raphe pathway in the rat as demonstrated by in vivo microdialysis: role of excitatory amino acids and GABA. *Brain Res.* 492, 187–202. doi: 10.1016/0006-8993(89)90901-3

Kaneko, T., and Fujiyama, F. (2002). Complementary distribution of vesicular glutamate transporters in the central nervous system. *Neurosci. Res.* 42, 243–250. doi: 10.1016/s0168-0102(02)00009-3

Kaneko, T., Fujiyama, F., and Hioki, H. (2002). Immunohistochemical localization of candidates for vesicular glutamate transporters in the rat brain. *J. Comp. Neurol.* 444, 39–62. doi: 10.1002/cne.10129

Kay, K. R., Smith, C., Wright, A. K., Serrano-Pozo, A., Pooler, A. M., Koffie, R., et al. (2013). Studying synapses in human brain with array tomography and electron microscopy. *Nat. Protoc.* 8, 1366–1380. doi: 10.1038/nprot.2013.078

Kerman, I. A., Bernard, R., Bunney, W. E., Jones, E. G., Schatzberg, A. F., Myers, R. M., et al. (2012). Evidence for transcriptional factor dysregulation in the dorsal raphe nucleus of patients with major depressive disorder. *Front. Neurosci.* 6:135. doi: 10.3389/fnins.2012.00135

Kirby, L. G., Pan, Y.-Z., Freeman-Daniels, E., Rani, S., Nunan, J. D., Akanwa, A., et al. (2007). Cellular effects of swim stress in the dorsal raphe nucleus. *Psychoneuroendocrinology* 32, 712–723. doi: 10.1016/j.psyneuen.2007.05.001

Kirouac, G. J., Li, S., and Mabrouk, G. (2004). GABAergic projection from the ventral tegmental area and substantia nigra to the periaqueductal gray region and the dorsal raphe nucleus. *J. Comp. Neurol.* 469, 170–184. doi: 10.1002/cne.11005

Koffie, R. M., Meyer-Luehmann, M., Hashimoto, T., Adams, K. W., Mielke, M. L., Garcia-Alloza, M., et al. (2009). Oligomeric amyloid beta associates with postsynaptic densities and correlates with excitatory synapse loss near senile plaques. *Proc. Natl. Acad. Sci. U S A* 106, 4012–4017. doi: 10.1073/pnas.0811698106

Kopeikina, K. J., Polydoro, M., Tai, H.-C., Yaeger, E., Carlson, G. A., Pitstick, R., et al. (2013). Synaptic alterations in the rTg4510 mouse model of tauopathy. *J. Comp. Neurol.* 521, 1334–1353. doi: 10.1002/cne.23234

Lacey, C. J., Bryant, A., Brill, J., and Huguenard, J. R. (2012). Enhanced NMDA receptor-dependent thalamic excitation and network oscillations in stargazer mice. *J. Neurosci.* 32, 11067–11081. doi: 10.1523/JNEUROSCI.5604-11.2012

Lavezzi, H. N., Parsley, K. P., and Zahm, D. S. (2012). Mesopontine rostromedial tegmental nucleus neurons projecting to the dorsal raphe and pedunculopontine tegmental nucleus: psychostimulant-elicited Fos expression and collateralization. *Brain Struct. Funct.* 217, 719–734. doi: 10.1007/s00429-011-0368-z

Lee, H. S., Kim, M. A., Valentino, R. J., and Waterhouse, B. D. (2003). Glutamatergic afferent projections to the dorsal raphe nucleus of the rat. *Brain Res.* 963, 57–71. doi: 10.1016/s0006-8993(02)03841-6

Matthews, P. R., and Harrison, P. J. (2012). A morphometric, immunohistochemical and in situ hybridization study of the dorsal raphe nucleus in major depression, bipolar disorder, schizophrenia and suicide. *J. Affect. Disord.* 137, 125–134. doi: 10.1016/j.jad.2011.10.043

Micheva, K. D., and Bruchez, M. P. (2012). The gain in brain: novel imaging techniques and multiplexed proteomic imaging of brain tissue ultrastructure. *Curr. Opin. Neurobiol.* 22, 94–100. doi: 10.1016/j.conb.2011.08.004

Micheva, K. D., Busse, B., Weiler, N. C., O'Rourke, N., and Smith, S. J. (2010). Single-synapse analysis of a diverse synapse population: proteomic imaging methods and markers. *Neuron* 68, 639–653. doi: 10.1016/j.neuron.2010.09.024

Micheva, K. D., and Smith, S. J. (2007). Array tomography: a new tool for imaging the molecular architecture and ultrastructure of neural circuits. *Neuron* 55, 25–36. doi: 10.1016/j.neuron.2007.06.014

Monti, J. M. (2010). The role of dorsal raphe nucleus serotonergic and non-serotonergic neurons and of their receptors, in regulating waking and rapid eye movement (REM) sleep. *Sleep Med. Rev.* 14, 319–327. doi: 10.1016/j.smrv.2009.10.003

Nakamura, K., Matsumoto, M., and Hikosaka, O. (2008). Reward-dependent modulation of neuronal activity in the primate dorsal raphe nucleus. *J. Neurosci.* 28, 5331–5343. doi: 10.1523/JNEUROSCI.0021-08.2008

Nitz, D., and Siegel, J. (1997). GABA release in the dorsal raphe nucleus: role in the control of REM sleep. *Am. J. Physiol.* 273, R451–R455.

O'Rourke, N. A., Weiler, N. C., Micheva, K. D., and Smith, S. J. (2012). Deep molecular diversity of mammalian synapses: why it matters and how to measure it. *Nat. Rev. Neurosci.* 13, 365–379. doi: 10.1038/nrn3170

Pugh, J. R., and Jahr, C. E. (2011). Axonal GABAA receptors increase cerebellar granule cell excitability and synaptic activity. *J. Neurosci.* 31, 565–574. doi: 10.1523/JNEUROSCI.4506-10.2011

Rah, J.-C., Bas, E., Colonell, J., Mishchenko, Y., Karsh, B., Fetter, R. D., et al. (2013). Thalamocortical input onto layer 5 pyramidal neurons measured using quantitative large-scale array tomography. *Front. Neural Circuits* 7:177. doi: 10.3389/fncir.2013.00177

Rozeske, R. R., Evans, A. K., Frank, M. G., Watkins, L. R., Lowry, C. A., and Maier, S. F. (2011). Uncontrollable, but not controllable, stress desensitizes 5-HT1A receptors in the dorsal raphe nucleus. *J. Neurosci.* 31, 14107–14115. doi: 10.1523/JNEUROSCI.3095-11.2011

Rust, M. J., Bates, M., and Zhuang, X. (2006). Sub-diffraction-limit imaging by stochastic optical reconstruction microscopy (STORM). *Nat. Methods* 3, 793–795. doi: 10.1038/nmeth929

Sego, C., Gonçalves, L., Lima, L., Furigo, I. C., Donato, J., and Metzger, M. (2014). Lateral habenula and the rostromedial tegmental nucleus innervate neurochemically distinct subdivisions of the dorsal raphe nucleus in the rat. *J. Comp. Neurol.* 522, 1454–1484. doi: 10.1002/cne.23533

Soiza-Reilly, M., Anderson, W. B., Vaughan, C. W., and Commons, K. G. (2013). Presynaptic gating of excitation in the dorsal raphe nucleus by GABA. *Proc. Natl. Acad. Sci. U S A* 110, 15800–15805. doi: 10.1073/pnas.1304505110

Soiza-Reilly, M., and Commons, K. G. (2011a). Glutamatergic drive of the dorsal raphe nucleus. *J. Chem. Neuroanat.* 41, 247–255. doi: 10.1016/j.jchemneu.2011.04.004

Soiza-Reilly, M., and Commons, K. G. (2011b). Quantitative analysis of glutamatergic innervation of the mouse dorsal raphe nucleus using array tomography. *J. Comp. Neurol.* 519, 3802–3814. doi: 10.1002/cne.22734

Steinbusch, H. W. M. (1984). Serotonin-immunoreactive neurons and their projections in the CNS. *Handb. Chem. Neuroanat.* 3, 68–125.

Stockmeier, C. A. (1997). Neurobiology of serotonin in depression and suicide. *Ann. N Y Acad. Sci.* 836, 220–232. doi: 10.1111/j.1749-6632.1997.tb52362.x

Takahashi, A., Shimamoto, A., Boyson, C. O., DeBold, J. F., and Miczek, K. A. (2010). GABA(B) receptor modulation of serotonin neurons in the dorsal raphé nucleus and escalation of aggression in mice. *J. Neurosci.* 30, 11771–11780. doi: 10.1523/JNEUROSCI.1814-10.2010.

Tao, R., and Auerbach, S. B. (2003). Influence of inhibitory and excitatory inputs on serotonin efflux differs in the dorsal and median raphe nuclei. *Brain Res.* 961, 109–120. doi: 10.1016/s0006-8993(02)03851-9

Taylor, S. R., Badurek, S., Dileone, R. J., Nashmi, R., Minichiello, L., and Picciotto, M. R. (2014). GABAergic and glutamatergic efferents of the mouse ventral tegmental area. *J. Comp. Neurol.* 522, 3308–3334. doi: 10.1002/cne.23603

Templin, J. S., Bang, S. J., Soiza-Reilly, M., Berde, C. B., and Commons, K. G. (2012). Patterned expression of ion channel genes in mouse dorsal raphe nucleus determined with the allen mouse brain atlas. *Brain Res.* 1457, 1–12. doi: 10.1016/j.brainres.2012.03.066

van Steensel, B., van Binnendijk, E. P., Hornsby, C. D., van der Voort, H. T., Krozowski, Z. S., de Kloet, E. R., et al. (1996). Partial colocalization of glucocorticoid and mineralocorticoid receptors in discrete compartments in nuclei of rat hippocampus neurons. *J. Cell Sci.* 109(Pt. 4), 787–792.

Varoqui, H., Schäfer, M. K. H., Zhu, H., Weihe, E., and Erickson, J. D. (2002). Identification of the differentiation-associated Na+/PI transporter as a novel vesicular glutamate transporter expressed in a distinct set of glutamatergic synapses. *J. Neurosci.* 22, 142–155.

Veenstra-VanderWeele, J., Muller, C. L., Iwamoto, H., Sauer, J. E., Owens, W. A., Shah, C. R., et al. (2012). Autism gene variant causes hyperserotonemia, serotonin receptor hypersensitivity, social impairment and repetitive behavior. *Proc. Natl. Acad. Sci. U S A* 109, 5469–5474. doi: 10.1073/pnas.1112345109

Wang, G., and Smith, S. J. (2012). Sub-diffraction limit localization of proteins in volumetric space using Bayesian restoration of fluorescence images from ultrathin specimens. *PLoS Comput. Biol.* 8:e1002671. doi: 10.1371/journal.pcbi.1002671

Warden, M. R., Selimbeyoglu, A., Mirzabekov, J. J., Lo, M., Thompson, K. R., Kim, S.-Y., et al. (2012). A prefrontal cortex-brainstem neuronal projection that controls response to behavioural challenge. *Nature* 492, 428–432. doi: 10.1038/nature11617

Conflict of Interest Statement: The authors declare that the research was conducted in the absence of any commercial or financial relationships that could be construed as a potential conflict of interest.

Received: 20 April 2014; accepted: 11 August 2014; published online: 26 August 2014.
Citation: Soiza-Reilly M and Commons KG (2014) Unraveling the architecture of the dorsal raphe synaptic neuropil using high-resolution neuroanatomy. Front. Neural Circuits ***8****:105. doi: 10.3389/fncir.2014.00105*
This article was submitted to the journal Frontiers in Neural Circuits.

frontiers in
NEURAL CIRCUITS

REVIEW ARTICLE
published: 03 September 2014
doi: 10.3389/fncir.2014.00098

Neuronal organization of olfactory bulb circuits

Shin Nagayama [1]***, Ryota Homma*** [1] ***and Fumiaki Imamura*** [2]

[1] *Department of Neurobiology and Anatomy, The University of Texas Medical School at Houston, Houston, TX, USA*
[2] *Department of Pharmacology, Pennsylvania State University College of Medicine, Hershey, PA, USA*

Edited by:
Benjamin R. Arenkiel, Baylor College of Medicine, USA

Reviewed by:
Kazushige Touhara, University of Tokyo, Japan
Veronica Egger, Ludwig-Maximilians-Universität, Germany
Kathleen Quast, Baylor College of Medicine, USA

****Correspondence:***
Shin Nagayama, Department of Neurobiology and Anatomy, The University of Texas Medical School at Houston, 6431 Fannin Street, MSB 7.046, Houston, TX, USA
e-mail: shin.nagayama@uth.tmc.edu

Olfactory sensory neurons extend their axons solely to the olfactory bulb, which is dedicated to odor information processing. The olfactory bulb is divided into multiple layers, with different types of neurons found in each of the layers. Therefore, neurons in the olfactory bulb have conventionally been categorized based on the layers in which their cell bodies are found; namely, juxtaglomerular cells in the glomerular layer, tufted cells in the external plexiform layer, mitral cells in the mitral cell layer, and granule cells in the granule cell layer. More recently, numerous studies have revealed the heterogeneous nature of each of these cell types, allowing them to be further divided into subclasses based on differences in morphological, molecular, and electrophysiological properties. In addition, technical developments and advances have resulted in an increasing number of studies regarding cell types other than the conventionally categorized ones described above, including short-axon cells and adult-generated interneurons. Thus, the expanding diversity of cells in the olfactory bulb is now being acknowledged. However, our current understanding of olfactory bulb neuronal circuits is mostly based on the conventional and simplest classification of cell types. Few studies have taken neuronal diversity into account for understanding the function of the neuronal circuits in this region of the brain. This oversight may contribute to the roadblocks in developing more precise and accurate models of olfactory neuronal networks. The purpose of this review is therefore to discuss the expanse of existing work on neuronal diversity in the olfactory bulb up to this point, so as to provide an overall picture of the olfactory bulb circuit.

Keywords: structure of olfactory bulb, cell type, layer formation

INTRODUCTION

Our environment is filled with odorant molecules, and our emotions, moods, and even behaviors can be controlled by olfactory stimuli. We are predisposed to discriminate between more than 10^{12} odors (Bushdid et al., 2014), in part due to the variety of odorant receptors that bind to different odorants with unique affinity profiles (Malnic et al., 1999). These odorant receptors are expressed by olfactory sensory neurons in the olfactory epithelium. Since the first rat odorant receptor was cloned in 1991, approximately 400 and 1000 different functional odorant receptors have been identified in the human and mouse genome, respectively (Buck and Axel, 1991; Zhang and Firestein, 2002; Nei et al., 2008; Adipietro et al., 2012). Because each olfactory sensory neuron expresses only a single odorant receptor, different odorants can activate distinct subsets of olfactory sensory neurons. Information from activated neurons is first transmitted to the olfactory bulb. Several reviews have summarized the elaborate neuronal network that extends from the olfactory epithelium to the olfactory bulb (Wilson and Mainen, 2006; Zou et al., 2009; Sakano, 2010; Mori and Sakano, 2011; Murthy, 2011; Lodovichi and Belluscio, 2012). In the olfactory bulb, multiple types of neurons form sophisticated networks to process information before transmitting it further to the olfactory cortex. Currently, there is a pressing demand for understanding the numerous neuronal types and networks to elucidate the mechanism(s) of olfactory information processing in the olfactory bulb.

Histologically, the olfactory bulb is divided into multiple layers. Intensive Golgi analyses in the 1970s succeeded in visualizing the morphology of neurons in each layer, and showed that the distinct layers were composed of morphologically distinct cells (Price and Powell, 1970a,b; Pinching and Powell, 1971a). Therefore, the neurons in the olfactory bulb have conventionally been categorized based on the layers in which their cell bodies are found. According to this categorization, juxtaglomerular (JG) cells, mitral cells, tufted cells, and granule cells were first defined. JG cells are now known to include three morphologically distinct cell types, the periglomerular (PG) cells, external tufted (ET) cells, and

Abbreviations: *Brain areas*: AON, anterior olfactory nucleus; AONpE, anterior olfactory nucleus pars externa; SVZ, subventicular zone; *Layers*: ONL, olfactory nerve layer; GL, glomerular layer; EPL, external plexiform layer; s-EPL, superficial EPL; i-EPL, intermediate EPL; d-EPL, deep EPL; MCL, mitral cell layer; IPL, internal plexiform layer; GCL, granule cell layer; *Cells*: JG cell, juxtaglomerular cell; PG cell, periglomerular cell; ET cell, external tufted cell; sSA cell, superficial short-axon cell; dSA cell, deep short-axon cell; SRIF-ir cell, somatostatinimmunoreactive cell; *Molecules*: BrdU, 5-bromo-2′-deoxyuridine; CaMKIV, CaM kinase IV; CB, calbindin; CCK, cholecystokinin; CR, calretinin; CRH, corticotropin-releasing hormone; DHPG, (RS)-3,5-dihydroxyphenylglycine; GAD, glutamic acid decarboxylase; GFP, green fluorescent protein; HCN, hyperpolarization-activated cyclic nucleotide gated channel; HRP, horseradish peroxidase; Kv, voltage-gated potassium channel; mGluRs, metabotropic glutamate receptors; nNOS, neuronal nitric oxide synthase; PV, parvalbumin; TH, tyrosine hydroxylase; VGAT, vesicular GABA transporter; VGLUT, vesicular glutamate transporter; VIP, vasoactive intestinal polypeptide.

superficial short-axon (sSA) cells. This categorization provides us with a basic model of the olfactory bulb network (**Figure 1**).

However, we are far away from forming a comprehensive model of the olfactory bulb network. An increasing number of studies suggest that conventionally categorized neurons in the brain comprise heterogeneous populations, and that the neuronal types in the olfactory bulb are among the most diverse (Shipley and Ennis, 1996). For example, PG cells are molecularly heterogeneous (Kosaka et al., 1995; Kosaka and Kosaka, 2005, 2007a; Panzanelli et al., 2007; Parrish-Aungst et al., 2007), and subgroups of mitral cells with different morphological and/or electrophysiological properties have been identified (Padmanabhan and Urban, 2010; Angelo et al., 2012). Furthermore, granule cells can be separated into morphologically distinct subgroups (Mori et al., 1983; Orona et al., 1983), and divergent properties between granule cells generated during developmental and adult stages are noted (Lemasson et al., 2005). In addition, some olfactory bulb neurons have not been typically included in conventional categories due to their relatively small numbers [e.g., short-axon cells in the External plexiform layer (EPL) and the granule cell layer (GCL)]. Nonetheless, recent technological advances now make it possible to target and analyze even these miniscule cell populations. Moreover, new neuronal types and connections in the olfactory bulb continue to be discovered (Merkle et al., 2014).

Nevertheless, new neuronal types and connections are often not taken into account in building a model of the olfactory bulb network. We are concerned with this trend of omission as it may hinder future progress in research. The major problem is that novel findings are scattered across many literary references, and recent reviews have not effectively summarized the neuronal diversity in the olfactory bulb. Here, we gather the scattered results and summarize the discoveries regarding the new neuronal types and connections in each layer. Since understanding the inputs and outputs of neurons is fundamental to building a network model, we focus mainly on somata locations, axon/dendrite extension patterns, neurotransmitters, and/or the physiological properties of neurons. We believe that this review greatly adds to our knowledge of the general model of the olfactory bulb network, and brings the information about this brain region to another level. In this article, we focus on neurons rather than on glia and the rodent main olfactory bulb rather than accessory olfactory bulb. The authors apologize to those whose work was not included here due to space limitations.

GLOMERULAR LAYER

NEURONS IN THE GLOMERULAR LAYER AND THEIR MORPHOLOGY

Neurons in the glomerular layer (GL) are morphologically heterogeneous and are of three identified types, PG cells, sSA cells,

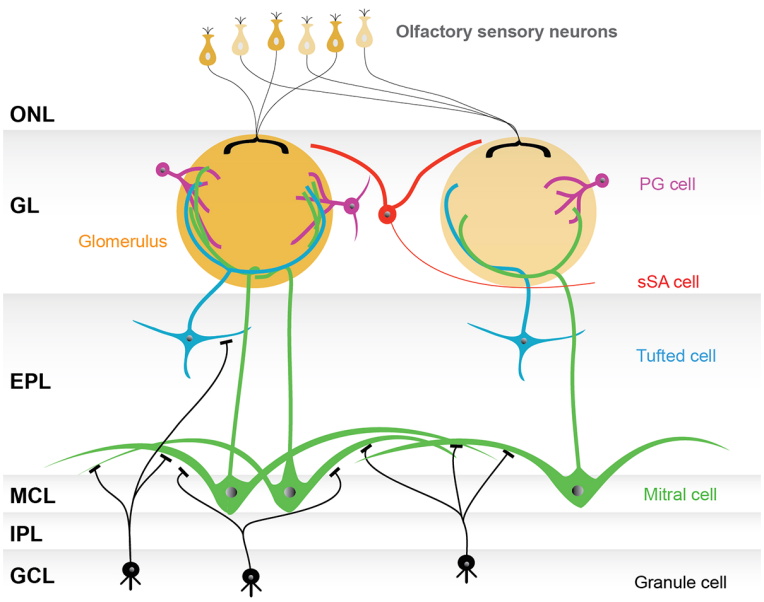

FIGURE 1 | Basic model of the olfactory bulb network. The illustrated olfactory bulb network is based on the conventional categorization of participating neurons. The axons of olfactory sensory neurons make synapses in the glomerular layer (GL), consisting of spherical structures called glomeruli. Although there are several thousand glomeruli at the surface of the rodent olfactory bulb, olfactory sensory neurons expressing the same type of odorant receptor converge their axons into only a few glomeruli, and thus each glomerulus represents a single odorant receptor. Neurons surrounding glomeruli in the GL are called juxtaglomerular cells (JG cells), consisting of three morphologically distinct cell types: periglomerular (PG) cells, external tufted (ET) cells (not shown), and superficial short-axon (sSA) cells. There are two types of projection neurons, the mitral cells and the tufted cells, which send their axons to the olfactory cortex. The somata of mitral cells are located in the mitral cell layer (MCL), while the tufted cells are scattered throughout the EPL. Both mitral and tufted cells project a single primary dendrite into a single glomerulus, where they receive synaptic inputs from the axons of olfactory sensory neurons and make reciprocal synapses with the dendrites of PG cells. Secondary dendrites of mitral and tufted cells are elongated in the external plexiform layer (EPL), where reciprocal synapses are formed with granule cell dendrites. The internal plexiform layer (IPL), in which axons from mitral cells and axon collaterals of ET cells run, and the granule cell layer (GCL), which is largely composed of granule cells, both lie beneath the MCL. Granule cells are axon-less interneurons extending dendrites apically into the EPL. Abbreviation: ONL, olfactory nerve layer.

and ET cells (Pinching and Powell, 1971a). Generically, they may also be referred to as JG cells when their morphological type is not specified. Most of these cells (PG cells, sSA cells, and a portion of the ET cells) are actually interneurons and do not innervate brain regions outside the olfactory bulb.

The PG cell is the most abundant type of neuron in the GL (Parrish-Aungst et al., 2007). These cells have the smallest cell body (5–10 μm in diameter) among the three morphological types. PG cells typically project their dendrites to a single glomerulus, and only occasionally to multiple glomeruli. Their dendrites ramify in a smaller portion of the glomerulus than the dendrites of ET cells. PG cells are generally thought to bear an axon (Pinching and Powell, 1971a), but axonless subtypes may also exist (Kosaka and Kosaka, 2011). The length of the axon is variable, and can extend as far as 5–6 glomeruli (∼600 μm; Pinching and Powell, 1971a). Axons of PG cells terminate in the interglomerular space.

The sSA cell was first reported by Pinching and Powell (Pinching and Powell, 1971a). The percentage of sSA cells among JG cells is thought to be small, although no estimate has been provided. The somata of sSA cells are slightly larger than those of PG cells, at 8–12 μm. These cells have dendrites that course exclusively in the interglomerular space, with an axon that extends as far as 1–2 glomeruli (Pinching and Powell, 1971a,c). No dendrodendritic connections have been found among this population (Pinching and Powell, 1971b,c). However, some recently described sSA cells have a somewhat distinct morphology from previously described sSA cells (Aungst et al., 2003; Kiyokage et al., 2010). This recently described population will be discussed in detail below.

The ET cell has the largest cell soma among the three types of JG cells, at 10–15 μm (Pinching and Powell, 1971a). The primary dendrites of ET cells are generally mono-glomerular, with a small subpopulation being di-glomerular (Ennis and Hayar, 2008). In contrast to PG cells, ET cell dendrites occupy a large volume of the glomerulus. To date, at least two morphologically distinctive subgroups of ET cells have been reported (Macrides and Schneider, 1982; Schoenfeld et al., 1985). One group has no secondary dendrites; the cell body is only found in the GL; and the axon is apparently restricted within the olfactory bulb. The other group of ET cells has secondary dendrites that extend to the EPL, with cell bodies generally found in the deeper one-third of the GL, or in the EPL near the boundary with the GL. The axons of the latter group project either to the internal plexiform layer (IPL) of the other side (medial-lateral) of the same bulb, or to the anterior olfactory nucleus (AON) pars externa (pE). The AONpE connects the circuits associated with homotypic glomeruli receiving input from olfactory sensory neurons that express the same odorant receptor between right and left olfactory bulb (Liu and Shipley, 1994; Lodovichi et al., 2003; Yan et al., 2008). As discussed later, these two groups may also be distinct in other attributes.

These JG neurons, including the subtypes discussed in the following subsections, are summarized in **Figure 2A** and **Table 1**. More detailed description about basic neuronal circuits in the GL can be found in an excellent review by Wachowiak and Shipley (2006).

DIVERSITY OF PERIGLOMERULAR CELLS REGARDING SYNAPTIC ORGANIZATION

PG cells can be divided into two subtypes based on its synaptic organization. A glomerulus in the olfactory bulb is composed of two distinct kinds of anatomical compartments (Kosaka et al., 1996, Kasowski et al., 1999). One compartment includes the processes of olfactory sensory neurons (ON zone), and the other compartment lacks these processes and is instead occupied by the processes of bulbar neurons (non-ON zone). Some PG cells extend their dendrites to both zones (referred to as type-I PG cells), but other PG cells extend their dendrites only to the non-ON zone (referred to as type-II PG cells; Kosaka et al., 1998). This observation suggests that type-II PG cells do not receive direct inputs from olfactory sensory neurons.

In parallel with the above-described anatomical heterogeneity, experiments using slice preparations suggested two types of synaptic organization in PG cells, based on their physiological properties (Shao et al., 2009; Kiyokage et al., 2010). The first type of neuron receives single spontaneous excitatory post-synaptic currents (EPSCs) and exhibits consistent and shorter delays in response to the electric stimulation of olfactory nerve bundles in the ONL. The second type of neuron receives a burst of spontaneous EPSCs and exhibits longer and varying delays to peri-threshold nerve stimulation. The former neuron is likely driven by direct monosynaptic inputs from olfactory sensory neurons (ON-driven cells), whereas the latter is likely driven by polysynaptic inputs through olfactory bulb neurons, such as ET cells (ET-driven cells; Shao et al., 2009).

It is tempting to relate type-I and type-II PG cells to ON-driven cells and ET-driven cells, respectively. However, the relationship may not be that straightforward. Type-II PG cells could be exclusively ET-driven, given that they have no connection to olfactory sensory neurons. On the other hand, type-I PG cells, which may connect to both olfactory sensory neurons and other cells, could in principle be driven by either pathway. Therefore, the dominant pathway is probably determined by as yet unidentified, additional factors (Kiyokage et al., 2010).

DIVERSITY OF PERIGLOMERULAR CELLS REGARDING NEURONAL TRANSMITTER

The neurotransmitters of PG cells are described largely on the basis of expression of related molecular markers. Among the many candidate markers related to neurotransmitters (Kosaka et al., 1998), glutamic acid decarboxylase (GAD), and tyrosine hydroxylase (TH) have attracted the most attention. Two isoforms of GAD (GAD65 and GAD67) are of particular interest. First, the expression of these proteins in a neuron implies its physiological function as a GABAergic neuron. Second, one or both of these isoforms is expressed in more than half of the entire JG cell population (Parrish-Aungst et al., 2007; Whitman and Greer, 2007). Even though the relative proportions of each isoform in a particular cell and/or their co-expression are of broad interest, no conclusive figures are yet available. One technical difficulty may be a potential mismatch between the population positive for GAD immunolabeling, genetic markers [e.g., green fluorescent protein (GFP)], and the true population of GABAergic neurons. Another problem is that a fraction of the PG cell population is not labeled by the general neuronal marker, NeuN (Panzanelli et al., 2007;

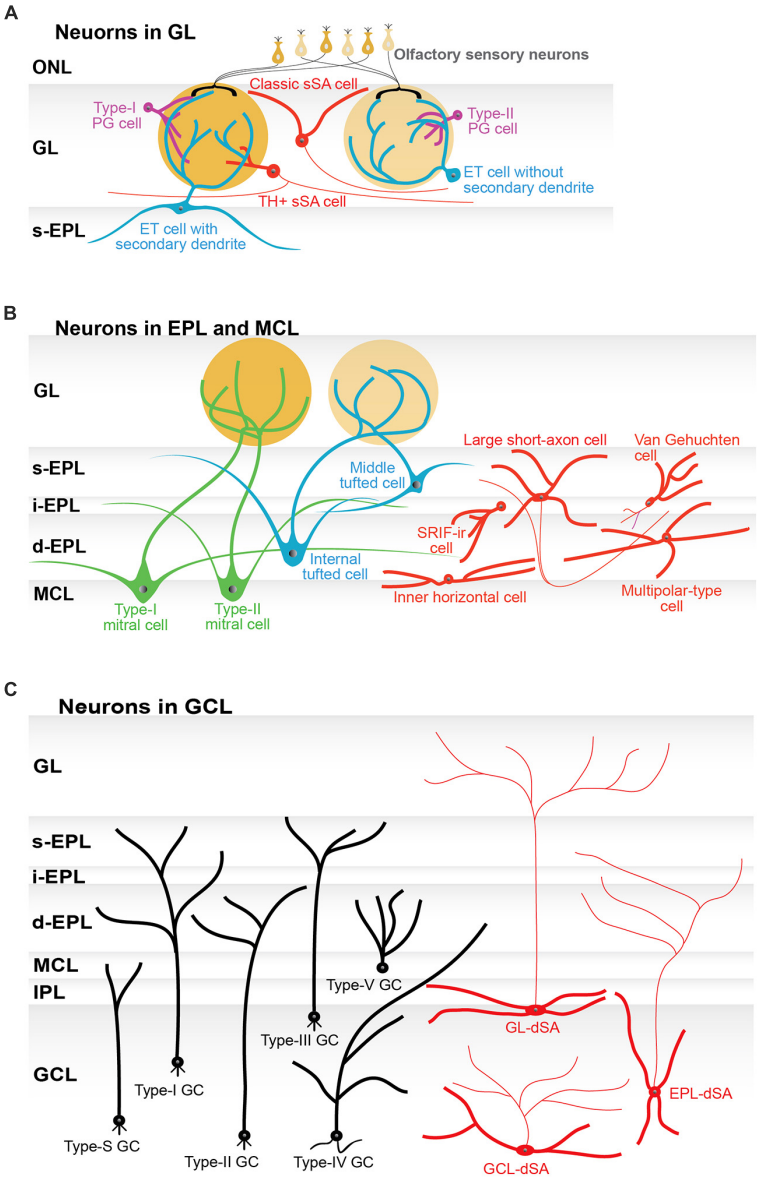

FIGURE 2 | Subtypes of neurons in the olfactory bulb. (A) Schematic illustration of the subtypes of periglomerular cells (PG cells; purple), superficial short-axon cells (sSA cells; red), and external tufted cells (ET cells; blue). Two subtypes of PG cells are based on their synaptic connections. Type-I PG cells receive synaptic inputs on their dendrites from both olfactory sensory neurons and neurons in the olfactory bulb. Type-II PG cells only receive inputs from neurons in the olfactory bulb. PG cells can be further divided into neurochemical subtypes (not shown in the figure). Classically, sSA cells had an axon and dendrites. The dendrites did not enter a glomerulus. More recently reported types of sSA cells are positive for tyrosine hydroxylase (TH) and connected to a few to tens of glomeruli. Subtypes of ET cells are determined by morphology: those without and those with secondary dendrites. The ET cells with secondary dendrites are more frequently found around the border between the GL and the superficial external plexiform layer (s-EPL). **(B)** Schematic illustration of subtypes of tufted cells (green) and mitral cells (blue), as well as interneurons (red) in the external plexiform layer (EPL) and the mitral cell layer (MCL). Tufted cells are classified as external, middle, and internal tufted cells based on their soma location. ET cells are discussed in the GL section of the main manuscript and thus are not shown here. The EPL itself can be divided into multiple sub-layers, including the s-EPL, the intermediate EPL (i-EPL), and the deep EPL (d-EPL). The two subtypes of mitral cells are based on the depth of their secondary (basal) dendrites in the EPL sub-layers and are referred to as type-I and type-II mitral cells, respectively. On average, middle tufted cells have smaller cell somata than internal tufted cells, and internal tufted cells have smaller cell somata than mitral cells. Among interneurons, only large short-axon cells have axons. Some of the neurons that had originally been categorized as short-axon cells have an axon-like process (see main text), but they are not shown in this figure to avoid any confusion. Van Gehuchten cells are axonless cells, while inner horizontal and multipolar-type cells are identified by their morphological features and locations. The majority of interneurons have been studied by parvalbumin (PV) labeling. In addition, somatostatin-immunoreactive (SRIF-ir) cells are located in the i-EPL/d-EPL and extend their dendrites specifically to the d-EPL. **(C)** Schematic illustration of six subtypes of granule cells (GC; black) and three subtypes of deep short-axon cells (dSA cells; red) in the granule cell layer (GCL). The subtypes of granule cells and dSA cells are determined based on the location (depth) of their cell somata in the GCL and the layer or sublayer to which their dendrites extend. These subtypes of GC are referred to as type-I, type-II, type-III, type-IV, type-V, and type-S cells. The subtypes of dSA cells are referred to as GL-dSA, EPL-dSA, and GCL-dSA cells, reflecting the distribution of their axons. Abbreviations: GL, glomerular layer, ONL, olfactory nerve layer; IPL, internal plexiform layer.

Table 1 | Glomerular layer.

Cell type	**Periglomerular cell (PG cell)**		**Superficial short-axon cell (sSA cell)**		**External tufted cell (ET cell)**	
Subtype	**Type-I**	**Type-II**	**Classic**	**TH+/GAD67+**	**No secondary dendrite**	**With secondary dendrite**
Soma size	5–10 μm		8–12 μm		10–15 μm	
Soma location	Interglomerular space		Interglomerular space		Interglomerular space	GL-EPL border
Dendrite extension	Single glomerulus (infrequently two glomeruli)		Interglomerular space	Multiple glomeruli	Single glomerulus (infrequently two glomeruli)	Superficial EPL
Input	ET cell, PG cell, sSA cell, tufted cell, mitral cell, GL-dSA cell, centrifugal fiber	OSN	PG cell, sSA cell, centrifugal fiber	ET cell (same glomerulus)	OSN, ET cell (VGLUT3+, same glomerulus)	GC
Output	Tufted cell, mitral cell, PG cell, OSN		PG cell, sSA cell (classic), tufted cell, mitral cell	ET cell (other glomeruli)	PG cell, sSA cell (TH+/GAD67+), ET cell (same glomerulus), mitral cell, tufted cell	neuron in AONpE
Transmitter	GABA, dopamine (in the TH+ subtype)		*Unknown*	GABA, dopamine	Glutamate, GABA (in the VGLUT3+ subtype)	CCK, vasopressin
Known neurochemical subtypes	TH+	CB+, CR+	*Unknown*	*Unknown*	VGLUT2+, VGLUT3+	
Other known molecules expressed (in subpopulation)	GAD65, GAD67, PV, neurocalcin, $GABA_A$-R α5 subunit		*Unknown*	GAD67, TH	CB, GAD67, $GABA_A$-R α1 and α3 subunits	CCK, vasopressin
Proportion to the total JG cell population	Majority		*Unknown* (minority)	Less than 10%*	*Unknown*	
Function	Inhibition within the glomerulus		*Unknown*	Inhibition across glomeruli	Excitation within the glomerulus	Connecting circuits associated with the glomeruli of the same ORN
Additional notes				May have been included in TH-positive PG cell in some studies		Also referred to as "superficial tufted cell"
References	Pinching and Powell (1971a), Pinching and Powell (1971c), Kosaka et al. (1998), Kosaka and Kosaka (2005), Wachowiak and Shipley (2006), Kosaka and Kosaka (2007a), Parrish-Aungst et al. (2007), Panzanelli et al. (2007), Shao et al. (2009)		Pinching and Powell (1971a), Pinching and Powell (1971c)	Aungst et al. (2003), Kiyokage et al. (2010)	Macrides and Schneider (1982), Panzanelli et al. (2005), Tatti et al. (2014)	Liu and Shipley (1994), Tobin et al. (2010)

**TH+ neurons (TH+ PG cell and TH+ sSA cell) represent ~10% of entire JG cell population (Parrish-Aungst et al., 2007).*

Parrish-Aungst et al., 2007; Whitman and Greer, 2007). These limitations make it difficult to reliably estimate the number of all PG cells and their expression of GAD.

TH is an essential enzyme for the synthesis of dopamine. TH-positive cells account for approximately 10% of all JG cells, and most of these, if not all, co-express GAD. Indeed, the majority of the cells, and perhaps the entire population, is positive for GAD67, while a minor percentage is positive for both GAD65 and GAD67, or possibly for GAD65 alone. TH-positive neurons were considered as belonging to the PG cell population (Kosaka et al., 1998; Kosaka and Kosaka, 2005). However, recent studies revealed that some of TH-positive neurons are in fact morphologically similar to sSA cells (see below).

MOLECULAR DIVERSITY OF PERIGLOMERULAR CELLS

A number of studies address the molecular diversity of JG cells (Panzanelli et al., 2007; Parrish-Aungst et al., 2007). Although many of these studies did not originally intend to focus on specific morphological cell types, ET cells are negative for most of the molecular markers employed in these studies (but see below). Other studies limited their analyses to only the GABAergic neurons. As a consequence, while the vast majority of these studies intended to address the molecular diversity of PG cells, they might have inadvertently included GABAergic sSA cells and/or GABAergic ET cells.

The calcium-binding proteins, and particularly calretinin (CR) and calbindin (CB), have been extensively studied for their expression in PG cells. The expression of CR, CB, and TH is mutually exclusive, suggesting that each of these markers corresponds to a specific subtype of PG cell. Nearly all TH-positive and CB-positive PG cells, as well as the majority of CR-positive PG cells, are positive for GAD (Kosaka and Kosaka, 2007a; Sawada et al., 2011). TH, CB, and CR are co-expressed in PG cells with both GAD isoforms, and therefore are not exclusively associated with any one isoform. TH-positive PG cells are type-I PG cells, while CB-positive and CR-positive PG cells are type-II PG cells (Kosaka and Kosaka, 2005, 2007a). Multiple research groups have made attempts to determine the proportions of subtypes expressing these neurochemicals in the mouse (Panzanelli et al., 2007; Parrish-Aungst et al., 2007; Whitman and Greer, 2007; Sawada et al., 2011). Although the results are not ideal for direct comparisons between studies, the percentages of each marker fall within certain ranges: 30.0–44.0% for CR, 12.6–20.0% for TH, and 9.8–15.0% for CB. The difficulty of direct comparison mainly stems from varying definitions of overall cell populations. As described previously, enumeration of PG cells is technically challenging. Each laboratory has taken different paths to estimate the overall population of PG cells in the olfactory bulb, including counting all neurons positive for any neuronal markers tested (Parrish-Aungst et al., 2007); counting all cells labeled with the fluorescent dye DRAQ-5, except for ET cells (Whitman and Greer, 2007); counting cells immunohistochemically positive for a mixture of anti-GAD65/67 and anti-GABA (Kosaka and Kosaka, 2007a); or using transgenic mice, such as GAD67-GFP knock-in mice (Panzanelli et al., 2007) or vesicular GABA transporter (VGAT)-venus mice (Sawada et al., 2011), in which GABAergic neurons are labeled with fluorescent proteins.

The expression of additional neurochemical markers, such as neurocalcin, parvalbumin (PV), and $GABA_A$ receptor α5 subunit, have also been explored in several studies (Panzanelli et al., 2007; Parrish-Aungst et al., 2007; Whitman and Greer, 2007). Although these markers have not been investigated as extensively as the molecular markers, CR, CB, and TH, no evidence for co-expression with CR, CB, TH, or any other co-tested markers has been found. Accordingly, PG cells positive for some of these markers may also represent distinct cell subtypes. There are also reports of other markers that may only partially co-localize in PG cells (Kosaka and Kosaka, 2012). Such studies imply that the number of cellular molecular subtypes will continue to grow in the future based on the combination of multiple molecular markers. However, expression of many molecular markers (e.g., calcium-binding proteins) does not suggest the function of the cell subtype in and of themselves. Functional characterization of each cell subtype will therefore be essential.

DIVERSITY OF SUPERFICIAL SHORT-AXON CELLS

There is little literature explicitly describing the diversity of sSA cells. However, two types of sSA cells have apparently been documented in the literature. The first type is the sSA cells described by Pinching and Powell (Pinching and Powell, 1971a; see above). Here we mainly discuss the second type that was reported more recently.

Retrograde tracing showed that a subpopulation of JG cells possess long neuronal processes (several 100 μm to 1 mm). This population of neurons is positive for both TH and GAD67 (TH+/GAD67+ neurons; Kiyokage et al., 2010; Kosaka and Kosaka, 2011). Kiyokage et al. (2010) proposed that interglomerular process-bearing TH+/GAD67+ neurons might be classified as sSA cells. These cells were once reported as glutamatergic sSA cells by the same group (Aungst et al., 2003).

However, the morphology of this proposed TH+/GAD67+ sSA cell is clearly distinct from that of the "classic" sSA cell reported by Pinching and Powell (Kosaka and Kosaka, 2011; Pinching and Powell, 1971a,c). A TH+/GAD67+sSA cell has an axon that extends for ∼1 mm, and its dendrites make contacts with up to 50 glomeruli. On the other hand, a classic sSA cell has an axon that extends for just one to two glomeruli, and its dendrites avoid glomeruli. This discrepancy suggests that TH+/GAD67+sSA cells are a different breed from the classic sSA cell, even though their morphology is typical of the short-axon cell. It seems possible that there are two (or more) types of short-axon cell-like neurons in the GL, considering the heterogeneity of short-axon cells in the EPL and the GCL, as discussed in more detail later in the review.

Finally, TH-positive JG cells show further heterogeneity in soma size, where the size forms a bimodal distribution (Pignatelli et al., 2005; Kosaka and Kosaka, 2008b). The "small-soma" group is typical of PG cells, whereas the "large-soma" group exhibits a slightly larger soma than the PG cells. It is worthwhile to point out that TH+/GAD67+sSA cells are included in the large-soma group (Kosaka and Kosaka, 2008b). Therefore, we suggest that TH+/GAD67+ cells account for only a subpopulation of TH-positive JG cells.

MORPHOLOGICAL DIVERSITY OF EXTERNAL TUFTED CELLS

As discussed previously, ET cells are historically divided into two morphologically distinct subtypes: those without and those with secondary (basal) dendrites (alternatively, the cells can be divided into three subtypes by further dividing the dendrite-bearing cells according to morphological differences in the secondary dendrites; Macrides and Schneider, 1982). More recently, these morphological differences were shown to correlate with physiological distinctions (Antal et al., 2006). Therefore, the non-basal-dendrite-bearing and basal-dendrite-bearing ET cells may form two (or potentially more) separate populations.

In several studies, the basal-dendrite-bearing cells are referred to as superficial tufted cells (Ezeh et al., 1993; Kiyokage et al., 2010). Note that tufted cells are most typically classified into three types: external, middle, and internal tufted cells (see below). On the other hand, even though some ET cells with secondary dendrites are located in the superficial part of the EPL, they can still be distinguished from the middle tufted cells, particularly because few axons from these cells travel beyond the AON. It is therefore of great interest to determine whether the synaptic organization within the glomerulus is the same or different among each subtype of ET cells and the middle tufted cells.

DIVERSITY OF EXTERNAL TUFTED CELLS REGARDING NEURONAL TRANSMITTER

ET cells have long been considered exclusively glutamatergic. However, the latest study has revealed a novel and interesting subtype of ET cells, which is identified by its expression of vesicular glutamate transporter (VGLUT)3. A portion of this subtype is found to be not only glutamatergic but also GABAergic (Tatti et al., 2014). The synaptic targets of ET cells include other JG cells and projection neurons (both tufted and mitral cells) in the same glomerulus that connect through dendrodendritic synapses. For projection neurons, ET cell mediated di-synaptic inputs are a major source of excitatory inputs, in addition to direct inputs from olfactory sensory neurons (Wachowiak and Shipley, 2006; Najac et al., 2011; Gire et al., 2012). VGLUT3-positive subtype has been exhibited unique connectivity, that is, it excites tufted cells but not mitral cells. VGLUT3-positive subtype also inhibits the other subtype of ET cells in the same glomerulus (Tatti et al., 2014).

Furthermore, to date, two peptide hormones are known to be released from subpopulations of ET cells. Liu and Shipley (1994) reported a subpopulation of ET cells (referred to as "superficially situated tufted cells") that are involved in intrabulbar (medial-lateral) connections by using the peptide hormone, cholecystokinin (CCK), as a neurotransmitter. However, it is not clear whether CCK is used only by this type of ET cell, or by other ET cells as well. Tobin et al. (2010) reported a subpopulation of ET cells that releases a peptide hormone vasopressin. These vasopressinergic ET cells are involved in processing olfactory signal related to social recognition. These CCKergic and vasopressinergic ET cells are most often located around the boundary of GL and EPL, and have secondary dendrites.

MOLECULAR DIVERSITY OF EXTERNAL TUFTED CELLS

The molecular diversity of ET cells began to be revealed recently. For example, ET cells can be divided into specific subpopulations based on immunoreactivity for different $GABA_A$ receptor subunits, such as the α1 and α3 subunits (Panzanelli et al., 2005). Another study has classified ET cells into VGLUT2-positive and VGLUT3-positive subpopulations. VGLUT2-positive and VGLUT3-positive subpopulations are also distinctive about the synaptic organization in the glomerulus (Tatti et al., 2014). In the latter study, a portion of VGLUT3-positive ET cells coexpressed CB, but few of them coexpressed CR or TH. Although these molecules may not be strictly specific as molecular markers, they would be enormously helpful for the future studies on ET cells.

ADULT-BORN NEURONS IN THE GLOMERULAR LAYER

Subpopulations of olfactory bulb neurons are generated during adulthood and continue to be replaced throughout the life of the organism. JG cells are included in these subpopulations, although the proportion of adult-born neurons in the GL is much lower than that in the GCL. These neurons are generated in subventicular zone (SVZ) or rostral migratory stream, and then migrate to the olfactory bulb through the rostral migratory stream. Adult-born JG cells are probably primarily composed of PG cells, based on their morphology. Whitman and Greer (2007) described two morphologically distinct adult-born JG cells, one with a dendritic arbor limited to one or two glomeruli, and the other with more extensive multi-glomerular dendrites. The latter cells also had slightly larger cell bodies. Nonetheless, TH-positive neurons with interglomerular processes (i.e., the TH+/GAD67+ sSA cells discussed earlier) may not be generated in adulthood (Kosaka and Kosaka, 2009).

As in the overall PG cell population, neurochemical subtypes have been revealed in adult-born JG cells. The vast majority of these subtypes are likely GABAergic (Whitman and Greer, 2007; Sawada et al., 2011). However, a recent study reported the presence of adult-born, glutamatergic JG cells (Brill et al., 2009). Even though their numbers are small, further characterization of these neurons would be of great interest.

Regarding other molecular markers, adult-born PG cells express all three typical molecular markers discussed above: TH, CR, and CB. Whitman and Greer (2007) determined the percentage of each PG cell subtype in adult-born JG cells of a specific age by using the thymidine analog, 5-bromo-2′-deoxyuridine (BrdU), to label cells generated at the time of injection. At 46 days post-BrdU injection, a date at which adult-born PG cells are morphologically mature, BrdU-positive cells (∼46 days old) contain higher percentages of TH-positive, CR-positive, and GAD67-positive neurons compared with BrdU-negative cells (cells of all other ages, including embryonic cells). This finding raises the possibility that the relative percentage of PG cell subtypes may not be static, but instead keeps changing throughout life.

EXTERNAL PLEXIFORM LAYER AND MITRAL CELL LAYER

PROJECTION NEURONS IN THE EXTERNAL PLEXIFORM LAYER AND MITRAL CELL LAYER

Odor signals, which are processed within the glomerulus, propagate in the EPL along the primary dendrite of two types of

projection neurons, mitral and tufted cells (**Figure 1**). The signal arrives at the cell body of tufted cells in the EPL and mitral cells in the mitral cell layer (MCL), then horizontally back-propagates through the secondary dendrites in the EPL. The back-propagation signal is considered not to be attenuated, but rather to be conducted throughout the dendrites until it is blocked by local inhibition from granule cells (Xiong and Chen, 2002). The horizontal signal propagation is believed to inhibit the activity of other mitral/tufted cells via the dendrodendritic interaction with granule cells and other interneurons. This process is called lateral inhibition. The EPL is mostly occupied by dendritic fibers that are secondary dendrites of mitral/tufted cells and apical dendrites of granule cells.

Mitral and tufted cells share many morphological properties. For example, they both extend a single primary dendrite to one of the several thousand glomeruli in the olfactory bulb. This observation signifies that each projection neuron receives odor information originating from only one type of odorant receptor. Therefore, even at the level of projection neurons, each neuron follows the "single cell – single odorant receptor" rule. Furthermore, neurons associated with the same glomerulus (sister cells) receive homogeneous input from the same olfactory sensory neurons and thus are thought to have similar odorant response properties. However, their odor-tuning specificity is variable, depending on odor concentration and spatial location (Tan et al., 2010; Kikuta et al., 2013). In addition, sister cells reportedly have various temporal activity patterns (Dhawale et al., 2010).

Mitral and tufted cells also share certain biophysical properties. For instance, the dendrodendritic reciprocal synapses between tufted and granule cells are both AMPA and NMDA receptor-mediated synapses but NMDA receptor is essential for the dendrodendritic inhibition (Christie et al., 2001), as are the synapses between mitral and granule cells (Isaacson and Strowbridge, 1998; Chen et al., 2000). Therefore, tufted cells tend to be regarded as smaller mitral cells, and they are often, especially in physiological studies, categorized into a single group termed "mitral/tufted cells." In other organisms frequently used in olfactory research, such as the fly and the fish, mitral, and tufted cells are not morphologically well segregated and are accordingly categorized into a single group of projection neurons (Satou, 1990; Bargmann, 2006).

However, in the mammal, the morphologies of mitral and tufted cells are discriminable, especially by the location of the cell body and the extension pattern of secondary dendrites in the EPL (Mori et al., 1983; Orona et al., 1983). The secondary dendrites of the majority of tufted cells extend to the superficial/outer EPL, while those of mitral cells mostly extend to the deep/inner EPL. Hence, the EPL could be subdivided into at least two sublayers, the superficial/outer and the deep/inner layers, although a clear marker for the sublayers is not known. Interestingly, an early report identified a third intermediate sublayer, which is labeled by cytochrome oxidase (Mouradian and Scott, 1988).

Cell bodies of tufted cells are sparsely distributed in the EPL, and it is rare for them to find adjacent tufted cells. To the contrary, the cell bodies of mitral cells are surrounded by adjacent mitral cells in the MCL. Given the idea that more closely situated neurons tend to interact more strongly via reciprocal synapses with granule cells, such interactions are expected to be stronger among mitral cells than among tufted cells. The difference may, at least partially, be responsible for functional discrepancies between mitral and tufted cells (e.g., differential odor selectivity; Kikuta et al., 2013).

Targets of axons also differ between tufted cells and mitral cells (Haberly and Price, 1977; Skeen and Hall, 1977; Scott et al., 1980). The axons of tufted cells project to the anterior olfactory cortex, including the olfactory peduncle, olfactory tubercle, and ventrorostral subdivision of the piriform cortex. By contrast, those of mitral cells project widely throughout the entire olfactory cortex (Nagayama et al., 2010; Igarashi et al., 2012). Thus, there may be two types of axon bundles in the lateral olfactory tract, where one bundle is composed of thicker axons, and the other is composed of thinner axons [Price and Sprich, 1975; see also Bartolomei and Greer (1998) for PCD mice]. It is speculated that the thicker axons represent projections from mitral cells, while the thinner axons represent projections from tufted cells.

Functionally, tufted cells have lower thresholds to induce spike discharges by electrical stimulation of olfactory sensory neurons (Ezeh et al., 1993). The same result was also obtained with odorant stimulation of sensory neurons (Igarashi et al., 2012; Kikuta et al., 2013). In addition, tufted cells show a higher firing frequency than mitral cells (Nagayama et al., 2004), and tufted cells respond to a broader range of odorants than mitral cells (Nagayama et al., 2004; Kikuta et al., 2013). Recent reports also indicated that tufted cells respond during an earlier phase of the respiratory cycle, while mitral cells are activated during a later phase of the respiratory cycle (Fukunaga et al., 2012; Igarashi et al., 2012).

Mitral and tufted cells are generated during different periods of development. Whereas most mitral cells are born between embryonic days 10 and 13, tufted cells are born during a later period (embryonic days 13–16; Hinds, 1968; Imamura et al., 2011). The distinction in the timing of the genesis of tufted cells and mitral cells may affect to the differential locations of their somata, extension patterns of secondary dendrites, axon projections, and terminal locations (Inaki et al., 2004; Imamura et al., 2011).

Below, we discuss the structural and functional features of subgroups of tufted cells, mitral cells, and interneurons. The morphological features of these various kinds of neurons are summarized in **Figure 2B** and **Table 2**.

SUBGROUPS OF TUFTED CELLS

Currently, tufted cells tend to be categorized into three subgroups: ET cells, middle tufted cells, and internal tufted cells. ET cells have relatively small cell bodies (10–15 μm) and are located around the boundary between the GL and the EPL (Pinching and Powell, 1971a). As discussed previously, ET cells can be separated into two distinct populations, one with no secondary dendrites, and the other with extended secondary dendrites in the superficial EPL.

Middle tufted cells are located in the intermediate and superficial EPL, which lies underneath the boundary between the GL and EPL. As might be expected, the cell body of these cells is of a medium size (15–20 μm; Shepherd et al., 2004). The majority of the middle tufted cells extend relatively short secondary dendrites in the superficial and intermediate EPL. They also extend axon collaterals in the IPL (Orona et al., 1984), which probably make

Table 2 | External plexiform layer and mitral cell layer.

Projection neurons				
Cell type	**Tufted cell**		**Mitral cell**	
	Middle	**Internal**	**Type-I**	**Type-II**
Soma size	15–20 μm	>20 μm	>20 μm	
Soma location	Superficial-intermediate EPL	Deep EPL	MCL	
Dendrite extension	Superficial-intermediate EPL		Deep EPL	Intermediate EPL
Output within OB	Dendrites of PG, granule (probably type-I and -III) and other interneurons in EPL		Dendrites of PG, granule (Probably type-I and -II) and other interneurons in EPL	
Output out of OB	Anterior part of olfactory cortex		Entire olfactory cortex	
Transmitter	Glutamate			
Molecular markers	Tbx21, Pcdh21			
Population	∼50 tufted cells/glomerulus		∼20 mitral cells/glomerulus	
Physiological properties	Higher sensitivity to the odor stimuli		Lower sensitivity to the odor stimuli	
	Odor evoked spike activity during early phase of respiratory cycle		Odor evoked spike activity during late phase of respiratory cycle	
Additional notes	Sometimes, it is called intermediate tufted cells	Sometimes, it is called displaced mitral cells		
References	Mori et al. (1983), Orona et al. (1984), Ezeh et al. (1993), Royet et al. (1998), Nakajima et al. (2001), Nagai et al. (2005), Shepherd et al. (2004), Igarashi et al. (2012), Fukunaga et al. (2012)			

Interneurons					
Cell type	**Van Gehuchten cell types**		**Multipolar types**		
	Van Gehuchten cell	**Somatostatin-immunoreactive cell**	**Inner horizontal cell**	**Other types**	**Large short axon cell**
Soma size	∼12 μm	∼10 μm	9–12 μm	9–15 μm	∼14 μm
Soma location	Throughout the EPL	Intermediate-deep EPL	Deep EPL and MCL	Throughout the EPL	Superficial EPL
Dendrite extension	Throughout the EPL	Deep EPL	MCL and just above MCL	Throughout the EPL	EPL and GL
Output	*Unknown*	Probably mitral cell	probably mitral cell	Mitral/tufted cell	*Unknown*
Transmitter	Almost all of EPL interneurons are GABAergic				
Molecular markers	CR	Somatostatin, CR, VIP	CR		
Axon	No				Yes
Additional notes	Fusiform shape soma				Relatively rare to be found
References	Schneider and Macrides (1978), Kosaka et al. (1994), Brinon et al. (1998), Kosaka and Kosaka (2008a), Lepousez et al. (2010)				

contact with the other side (lateral-medial) of olfactory bulb like ET cells (Belluscio et al., 2002).

Internal tufted cells have relatively large cell bodies (>20 μm) and are located in the deep portion of the EPL (Orona et al., 1984). Internal tufted cells are sometimes called displaced mitral cells, because they reportedly have structural and functional properties similar to mitral cells. They also extend secondary dendrites in the intermediate and superficial EPL, as found with middle tufted cells. No tufted cells have been observed to extend secondary dendrites in the deep EPL.

SUBGROUPS OF MITRAL CELLS

Mitral cells have large cell bodies (>20 μm) and are found in the MCL. The majority of these cells extend long secondary dendrites predominantly in the deep EPL and are termed type-I mitral cells (Mori et al., 1983; Orona et al., 1984). However, some mitral cells extend secondary dendrites predominantly in the intermediate EPL and are termed type-II mitral cells (Orona et al., 1984; Mouradian and Scott, 1988). In addition, subsets of mitral cells extend secondary dendrites in the superficial EPL (Imamura and Greer, unpublished data) and may not represent either type-I or type-II mitral cells. This new type of mitral cell may thus make a unique odor-processing contribution and receive dendritic inhibition in the superficial EPL (like tufted cells), as well as strong somatic inhibition in the MCL from type-S granule cells (also see GCL section). Recently, several reports have suggested the presence of different types of mitral cells based on their structural and functional properties (Padmanabhan and Urban, 2010; Angelo and Margrie, 2011; Angelo et al., 2012; Kikuta et al., 2013). By using *in vivo* two-photon imaging microscopy, mitral cells were recently grouped into three subtypes according to cell body shape: triangular, round, and fusiform type (Kikuta et al., 2013). Due to the lack of detailed evidence about the secondary dendrite extension pattern for each of these three subtypes, it is still unclear whether these cells are related to type-I or type-II mitral cells.

Mitral cells vary in molecular expression profiles. Subsets of the cells express the α3 subunit of the $GABA_A$ receptor (Panzanelli et al., 2005), and variably express the voltage-gated potassium channel (e.g., Kv1.2) and the hyperpolarization-activated cyclic nucleotide gated channel (e.g., HCN2; Padmanabhan and Urban, 2010; Angelo and Margrie, 2011). Because HCN2 channel expression levels may be strongly associated with the parental glomerulus, olfactory sensory neuronal activity likely influences channel expression in mitral cells (Angelo et al., 2012). These data suggest the possibility that mitral cells can be subdivided based on the expression levels of specific molecules. Recent reports revealed that intrinsic biophysical properties also vary among mitral cells, such as firing frequency (Padmanabhan and Urban, 2010) and the I_h sag current (Angelo et al., 2012). The I_h sag current is probably associated with HCN2 expression levels. These studies highlight the possibility that the activity of mitral cells is controlled not only by inhibitory neurons in the olfactory bulb circuit, but also by intrinsic physiological properties.

As noted above, several reports indicate variations in mitral cell morphology, molecular expression profiles, and biophysical properties. However, it is uncertain whether these properties are related to one another. Connecting information and drawing a detailed profile of each mitral cell subtype will undoubtedly promote an understanding of odor coding.

INTERNEURONS IN THE EXTERNAL PLEXIFORM LAYER AND MITRAL CELL LAYER

Several types of local neurons exist in the EPL (Schneider and Macrides, 1978; Shepherd et al., 2004). The majority are GABAergic neurons and make reciprocal synaptic contacts with mitral cells (Kosaka et al., 1994; Toida et al., 1994). These neurons reportedly express several calcium-binding proteins, such as PV, CB, CR, and neurocalcin (Brinon et al., 1999). Almost all EPL interneurons express CR. One-third are PV-positive neurons, which are well-studied, especially regarding their structural features (Lepousez et al., 2010; Huang et al., 2013). Nonetheless, PV is expressed in multiple morphological subtypes and thus, cannot be used as a definitive marker for a specific neuronal subtype. We first discuss PV-positive neurons below, and then briefly introduce several morphologically identified subtypes of EPL interneurons.

Parvalbumin-positive neurons

PV-positive cells in the EPL have quite varied structural properties. They can be categorized into five groups: sSA cells, Van Gehuchten cells, multipolar-type cells, inner short-axon cells, and inner horizontal cells (Kosaka et al., 1994). The latter two are regarded as particular subtypes or variations of the multipolar-type cell. Although some of the neurons are termed short-axon cells, it is not clear whether these PV-positive cells have axons or not (also see the following section, "short-axon cells in the external plexiform layer"; Kosaka et al., 1994; Kosaka and Kosaka, 2008a). PV-positive cells show reciprocal interactions with mitral cells, receiving excitatory inputs from mitral/tufted cells and returning inhibition to mitral/tufted cells, as seen with granule cells (Toida et al., 1994; Huang et al., 2013; Kato et al., 2013; Miyamichi et al., 2013). An interesting finding is that PV-positive cells have quite wide odorant selectivity, and odors can activate them in a broad area. Therefore, PV-positive neurons are expected to contribute to the non-specific gain control signals in the olfactory bulb circuit (Kato et al., 2013; Miyamichi et al., 2013).

A recent study reported that ∼80% of corticotropin-releasing hormone (CRH)-positive neurons express PV, and that the number of CRH-expressing cells is almost the same as the number of PV-positive cells in the EPL (Huang et al., 2013). This implies that the majority of CRH- and PV-expressing cells represent the same population. CRH-positive cells have a relatively low input resistance, a high capacitance, and a high firing rate response to current injection. Therefore, CRH-positive interneurons are considered to comprise a population of medium-sized and fast-spiking interneurons in the EPL (Huang et al., 2013).

Short-axon cells in the external plexiform layer

Historically, short-axon cells in the EPL were visualized by using Golgi techniques (Schneider and Macrides, 1978), and their structural details were studied by using PV immunostaining (Kosaka et al., 1994; Brinon et al., 1998). In some PV-positive cells, the axon initial segments of axon-like processes lack βIV-spectrin, an essential protein for spike propagation in axon. This observation suggests that the processes might not function as typical axons.

Therefore, only large, multipolar cells with distinctive axons are defined as short-axon cells among PV-positive cells (Kosaka and Kosaka, 2008a). Interestingly, trans-synaptic tracing methods indicated that some of the short-axon cells in the EPL are presynaptic to adult-born neurons (Arenkiel et al., 2011). This implies that short-axon cell-like interneurons in this region may act to recruit or navigate newly generated granule cells into proper connections with mitral/tufted cells.

Van Gehuchten cells

This neuron type is considered an axonless cell. Van Gehuchten cells have medium-sized somata (∼12 μm) and few dendrites with polarized extension patterns. The thicker and longer dendrites (<150 μm) extend toward one side of the EPL, and the thinner and relatively shorter dendrites (<100 μm) extend toward the opposite pole (Schneider and Macrides, 1978). Half of these cells are PV-positive (Kosaka et al., 1994; Toida et al., 1996). Neurocalcin- or CB-positive cells are rarely found (Brinon et al., 1998).

Somatostatin-immunoreactive neurons

These neurons are recently identified and share some of the same morphological features as Van Gehuchten cells. They are also considered axonless cells. The soma size is approximately 10 μm. The majority of somatostatin-immunoreactive (SRIF-ir) neurons (∼95%) are located in the intermediate and deep EPL and extend dendrites specifically into the deep EPL (Lepousez et al., 2010). Because most mitral cells (type-I) extend secondary dendrites in the deep EPL, the SRIF-ir neurons may connect specifically with mitral cell secondary dendrites. SRIF-ir neurons are also GABAergic (99.4%), CR-positive (99.9%), and vasoactive intestinal polypeptide (VIP)-positive (96.7%) cells. Half of these cells are also PV-positive.

GRANULE CELL LAYER

The GCL of the olfactory bulb is occupied mostly by granule cells, which are inhibitory interneurons with a small cell body (6–8 μm in diameter; Price and Powell, 1970b). Their somata are localized mostly in the GCL, but some granule cells are also found in the IPL and the MCL. An apical dendrite typically extends radially toward the surface of the olfactory bulb and rarely branches in the GCL, until it ramifies in the EPL. In the EPL, granule cells have dendritic spines that form reciprocal synapses with the secondary dendrites of mitral and/or tufted cells. Due to their axonless morphology, the output of granule cells relies solely on dendrodendritic synapses.

The other interneurons in the GCL are deep short-axon (dSA) cells. Short-axon cells comprise heterogeneous populations, and they were previously classified into multiple subpopulations based on their soma location and morphology (Schneider and Macrides, 1978; Shepherd et al., 2004). Among these short-axon cells, the Blanes cells, Golgi cells, Cajal cells, and horizontal cells have their cell bodies in the deeper regions of the olfactory bulb, including the MCL, IPL, and GCL. These cells are now collectively re-classified as dSA cells (Eyre et al., 2008). Compared with granule cells, dSA cells have larger cell bodies (10–20 μm in diameter), and their dendrites do not usually extend beyond the MCL. On the other hand, they have axons that project to different layers of the olfactory bulb (see below).

Granule cells and dSA cells are divided into subgroups, mostly based on morphological differences between the groups. These cells are discussed in detail below, and their properties are summarized in **Figure 2C** and **Table 3**.

MORPHOLOGICAL DIVERSITY OF GRANULE CELLS

Intracellular horseradish peroxidase (HRP) injection into the rabbit olfactory bulb cells revealed at least three morphologically distinct subpopulations of granule cells based on their dendritic extension patterns in the EPL (Mori et al., 1983; Mori, 1987). The type-I granule cell (GI) ramifies spiny dendrites at any depth of the EPL. Dendrites of the type-II granule cell (GII) extend only in the deep EPL, while the type-III granule cell (GIII) ramifies spiny dendrites predominantly in the superficial EPL. Therefore, type-II and type-III granule cells are thought to preferentially regulate the activity of mitral cells and tufted cells, respectively. In an early work, Orona et al. (1983) injected HRP into the EPL of the rat olfactory bulb to label granule cells extending dendrites to the injection site. Injection of HRP into the superficial EPL preferentially labeled the granule cells localized in the superficial portion of the GCL (superficial granule cells). In contrast, HRP injection into the deep EPL labeled additional granule cells in the deep GCL (deep granule cells). These results strongly indicate a correlation between somata location and dendrite-ramifying area. Nonetheless, the location of somata is not a definitive determinant of type-I, II, or III cells, because some superficial granule cells ramified dendrites in the deep EPL, while some deep granule cells sent dendrites up to the superficial EPL.

Several other types of granule cells do not fit into type-I, II, or III categories. Naritsuka et al. (2009) discovered a novel type of cell in the GCL of a transgenic mouse expressing GFP under the control of the nestin promoter. The cell was named a type-S cell based on its strong GFP expression. Although neuronal progenitor cells usually express nestin, the type-S cell was defined as a mature neuron due to its expression of NeuN, a marker of mature neurons, and the existence of dendritic spines. The cell was also considered a granule cell based on its GABAergic phenotype and axonless morphology. The especially unique feature of the type-S granule cell was that the apical dendrites did not penetrate into the EPL, but rather formed reciprocal synapses with the perisomatic region of mitral cells. Therefore, the dendrites might regulate the production of action potentials in mitral cells. This hypothesis could be tested by experiments using electrophysiology and/or optogenetics.

Recently, Merkle et al. (2014) reported four previously unknown interneuron types that are generated in the adult mouse ventricular zone-SVZ and migrate to the GCL. Based on soma size/location, dendritic arbors bearing spines, and axonless morphology, two of the cells were termed type-IV granule cells (GIV) and type-V granule cells (GV). The type-IV granule cell was frequent dendritic branching in the GCL, and often failed to reach beyond the IPL. Somata of type-V granule cells lacked basal dendrites and were restricted to the MCL. These cells extended spiny shrub-like apical dendrites predominantly into the deep EPL. Due to their characteristic features, the authors also called type-IV and -V granule cells deep-branching granule cells and shrub granule cells, respectively. However, neurotransmitter and existence of

Table 3 | Granule cell layer.

Granule cell						
Cell type	**Type-I**	**Type-II**	**Type-III**	**Type-IV (deep-branching)**	**Type-V (shrub)**	**Type-S**
Soma size	6–8 μm					
Soma location (primary)	*Unspecified*	Deep GCL	Superficial GCL to MCL	*Unspecified*	MCL	Middle GCL
Dendrite extension	All through EPL	Deep EPL	Superficial EPL	Frequently branch in GCL	Deep EPL (no basal dendrite)	MCL
Transmitter	GABA			GABA?		GABA
Output	Mitral/tufted cell	Mitral cell?	Tufted cell?	*Unknown*	Mitral cell?	Mitral cell soma
References	Mori et al. (1983), Orona et al. (1983)			Merkle et al. (2014)		Naritsuka et al. (2009)

Deep short-axon cell			
Cell type	**GL-dSA**	**EPL-dSA**	**GCL-dSA**
Soma size	14–20 μm	11–15 μm	10–20 μm
Soma location (primary)	IPL	GCL	GCL
Dendrite extension	Predominantly confined to the IPL	MCL, IPL, GCL	MCL, IPL, GCL
Axon extension	GL (some in EPL)	EPL (some in IPL and superficial GCL)	GCL (some to the olfactory cortex)
Output	PG cell (granule cell)	Granule cell	Granule cell
Transmitter	GABA		
Additional notes	Horizontal cells, Golgi cells	Blanes cells, Cajal cells	Horizontal cells, Golgi cells
References	Schneider and Macrides (1978), Eyre et al. (2008, 2009)		

reciprocal synapses are still necessary to be specified, which will increase our knowledge of granule cell diversity.

MOLECULAR DIVERSITY OF GRANULE CELLS

To date, only GABA has been identified as a neurotransmitter of the granule cell. Although glycine evokes an inhibitory response in both mitral/tufted cells and granule cells, and immunoreactivity for glycine, the glycine receptor, and glycine transporters is found in the olfactory bulb (van Den Pol and Gorcs, 1988; Trombley and Shepherd, 1994), there is no direct evidence suggesting the existence of glycinergic neurons in the GCL (Zeilhofer et al., 2005). Therefore, glycinergic axons may originate outside the olfactory bulb.

In contrast to PG cells, granule cells are molecularly less diverse. Among known molecular markers expressed by subpopulations of PG cells (i.e., TH, CR, CB, and PV), only CR is expressed by a subset of granule cells that are localized in superficial GCL (Batista-Brito et al., 2008). In addition, 5T4, a leucine-rich-repeat transmembrane protein, also labels a subpopulation of superficial granule cells (Imamura et al., 2006; Yoshihara et al., 2012). Because dendrites of the 5T4-positive granule cells preferentially ramify in the superficial EPL, these cells most likely represent type-III granule cells. On the other hand, 5T4-positive granule cells are mostly found in the MCL and IPL, but rarely in the GCL, suggesting that they account for only a subset of type-III granule cells.

Curiously, few molecules specifically expressed by deep granule cells have been identified. As an exception, electrophysiological analyses suggested that expression levels of Group I metabotropic glutamate receptors (mGluRs) differed between superficial and deep granule cells (Heinbockel et al., 2007). (RS)-3,5-dihydroxyphenylglycine (DHPG), an agonist of Group I mGluRs, directly depolarized both superficial and deep granule cells in the wild-type mouse olfactory bulb slice. In mGluR5$^{-/-}$ and mGluR1$^{-/-}$ mice, only superficial and deep granule cells, respectively, were depolarized with DHPG. Further confirmation of differential expression of these molecules could be achieved

by immunohistochemical analyses with antibodies specific to mGluR1 and mGluR5.

Recently, Saino-Saito et al. (2007) reported that CaM kinase IV (CaMKIV) expression is restricted to deep granule cells. However, according to the immunohistochemical staining pattern, CaMKIV-positive cells localized to the entire GCL, but rarely to the MCL. The authors apparently defined granule cells in the whole GCL as deep granule cells. Therefore, albeit an interesting observation, CaMKIV might not be specific to deep granule cells under the definition in this review, in which the GCL is divided into superficial and deep layers. One possible reason for the lack of identification of any molecule specifically expressed by deep granule cells is simply that we have not yet examined the expression of the appropriate molecules. However, an alternative possibility is that granule cells innately have properties to differentiate into deep granule cells, and are thus redirected toward superficial granule cells by the expression of alternative molecules, such as Pax6 (see below).

ADULT-BORN GRANULE CELLS

An estimated 10,000 new neurons are generated in the adult mouse SVZ and enter into the olfactory bulb via the rostral migratory stream every day. Approximately half of these new neurons are integrated into the existing neuronal circuit as adult-born granule cells (Petreanu and Alvarez-Buylla, 2002; Yamaguchi and Mori, 2005). On the other hand, many pre-existing granule cells are eliminated from the circuit via apoptotic cell death every day. Whether specific types of granule cells are replaced with adult-born granule cells is an interesting question. Both morphologically and molecularly, all types of granule cells mentioned above, except for type-S cells, are generated in the adult olfactory bulb (Merkle et al., 2007, 2014). To date, the replacement of type-S cells has not been investigated. Although adult-born granule cells are distributed throughout the MCL, IPL, and GCL, several studies have suggested that adult-born granule cells are located in the deep GCL with higher density, while embryonically/perinatally born granule cells are preferentially located in the MCL, IPL, and the superficial GCL (Lemasson et al., 2005; Imayoshi et al., 2008). Intriguingly, retroviral fate mapping in the rat revealed that more adult-born granule cells ramified their dendrites in the deep EPL, even though their somata were located in the superficial GCL (Kelsch et al., 2007). These studies raise the idea that the microcircuit formed in the deep EPL is more plastic than that in the superficial EPL in the adult olfactory bulb.

DETERMINANTS OF GRANULE CELL DIVERSITY

What determines the final morphology and molecular phenotype of granule cells? Deep granule cells are mainly generated during postnatal stages, while superficial granule cells have a generation peak around the perinatal period (Hinds, 1968). Thus, the timing of neurogenesis influences the fate of granule cells. However, the factor that probably has the largest influence on granule cell diversity is the SVZ region in which the granule cell is generated. Neural stem cells in different portions of the SVZ produce different types of granule cells. Lineage tracing analyses of cells generated in various SVZ regions revealed that superficial and deep granule cells are preferentially produced in the dorsal and ventral SVZ, respectively (Merkle et al., 2007). Kelsch et al. (2007) used retroviral injection into the SVZ to show that the anterior and posterior axis also influenced the production of superficial and deep granule cells. In addition, Merkle et al. (2007) showed that CR-positive granule cells were mostly produced from the rostral migratory stream or the medial wall of the anterior SVZ. Furthermore, grafting experiments from these groups suggested that SVZ stem cells are highly resistant to respecification by environmental cues.

The molecular mechanisms regulating the production of specific granule cell types are not well known. Two transcription factors, Pax6 and ER81, are reportedly expressed only in subsets of superficial granule cells (Kohwi et al., 2005; Saino-Saito et al., 2007; Haba et al., 2009). Moreover, Pax6-deficient stem cells grafted into the wild-type SVZ produced many deep granule cells, but failed to produce superficial granule cells or TH-positive PG cells (Kohwi et al., 2005). These results may indicate that newly generated granule cells have innate properties to differentiate into deep granule cells, and are directed to become superficial granule cells via the expression of an additional set of transcription factors.

DIVERSITY OF DEEP SHORT-AXON CELLS

Based on morphological diversity revealed by Golgi staining, dSA cells in the rodent olfactory bulb were initially defined belonging to one of four cell types: Blanes cells, Golgi cells, horizontal cells, and Cajal cells. Schneider and Macrides (1978) described the morphology and location of the various dSA cells in the hamster olfactory bulb. Blanes cells are mostly found in the GCL or the IPL and have the largest cell body (16–23 μm) of the four dSA cells. They also have stellate dendrites covered with many spines. Golgi cells likewise are found in the GCL. Their cell bodies are slightly smaller than those of Blanes cells (12–22 μm), and their dendrites rarely have spines. Both horizontal cells and Cajal cells have the smallest cell bodies (15–18 μm), are restricted to the IPL and MCL, and have smooth dendrites. To date, all dSA cells are considered to be GABAergic, as are their post-synaptic target cells. Recently, dSA cell morphologies were reconstructed after electrophysiological recording in a rat olfactory bulb slice (Eyre et al., 2008). Overall, the dendrites of all four dSA cell types were restricted to the layers below the MCL. Despite the Schneider and Macrides report of the extension of Cajal cell dendrites to the EPL, this was not described by Eyre et al. Although the input sources were not revealed in detail, both excitatory and inhibitory inputs apparently modulated the activity of dSA cells.

Eyre et al. (2008) next re-classified dSA cells into three subpopulations according to their axonal distribution patterns in the olfactory bulb. The first subpopulation corresponds to the GL-dSA cell. The axons of these cells travel in the EPL up to the GL, where they extensively ramify with a few axon collaterals extending into the EPL and GCL. The major post-synaptic targets of GL-dSA cells are PG cells in the GL, while symmetrical synapses between axons of GL-dSA cells and the dendrites of granule cells are found in the EPL and GCL. The somata of many GL-dSA cells elongate in a direction parallel to the MCL, and are mostly found in the MCL and IPL. The dendrites of these cells are

predominantly confined to the IPL. According to the authors, GL-dSA cells have an overall appearance of horizontal cells or Golgi cells.

The second re-classified dSA cell population is the EPL-dSA cell. Axons of EPL-dSA cells ramify predominantly within the EPL, and never enter the GL. Their somata are mostly found in the GCL, and the majority have stellate or vertically oriented dendrites with spines. However, some EPL-dSA cell dendrites are devoid of spines. Morphological features suggest that the bulk of EPL-dSA cells are Blanes cells, along with some Cajal cells. The post-synaptic targets of EPL-dSA cells in the EPL are the dendritic shaft and spines of granule cells, but some synapses are also found in the GCL. Pressler and Strowbridge (2006) showed that Blanes cells monosynaptically inhibited granule cells, and that the persisting firing of Blanes cell caused long-lasting inhibition of granule cells.

The third re-classified population is the GCL-dSA cell. Axonal arbors of GCL-dSA cells are mostly restricted to the GCL and contact the proximal dendrites and somata of granule cells. Some axons also project to the olfactory cortices. The dendrites of these cells are usually sparsely spiny. Eyre et al. (2008) described GCL-dSA cells as having an overall appearance of horizontal cells or Golgi cells.

Certain molecules, such as neuropeptide Y (Gall et al., 1986), CB (Brinon et al., 1992), VIP (Gracia-Llanes et al., 2003), neuronal nitric oxide synthase (nNOS) (Kosaka and Kosaka, 2007b), and neurocalcin (Brinon et al., 1998), are expressed by subpopulations of dSA cells. However, dSA cell subtypes that express these molecules have not been well identified. Assorted dSA cells seem to have divergent electrophysiological properties, which is probably related to the differential expression of channels and neurotransmitter receptors (Eyre et al., 2008, 2009).

SUMMARY

THE OLFACTORY BULB CIRCUIT AS BASED ON RECENTLY IDENTIFIED NEURONAL GROUPS

This review summarizes the properties of numerous neurons in the olfactory bulb by focusing on their morphology, protein expression, and function. As the motivation behind this work is to have a more advanced model of olfactory bulb circuit, we assembled the recognized neuronal connections into a diagram (**Figure 3**). We included the connections suggested from the dendritic arborization, axonal projection pattern and physiological data in addition to the established connections. Although the diagram is still far from complete, it would be helpful for neuronal researches in the olfactory bulb circuits. In addition, we discuss some of the issues not highlighted above to bridge the recent research results and the conventional diagram of the circuit.

External tufted cells and superficial tufted cells

In the course of defining the neuronal groups, the categorization of ET cells and superficial tufted cells creates some confusion. More specifically, there seems to be little consensus regarding the exact definition of a superficial tufted cell. In literature, the term superficial tufted cell could be just a synonym of ET cell, or it could represent a tufted cell whose cell body is located in the superficial part of the EPL (Kosaka et al., 1998; Luo and Katz, 2001; Hamilton et al., 2005). As discussed in the GL section, ET cells consist of two subtypes that are morphologically and physiologically distinct. In some reports, the superficial tufted cell is described as the subtype with secondary dendrites and therefore the term ET cell only represents the subtype without secondary dendrites (Ezeh et al., 1993; Kiyokage et al., 2010). In our opinion, this seems the most sensible use of the terms.

A fraction of putative middle tufted cells located in the superficial EPL potentially belongs to the superficial tufted cells as well. Both of two ET cell/superficial tufted cell subpopulations that release peptide hormones CCK and vasopressin, respectively (Liu and Shipley, 1994; Tobin et al., 2010), have secondary dendrites and are thus most likely involved in the superficial tufted cells, implying the further functional heterogeneity of superficial tufted cells. Additional investigations are required to definitively conclude how superficial tufted cells differ from ET cells (i.e., without secondary dendrites) or from middle tufted cells. For example, it is an interesting question whether the targets of their axon and/or axon collaterals are the same, partially overlapping, or mutually exclusive.

Tufted cells and mitral cells

Here, we regard mitral and tufted cells as different cell types due to their divergent properties, including the location of the cell body, patterns of secondary dendrite extension and axonal projection, firing frequency, odor sensitivity, tuning specificity, and odor response phase on the respiratory rhythm. However, as stated above, recent investigations have identified certain projection neurons that have features of both tufted and mitral cells, such as mitral cells that extend secondary dendrites into the superficial EPL. These reports raise the question of whether mitral and tufted cells actually compose segregated circuits, and whether they are clearly distinguishable cell types or not.

A provocative idea is that mitral and tufted cells are on a continuum of neurons physically aligned from the superficial to deep portions of the EPL–MCL area, where the continuum comprises ET, superficial tufted, middle tufted, internal tufted, type-II mitral, and type-I mitral cells. The alignment may be also associated with the birth date of the neurons during the embryonic stage. A key point to examine within this hypothesis is the existence of any molecule(s) with a differential expression pattern between mitral and tufted cells.

Granule cells

This review describes morphologically distinct granule cells in the rodent olfactory bulb, particularly in regard to dendritic extension patterns in the EPL. In fact, at least three subgroups of granule cells have been identified according to dendritic morphology: type-I, II, and III granule cells. However, these three subtypes do not cover the entire granule cell population, because some granule cells have morphologies that do not resemble any of these types. One example is the type-S cell. More recently, Merkle et al. (2014) reported novel granule cells

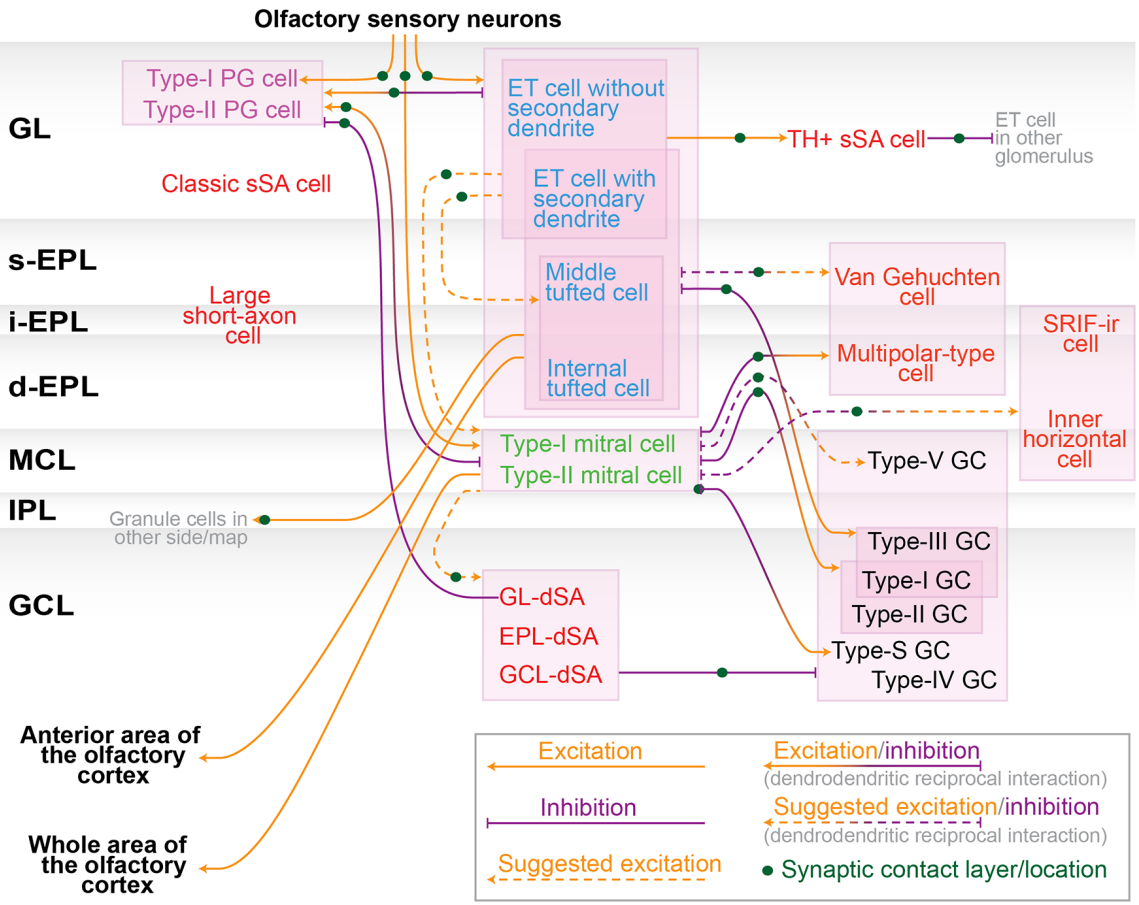

FIGURE 3 | Neuronal connection in the olfactory bulb. Schematic diagram of the neuronal synaptic connection among nerve terminal of olfactory sensory neurons, subtypes of periglomerular (PG) cells (purple), tufted cells (blue), mitral cells (green), granule (GC) cells (black), and other interneurons including various short-axon cells (red). These colors are consistent with previous figures. Orange and purple arrows represent excitatory and inhibitory inputs, respectively. Dendrodendritic excitatory/inhibitory interaction is represented by orange/purple bidirectional arrows. Connections suggested from the dendritic arborization, axonal projection pattern and physiological data are shown in dashed lines. Several neuron types are left unwired due to lack of sufficient information. Note that there are interactions not appeared in this diagram, including electric couplings between divergent neurons (e.g., mitral–mitral, mitral–tufted, tufted–tufted and mitral–interneurons; Kosaka and Kosaka, 2003; Christie et al., 2005; Hayar et al., 2005; Kosaka et al., 2005; Ma and Lowe, 2010), spillover of glutamate (Aroniadou-Anderjaska et al., 1999; Carlson et al., 2000), GABA (Aroniadou-Anderjaska et al., 2000; Smith and Jahr, 2002; Murphy et al., 2005) and dopamine (Ennis et al., 2001). Abbreviations: dSA, deep short-axon; GL, glomerular layer; s/i/d-EPL, superficial/intermediate/deep external plexiform layer; MCL, mitral cell layer; IPL, internal plexiform layer.

in the GCL: the type-IV and V granule cells. There are possibly more unidentified granule cells in the GCL. Again, the identification of any molecules that could segregate the different types of granule cells is a question of interest for future exploration.

Another unanswered question is whether different types of granule cells have divergent functions in the neuronal network in the olfactory bulb. Very limited information is available about the electrophysiological properties, target cells, and responses to odorants among various granule cells. For example, the dendritic morphologies in the EPL suggest that type-II and III granule cells regulate mostly mitral and tufted cells, respectively, although this hypothesis has not yet been tested.

Also unknown is the matter of any functional structure in the GCL. Recent explorations have used virus tracing methods to show that the GCL has a columnar structure (Willhite et al., 2006). Although it is not known whether the columnar structure of the GCL reflects the spatial pattern of a group of neurons strongly connected to each other or the expression of specific synaptic molecules that are essential for trans-synaptic virus infection, this observation lends support to the idea that the GCL may indeed have a functional structure. Future research to uncover the organization of the GCL will be an important challenge to more clearly understand the olfactory bulb circuit.

Short-axon cells

One might consider that interneurons in the olfactory bulb other than PG cells and granule cells are the same type of neuron, since they are all called short-axon cells. Nonetheless, short-axon cells are a diverse population with varied morphologies and functions, and, thus, they should not be regarded as a single

group. In addition, as discussed in the EPL section, some EPL interneurons, which were conventionally categorized as short-axon cells, may not have an actual axon, but instead have only an axon-like process (Kosaka and Kosaka, 2008a). These various short-axon cells deserve re-investigation with the aid of contemporary technology, similar to the recent re-investigations of dSA cells (Eyre et al., 2008, 2009).

Horizontal interactions in the olfactory bulb

The remarkable change from the conventional to updated olfactory bulb circuit diagram is that various types of cells can contribute to horizontal interactions in the GL and EPL. Conventionally, horizontal interactions were thought to be mediated mainly by dendrodendritic reciprocal synapses formed between mitral/tufted cells and granule cells. However, recent work revealed that sSA cells in the GL and PV-positive neurons in the EPL also contribute to horizontal interactions in each layer. Interestingly, the locations of the interaction sites are clearly segregated. The sSA cells mediate horizontal interactions only in the GL, while PV-positive cells mediate such interactions only in the EPL. Moreover, these cells differ in morphology. While the sSA cell has an axon, most PV-positive cells are axonless and send outputs from dendrites alone, similar to granule cells (Huang et al., 2013; Kato et al., 2013; Miyamichi et al., 2013). The locational and morphological variances probably reflect the functional distinctions between these neurons. Further clarification of such functional distinctions is essential for understanding how convergent odor information is processed through the interaction of multiple glomerular modules.

CONCLUDING REMARKS

In general, recent studies in neuroscience have increasingly revealed the intricacy and complexity of the olfactory system, providing more a detailed, albeit a more complicated, diagram of the olfactory bulb network. However, many issues must still be addressed to accurately categorize neuronal types and to complete a comprehensive diagram of this network. The rapid progress in developing new techniques and technologies (e.g., *in vivo* two-photon imaging, CLARITY) is essential and quite helpful in overcoming some of the challenges that we still face in understanding the structure and function of neuronal networks with single cell resolution. Steady progress in characterizing each neuronal type along the full spectrum of its properties is one of our most immediate needs. Ultimately, as we dissect and begin to understand the detailed nature of the olfactory circuit networks, our next questions must focus on understanding how odorants within these circuits play a role in regulating behavior.

ACKNOWLEDGMENTS

We thank Dr. Charles Greer for his helpful comments on the earlier version of this manuscript. This work was supported by NIH grants DC009666 and DC013802 (to Shin Nagayama) and DC011134 (to Fumiaki Imamura).

REFERENCES

Adipietro, K. A., Mainland, J. D., and Matsunami, H. (2012). Functional evolution of mammalian odorant receptors. *PLoS Genet.* 8:e1002821. doi: 10.1371/journal.pgen.1002821

Angelo, K., and Margrie, T. W. (2011). Population diversity and function of hyperpolarization-activated current in olfactory bulb mitral cells. *Sci. Rep.* 1, 50. doi: 10.1038/srep00050

Angelo, K., Rancz, E. A., Pimentel, D., Hundahl, C., Hannibal, J., Fleischmann, A., et al. (2012). A biophysical signature of network affiliation and sensory processing in mitral cells. *Nature* 488, 375–378. doi: 10.1038/nature11291

Antal, M., Eyre, M., Finklea, B., and Nusser, Z. (2006). External tufted cells in the main olfactory bulb form two distinct subpopulations. *Eur. J. Neurosci.* 24, 1124–1136. doi: 10.1111/j.1460-9568.2006.04988.x

Arenkiel, B. R., Hasegawa, H., Yi, J. J., Larsen, R. S., Wallace, M. L., Philpot, B. D., et al. (2011). Activity-induced remodeling of olfactory bulb microcircuits revealed by monosynaptic tracing. *PLoS ONE* 6:e29423. doi: 10.1371/journal.pone.0029423

Aroniadou-Anderjaska, V., Ennis, M., and Shipley, M. T. (1999). Dendrodendritic recurrent excitation in mitral cells of the rat olfactory bulb. *J. Neurophysiol.* 82, 489–494.

Aroniadou-Anderjaska, V., Zhou, F. M., Priest, C. A., Ennis, M., and Shipley, M. T. (2000). Tonic and synaptically evoked presynaptic inhibition of sensory input to the rat olfactory bulb via GABA(B) heteroreceptors. *J. Neurophysiol.* 84, 1194–1203.

Aungst, J. L., Heyward, P. M., Puche, A. C., Karnup, S. V., Hayar, A., Szabo, G., et al. (2003). Centre-surround inhibition among olfactory bulb glomeruli. *Nature* 426, 623–629. doi: 10.1038/nature02185

Bargmann, C. I. (2006). Comparative chemosensation from receptors to ecology. *Nature* 444, 295–301. doi: 10.1038/nature05402

Bartolomei, J. C., and Greer, C. A. (1998). The organization of piriform cortex and the lateral olfactory tract following the loss of mitral cells in PCD mice. *Exp. Neurol.* 154, 537–550. doi: 10.1006/exnr.1998.6947

Batista-Brito, R., Close, J., Machold, R., and Fishell, G. (2008). The distinct temporal origins of olfactory bulb interneuron subtypes. *J. Neurosci.* 28, 3966–3975. doi: 10.1523/JNEUROSCI.5625-07.2008

Belluscio, L., Lodovichi, C., Feinstein, P., Mombaerts, P., and Katz, L. C. (2002). Odorant receptors instruct functional circuitry in the mouse olfactory bulb. *Nature* 419, 296–300. doi: 10.1038/nature01001

Brill, M. S., Ninkovic, J., Winpenny, E., Hodge, R. D., Ozen, I., Yang, R., et al. (2009). Adult generation of glutamatergic olfactory bulb interneurons. *Nat. Neurosci.* 12, 1524–1533. doi: 10.1038/nn.2416

Brinon, J. G., Alonso, J. R., Arevalo, R., Garcia-Ojeda, E., Lara, J., and Aijon, J. (1992). Calbindin D-28k-positive neurons in the rat olfactory bulb. An immunohistochemical study. *Cell Tissue Res.* 269, 289–297. doi: 10.1007/BF00319620

Brinon, J. G., Arevalo, R., Crespo, C., Bravo, I. G., Okazaki, K., Hidaka, H., et al. (1998). Neurocalcin immunoreactivity in the rat main olfactory bulb. *Brain Res.* 795, 204–214. doi: 10.1016/S0006-8993(98)00311-4

Brinon, J. G., Martinez-Guijarro, F. J., Bravo, I. G., Arevalo, R., Crespo, C., Okazaki, K., et al. (1999). Coexpression of neurocalcin with other calcium-binding proteins in the rat main olfactory bulb. *J. Comp. Neurol.* 407, 404–414. doi: 10.1002/(SICI)1096-9861(19990510)407:3<404::AID-CNE8>3.0.CO;2-9

Buck, L., and Axel, R. (1991). A novel multigene family may encode odorant receptors: a molecular basis for odor recognition. *Cell* 65, 175–187. doi: 10.1016/0092-8674(91)90418-X

Bushdid, C., Magnasco, M. O., Vosshall, L. B., and Keller, A. (2014). Humans can discriminate more than 1 trillion olfactory stimuli. *Science* 343, 1370–1372. doi: 10.1126/science.1249168

Carlson, G. C., Shipley, M. T., and Keller, A. (2000). Long-lasting depolarizations in mitral cells of the rat olfactory bulb. *J. Neurosci.* 20, 2011–2021.

Chen, W. R., Xiong, W., and Shepherd, G. M. (2000). Analysis of relations between NMDA receptors and GABA release at olfactory bulb reciprocal synapses. *Neuron* 25, 625–633. doi: 10.1016/S0896-6273(00)81065-X

Christie, J. M., Bark, C., Hormuzdi, S. G., Helbig, I., Monyer, H., and Westbrook, G. L. (2005). Connexin36 mediates spike synchrony in olfactory bulb glomeruli. *Neuron* 46, 761–772. doi: 10.1016/j.neuron.2005.04.030

Christie, J. M., Schoppa, N. E., and Westbrook, G. L. (2001). Tufted cell dendrodendritic inhibition in the olfactory bulb is dependent on NMDA receptor activity. *J. Neurophysiol.* 85, 169–173.

Dhawale, A. K., Hagiwara, A., Bhalla, U. S., Murthy, V. N., and Albeanu, D. F. (2010). Non-redundant odor coding by sister mitral cells revealed by light addressable glomeruli in the mouse. *Nat. Neurosci.* 13, 1404–1412. doi: 10.1038/nn.2673

Ennis, M., and Hayar, A. (2008). "Physiology of the main olfactory bulb," in *The Senses: A Comprehensive Reference, Volume 4: Olfaction and Taste*, eds S. Firestein and G. K. Beauchamp (San Diego, CA: Academic Press), 641–686.

Ennis, M., Zhou, F. M., Ciombor, K. J., Aroniadou-Anderjaska, V., Hayar, A., Borrelli, E., et al. (2001). Dopamine D2 receptor-mediated presynaptic inhibition of olfactory nerve terminals. *J. Neurophysiol.* 86, 2986–2997.

Eyre, M. D., Antal, M., and Nusser, Z. (2008). Distinct deep short-axon cell subtypes of the main olfactory bulb provide novel intrabulbar and extrabulbar GABAergic connections. *J. Neurosci.* 28, 8217–8229. doi: 10.1523/JNEUROSCI.2490-08.2008

Eyre, M. D., Kerti, K., and Nusser, Z. (2009). Molecular diversity of deep short-axon cells of the rat main olfactory bulb. *Eur. J. Neurosci.* 29, 1397–1407. doi: 10.1111/j.1460-9568.2009.06703.x

Ezeh, P. I., Wellis, D. P., and Scott, J. W. (1993). Organization of inhibition in the rat olfactory bulb external plexiform layer. *J. Neurophysiol.* 70, 263–274.

Fukunaga, I., Berning, M., Kollo, M., Schmaltz, A., and Schaefer, A. T. (2012). Two distinct channels of olfactory bulb output. *Neuron* 75, 320–329. doi: 10.1016/j.neuron.2012.05.017

Gall, C., Seroogy, K. B., and Brecha, N. (1986). Distribution of VIP- and NPY-like immunoreactivities in rat main olfactory bulb. *Brain Res.* 374, 389–394. doi: 10.1016/0006-8993(86)90436-1

Gire, D. H., Franks, K. M., Zak, J. D., Tanaka, K. F., Whitesell, J. D., Mulligan, A. A., et al. (2012). Mitral cells in the olfactory bulb are mainly excited through a multistep signaling path. *J. Neurosci.* 32, 2964–2975. doi: 10.1523/JNEUROSCI.5580-11.2012

Gracia-Llanes, F. J., Crespo, C., Blasco-Ibanez, J. M., Marques-Mari, A. I., and Martinez-Guijarro, F. J. (2003). VIP-containing deep short-axon cells of the olfactory bulb innervate interneurons different from granule cells. *Eur. J. Neurosci.* 18, 1751–1763. doi: 10.1046/j.1460-9568.2003.02895.x

Haba, H., Nomura, T., Suto, F., and Osumi, N. (2009). Subtype-specific reduction of olfactory bulb interneurons in Pax6 heterozygous mutant mice. *Neurosci. Res.* 65, 116–121. doi: 10.1016/j.neures.2009.05.011

Haberly, L. B., and Price, J. L. (1977). The axonal projection patterns of the mitral and tufted cells of the olfactory bulb in the rat. *Brain Res.* 129, 152–157. doi: 10.1016/0006-8993(77)90978-7

Hamilton, K. A., Heinbockel, T., Ennis, M., Szabó, G., Erdélyi, F., and Hayar, A. (2005). Properties of external plexiform layer interneurons in mouse olfactory bulb slices. *Neuroscience* 133, 819–829. doi: 10.1016/j.neuroscience.2005.03.008

Hayar, A., Shipley, M. T., and Ennis, M. (2005). Olfactory bulb external tufted cells are synchronized by multiple intraglomerular mechanisms. *J. Neurosci.* 25, 8197–8208. doi: 10.1523/JNEUROSCI.2374-05.2005

Heinbockel, T., Hamilton, K. A., and Ennis, M. (2007). Group I metabotropic glutamate receptors are differentially expressed by two populations of olfactory bulb granule cells. *J. Neurophysiol.* 97, 3136–3141. doi: 10.1152/jn.01202.2006

Hinds, J. W. (1968). Autoradiographic study of histogenesis in the mouse olfactory bulb. I. Time of origin of neurons and neuroglia. *J. Comp. Neurol.* 134, 287–304. doi: 10.1002/cne.901340304

Huang, L., Garcia, I., Jen, H. I., and Arenkiel, B. R. (2013). Reciprocal connectivity between mitral cells and external plexiform layer interneurons in the mouse olfactory bulb. *Front. Neural Circuits* 7:32. doi: 10.3389/fncir.2013.00032

Igarashi, K. M., Ieki, N., An, M., Yamaguchi, Y., Nagayama, S., Kobayakawa, K., et al. (2012). Parallel mitral and tufted cell pathways route distinct odor information to different targets in the olfactory cortex. *J. Neurosci.* 32, 7970–7985. doi: 10.1523/JNEUROSCI.0154-12.2012

Imamura, F., Ayoub, A. E., Rakic, P., and Greer, C. A. (2011). Timing of neurogenesis is a determinant of olfactory circuitry. *Nat. Neurosci.* 14, 331–337. doi: 10.1038/nn.2754

Imamura, F., Nagao, H., Naritsuka, H., Murata, Y., Taniguchi, H., and Mori, K. (2006). A leucine-rich repeat membrane protein, 5T4, is expressed by a subtype of granule cells with dendritic arbors in specific strata of the mouse olfactory bulb. *J. Comp. Neurol.* 495, 754–768. doi: 10.1002/cne.20896

Imayoshi, I., Sakamoto, M., Ohtsuka, T., Takao, K., Miyakawa, T., Yamaguchi, M., et al. (2008). Roles of continuous neurogenesis in the structural and functional integrity of the adult forebrain. *Nat. Neurosci.* 11, 1153–1161. doi: 10.1038/nn.2185

Inaki, K., Nishimura, S., Nakashiba, T., Itohara, S., and Yoshihara, Y. (2004). Laminar organization of the developing lateral olfactory tract revealed by differential expression of cell recognition molecules. *J. Comp. Neurol.* 479, 243–256. doi: 10.1002/cne.20270

Isaacson, J. S., and Strowbridge, B. W. (1998). Olfactory reciprocal synapses: dendritic signaling in the CNS. *Neuron* 20, 749–761. doi: 10.1016/S0896-6273(00)81013-2

Kasowski, H. J., Kim, H., and Greer, C. A. (1999). Compartmental organization of the olfactory bulb glomerulus. *J. Comp. Neurol.* 407, 261–274. doi: 10.1002/(SICI)1096-9861(19990503)407:2<261::AID-CNE7>3.0.CO;2-G

Kato, H. K., Gillet, S. N., Peters, A. J., Isaacson, J. S., and Komiyama, T. (2013). Parvalbumin-expressing interneurons linearly control olfactory bulb output. *Neuron* 80, 1218–1231. doi: 10.1016/j.neuron.2013.08.036

Kelsch, W., Mosley, C. P., Lin, C. W., and Lois, C. (2007). Distinct mammalian precursors are committed to generate neurons with defined dendritic projection patterns. *PLoS Biol.* 5:e300. doi: 10.1371/journal.pbio.0050300

Kikuta, S., Fletcher, M. L., Homma, R., Yamasoba, T., and Nagayama, S. (2013). Odorant response properties of individual neurons in an olfactory glomerular module. *Neuron* 77, 1122–1135. doi: 10.1016/j.neuron.2013.01.022

Kiyokage, E., Pan, Y.-Z., Shao, Z., Kobayashi, K., Szabo, G., Yanagawa, Y., et al. (2010). Molecular identity of periglomerular and short axon cells. *J. Neurosci.* 30, 1185–1196. doi: 10.1523/JNEUROSCI.3497-09.2010

Kohwi, M., Osumi, N., Rubenstein, J. L., and Alvarez-Buylla, A. (2005). Pax6 is required for making specific subpopulations of granule and periglomerular neurons in the olfactory bulb. *J. Neurosci.* 25, 6997–7003. doi: 10.1523/JNEUROSCI.1435-05.2005

Kosaka, K., Aika, Y., Toida, K., Heizmann, C. W., Hunziker, W., Jacobowitz, D. M., et al. (1995). Chemically defined neuron groups and their subpopulations in the glomerular layer of the rat main olfactory bulb. *Neurosci. Res.* 23, 73–88. doi: 10.1016/0168-0102(95)90017-9

Kosaka, K., Heizmann, C. W., and Kosaka, T. (1994). Calcium-binding protein parvalbumin-immunoreactive neurons in the rat olfactory bulb. 1. Distribution and structural features in adult rat. *Exp. Brain Res.* 99, 191–204. doi: 10.1007/BF00239586

Kosaka, K., and Kosaka, T. (2005). Synaptic organization of the glomerulus in the main olfactory bulb: compartments of the glomerulus and heterogeneity of the periglomerular cells. *Anat. Sci. Int.* 80, 80–90. doi: 10.1111/j.1447-073x.2005.00092.x

Kosaka, K., and Kosaka, T. (2007a). Chemical properties of type 1 and type 2 periglomerular cells in the mouse olfactory bulb are different from those in the rat olfactory bulb. *Brain Res.* 1167, 42–55. doi: 10.1016/j.brainres.2007.04.087

Kosaka, T., and Kosaka, K. (2007b). Heterogeneity of nitric oxide synthase-containing neurons in the mouse main olfactory bulb. *Neurosci. Res.* 57, 165–178. doi: 10.1016/j.neures.2006.10.005

Kosaka, K., Toida, K., Aika, Y., and Kosaka, T. (1998). How simple is the organization of the olfactory glomerulus?: the heterogeneity of so-called periglomerular cells. *Neurosci. Res.* 30, 101–110. doi: 10.1016/S0168-0102(98)00002-9

Kosaka, K., Toida, K., Margolis, F. L., and Kosaka, T. (1996). Chemically defined neuron groups and their subpopulations in the glomerular layer of the rat main olfactory bulb: prominent differences in the intraglomerular dendritic arborization and their relationship to olfactory nerve terminals. *Neuroscience* 76, 775–786. doi: 10.1016/S0306-4522(96)00308-9

Kosaka, T., Deans, M. R., Paul, D. L., and Kosaka, K. (2005). Neuronal gap junctions in the mouse main olfactory bulb: morphological analyses on transgenic mice. *Neuroscience* 134, 757–769. doi: 10.1016/j.neuroscience.2005.04.057

Kosaka, T., and Kosaka, K. (2003). Neuronal gap junctions in the rat main olfactory bulb, with special reference to intraglomerular gap junctions. *Neurosci. Res.* 45, 189–209. doi: 10.1016/S0168-0102(02)00222-5

Kosaka, T., and Kosaka, K. (2008a). Heterogeneity of parvalbumin-containing neurons in the mouse main olfactory bulb, with special reference to short-axon cells and betaIV-spectrin positive dendritic segments. *Neurosci. Res.* 60, 56–72. doi: 10.1016/j.neures.2007.09.008

Kosaka, T., and Kosaka, K. (2008b). Tyrosine hydroxylase-positive GABAergic juxtaglomerular neurons are the main source of the interglomerular connections in the mouse main olfactory bulb. *Neurosci. Res.* 60, 349–354. doi: 10.1016/j.neures.2007.11.012

Kosaka, T., and Kosaka, K. (2009). Two types of tyrosine hydroxylase positive GABAergic juxtaglomerular neurons in the mouse main olfactory bulb

are different in their time of origin. *Neurosci. Res.* 64, 436–441. doi: 10.1016/j.neures.2009.04.018

Kosaka, T., and Kosaka, K. (2011). "Interneurons" in the olfactory bulb revisited. *Neurosci. Res.* 69, 93–99. doi: 10.1016/j.neures.2010.10.002

Kosaka, T., and Kosaka, K. (2012). Further characterization of the juxtaglomerular neurons in the mouse main olfactory bulb by transcription factors, Sp8 and Tbx21. *Neurosci. Res.* 73, 24–31. doi: 10.1016/j.neures.2012.02.013

Lemasson, M., Saghatelyan, A., Olivo-Marin, J. C., and Lledo, P. M. (2005). Neonatal and adult neurogenesis provide two distinct populations of newborn neurons to the mouse olfactory bulb. *J. Neurosci.* 25, 6816–6825. doi: 10.1523/JNEUROSCI.1114-05.2005

Lepousez, G., Csaba, Z., Bernard, V., Loudes, C., Videau, C., Lacombe, J., et al. (2010). Somatostatin interneurons delineate the inner part of the external plexiform layer in the mouse main olfactory bulb. *J. Comp. Neurol.* 518, 1976–1994. doi: 10.1002/cne.22317

Liu, W. L., and Shipley, M. T. (1994). Intrabulbar associational system in the rat olfactory bulb comprises cholecystokinin-containing tufted cells that synapse onto the dendrites of GABAergic granule cells. *J. Comp. Neurol.* 346, 541–558. doi: 10.1002/cne.903460407

Lodovichi, C., and Belluscio, L. (2012). Odorant receptors in the formation of the olfactory bulb circuitry. *Physiology (Bethesda)* 27, 200–212. doi: 10.1152/physiol.00015.2012

Lodovichi, C., Belluscio, L., and Katz, L. C. (2003). Functional topography of connections linking mirror-symmetric maps in the mouse olfactory bulb. *Neuron* 38, 265–276. doi: 10.1016/S0896-6273(03)00194-6

Luo, M., and Katz, L. C. (2001). Response correlation maps of neurons in the mammalian olfactory bulb. *Neuron* 32, 1165–1179. doi: 10.1016/S0896-6273(01)00537-2

Ma, J., and Lowe, G. (2010). Correlated firing in tufted cells of mouse olfactory bulb. *Neuroscience* 169, 1715–1738. doi: 10.1016/j.neuroscience.2010.06.033

Macrides, F., and Schneider, S. P. (1982). Laminar organization of mitral and tufted cells in the main olfactory bulb of the adult hamster. *J. Comp. Neurol.* 208, 419–430. doi: 10.1002/cne.902080410

Malnic, B., Hirono, J., Sato, T., and Buck, L. B. (1999). Combinatorial receptor codes for odors. *Cell* 96, 713–723. doi: 10.1016/S0092-8674(00)80581-4

Merkle, F. T., Fuentealba, L. C., Sanders, T. A., Magno, L., Kessaris, N., and Alvarez-Buylla, A. (2014). Adult neural stem cells in distinct microdomains generate previously unknown interneuron types. *Nat. Neurosci.* 17, 207–214. doi: 10.1038/nn.3610

Merkle, F. T., Mirzadeh, Z., and Alvarez-Buylla, A. (2007). Mosaic organization of neural stem cells in the adult brain. *Science* 317, 381–384. doi: 10.1126/science.1144914

Miyamichi, K., Shlomai-Fuchs, Y., Shu, M., Weissbourd, B. C., Luo, L., and Mizrahi, A. (2013). Dissecting local circuits: parvalbumin interneurons underlie broad feedback control of olfactory bulb output. *Neuron* 80, 1232–1245. doi: 10.1016/j.neuron.2013.08.027

Mori, K. (1987). Membrane and synaptic properties of identified neurons in the olfactory bulb. *Prog. Neurobiol.* 29, 275–320. doi: 10.1016/0301-0082(87)90024-4

Mori, K., Kishi, K., and Ojima, H. (1983). Distribution of dendrites of mitral, displaced mitral, tufted, and granule cells in the rabbit olfactory bulb. *J. Comp. Neurol.* 219, 339–355. doi: 10.1002/cne.902190308

Mori, K., and Sakano, H. (2011). How is the olfactory map formed and interpreted in the mammalian brain? *Annu. Rev. Neurosci.* 34, 467–499. doi: 10.1146/annurev-neuro-112210-112917

Mouradian, L. E., and Scott, J. W. (1988). Cytochrome oxidase staining marks dendritic zones of the rat olfactory bulb external plexiform layer. *J. Comp. Neurol.* 271, 507–518. doi: 10.1002/cne.902710404

Murphy, G. J., Darcy, D. P., and Isaacson, J. S. (2005). Intraglomerular inhibition: signaling mechanisms of an olfactory microcircuit. *Nat. Neurosci.* 8, 354–364. doi: 10.1038/nn1403

Murthy, V. N. (2011). Olfactory maps in the brain. *Annu. Rev. Neurosci.* 34, 233–258. doi: 10.1146/annurev-neuro-061010-113738

Nagai, Y., Sano, H., and Yokoi, M. (2005). Transgenic expression of Cre recombinase in mitral/tufted cells of the olfactory bulb. *Genesis* 43, 12–16. doi: 10.1002/gene.20146

Nagayama, S., Enerva, A., Fletcher, M. L., Masurkar, A. V., Igarashi, K. M., Mori, K., et al. (2010). Differential axonal projection of mitral and tufted cells in the mouse main olfactory system. *Front. Neural Circuits* 4:120. doi: 10.3389/fncir.2010.00120

Nagayama, S., Takahashi, Y. K., Yoshihara, Y., and Mori, K. (2004). Mitral and tufted cells differ in the decoding manner of odor maps in the rat olfactory bulb. *J. Neurophysiol.* 91, 2532–2540. doi: 10.1152/jn.01266.2003

Najac, M., De Saint Jan, D., Reguero, L., Grandes, P., and Charpak, S. (2011). Monosynaptic and polysynaptic feed-forward inputs to mitral cells from olfactory sensory neurons. *J. Neurosci.* 31, 8722–8729. doi: 10.1523/JNEUROSCI.0527-11.2011

Nakajima, D., Nakayama, M., Kikuno, R., Hirosawa, M., Nagase, T., and Ohara, O. (2001). Identification of three novel non-classical cadherin genes through comprehensive analysis of large cDNAs. *Brain Res. Mol. Brain Res.* 94, 85–95. doi: 10.1016/S0169-328X(01)00218-2

Naritsuka, H., Sakai, K., Hashikawa, T., Mori, K., and Yamaguchi, M. (2009). Perisomatic-targeting granule cells in the mouse olfactory bulb. *J. Comp. Neurol.* 515, 409–426. doi: 10.1002/cne.22063

Nei, M., Niimura, Y., and Nozawa, M. (2008). The evolution of animal chemosensory receptor gene repertoires: roles of chance and necessity. *Nat. Rev. Genet.* 9, 951–963. doi: 10.1038/nrg2480

Orona, E., Rainer, E. C., and Scott, J. W. (1984). Dendritic and axonal organization of mitral and tufted cells in the rat olfactory bulb. *J. Comp. Neurol.* 226, 346–356. doi: 10.1002/cne.902260305

Orona, E., Scott, J. W., and Rainer, E. C. (1983). Different granule cell populations innervate superficial and deep regions of the external plexiform layer in rat olfactory bulb. *J. Comp. Neurol.* 217, 227–237. doi: 10.1002/cne.902170209

Padmanabhan, K., and Urban, N. N. (2010). Intrinsic biophysical diversity decorrelates neuronal firing while increasing information content. *Nat. Neurosci.* 13, 1276–1282. doi: 10.1038/nn.2630

Panzanelli, P., Fritschy, J. M., Yanagawa, Y., Obata, K., and Sassoe-Pognetto, M. (2007). GABAergic phenotype of periglomerular cells in the rodent olfactory bulb. *J. Comp. Neurol.* 502, 990–1002. doi: 10.1002/cne.21356

Panzanelli, P., Perazzini, A. Z., Fritschy, J. M., and Sassoe-Pognetto, M. (2005). Heterogeneity of gamma-aminobutyric acid type A receptors in mitral and tufted cells of the rat main olfactory bulb. *J. Comp. Neurol.* 484, 121–131. doi: 10.1002/cne.20440

Parrish-Aungst, S., Shipley, M. T., Erdelyi, F., Szabo, G., and Puche, A. C. (2007). Quantitative analysis of neuronal diversity in the mouse olfactory bulb. *J. Comp. Neurol.* 501, 825–836. doi: 10.1002/cne.21205

Petreanu, L., and Alvarez-Buylla, A. (2002). Maturation and death of adult-born olfactory bulb granule neurons: role of olfaction. *J. Neurosci.* 22, 6106–6113.

Pignatelli, A., Kobayashi, K., Okano, H., and Belluzzi, O. (2005). Functional properties of dopaminergic neurones in the mouse olfactory bulb. *J. Physiol.* 564, 501–514. doi: 10.1113/jphysiol.2005.084632

Pinching, A. J., and Powell, T. P. (1971a). The neuron types of the glomerular layer of the olfactory bulb. *J. Cell Sci.* 9, 305–345.

Pinching, A. J., and Powell, T. P. (1971b). The neuropil of the glomeruli of the olfactory bulb. *J. Cell Sci.* 9, 347–377.

Pinching, A. J., and Powell, T. P. S. (1971c). The neuropil of the periglomerular region of the olfactory bulb. *J. Cell Sci.* 9, 379–409.

Pressler, R. T., and Strowbridge, B. W. (2006). Blanes cells mediate persistent feed-forward inhibition onto granule cells in the olfactory bulb. *Neuron* 49, 889–904. doi: 10.1016/j.neuron.2006.02.019

Price, J. L., and Powell, T. P. (1970a). The mitral and short axon cells of the olfactory bulb. *J. Cell Sci.* 7, 631–651.

Price, J. L., and Powell, T. P. (1970b). The morphology of the granule cells of the olfactory bulb. *J. Cell Sci.* 7, 91–123.

Price, J. L., and Sprich, W. W. (1975). Observations on the lateral olfactory tract of the rat. *J. Comp. Neurol.* 162, 321–336. doi: 10.1002/cne.901620304

Royet, J. P., Distel, H., Hudson, R., and Gervais, R. (1998). A re-estimation of the number of glomeruli and mitral cells in the olfactory bulb of rabbit. *Brain Res.* 788, 35–42. doi: 10.1016/S0006-8993(97)01504-7

Saino-Saito, S., Cave, J. W., Akiba, Y., Sasaki, H., Goto, K., Kobayashi, K., et al. (2007). ER81 and CaMKIV identify anatomically and phenotypically defined subsets of mouse olfactory bulb interneurons. *J. Comp. Neurol.* 502, 485–496. doi: 10.1002/cne.21293

Sakano, H. (2010). Neural map formation in the mouse olfactory system. *Neuron* 67, 530–542. doi: 10.1016/j.neuron.2010.07.003

Satou, M. (1990). Synaptic organization, local neuronal circuitry, and functional segregation of the teleost olfactory bulb. *Prog. Neurobiol.* 34, 115–142. doi: 10.1016/0301-0082(90)90004-Z

Sawada, M., Kaneko, N., Inada, H., Wake, H., Kato, Y., Yanagawa, Y., et al. (2011). Sensory input regulates spatial and subtype-specific patterns of neuronal turnover in the adult olfactory bulb. *J. Neurosci.* 31, 11587–11596. doi: 10.1523/JNEUROSCI.0614-11.2011

Schneider, S. P., and Macrides, F. (1978). Laminar distributions of internuerons in the main olfactory bulb of the adult hamster. *Brain Res. Bull.* 3, 73–82. doi: 10.1016/0361-9230(78)90063-1

Schoenfeld, T. A., Marchand, J. E., and Macrides, F. (1985). Topographic organization of tufted cell axonal projections in the hamster main olfactory bulb: an intrabulbar associational system. *J. Comp. Neurol.* 235, 503–518. doi: 10.1002/cne.902350408

Scott, J. W., Mcbride, R. L., and Schneider, S. P. (1980). The organization of projections from the olfactory bulb to the piriform cortex and olfactory tubercle in the rat. *J. Comp. Neurol.* 194, 519–534. doi: 10.1002/cne.901940304

Shao, Z., Puche, A. C., Kiyokage, E., Szabo, G., and Shipley, M. T. (2009). Two GABAergic intraglomerular circuits differentially regulate tonic and phasic presynaptic inhibition of olfactory nerve terminals. *J. Neurophysiol.* 101, 1988–2001. doi: 10.1152/jn.91116.2008

Shepherd, G. M., Chen, W. R., and Greer, C. A. (2004). "Olfactory bulb," in *The Synaptic Organization of the Brain*, ed. G. M. Shepherd, 5th Edn (New York: Oxford University Press), 165–216. doi: 10.1093/acprof:oso/9780195159561.003.0005

Shipley, M. T., and Ennis, M. (1996). Functional organization of olfactory system. *J. Neurobiol.* 30, 123–176. doi: 10.1002/(SICI)1097-4695(199605)30:1<123::AID-NEU11>3.0.CO;2-N

Skeen, L. C., and Hall, W. C. (1977). Efferent projections of the main and the accessory olfactory bulb in the tree shrew (*Tupaia glis*). *J. Comp. Neurol.* 172, 1–35. doi: 10.1002/cne.901720102

Smith, T. C., and Jahr, C. E. (2002). Self-inhibition of olfactory bulb neurons. *Nat. Neurosci.* 5, 760–766.

Tan, J., Savigner, A., Ma, M., and Luo, M. (2010). Odor information processing by the olfactory bulb analyzed in gene-targeted mice. *Neuron* 65, 912–926. doi: 10.1016/j.neuron.2010.02.011

Tatti, R., Bhaukaurally, K., Gschwend, O., Seal, R. P., Edwards, R. H., Rodriguez, I., et al. (2014). A population of glomerular glutamatergic neurons controls sensory information transfer in the mouse olfactory bulb. *Nat. Commun.* 5, 3791. doi: 10.1038/ncomms4791

Tobin, V. A., Hashimoto, H., Wacker, D. W., Takayanagi, Y., Langnaese, K., Caquineau, C., et al. (2010). An intrinsic vasopressin system in the olfactory bulb is involved in social recognition. *Nature* 464, 413–417. doi: 10.1038/nature08826

Toida, K., Kosaka, K., Heizmann, C. W., and Kosaka, T. (1994). Synaptic contacts between mitral/tufted cells and GABAergic neurons containing calcium-binding protein parvalbumin in the rat olfactory bulb, with special reference to reciprocal synapses between them. *Brain Res.* 650, 347–352. doi: 10.1016/0006-8993(94)91804-X

Toida, K., Kosaka, K., Heizmann, C. W., and Kosaka, T. (1996). Electron microscopic serial-sectioning/reconstruction study of parvalbumin-containing neurons in the external plexiform layer of the rat olfactory bulb. *Neuroscience* 72, 449–466. doi: 10.1016/0306-4522(95)00521-8

Trombley, P. Q., and Shepherd, G. M. (1994). Glycine exerts potent inhibitory actions on mammalian olfactory bulb neurons. *J. Neurophysiol.* 71, 761–767.

van Den Pol, A. N., and Gorcs, T. (1988). Glycine and glycine receptor immunoreactivity in brain and spinal cord. *J. Neurosci.* 8, 472–492.

Wachowiak, M., and Shipley, M. T. (2006). Coding and synaptic processing of sensory information in the glomerular layer of the olfactory bulb. *Semin. Cell Dev. Biol.* 17, 411–423. doi: 10.1016/j.semcdb.2006.04.007

Whitman, M. C., and Greer, C. A. (2007). Adult-generated neurons exhibit diverse developmental fates. *Dev. Neurobiol.* 67, 1079–1093. doi: 10.1002/dneu.20389

Willhite, D. C., Nguyen, K. T., Masurkar, A. V., Greer, C. A., Shepherd, G. M., and Chen, W. R. (2006). Viral tracing identifies distributed columnar organization in the olfactory bulb. *Proc. Natl. Acad. Sci. U.S.A.* 103, 12592–12597. doi: 10.1073/pnas.0602032103

Wilson, R. I., and Mainen, Z. F. (2006). Early events in olfactory processing. *Annu. Rev. Neurosci.* 29, 163–201. doi: 10.1146/annurev.neuro.29.051605.112950

Xiong, W., and Chen, W. R. (2002). Dynamic gating of spike propagation in the mitral cell lateral dendrites. *Neuron* 34, 115–126. doi: 10.1016/S0896-6273(02)00628-1

Yamaguchi, M., and Mori, K. (2005). Critical period for sensory experience-dependent survival of newly generated granule cells in the adult mouse olfactory bulb. *Proc. Natl. Acad. Sci. U.S.A.* 102, 9697–9702. doi: 10.1073/pnas.0406082102

Yan, Z., Tan, J., Qin, C., Lu, Y., Ding, C., and Luo, M. (2008). Precise circuitry links bilaterally symmetric olfactory maps. *Neuron* 58, 613–624. doi: 10.1016/j.neuron.2008.03.012

Yoshihara, S., Takahashi, H., Nishimura, N., Naritsuka, H., Shirao, T., Hirai, H., et al. (2012). 5T4 glycoprotein regulates the sensory input-dependent development of a specific subtype of newborn interneurons in the mouse olfactory bulb. *J. Neurosci.* 32, 2217–2226. doi: 10.1523/JNEUROSCI.5907-11.2012

Zeilhofer, H. U., Studler, B., Arabadzisz, D., Schweizer, C., Ahmadi, S., Layh, B., et al. (2005). Glycinergic neurons expressing enhanced green fluorescent protein in bacterial artificial chromosome transgenic mice. *J. Comp. Neurol.* 482, 123–141. doi: 10.1002/cne.20349

Zhang, X., and Firestein, S. (2002). The olfactory receptor gene superfamily of the mouse. *Nat. Neurosci.* 5, 124–133.

Zou, D. J., Chesler, A., and Firestein, S. (2009). How the olfactory bulb got its glomeruli: a just so story? *Nat. Rev. Neurosci.* 10, 611–618. doi: 10.1038/nrn2666

Conflict of Interest Statement: The authors declare that the research was conducted in the absence of any commercial or financial relationships that could be construed as a potential conflict of interest.

Received: 30 April 2014; accepted: 29 July 2014; published online: 03 September 2014.
Citation: Nagayama S, Homma R and Imamura F (2014) Neuronal organization of olfactory bulb circuits. Front. Neural Circuits ***8****:98. doi: 10.3389/fncir.2014.00098*
This article was submitted to the journal Frontiers in Neural Circuits.

frontiers in
NEURAL CIRCUITS

ORIGINAL RESEARCH ARTICLE
published: 10 July 2014
doi: 10.3389/fncir.2014.00076

Anatomical characterization of Cre driver mice for neural circuit mapping and manipulation

Julie A. Harris*, Karla E. Hirokawa, Staci A. Sorensen, Hong Gu, Maya Mills, Lydia L. Ng, Phillip Bohn, Marty Mortrud, Benjamin Ouellette, Jolene Kidney, Kimberly A. Smith, Chinh Dang, Susan Sunkin, Amy Bernard, Seung Wook Oh, Linda Madisen and Hongkui Zeng

Allen Institute for Brain Science, Seattle, WA, USA

Edited by:
Benjamin R. Arenkiel, Baylor College of Medicine, USA

Reviewed by:
Josh Huang, Cold Spring Harbor Laboratory, USA
Petr Tvrdik, University of Utah, USA

****Correspondence:***
Julie A. Harris, Allen Institute for Brain Science, 551 N 34th St., Seattle, WA 98103, USA
e-mail: julieha@alleninstitute.org

Significant advances in circuit-level analyses of the brain require tools that allow for labeling, modulation of gene expression, and monitoring and manipulation of cellular activity in specific cell types and/or anatomical regions. Large-scale projects and individual laboratories have produced hundreds of gene-specific promoter-driven Cre mouse lines invaluable for enabling genetic access to subpopulations of cells in the brain. However, the potential utility of each line may not be fully realized without systematic whole brain characterization of transgene expression patterns. We established a high-throughput *in situ* hybridization (ISH), imaging and data processing pipeline to describe whole brain gene expression patterns in Cre driver mice. Currently, anatomical data from over 100 Cre driver lines are publicly available via the Allen Institute's Transgenic Characterization database, which can be used to assist researchers in choosing the appropriate Cre drivers for functional, molecular, or connectional studies of different regions and/or cell types in the brain.

Keywords: Cre driver mice, genetic tools, anatomical characterization, *in situ* hybridization, neuronal cell types

INTRODUCTION

Experimental access to neural components, i.e., the specific cell types and neuronal populations which constitute a circuit, is critical for understanding the complexity of network connectivity and functional roles in perception and behavior. The most advanced set of tools to label, monitor, and manipulate specific cell populations to date are genetically engineered mouse lines and viral vectors, which utilize several common strategies to drive expression of transgenes in cells of interest (Huang and Zeng, 2013). One of the most widely used approaches is the Cre/loxP binary system, in which the Cre recombinase transgene activates a reporter gene through recombination at loxP sites. This genetic strategy is highly flexible, enabling cell type-specific and regional control of Cre expression by unique gene promoters combined with an increasing variety of reporter genes, including fluorescent proteins, optogenetic molecules, and calcium indicators that become active in the presence of Cre (Madisen et al., 2010, 2012; Zariwala et al., 2012; Zeng and Madisen, 2012). Using this binary system, cell-specific transgene expression is accomplished practically through breeding of Cre driver and reporter transgenic mouse lines, co-injection of Cre driver and reporter engineered recombinant viruses into wild type mice, or the injection of recombinant viruses into transgenic mouse lines, which allows for additional spatial and temporal control of reporter gene expression. These approaches are becoming common tools in many neuroscience laboratories and have contributed to significant advances in understanding a variety of specific functional circuits (O'Connor et al., 2013; Ramirez et al., 2013; Anthony et al., 2014).

Large numbers of Cre driver lines with expression in the central nervous system have been generated by projects such as GENSAT (Gong et al., 2007), the NIH Neuroscience Blueprint Cre Driver Network (Taniguchi et al., 2011), at the Allen Institute, and by many individual laboratories. Many of these lines have been made publicly available to the broader neuroscience community through repositories such as Jackson Laboratory and MMRRC. There are two major approaches to genetic engineering of Cre lines, conventional or bacterial artificial chromosome (BAC) transgenics, and genetic targeting (knock-in). Conventional transgenic approaches for Cre expression are generally more straightforward from a technical standpoint, but can result in ectopic expression patterns that do not match expected endogenous gene expression patterns. This is thought to be due to either the lack of all required regulatory elements driving a Cre transgene cassette or random integration into the genome. However, for specifically defined questions, novel expression patterns may prove serendipitous and should not immediately be ruled out as useless. Knock-in techniques use homologous recombination to insert the Cre transgene cassette directly into the endogenous gene locus, sometimes disrupting gene expression depending on the location of the knock-in. Knock-ins generally capture endogenous gene expression patterns better than transgenic strategies, but there are surprising exceptions. Robust interpretation of results using Cre lines generated by either method requires knowledge of whether the Cre-defined cells are in fact the same populations endogenously expressing the corresponding gene. In fact, there may be and often are differences between Cre recombination patterns and the target gene's endogenous

expression; it cannot be assumed for any Cre line that the recombined cells are the same cells which normally express the gene from that specific promoter. These differences and similarities can also depend on brain region. The GENSAT project has publicly provided a critical first characterization step for over 250 BAC transgenic lines by showing Cre reporter expression across the brain (http://www.gensat.org). However, there has been limited brain-wide systematic characterization of Cre driver lines and comparison with endogenous gene expression patterns, as many researchers tend to focus on analyzing the expression of Cre in specific brain areas or circuits of interest. Thus, the full potential and utility of the various Cre lines already available for providing genetic access to specific cell populations within networks across the entire brain is likely not completely realized.

Using the pipeline developed first for the Allen Mouse Brain Atlas (ABA) (Lein et al., 2007), we systematically characterized transgenic mRNA expression patterns from 135 Cre driver lines across the entire brain. Here, we present the Transgenic Characterization database and provide an informatics-based and manual analysis of the expression patterns in these Cre lines, summarizing possible ways in which this database can guide researchers selecting Cre lines for research into neural circuits of interest. All image data are publicly available on the Allen Brain Atlas Data Portal (http://connectivity.brain-map.org/transgenic/), and are integrated with other Institute resources.

MATERIALS AND METHODS

TRANSGENIC MICE

All animal procedures were approved by the Institutional Animal Care and Use Committee at the Allen Institute for Brain Science. Cre lines were generated at the Allen Institute or imported from external sources for characterization. Methods used to generate BAC transgenic and knock-in Cre lines at the Allen Institute have been described previously (Madisen et al., 2010). External sources included Cre lines generated as part of the NIH Neuroscience Blueprint Cre Driver Network (www.credrivermice.org) and the GENSAT project (http://gensat.org/), as well as individual labs. Cre lines were on mixed or various backgrounds, but the majority were crossed to C57Bl6/J mice and maintained as heterozygous lines upon arrival. All Cre driver lines included in this study ($n = 135$) are shown in Supplemental Table 1, along with information on the method of generation (e.g., knock-in or transgenic), availability at public repositories and links to image series data available for each line through the Transgenic Characterization data portal (http://connectivity.brain-map.org/transgenic/). Lines were generated using conventional and BAC transgenic, or knock-in strategies. Knock-ins include either direct insertion of Cre at ATG start site, which disrupts endogenous gene expression, or bicistronic cassettes inserted after the targeted gene, usually in the 3′UTR using IRES, IRES2, or 2A sequences to mediate ribosomal entry or skipping (Bochkov and Palmenberg, 2006; Trichas et al., 2008). The IRES2 sequence (Clontech) is a non-attenuated IRES that could result in higher levels of expression of the downstream gene (e.g., Cre). The 2A sequence used for new lines generated at the Allen Institute (**Table 1**) was a modified T2A (5′-ggaagcggcgagggcagaggaagtcttctgacatgcggag acgtggaagagaatcccggccctgccccaggctca-3′) or F2A (5′cgggctaagaga ggttctggagcaccggtgaaacagactttgaattttgaccttctcaagttggcgggagacgtgg agtccaacccagggccc-3′), as indicated in Supplemental Table 1. Lines imported from external sources have been renamed in specific cases to maintain a standard convention across all lines characterized in our pipeline; see Supplemental Table 1. Line names typically follow this order: (1) NCBI symbol for specific gene promoter, (2) an IRES, IRES2 or 2A sequence preceding Cre if present, (3) Cre, and, for all GENSAT lines, the (4) line number given by GENSAT, e.g., Ntsr1-Cre_GN220. Regulatable versions of Cre are noted by modifying "Cre" to "CreERT2" for the tamoxifen-inducible fusion protein (Feil et al., 1997) and "dCre" for a destabilized Cre fusion gene that allows recombination at loxP sites following administration of trimethoprim (Sando et al., 2013).

CHARACTERIZATION PIPELINE FOR Cre MICE

To systematically characterize whole brain gene expression patterns by *in situ* hybridization (ISH), Cre driver mice from every line were crossed with a reporter strain, typically the tdTomato reporters Ai9 or Ai14 (Madisen et al., 2010). Data analyses in the current study focus on postnatal day 56 (P56) and older mice, but for many of the Cre lines, whole brain characterization was also completed at P4, P14, and P28 and this data can also be found online. We adapted the high-throughput pipeline established for the ABA (Figure 1, Lein et al., 2007), which includes tissue processing, probe hybridization, image capture, and informatics data processing; brief details are described below.

TAMOXIFEN AND TRIMETHOPRIM INDUCTION

For brain collection at P56, young adult tamoxifen-inducible Cre mice (CreERT2) were treated with ∼200 μl of tamoxifen solution (0.2 mg/g body weight) via oral gavage once per day for 5 consecutive days. Trimethoprim (TMP)-inducible Cre mice (dCre) received one i.p. injection of TMP (0.25 mg/g body weight), or one oral gavage dosing of TMP (0.3 mg/g body weight), per day for 1–3 days to activate Cre recombinase. Tissue was collected 1 week after the treatments ended.

TISSUE PROCESSING, *IN SITU* HYBRIDIZATION, AND IMAGE CAPTURE

Mice were deeply anesthetized with 5% isoflurane, and brains rapidly dissected and frozen. Fresh frozen brains were sectioned at 25 μm thickness directly onto slides using a cryostat. Brains were sectioned into eight series in either sagittal or coronal planes, depending in part on expected patterns of expression for a particular Cre line. One series of sections uniformly samples every 200 μm across the brain. One series was used for each probe or probe pair hybridization. Colorimetric ISH (for tdTomato or Cre) and double-fluorescent ISH (DFISH, for tdTomato and other genes of interest) were carried out using previously established and published procedures, with minor differences for DFISH (e.g., TSA biotin was used instead of TSA biotin Plus, and anti-DIG-POD was used at a concentration of 0.10 U/ml instead of 0.25 U/ml) (http://help.brain-map.org/display/mousebrain/Documentation) (Lein et al., 2007; Thompson et al., 2008). Specific information on the probes used to detect the tdTomato

Table 1 | A list of newly generated Cre driver lines at the Allen Institute with a summary overview of the resulting whole brain expression patterns characterized by ISH.

New Cre lines	Gene name	Expression pattern summary
Adcyap1-2A-Cre	Adenylate cyclase activating polypeptide 1	Cre expression is enriched in restricted populations within the olfactory areas, hippocampus, striatum, thalamus, midbrain, pons, and medulla. Expression is scattered within the isocortex and hypothalamus. Reporter expression is widespread.
Avp-IRES2-Cre	Arginine vasopressin	Expressed in restricted populations within the hypothalamus.
Nxph4-2A-CreERT2	Neurexophilin	Strong expression in locus coeruleus and dorsal medial hypothalamus. Very sparse in other regions of hypothalamus, and layer 6b of cortex and other brain regions.
Pvalb-2A-CreERT2	Parvalbumin	Scattered expression throughout the cortex. Enriched in restricted populations in the cerebellum, medulla, pons, pallidum, and thalamus.
Pvalb-2A-dCre	Parvalbumin	Scattered expression throughout the cortex. Enriched in restricted populations in the cerebellum, medulla, pons, pallidum, and thalamus.
Penk-2A-CreERT2	Preproenkephalin	Weak widespread expression throughout the brain. Strong expression in striatum, olfactory tubercle, and very sparsely in dentate gyrus and cortex.
Rasgrf2-2A-dCre	RAS protein-specific guanine nucleotide-releasing factor 2	Scattered expression throughout the cortex with enriched expression in layers 2/3. Scattered expression in striatum, amygdala, and hypothalamus. Enriched expression in the ventromedial hypothalamic nucleus and the paraventricular nucleus of the thalamus.
Rorb-IRES2-Cre	RAR-related orphan receptor beta	Strong expression in the zonal layer of the superior colliculus and subregions of thalamus. Dense, patchy expression in layer 4 and sparse expression in layer 5 and 6 in cortex. Also expressed in trigeminal nucleus and small patches of cells in cerebellum.
Slc17a7-IRES2-Cre	Solute carrier family 17 (sodium-dependent inorganic phosphate cotransporter), member 7	Strong expression throughout the cortex, olfactory bulb, and anterior olfactory nuclei. Scattered expression in striatum, hippocampus. Enriched in restricted populations in pons, superior colliculus, and anterodorsal nucleus of thalamus.
Snap25-IRES2-Cre	Synaptosomal-associated protein 25	Strong widespread expression throughout the brain.
Sst-Cre	Somatostatin	Sparse, scattered cells throughout most of the brain.
Tac1-IRES2-Cre	Tachykinin 1	Scattered expression in caudate, septum, hypothalamus, midbrain, hindbrain, and cerebellum. Dense expression in accessory olfactory bulb and anterior olfactory nucleus, thalamus, VMH, and midbrain structures such as superior colliculus.
Tac2-IRES2-Cre	Tachykinin 2	Cre expression is enriched in habenula and restricted populations of the hypothalamus. Sparse expression in cortex, hippocampus, and cerebellum.
Trib2-2A-CreERT2	Tribbles homolog 2 (Drosophila)	Enriched in superficial layer 5 neurons of cortex. In scattered cells in the cortex and throughout the brain. Also widespread in vasculature.

and Cre transgenes for ISH and additional probes for DFISH can be found in the Transgenic Characterization database (http://connectivity.brain-map.org/transgenic/). Full slide images of colorimetric ISH were acquired with a 10× objective using the ScanScope (Aperio Technologies, Inc.). DFISH images were captured on VS110 or VS120 systems (Olympus), fully automated, high speed multi-channel fluorescent scanning systems, with a 10× objective.

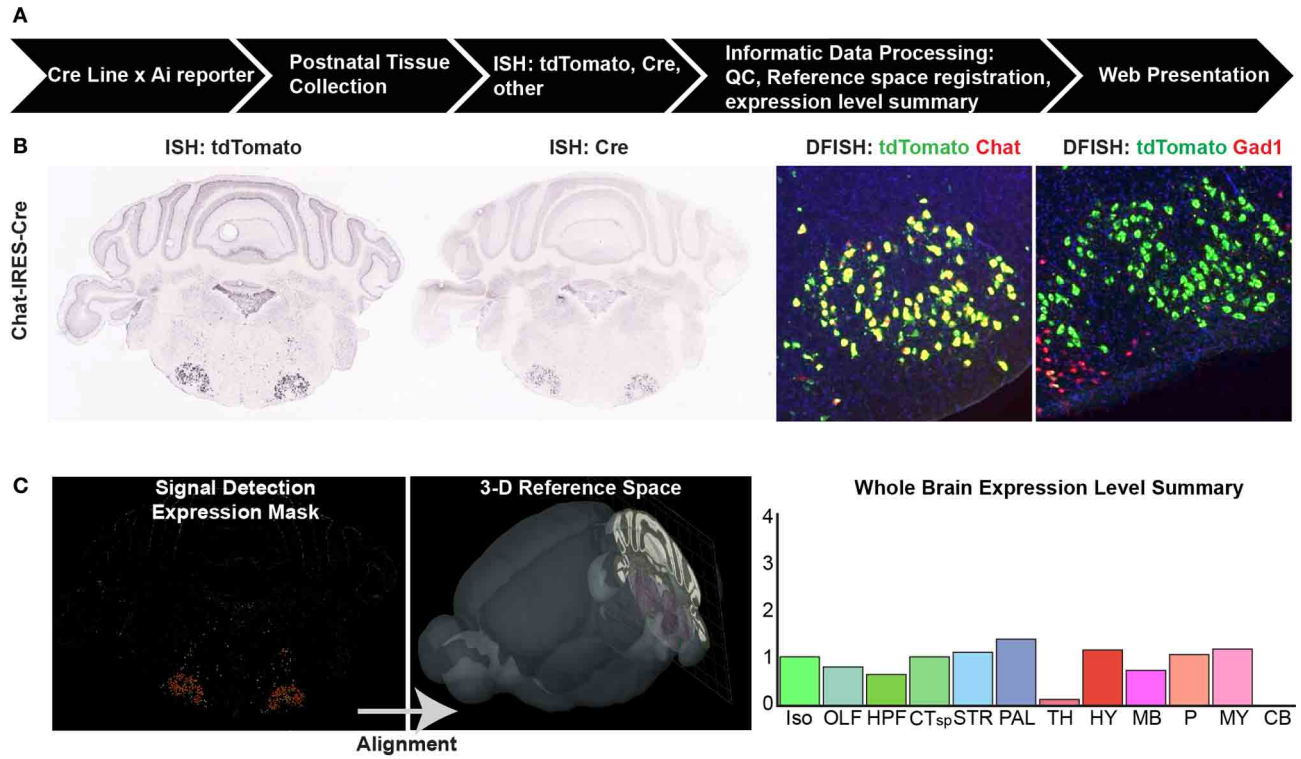

FIGURE 1 | Cre characterization data types and processing pipeline. **(A)** An overview of the high-throughput pipeline starting with crosses of mice from every characterized Cre line to a Cre reporter strain (e.g., Ai9, Ai14) to generate double positive mice for brain collection at up to four postnatal ages. The entire brain is sectioned and tissue subjected to *in situ* hybridization (ISH) before informatics data processing and web presentation. **(B)** Types of ISH data collected. For every Cre/reporter line, ISH was used to detect the tdTomato reporter gene at P56. For most Cre lines, additional data types include ISH to detect the Cre gene itself at P56, and double-fluorescent ISH (DFISH) using probes for the tdTomato gene and corresponding endogenous gene to the Cre line promoter or to another cell type marker (e.g., Gad1 for inhibitory neurons). Image series throughout the rostral-caudal extent of the brain were collected to gather whole brain expression patterns. **(C)** Informatics data processing includes signal detection, quantification, and registration of each image series into the 3D Allen Reference Atlas (ARA) space to assign signal (expression energy) to all annotated brain regions within the ARA. A whole brain expression summary is presented online at a coarse level across 12 major brain divisions along with the image series for each brain. Abbreviations are Iso, isocortex; OLF, olfactory areas; HPF, hippocampal formation; CTsp, cortical subplate; STR, striatum; PAL, pallidum; TH, thalamus; HY, hypothalamus; MB, midbrain; P, pons; MY, medulla; and CB, cerebellum.

INFORMATICS DATA PROCESSING (IDP) PIPELINE

The IDP has also been described in detail previously (Ng et al., 2007), and was adopted for use in the Transgenic Characterization pipeline. Briefly, each ISH image series undergoes pre-processing (e.g., white-balancing, cropping, and quality control assessment) and then registration to the 3D Allen Reference Atlas (ARA, Dong, 2008) which contains ∼800 annotated structures. ISH data are presented as 2D image series on the public Transgenic Characterization database (http://connectivity.brain-map.org/transgenic/), with the ability to "sync" to the ARA, enabling identification of the same approximate positions between different image series and the ARA using the transforms from the 3D registration process. In addition, a signal detection algorithm is applied to segment ISH expression above background for each image and to generate an expression mask (**Figure 1C**). Each image is divided into 200 μm grids that can be projected back into the 3D ARA space and assigned to specific annotated brain regions. Within each grid, the total intensity of detected pixels is calculated. The expression level per brain structure is measured here as "expression energy," or the sum of expressing pixel intensity/sum of all pixels for all grids associated with that structure in 3D. A coarse level summary of expression across 12 major brain divisions is presented online for each image series (e.g., **Figure 1C**, far right).

STATISTICAL ANALYSES

Statistical analyses were conducted with GraphPad Prism version 6.0. Differences between means were analyzed with two-tailed *t*-tests; $p < 0.05$ was considered significant.

RESULTS

SYSTEMATIC CHARACTERIZATION OF WHOLE-BRAIN EXPRESSION PATTERNS FROM >100 Cre DRIVER LINES

The Transgenic Characterization pipeline (**Figure 1A**) was developed to provide data for researchers to evaluate whole brain Cre recombination patterns in a standardized and publicly available format (http://connectivity.brain-map.org/transgenic/). The data consists of high resolution images of ISH for Cre reporters,

Cre, and combinations of genes and reporters (e.g., DFISH) on tissue sections covering the entire brain (**Figure 1B**). Each image series is registered to the 3D ARA, allowing for informatics-based quantification of signal across different annotated brain structures and subsequent data mining (**Figure 1C**). As of April 2014, we have characterized 135 Cre lines driven by specific gene promoters from various sources (Supplemental Table 1); 37 from GENSAT, 28 from the NIH Blueprint Cre Driver Network (Drs. Z. Josh Huang and Ulrich Mueller), 10 from Dr. Bradford Lowell, 30 from other individual laboratories, and 30 generated at the Allen Institute. Of the Allen Institute lines, here we report for the first time 14 new knock-in Cre drivers (**Table 1**). The online Transgenic Characterization database also contains data from lines with Cre driven by enhancer elements, a small number of other driver lines (Flp, Dre, tTA, GFP), and reporter lines, which were excluded from the analyses here.

We derived quantitative values across all gridded voxels in each brain after signal segmentation and registration to the ARA. For this analysis, we focused on calculating the strength of expression in 295 non-overlapping brain structures which tile the entire brain space as defined in the ARA at a mid-ontology level (see Supplemental Table 2, ARA ontology key for structures and abbreviations). Expression strength is related to the number of recombined cells per region. For each of the 135 Cre lines, an exemplar image series of tdTomato reporter expression was chosen; quantitative measurements of reporter expression in each of these 295 brain structures are shown in Supplemental Table 2. These values can be mined to generate a candidate list of brain regions with the highest levels of expression in a particular Cre line. However, due to unavoidable artifacts in segmentation, sometimes poor registration with the ARA, or issues with annotation and border definition within the ARA itself, there can be many false positives on these lists. Therefore, it is critical to also visually inspect the images and areas of interest for Cre expression. We performed a comprehensive visual, manual analysis for a subset of all Cre lines ($n = 70$ lines with complete analyses across all 295 structures, 65 are only partially complete). Each of the 295 structures was identified using the ARA and the "sync" function was used to locate the most closely matched locations in the tdTomato ISH image series. The corresponding tdTomato ISH expression pattern was then classified into one of six patterns (**Figure 2**); (1) Widespread: very dense expression across neighboring structures (i.e., sharing boundaries) within or across a major brain division, (2) Scattered: less dense expression across neighboring structures, (3) Sparse: low density of expression across neighboring structures, (4) Enriched: some specificity or boundary definition of a particular structure from its neighbors, (5) Restricted (or laminar if in cortex): very specific expression within a particular structure or cortical layer that clearly defines borders with neighboring structures, and (6) Restricted, but sparse: sparse, specific expression within a particular structure. These descriptive categories are included in Supplemental Tables 2, 3, and can be used when mining the quantitative values for visually verified expression and/or determination of enrichment of Cre reporter to specific regions.

COMPARISON OF WHOLE BRAIN Cre EXPRESSION PATTERNS WITH ENDOGENOUS GENE EXPRESSION

To compare expression patterns across the entire brain between genes and the same gene promoter-driven Cre expression, we identified ISH datasets from P56 mice generated as part of the ABA (Lein et al., 2007), which corresponded to the specific promoters of Cre lines in the Transgenic Characterization pipeline. After matching for plane of sectioning (sagittal to sagittal and coronal to coronal), ABA expression data within the same 295 structures were correlated with tdTomato ISH expression values for 119 Cre lines, and with Cre ISH for 83 lines. Each dataset was represented by an $n = 1$–6. Average Spearman rank correlation coefficients were calculated for each line (ABA vs. tdTomato and ABA vs. Cre), and across all Cre lines. The overall correlation

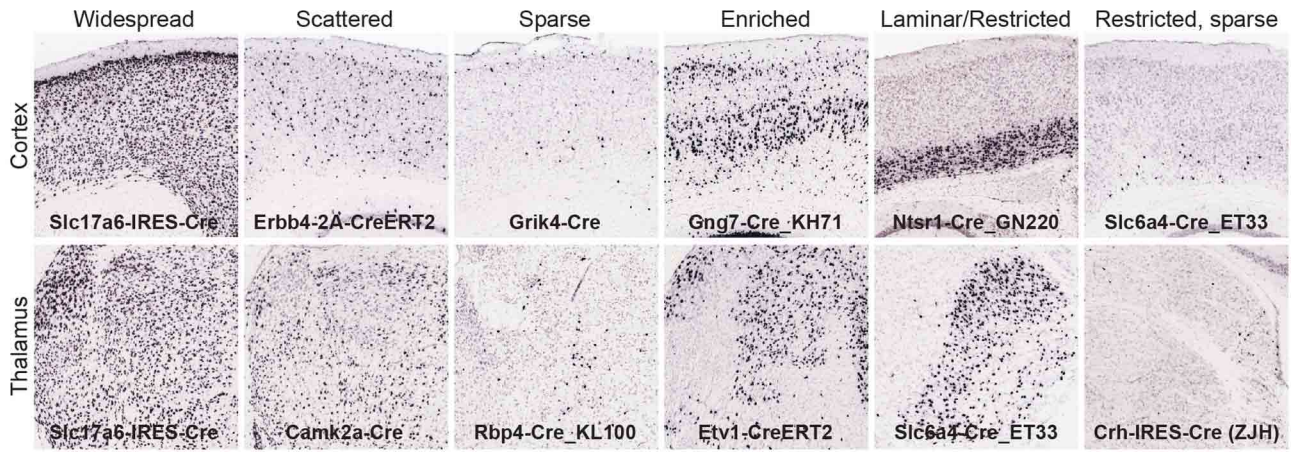

FIGURE 2 | Manual analysis of Cre reporter expression patterns across the brain. To aid in interpretation and further mining of the informatics-derived expression energy values, expression patterns were visually classified into one of six categories and recorded in Supplemental Tables 2, 3; (1) widespread, (2) scattered, (3) sparse, (4) enriched, (5) laminar or restricted, and (6) restricted but sparse. Examples from the cortex (top) and thalamus (bottom) are shown for each category.

was significantly higher when comparing expression of Cre itself to the corresponding ABA expression values, as opposed to the tdTomato reporter ($r^2 = 0.41$ vs. 0.32, **Figure 3A**), perhaps due to transient developmental expression of Cre permanently turning on reporter expression. Expression of Cre itself is therefore a better overall indicator of adult Cre expression patterns than the tdTomato reporter, but in general the Cre ISH probe is not as robust at detecting low levels of expression compared to the probe used for tdTomato. Due to this and for the reason that more Cre lines have tdTomato datasets than Cre ISH datasets, subsequent analyses used the tdTomato reporter ISH image series only. Researchers are encouraged to take advantage of the Cre datasets that exist when selecting a particular Cre line. Endogenous gene expression patterns may be more faithfully recapitulated in knock-in mice than those generated using transgenic strategies. We found that the average correlation of tdTomato expression across all Cre lines at P56 with ABA gene expression at P56 was significantly higher in knock-in as compared to transgenic Cre lines ($r^2 = 0.37$ vs. 0.25, **Figure 3B**). No significant differences were seen in the average correlation coefficients between this collection of knock-in lines generated using 2A, IRES/IRES2, or direct methods of insertion, or between BAC and conventional transgenics. The average ABA and tdTomato correlation coefficients from each Cre line ranged from −0.47 to 0.88 (**Figure 3C**). In comparison, the average correlation between biological replicates of tdTomato, Cre, or ABA expression values was 0.57 (shown on far right in **Figure 3C**). The Cre lines can thus be broken into groups with high (similar to replicate comparisons, above the 75th percentile), mid-level (50–75th percentile), low (25–50th percentile), and very low correlations (below 25th percentile).

The overall correlation coefficient per Cre line may be impacted by several different factors. Across all Cre lines, recombination patterns relative to the corresponding gene can be roughly classified into three categories; (1) Faithful recapitulation in all brain areas, (2) Faithful recapitulation in areas where endogenous gene is expressed *plus* additional brain areas where it is not, and (3) Faithful recapitulation in a subset of all areas where endogenous gene is expressed. There may also be a mixture of (2) and (3) in some Cre lines. One of the Cre lines with a high correlation coefficient, representing category (1), is the knock-in line Erbb4-2A-CreERT2 ($r^2 = 0.81$, **Figure 4A**) (Madisen et al., 2010). Erbb4 is expressed in scattered populations of GABAergic cells in many brain regions including the cortex and hippocampus (Yau et al., 2003). Cre and tdTomato ISH patterns are strikingly similar to ABA when visually inspected. *Erbb4* and tdTomato mRNAs are also highly co-localized within single cells, shown by DFISH. A scatterplot of the expression energy value for each of 295 brain structures in the ABA vs. tdTomato dataset shows the strong positive relationship between the two genes across most structures. Within a Cre line, expression patterns can be similar to the endogenous pattern in most brain structures, but dissimilar in others, e.g., category (2) above. For example, the BAC transgenic Cre line Drd2-Cre_ER44 (**Figure 4B**) captures the dopamine D2 receptor expression in the caudoputamen, but shows ectopic expression of both Cre and tdTomato in cortical areas. However, it is also possible that the expression of *Drd2* in cortical regions is below the detection level of the *Drd2* ISH. A similar example of Cre reporter expression both within and outside areas where endogenous gene is expressed at P56 is the knock-in Slc6a3-Cre line (Zhuang et al., 2005) ($r^2 = 0.2$, **Figure 4C**). Here, strong and highly co-localized expression is observed in the VTA and SNc for both the *Slc6a3* and tdTomato reporter genes, but tdTomato is observed in additional areas, such as the lateral reticular nucleus of the medulla, which does not express detectable *Slc6a3* at any point across development (data not shown, but available at http://developingmouse.brain-map.org/). An example of category (3), where Cre is expressed in a subset of all regions with endogenous

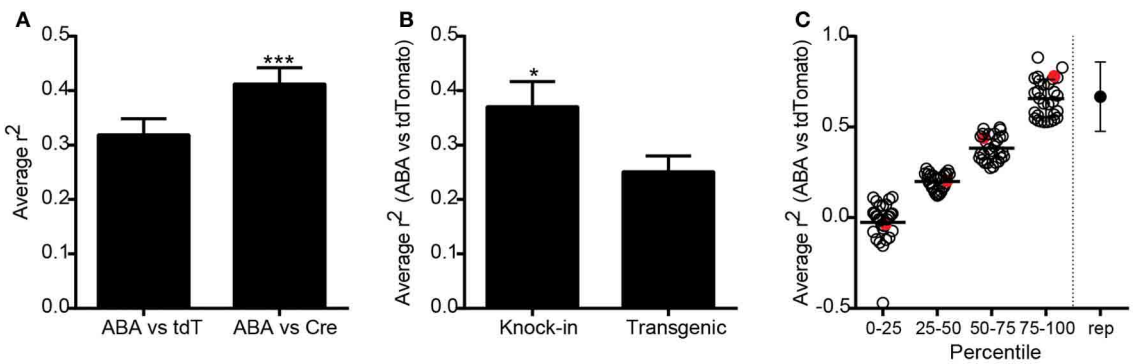

FIGURE 3 | Overall correlations between Cre expression and corresponding endogenous gene expression across all Cre lines. **(A)** Expression energy values across 295 annotated structures covering the entire brain were correlated between tdTomato or Cre ISH datasets, and each endogenous gene profile corresponding to the unique promoter driving Cre expression from the Allen Brain Atlas (ABA). The average correlation between ABA and tdTomato datasets was positive ($n = 119$ lines, $r^2 = 0.32$, Spearman correlation). The average correlation between ABA and Cre ISH datasets was significantly higher ($n = 83$ paired lines, $r^2 = 0.41$, paired t-test $^{***}p < 0.001$). **(B)** Cre reporter (tdTomato) expression values across the whole brain were significantly more similar to the corresponding ABA gene expression values in knock-in compared with transgenic Cre lines (unpaired t-test, $n = 52$ knock-in and 66 transgenic, $^{*}p < 0.05$). **(C)** Scatter plot showing the ABA vs. tdTomato whole brain r^2-value for each of the 119 Cre lines grouped by percentile rank. The point on the far right shows the average r^2-value between biological replicates within a Cre line for comparison. Red circles indicate examples shown in **Figure 4**.

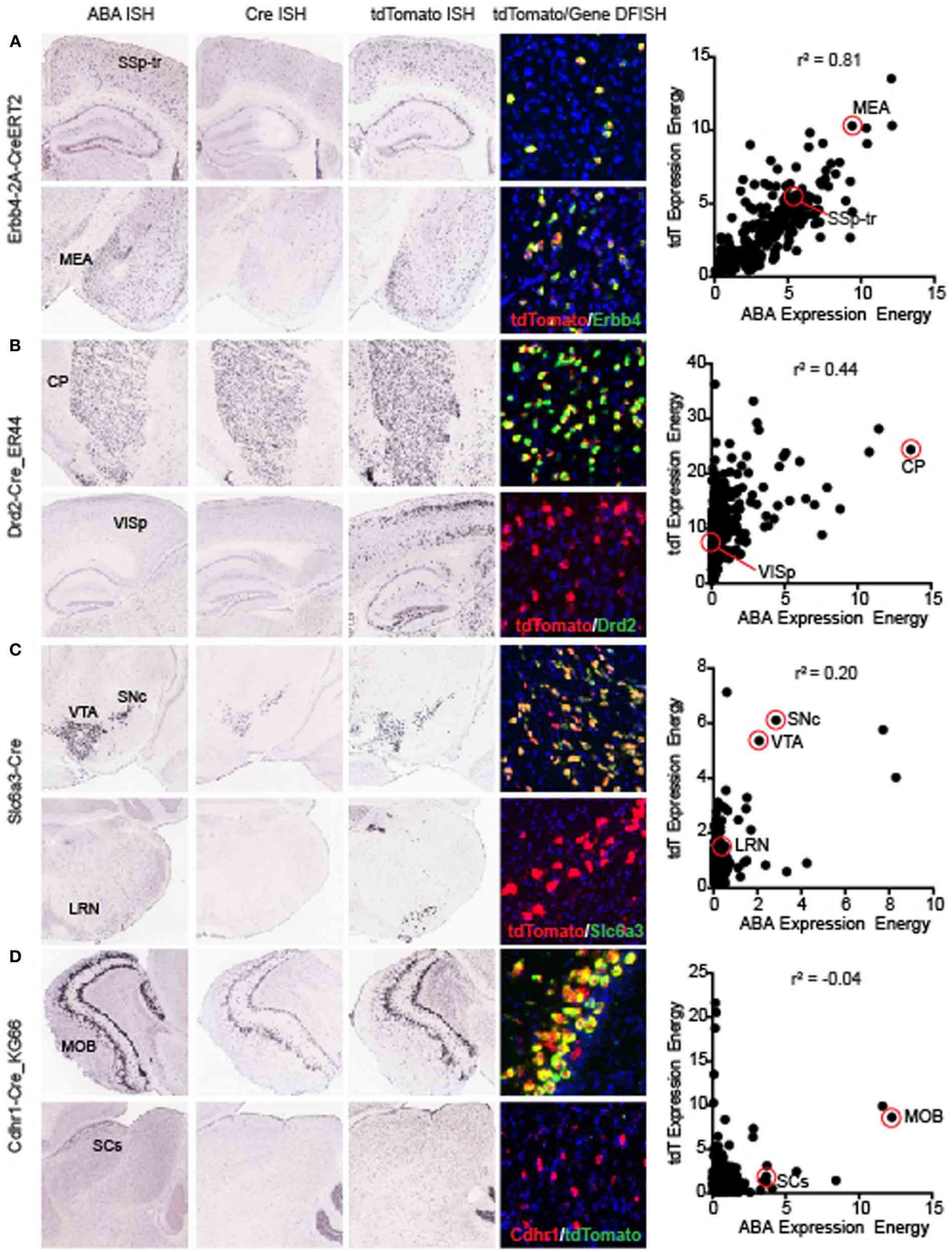

FIGURE 4 | Representative examples of the correlations between individual Cre lines and the corresponding endogenous gene expression. Images of ABA, Cre, tdTomato ISH, and tdTomato/endogenous gene DFISH are shown at two positions in the brain (top and bottom panels for each line). For each Cre line, a scatterplot comparing the expression energy in each of

(Continued)

FIGURE 4 | Continued
295 brain structures from ABA vs. tdTomato data is shown on the far right. The examples shown here are representative of lines with high **(A)** Erbb4-CreERT2, mid **(B)** Drd2-Cre_ER44, low **(C)** Slc6a3-Cre, and very low **(D)** Cdhr1-Cre_KG66 overall correlations with the corresponding ABA gene expression profiles. In each case shown, DFISH demonstrates that for highly correlated areal gene expression, cell-specific gene expression is also mostly overlapping, whereas when expression energy at the areal level is not correlated, tdTomato and endogenous gene expression are not usually expressed in the same cells. Abbreviations are SSp-tr, primary somatosensory area, trunk region; MEA, medial amygdalar nucleus; CP, caudoputamen; VISp, primary visual area; SNc, substantia nigra, compact part; VTA, ventral tegmental area; LRN, lateral reticular nucleus; MOB, main olfactory bulb; and SCs, superior colliculus, sensory related.

gene expression, is seen in the BAC transgenic Cdhr1-Cre_KG66 line (**Figure 4D**). Cre and the tdTomato reporter are both highly expressed in the olfactory bulb, similar to *Cdhr1*, but not in the sensory region of the superior colliculus (SCs).

Cre LINES ALLOW GENETIC ACCESS TO SPECIFIC BRAIN STRUCTURES

One main advantage of systematic whole brain expression characterization across many Cre lines is the ability to identify both known and novel Cre lines with expression in specific brain regions and circuits of interest. To enable comparison across Cre lines and mine the tdTomato ISH datasets for Cre lines with expression enriched in any of the 295 brain structures, we calculated the fold change difference between the tdTomato expression value within each structure and the average whole brain signal per Cre line (Supplemental Table 3). Note that this calculation will only highlight those regions that are specifically enriched over the entire brain, and will not highlight areas with expression enriched relative to local subdivisions of the brain, e.g., the lateral geniculate nucleus relative to the thalamus as a whole, although these values could also be generated from Supplemental Table 2. Fold change values can be sorted within each brain structure to identify Cre lines showing the most enrichment to the area(s) of interest. Note also that we did not impose a threshold for expression energy values prior to this fold change calculation, due to the high level of variability between expression energy values that correspond to expressed or not expressed across Cre lines and image series. Therefore, care must be taken in assessing the Cre lines with the highest fold change values as the absolute expression energy is not taken into account, and may in fact be very low or not expressed. The manual, visual inspection notes on expression patterns (described for Supplemental Table 2 and **Figure 2**) for the set of Cre lines with either full or partial manual annotation can also be used as a preliminary and associated guide to determine whether Cre reporter is expressed or not expressed. The structure columns can be sorted or filtered for "enriched" or "restricted" to identify Cre lines with manually verified anatomically-selective expression patterns. All brain structures have at least one Cre line with detectable expression of Cre reporter, although not all have anatomically-enriched or restricted expression (e.g., they define borders with neighboring nuclei).

At a coarse level, subcortical regions can be broken down into olfactory areas, hippocampal formation, cortical subplate, striatum, pallidum, thalamus, hypothalamus, midbrain, pons, medulla, and cerebellum. There are between 7 and 43 unique structures within each of these coarse divisions at the 295 structure ARA ontology level described above. Overall, the variety of Cre lines with regionally enriched expression patterns throughout subcortical brain regions is quite rich, providing diverse possibilities for genetic access to specific regions involved in a large number of brain networks. **Figure 5** shows examples of enriched or restricted Cre reporter expression patterns in representative structures within each of the major subcortical brain divisions. Note that the vast majority of Cre lines express Cre in multiple regions throughout the brain, but specific areas are highlighted here for each line. For example, in olfactory areas GENSAT BAC transgenic lines Rbp4-Cre_KL100 has expression restricted to the accessory olfactory bulb, while Sim1-Cre_KJ18 shows Cre reporter expression within the nucleus of the lateral olfactory tract. In the hippocampal formation, there are Cre lines with expression restricted to the dentate gyrus [Pomc-Cre (ST), McHugh et al., 2007] and the CA1 region (Gpr26-Cre_KO250). In cortical subplate regions, the dorsal endopiriform nucleus could be accessed using the Syt17-Cre_NO14 line and the basolateral amygdala in the Grik4-Cre line (Nakazawa et al., 2002). Several Cre lines also have region-specific expression within striatal regions, including the caudoputamen. Within the CP, many lines show cell type-selective expression which also defines borders with neighboring areas (e.g., Penk-2A-CreERT2, Drd1-Cre, Drd2-Cre_ER44, Heusner et al., 2008). Specific expression patterns can also be found within the lateral septum (e.g., Sst-Cre) and central amygdala (e.g., Prkcd-GluCla-CFP-IRES-Cre, Haubensak et al., 2010). In the hypothalamus, there are also several examples of Cre lines that have expression patterns which both define an anatomical region's boundaries with other nuclei (e.g., suprachiasmatic nucleus, Lypd6-Cre_KL56) and mark specific cell types (e.g., Nr5a1-Cre in ventromedial hypothalamus, and Pomc-Cre (BL) in the arcuate nucleus, Balthasar et al., 2004; Dhillon et al., 2006). In pallidum regions, Slc6a3-Cre (Zhuang et al., 2005) expresses Cre reporter specifically within the bed nuclei of the stria terminalis and Gnrh-Cre (Yoon et al., 2005) has strong expression within the medial septum. Cre lines are also available which isolate specific thalamic nuclei, including the paraventricular nucleus of the thalamus (e.g., Ntrk1-IRES-Cre) and anterodorsal and anteroventral nuclei (Gal-Cre_KI87). In the midbrain, Rorb-IRES2-Cre directs specific restricted expression to the sensory regions of the SCs and the oculomotor nucleus can be accessed separately from its neighbors using the Pvalb-IRES-Cre line (Hippenmeyer et al., 2005). Nuclei within the pons with restricted expression of Cre include the motor nucleus of the trigeminal (Scnn1a-Tg2-Cre, Madisen et al., 2010) and the pontine gray (Th-Cre_FI172). In the medulla, the inferior olivary nucleus specifically expresses Cre in Crh-IRES-Cre (ZJH) mice (Taniguchi et al., 2011) and the dorsal cochlear nucleus has anatomically restricted expression of Cre in the Pnmt-Cre line (Ebert et al., 2004). Finally, several Cre lines show expression in the cerebellum, including Purkinje cells (e.g., Pcp2-Cre_GN135)

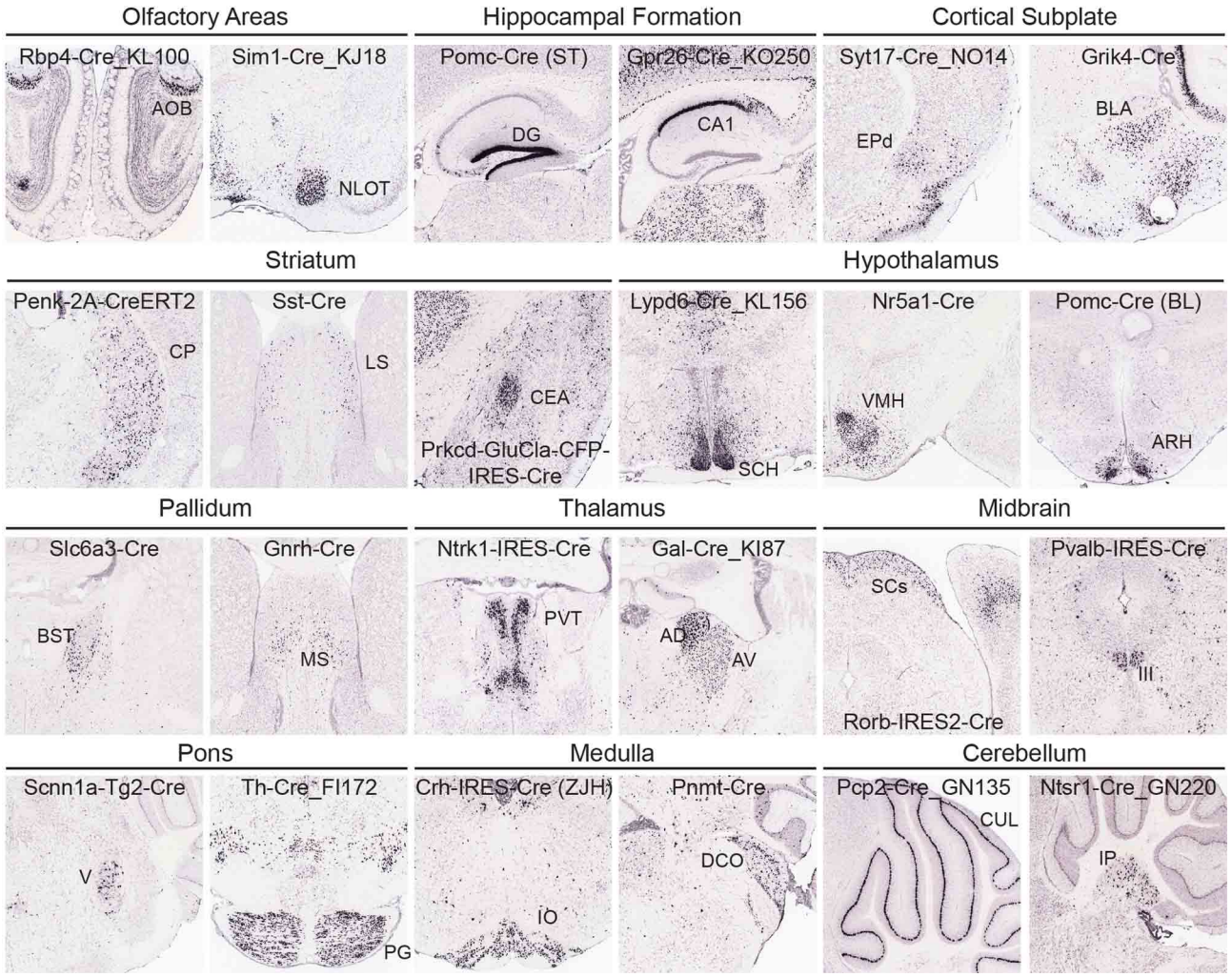

FIGURE 5 | Cre lines provide genetic access to specific brain areas through enriched or restricted gene expression patterns. Within this collection of 135 characterized Cre lines, enriched expression patterns can be seen in nuclei from all major brain regions. Representative examples of Cre lines with region-selective expression patterns of the tdTomato reporter are shown within olfactory areas (Rbp4-Cre_KL100, Sim1-Cre_KJ18), hippocampal formation (Pomc-Cre (ST), Gpr26-Cre_KO250), cortical subplate (Syt17-Cre_NO14, Grik4-Cre), striatum (Penk-2A-CreERT2, Sst-Cre, Prkcd-GluCla-CFP-IRES-Cre), hypothalamus [Lypd6-Cre_KL156, Nr5a1-Cre, Pomc-Cre (BL)], pallidum (Slc6a3-Cre, Gnrh-Cre), thalamus (Ntrk1-IRES-Cre, Gal-Cre_KI87), midbrain (Rorb-IRES2-Cre, Pvalb-IRES-Cre), pons (Scnn1a-Tg2-Cre, Th-Cre_FI172), medulla (Crh-IRES-Cre(ZJH), Pnmt-Cre), and cerebellum (Pcp2-Cre_GN135, Ntsr1-Cre_GN220). Abbreviations are: AOB, accessory olfactory bulb; NLOT, nucleus of the lateral olfactory tract; DG, dentate gyrus; field CA1; EPd, endopiriform nucleus, dorsal part; BLA, basolateral amygdalar nucleus; CP, caudoputamen; LS, lateral septal nucleus; CEA, central amygdalar nucleus; SCH, suprachiasmatic nucleus; VMH, ventromedial hypothalamic nucleus; ARH, arcuate nucleus; BST, bed nuclei of the stria terminalis; MS, medial septal nucleus; PVT, paraventricular nucleus of the thalamus; AD, anterodorsal; and AV, anteroventral nucleus of the thalamus; SCs, superior colliculus, sensory related; III, oculomotor nucleus; V, motor nucleus of trigeminal; PG, pontine gray; IO, inferior olivary complex; DCO, dorsal cochlear nucleus; CUL, culmen; and IP, interposed nucleus.

in the cerebellar lobules and in the deep cerebellar nuclei (e.g., Ntsr1-Cre_GN220).

Cre LINES FOR GENETIC ACCESS TO SPECIFIC CELL TYPES WITHIN CORTICAL CIRCUITS

As shown above, a large variety of whole brain expression patterns exist within these 135 Cre lines, but there was an initial selection bias toward including in the database Cre lines with cortical expression, either laminar-restricted Cre or cortical interneurons. Most of these cortical Cre lines also have regionally-specific expression patterns in subcortical brain regions. Each Cre line was placed into a *single* coarse-level group depending on its dominant pattern of expression (**Table 2**), although many Cre lines actually belong to multiple categories. For example, here we placed several lines with neuropeptide promoters (VIP-Cre, vasoactive intestinal polypeptide, Sst-Cre, somatostatin, and Cck-Cre, cholecystokinin) into the cortical interneuron group as they have been well studied there, but they also belong to the neuropeptide group. Of note, we also characterized very general cell type-specific Cre lines that may be

Table 2 | Cre lines listed only once according to major categorie.

Cortical layer selective lines	Cortical interneuron lines	Neuropeptide/ neuromodulator lines	Widespread lines	Regionally enriched lines
A930038C07Rik-Tg1-Cre (layer 5)	Calb2-CreERT2	Adcyap1-2A-Cre	Dcx-Cre-35	Camk2a-Cre
A930038C07Rik-Tg4-Cre (layer 5)	Calb2-IRES-Cre	Agrp-IRES-Cre	Dcx-Cre-38	Camk2a-CreERT2
Chrna2-Cre_OE25 (layer 5)	Cck-CreERT2	Avp-IRES2-Cre	Dcx-CreERT2	Cart-Tg1-Cre
Chrnb4-Cre_OL57 (layer 2/3/5)	Cck-IRES-Cre	Chat-IRES-Cre	Eno2-Cre	Cdhr1-Cre_KG66
Ctgf-Tg1-Cre (layer 6b)	Cort-T2A-Cre	Chat-IRES-CreER	Gfap-Cre	Cnnm2-Cre_KD18
Ctgf-Tg2-Cre (layer 6b)	Crh-IRES-Cre (BL)	Dbh-Cre_KH212	Nefh-Cre	Cyp39a1-Tg1-Cre
Cux2-Cre (layer 2/3/4)	Crh-IRES-Cre (ZJH)	Gal-Cre_KI87	Nes-Cre	Cyp39a1-Tg7-Cre
Cux2-CreERT2 (layer 2/3/4)	Dlx1-CreERT2	Gnrh1-Cre	Otof-CreERT2	Dbx1-IRES-Cre
Cux2-IRES-Cre (layer 2/3/4)	Dlx5-CreERT2	Hdc-Cre_IM1	Slc17a8-iCre	Drd1a-Cre
Efr3a-Cre_NO108 (layer 5)	Erbb4-2A-CreERT2	Ins2-Cre	Snap25-IRES2-Cre	Drd2-Cre_ER44
Etv1-CreERT2 (layer 5)	Gad2-CreERT2	Kiss1-Cre	Syn1-Cre	Drd3-Cre_KI196
Gng7-Cre_KH71 (layer 2/5)	Gad2-IRES-Cre	Oxt-IRES-Cre	Vamp2-IRES-CreER	Emx1-IRES-Cre
Gpr26-Cre_KO250 (layer 5)	Nkx2-1-CreERT2	Penk-2A-CreERT2		Esr1-2A-Cre
Grp-Cre_KH288 (layer 2/3)	Nos1-CreERT2	Pmch-Cre		Gabra6-IRES-Cre
Htr2a-Cre_KM207 (layer 5)	Pvalb-2A-Cre	Pomc-Cre (BL)		Gabrr3-Cre_KC112
Nr5a1-Cre (layer 4)	Pvalb-2A-CreERT2	Pomc-Cre (ST)		Grik4-Cre
Ntsr1-Cre_GN220 (layer 6)	Pvalb-2A-dCre	Slc6a3-Cre		Grm2-Cre_MR90
Nxph4-2A-CreERT2 (layer 6b)	Pvalb-CreERT2	Slc6a4-Cre_ET33		Kcnc2-Cre
Otof-Cre (layer 6)	Pvalb-IRES-Cre	Slc6a4-CreERT2_EZ13		Lepr-IRES-Cre
Rasgrf2-2A-dCre (layer 2/3)	Slc32a1-IRES-Cre	Slc18a2-Cre_OZ14		Lhx6-CreERT2
Rbp4-Cre_KL100 (layer 5)	Sst-Cre	Th-IRES-CreER		Lypd6-Cre_KL156
Rorb-IRES2-Cre (layer 4)	Sst-CreERT2	Th-Cre_FI172		Mybpc1-Cre
Scnn1a-Tg1-Cre (layer 4)	Sst-IRES-Cre	Ucn3-Cre_KF43		Nefl-IRES-CreER
Scnn1a-Tg2-Cre (layer 4)	Tac1-IRES2-Cre			Ntrk1-IRES-Cre
Scnn1a-Tg3-Cre (layer 4)	Tac2-IRES2-Cre			Oxtr-Cre_ON66
Sim1-Cre_KJ18 (layer 5)	Vip-IRES-Cre			Pcdh9-Cre_NP276
Six3-Cre (layer 4)				Pcp2-Cre (AM)
Syt6-Cre_KI148 (layer 6)				Pcp2-Cre_GN135
Trib2-2A-CreERT2 (layer 5)				Pdzk1ip1-Cre_KD31
Wfs1-Tg2-CreERT2 (layer 2/3)				Plxnd1-Cre_OG1
Wfs1-Tg3-CreERT2 (layer 2/3)				Pnmt-Cre
				Ppp1r17-Cre_NL146
				Prkcd-GluCla-CFP-IRES-Cre
				Satb2-Cre_MO23
				Sim1-Cre
				Slc6a5-Cre_KF109
				Slc17a6-IRES-Cre
				Slc17a7-IRES2-Cre
				Syn1-icre/mRFP1
				Syt17-Cre_NO14
				Tlx3-Cre
				Vipr2-Cre_KE2
				Wnt3a-IRES-Cre

Lines in bold indicate those for which expression of Cre itself (unlike reporter) shows laminar restriction in the cortex.

widespread or regionally enriched, including pan-neuronal (e.g., Nes-Cre, Snap25-IRES2-Cre, Eno2-Cre), pan-glial (Gfap-Cre), pan-glutamatergic (e.g., Slc17a6-IRES-Cre, Slc17a7-IRES2-Cre), and pan-GABAergic (e.g., Gad2-IRES-Cre, Slc32a1-IRES-Cre).

Approximately 30 Cre lines were characterized in which expression is highly selective to cells within one cortical layer; 10 example images from the primary somatosensory cortex are shown in **Figure 6**. Cux2-CreERT2 (Franco et al., 2012) and Rasgrf2-2A-dCre are enriched in cells within superficial layers 2/3/4 or 2/3, respectively. In layer 4, three Cre lines with laminar-selective expression are Nr5a1-Cre (Dhillon et al., 2006), Rorb-IRES2-Cre, and Scnn1a-Tg3-Cre (Madisen et al., 2010). GENSAT lines Rbp4-Cre_KL100 and Chrna2-Cre_OE25, as well as the Etv1-CreERT2 line (Taniguchi et al., 2011) are enriched

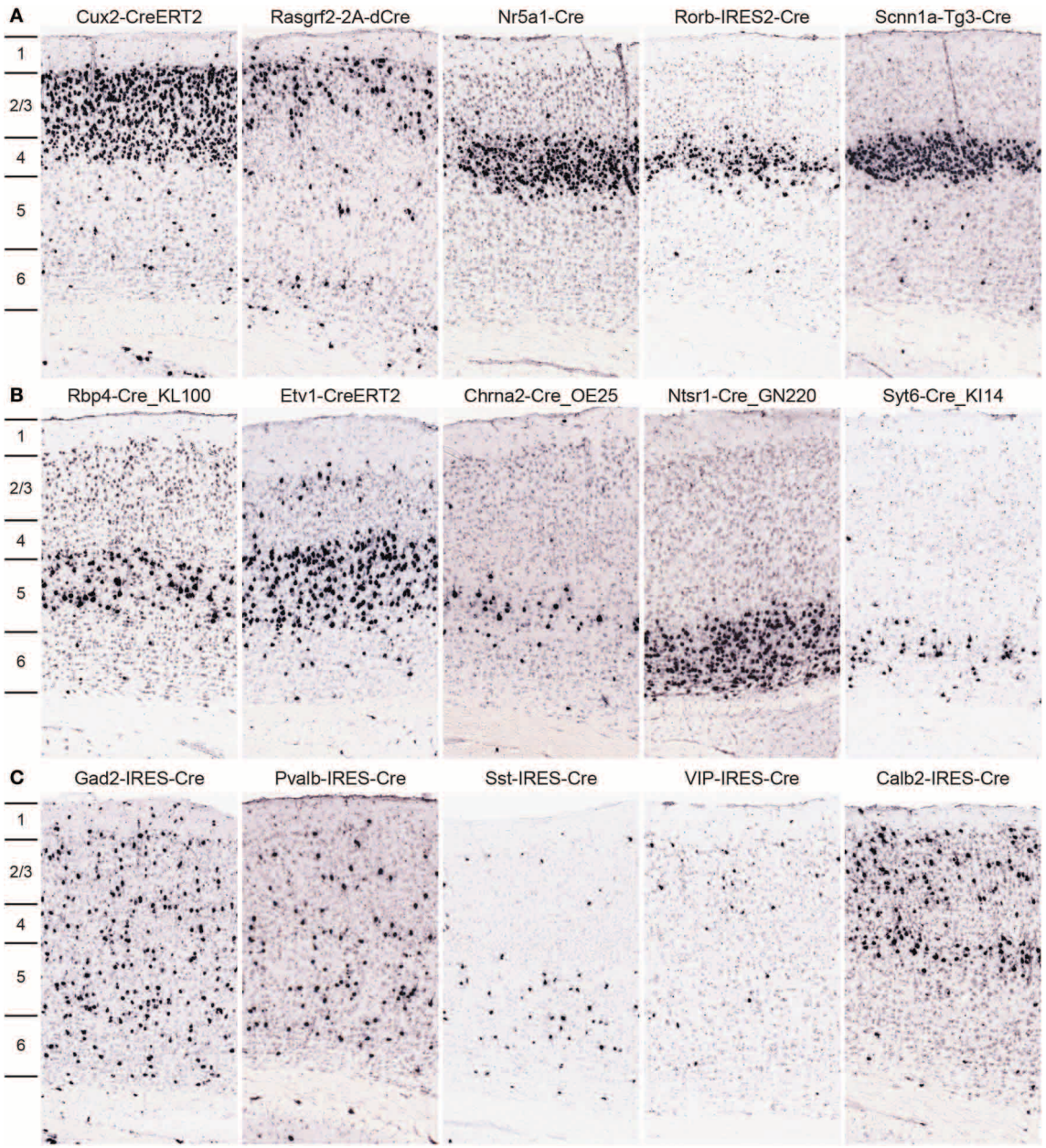

FIGURE 6 | Cre lines provide genetic access to specific cortical layers and cortical interneurons for circuit analyses. (A,B) Many Cre lines have been generated with selective expression in distinct cortical layers. Representative tdTomato ISH images are shown from a subset of Cre lines with preferential expression in neurons of layers 2/3 (Cux2-CreERT2, Rasgrf2-2A-dCre), layer 4 (Nr5a1-Cre, Rorb-IRES2-Cre, Scnn1a-Tg3-Cre), layer 5 (Rbp4-Cre_KL100, Etv1-CreERT2, Chrna2-Cre_OE25), and layer 6 (Ntsr1-Cre_GN220, Syt6-Cre_KI14). **(C)** Representative images from Cre lines with tdTomato expression driven by cortical interneuron marker promoters (Gad2-IRES-Cre, Pvalb-IRES-Cre, Sst-IRES-Cre, VIP-IRES-Cre, Calb2-IRES-Cre). Density and level of restriction to specific layers varies and is often dependent on the specific cortical region of interest, thus researchers should use the entire whole brain image series to confirm expression in other areas.

in layer 5. Layer 6 cells express Cre in the Ntsr1-Cre_GN220 and Syt6-Cre_KI14 lines. For all Cre lines, expression is rarely perfectly restricted to a single layer, but these lines are still incredibly useful for much more precise spatial control of genetic tools for circuit analyses. In addition, most of these Cre lines have roughly equal expression throughout all cortical areas, but a minority are anatomically restricted to specific cortical regions (e.g., Grp-Cre_KH288 is restricted to frontal cortex, Gerfen et al., 2013). Therefore, the whole brain/cortex image series should be viewed by researchers for confirmation in specific regions. Cortical interneuron types within cortical circuits can also be genetically accessed via specific Cre lines, many of which were described previously in the cortex, used successfully for functional studies of circuit components, and for the most part

faithfully recapitulate endogenous expression (Taniguchi et al., 2011; Pfeffer et al., 2013; Pi et al., 2013), but are now fully characterized across the brain due to our pipeline processing, including Gad2-IRES-Cre, Pvalb-IRES-Cre, Sst-IRES-Cre, VIP-IRES-Cre, and Calb2-IRES-Cre.

Cre LINES FOR GENETIC ACCESS TO SPECIFIC NEUROMODULATORY CELL TYPES IN BRAIN-WIDE CIRCUITS

Another large group of Cre lines for which we have produced whole brain anatomical expression data include those driven by specific promoters involved in neuromodulatory or neuropeptide signaling. Any Cre line to be used for investigations into cell type-specific roles (as opposed to taking advantage of regional, perhaps serendipitous ectopic expression) should have verified Cre expression patterns that mimic the corresponding endogenous gene expression. In many cases, DFISH data is available in the Transgenic Characterization database to confirm or refute this, or reporter and Cre ISH can be viewed together with ABA data to allow for comparisons of expression within brain regions. Four examples from each of the major neuromodulatory systems where Cre reporter expression matches the corresponding endogenous gene patterns include cholinergic cells expressing Cre in the Chat-IRES-Cre line (Rossi et al., 2011) (**Figure 7A**), noradrenergic cells expressing Cre in the Dbh-Cre_KH212 line (**Figure 7B**), dopaminergic cells expressing Cre in the Slc6a3-Cre line (Zhuang et al., 2005) (**Figure 7C**), and serotonergic cells expressing Cre in the Slc6a4-Cre_ET33 line (**Figure 7D**).

DISCUSSION

Promoter-specific Cre lines can provide both cell type and/or regional specificity to label and manipulate network components when used with reporter lines or recombinant viruses. Large scale projects such as GENSAT (Gong et al., 2007; Gerfen et al., 2013) and the NIH Blueprint for Neuroscience Research (Taniguchi et al., 2011) produced a large collection of Cre driver lines in a systematic fashion, but not all lines were comprehensively characterized. GENSAT provided whole brain data by crossing their >250 BAC transgenic Cre lines with a reporter line (Rosa26-EGFP) and presenting images of immunohistological staining on its public website (http://www.gensat.org). We also characterized Cre reporter expression for the collection of lines presented here, but include different and additional data types critical for assessing whole brain recombination patterns in a particular Cre line. Specifically we used ISH to detect reporter and Cre mRNA, and included DFISH for a subset of lines to characterize expression within single cells. We did not include immunohistological analyses of protein levels. Our extensive dataset also benefits from integration with other Allen Institute data, specifically registration with the ARA, links to endogenous gene expression data through the Allen Brain Atlas, and links to related data from other Institute projects. The Transgenic Database presented here is meant as a reference guide for researchers interested in using and identifying Cre driver lines for investigation into specific cell populations and networks.

Two simple, yet powerful, searches made possible through our database and the tables provided here are: (1) Where in the brain is Cre expressed in my line of interest; and (2) Are there driver lines with Cre expression in my area(s) of interest? For the first question, users can view 2D image series (e.g., tdTomato reporter, Cre, or DFISH) sampled across the entire brain for each Cre driver line side-by-side with the ARA to help identify brain structures. In addition, we provide here (Supplemental Table 2) expression values from 295 brain areas per Cre line, which can be sorted to identify regions with the highest Cre expression per line, and also supply associated visual descriptions of these expression patterns for a subset of all lines. Supplemental Table 3 makes it possible to perform the second search by providing fold change ratios of expression value per structure normalized to the average whole brain expression value. High fold change ratios in a particular structure indicate enrichment in that structure over the rest of brain. Again, we provide visually annotated categories to describe expression patterns (and note when there is no expression) associated with the informatics values, but users should also refer to the images online to confirm for themselves.

Major considerations when using Cre driver lines are common across various experiments investigating the roles of cell populations and circuit function, and several of them can be addressed using the Transgenic Characterization resource. One is whether Cre expression faithfully represents endogenous gene expression patterns. We present two data types to aid in this determination: (1) comparison of regional expression patterns between the Cre line and the corresponding gene in the ABA; or (2) DFISH to assess co-localization of Cre reporter and the corresponding endogenous gene mRNAs within the same cells. We performed correlation analyses using the informatics-derived expression values assigned from each data type (ABA or Transgenic Data). There was a wide range of results, with some Cre lines very faithfully capturing whole brain expression patterns, and others performing poorly or at intermediate levels. Lines with lower overall correlation coefficients generally captured a combination of all areas with endogenous gene expression plus ectopic regions, or captured a subset of all endogenous regions. Knock-in lines had expression patterns better predicted from the endogenous gene expression, but still showed variation in results.

A second consideration that can be addressed using this resource is whether reporter expression is consistent with Cre expression (or endogenous gene expression) at the desired age for experiments. When viewing reporter expression at P56, it is important to bear in mind that transient developmental expression of Cre can contribute to seemingly "ectopic" patterns of expression. Indeed, we found that the overall correlation between Cre itself and ABA across all lines was significantly higher than with tdTomato reporter ISH. Cre ISH data in P56 mice is supplied for ∼60% of the 135 driver lines characterized here, and should be consulted when available to confirm adult expression of Cre itself. However, transient developmental expression does not account for all seemingly ectopic expression patterns (e.g., see **Figure 4B**, Cre and tdTomato ISH in cortex, but not in ABA). Care must also be taken in interpreting negative ISH results; very low levels of mRNA may not be detectable by this method. Ectopic expression may also provide serendipitous access to specific circuits. For example, the Ntsr1-Cre_ GN220 line has strong Cre and reporter expression in layer 6 of the cortex, but *Ntsr1* is not endogenously expressed in those cells (at least as detectable by ISH), even so the

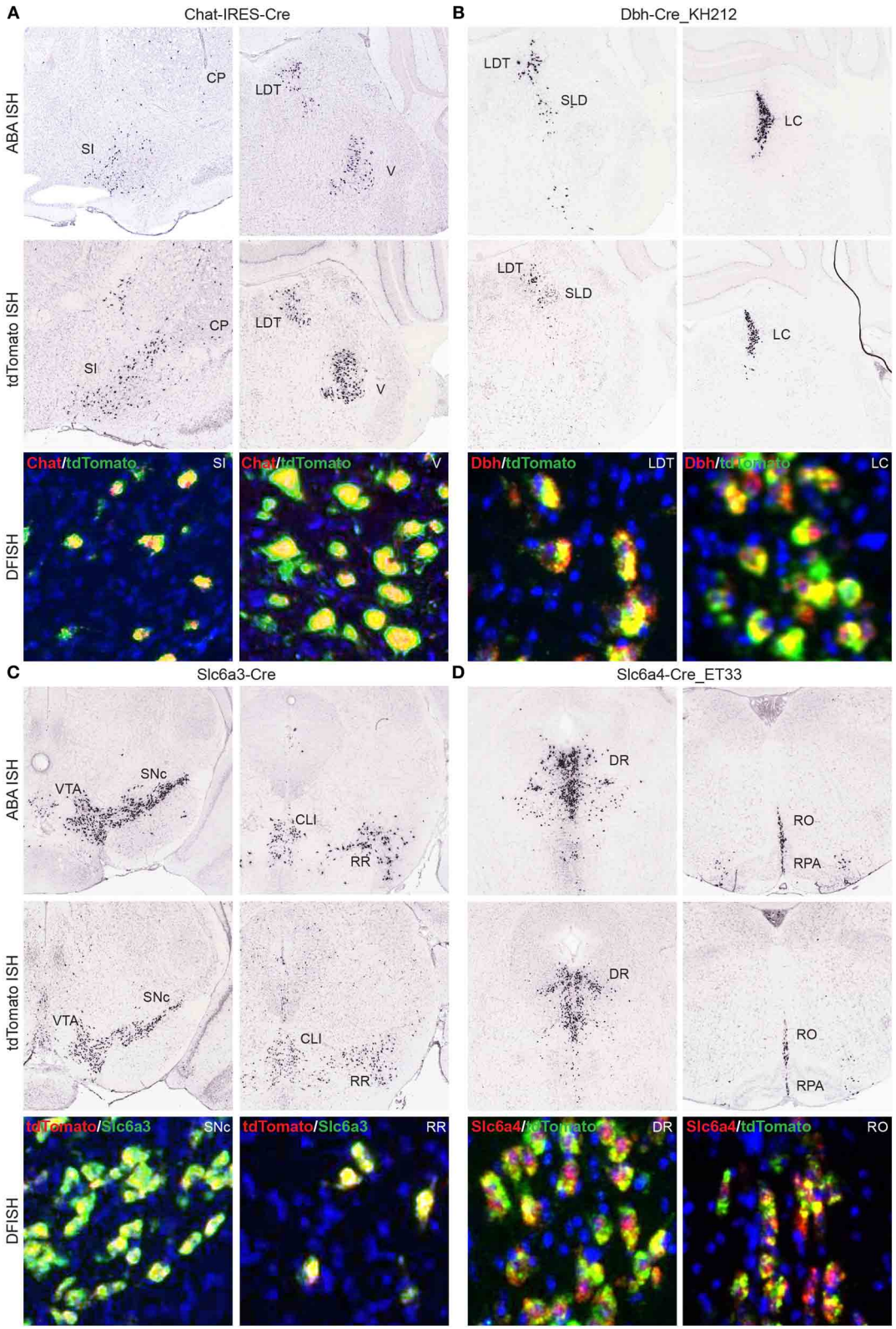

FIGURE 7 | Cre lines provide genetic access to specific neuromodulatory cell types and brain regions. Endogenous gene expression and tdTomato reporter ISH images show the faithful recapitulation of regional expression patterns between Cre line reporter expression at P56 and the corresponding endogenous gene expression patterns from the ABA for four major neuromodulatory systems. DFISH data from each line also demonstrates high levels of correspondence between the endogenous gene and reporter

(Continued)

FIGURE 7 | Continued
expression within the same cell. **(A)** Cholinergic neurons in the SI, basal forebrain; CP, caudoputamen; LDT, laterodorsal tegmental nucleus; and V, motor nucleus of the trigeminal; that express choline acetyltransferase mRNA (*Chat*), among other regions not shown, are also specifically labeled in the Chat-IRES-Cre line. **(B)** Noradrenergic neurons labeled for dopamine beta-hydroxylase mRNA (*Dbh*) are specifically located with the LDT, SLD, sublaterodorsal nucleus; and LC, locus ceruleus. The same regions have enriched expression of the tdTomato reporter in the Dbh-Cre_KH212 transgenic line. **(C)** Dopaminergic cells expressing dopamine transporter mRNA (*Slc6a3*) and Cre reporter mRNA in the Slc6a3-Cre line are found within the VTA, ventral tegmental area; SNc, substantia nigra, pars compacta; CLI, central linear nucleus raphe; and RR, retrorubral area. **(D)** Serotonergic neurons, shown labeled with a probe against the serotonin transporter gene, *Slc6a4*, are located with the dorsal raphe nucleus (DR), and the brainstem raphe nuclei, obscurus (RO) and pallidus (RPA). The same expression pattern is observed in the transgenic Slc6a4-Cre_ET33 line.

line has already been used to uncover a role for layer six neurons in gain control in visual cortex (Olsen et al., 2012).

More research and data types will be required to realize the full potential and limitations of available Cre driver lines for genetic access to specific cell types and regions. For example, characterization of the axonal projections originating from different Cre lines provides additional information on whether a subtype of projection neuron is labeled (Gerfen et al., 2013). We are actively pursuing this method of characterization now in the context of mapping whole brain projections using Cre drivers, by injecting Cre-dependent rAAV tracer into brain regions with enriched or restricted expression in over 100 Cre lines as part of our Allen Mouse Brain Connectivity Atlas project (http://connectivity.brain-map.org) (Oh et al., 2014).

Cre lines may be among the best available tools for systematically generating a census of cell types in the mouse brain by providing access to genetically defined cell populations, although it cannot be assumed that a Cre driver equals a single cell type. Many characteristics, or combinations of characteristics, can be used to classify cells into types, including gene expression, morphology, physiological properties, and connectivity. Hetero- or homo-geneity of cell type characteristics within a particular Cre line can be determined through direct labeling using Cre reporters in combination with various experimental techniques; e.g., (1) morphological reconstruction of Cre+ cells (Rotolo et al., 2008), (2) FACS sorting or single cell collection of labeled Cre+ cells for genetic profiling (Siegert et al., 2012; Pfeffer et al., 2013), (3) electrophysiological recording of fluorescent Cre+ cells *in vitro* or *in vivo* (Miyamichi et al., 2013; Runyan and Sur, 2013), and (4) connectivity profiling in local circuits by dual patching of Cre+ and/or Cre- cells (Pfeffer et al., 2013). Analyses at the single cell level will inform us as to whether and which Cre lines label heterogeneous cell populations, as most cell types are not likely defined by single genes. Already genetic strategies are in use to capture more homogenous cell populations using Cre/Flp intersectional techniques (Dymecki et al., 2010); the generation of more Flp drivers will aid this process. Knowledge of specific developmental lineages and timing of Cre induction can also be used to isolate some pure cell types (Taniguchi et al., 2013).

Regardless of whether a Cre line provides genetic access to a "single" cell type, they are commonly used together with a variety of reporter genes for analyses of gene function and the role of different components within specific neural circuits (Gore and Zweifel, 2013). Using Cre lines to target specific cell populations has greatly enhanced our knowledge of the dynamic organization of neural circuits, obtained from tools to monitor and manipulate neural activity (Atasoy et al., 2008; Madisen et al., 2012; Zariwala et al., 2012). Full characterization of Cre expression and understanding the variability of different characteristics in specific gene promoter driver lines will continue to improve the analytical potential of various tools in dissecting circuit functions, and aid in the classification of cell types.

AUTHOR CONTRIBUTIONS

Julie A. Harris, Seung Wook Oh, Susan Sunkin, Staci A. Sorensen, Amy Bernard, Linda Madisen, and Hongkui Zeng contributed to overall project design and management. Karla E. Hirokawa, Julie A. Harris, Staci A. Sorensen, Phillip Bohn, Marty Mortrud, and Benjamin Ouellette, were main contributors to data and image analysis. Linda Madisen, Maya Mills, Hong Gu, and Hongkui Zeng were responsible for generation of new Cre lines. Lydia L. Ng and Chinh Dang conducted informatics data processing and web presentation. Amy Bernard, Kimberly A. Smith, and Jolene Kidney performed managerial roles in ISH, imaging, and mouse colony planning processes. Julie A. Harris wrote the manuscript with input from other authors.

ACKNOWLEDGMENTS

We are grateful to the individuals and programs which supplied Cre driver lines or made them available at public repositories. We would also like to thank the many staff members at the Allen Institute who did not author the paper for expert technical support. This work was funded by the Allen Institute for Brain Science. We are grateful to the Allen Institute founders, P.G. Allen and J. Allen, for their vision, encouragement, and support.

SUPPLEMENTARY MATERIAL

The Supplementary Material for this article can be found online at: http://www.frontiersin.org/journal/10.3389/fncir.2014.00076/abstract

REFERENCES

Anthony, T. E., Dee, N., Bernard, A., Lerchner, W., Heintz, N., and Anderson, D. J. (2014). Control of stress-induced persistent anxiety by an extra-amygdala septohypothalamic circuit. *Cell* 156, 522–536. doi: 10.1016/j.cell.2013.12.040

Atasoy, D., Aponte, Y., Su, H. H., and Sternson, S. M. (2008). A FLEX switch targets Channelrhodopsin-2 to multiple cell types for imaging and long-range circuit mapping. *J. Neurosci.* 28, 7025–7030. doi: 10.1523/JNEUROSCI.1954-08.2008

Balthasar, N., Coppari, R., McMinn, J., Liu, S. M., Lee, C. E., Tang, V., et al. (2004). Leptin receptor signaling in POMC neurons is required for normal body weight homeostasis. *Neuron* 42, 983–991. doi: 10.1016/j.neuron.2004.06.004

Bochkov, Y. A., and Palmenberg, A. C. (2006). Translational efficiency of EMCV IRES in bicistronic vectors is dependent upon IRES sequence and gene location. *Biotechniques* 41, 283–284, 286, 288 passim. doi: 10.2144/000112243

Dhillon, H., Zigman, J. M., Ye, C., Lee, C. E., McGovern, R. A., Tang, V., et al. (2006). Leptin directly activates SF1 neurons in the VMH, and this action by leptin is required for normal body-weight homeostasis. *Neuron* 49, 191–203. doi: 10.1016/j.neuron.2005.12.021

Dong, H. (2008). *The Allen Reference Atlas: A Digital Color Brain Atlas of the C57BL/6J Male Mouse*. Hoboken, NJ: John Wiley & Sons, Inc.

Dymecki, S. M., Ray, R. S., and Kim, J. C. (2010). Mapping cell fate and function using recombinase-based intersectional strategies. *Meth. Enzymol.* 477, 183–213. doi: 10.1016/S0076-6879(10)77011-7

Ebert, S. N., Rong, Q., Boe, S., Thompson, R. P., Grinberg, A., and Pfeifer, K. (2004). Targeted insertion of the Cre-recombinase gene at the phenylethanolamine n-methyltransferase locus: a new model for studying the developmental distribution of adrenergic cells. *Dev. Dyn.* 231, 849–858. doi: 10.1002/dvdy.20188

Feil, R., Wagner, J., Metzger, D., and Chambon, P. (1997). Regulation of Cre recombinase activity by mutated estrogen receptor ligand-binding domains. *Biochem. Biophys. Res. Commun.* 237, 752–757. doi: 10.1006/bbrc.1997.7124

Franco, S. J., Gil-Sanz, C., Martinez-Garay, I., Espinosa, A., Harkins-Perry, S. R., Ramos, C., et al. (2012). Fate-restricted neural progenitors in the mammalian cerebral cortex. *Science* 337, 746–749. doi: 10.1126/science.1223616

Gerfen, C. R., Paletzki, R., and Heintz, N. (2013). GENSAT BAC cre-recombinase driver lines to study the functional organization of cerebral cortical and basal ganglia circuits. *Neuron* 80, 1368–1383. doi: 10.1016/j.neuron.2013.10.016

Gong, S., Doughty, M., Harbaugh, C. R., Cummins, A., Hatten, M. E., Heintz, N., et al. (2007). Targeting Cre recombinase to specific neuron populations with bacterial artificial chromosome constructs. *J. Neurosci.* 27, 9817–9823. doi: 10.1523/JNEUROSCI.2707-07.2007

Gore, B. B., and Zweifel, L. S. (2013). Genetic reconstruction of dopamine D1 receptor signaling in the nucleus accumbens facilitates natural and drug reward responses. *J. Neurosci.* 33, 8640–8649. doi: 10.1523/JNEUROSCI.5532-12.2013

Haubensak, W., Kunwar, P. S., Cai, H., Ciocchi, S., Wall, N. R., Ponnusamy, R., et al. (2010). Genetic dissection of an amygdala microcircuit that gates conditioned fear. *Nature* 468, 270–276. doi: 10.1038/nature09553

Heusner, C. L., Beutler, L. R., Houser, C. R., and Palmiter, R. D. (2008). Deletion of GAD67 in dopamine receptor-1 expressing cells causes specific motor deficits. *Genesis* 46, 357–367. doi: 10.1002/dvg.20405

Hippenmeyer, S., Vrieseling, E., Sigrist, M., Portmann, T., Laengle, C., Ladle, D. R., et al. (2005). A developmental switch in the response of DRG neurons to ETS transcription factor signaling. *PLoS Biol.* 3:e159. doi: 10.1371/journal.pbio.0030159

Huang, Z. J., and Zeng, H. (2013). Genetic approaches to neural circuits in the mouse. *Annu. Rev. Neurosci.* 36, 183–215. doi: 10.1146/annurev-neuro-062012-170307

Lein, E. S., Hawrylycz, M. J., Ao, N., Ayres, M., Bensinger, A., Bernard, A., et al. (2007). Genome-wide atlas of gene expression in the adult mouse brain. *Nature* 445, 168–176. doi: 10.1038/nature05453

Madisen, L., Mao, T., Koch, H., Zhuo, J. M., Berenyi, A., Fujisawa, S., et al. (2012). A toolbox of Cre-dependent optogenetic transgenic mice for light-induced activation and silencing. *Nat. Neurosci.* 15, 793–802. doi: 10.1038/nn.3078

Madisen, L., Zwingman, T. A., Sunkin, S. M., Oh, S. W., Zariwala, H. A., Gu, H., et al. (2010). A robust and high-throughput Cre reporting and characterization system for the whole mouse brain. *Nat. Neurosci.* 13, 133–140. doi: 10.1038/nn.2467

McHugh, T. J., Jones, M. W., Quinn, J. J., Balthasar, N., Coppari, R., Elmquist, J. K., et al. (2007). Dentate gyrus NMDA receptors mediate rapid pattern separation in the hippocampal network. *Science* 317, 94–99. doi: 10.1126/science.1140263

Miyamichi, K., Shlomai-Fuchs, Y., Shu, M., Weissbourd, B. C., Luo, L., and Mizrahi, A. (2013). Dissecting local circuits: parvalbumin interneurons underlie broad feedback control of olfactory bulb output. *Neuron* 80, 1232–1245. doi: 10.1016/j.neuron.2013.08.027

Nakazawa, K., Quirk, M. C., Chitwood, R. A., Watanabe, M., Yeckel, M. F., Sun, L. D., et al. (2002). Requirement for hippocampal CA3 NMDA receptors in associative memory recall. *Science* 297, 211–218. doi: 10.1126/science.1071795

Ng, L., Pathak, S. D., Kuan, C., Lau, C., Dong, H., Sodt, A., et al. (2007). Neuroinformatics for genome-wide 3D gene expression mapping in the mouse brain. *IEEE/ACM Trans. Comput. Biol. Bioinform.* 4, 382–393. doi: 10.1109/tcbb.2007.1035

O'Connor, D. H., Hires, S. A., Guo, Z. V., Li, N., Yu, J., Sun, Q. Q., et al. (2013). Neural coding during active somatosensation revealed using illusory touch. *Nat. Neurosci.* 16, 958–965. doi: 10.1038/nn.3419

Oh, S. W., Harris, J. A., Ng, L., Winslow, B., Cain, N., Mihalas, S., et al. (2014). A mesoscale connectome of the mouse brain. *Nature* 508, 207–214. doi: 10.1038/nature13186

Olsen, S. R., Bortone, D. S., Adesnik, H., and Scanziani, M. (2012). Gain control by layer six in cortical circuits of vision. *Nature* 483, 47–52. doi: 10.1038/nature10835

Pfeffer, C. K., Xue, M., He, M., Huang, Z. J., and Scanziani, M. (2013). Inhibition of inhibition in visual cortex: the logic of connections between molecularly distinct interneurons. *Nat. Neurosci.* 16, 1068–1076. doi: 10.1038/nn.3446

Pi, H. J., Hangya, B., Kvitsiani, D., Sanders, J. I., Huang, Z. J., and Kepecs, A. (2013). Cortical interneurons that specialize in disinhibitory control. *Nature* 503, 521–524. doi: 10.1038/nature12676

Ramirez, S., Liu, X., Lin, P. A., Suh, J., Pignatelli, M., Redondo, R. L., et al. (2013). Creating a false memory in the hippocampus. *Science* 341, 387–391. doi: 10.1126/science.1239073

Rossi, J., Balthasar, N., Olson, D., Scott, M., Berglund, E., Lee, C. E., et al. (2011). Melanocortin-4 receptors expressed by cholinergic neurons regulate energy balance and glucose homeostasis. *Cell Metab.* 13, 195–204. doi: 10.1016/j.cmet.2011.01.010

Rotolo, T., Smallwood, P. M., Williams, J., and Nathans, J. (2008). Genetically-directed, cell type-specific sparse labeling for the analysis of neuronal morphology. *PLoS ONE* 3:e4099. doi: 10.1371/journal.pone.0004099

Runyan, C. A., and Sur, M. (2013). Response selectivity is correlated to dendritic structure in parvalbumin-expressing inhibitory neurons in visual cortex. *J. Neurosci.* 33, 11724–11733. doi: 10.1523/JNEUROSCI.2196-12.2013

Sando, R. 3rd., Baumgaertel, K., Pieraut, S., Torabi-Rander, N., Wandless, T. J., Mayford, M., et al. (2013). Inducible control of gene expression with destabilized Cre. *Nat. Methods* 10, 1085–1088. doi: 10.1038/nmeth.2640

Siegert, S., Cabuy, E., Scherf, B. G., Kohler, H., Panda, S., Le, Y. Z., et al. (2012). Transcriptional code and disease map for adult retinal cell types. *Nat. Neurosci.* 15, 487–495, S481–S482. doi: 10.1038/nn.3032

Taniguchi, H., He, M., Wu, P., Kim, S., Paik, R., Sugino, K., et al. (2011). A resource of Cre driver lines for genetic targeting of GABAergic neurons in cerebral cortex. *Neuron* 71, 995–1013. doi: 10.1016/j.neuron.2011.07.026

Taniguchi, H., Lu, J., and Huang, Z. J. (2013). The spatial and temporal origin of chandelier cells in mouse neocortex. *Science* 339, 70–74. doi: 10.1126/science.1227622

Thompson, C. L., Pathak, S. D., Jeromin, A., Ng, L. L., Macpherson, C. R., Mortrud, M. T., et al. (2008). Genomic anatomy of the hippocampus. *Neuron* 60, 1010–1021. doi: 10.1016/j.neuron.2008.12.008

Trichas, G., Begbie, J., and Srinivas, S. (2008). Use of the viral 2A peptide for bicistronic expression in transgenic mice. *BMC Biol.* 6:40. doi: 10.1186/1741-7007-6-40

Yau, H. J., Wang, H. F., Lai, C., and Liu, F. C. (2003). Neural development of the neuregulin receptor ErbB4 in the cerebral cortex and the hippocampus: preferential expression by interneurons tangentially migrating from the ganglionic eminences. *Cereb. Cortex* 13, 252–264. doi: 10.1093/cercor/13.3.252

Yoon, H., Enquist, L. W., and Dulac, C. (2005). Olfactory inputs to hypothalamic neurons controlling reproduction and fertility. *Cell* 123, 669–682. doi: 10.1016/j.cell.2005.08.039

Zariwala, H. A., Borghuis, B. G., Hoogland, T. M., Madisen, L., Tian, L., De Zeeuw, C. I., et al. (2012). A Cre-dependent GCaMP3 reporter mouse for neuronal imaging *in vivo*. *J. Neurosci.* 32, 3131–3141. doi: 10.1523/JNEUROSCI.4469-11.2012

Zeng, H., and Madisen, L. (2012). Mouse transgenic approaches in optogenetics. *Prog. Brain Res.* 196, 193–213. doi: 10.1016/B978-0-444-59426-6.00010-0

Zhuang, X., Masson, J., Gingrich, J. A., Rayport, S., and Hen, R. (2005). Targeted gene expression in dopamine and serotonin neurons of the mouse brain. *J. Neurosci. Methods* 143, 27–32. doi: 10.1016/j.jneumeth.2004.09.020

Conflict of Interest Statement: The authors declare that the research was conducted in the absence of any commercial or financial relationships that could be construed as a potential conflict of interest.

Received: 18 April 2014; accepted: 18 June 2014; published online: 10 July 2014.
Citation: Harris JA, Hirokawa KE, Sorensen SA, Gu H, Mills M, Ng LL, Bohn P, Mortrud M, Ouellette B, Kidney J, Smith KA, Dang C, Sunkin S, Bernard A, Oh SW, Madisen L and Zeng H (2014) Anatomical characterization of Cre driver mice for neural circuit mapping and manipulation. Front. Neural Circuits ***8****:76. doi: 10.3389/fncir.2014.00076*
This article was submitted to the journal Frontiers in Neural Circuits.

frontiers in
NEURAL CIRCUITS

ORIGINAL RESEARCH ARTICLE
published: 11 July 2014
doi: 10.3389/fncir.2014.00074

Deep layer neurons in the rat medial entorhinal cortex fire sparsely irrespective of spatial novelty

Andrea Burgalossi*[1,2]*†, *Moritz von Heimendahl*[1†] *and Michael Brecht*[1]

[1] *Bernstein Center for Computational Neuroscience, Humboldt University of Berlin, Berlin, Germany*
[2] *Werner Reichardt Centre for Integrative Neuroscience, University of Tübingen, Tübingen, Germany*

Edited by:
Mariano Soiza-Reilly, Institut du Fer à Moulin (U839), INSERM, France

Reviewed by:
Kevin Allen, University of Heidelberg, Germany
Caswell Barry, University College London, UK

***Correspondence:**
Andrea Burgalossi, Werner Reichardt Centre for Integrative Neuroscience, University of Tübingen Otfried-Müller-Str. 25, 72076 Tübingen, Germany
e-mail: andrea.burgalossi@cin.uni-tuebingen.de;
Michael Brecht, Bernstein Center for Computational Neuroscience, Humboldt University of Berlin, Philippstr. 13 Haus 6, 10115 Berlin, Germany
e-mail: michael.brecht@bccn-berlin.de

† *These authors have contributed equally to this work.*

Extracellular recordings in medial entorhinal cortex have revealed the existence of spatially-modulated firing patterns, which are thought to contribute to a cognitive map of external space. Previous work indicated that during exploration of novel environments, spiking activity in deep entorhinal layers is much sparser than in superficial layers. In the present report, we ask whether this laminar activity profile is a consequence of environmental novelty. We report on a large dataset of juxtacellularly-recorded neurons ($n = 70$) whose spiking activity was monitored while rats explored either a novel or a familiar environment, or both within the same session. Irrespective of previous knowledge of the environment, deep layer activity was very low during exploration (median firing rate 0.4 Hz for non-silent cells), with a large fraction of silent cells ($n = 19$ of a total 37), while superficial layer activity was several times higher (median firing rate 2.4 Hz; $n = 33$). The persistence of laminar differences in firing activity both under environmental novelty and familiarity, and even in head-restrained stationary animals, suggests that sparse coding might be a constitutive feature of deep entorhinal layers.

Keywords: sparse coding, medial entorhinal cortex, novelty, rat, spatial

INTRODUCTION

The medial entorhinal cortex (MEC) is a key structure involved in processing of spatial information (Fyhn et al., 2004; Hafting et al., 2005; Derdikman and Moser, 2010). Superficial (L2-3) and deep layers (L5-6) of the MEC show clear differences in anatomical connectivity, as well as intrinsic and functional neuronal properties (Sargolini et al., 2006; Canto and Witter, 2012). While the superficial layers of the MEC are the main recipient of processed sensory information and give rise to the major projection to the hippocampal formation via the perforant path, the deep layers receive feedback from the hippocampal subfields CA1 and subiculum. Although there are many exceptions from this simplified picture (Van Strien et al., 2009), the layer differences seem to predict distinct functional roles of entorhinal layers in spatial processing.

In a recent study (Burgalossi et al., 2011), we employed the juxtacellular recording method (Pinault, 1996) to sample individual MEC neurons in behaving animals. An advantage of the juxtacellular recording technique over conventional extracellular methods is that neurons can be identified irrespective of their spiking activity (Herfst et al., 2012). Neurons contributing very few spikes during the recording session, and even silent cells can be reliably recorded (Zhang and Deschênes, 1997). Sampling of individual neurons by juxtacellular method revealed strong laminar differences in firing rates in animals exploring novel environments: deep layer neurons displayed much lower rates (all below 1 Hz, with nearly half of them silent) than superficially recorded cells (Burgalossi et al., 2011). While layer differences might be expected due to the marked differences in anatomical connectivity and intrinsic neuronal properties, the reason for the reported low rates in deep layers remains unclear.

Spatial novelty appears to be one important trigger for the creation of new spatial maps in the rodent hippocampus (Muller and Kubie, 1987), and the expansion (Barry et al., 2012) and re-alignment of grid maps in the MEC modules (Fyhn et al., 2007). Furthermore, novelty can modulate theta (4–12 Hz) oscillatory dynamics (Wells et al., 2013) and firing activity of neurons in the hippocampal circuit (Nitz and McNaughton, 2004; Larkin et al., 2014). We therefore asked whether environmental novelty contributes to the low activity of deep layer neurons. To this end, we juxtacellularly recorded single neurons while rats explored either a novel or a familiar environment, or both within the same session. The present study, which is based on a large dataset of juxtacellularly recorded neurons ($n = 70$) indicates that firing activity is not significantly modulated by environmental novelty, but the activity's laminar differences might rather be a constitutive feature of entorhinal circuits.

MATERIALS AND METHODS

RECORDING APPARATUS AND BEHAVIORAL TRAINING

Two types of arenas were used in this study: an O-maze ($n = 45$ experiments) and a two-compartment maze ($n = 25$ experiments). The O-maze (60×120 cm) had 22-cm high inner and outer walls, with a 12-cm wide path in between. A small subset of neurons from our previous study (Burgalossi et al., 2011) were recorded in a smaller O-maze (40×80 cm, $n = 6$). The two-compartment maze was comprised of a novel and a familiar compartment. The novel one was square-shaped (55×55 cm) and had 80 cm high walls, whose inner face was covered with black and white stripes of tape, and a soft texture was added to the floor (a 0.5-cm thick sponge layer covered with black insulating adhesive foil). The familiar compartment was a rectangular arena (81×25 cm) with 21-cm high walls. The familiar and novel compartment communicated via a gate, which could be manually opened.

For recordings in familiar environments (either O-maze or two-compartment maze) the rats were placed in the arena for 2–4 sessions per day (lasting between 15 min and 1 h each) for 3–7 days. In the two-compartment maze, in order to limit use of distal visual cues, the novel compartment was dimly illuminated from the top. During habituation in the familiar compartment, the access gate to the novel compartment was always closed. These measures were taken to ensure complete novelty of the novel compartment in the two-compartment maze, as opposed to a mixed situation where only local cues are novel, which leads to different cognitive processing (Leutgeb et al., 2005). After each session, the floor of the mazes was cleaned with ethanol.

IN-VIVO JUXTACELLULAR RECORDINGS

Juxtacellular recordings in freely-moving animals were obtained according to previously published procedures (Burgalossi et al., 2011; Herfst et al., 2012). For recordings in novel environments, naïve Wistar rats were initially anesthetized with a mixture of medetomidine (225 μg/kg), midazolam (6 mg/kg), and fentanyl (7.5 μg/kg). After a juxtacellular recording was obtained and mechanically stabilized (Herfst et al., 2012), the rat was placed in the novel environment and the anesthetics were reversed by a fast-acting mix of antagonists (antipamezole, 1 mg/kg; flumazenil, 600 μg/kg; naloxone, 180 μg/kg; Lee et al., 2006; Burgalossi et al., 2011; Herfst et al., 2012) and the spiking activity of the neuron monitored while the rat explored the environment.

For recordings in familiar environments, animals were habituated to the O-maze for 3–7 days (2–4 sessions per day, of 15 min–1 h duration each). On the day of the experiment, animals were anesthetized with the antagonizable anesthetic (see above) and the recordings performed as described above.

For recordings in the two-compartment maze ($n = 17$), animals were pre-implanted under ketamine/xylazine anesthesia (intraperitoneal doses of 100 and 10 mg/kg, respectively) according to previously published procedures (Houweling and Brecht, 2008; Herfst et al., 2012). After a recovery period (typically 2–3 days) animals were habituated to the familiar compartment of the two-compartment maze for 3–7 days (2–4 sessions per day, of 15 min–1 h duration each). Habituation was performed either before and after implantation, or only after implantation. On the day of the experiment, animals were anesthetized with the antagonizable anesthetic (see above) and the recordings performed as described above.

One cell per animal was recorded. In all cases, recording sites could be clearly identified by biocytin/neurobiotin spillover at the ejection site, thereby providing unequivocal assignment of the recording layer even when cell recovery failed.

Juxtacellular recordings in drug-free, head-fixed rats were performed as previously described (Houweling and Brecht, 2008; Doron et al., 2014). Briefly, animals were pre-implanted with a metal post and a recording chamber under ketamine/xylazine anesthesia, and a craniotomy was performed at the coordinates for targeting MEC (Burgalossi et al., 2011). The craniotomy was then closed with silicone (Kwik-Cast, World Precision Instruments). After a recovery period (2–3 days), animals were slowly habituated to the head-fixation. After successful habituation (3–7 days) animals were head-fixed, the silicone plug was removed and the craniotomy carefully cleaned. Before juxtacellular recordings, mapping experiments with low-resistance electrodes (0.5–1 MΩ) were performed to estimate the recording depth of the entorhinal layers, based on known electrophysiological features of the entorhinal laminar structure (Quilichini et al., 2010). Juxtacellular recordings in head-fixed animals ($n = 49$) were assigned to superficial and deep layers based on (1) cortical depth and mapping experiments and (2) morphological identification of a subset of the recorded neurons ($n = 9$), which confirmed the layer assessment. Recordings and habituation sessions were performed under dim ambient illumination.

The juxtacellular signal was amplified by an ELC Ultra miniature headstage (NPI Electronic), and an ELC-03XS amplifier (NPI Electronic), sampled at 20–50 kHz by a LIH 1600 data-acquisition interface (HEKA Electronic) under the control of PatchMaster 2.20 software (HEKA Electronic). The location of the animal was tracked at 25 Hz by the Digital Lynx video-tracking system (Neuralynx) using two LEDs (red and blue) mounted on the rat's head. All experimental procedures were performed according to German guidelines on animal welfare under the supervision of local ethics committees.

HISTOLOGICAL ANALYSIS

At the end of each recording, the animal was injected with an overdose of ketamine or urethane and quickly perfused transcardially with 0.1 M phosphate-buffered saline followed by a 4% paraformaldehyde solution. To reveal the morphology of juxtacellularly labeled cells, 100–150 μm thick brain slices were processed with the avidin-biotin-peroxidase method as described previously (Lee et al., 2006, 2009; Epsztein et al., 2010). Neurons were manually reconstructed with Neurolucida software (MBF Bioscience) and displayed as a two-dimensional projection.

DATA ANALYSIS

Behavior

The position of the rat was defined as the midpoint between the two head-mounted LEDs. To determine running speed, the rat's head positions was first smoothed with a square window of length 600 ms, to decrease the impact of jerky head motion.

Center field avoidance in the square, novel part of the two-compartment maze was quantified by measuring the relative occupancy in an inner square half the side length of the full

square. This inner square occupied one quarter of the total area, and therefore center field avoidance was assessed by comparing its relative occupancy to 25%.

Preference for the familiar part of the two-compartment maze was measured as the share of time spent in the familiar compartment, counting from the moment the rat entered it first. To avoid bias, a characteristic time T was estimated as the time required to traverse the familiar part of the maze, $T = L/v$, with L the length of the maze and v the rat-specific average speed. Values of T ranged from 9 to 53 s. T was used for two corrective steps: Immediately after the first entry into the familiar compartment, a period of T was ignored for analysis. This was done to eliminate bias because initially, the rat had to be in the familiar compartment, by definition. Second, an adjusted share of time spent in the familiar maze was calculated as

$$s_{\text{adj}} = (t_{\text{fam}} + T/2)/(t_{\text{total}} + T),$$

with t_{fam} the time spent in the familiar compartment, t_{total} the total time, T the characteristic time and s_{adj} the adjusted familiar share. The adjustment with $T/2$ and T is a standard statistical measure to avoid edge problems and give appropriate weight to null and full shares. The distribution across rats of familiar shares was guessed to be logit-normal, which was verified by logit-transforming all s_{adj} and testing for normality (Lilliefors test for normality, $p = 0.5$). Then, the logit-transformed values were tested for a mean of 0 (because logit of the critical value of 50% is 0) using a t-test.

Physiology

A fraction of recordings performed in novel environments ($n = 31$) have been published elsewhere (Burgalossi et al., 2011). For spike analysis, juxtacellular traces were high-pass filtered at 100 Hz, and a three-dimensional analysis using time and the first two principal components of the waveform was performed to visualize and assess the stability of spikes amplitude over time, and to isolate spikes from recording artifacts. For most recordings (including silent cells) the electrode resistance was monitored by small (<1 nA) hyperpolarizing current pulses delivered every 20–30 s. Loss of the juxtacellular configuration was signaled by a sudden loss of the spike signals (for spiking cells) and/or a concomitant drop in the electrode tip resistance. In a large fraction of recordings from silent cells (70%; $n = 12/17$) the neurons were fired at the end of the recording session by positive current injections to directly confirm the presence of the cell.

For the calculation of firing rates (including the identification of silent cells), only epochs with speeds greater than 1 cm/s were considered. An exception was the inclusion criterion for the paired test used in the two-compartment maze, where cells were included if only they fired a single spike ever, in either compartment.

Firing rate distributions were tested for bimodality on a logarithmic scale. To resolve the rates without any recorded spike, a virtual spike was added to all counts. This is a standard measure to resolve singularity problems and, at the same time, give appropriate weight to zero-count samples; e.g., a recording without observed spikes of 10 s is represented as a rate of $1 * 10^{-1}$ Hz, but 10 min without a spike as $0.2 * 10^{-2}$ Hz, effectively a "stronger" zero.

The firing rate distribution was tested for bimodality by calculation of the bimodality coefficient described by Pfister et al. (2013).

$$\text{BC} = \frac{m_3^2 + 1}{m_4 + 3 \cdot \frac{(n-1)^2}{(n-2)(n-3)}},$$

with m_3 referring to the skewness of the distribution, m_4 its excess kurtosis and n the sample size. Values of BC greater than 0.55 are considered an indication of bimodality (Pfister et al., 2013). As another independent measure, Hartigan's dip test was performed (Hartigan and Hartigan, 1985). To test for significance, the dip value was calculated on 1000 random samples of uniform distributions of sample size equal to the real data, and the real dip value ranked in the random distribution.

RESULTS

DEEP LAYER NEURONS FIRE AT LOW RATES IRRESPECTIVE OF SPATIAL EXPERIENCE

Juxtacellular recordings in freely-moving animals were obtained according to previously published procedures (Burgalossi et al., 2011; Herfst et al., 2012). Briefly, animals were anesthetized with an antagonizable anesthetic mix (Lee et al., 2006, 2009; Burgalossi et al., 2011; see Materials and Methods). After a juxtacellular recording was obtained, it was mechanically stabilized (Herfst et al., 2012) and the neuron labeled. Animals were woken up by injection of fast-acting antagonists (see Materials and Methods) and single cell spiking activity was monitored while rats explored an O-maze, either for the first time ("novel") or after several days of habituation ("familiar") (median recording duration = 198 s, interquartile range 114–370 s).

Recordings were targeted to deep layers (L5-6) of MEC; **Figure 1A** shows a representative L5 pyramidal neuron, recorded and identified in a freely-moving animal. During exploration of a novel environment, juxtacellularly recorded neurons in deep layers displayed very low levels of activity (median 0.01 Hz, $n = 11$; see **Figure 1B** for an example), with 5 of 11 neurons being completely silent (see also Burgalossi et al., 2011). To test whether the low firing activity in deep layers was attributable to the novelty of the environment, we performed nine additional juxtacellular recordings from rats which were habituated to the same O-maze prior to the recording session (see Materials and Methods). Even under these conditions, we observed a large fraction of silent cells (5/9; see **Figure 1C** for an example) and a similar distribution of firing rates (novel: median 0.01 Hz, range 0.0–1.3 Hz; familiar: median 0.0 Hz, range 0.0–1.5 Hz; $p = 0.9$, Wilcoxon rank-sum test, two-tailed).

To more directly assess the effect of spatial experience on the firing activity of deep layer neurons, we performed an additional set of experiments ($n = 17$) where single neuron spiking activity was recorded while rats explored both a novel and a familiar environment in a two-compartment maze (**Figure 1D**). In 11 of the 17 recordings, the animal explored both environments; in seven of these, the cell was active in at least one of

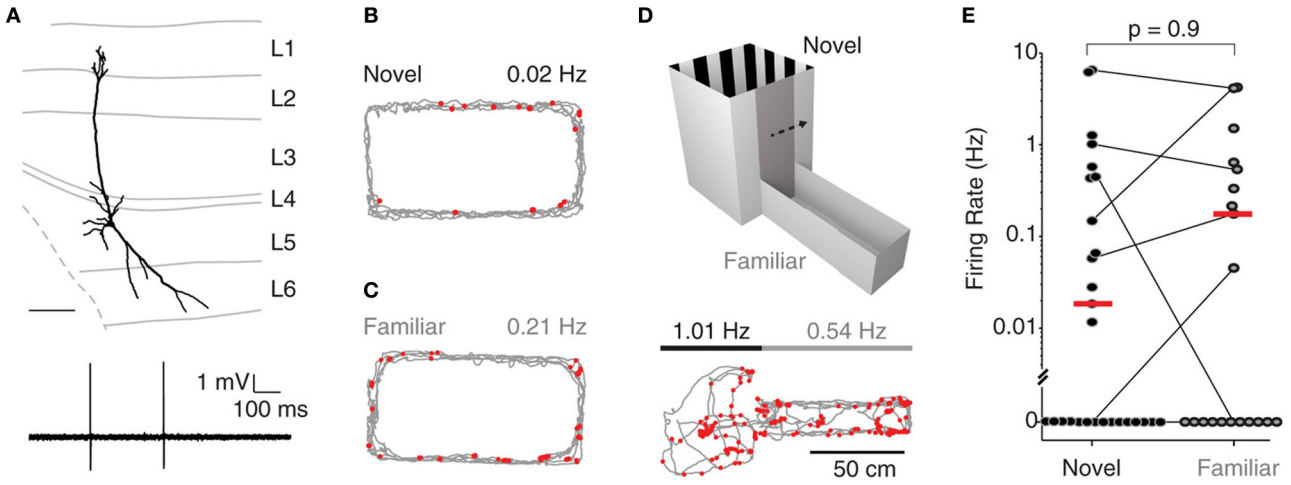

FIGURE 1 | Deep layer neurons in MEC fire at low rates irrespective of spatial experience. (A) Top, reconstruction of the dendritic morphology of the L5 neuron of MEC recorded during exploration of a two-compartment maze (recording shown in **D**). Scale bar = 200 μm. Bottom, representative spike trace recorded during freely-moving behavior. **(B)** Firing locations of spikes (red) and trajectory of the rat (gray) during running in a novel environment (O-maze). Average firing rate is indicated. **(C)** Same as in **(B)**, but for a familiar environment. **(D)** Top: The two-compartment maze used for the combined novel/familiar experiments. Bottom: as in **(B)**, but for a recording in the two-compartment maze (square compartment, novel; rectangular compartment, familiar). Average firing rates in novel and familiar compartments are indicated. **(E)** Average firing rates of all juxtacellularly recorded neurons in novel and familiar environments. Horizontal lines connect recordings from the two-compartment maze, where novel and familiar compartments where sampled within the same recording session. Red lines indicate medians.

the two environments. The two-compartment maze consisted of a square maze ("novel compartment") connected to a rectangular maze ("familiar compartment") separated by a sliding door (see Materials and Methods). Rats were first habituated to the familiar compartment of the maze for several days, and then a juxtacellular recording was obtained from a deep layer neuron and the rat woken up in the novel compartment. After exploring the novel compartment (range of traveled distances: 131–523 cm; $n = 7$) the gate was opened and the rat allowed to transition to the familiar compartment. **Figure 1D** shows a representative recording from a pyramidal neuron (reconstruction shown in **Figure 1A**) which was similarly active in both compartments. At the population level, there was no significant difference between firing rates in the novel and the familiar compartment (**Figure 1E**; median rates = 0.15 Hz (novel) and 0.17 Hz (familiar), $p = 0.8$, $n = 7$; Wilcoxon signed rank test, two-tailed). This remained true when all data from the O-mazes and the two-compartment maze were analyzed jointly (novel: median 0.00 Hz, range 0.0–6.5 Hz, $n = 28$; familiar: median 0.0 Hz, range 0.0–4.3 Hz, $n = 20$; medians not significantly different, $p = 0.9$, Wilcoxon rank-sum test, two-tailed). These data indicate that at the population level, spiking activity in deep layers of MEC is not significantly modulated by spatial experience.

SUPERFICIAL LAYER NEURONS FIRE AT HIGHER RATES IRRESPECTIVE OF SPATIAL EXPERIENCE

A subset of recordings ($n = 33$) was targeted to the superficial layers (L2-3) of MEC, and spiking activity from single neurons was monitored while rats explored either a novel, a familiar or a two-compartment maze. **Figure 2A** shows a representative L3 pyramidal neuron, recorded and identified in a freely-moving animal. During exploration of an O-maze novel to the rat, neurons juxtacellularly recorded from superficial layers displayed higher levels of activity compared to deep layer neurons, with only 1 of 21 neurons being silent (median 3.2 Hz, $n = 21$; see **Figure 2B** for an example; inter-layer comparison statistics in the next section). To test whether spatial experience has an impact on the activity of superficial layer neurons, we also recorded single neurons while rats explored a familiar O-maze ($n = 4$; **Figure 2C**, corresponding reconstruction shown in **Figure 2A**), and a two-compartment maze ($n = 7$; **Figure 2D**). Firing rates in novel and familiar environments did not differ significantly (median firing rate novel = 2.3 Hz, $n = 29$; median firing rate familiar = 1.9 Hz, $n = 11$; $p = 0.5$, Wilcoxon rank-sum test, **Figure 2E**), suggesting that superficial layer activity is not significantly modulated by spatial experience.

The absence of any difference in firing rates under manipulation of novelty raises the concern that the familiarity may not have been detected by the animals. To address this, the behavior was analyzed for novelty-driven patterns. Indeed, in the O-maze experiments, rats were more active in novel environments than in familiar ones (median of rats' average speeds: novel, 4.6 cm/s; familiar, 3.1 cm/s; $p = 0.035$, Wilcoxon rank-sum test, one-tailed; see **Figure S1A**), consistent with novelty-driven exploration. Similarly, in the two-compartment maze, rats were more active in the novel part (median of rats' average speeds: novel, 4.4 cm/s; familiar, 3.7 cm/s; $p = 0.037$, Wilcoxon rank-sum test, one-tailed; **Figure S1B**). Consistent with well described neophobic behaviors in rodents (Barnett, 1958), our rats showed open field avoidance in the novel part of the two-compartment maze (median center field occupancy 18%, less than the uniformly expected 25%, $p = 0.048$, sign test, one-tailed; **Figure S1C**) and once in the familiar, they avoided return to the novel environment (average share of time spent in the

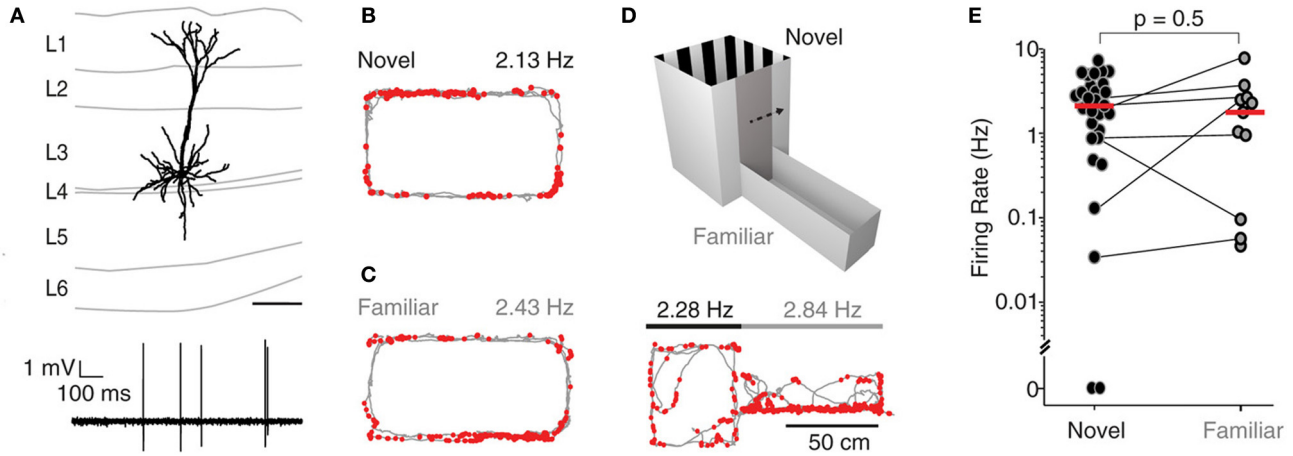

FIGURE 2 | Superficial layer neurons in MEC fire at higher rates irrespective of spatial experience. (A) Top, reconstruction of the dendritic morphology of the L3 neuron of MEC recorded during exploration of a familiar O-maze [recording shown in **(C)**]. Bottom, representative spike trace. Scale bar = 200 during freely-moving behavior. **(B)** Firing locations of spikes (red) and trajectory of the rat (gray) during running in a novel environment (O-maze). Average firing rate is indicated. **(C)** Same as in **(B)**, but for a familiar environment. **(D)** Top: the two-compartment maze used for the combined novel/familiar experiments. Bottom: as in **(B)**, but for a recording in the two-compartment maze (square compartment, novel; rectangular compartment, familiar). Average firing rates in novel and familiar compartments are indicated. **(E)** Average firing rates of all juxtacellularly recorded neurons in novel and familiar environments. Horizontal lines connect recordings from the two-compartment maze, where novel and familiar compartments where sampled within the same recording session. Red lines indicate medians.

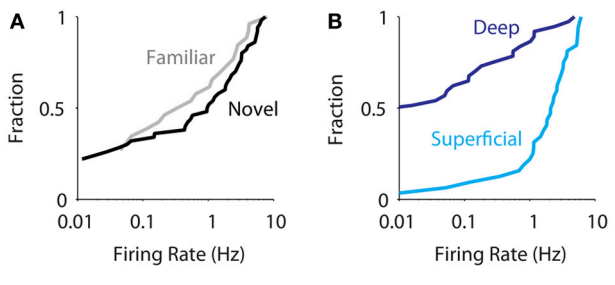

FIGURE 3 | Layer is a strong determinant of average firing rate in MEC. (A) Cumulative distribution of average firing rates for all juxtacellularly recorded neurons recorded in novel (black, $n = 57$) and familiar environments (gray, $n = 31$). The two distributions are not statistically different [median for novel 0.54 ($n = 57$), familiar 0.17 ($n = 31$); $p = 0.4$, Wilcoxon rank-sum test]. **(B)** Cumulative distribution of average firing rates for all juxtacellularly recorded neurons recorded in superficial (light blue, $n = 33$) vs. deep layers (dark blue, $n = 37$), irrespective of spatial experience. The two distributions are statistically different (median for superficial 2.3, deep 0.0, $p = 1.4\ 10^{-7}$, Wilcoxon rank-sum test).

familiar compartment: 0.82, greater than 0.5 with $p = 7.10^{-7}$, t-test, two-sided; **Figure S1D**, see Materials and Methods for details).

LAYER IS A STRONG DETERMINANT OF AVERAGE FIRING RATE

Altogether, we juxtacellularly sampled the activity of 33 and 37 neurons in superficial and deep layers of MEC, respectively. At the population level ($n = 70$) we did not observe an effect of spatial experience in modulating the activity of MEC neurons [**Figure 3A**, median for novel 0.54 Hz ($n = 57$), familiar 0.17 Hz ($n = 31$); $p = 0.4$, Wilcoxon rank-sum test] in agreement with data obtained from extracellular recordings (Barry et al., 2012). On the other hand, we observed a robust difference in firing activity between superficial and deep neurons (**Figure 3B**, median for superficial 2.4 Hz, deep 0.0 Hz, $p = 10^{-7}$, Wilcoxon rank-sum test). This was true for the new dataset alone [superficial layers: median 1.5 ($n = 12$), deep layers: median 0.00 ($n = 27$), $p = 0.006$, Wilcoxon rank-sum test, two-tailed], in line with the previously published data (Burgalossi et al., 2011). Within the deep and superficial layer groups, there were no significant differences either in firing rates [layers 2 vs. 3: medians 2.0 ($n = 14$) and 2.8 ($n = 18$), respectively, $p = 0.3$; layers 5 vs. 6: medians 0.0 ($n = 26$) and 0.14 ($n = 11$), $p = 0.33$; Wilcoxon rank-sum tests] or in the fraction of silent cells [layers 2 vs. 3: silent cells 1/14 and 1/18, respectively, $p = 1$; layers 5 vs. 6, silent cells 14/26 and 5/11, $p = 0.7$, Fisher exact tests]. Notably, the strong differences in firing activity between superficial and deep layer neurons were observed also in drug-free, awake, head-fixed animals (see Materials and Methods; median firing rates: superficial, 2.0 Hz, $n = 28$; deep, 0.1 Hz, $n = 21$; $p = 9.10^{-8}$, Wilcoxon rank-sum test), suggesting they occur even in the absence of locomotor activity.

A difference in median firing rate between two populations can have different structures. Inspection of the firing rate histograms for all cells (**Figure S2A**) as well as by layer (**Figure S2B**) suggested that the median difference between deep and superficial cells may be due to different mixtures of two distributions: one with mainly silent and one with active neurons. We therefore tested for bimodality by applying two established criteria. While the bimodality coefficient (Pfister et al., 2013) was found to be 0.70 (greater than the conventional cut-off of 0.55, and therefore considered bimodal), Hartigan's dip test (Hartigan and

Hartigan, 1985) did not indicate significant bimodality (dip = 0.029, $p = 0.97$, bootstrap test). Also, firing rate distributions differed between deep and superficial layers even considering non-silent cells only (superficial layers, median firing rate = 2.6 Hz, $n = 31$; deep layers, median firing rate = 0.38 Hz, $n = 18$, $p = 0.0007$, Wilcoxon rank-sum test). We therefore conclude that there is no conclusive evidence for a bimodal distribution of firing rates in MEC.

Irrespective of the statistically rigorous concept of bimodality, one striking feature of the firing rate distributions are the contrasting shares of silent cells between superficial and deep layers (see above), which can be interpreted as a measure of population sparseness (Willmore and Tolhurst, 2001). Deep layer neurons have a higher population sparseness than superficial layer neurons, and sparseness is unaffected by familiarity (number of silent cells; deep layers: familiar 11/20, novel 15/28, $p = 1$; superficial layers: familiar 0/11, novel 2/29, $p = 1$, both Fisher exact tests). Together, these findings indicate that population sparseness and neuronal firing rates in MEC differ strongly by layer but are not affected by environmental novelty.

DISCUSSION

It has been suggested that the cerebral cortex employs a sparse code for encoding information (Field, 1994). This has, indeed, been observed in sensory cortices (Huber et al., 2008; Wolfe et al., 2010; Barth and Poulet, 2012) and, notably, in the hippocampus (Thompson and Best, 1989). The present study indicates that environments are differentially encoded across layers of MEC, irrespective of their familiarity. While superficial neurons were equally active in both conditions (**Figures 2**, **3**), deep layer neurons were mostly inactive, irrespective of previous knowledge of the environment (**Figures 1**, **3**). These findings suggest that encoding of spatial information by deep entorhinal layers is sparser than previously assumed based on extracellular sampling of neuronal spiking activity (Sargolini et al., 2006). So far, layer specific differences in MEC have been reported with respect to neuronal functional properties: In rats exploring familiar environments, pure grid responses were abundant in layer 2, while conjunctive, head-direction and grid cells were present in different proportions across layers 3–6 (Sargolini et al., 2006). Here we extend previous observations on laminar activity differences in MEC (Burgalossi et al., 2011) by showing that they persist under environmental familiarity.

The juxtacellular method provides unique advantages over classical extracellular recording techniques. First, it allows identification of the recorded unit and unequivocal laminar localization of the recording site (Herfst et al., 2012; see Materials and Methods). Second, it provides more realistic estimates of layer activity, since neurons can be sampled irrespective of their spiking activity (Zhang and Deschênes, 1997; Herfst et al., 2012). Silent cells, or cells which contribute very few spikes during the behavioral recording session, cannot be easily detected with extracellular recording methods, and their presence can only be indirectly inferred (Thompson and Best, 1989; Neunuebel and Knierim, 2012).

The anesthesia/wake-up protocol used in the present study has limitations, which might potentially have occluded a physiological novelty effect. Although the behavior of the rats appeared to be largely unaffected (see below), potential residual effects of the anesthetics cannot be ruled out, as acknowledged previously (Burgalossi et al., 2011; Herfst et al., 2012). However, the concerns of anesthesia side-effects are diminished by the fact that laminar differences persisted even in awake, drug-free animals. Another concern is that exposure to a novel context occurred immediately after wake up, which might be source of confusion and spatial disorientation in the rats. Behavioral analysis however indicated that animals were generally able to discriminate novel from familiar environments (**Figure S1**). While there are possible confounding factors in the behavioral assessment in the two-compartment maze because the conditions differ systematically in order, time after wake-up and environmental geometry, the data from the O-maze experiments suggest behavioral novelty detection (**Figure S1A**). We therefore conclude that firing rates were unaffected by novelty despite its detection by the animal.

Although novelty detection appeared to be largely intact under our experimental conditions, spatial disorientation in the novel environment immediately following wake up, together with associated emotional responses (i.e. fear, stress, anxiety), might have acted in concert with contextual novelty to account for the observed low activity of deep layer neurons. Novelty signals are inevitably associated with complex emotional responses in animals (Beerling et al., 2011) and a large variety of neuromodulatory transmitters appear to mediate these responses (Ihalainen et al., 1999; Barry and Hasselmo, 2012). Indeed the MEC receives prominent innervation from midbrain dopaminergic neurons (Björklund and Dunnett, 2007), as well as from adrenergic (Fallon et al., 1978), and serotoninergic neurons (Bobillier et al., 1975). However, the fact that low levels of activity were also observed under conditions of reduced stress, such as in familiar environments, indicates that sparse firing is a constitutive property of deep layers of MEC. Further work will elucidate whether sparse firing is inherited from upstream regions (i.e., CA1), or whether it is a result of local synaptic interactions.

AUTHOR CONTRIBUTIONS

Andrea Burgalossi performed the experiments, Michael Brecht supervised the experiments. Moritz von Heimendahl wrote MATLAB analysis code, Andrea Burgalossi and Moritz von Heimendahl analyzed data. All authors wrote the manuscript.

ACKNOWLEDGMENTS

We thank Brigitte Geue, Maik Kunert, Undine Schneeweiß, and Arnold Stern for outstanding technical assistance. Shimpei Ishiyama provided illustrative artwork for figures. This work was supported by Neurocure, the Bernstein Center for Computational Neuroscience (BMBF) and Humboldt University, the EU Biotact-grant and the Neuro-behavior ERC grant.

SUPPLEMENTARY MATERIAL

The Supplementary Material for this article can be found online at: http://www.frontiersin.org/journal/10.3389/fncir.2014.00074/abstract

Figure S1 | Rats' behavior indicates novelty detection. (A) Per-rat mean speed during exploration of either a novel or a familiar O-maze. **(B)** As in **(A)**, but for rats in the two-compartment maze. **(C)** For rats in the novel environment of the two-compartment maze, share of time spent in the central quarter of the maze. The red line indicates the expected share assuming a uniform sampling of the space by the rat. **(D)** In the two-compartment maze, share of time spent in the familiar environment after first entering it. The red line indicates indifferent choice (50%).

Figure S2 | Distribution of neuronal firing rates in medial entorhinal cortex. (A) Firing rate histogram for all cells ($n = 70$). To better resolve low firing rates all cells were assigned an extra virtual spike, leading to different rates for a recording without observed spikes of, e.g., 10 s (rate $1{\cdot}10^{-1}$ Hz) as opposed to 10 min (rate $0.2{\cdot}10^{-2}$ Hz) (see Materials and Methods). **(B)** Firing rate histograms as in **(A)**, but for superficial (light blue; $n = 33$) and deep layer cells (dark blue, $n = 37$).

REFERENCES

Barnett, S. A. (1958). Experiments on "neophobia" in wild and laboratory rats. *Br. J. Psychol.* 49, 195–201. doi: 10.1111/j.2044-8295.1958.tb00657.x

Barry, C., Ginzberg, L. L., O'Keefe, J., and Burgess, N. (2012). Grid cell firing patterns signal environmental novelty by expansion. *Proc. Natl. Acad. Sci. U.S.A.* 109, 17687–17692. doi: 10.1073/pnas.1209918109

Barry, C., and Hasselmo, M. E. (2012). Possible role of acetylcholine in regulating spatial novelty effects on theta rhythm and grid cells. *Front. Neural Circuits* 6:5. doi: 10.3389/fncir.2012.00005

Barth, A. L., and Poulet, J. F. A. (2012). Experimental evidence for sparse firing in the neocortex. *Trends Neurosci.* 35, 345–355. doi: 10.1016/j.tins.2012.03.008

Beerling, W., Koolhaas, J. M., Ahnaou, A., Bouwknecht, J. A., de Boer, S. F., Meerlo, P., et al. (2011). Physiological and hormonal responses to novelty exposure in rats are mainly related to ongoing behavioral activity. *Physiol. Behav.* 103, 412–420. doi: 10.1016/j.physbeh.2011.03.014

Björklund, A., and Dunnett, S. B. (2007). Dopamine neuron systems in the brain: an update. *Trends Neurosci.* 30, 194–202. doi: 10.1016/j.tins.2007.03.006

Bobillier, P., Petitjean, F., Salvert, D., Ligier, M., and Seguin, S. (1975). Differential projections of the nucleus raphe dorsalis and nucleus raphe centralis as revealed by autoradiography. *Brain Res.* 85, 205–210. doi: 10.1016/0006-8993(75)90071-2

Burgalossi, A., Herfst, L., von Heimendahl, M., Förste, H., Haskic, K., Schmidt, M., et al. (2011). Microcircuits of functionally identified neurons in the rat medial entorhinal cortex. *Neuron* 70, 773–786. doi: 10.1016/j.neuron.2011.04.003

Canto, C. B., and Witter, M. P. (2012). Cellular properties of principal neurons in the rat entorhinal cortex. II. The medial entorhinal cortex. *Hippocampus* 22, 1277–1299. doi: 10.1002/hipo.20993

Derdikman, D., and Moser, E. I. (2010). A manifold of spatial maps in the brain. *Trends Cogn. Sci.* 14, 561–569. doi: 10.1016/j.tics.2010.09.004

Doron, G., von Heimendahl, M., Schlattmann, P., Houweling, A. R., and Brecht, M. (2014). Spiking irregularity and frequency modulate the behavioral report of single-neuron stimulation. *Neuron* 81, 653–663. doi: 10.1016/j.neuron.2013.11.032

Epsztein, J., Lee, A. K., Chorev, E., and Brecht, M. (2010). Impact of spikelets on hippocampal CA1 pyramidal cell activity during spatial exploration. *Science* 327, 474–477. doi: 10.1126/science.1182773

Fallon, J. H., Koziell, D. A., and Moore, R. Y. (1978). Catecholamine innervation of the basal forebrain II. Amygdala, suprarhinal cortex and entorhinal cortex. *J. Comp. Neurol.* 180, 509–531. doi: 10.1002/cne.901800308

Field, D. J. (1994). What is the goal of sensory coding? *Neural Comput.* 6, 559–601. doi: 10.1162/neco.1994.6.4.559

Fyhn, M., Hafting, T., Treves, A., Moser, M.-B., and Moser, E. I. (2007). Hippocampal remapping and grid realignment in entorhinal cortex. *Nature* 446, 190–194. doi: 10.1038/nature05601

Fyhn, M., Molden, S., Witter, M. P., Moser, E. I., and Moser, M.-B. (2004). Spatial representation in the entorhinal cortex. *Science* 305, 1258–1264. doi: 10.1126/science.1099901

Hafting, T., Fyhn, M., Molden, S., Moser, M.-B., and Moser, E. I. (2005). Microstructure of a spatial map in the entorhinal cortex. *Nature* 436, 801–806. doi: 10.1038/nature03721

Hartigan, J. A., and Hartigan, P. M. (1985). The dip test of unimodality. *Ann. Stat.* 13, 70–84.

Herfst, L., Burgalossi, A., Haskic, K., Tukker, J. J., Schmidt, M., and Brecht, M. (2012). Friction-based stabilization of juxtacellular recordings in freely moving rats. *J. Neurophysiol.* 108, 697–707. doi: 10.1152/jn.00910.2011

Houweling, A. R., and Brecht, M. (2008). Behavioural report of single neuron stimulation in somatosensory cortex. *Nature* 451, 65–68. doi: 10.1038/nature06447

Huber, D., Petreanu, L., Ghitani, N., Ranade, S., Hromádka, T., Mainen, Z., et al. (2008). Sparse optical microstimulation in barrel cortex drives learned behaviour in freely moving mice. *Nature* 451, 61–64. doi: 10.1038/nature06445

Ihalainen, J., Riekkinen, P. Jr., and Feenstra, M. G. (1999). Comparison of dopamine and noradrenaline release in mouse prefrontal cortex, striatum and hippocampus using microdialysis. *Neurosci. Lett.* 277, 71–74. doi: 10.1016/S0304-3940(99)00840-X

Larkin, M. C., Lykken, C., Tye, L. D., Wickelgren, J. G., and Frank, L. M. (2014). Hippocampal output area CA1 broadcasts a generalized novelty signal during an object-place recognition task. *Hippocampus* 7, 773–783. doi: 10.1002/hipo.22268

Lee, A. K., Epsztein, J., and Brecht, M. (2009). Head-anchored whole-cell recordings in freely moving rats. *Nat. Protoc.* 4, 385–392. doi: 10.1038/nprot.2009.5

Lee, A. K., Manns, I. D., Sakmann, B., and Brecht, M. (2006). Whole-cell recordings in freely moving rats. *Neuron* 51, 399–407. doi: 10.1016/j.neuron.2006.07.004

Leutgeb, S., Leutgeb, J. K., Barnes, C. A., Moser, E. I., McNaughton, B. L., and Moser, M.-B. (2005). Independent codes for spatial and episodic memory in hippocampal neuronal ensembles. *Science* 309, 619–623. doi: 10.1126/science.1114037

Muller, R. U., and Kubie, J. L. (1987). The effects of changes in the environment on the spatial firing of hippocampal complex-spike cells. *J. Neurosci.* 7:1951

Neunuebel, J. P., and Knierim, J. J. (2012). Spatial firing correlates of physiologically distinct cell types of the rat dentate gyrus. *J. Neurosci.* 32, 3848–3858. doi: 10.1523/JNEUROSCI.6038-11.2012

Nitz, D., and McNaughton, B. (2004). Differential modulation of CA1 and dentate gyrus interneurons during exploration of novel environments. *J. Neurophysiol.* 91, 863–872. doi: 10.1152/jn.00614.2003

Pfister, R., Schwarz, K. A., Janczyk, M., Dale, R., and Freeman, J. (2013). Good things peak in pairs: a note on the bimodality coefficient. *Front. Psychol.* 4:700. doi: 10.3389/fpsyg.2013.00700

Pinault, D. (1996). A novel single-cell staining procedure performed *in vivo* under electrophysiological control: morpho-functional features of juxtacellularly labeled thalamic cells and other central neurons with biocytin or Neurobiotin. *J. Neurosci. Methods* 65, 113–136. doi: 10.1016/0165-0270(95)00144-1

Quilichini, P., Sirota, A., and Buzsáki, G. (2010). Intrinsic circuit organization and theta–gamma oscillation dynamics in the entorhinal cortex of the rat. *J. Neurosci.* 30, 11128–11142. doi: 10.1523/JNEUROSCI.1327-10.2010

Sargolini, F., Fyhn, M., Hafting, T., McNaughton, B. L., Witter, M. P., Moser, M.-B., et al. (2006). Conjunctive representation of position, direction, and velocity in entorhinal cortex. *Science* 312, 758–762. doi: 10.1126/science.1125572

Thompson, L. T., and Best, P. J. (1989). Place cells and silent cells in the hippocampus of freely-behaving rats. *J. Neurosci.* 9, 2382–2390.

Van Strien, N. M., Cappaert, N. L. M., and Witter, M. P. (2009). The anatomy of memory: an interactive overview of the parahippocampal-hippocampal network. *Nat. Rev. Neurosci.* 10, 272–282. doi: 10.1038/nrn2614

Wells, C. E., Amos, D. P., Jeewajee, A., Douchamps, V., Rodgers, J., O'Keefe, J., et al. (2013). Novelty and anxiolytic drugs dissociate two components of hippocampal theta in behaving rats. *J. Neurosci.* 33, 8650–8667. doi: 10.1523/JNEUROSCI.5040-12.2013

Willmore, B., and Tolhurst, D. J. (2001). Characterizing the sparseness of neural codes. *Netw. Comput. Neural Syst.* 12, 255–270. doi: 10.1080/net.12.3.255.270

Wolfe, J., Houweling, A. R., and Brecht, M. (2010). Sparse and powerful cortical spikes. *Curr. Opin. Neurobiol.* 20, 306–312. doi: 10.1016/j.conb.2010.03.006

Zhang, Z.-W., and Deschênes, M. (1997). Intracortical axonal projections of lamina VI cells of the primary somatosensory cortex in the rat: a single-cell labeling study. *J. Neurosci.* 17, 6365–6379.

Conflict of Interest Statement: The authors declare that the research was conducted in the absence of any commercial or financial relationships that could be construed as a potential conflict of interest.

Received: 10 April 2014; accepted: 13 June 2014; published online: 11 July 2014.
Citation: Burgalossi A, von Heimendahl M and Brecht M (2014) Deep layer neurons in the rat medial entorhinal cortex fire sparsely irrespective of spatial novelty. Front. Neural Circuits ***8****:74. doi: 10.3389/fncir.2014.00074*
This article was submitted to the journal Frontiers in Neural Circuits.

frontiers in
NEURAL CIRCUITS

ORIGINAL RESEARCH ARTICLE
published: 03 July 2014
doi: 10.3389/fncir.2014.00073

Functional imaging of cortical feedback projections to the olfactory bulb

Markus Rothermel* and Matt Wachowiak

Brain Institute and Department of Neurobiology and Anatomy, University of Utah, Salt Lake City, UT, USA

Edited by:
Benjamin R. Arenkiel, Baylor College of Medicine, USA

Reviewed by:
Peter Brunjes, University of Virginia, USA
Ian Davison, Boston University, USA

****Correspondence:***
Markus Rothermel, Brain Institute and Department of Neurobiology and Anatomy, University of Utah, Sorenson Molecular Biotechnology Building (SMBB), 36 South Wasatch Drive, Salt Lake City, UT 84103, USA
e-mail: Markus.Rothermel@utah.edu

Processing of sensory information is substantially shaped by centrifugal, or feedback, projections from higher cortical areas, yet the functional properties of these projections are poorly characterized. Here, we used genetically-encoded calcium sensors (GCaMPs) to functionally image activation of centrifugal projections targeting the olfactory bulb (OB). The OB receives massive centrifugal input from cortical areas but there has been as yet no characterization of their activity *in vivo*. We focused on projections to the OB from the anterior olfactory nucleus (AON), a major source of cortical feedback to the OB. We expressed GCaMP selectively in AON projection neurons using a mouse line expressing Cre recombinase (Cre) in these neurons and Cre-dependent viral vectors injected into AON, allowing us to image GCaMP fluorescence signals from their axon terminals in the OB. Electrical stimulation of AON evoked large fluorescence signals that could be imaged from the dorsal OB surface *in vivo*. Surprisingly, odorants also evoked large signals that were transient and coupled to odorant inhalation both in the anesthetized and awake mouse, suggesting that feedback from AON to the OB is rapid and robust across different brain states. The strength of AON feedback signals increased during wakefulness, suggesting a state-dependent modulation of cortical feedback to the OB. Two-photon GCaMP imaging revealed that different odorants activated different subsets of centrifugal AON axons and could elicit both excitation and suppression in different axons, indicating a surprising richness in the representation of odor information by cortical feedback to the OB. Finally, we found that activating neuromodulatory centers such as basal forebrain drove AON inputs to the OB independent of odorant stimulation. Our results point to the AON as a multifunctional cortical area that provides ongoing feedback to the OB and also serves as a descending relay for other neuromodulatory systems.

Keywords: olfactory bulb, centrifugal systems, anterior olfactory nucleus, GCaMP, *in vivo*

INTRODUCTION

Sensory systems enable an animal to detect and act upon relevant environmental information in order to navigate and survive in a complex world. Sensation is an active process in which external stimuli are selectively sampled in space and time, and the processing of incoming sensory information is strongly and dynamically modulated depending on behavioral state and past experience. Thus, activity at all stages of sensory pathways is not solely determined by sensory input but also by ongoing activity in other brain areas. Understanding the neural mechanisms underlying sensation thus requires understanding the neural circuits mediating this modulation.

Similar to other systems such as the visual system where behavioral state modulates early sensory processing (Niell and Stryker, 2010; Fu et al., 2014), response properties of neurons in the early olfactory pathway are modulated in the behaving animal. Numerous studies have investigated the modulation of activity in the olfactory bulb (OB)—the first stage of synaptic processing of olfactory sensory input—as a function of behavioral state and found rapid and profound effects (Karpov, 1980; Kay and Laurent, 1999; Doucette and Restrepo, 2008; Kato et al., 2012; Wachowiak et al., 2013; Nunez-Parra et al., 2014). It has been hypothesized that centrifugal modulation from diverse brain centers plays an important role in mediating these effects (Matsutani and Yamamoto, 2008; Shea et al., 2008; Petzold et al., 2009; Nunez-Parra et al., 2013; Rothermel et al., 2014). The OB receives centrifugal input from fibers originating in classical neuromodulatory centers including noradrenergic inputs from locus coeruleus (Shipley et al., 1985; McLean et al., 1989; Shea et al., 2008), serotonergic inputs from raphe (Mclean and Shipley, 1987; Petzold et al., 2009) and cholinergic and GABA-ergic inputs from the basal forebrain (Ichikawa and Hirata, 1986; Ojima et al., 1988; Nunez-Parra et al., 2013; Rothermel et al., 2014). The OB is also heavily innervated by centrifugal projections originating throughout olfactory cortex (Price and Powell, 1970; Davis et al., 1978; de Olmos et al., 1978; Haberly and Price, 1978; Reyher et al., 1988; De Carlos et al., 1989; Matsutani, 2010). Despite extensive characterization

of these projections, the functional properties of centrifugal input to the OB *in vivo* has yet to be described for any system.

The anterior olfactory nucleus (AON) constitutes the largest source of OB centrifugal inputs to the OB (Carson, 1984; Shipley and Adamek, 1984). It is the most anterior subdivision of olfactory cortex and can be divided into two distinct zones: pars externa, consisting of a thin ring of cells surrounding the rostral end of the AON, and the remainder, pars principalis which itself can be further subdivided into 4 parts (dorsal, lateral, medial and ventral) (Valverde et al., 1989; Brunjes et al., 2005). The AON receives sensory input from the OB and sends "ascending" outputs to other olfactory and non-olfactory areas including anterior piriform cortex, olfactory tubercle, entorhinal cortex and periamygdaloid cortex (for review, see Brunjes et al., 2005). Features of the connections between the AON and the OB include a coarse topography in the centripetal projections from the OB to the AON (Schoenfeld et al., 1985; Scott et al., 1985; Yan et al., 2008; Miyamichi et al., 2011) as well as descending projections that innervate not only the ipsilateral but also the contralateral OB (Schoenfeld and Macrides, 1984; Shipley and Adamek, 1984; Kay and Brunjes, 2014). In addition, laminar differences in the distribution of AON projections to OB have been observed for both zones (Davis and Macrides, 1981; Luskin and Price, 1983). Finally, the AON itself receives robust centrifugal inputs from other olfactory cortical areas including anterior piriform cortex (Haberly and Price, 1978; Luskin and Price, 1983; Haberly, 2001) and amygdala (De Carlos et al., 1989; Gomez and Newman, 1992; Canteras et al., 1995; Petrovich et al., 1996) as well as higher-order centers such as basal forebrain (Broadwell and Jacobowitz, 1976; Luiten et al., 1987; De Carlos et al., 1989; Carnes et al., 1990; Gaykema et al., 1990; Zaborszky et al., 2012) and the hippocampus (Swanson and Cowan, 1977; van Groen and Wyss, 1990). This extensive connectivity with primary and secondary olfactory processing centers and its position as both a relay of ascending sensory input from the OB and a source of "top-down", centrifugal input to the OB makes this structure an interesting model system for investigating higher-order olfactory processing.

The AON has been implicated in a range of different functions in odor perception, including serving as the first site of integrated odor percept formation, reconstructing olfactory memory traces (Haberly, 2001), and integrating activity within and between the two OBs (Schoenfeld and Macrides, 1984; Lei et al., 2006; Kikuta et al., 2010). However, the role of centrifugal AON projections in modulating ongoing OB activity remains poorly characterized, especially in a functional and behavioral context. So far, only one study has investigated the influence of centrifugal AON projections on OB circuit function (Markopoulos et al., 2012); this study demonstrated that optogenetically activating these inputs directly depolarizes as well as disynaptically inhibits mitral/tufted cells, thereby enabling precisely timed spikes in a population of mitral/tufted cells and shaping OB output. However, how centrifugal AON fibers are activated naturally remains unclear.

In the present study, we used genetically-encoded calcium reporters (GCaMPs) to functionally image the activation of AON projections innervating the OB in the anesthetized and awake mouse. We found that olfactory sensory input rapidly and robustly activates AON feedback projections to the ipsi- as well as contralateral OB which are transient and coupled to inhalation in both the anesthetized and the awake animal. AON feedback projections could also be activated by higher-order neuromodulatory centers. Two-photon imaging revealed distinct spatiotemporal patterns of AON feedback evoked by different odorants. These results provide the first *in vivo* functional characterization of centrifugal inputs to the OB, and point to the AON as an integral olfactory processing center that provides robust, ongoing and odorant-specific feedback to the OB and also serves as a relay for other neuromodulatory systems.

MATERIALS AND METHODS

ANIMALS STRAIN AND CARE

We used a mouse line (Chrna7-Cre, kindly provided by S. Rogers and P. Tvrdik, University of Utah) in which an IRES-Cre bi-cistronic cassette was introduced into the 3'noncoding region of the cholinergic nicotinic receptor alpha7 (*Chrna7*) (Rogers and Gahring, 2012; Rogers et al., 2012a,b; Gahring et al., 2013). Additional experiments were performed on mice expressing Cre recombinase (Cre) under the olfactory marker protein promotor (OMP; Li et al., 2004), JAX Stock #006668 (The Jackson Laboratory) crossed to the Ai38 reporter line (Zariwala et al., 2012), JAX Stock #014538 (The Jackson Laboratory). Animals of either sex were used. Animals were housed under standard conditions in ventilated racks. Mouse colonies were bred and maintained at the University of Utah animal care facilities. All procedures were carried out following National Institutes of Health Guide for the Care and Use of Laboratory Animals and were approved by the University of Utah Institutional Animal Care and Use Committee.

VIRAL VECTORS

Viral vectors were obtained from the viral vector core of the University of Pennsylvania. Vectors were from stock batches available for general distribution. Injection of Cre-dependent vector was performed in either heterozygous or homozygous Chrna7-Cre mice. Virus injection was targeted to the dorsal OB at a depth of 200–300 μm or to the AON using stereotaxic targeting (relative to Bregma (in mm) +2.8 anteroposterior, 1.25 mediolateral, −2.6 dorsoventral) using previously-described procedures (Wachowiak et al., 2013). Virus (0.1–0.2 μl for OB injections; 0.5 μl for AON injections) was delivered through a 33 or 30 gauge metal needle (AON injections) or a pulled glass pipette (OB injections) at a rate of 0.1 μl/min. Mice were between 4 and 12 weeks of age at the time of virus injection and were individually housed for 14–28 days before evaluating for transgene expression or imaging. In a few cases (see Section Results), we injected virus into the OB of postnatal pups (P 1–3) and evaluated expression at 6–16 weeks of age. The viral vectors used, with their abbreviated names as used in the text, were: AAV2/1.hSynap.FLEX.GCaMP3.3.WPRE.SV40 (*2/1.FLEX.GCaMP3*) and AAV2/9.Syn.Flex.GCaMP6s.WPRE.SV40 (*2/9.FLEX.GCaMP6s*).

OLFACTOMETRY

Odorants were presented as dilutions from saturated vapor in cleaned, humidified air using a custom olfactometer under computer control (Bozza et al., 2004; Verhagen et al., 2007). Odorants were typically presented for 4 s. All odorants were obtained at 95–99% purity from Sigma-Alrich and stored under nitrogen. The concentration of the odorants ranged from 0.1 to 2% saturated vapor (s.v.).

EPIFLUORESCENCE IMAGING

For acute imaging experiments, mice were anesthetized with pentobarbital (50 mg/kg). Body temperature and heart rate were maintained at 37°C and ∼400 beats per minute. Unless otherwise stated, a double tracheotomy was performed and an artificial inhalation paradigm used (Wachowiak and Cohen, 2001; Spors et al., 2006). Animals were secured in a stereotaxic device (Kopf Instrument) for further procedures and imaging followed previously established protocols (Wachowiak and Cohen, 2001; Bozza et al., 2004; Spors et al., 2006). Imaging in awake, head-fixed mice was performed using an identical optical setup that accommodated a custom restraint and behavioral training apparatus (described below). Wide-field epifluorescence signals were acquired through the thinned bone overlying the dorsal OB. The optical setup included an Olympus BX51 illumination turret, an Olympus 4x 0.28 numerical aperture objective, a filter set optimized for GFP (exciter: HQ480/40, dichroic: Q505LP, emitter: HQ535/50, Semrock), and a 470 nm light-emitting diode (LED) source (Thorlabs) or 150W Xenon arc lamp (Opti-quip). Light was attenuated using neutral density filters. Optical signals were acquired at 256 × 256 pixel resolution and a frame rate of 25 Hz and digitized at 14-bit resolution using a back-illuminated charge-coupled device (CCD) camera (NeuroCCD, SM-256, RedShirtImaging), then synchronized with other experimental signals (respiration, odor control) and stored to disk using Neuroplex software (RedShirtImaging).

ELECTRICAL STIMULATION

Electrical stimulation of AON or horizontal limb of the diagonal band of Broca (HDB) was performed using a concentric bipolar electrode (CBCPH-75, FHC) inserted through a small craniotomy to the same stereotaxic coordinates used for virus injection or, in the case of HDB stimulation, to coordinates (relative to Bregma (in mm) +0.74 anteroposterior, 0.65 mediolateral, −4.8 dorsoventral. Stimulus trains were composed of 300 μA, 300 μs duration pulses delivered at 50 Hz for 0.1–1 s, as specified in the text.

AWAKE, HEAD-FIXED PREPARATION

Epifluorescence imaging in awake, head-fixed mice was performed as described previously (Wachowiak et al., 2013). Mice were acclimated to head restraint for 1–2 daily sessions prior to imaging, with no operant conditioning. Persistent limb movement or severely attenuated respiration was used as an indicator of excessive stress, in which case the session was terminated. A single imaging session lasted for up to 60 min and data were collected over as many as two consecutive daily sessions. To compare optical signals during wakefulness and anesthesia (**Figure 4**), head-fixed mice were briefly anesthetized with isoflurane, then responses to odorants imaged in the 1–2 min after anesthetic was removed (Wachowiak et al., 2013).

EPIFLUORESCENCE DATA ANALYSIS

Basic processing and analysis of optical signals followed protocols previously described for epifluorescence imaging from olfactory sensory neurons (OSNs; Wachowiak and Cohen, 2001; Verhagen et al., 2007; Wesson et al., 2008; Carey et al., 2009). Initial data processing included extracting fluorescence time-courses from visually-selected regions of interest (ROIs; ROIs consisted of 9–12 pixels and were distributed equally across activated areas on the dorsal OB) and upsampling of optical signals to 100 Hz to match the acquisition rate of respiratory signals. Repeated trials (3–8 trials) were averaged before analysis to improve signal to noise ratio.

For odorant response maps, $\Delta F/F$ values were calculated from temporal averages of 10 frames before odorant onset and 10 frames after the first inhalation of odorant. For display in the figures, maps were scaled from 0 to 95% of the maximal $\Delta F/F$ and pixel resolution doubled (to 512 × 512) using bilinear interpolation. Measurement of inhalation-evoked response amplitudes, peak odorant-evoked response amplitudes and signal onset latencies were made as described previously using a custom algorithm that fit the optical signals to a double sigmoid function (Wesson et al., 2008). The algorithm was modified slightly to fit the higher respiration frequencies in awake mice. Onset time was defined as the time the fitted optical signal reached 10% of its maximal amplitude (t_{10}). Response onset latencies were measured relative to the start of the first inhalation after odorant onset. Latencies were measured from multiple foci and multiple odorants and averaged across inhalations of odorant before computing a grand average across animals. ROIs were counted as showing detectable inhalation-locked responses if the algorithm was able to fit responses to at least four sniffs in a given trial. All analyses were performed using custom software written in Matlab or LabVIEW. Summary data are reported as mean (or median) ± standard deviation (SD) unless noted otherwise. All statistical tests were performed using the Matlab statistics toolbox. An exponential function was used to compute τ_{off} values.

AWAKE *IN VIVO* TWO PHOTON IMAGING

Animals were prepared for two-photon imaging in the same manner as described for the awake head fixed epifluorescence imaging experiments, except that animal were habituated to run on a free floating Styrofoam ball. Imaging was carried out with a two-photon microscope (MOM; Sutter Instruments) coupled to a pulsed Ti:Sapphire laser (Mai Tai HP; Spectra-Physics) and controlled by Scanimage 3.9 (Pologruto et al., 2003). In all experiments, imaging was performed through a 16 × 0.8 numerical aperture objective (Nikon) and emitted light was collected by multialkali photomultiplier tubes (Hamamatsu R6357). Images were acquired at 3.7 Hz in most experiments. Fluorescence time series were extracted and analyzed with custom Matlab scripts, and $\Delta F/F$ was calculated as in *in vitro* experiments. Pseudocolor activation maps reflect an average of 8 trials in which movies were spatially filtered using a Gaussian window with a

sigma of 0.75 pixels and temporally filtered using a fourth-order Butterworth filter with a cutoff frequency of 0.25 Hz. Correlation coefficients of odor evoked activity maps were calculated from pairwise correlations of averaged (8 odor presentations) ΔF maps.

INACTIVATION OF THE AON

Microinjection of TTX (0.5 µl, 50 µM, Sigma-Aldrich) or muscimol (0.5 µl, 0.8 mM, Sigma-Aldrich) was performed using a glass pipette connected to a Picospritzer III (Parker Instruments). The tip of the glass pipette was lowered to the AON using the same stereotaxic coordinates as for viral vector injection. The glass pipette was left in the AON for approximately 5 min after the injection to allow for drug diffusion into the targeted structure. The amount of drug injected (approximately 10 ng and 50 ng for TTX and muscimol, respectively) is similar to that reported previously for *in vivo* inactivation (Zhuravin and Bures, 1991; Meyer and Louilot, 2012; Stratford and Wirtshafter, 2012).

HISTOLOGY

Transgene expression was evaluated with post hoc histology in all experiments to confirm accurate targeting of AON neurons and a lack of expression in OB neurons. Mice were deeply anesthetized with an overdose of sodium pentobarbital and perfused with phosphate-buffered saline (PBS) followed by 4% paraformaldehyde in PBS. Tissue was vibratome-sectioned as described previously (Wachowiak et al., 2013) and expression evaluated from native fluorescence without immunohistochemical amplification. For display, image stacks were obtained with an Olympus FV10i confocal laser scanning microscope.

RESULTS

EXPRESSION OF GCaMP IN AON NEURONS

We used a mouse line, Chrna7-Cre, in which an IRES-Cre bi-cistronic cassette was introduced into the 3'noncoding region of the cholinergic nicotinic receptor alpha7 gene (Chrna7) (Rogers et al., 2012b) to achieve expression of genetically-encoded calcium reporters in neurons within the AON (**Figure 1A**).

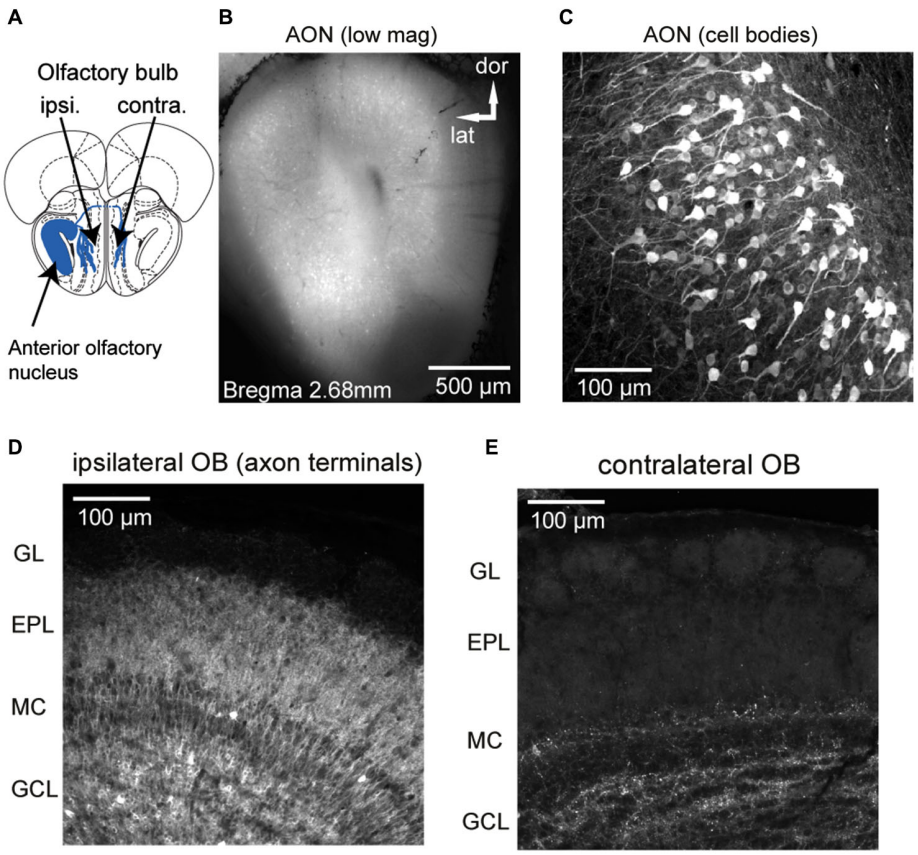

FIGURE 1 | GCaMP3 expression after unilateral viral injection into AON of a Chrna7-Cre mouse. (A) Schematic diagram (Bregma 3.08 mm, section from atlas (Paxinos and Franklin, 2001)) depicting genetically-targeted AON projections to the ipsilateral and contralateral OB. **(B)** Low-magnification, epifluorescence image showing heavy expression in AON neurons in all AON subdivisions. **(C)** Confocal stack showing GCaMP3 expression in AON cell bodies and neurites. Note thick apical dendrites and "pyramidal-type" morphology of expressing neurons. **(D and E)** Confocal stack from the ipsilateral **(D)** and contralateral **(E)** dorsal OB displaying AON terminals ending in different layers. The ipsilateral OB shows expression predominately in the granule cell and external plexiform layers whereas in the contralateral OB fewer fibers in granule cell and deep external plexiform layer are labeled. GL: glomerular layer, EPL: external plexiform layer, MC: mitral cell layer, GCL: granule cell layer.

The nicotinic receptor alpha7 (α7) is expressed in both neuronal and nonneuronal tissues throughout the body and expression is especially high in AON neurons (Dominguez del Toro et al., 1994; Brunjes et al., 2005). Stereotaxic injection of the Cre-dependent viral vectors rAAV 2/1.FLEX.GCaMP3 (Atasoy et al., 2008; Tian et al., 2009; Betley and Sternson, 2011) or rAAV2/9.FLEX.GCaMP6s (Chen et al., 2013) centrally into the AON resulted in strong GCaMP expression in principal neurons in all major AON subdivisions (dorsal, lateral, medial and ventral part; expression in pars externa was not systematically analyzed, but observed in most animals; **Figure 1B**). The basic morphology of the labeled cells is dominated by one or more thick apical dendrites typical of pyramidal neurons (**Figure 1C**), in agreement with previous morphological descriptions of AON projection neurons (Brunjes and Kenerson, 2010).

GCaMP fluorescence was readily apparent in axonal projections from the AON to the OB, with expression predominately in the granule cell and external plexiform layers of the ipsilateral OB (**Figure 1D**) and fewer fibers in the external plexiform layer of the contralateral OB (**Figure 1E**), consistent with earlier characterizations of AON–OB projections (Reyher et al., 1988). Importantly, in the majority of animals AON infection resulted in no or only a few neuron somata in the OB expressing GCaMP (**Figure 1D**; the dense axonal terminations in the granule cell layer lead to the appearance of cellular labeling here due to a "shadowing" effect, but high-resolution confocal microscopy confirmed only sparse cellular expression). We were also able to drive expression of GCaMP in AON-OB projection neurons via retrograde infection with the same virus after injection into the OB of young (postnatal day 1–3) (7 mice) or adult Chrna7-Cre (2 mice) animals, as previously reported for cholecystokinin (CCK)-expressing neurons in AON (Rothermel et al., 2013). Retrograde infection via OB injection led to GCaMP expression in a large population of AON neurons on the ipsilateral side and fewer neurons in the contralateral AON, with expression in few if any neurons in the OB (not shown). As for the AON injections, sparsely labeled cells could be observed below the mitral cell layer as well as in the granule cell layer. Thus, projections from the AON to the OB appear to be largely comprised of α7—expressing neurons which can be selectively targeted with viral vectors, while infection of resident neurons in the postnatal OB appears to very sparse.

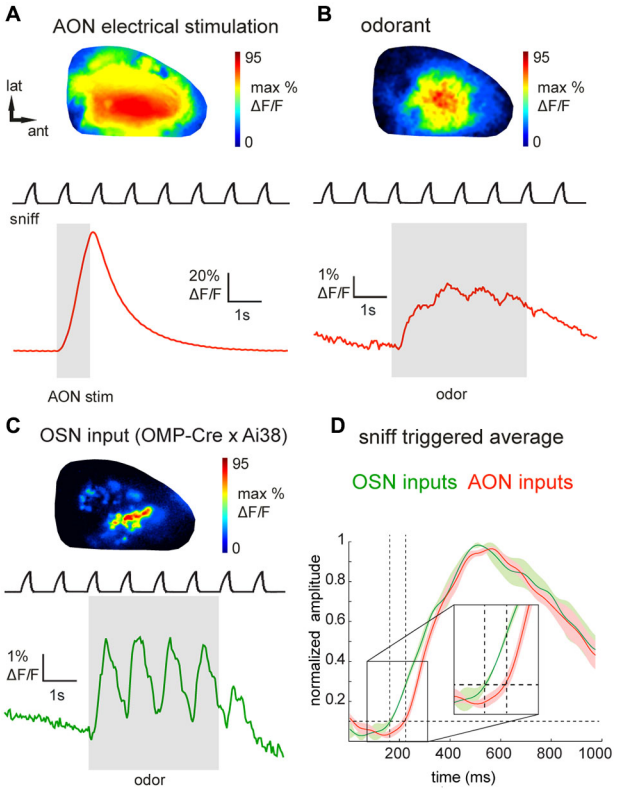

FIGURE 2 | Epifluorescence imaging of centrifugal and olfactory sensory neuron inputs to the OB *in vivo* using GCaMP3. (A) GCaMP3 signals imaged from the dorsal OB of an anesthetized Chrna7-Cre mouse after viral injection into ipsilateral AON. Top: Map of response to electrical stimulation of AON showing widespread fluorescence increases. Map is normalized to its own maximum. Bottom: Time-course of the optical signal. AON stimulation causes a large, transient increase in GCaMP3 fluorescence that decays rapidly. Upper trace ("sniff") shows intranasal pressure transients during artificial inhalation. **(B)** Map (top) and time-course (bottom) of odorant-evoked (1% hexanal) GCaMP3 signals, displayed as in **(A)**. Odorant presentation evokes large fluorescence changes that are driven by inhalation and broadly distributed across the dorsal OB. **(C)** Map (top) and time-course (bottom) of odorant-evoked (1% ethyl butyrate) GCaMP3 signals imaged from OSN axonal terminals in an anesthetized OMP-Cre:Ai38 mouse. Signals appear as discrete, glomerular foci and display strongly-modulated inhalation-linked response dynamics. **(D)** "Sniff-triggered" average GCaMP3 signals comparing responses from OMP-Cre:Ai38 animals (green trace) to Chrna7-Cre animals expressing GCaMP3 in the AON (red trace). Both traces are normalized to their own maxima. Traces show mean ± SEM of the inhalation-aligned response. Sensory neuron signals display a faster onset (see also insert) compared to the signals imaged in the Chrna7-Cre animals.

FUNCTIONAL IMAGING OF AON INPUTS TO THE OB *IN VIVO*

We next attempted to visualize the activation of AON projections to the dorsal OB as reported by GCaMP3 expression in their axon terminals. Using epifluorescence imaging focused slightly below the glomerular layer, electrical stimulation of the AON (50 pulses at 50 Hz, see Section Materials and Methods for details) evoked a large, transient increase in GCaMP3 fluorescence across the dorsal OB (**Figure 2A**). Electrically-evoked activity was evenly distributed over the dorsal surface of the OB in all recorded animals (**Figure 2A**). The mean stimulation-evoked increase across the dorsal OB was 21.6 ± 19.8% ΔF/F (n = 5 mice), with signals reaching as high as 80% ΔF/F in the strongest-activated areas. The minimum number of pulses necessary to evoke a response ranged between 4 and 8 pulses. AON stimulation-evoked GCaMP3 fluorescence increases decayed with a time-constant of 1.0 ± 0.16 s (n = 5 mice), comparable to that reported for the decay of GCaMP3 signals expressed in mitral and pyramidal cells after a brief spike burst (Wachowiak et al., 2013). The strong amplitude and rapid decay of this signal is consistent with it reflecting stimulation-evoked action potentials at the axon terminals of AON projections to the OB.

Next we asked whether sensory inputs to the OB are capable of activating feedback projections from AON. We and others have previously reported that inhalation alone can weakly activate olfactory sensory input to the OB and drive mitral/tufted cell activity (Grosmaitre et al., 2007; Carey et al., 2009; Wachowiak et al., 2013; Rothermel et al., 2014). In mice expressing GCaMP3 in AON projections (n = 8), we found that artificial inhalation of clean air at 1 Hz (see Section Materials and Methods) evoked small-amplitude fluorescence transients detectable above baseline noise in some regions (60 out of 144 ROIs, n = 301 sniffs, eight mice, see Section Materials and Methods for detection criteria). The mean peak amplitude of these detectable transients was 1.7 ± 0.9% ΔF/F. In five mice in which AON was also stimulated electrically, detectable inhalation-evoked signals reached a magnitude of 3.0 ± 2.2% of the magnitude of the AON stimulation response. This result suggests that even weak sensory inputs driven by inhalation are capable of driving descending AON inputs to the OB, and that these descending inputs are temporally patterned by inhalation.

Odorant presentation evoked larger GCaMP3 fluorescence changes that were, like the electrically-evoked signals, broadly but heterogeneously distributed across the dorsal OB (**Figure 2B**). The peak amplitude of odorant-evoked GCaMP3 signals reached up to 30% ΔF/F (mean across the imaged region, 5.6 ± 6.2%; n = 8 mice), and ranged from 1.9–36.5% of the peak response evoked by electrical AON stimulation (n = 5 mice). Responses to individual inhalations could be clearly resolved within the evoked GCaMP3 signals (**Figure 2B**). Odorant-evoked responses displayed a latency relative to inhalation onset of 234 ± 45 ms (n = 5 mice, 271 responses); these times were slower than previously-reported response latencies of OB interneurons (Wachowiak et al., 2013). To compare AON response latencies to those of primary sensory inputs imaged with the same optical reporter, we crossed OMP-Cre animals to the Ai38 GCaMP3 reporter line (Zariwala et al., 2012), which resulted in expression of GCaMP3 in olfactory sensory neuron axon terminals. In OMP-Cre:Ai38 mice, odorants evoked spatially organized, glomerular signals which showed robust inhalation-linked response dynamics (**Figure 2C**) as observed previously using synthetic calcium indicators and GCaMP2 (Wachowiak and Cohen, 2001; Bozza et al., 2004; Soucy et al., 2009; Ma et al., 2012; Wachowiak et al., 2013). Odorant-evoked response latencies relative to inhalation onset were 146 ± 30 ms (n = 2 mice, 32 responses), and so were substantially faster than those of AON projections to the OB (**Figure 2D**).

To ensure that odorant-evoked responses were not due to spurious GCaMP expression in neurons with the OB, we locally inactivated AON neurons by microinjecting tetrodotoxin (TTX). Local TTX application into the AON (50 μM, 0.5 μl) dramatically reduced odorant-evoked responses in the OB (**Figure 3A**, reduction to 13.2 ± 12.9% (median ± SD) of the peak ΔF under control conditions; n = 3 mice). Thus, sensory-evoked GCaMP signals in the OB originate largely, if not entirely, from AON feedback to the OB. Overall, these results suggest that AON input to the OB can be triggered by both weak and strong sensory input, is patterned by respiration, and may therefore provide rapid feedback to the OB that is updated with each inhalation.

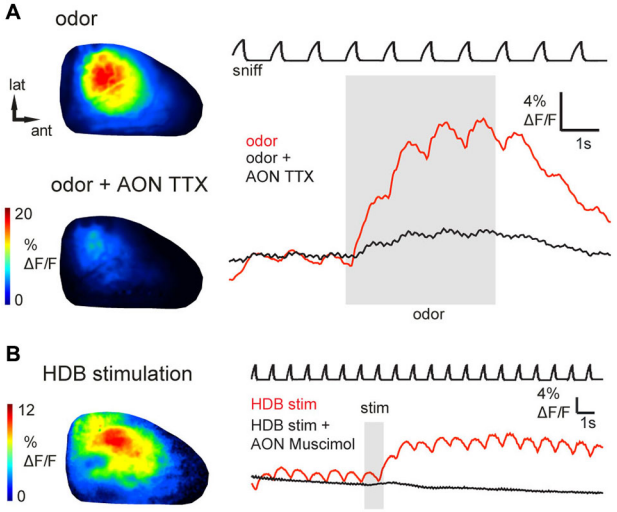

FIGURE 3 | Epifluorescence signals arise from AON activity and can be activated by basal forebrain stimulation. (A) Odorant-evoked (1% ethyl butyrate) GCaMP6s signals before and after injection of TTX into AON (see Text for details). Shown are odorant response maps (left) and optical signal traces (right) taken immediately before (upper map, red trace) or after (lower map, black trace) TTX injection. TTX injection into the AON reduced odorant-evoked responses in the OB. **(B)** Response maps and time-course of GCaMP6s signals evoked by electrical HDB stimulation, displayed as in **(A)**. HDB stimulation caused prolonged fluorescence increases in AON axon terminals (red trace). Black trace shows GCaMP6s signal from the same region of interest shortly after injection of muscimol into AON. AON inactivation with muscimol abolished inhalation- and HDB stimulation-evoked responses in the OB.

BASAL FOREBRAIN ACTIVATION ALSO DRIVES INPUT FROM AON TO THE OB

In addition to ascending sensory signals from the OB, the AON receives centrifugal input from higher-order brain areas including classical neuromodulatory centers. The horizontal limb of the HDB, for example, sends cholinergic and GABA-ergic projections to the OB, piriform cortex and AON (Woolf et al., 1984; Linster et al., 1999; Zaborszky et al., 2012; Rothermel et al., 2014). To assess whether neuromodulatory centers might modulate OB activity via their impact on AON projections, we investigated the effects of HDB stimulation on AON inputs to the OB. Brief electrical stimulation of HDB (same stimulus parameters as for AON stimulation; see Section Materials and Methods) evoked a modest increase in GCaMP3 fluorescence that outlasted the stimulus train by as much as 10 s (n = 4 mice; **Figure 3B**). The peak amplitude of HDB stimulation-evoked GCaMP3 signals reached up to 12% ΔF/F (mean, 3.1 ± 2.7%; n = 4 mice), corresponding to 4.9–9.8% of the maximal AON stimulation-evoked response observed in the same animals (n = 2 mice). The prolonged effect of HDB stimulation-evoked GCaMP3 fluorescence increases suggests a modulation of ongoing AON output rather than a direct excitation of AON projection neurons or direct cholinergic activation of AON axon terminals in the OB. To confirm this, in one animal we locally inactivated AON neurons by microinjecting the $GABA_A$ receptor agonist muscimol into AON. We predicted that muscimol should inactivate AON

throughput without affecting axons of passage projecting directly from HDB to the OB. As expected, muscimol injection into the AON (0.8 mM, 0.5 μl) eliminated HDB stimulation-evoked responses in the OB (**Figure 3B**). Muscimol also eliminated inhalation- and odor-evoked signals in the OB. Together these results indicate that basal forebrain, in addition to the known direct projections from basal forebrain to the OB (Macrides et al., 1981; Shipley and Adamek, 1984; Rothermel et al., 2013, 2014), can indirectly modulate OB processing via its enhancement of AON inputs to the OB.

SENSORY-EVOKED AON FEEDBACK TO THE OB IMAGED IN THE AWAKE MOUSE

Centrifugal inputs from higher-order centers can play a major role in shaping processing in primary sensory areas as a function of behavioral state. We thus imaged AON inputs to the OB during passive and active sampling of olfactory stimuli in the awake, head-fixed mouse using epifluorescence and two-photon imaging. Under epifluorescence, odorants robustly activated AON projections to the OB during wakefulness, with peak GCaMP3 signals reaching up to 18% ΔF/F (n = 2 mice). Odorant-evoked responses were reliable across repeated odorant presentations and modulated by respiration (**Figures 4A,B**). While the degree of respiratory modulation appeared smaller than in the anesthetized mouse, transient GCaMP3 signals were nonetheless clearly linked to inhalation (**Figures 4B,C**). Bouts of higher frequency sniffing (**Figure 4A**, stippled lines) or even a single strong inhalation (arrowheads) transiently activated AON inputs to the OB even in the absence of odorant, consistent with the results of the artificial inhalation experiments.

We also found evidence that the strength of AON input to the OB was itself modulated by wakefulness. In order to compare responses in the awake versus anesthetized states, we briefly (1–3 min) anesthetized head-fixed mice with isoflurane, then imaged GCaMP signals as the animal returned to the waking state over the next 1–2 min (Wachowiak et al., 2013). Odorant-evoked GCaMP signals under anesthesia were significantly smaller than those observed during wakefulness (**Figure 4C**), with peak amplitudes just after removal of isoflurane being reduced to 34 and 25% of those before anesthesia (n = 2 mice). This result is in contrast to what we and others have observed for OB output neurons, where mitral/tufted cell responses imaged with GCaMPs are larger under anesthesia than during wakefulness. These results suggest that the strength of sensory-evoked

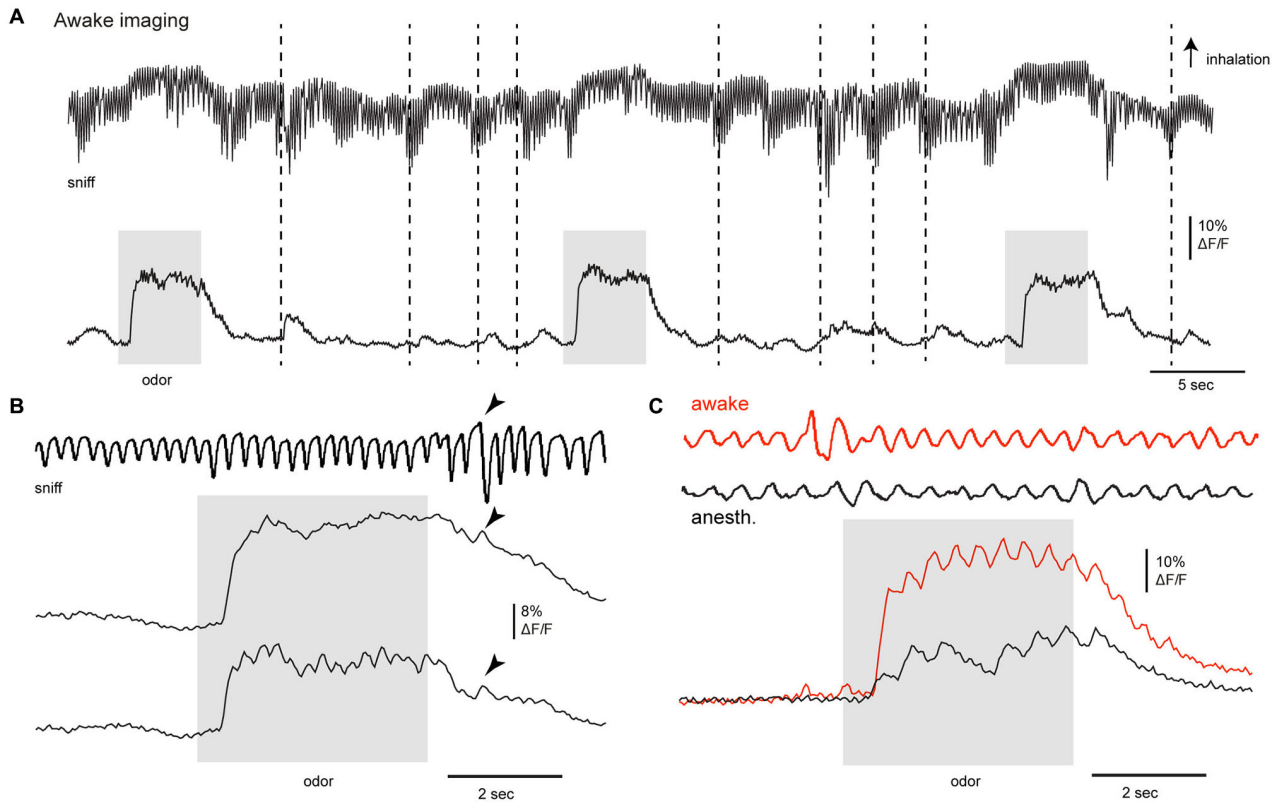

FIGURE 4 | Activation of centrifugal AON inputs to the olfactory bulb in the awake animal. (A–C) GCaMP3 signals imaged from AON terminals in the dorsal OB of an awake animal after viral injection to the AON in Chrna7-Cre mice. **(A)** GCaMP3 signals imaged from the dorsal OB in an awake, head fixed mouse; odorant (0.5% of a mixture of 4 odorants: 2-hexanone, butyl acetate, ethyl butyrate, methyl valerate) is presented three times; activity from one ROI is displayed. Top trace in **(A, B and C)** shows respiration measured via thermocouple (placed in front of the nose in the depicted example), with inhalation up in all cases. Stippled lines indicate bouts of higher frequency sniffing; arrowhead points to a single deep inhalation. Odorant application as well as high-frequency sniffing in the absence of odorants activated AON inputs as reported with GCaMP3.

descending inputs from AON to the OB may itself vary with brain state.

Next we further evaluated the spatiotemporal organization of AON feedback to the OB using two-photon imaging in the awake mouse (see Section Materials and Methods for details). Imaging was performed at a single focal plane set at the superficial external plexiform layer (see insert, **Figure 5C**), which receives dense axonal projections from AON (also compare to **Figure 1D**). Apparent foci in the average projection image at the bottom of **Figure 5A** are artifacts from anatomical features (blood vessels).

We imaged responses to several odorants *per session*, presenting each odorant eight times with an inter-stimulus interval of 36 s. **Figure 5** shows response maps evoked by three sample odorants (**Figure 5A**) as well as example traces depicting the fluorescence signals recorded from three ROIs (**Figure 5B**), using these odorants. Odorant-evoked responses were reliably repeated across multiple presentations and showed peak amplitudes of up to 117% ΔF/F (mean peak response across all odorants, 35.8 ± 27.2%; n = 3 mice, 52 odorant responses). Notably, odorant-evoked responses had diverse temporal characteristics

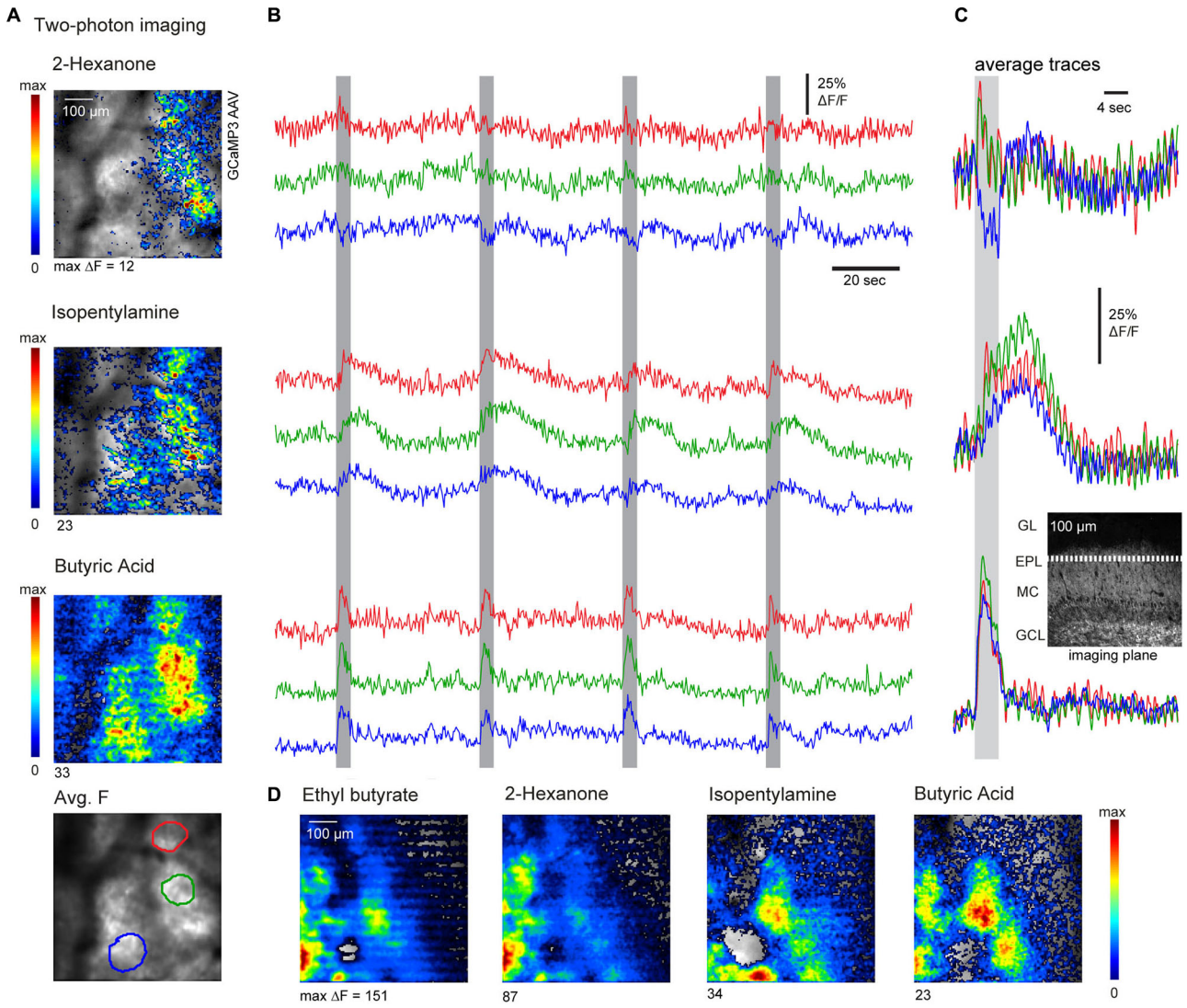

FIGURE 5 | Two-photon imaging reveals odorant-specific patterns of AON feedback to the OB. (A) Resting fluorescence (grayscale) and pseudocolor overlay of odorant-evoked GCaMP3 fluorescence changes imaged with two-photon microscopy in an awake, head-fixed mouse. Odorant-evoked responses were broadly but heterogeneously distributed and varied across odorants. Bottom: Regions of interest (ROIs) used for the time-courses shown in **(B)**. **(B)** Traces showing the time-course of GCaMP3 signals imaged from different ROIs during four consecutive odorant presentations. Odorant presentation elicited reproducible responses which differed in different ROIs. Responses also differed in their temporal dynamics and could also include fluorescence decreases. **(C)** Average odorant-evoked signals from the same ROIs and same odorants as in **(A)** and **(B)**, averaged over eight trials. Inset: approximate imaging plane shown in a reference section. **(D)** Odorant-evoked response maps imaged with two-photon microscopy in a different animal, again showing odorant-specific patterns of fluorescence signals (GCaMP3).

that were reproducible for individual odorants but substantially differed between them (**Figure 5C**; compare the prolonged odor response to isopentamylamine to the brief response evoked by butyric acid). The same odorant could also evoke distinct temporal response patterns in different areas of the imaged region (for example, compare red and green trace to blue trace for 2-hexanone). Response maps of AON input activity also revealed that different odorants could evoke distinct spatial patterns of feedback activity (**Figures 5A,D**). To quantify this spatial heterogeneity, we correlated averaged response maps evoked by different odorants or by blocks of repeated trials of the same odorant. The correlation coefficients between responses to different odorants ($r = 0.54 \pm 0.17$, 69 pair-wise comparisons, 11 imaging sessions, $n = 3$ mice) were significantly lower than correlation coefficients calculated for trials of the same odorant ($r = 0.73 \pm 0.14$, 5 pair-wise comparisons, 3 imaging sessions, $p = 0.03$ Mann–Whitney U-test), indicating some degree of spatial specificity in AON feedback to the OB. Overall, these results suggest that sensory-evoked AON feedback to the OB is not homogenous, but instead displays distinct spatiotemporal patterns evoked by different odorants.

AON MEDIATES ODORANT-SPECIFIC FEEDBACK TO THE CONTRALATERAL OB

The AON has been proposed to mediate the communication of olfactory information between each OB via its projections to the contralateral OB (Schoenfeld and Macrides, 1984; Lei et al., 2006; Yan et al., 2008; Kikuta et al., 2010; Kay and Brunjes, 2014). Thus, in a final experiment, we attempted to image from individual axons projecting from AON to the contralateral OB. Epifluorescence imaging in an anesthetized mouse revealed broadly distributed and inhalation-driven odorant evoked GCaMP6s fluorescence signals that were qualitatively similar to those observed in ipsilateral imaging (**Figure 6A**). Because contralateral projections showed sparser labeling than ipsilateral projections in all preparations (e.g., **Figure 1E**), discrete axons and axonal varicosities could be visualized using two-photon imaging in the deep external plexiform layer of the contralateral OB (**Figure 6B**, average fluorescence map), allowing us to map odorant-evoked feedback from individual contralaterally-projecting axons (**Figure 6B**). Examples of GCaMP6s signals recorded from four ROI centered on putative axon terminals are shown in **Figure 6C**. Odorants evoked responses in distinct combinations of axon terminals with temporally diverse responses that included "simple" fluorescence increases during odorant stimulation, "off" responses, as well as apparent suppression of ongoing activity (**Figure 6C**). In each case, responses were repeated across successive odorant presentations. These results indicate that AON sends odorant-specific feedback signals to both ipsi- and contralateral OBs.

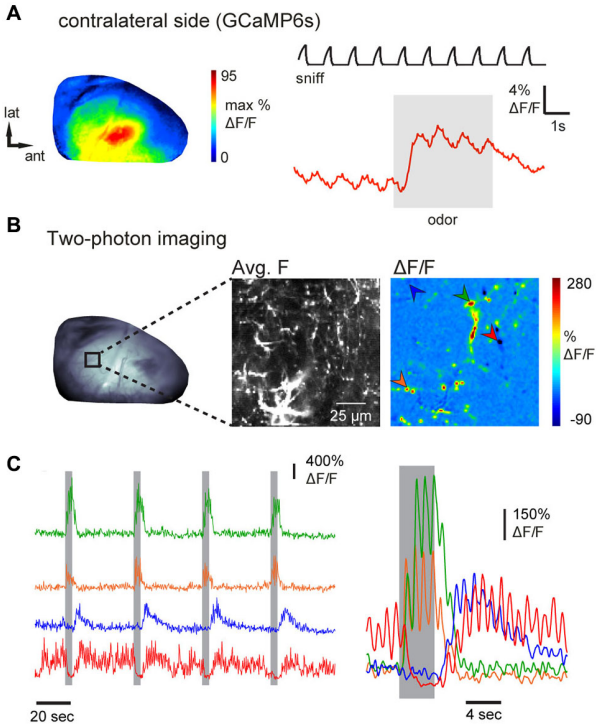

FIGURE 6 | Inhalation-driven and odorant-specific centrifugal AON inputs to the contralateral OB. (A) Response map (left) and time-course (right) of odorant-evoked (1% ethyl butyrate) GCaMP6s signals imaged from AON terminals in the contralateral dorsal OB of an anesthetized mouse, displayed as in **Figure 2**. As with ipsilateral signals, contralateral AON input responses were driven by inhalation and broadly distributed across the dorsal OB. **(B)** Contralateral AON inputs imaged with two-photon microscopy in an anesthetized mouse. Left: epifluorescence image of the dorsal OB. Middle: Two-photon images showing resting GCaMP6s fluorescence (average fluorescence map) in AON axons in the indicated region. Right: Odorant-evoked response map showing strong fluorescence changes in small, sparsely-distributed foci likely corresponding to individual axonal fibers and varicosities. Arrowheads indicate foci used for the time-courses shown in **(C)**. **(C)** Traces demonstrating diverse responses of different contralateral AON inputs. Left traces show continuous fluorescence signals taken from the regions indicated in **(B)** during four consecutive odorant presentations. Right traces show the same responses averaged across eight trials. Fluctuations indicate inhalation-driven fluorescence increases (sniff trace not shown). Responses were consistent across trials and included "off" responses (blue trace) as well as suppression of ongoing activity (red trace).

DISCUSSION

Olfactory cortex sends strong feedback projections to the OB, the first stage of synaptic processing in the olfactory system. While this cortical feedback has been shown to profoundly modulate OB output and hypothesized to play an integral role in olfactory processing in the awake animal (Strowbridge, 2009; Boyd et al., 2012; Markopoulos et al., 2012; Soria-Gómez et al., 2014), the functional properties of feedback to the OB from any neuronal population have yet to be characterized *in vivo*. Centrifugal projections from the AON—a simplified cortical structure interconnected with the OB and piriform cortex—are among the most numerous of centrifugal inputs to the OB (Carson, 1984; Shipley and Adamek, 1984). Here, we selectively labeled descending AON projection neurons and imaged activation of their axon terminals in the OB, an approach similar to recent studies imaging from axonal processes in visual or somatosensory cortex (Petreanu et al., 2012; Glickfeld et al., 2013). We found that Cre-dependent viral vector injection into Chrna7-Cre animals was sufficient to drive GCaMP expression in principal neurons throughout the AON. GCaMP expression in AON was sufficient to report the

arrival of action potentials at their axon terminals in the OB. AON neurons could be labeled either by direct virus injection into the AON or by retrograde viral transport after virus injection into the OB, consistent with our recent report of the retrograde infection capabilities of many recombinant AAV vectors (Rothermel et al., 2013). In either case, a key feature of our approach was the ability to selectively image the activation of centrifugal projections to the OB. The AON is composed of at least five major subdivisions which appear functionally distinct on the basis of their anatomical projections, intrinsic cellular makeup and chemoarchitecture (Reyher et al., 1988; Brunjes et al., 2005; Meyer et al., 2006; Illig and Eudy, 2009; Kay and Brunjes, 2014). While clearly a simplification, as a first step we did not attempt to selectively investigate these subdivisions and instead considered AON output signals as a whole.

There are several lines of evidence indicating that the fluorescence signals imaged from the dorsal OB in our experiments originated largely or entirely from GCaMP expressed in centrifugal projections from the AON. First, even with direct bulbar virus injections we observed only a very sparse cellular labeling in the OB which was consistent with the sparse distribution of Chrna7-expressing neurons in adult mice using transgenic markers (The Gene Expression Nervous System Atlas (GENSAT) Project[1]) (Gong et al., 2003); virus injection into AON, as used in the majority of experiments, should further minimize the chances of expression in OB neurons. Second, strong and short-latency responses could be triggered by direct electrical stimulation of the AON. Third, odorant-evoked responses imaged from the OB showed longer response latencies relative to inhalation compared to responses imaged from olfactory sensory neuron axon terminals expressing the same GCaMP3 reporter (i.e., **Figure 2D**), and also slightly longer than those reported for OB interneurons and mitral/tufted cells (Wachowiak et al., 2013), as would be expected for a sensory-evoked feedback projection. Finally, TTX and muscimol blockade experiments confirmed the AON as the major signal source for fluorescence activity measured at the dorsal OB.

While AON projections to the OB have been well-described anatomically (Brunjes et al., 2005), their functional properties *in vivo* have, until now, been completely uncharacterized. For example, earlier studies have proposed that AON pars externa mediates rapid feedback of OB output to the contralateral OB (Schoenfeld and Macrides, 1984; Yan et al., 2008), a prediction now confirmed by our results. In addition, our experiments provide the first functional evidence in support of an indirect modulation of OB function mediated by higher-order areas such as basal forebrain, as predicted from earlier anatomical findings (Zaborszky et al., 2012; Rothermel et al., 2014). Other results—for example, the strong respiratory coupling of AON feedback neurons to the ipsilateral OB and the rich diversity of odorant response specificities and response polarities apparent with high-resolution two-photon imaging—are not easily predicted from anatomical studies. The implications of such findings for the functional role of the AON in olfactory processing are discussed in more detail below.

[1]http://www.gensat.org/index.html

SENSORY-EVOKED FEEDBACK PROJECTIONS FROM AON TO THE OB

Odorants evoked fluorescence changes that were transient and driven by inhalation, suggesting that even in the anesthetized animal there are strong sensory-evoked feedback projections from AON to the OB. Rapid inhalation-driven bursts of AON input to the OB were also robust in the awake mouse. The persistence of strong respiratory coupling in AON feedback to the OB is somewhat surprising given that OB output neurons show diverse temporal responses which span the respiratory cycle (Chaput, 1986; Carey and Wachowiak, 2011; Shusterman et al., 2011). One explanation for this result may be that the AON receives input preferentially from OB tufted (as opposed to mitral) cells (Haberly and Price, 1977; Scott et al., 1980; Scott, 1981; Macrides and Schneider, 1982; Nagayama et al., 2010; Sosulski et al., 2011). Functionally, tufted cells are more excitable, have higher firing frequencies and display stronger respiratory locking compared to mitral cells (Schneider and Scott, 1983; Ezeh et al., 1993; Nagayama et al., 2004; Griff et al., 2008; Burton and Urban, 2014) and so may preserve the timing of odor sampling more faithfully across their population. Inhalation-coupled feedback from AON may play several roles in shaping how the OB processes incoming olfactory information. First, inhalation-coupled feedback may provide a real-time report of sensory input referenced to the respiratory cycle. Inhalation alone evokes weak OSN inputs to the OB (Grosmaitre et al., 2007; Carey et al., 2009), which are presumably relayed to the AON and which may, as our recordings suggest, trigger inhalation-coupled AON feedback even in the absence of odorant. Since AON projection terminals innervate all major OB layers, inhalation-coupled AON activity may impose a feedback signal on OB circuits that can serve as a reference for the timing of the respiratory cycle across different OB cells types; this timing signal may be important in shaping the odor-specific, respiratory patterning of mitral/tufted cell dynamics that is thought to be important in encoding odor information (Bathellier et al., 2008; Cury and Uchida, 2010; Shusterman et al., 2011).

The circuit mechanisms underlying rapid, sensory-evoked feedback to the OB remain to be elucidated. So far, only one study has selectively investigated the influence of centrifugal AON inputs on defined OB circuits including OB output neurons (Markopoulos et al., 2012). Using optical AON stimulation, Markopoulos et al. (2012) found evidence that AON inputs drive a fast direct depolarization of mitral/tufted cells as well as a delayed disynaptic inhibition mainly mediated by granule cells. AON effects on mitral/tufted cells were independent of the exact phase of the respiration but strongly dependent on mitral/tufted cell basal firing rate. The authors concluded that AON feedback might shape OB output by creating a window of opportunity for mitral/tufted cell spikes and enforcing a broad inhibition that could suppress background activity. Our observation that AON feedback activity shows strong modulations with the respiration cycle is consistent with this hypothesis and supports the idea that the timing of cortical feedback projections to the OB is important for modulating OB activity.

High-resolution two-photon imaging revealed that, on a small spatial scale, AON feedback to the OB shows considerable diversity in odorant specificity and temporal dynamics, with different individual axons—or small populations of axons—showing

distinct odorant response profiles and even distinct combinations of excitatory and suppressive responses. These results suggest an unforeseen richness in the representation of odor information carried by centrifugal feedback to the OB. The logic of such specific feedback projections remains to be explored; however these results suggest that AON feedback functions as more than just a global, activity-dependent regulator of OB output. One possibility is that AON feedback might selectively modulate sensory inputs to different functional domains of the OB. It has been reported that the AON is (in part) topographically organized with AON outputs to the OB showing a dorsal to ventral topography and different AON subdivisions targeting different OB layers (Davis and Macrides, 1981; Luskin and Price, 1983; Reyher et al., 1988; Brunjes et al., 2005). Ascending projections from the OB to the AON (both pars externa and pars principalis) also maintain a rough topographic organization (Schoenfeld et al., 1985; Scott et al., 1985; Ghosh et al., 2011; Miyamichi et al., 2011), and different odorants activate topographically distinct groups of neuron in pars externa (but not pars pricipalis) (Kay et al., 2011). It is thus possible that centrifugal projections from the AON may modulate neural activity in homotopic OB areas, meaning that domains within the OB that were activated by a specific odorant could receive selective and targeted feedback from the AON. Sensory-evoked feedback from the AON that targets specific OB regions would be in a powerful position to selectively modulate the gain of particular functional domains and therefore dynamically adjust the relative responsiveness of OB output to different odorant classes. Odorant-specific feedback to the OB might also play a role in experience-dependent plasticity of early odor representations—for example, mediating glomerulus-specific changes in response gain for glomeruli involved in representing odor objects associated with aversive or appetitive stimuli (Kass et al., 2013; Abraham et al., 2014). While speculative at this point, such a role would be consistent with that proposed earlier for AON on the basis of its anatomical connections with the OB and piriform cortex (Haberly, 2001).

THE AON AS A MULIFUNCTIONAL HUB FOR SHAPING EARLY OLFACTORY PROCESSING

In addition to being activated by incoming olfactory information, we also found that AON projections to the OB were activated by stimulating basal forebrain, illustrating that the AON functions not only as a low-level feedback center or a relay nucleus but also as a mediator of "top-down" signals from higher-order areas. This finding is consistent with anatomical studies showing that the AON not only receives direct input from the OB but also from diverse brain areas including basal forebrain (Zaborszky et al., 2012; Rothermel et al., 2014), piriform cortex (Haberly and Price, 1978; Luskin and Price, 1983; Hagiwara et al., 2012) and the contralateral AON (Brunjes et al., 2005). Thus, the role of the AON in modulating incoming olfactory information may be analogous to pre-cortical nuclei in other sensory systems. In the auditory system for example, olivocochlear efferents mediate central control of the sensitivity of hair cells to external sounds (reviewed in Rabbitt and Brownell, 2011). This system can be activated by auditory input from the cochlear nucleus, thus constituting a rapid sensory feedback pathway, but can also be driven by "top-down" signals arising, for example, from the vocal motor system to modulate auditory sensitivity to self-generated sounds (Weeg et al., 2005).

We hypothesize that the AON serves a similar multifunctional role, acting as modulatory hub that integrates incoming sensory information with inputs from other brain areas in order to rapidly shape OB output according to ongoing olfactory sampling as well as overall behavioral state. The AON likely also plays an important role in olfactory processing by shaping odor representations as they ascend to other cortical areas; indeed, there are robust projections from the AON to anterior piriform cortex (Hagiwara et al., 2012), and AON neurons display unique odorant response properties consistent with their integrating and transforming sensory inputs from the OB (Lei et al., 2006; Kikuta et al., 2010; Kay et al., 2011). Whether these multiple functional pathways are mediated by separate or overlapping circuits, or mediated by distinct subdivisions of AON, remains unexplored. Genetically-targeted, optical approaches similar to those used here to functionally characterize, for the first time, centrifugal AON projections to the OB should be useful in further dissecting these pathways in order to understand how each is engaged to shape olfactory processing during behavior.

AUTHOR CONTRIBUTIONS

Markus Rothermel and Matt Wachowiak designed the experiments, Markus Rothermel performed the imaging experiments and data analysis, Markus Rothermel and Matt Wachowiak wrote the paper.

ACKNOWLEDGMENTS

We thank Scott W. Rogers and Petr Tvrdik for kindly providing the Chrna7-Cre mice and for advice on colony maintenance. Chrna7-Cre mice were generated with funding from NIH AG017517 to S. Rogers. We thank Justus Verhagen for kindly providing the OMP-Cre mice. We thank Loren L. Looger, Jasper Akerboom, Douglas S. Kim, and the Genetically Encoded Calcium Indicator (GECI) Project at Janelia Farm Research Campus Howard Hughes Medical Institute for providing constructs. We also thank Michael T. Shipley and Adam C. Puche for helpful discussions in initial phases of this project, Christine Zabawa for technical assistance, Daniela Brunert and Jackson Ball for providing recordings in the OMP-Cre:Ai38 mice and Michael N. Economo and Kyle Hansen for providing analysis software. This work was supported by funding from the NIH (DC010915, DC06441) and the DFG (to Markus Rothermel).

REFERENCES

Abraham, N. M., Vincis, R., Lagier, S., Rodriguez, I., Carleton, A., and Eichenbaum, H. (2014). Long term functional plasticity of sensory inputs mediated by olfactory learning. *Elife* 3:e02109. doi: 10.7554/elife.02109

Atasoy, D., Aponte, Y., Su, H. H., and Sternson, S. M. (2008). A FLEX switch targets Channelrhodopsin-2 to multiple cell types for imaging and long-range circuit mapping. *J. Neurosci.* 28, 7025–7030. doi: 10.1523/JNEUROSCI.1954-08.2008

Bathellier, B., Buhl, D. L., Accolla, R., and Carleton, A. (2008). Dynamic ensemble odor coding in the mammalian olfactory bulb: sensory information at different timescales. *Neuron* 57, 586–598. doi: 10.1016/j.neuron.2008.02.011

Betley, J. N., and Sternson, S. M. (2011). Adeno-associated viral vectors for mapping, monitoring and manipulating neural circuits. *Hum. Gene Ther.* 22, 669–677. doi: 10.1089/hum.2010.204

Boyd, A. M., Sturgill, J. F., Poo, C., and Isaacson, J. S. (2012). Cortical feedback control of olfactory bulb circuits. *Neuron* 76, 1161–1174. doi: 10.1016/j.neuron.2012.10.020

Bozza, T., Mcgann, J. P., Mombaerts, P., and Wachowiak, M. (2004). In vivo imaging of neuronal activity by targeted expression of a genetically encoded probe in the mouse. *Neuron* 42, 9–21. doi: 10.1016/S0896-6273(04)00144-8

Broadwell, R. D., and Jacobowitz, D. M. (1976). Olfactory relationships of the telencephalon and diencephalon in the rabbit. III. The ipsilateral centrifugal fibers to the olfactory bulbar and retrobulbar formations. *J. Comp. Neurol.* 170, 321–345. doi: 10.1002/cne.901700305

Brunjes, P. C., Illig, K. R., and Meyer, E. A. (2005). A field guide to the anterior olfactory nucleus (cortex). *Brain Res. Brain Res. Rev.* 50, 305–335. doi: 10.1016/j.brainresrev.2005.08.005

Brunjes, P. C., and Kenerson, M. C. (2010). The anterior olfactory nucleus: quantitative study of dendritic morphology. *J. Comp. Neurol.* 518, 1603–1616. doi: 10.1002/cne.22293

Burton, S. D., and Urban, N. N. (2014). Greater excitability and firing irregularity of tufted cells underlies distinct afferent-evoked activity of olfactory bulb mitral and tufted cells. *J. Physiol.* 592(Pt. 10), 2097–2118. doi: 10.1113/jphysiol.2013.269886

Canteras, N. S., Simerly, R. B., and Swanson, L. W. (1995). Organization of projections from the medial nucleus of the amygdala: a PHAL study in the rat. *J. Comp. Neurol.* 360, 213–245. doi: 10.1002/cne.903600203

Carey, R. M., Verhagen, J. V., Wesson, D. W., Pirez, N., and Wachowiak, M. (2009). Temporal structure of receptor neuron input to the olfactory bulb imaged in behaving rats. *J. Neurophysiol.* 101, 1073–1088. doi: 10.1152/jn.90902.2008

Carey, R. M., and Wachowiak, M. (2011). Effect of sniffing on the temporal structure of mitral/tufted cell output from the olfactory bulb. *J. Neurosci.* 31, 10615–10626. doi: 10.1523/JNEUROSCI.1805-11.2011

Carnes, K. M., Fuller, T. A., and Price, J. L. (1990). Sources of presumptive glutamatergic/aspartatergic afferents to the magnocellular basal forebrain in the rat. *J. Comp. Neurol.* 302, 824–852. doi: 10.1002/cne.903020413

Carson, K. A. (1984). Quantitative localization of neurons projecting to the mouse main olfactory bulb. *Brain Res. Bull.* 12, 629–634. doi: 10.1016/0361-9230(84)90143-6

Chaput, M. A. (1986). Respiratory-phase-related coding of olfactory information in the olfactory bulb of awake freely-breathing rabbits. *Physiol. Behav.* 36, 319–324. doi: 10.1016/0031-9384(86)90023-5

Chen, T.-W., Wardill, T. J., Sun, Y., Pulver, S. R., Renninger, S. L., Baohan, A., et al. (2013). Ultrasensitive fluorescent proteins for imaging neuronal activity. *Nature* 499, 295–300. doi: 10.1038/nature12354

Cury, K. M., and Uchida, N. (2010). Robust odor coding via inhalation-coupled transient activity in the mammalian olfactory bulb. *Neuron* 68, 570–585. doi: 10.1016/j.neuron.2010.09.040

Davis, B. J., and Macrides, F. (1981). The organization of centrifugal projections from the anterior olfactory nucleus, ventral hippocampal rudiment and piriform cortex to the main olfactory bulb in the hamster: an autoradiographic study. *J. Comp. Neurol.* 203, 475–493. doi: 10.1002/cne.902030310

Davis, B. J., Macrides, F., Youngs, W. M., Schneider, S. P., and Rosene, D. L. (1978). Efferents and centrifugal afferents of the main and accessory olfactory bulbs in the hamster. *Brain Res. Bull.* 3, 59–72. doi: 10.1016/0361-9230(78)90062-x

De Carlos, J. A., Lopez-Mascaraque, L., and Valverde, F. (1989). Connections of the olfactory bulb and nucleus olfactorius anterior in the hedgehog (Erinaceus europaeus): fluorescent tracers and HRP study. *J. Comp. Neurol.* 279, 601–618. doi: 10.1002/cne.902790408

de Olmos, J., Hardy, H., and Heimer, L. (1978). The afferent connections of the main and the accessory olfactory bulb formations in the rat: an experimental HRP-study. *J. Comp. Neurol.* 181, 213–244. doi: 10.1002/cne.901810202

Dominguez del Toro, E., Juiz, J. M., Peng, X., Lindstrom, J., and Criado, M. (1994). Immunocytochemical localization of the alpha 7 subunit of the nicotinic acetylcholine receptor in the rat central nervous system. *J. Comp. Neurol.* 349, 325–342. doi: 10.1002/cne.903490302

Doucette, W., and Restrepo, D. (2008). Profound context-dependent plasticity of mitral cell responses in olfactory bulb. *PLoS Biol.* 6:e258. doi: 10.1371/journal.pbio.0060258

Ezeh, P. I., Wellis, D. P., and Scott, J. W. (1993). Organization of inhibition in the rat olfactory bulb external plexiform layer. *J. Neurophysiol.* 70, 263–274.

Fu, Y., Tucciarone, J. M., Espinosa, J. S., Sheng, N., Darcy, D. P., Nicoll, R. A., et al. (2014). A cortical circuit for gain control by behavioral state. *Cell* 156, 1139–1152. doi: 10.1016/j.cell.2014.01.050

Gahring, L. C., Enioutina, E. Y., Myers, E. J., Spangrude, G. J., Efimova, O. V., Kelley, T. W., et al. (2013). Nicotinic receptor alpha7 expression identifies a novel hematopoietic progenitor lineage. *PLoS One* 8:e57481. doi: 10.1371/journal.pone.0057481

Gaykema, R. P., Luiten, P. G., Nyakas, C., and Traber, J. (1990). Cortical projection patterns of the medial septum-diagonal band complex. *J. Comp. Neurol.* 293, 103–124. doi: 10.1002/cne.902930109

Ghosh, S., Larson, S. D., Hefzi, H., Marnoy, Z., Cutforth, T., Dokka, K., et al. (2011). Sensory maps in the olfactory cortex defined by long-range viral tracing of single neurons. *Nature* 472, 217–220. doi: 10.1038/nature09945

Glickfeld, L. L., Andermann, M. L., Bonin, V., and Reid, R. C. (2013). Cortico-cortical projections in mouse visual cortex are functionally target specific. *Nat. Neurosci.* 16, 219–226. doi: 10.1038/nn.3300

Gomez, D. M., and Newman, S. W. (1992). Differential projections of the anterior and posterior regions of the medial amygdaloid nucleus in the Syrian hamster. *J. Comp. Neurol.* 317, 195–218. doi: 10.1002/cne.903170208

Gong, S., Zheng, C., Doughty, M. L., Losos, K., Didkovsky, N., Schambra, U. B., et al. (2003). A gene expression atlas of the central nervous system based on bacterial artificial chromosomes. *Nature* 425, 917–925. doi: 10.1038/nature02033

Griff, E. R., Mafhouz, M., and Chaput, M. A. (2008). Comparison of identified mitral and tufted cells in freely breathing rats: II. Odor-evoked responses. *Chem. Senses* 33, 793–802. doi: 10.1093/chemse/bjn040

Grosmaitre, X., Santarelli, L. C., Tan, J., Luo, M., and Ma, M. (2007). Dual functions of mammalian olfactory sensory neurons as odor detectors and mechanical sensors. *Nat. Neurosci.* 10, 348–354. doi: 10.1038/nn1856

Haberly, L. B. (2001). Parallel-distributed processing in olfactory cortex: new insights from morphological and physiological analysis of neuronal circuitry. *Chem. Senses* 26, 551–576. doi: 10.1093/chemse/26.5.551

Haberly, L. B., and Price, J. L. (1977). The axonal projection patterns of the mitral and tufted cells of the olfactory bulb in the rat. *Brain Res.* 129, 152–157. doi: 10.1016/0006-8993(77)90978-7

Haberly, L. B., and Price, J. L. (1978). Association and commissural fiber systems of the olfactory cortex of the rat. *J. Comp. Neurol.* 178, 711–740. doi: 10.1002/cne.901780408

Hagiwara, A., Pal, S. K., Sato, T. F., Wienisch, M., and Murthy, V. N. (2012). Optophysiological analysis of associational circuits in the olfactory cortex. *Front. Neural Circuits* 6:18. doi: 10.3389/fncir.2012.00018

Ichikawa, T., and Hirata, Y. (1986). Organization of choline acetyltransferase-containing structures in the forebrain of the rat. *J. Neurosci.* 6, 281–292.

Illig, K. R., and Eudy, J. D. (2009). Contralateral projections of the rat anterior olfactory nucleus. *J. Comp. Neurol.* 512, 115–123. doi: 10.1002/cne.21900

Karpov, A. P. (1980). "Analysis of neuron activity in the rabbit's olfactory bulb during food-acquisition behavior," in *Neural Mechanisms of Goal-Directed Behavior and Learning*, eds R. F. Thompson, L. H. Hicks and V. B. Shvyrkov (New York: Academic Press), 273–282.

Kass, M. D., Rosenthal, M. C., Pottackal, J., and Mcgann, J. P. (2013). Fear learning enhances neural responses to threat-predictive sensory stimuli. *Science* 342, 1389–1392. doi: 10.1126/science.1244916

Kato, H. K., Chu, M. W., Isaacson, J. S., and Komiyama, T. (2012). Dynamic sensory representations in the olfactory bulb: modulation by wakefulness and experience. *Neuron* 76, 962–975. doi: 10.1016/j.neuron.2012.09.037

Kay, R. B., and Brunjes, P. C. (2014). Diversity among principal and GABAergic neurons of the anterior olfactory nucleus. *Front. Cell. Neurosci.* 8:111. doi: 10.3389/fncel.2014.00111

Kay, L. M., and Laurent, G. (1999). Odor- and context-dependent modulation of mitral cell activity in behaving rats. *Nat. Neurosci.* 2, 1003–1009. doi: 10.1038/14801

Kay, R. B., Meyer, E. A., Illig, K. R., and Brunjes, P. C. (2011). Spatial distribution of neural activity in the anterior olfactory nucleus evoked by odor and electrical stimulation. *J. Comp. Neurol.* 519, 277–289. doi: 10.1002/cne.22519

Kikuta, S., Sato, K., Kashiwadani, H., Tsunoda, K., Yamasoba, T., and Mori, K. (2010). Neurons in the anterior olfactory nucleus pars externa detect right or left localization of odor sources. *Proc. Natl. Acad. Sci. U S A* 107, 12363–12368. doi: 10.1073/pnas.1003999107

Lei, H., Mooney, R., and Katz, L. C. (2006). Synaptic integration of olfactory information in mouse anterior olfactory nucleus. *J. Neurosci.* 26, 12023–12032. doi: 10.1523/jneurosci.2598-06.2006

Li, J., Ishii, T., Feinstein, P., and Mombaerts, P. (2004). Odorant receptor gene choice is reset by nuclear transfer from mouse olfactory sensory neurons. *Nature* 428, 393–399. doi: 10.1038/nature02433

Linster, C., Wyble, B. P., and Hasselmo, M. E. (1999). Electrical stimulation of the horizontal limb of the diagonal band of broca modulates population EPSPs in piriform cortex. *J. Neurophysiol.* 81, 2737–2742.

Luiten, P. G., Gaykema, R. P., Traber, J., and Spencer, D. G. Jr. (1987). Cortical projection patterns of magnocellular basal nucleus subdivisions as revealed by anterogradely transported Phaseolus vulgaris leucoagglutinin. *Brain Res.* 413, 229–250. doi: 10.1016/0006-8993(87)91014-6

Luskin, M. B., and Price, J. L. (1983). The topographic organization of associational fibers of the olfactory system in the rat, including centrifugal fibers to the olfactory bulb. *J. Comp. Neurol.* 216, 264–291. doi: 10.1002/cne.902160305

Ma, L., Qiu, Q., Gradwohl, S., Scott, A., Yu, E. Q., Alexander, R., et al. (2012). Distributed representation of chemical features and tunotopic organization of glomeruli in the mouse olfactory bulb. *Proc. Natl. Acad. Sci. U S A* 109, 5481–5486. doi: 10.1073/pnas.1117491109

Macrides, F., Davis, B. J., Youngs, W. M., Nadi, N. S., and Margolis, F. L. (1981). Cholinergic and catecholaminergic afferents to the olfactory bulb in the hamster: a neuroanatomical, biochemical and histochemical investigation. *J. Comp. Neurol.* 203, 495–514. doi: 10.1002/cne.902030311

Macrides, F., and Schneider, S. P. (1982). Laminar organization of mitral and tufted cells in the main olfactory bulb of the adult hamster. *J. Comp. Neurol.* 208, 419–430. doi: 10.1002/cne.902080410

Markopoulos, F., Rokni, D., Gire, D. H., and Murthy, V. N. (2012). Functional properties of cortical feedback projections to the olfactory bulb. *Neuron* 76, 1175–1188. doi: 10.1016/j.neuron.2012.10.028

Matsutani, S. (2010). Trajectory and terminal distribution of single centrifugal axons from olfactory cortical areas in the rat olfactory bulb. *Neuroscience* 169, 436–448. doi: 10.1016/j.neuroscience.2010.05.001

Matsutani, S., and Yamamoto, N. (2008). Centrifugal innervation of the mammalian olfactory bulb. *Anat. Sci. Int.* 83, 218–227. doi: 10.1111/j.1447-073x.2007.00223.x

Mclean, J. H., and Shipley, M. T. (1987). Serotonergic afferents to the rat olfactory bulb: I. Origins and laminar specificity of serotonergic inputs in the adult rat. *J. Neurosci.* 7, 3016–3028.

McLean, J. H., Shipley, M. T., Nickell, W. T., Aston-Jones, G., and Reyher, C. K. (1989). Chemoanatomical organization of the noradrenergic input from locus coeruleus to the olfactory bulb of the adult rat. *J. Comp. Neurol.* 285, 339–349. doi: 10.1002/cne.902850305

Meyer, E. A., Illig, K. R., and Brunjes, P. C. (2006). Differences in chemo- and cytoarchitectural features within pars principalis of the rat anterior olfactory nucleus suggest functional specialization. *J. Comp. Neurol.* 498, 786–795. doi: 10.1002/cne.21077

Meyer, F., and Louilot, A. (2012). Early prefrontal functional blockade in rats results in schizophrenia-related anomalies in behavior and dopamine. *Neuropsychopharmacology* 37, 2233–2243. doi: 10.1038/npp.2012.74

Miyamichi, K., Amat, F., Moussavi, F., Wang, C., Wickersham, I., Wall, N. R., et al. (2011). Cortical representations of olfactory input by trans-synaptic tracing. *Nature* 472, 191–196. doi: 10.1038/nature09714

Nagayama, S., Enerva, A., Fletcher, M. L., Masurkar, A. V., Igarashi, K. M., Mori, K., et al. (2010). Differential axonal projection of mitral and tufted cells in the mouse main olfactory system. *Front. Neural Circuits* 4:120. doi: 10.3389/fncir.2010.00120

Nagayama, S., Takahashi, Y. K., Yoshihara, Y., and Mori, K. (2004). Mitral and tufted cells differ in the decoding manner of odor maps in the rat olfactory bulb. *J. Neurophysiol.* 91, 2532–2540. doi: 10.1152/jn.01266.2003

Niell, C. M., and Stryker, M. P. (2010). Modulation of visual responses by behavioral state in mouse visual cortex. *Neuron* 65, 472–479. doi: 10.1016/j.neuron.2010.01.033

Nunez-Parra, A., Li, A., and Restrepo, D. (2014). Coding odor identity and odor value in awake rodents. *Prog. Brain Res.* 208, 205–222. doi: 10.1016/b978-0-444-63350-7.00008-5

Nunez-Parra, A., Maurer, R. K., Krahe, K., Smith, R. S., and Araneda, R. C. (2013). Disruption of centrifugal inhibition to olfactory bulb granule cells impairs olfactory discrimination. *Proc. Natl. Acad. Sci. U S A* 110, 14777–14782. doi: 10.1073/pnas.1310686110

Ojima, H., Yamasaki, T., Kojima, H., and Akashi, A. (1988). Cholinergic innervation of the main and the accessory olfactory bulbs of the rat as revealed by a monoclonal antibody against choline acetyltransferase. *Anat. Embryol. (Berl)* 178, 481–488. doi: 10.1007/bf00305035

Paxinos, G., and Franklin, K. B. J. (2001). *The Mouse Brain in Stereotaxic Coordinates*. 2nd Edn. San Diego: Academic Press.

Petreanu, L., Gutnisky, D. A., Huber, D., Xu, N. L., O'connor, D. H., Tian, L., et al. (2012). Activity in motor-sensory projections reveals distributed coding in somatosensation. *Nature* 489, 299–303. doi: 10.1038/nature11321

Petrovich, G. D., Risold, P. Y., and Swanson, L. W. (1996). Organization of projections from the basomedial nucleus of the amygdala: a PHAL study in the rat. *J. Comp. Neurol.* 374, 387–420. doi: 10.1002/(sici)1096-9861(19961021)374:3<387::aid-cne6>3.0.co;2-y

Petzold, G. C., Hagiwara, A., and Murthy, V. N. (2009). Serotonergic modulation of odor input to the mammalian olfactory bulb. *Nat. Neurosci.* 12, 784–791. doi: 10.1038/nn.2335

Pologruto, T., Sabatini, B., and Svoboda, K. (2003). ScanImage: flexible software for operating laser scanning microscopes. *Biomed. Eng. Online* 2:13. doi: 10.1186/1475-925X-2-13

Price, J. L., and Powell, T. P. (1970). An experimental study of the origin and the course of the centrifugal fibres to the olfactory bulb in the rat. *J. Anat.* 107, 215–237.

Rabbitt, R. D., and Brownell, W. E. (2011). Efferent modulation of hair cell function. *Curr. Opin. Otolaryngol. Head Neck Surg.* 19, 376–381. doi: 10.1097/MOO.0b013e32834a5be1

Reyher, C. K., Schwerdtfeger, W. K., and Baumgarten, H. G. (1988). Interbulbar axonal collateralization and morphology of anterior olfactory nucleus neurons in the rat. *Brain Res. Bull.* 20, 549–566. doi: 10.1016/0361-9230(88)90214-6

Rogers, S. W., and Gahring, L. C. (2012). Nicotinic receptor Alpha7 expression during tooth morphogenesis reveals functional pleiotropy. *PLoS One* 7:e36467. doi: 10.1371/journal.pone.0036467

Rogers, S. W., Myers, E. J., and Gahring, L. C. (2012a). The expression of nicotinic receptor alpha7 during cochlear development. *Brain Behav.* 2, 628–639. doi: 10.1002/brb3.84

Rogers, S. W., Tvrdik, P., Capecchi, M. R., and Gahring, L. C. (2012b). Prenatal ablation of nicotinic receptor alpha7 cell lineages produces lumbosacral spina bifida the severity of which is modified by choline and nicotine exposure. *Am. J. Med. Genet. A* 158A, 1135–1144. doi: 10.1002/ajmg.a.35372

Rothermel, M., Brunert, D., Zabawa, C., Díaz-Quesada, M., and Wachowiak, M. (2013). Transgene expression in target-defined neuron populations mediated by retrograde infection with adeno-associated viral vectors. *J. Neurosci.* 33, 15195–15206. doi: 10.1523/JNEUROSCI.1618-13.2013

Rothermel, M., Carey, R. M., Puche, A., Shipley, M. T., and Wachowiak, M. (2014). Cholinergic inputs from basal forebrain add an excitatory bias to odor coding in the olfactory bulb. *J. Neurosci.* 34, 4654–4664. doi: 10.1523/JNEUROSCI.5026-13.2014

Schneider, S. P., and Scott, J. W. (1983). Orthodromic response properties of rat olfactory bulb mitral and tufted cells correlate with their projection patterns. *J. Neurophysiol.* 50, 358–378.

Schoenfeld, T. A., and Macrides, F. (1984). Topographic organization of connections between the main olfactory bulb and pars externa of the anterior olfactory nucleus in the hamster. *J. Comp. Neurol.* 227, 121–135. doi: 10.1002/cne.902270113

Schoenfeld, T. A., Marchand, J. E., and Macrides, F. (1985). Topographic organization of tufted cell axonal projections in the hamster main olfactory bulb: an intrabulbar associational system. *J. Comp. Neurol.* 235, 503–518. doi: 10.1002/cne.902350408

Scott, J. W. (1981). Electrophysiological identification of mitral and tufted cells and distributions of their axons in olfactory system of the rat. *J. Neurophysiol.* 46, 918–931.

Scott, J. W., Mcbride, R. L., and Schneider, S. P. (1980). The organization of projections from the olfactory bulb to the piriform cortex and olfactory tubercle in the rat. *J. Comp. Neurol.* 194, 519–534. doi: 10.1002/cne.901940304

Scott, J. W., Ranier, E. C., Pemberton, J. L., Orona, E., and Mouradian, L. E. (1985). Pattern of rat olfactory bulb mitral and tufted cell connections to the anterior

olfactory nucleus pars externa. *J. Comp. Neurol.* 242, 415–424. doi: 10.1002/cne.902420309

Shea, S. D., Katz, L. C., and Mooney, R. (2008). Noradrenergic induction of odor-specific neural habituation and olfactory memories. *J. Neurosci.* 28, 10711–10719. doi: 10.1523/JNEUROSCI.3853-08.2008

Shipley, M. T., and Adamek, G. D. (1984). The connections of the mouse olfactory bulb: a study using orthograde and retrograde transport of wheat germ agglutinin conjugated to horseradish peroxidase. *Brain Res. Bull.* 12, 669–688. doi: 10.1016/0361-9230(84)90148-5

Shipley, M. T., Halloran, F. J., and de la Torre, J. (1985). Surprisingly rich projection from locus coeruleus to the olfactory bulb in the rat. *Brain Res.* 329, 294–299. doi: 10.1016/0006-8993(85)90537-2

Shusterman, R., Smear, M. C., Koulakov, A. A., and Rinberg, D. (2011). Precise olfactory responses tile the sniff cycle. *Nat. Neurosci.* 14, 1039–1044. doi: 10.1038/nn.2877

Soria-Gómez, E., Bellocchio, L., Reguero, L., Lepousez, G., Martin, C., Bendahmane, M., et al. (2014). The endocannabinoid system controls food intake via olfactory processes. *Nat. Neurosci.* 17, 407–415. doi: 10.1038/nn.3647

Sosulski, D. L., Lissitsyna Bloom, M., Cutforth, T., Axel, R., and Datta, S. R. (2011). Distinct representations of olfactory information in different cortical centres. *Nature* 472, 213–216. doi: 10.1038/nature09868

Soucy, E. R., Albeanu, D. F., Fantana, A. L., Murthy, V. N., and Meister, M. (2009). Precision and diversity in an odor map on the olfactory bulb. *Nat. Neurosci.* 12, 210–220. doi: 10.1038/nn.2262

Spors, H., Wachowiak, M., Cohen, L. B., and Friedrich, R. W. (2006). Temporal dynamics and latency patterns of receptor neuron input to the olfactory bulb. *J. Neurosci.* 26, 1247–1259. doi: 10.1523/jneurosci.3100-05.2006

Stratford, T. R., and Wirtshafter, D. (2012). Effects of muscimol, amphetamine and DAMGO injected into the nucleus accumbens shell on food-reinforced lever pressing by undeprived rats. *Pharmacol. Biochem. Behav.* 101, 499–503. doi: 10.1016/j.pbb.2012.02.010

Strowbridge, B. W. (2009). Role of cortical feedback in regulating inhibitory microcircuits. *Ann. N Y Acad. Sci.* 1170, 270–274. doi: 10.1111/j.1749-6632.2009.04018.x

Swanson, L. W., and Cowan, W. M. (1977). An autoradiographic study of the organization of the efferent connections of the hippocampal formation in the rat. *J. Comp. Neurol.* 172, 49–84. doi: 10.1002/cne.901720104

Tian, L., Hires, S. A., Mao, T., Huber, D., Chiappe, M. E., Chalasani, S. H., et al. (2009). Imaging neural activity in worms, flies and mice with improved GCaMP calcium indicators. *Nat. Methods* 6, 875–881. doi: 10.1038/nmeth.1398

Valverde, F., Lopez-Mascaraque, L., and De Carlos, J. A. (1989). Structure of the nucleus olfactorius anterior of the hedgehog (Erinaceus europaeus). *J. Comp. Neurol.* 279, 581–600. doi: 10.1002/cne.902790407

van Groen, T., and Wyss, J. M. (1990). Extrinsic projections from area CA1 of the rat hippocampus: olfactory, cortical, subcortical and bilateral hippocampal formation projections. *J. Comp. Neurol.* 302, 515–528. doi: 10.1002/cne.903020308

Verhagen, J. V., Wesson, D. W., Netoff, T. I., White, J. A., and Wachowiak, M. (2007). Sniffing controls an adaptive filter of sensory input to the olfactory bulb. *Nat. Neurosci.* 10, 631–639. doi: 10.1038/nn1892

Wachowiak, M., and Cohen, L. B. (2001). Representation of odorants by receptor neuron input to the mouse olfactory bulb. *Neuron* 32, 723–735. doi: 10.1016/s0896-6273(01)00506-2

Wachowiak, M., Economo, M. N., Díaz-Quesada, M., Brunert, D., Wesson, D. W., White, J. A., et al. (2013). Optical dissection of odor information processing in vivo using GCaMPs expressed in specified cell types of the olfactory bulb. *J. Neurosci.* 33, 5285–5300. doi: 10.1523/JNEUROSCI.4824-12.2013

Weeg, M. S., Land, B. R., and Bass, A. H. (2005). Vocal pathways modulate efferent neurons to the inner ear and lateral line. *J. Neurosci.* 25, 5967–5974. doi: 10.1523/jneurosci.0019-05.2005

Wesson, D. W., Carey, R. M., Verhagen, J. V., and Wachowiak, M. (2008). Rapid encoding and perception of novel odors in the rat. *PLoS Biol.* 6:e82. doi: 10.1371/journal.pbio.0060082

Woolf, N. J., Eckenstein, F., and Butcher, L. L. (1984). Cholinergic systems in the rat brain: I. projections to the limbic telencephalon. *Brain Res. Bull.* 13, 751–784. doi: 10.1016/0361-9230(84)90236-3

Yan, Z., Tan, J., Qin, C., Lu, Y., Ding, C., and Luo, M. (2008). Precise circuitry links bilaterally symmetric olfactory maps. *Neuron* 58, 613–624. doi: 10.1016/j.neuron.2008.03.012

Zaborszky, L., Van Den Pol, A. N., and Gyengesi, E. (2012). "The basal forebrain cholinergic projection system in mice," in *The Mouse Nervous System*, eds C. Watson, G. Paxinos and L. Puelles (Amsterdam: Elsevier), 684–718.

Zariwala, H. A., Borghuis, B. G., Hoogland, T. M., Madisen, L., Tian, L., De Zeeuw, C. I., et al. (2012). A cre-dependent GCaMP3 reporter mouse for neuronal imaging in vivo. *J. Neurosci.* 32, 3131–3141. doi: 10.1523/JNEUROSCI.4469-11.2012

Zhuravin, I. A., and Bures, J. (1991). Extent of the tetrodotoxin induced blockade examined by pupillary paralysis elicited by intracerebral injection of the drug. *Exp. Brain Res.* 83, 687–690. doi: 10.1007/bf00229849

Conflict of Interest Statement: The authors declare that the research was conducted in the absence of any commercial or financial relationships that could be construed as a potential conflict of interest.

Received: 02 May 2014; accepted: 12 June 2014; published online: 03 July 2014.
Citation: Rothermel M and Wachowiak M (2014) Functional imaging of cortical feedback projections to the olfactory bulb. Front. Neural Circuits ***8****:73. doi: 10.3389/fncir.2014.00073*
This article was submitted to the journal Frontiers in Neural Circuits.

frontiers in
NEURAL CIRCUITS

REVIEW ARTICLE
published: 23 April 2014
doi: 10.3389/fncir.2014.00037

A new era for functional labeling of neurons: activity-dependent promoters have come of age

Takashi Kawashima[1†], Hiroyuki Okuno[1†] and Haruhiko Bito[1,2]*

[1] *Department of Neurochemistry, Graduate School of Medicine, The University of Tokyo, Tokyo, Japan*
[2] *Core Research for Evolutionary Science and Technology, Japan Science and Technology Agency, Saitama, Japan*

Edited by:
Benjamin R. Arenkiel, Baylor College of Medicine, USA

Reviewed by:
Jason D. Shepherd, University of Utah, USA
Matthew Kennedy, University of Colorado Denver, School of Medicine, USA

***Correspondence:**
Haruhiko Bito, Department of Neurochemistry, Graduate School of Medicine, The University of Tokyo, 7-3-1 Hongo, Bunkyo-ku, Tokyo 113-0033, Japan
e-mail: hbito@m.u-tokyo.ac.jp

†Present address:
Takashi Kawashima, Howard Hughes Medical Institute, Janelia Farm Research Campus, Ashburn, VA, USA; Hiroyuki Okuno, Medical Innovation Center, Kyoto University Graduate School of Medicine, Kyoto, Japan

Genetic labeling of neurons with a specific response feature is an emerging technology for precise dissection of brain circuits that are functionally heterogeneous at the single-cell level. While immediate early gene mapping has been widely used for decades to identify brain regions which are activated by external stimuli, recent characterization of the promoter and enhancer elements responsible for neuronal activity-dependent transcription have opened new avenues for live imaging of active neurons. Indeed, these advancements provided the basis for a growing repertoire of novel experiments to address the role of active neuronal networks in cognitive behaviors. In this review, we summarize the current literature on the usage and development of activity-dependent promoters and discuss the future directions of this expanding new field.

Keywords: *Arc*, neuronal ensemble, E-SARE, live imaging, activity-dependent gene expression, c-*fos*

INTRODUCTION

The central nervous systems of animals, including insects, vertebrates, and primates, are controlled by coordinated action of multiple brain regions. Each brain region consists of thousands of homologous neurons composed of multiple anatomical types. Interestingly, functional neuronal subsets that share similar response features or are coactivated during one behavioral task are usually sparsely scattered within homologous neural populations. For example, in the visual cortex of rodents, neurons of different orientation preferences are intermingled together at the single-cell level (Ohki et al., 2005). Thus, for precise understanding of circuit dynamics underlying cognitive brain function at the cellular level, it is of primary importance to selectively label these functionally defined subsets of neurons and analyze their nature in detail.

One approach towards this goal is to use genomic sequences, e.g., promoters and enhancers, that control the expression of neuronal immediate early genes (IEGs) which are rapidly induced by neuronal activity (Smeyne et al., 1992; Barth, 2007; Inoue et al., 2010; Okuno, 2011). The mechanisms underlying such gene induction events have been characterized in detail in the past. When a neuron receives large amounts of synaptic inputs, calcium ions rapidly flow into neurons through synaptic N-methyl-D-aspartic acid (NMDA) receptors or voltage-gated calcium channels (VGCCs). This turns on several calcium-dependent kinase cascades, which then activate a set of transcription factors and trigger rapid induction of target genes (Bito et al., 1997; Flavell and Greenberg, 2008). In combination with a variety of reporter proteins that can be driven to label neurons, IEG promoters have thus been exploited to map neuronal activation patterns associated with a specific animal sensation or behavior at a cellular resolution.

Among neuronal IEGs, promoters for c-*fos* (Schilling et al., 1991) and *Arc/Arg*3.1 (Waltereit et al., 2001; Kawashima et al., 2009; Pintchovski et al., 2009) were well characterized and widely used as a tool to facilitate neuronal activity mapping *in situ* on histological sections. The availability of novel genetic methods to artificially manipulate neural activity further provided an opportunity to expand the application of activity-dependent promoters, to address new questions in anatomical, electrophysiological, and cognitive research. The promoter of c-*fos* was successfully employed for investigating the formation of memory engram in rodents (Garner et al., 2012; Liu et al., 2012; Ramirez et al., 2013). Furthermore, the promoter of *Arc/Arg*3.1 was successfully employed for live imaging of cortical activation both at the cellular scale (Wang et al., 2006; Kawashima et al., 2013) and at the whole-cortex scale (Eguchi and Yamaguchi, 2009; Izumi et al., 2011). Recently, a novel activity-dependent promoter E-SARE (enhanced synaptic activity-responsive element) was engineered, which enabled an activity-based, long-distance axonal tracing in living animals (Kawashima et al., 2013). In this review, we summarize the latest advances and discuss future directions of this expanding new field.

THE RISE OF BRAIN ACTIVITY MAPPING BASED ON IEG EXPRESSION

During the 1970s, several important strategies were developed to selectively label activated brain regions. The first visualization was achieved by the autoradiography of a metabolic marker 2-deoxy-D-glucose (2-DG; Sokoloff et al., 1977). 2-DG was incorporated into tissues with ongoing high energy consumption and, since it could not undergo glycolysis, remained in the incorporated tissue. In the brain, 2-DG was incorporated into active brain regions, serving as a marker for neuronal activation. A less invasive, blood oxygenation level dependent (BOLD) contrast-based method further enabled functional magnetic resonance imaging of live brain activity (Ogawa et al., 1990). However, these whole-brain tissue imaging showed only limited spatial resolution and did not confer cellular resolution.

The first activity mapping with cellular resolution was achieved by immunostaining of inducible gene expression. Preceding studies showed that the proto-oncogene c-*fos* in cultured cells could be rapidly induced by application of growth factors (Greenberg and Ziff, 1984; Müller et al., 1984; Curran and Morgan, 1985). Taking advantage of this, neurons in the brain that were activated by electrical seizure, tactile stimulation, and water starvation were visualized by immunostaining of c-Fos (Morgan et al., 1987; Sagar et al., 1988). Largely based on these pioneering studies, monitoring of up-regulated expression of IEGs, such as c-*fos* or *zif*268/*egr*-1 (Saffen et al., 1988), and also of activated transcription factors, such as phosphorylated cAMP response element-binding protein (CREB) (Ginty et al., 1993; Bito et al., 1996; Deisseroth et al., 1996), either using immunostaining or *in situ* hybridization, has become accepted as a widely applicable method to map activated circuits at cellular scale.

Attempts to identify activity-induced genes in the hippocampus led to the cloning of a new IEG, *Arc* (aka *Arg*3.1; Link et al., 1995; Lyford et al., 1995). Subsequently, the unique transport kinetics of *Arc* mRNAs from nucleus to cytoplasm was exploited to build a catFISH (cellular compartment analysis of temporal activity by fluorescent *in situ* hybridization) assay: by examining the differential localization of *Arc* mRNA, distinct neuronal ensembles that were activated in two different environments at a 20 min interval could be clearly discriminated (Guzowski et al., 1999). Detailed spatiotemporal analyses of *Arc* expression further indicated a strong correlation between *Arc* induction with cognitive behavior in normal as well as aged animals (Small et al., 2004; Ramírez-Amaya et al., 2005; Hartzell et al., 2013).

However, the signal-to-noise ratio of gene expression mapping heavily depended on the labeling protocol and the quality of antibodies or hybridization probes, which sometimes caused high variability/low reliability of the mapping results. To address this issue, the promoter of the c-*fos* gene was isolated and fused with an expression cassette of a reporter protein, beta-galactosidase (LacZ; Schilling et al., 1991). This led to a generation of *fos-lacZ* transgenic mice and enabled the activity mapping at a cellular scale with higher signal-to-noise ratio based on β-gal staining (Smeyne et al., 1992; Robertson et al., 1995). These studies also demonstrated the utility of IEG promoters as a versatile tool to label a functionally defined subset of neurons within a heterogeneous neural population.

BRAIN ACTIVITY MAPPING BASED ON ACTIVITY-DEPENDENT PROMOTERS

Following the generation of the first line of *fos-lacZ* mice, several other transgenic mice that expressed *lacZ* downstream of activity-dependent promoters were generated such as cAMP response element (CRE)-*lacZ* (Impey et al., 1996), *egr*-1-*lacZ* (Tsai et al., 2000) and *fos-tau-lacZ* (Wilson et al., 2002) mice. These *lacZ* transgenic mice enabled histological visualization of active circuits during seizure (Smeyne et al., 1992), development during critical period (Pham et al., 1999) and water deprivation (Wilson et al., 2002). The reliance on LacZ as a reporter, however, required fixation and staining of tissue sections, and this method was therefore not suited for anatomical and physiological investigation of live animals. Furthermore, the relative stability of the LacZ reporter protein caused a high signal background, thus hampering a clean mapping of authentic neural activity.

With the advent and improvement of fluorescent proteins, the destabilized green fluorescent protein (GFP) has become the preferred choice as a reporter of activity-dependent promoters in transgenic mice and virus vectors (Barth et al., 2004; Wang et al., 2006; Eguchi and Yamaguchi, 2009; Grinevich et al., 2009; Kawashima et al., 2009; Okuno et al., 2012). As GFP fluorescence enabled high S/N observation of live neurons, these mice and virus vectors widely expanded the scope of gene expression mapping based on activity-dependent promoters. Two-photon fluorescence microscopy visualized orientation-specific neuronal activation in living animals at single-cell resolution (Wang et al., 2006; Kawashima et al., 2013). Fluorescent live imaging of whole cortical areas revealed brain regions that were visually activated (Eguchi and Yamaguchi, 2009; Grinevich et al., 2009). The use of a bioluminescent protein, *firefly* luciferase, also enabled visualization of plastic changes in sensory cortices after sensory deprivation (Wada et al., 2010; Izumi et al., 2011).

One drawback of activity mapping based on histological methods is the time-consuming and labor-intensive processing and analysis of histological sections. However, a recent technological advancement, a serial two-photon tomography (STP; Ragan et al., 2012), holds great promise for overcoming this bottleneck. This technique allows automated acquisition of fluorescent images of a histological block surface, which is sequentially cut by an automated microtome. This dramatically reduces the burden of manually preparing serial histological sections and enables serial acquisition of fluorescent images of the entire mouse brain within a couple of days. When appropriately combined with transgenic mice expressing fluorescent reporters downstream of activity-dependent promoters (Osten and Margrie, 2013), this technique provides whole-brain datasets of cellular level activation under various behavioral conditions (Vousden et al., in press).

NEURONAL CELL TYPES LABELED BY THE ACTIVITY-DEPENDENT GENE PROMOTERS

Accumulating histological evidences suggest that activity-dependent genes are differentially regulated in different cell types in distinct brain areas. In the neocortex and the hippocampus, IEGs are mostly up-regulated in excitatory pyramidal neurons (Chaudhuri et al., 1995; Filipkowski, 2000), although inhibitory neurons can also express some IEGs, such as c-*fos* and *Arc*,

after strong stimulation (Staiger et al., 2002; Vazdarjanova et al., 2006). In contrast, inhibitory granule cells, rather than excitatory mitral cells, mainly express c-*fos* and *Arc* in the olfactory bulb (Guenthner et al., 2013). In the striatum, *Arc* and *egr*-1, but not c-*fos*, are strongly expressed by GABAergic medium spiny neurons (Moratalla et al., 1993; Vazdarjanova et al., 2006; Guenthner et al., 2013). In contrast, thalamic areas tend to express c-*fos* rather than *Arc* or *egr*-1 (Steiner and Gerfen, 1994; Link et al., 1995; Lyford et al., 1995). In the cerebellum, c-*fos* is more expressed than *Arc* in excitatory granule cells (Guenthner et al., 2013), while both c-*fos* and *Arc* can be expressed in cerebellar Purkinje cells (Tian and Bishop, 2002; Smith-Hicks et al., 2010; Mikuni et al., 2013).

Such a variety in cell-type and regional specificity of activity-regulated IEG expression is thought arise from a combination of distinct transcriptional regulation and cellular calcium kinetics. Reporter expression from isolated promoter elements also appears to recapitulate the cell-type or regional preference of the original genes (Eguchi and Yamaguchi, 2009; Yassin et al., 2010; Kawashima et al., 2013). This suggests that it is of primary importance to select the type of activity-dependent promoters depending on the target cell type and brain region in which one wishes to achieve significant activity-dependent reporter expression. Also, to the best of our knowledge, there are as yet no IEGs that are expressed exclusively in a particular cell type, such as GABAergic or dopaminergic. It would thus seem a worthy challenge to seek and characterize novel IEGs and design new synthetic activity-dependent promoters that possess restricted cell-type preferences.

MECHANISMS UNDERLYING ACTIVATION OF ACTIVITY-DEPENDENT GENE PROMOTERS

The mechanisms underlying activation of IEG promoters have been the subject of detailed studies for decades. These core regulatory mechanisms may be largely divided into three steps: influx of calcium ions triggered by synaptic inputs and neural firing, activation of calcium-dependent kinase cascades, and activation of transcription factors by kinases (Bito et al., 1997; Flavell and Greenberg, 2008). When a neuron receives intense synaptic inputs, calcium ions flow into the cytoplasm through NMDA-type glutamate receptors (NMDARs) present at activated synapses as well as through VGCCs that open upon neuronal firing. This in turn stimulates the activation of several calcium-dependent kinase cascades, that comprise Ca^{2+}/calmodulin-dependent protein kinases (CaMKs; Bito et al., 1996; Fujii et al., 2013) and mitogen-activated protein kinases (MAPKs; Dolmetsch et al., 2001; Zhai et al., 2013). Finally, activation of these kinases cascades leads to site-specific modulation of activity-dependent transcription factors, such as CREB (Bito et al., 1996), myocyte enhancer factor-2 (MEF2; Mao et al., 1999), and serum-responsive factor (SRF; Norman et al., 1988), thereby turning on rapid transcription of downstream IEGs.

We recently discovered a SARE from the *Arc* promoter/enhancer region (Kawashima et al., 2009). Our studies on SARE revealed that three different transcription factors, CREB, MEF2, and SRF, cooperated within this ∼100 bp locus to induce activity-dependent transcription that was substantially more potent than through the action of each individual factor alone. This finding demonstrated that activity-dependent promoters performed a supralinear integration of the output of several co-activated signaling pathways, in keeping with previous analyses on c-*fos* (Robertson et al., 1995) and *bdnf* promoters (West et al., 2001).

At the physiological level, activation of IEG promoters is thought to be an event critical for the conversion of short-term stimuli that transiently activate neurons (with a timescale of milliseconds to minutes) into a long-term neuronal plasticity that requires gene expression (with a timescale of days to years). Such an ability to re-scale information in the time axis seems to be one of the key features of IEG promoter activity, and this may be pivotal in producing persistent traces of neuronal activity. Thus, once a subset of neurons received external stimuli during plasticity induction, they may express a "plasticity-related reporter protein" for a certain period of time (from several hours to a couple of days). Consistently blockade of activity-dependent gene expression pathways led to strong impairment of late-phase LTP and long-term memory without affecting early phase LTP and short-term memory (Bourtchuladze et al., 1994; Abel et al., 1997; Kang et al., 2001; Kida et al., 2002).

ENGINEERING A POTENT SYNTHETIC ACTIVITY-DEPENDENT PROMOTER

Although a large amount of effort has been spent in the past on the application of activity-dependent IEG promoters, very little effort was made to improve endogenous promoters, and create an experimentally optimized synthetic activity-dependent promoter. Notable exceptions were the use of synthetic binding sites for activity-regulated transcription factors (such as multiplexed CRE) to drive expression of several reporter proteins (Impey et al., 1996; Böer et al., 2007). In most of these cases, however, the expression levels of the reporters remained relatively weak, presumably because these artificial promoters did not adequately replicate the coordinated action of multiple transcription factors as found in the context of endogenous IEG promoters (Kawashima et al., 2009).

Recently, a novel engineered synthetic promoter, E-SARE, was successfully constructed based on the SARE enhancer element of the *Arc* promoter (Kawashima et al., 2009, 2013; **Figure 1**). The SARE element had a unique "modular" structure: it was short (∼100 base pairs); it had cooperative binding sites for three activity-dependent transcription factors, CREB, MEF2, and SRF/TCF; and this element was sufficient to induce a strong transcription independently of the type of the downstream minimal promoters that contains TATA-box (Kawashima et al., 2009). To generate an enhanced promoter based on this modularity, multiple SARE elements were connected in tandem with an adequate linker length. We found combinations with a 5 tandem repeat to yield a sevenfold increase in the reporter expression level. The resulting synthetic promoter, E-SARE, had more than 20-fold higher expression level and 30-fold higher induction ratio than the c-*fos* promoter (Kawashima et al., 2013; **Figure 1**).

The discovery of SARE and the resulting rational synthesis of the E-SARE promoter was a significant breakthrough, not only because this expanded the palette of available activity-regulated promoters, but mainly because this greatly facilitated the introduction of viral vector strategies into the labeling of active

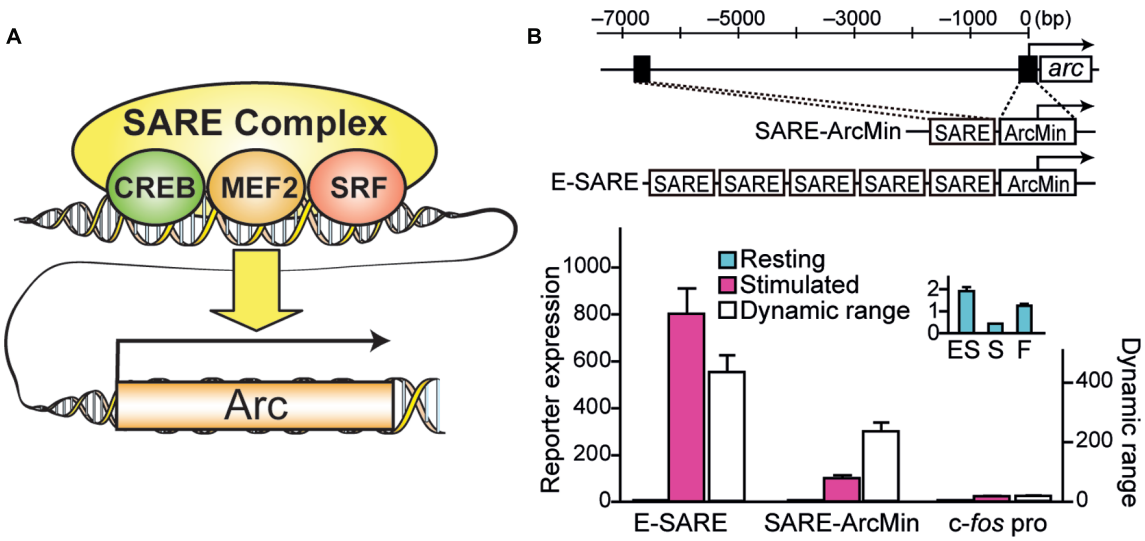

FIGURE 1 | Engineering of a synthetic E-SARE promoter. (A) The structure of SARE enhancer element which regulates activity-dependent expression of *Arc/Arg3.1*. Three distinct transcription factors, CREB, MEF2, and SRF, cooperate to induce strong transcription. **(B)** Top, construction strategy of E-SARE promoter. The locations of SARE and TATA-containing ArcMin in the *Arc* promoter are represented by black boxes. E-SARE is constructed by connecting SARE elements in tandem. Bottom, comparison of E-SARE with SARE-ArcMin and c-*fos* promoters by luciferase reporter assay in cultured neurons under resting (blue) and stimulated (pink) conditions. Dynamic ranges (calculated based on the ratio between stimulated and resting conditions; white) are also shown. Inset, expanded values obtained under resting conditions. Adapted from Kawashima et al. (2013).

neuronal ensemble. Because of their shortness (<1000 base pairs) and high reporter expression, SARE and E-SARE can be implemented into viral vector backbones such as lentivirus (LV) and adeno-associated virus (AAV), both of which have relatively limited genomic capacities, while allowing substantial flexibility in expression cassette design. As compared with developing transgenic rodents, viral vectors have the further advantage of requiring only a shorter time and much lower cost for production. Finally, it also opens a new avenue by potentially enabling an active ensemble mapping in larger mammalian species other than rodents, such as non-human primates, whose genomic engineering remains technically more challenging.

Table 1 summarizes a list of previously published transgenic animals and viral vectors that took advantage of various activity-dependent promoters to drive a reporter protein in the brain. The downstream reporter proteins were limited to LacZ and EGFP until late 2000s. With the explosion of newly available genetic methods, the genetic resources based on activity-dependent promoters have much broadened in scope and in sophistication (**Table 1**).

ELECTROPHYSIOLOGICAL CHARACTERIZATION OF NEURONS LABELED WITH ACTIVITY-DEPENDENT PROMOTERS

Despite our detailed understanding of the molecular pathways leading to activity-dependent gene expression, we understand much less about the input patterns of endogenous neuronal activities that trigger activity-dependent gene expression *in vivo*. Early studies demonstrated that *in vivo* high-frequency stimulation of medial perforant path axons from the entorhinal cortex triggered *Arc* mRNA expression in the dentate gyrus of the hippocampus (Link et al., 1995; Steward et al., 1998). *In vitro* experiments using cultured neurons further indicated that both LTP-inducing and LTD-inducing stimuli induces phosphorylation of an activity-dependent transcription factor CREB (Deisseroth et al., 1996). Consistently, either repeated high-frequency bursts (50Hz) or prolonged, low- frequency stimuli (5Hz) was shown to induce c-Fos expression (Bito et al., 1996).

However, electrophysiological characterization of individual neurons in which activity-dependent transcription has been turned on in living animals was achieved much later. Two studies based on single-cell recording guided by *in vivo* two-photon fluorescent microscopy provided critical insights into the type of neuronal activity which triggers activity-dependent gene expression. One study was based on FosGFP transgenic mice, in which a cFos-GFP fusion protein was expressed downstream of a c-*fos* promoter (Barth et al., 2004). This study showed that an increased spontaneous activity was correlated with the FosGFP expression in layer 2/3 pyramidal neurons of the somatosensory barrel cortex (Yassin et al., 2010). Because synaptic connectivity was enriched between FosGFP-positive neurons, the results were indicative of a functional sub-network of highly excitable neurons sparsely embedded in the barrel cortex (Yassin et al., 2010). Another study used a virus vector which expressed destabilized GFP under the E-SARE promoter, and cortical layer 2/3 pyramidal neurons in the barrel cortex were recorded (Kawashima et al., 2013). When the whisker-evoked activity and spontaneous activity were measured, interestingly, only the whisker-evoked activity showed a significant correlation with reporter GFP expression; in sharp contrast, spontaneous activity revealed little correlation (**Figure 2**). This labeling selectivity for neuronal activity constituted a characteristic feature of E-SARE activation (Kawashima et al., 2013). These results highlighted the critical

Table 1 | Reporter mouse lines and viruses based on activity-dependent promoters.

Gene	Type of promoter	Reporter protein	Resource type	Reference
c-fos	Mouse 5′ regulatory region (600 base pairs)	cFos-LacZ fusion	Transgenic mouce	Smeyne et al. (1992)
		Tau-LacZ fusion		Wilson et al. (2002)
		cFos-EGFP fusion		Barth et al. (2004)
		firefly luciferase		Geusz et al. (1997)
		cFos-LacZ fusion	Transgenic rat	Kasof et al. (1995)
		cFos-EGFP fusion		Cifani et al. (2012)
		PSD95-Venus fusion		Knapska et al. (2012)
		tTA\d2EGFP	Double transgenic mouse	Reijmers et al. (2007)
	Knock-in	$CreER^{T2}$	Knock-in mouse	Guenthner et al. (2013)
Arc/Arg3.1	Knock-in	d2EGFP	Knock-in mouse	Wang et al. (2006)
		$CreER^{T2}$		Guenthner et al. (2013)
	Mouse 5′regulatory region (7k base pairs)	d2Venus	Transgenic mouse	Eguchi and Yamaguchi (2009), Mikuni et al. (2013)
		EGFP-Arc fusion		Okuno et al. (2012)
	mouse BAC clone	d4EGFP		Grinevich et al. (2009)
		firefly luciferase		Izumi et al. (2011)
	SARE enhancer	d2EGFP	Lentiviral vector	Kawashima et al. (2009)
	E-SARE promoter	d2EGFP	Adeno-associated virus	Kawashima et al. (2013)
		ER^{T2}-Cre-ER^{T2}		
Egr-1	Mouse 5′ regulatory region (1.5 K base pairs)	d2EGFP	Transgenic rat	Man et al. (2007)
CREB binding sites	6xCRE-RSV promoter	LacZ	Transgenic mouse	Impey et al. (1996)
	4xCRE-TK promoter	*firefly* Luciferase		Böer et al. (2007)

Note that this is not an exclusive survey.

importance of choosing the right type of the activity-dependent promoters and reporter proteins to correctly target the neural activity to be studied.

Multiple lines of evidences suggest that neurons that were marked with activity-dependent promoters might undergo robust changes in electrophysiological and anatomical properties when animals are exposed to various memory-related tasks. In one study, FosGFP mice were trained with repetitive "trace" fear conditioning, and an increase in postsynaptic calcium-permeable AMPA receptors (CP-AMPAR) was exclusively observed in FosGFP-positive neurons, but not in FosGFP-negative neurons, in the anterior cingulate cortex (Descalzi et al., 2012). When FosGFP mice were exposed to repetitive administration of cocaine to evoke psychomotor sensitization, a sign of cocaine addiction, "silent synapses" containing functional NMDA receptors but few functional AMPA receptors were significantly increased in FosGFP-positive neurons in the nucleus accumbens (Koya et al., 2012). Furthermore, a third study showed that upon establishment of contextual fear conditioning, GFP-GluR1$^{c\text{-}fos}$ transgenic mice, which express GFP-GluR1 downstream of tetracycline transactivator (tTA) driven by c-*fos* promoter (Matsuo et al., 2008), revealed a selective decrease of dendritic spines in GFP-positive neurons in the CA1 neurons of the hippocampus (Sanders et al., 2012). These studies, together, demonstrate the usefulness of activity-dependent promoters in identifying a small number of neurons in which important electrophysiological and morphological changes do occur, which otherwise would have been inevitably missed. Furthermore, this illustrates the reliability of activity-dependent promoters in specifically labeling behaviorally relevant neurons among a majority of functionally heterogenous neurons.

BEHAVIORAL MANIPULATION OF COGNITION IN LIVING ANIMALS BASED ON ACTIVITY-DEPENDENT PROMOTERS

Following recent advancement of genetic and chemical methods for manipulation of neural activity, activity-dependent promoters are now widely being used to modulate neural circuits which underlie cognitive behaviors in living animals. In a pioneering study, Reijmers et al. (2007) developed a "TetTag" method based on a tTA (Gossen and Bujard, 1992). This combinatorial strategy takes advantage of a first transgenic mouse line in which tTA was expressed downstream of c-*fos* promoter, and a second transgenic mouse line in which a reporter LacZ protein was expressed downstream of tetracycline responsive element (TRE) which is activated by tTA. This double-transgenic design enabled prolonged marker expression (<1–2 weeks) in neurons which were activated during a specific time period that was experimentally defined by doxycycline administration. Based on this system, they found that

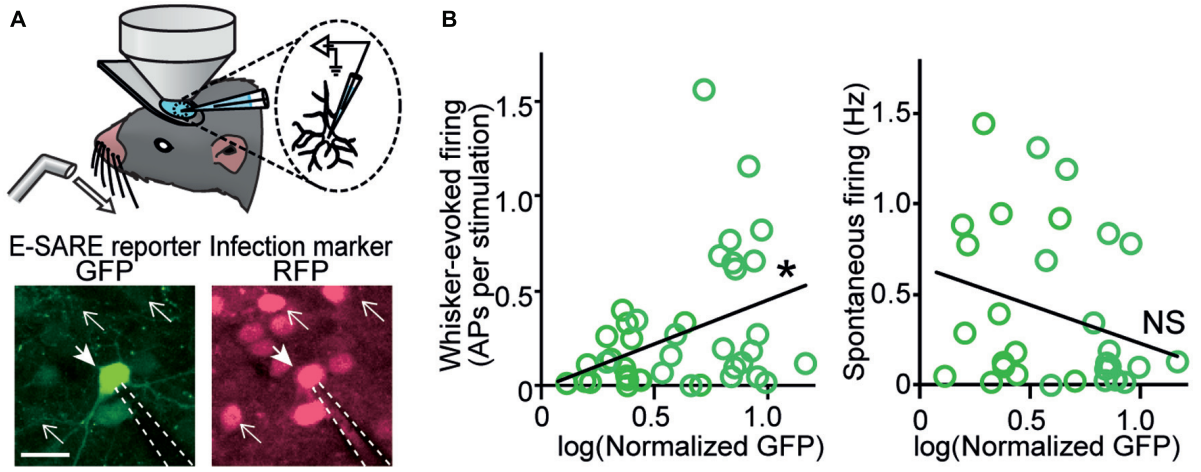

FIGURE 2 | ***In vivo*** **recording reveals a strong correlation between evoked neuronal activity and E-SARE expression. (A)** Top, experimental setup. Single-cell responses of E-SARE-driven GFP-positive and – negative neurons were recorded under the observation by two-photon microscopy. Bottom, representative images of a recorded neuron that is GFP reporter-positive (filled arrow). The dashed lines and line arrows indicate the recording electrode and GFP-negative neurons, respectively. Scale bar, 20 μm. **(B)** GFP brightness of recorded neurons correlates with their whisker-evoked activity (left) but not with spontaneous activity rate (right). Adapted from Kawashima et al. (2013).

a subset of the basolateral amygdala (BLA) neurons was activated at the acquisition of fear memory and, 3 days later, the same population was again activated during the retrieval of memory (Reijmers et al., 2007).

This TetTag method has paved the way for a new series of behavioral studies based on manipulation of functionally defined neurons in behaving animals. These studies involve two steps of experiments. First, a specific neuronal subset is labeled using TetTag under a certain behavioral condition through combination of an activity-dependent promoter and a time-restrictive drug administration. The resulting reporter proteins, which persist for several days, are subsequently used for controlling the activity of labeled neurons and their effects on behaviors are examined. A couple of recent studies (Liu et al., 2012; Ramirez et al., 2013) adopted the TetTag system in combination with with AAVs expressing light-gated cation channel channelrhodopsin-2 (ChR2; Boyden et al., 2005), to specifically label activated hippocampal dentate gyrus neurons during the acquisition of contextual fear memory. When this ChR2-TetTag system was combined with aversive experiences (foot shocks), light-driven excitation of the labeled neurons evoked an "artificial" fear response, demonstrating that the reactivation of an "engram" of fear memory was sufficient for memory recall in the hippocampus (Liu et al., 2012). Another study (Garner et al., 2012) used a mouse which expressed designer receptors exclusively activated by designer drugs (DREADD), hM3Dq (Alexander et al., 2009), downstream of TRE. Neurons that were activated in one context was first labeled with hM3Dq in the absence of chemical stimuli, and when these neurons were chemically excited during acquisition of fear memory in another context, a "synthetic memory" was formed in association with the first context (Garner et al., 2012).

An original chemical genetic approach was used by Koya et al. (2009). In this study, a chemical compound Daun02, which is converted into a neuronal silencer daunorubicin by beta-galactosidase activity of LacZ, was used in combination with Fos-LacZ rats. Local injection of Daun02 incapacitated a dominant subset of nucleus accumbens neurons which were previously activated by cocaine administration and thus impaired the formation of context-specific psychomotor sensitization, indicating the presence a functional sub-network which associates the environment and addiction behaviors (Koya et al., 2009).

These newly discovered aspects of learned behaviors demonstrate the unique power of functional labeling based on activity-dependent promoters over conventional anatomy- or cell-type-based labeling. The majority of the publications that used functional labeling so far employed this technique to mark a hippocampal circuit that participated in encoding of external contexts during fear conditioning. However, we recently showed that the scope of functional labeling can be extended to different types of circuits, such as stimulus feature (orientation)-specific circuits in the visual cortex (Kawashima et al., 2013). We anticipate that many exciting discoveries lie ahead when it will become common to selectively manipulate functional neuronal ensembles that are associated with various brain functions.

PERSISTENT LABELING OF FUNCTIONAL NEURONS USING ACTIVITY-DEPENDENT PROMOTERS

One new direction of functional labeling involves conversion of transient expression from activity-dependent promoters into a permanent labeling based on tamoxifen-dependent recombinases, such as CreER^{T2} (Feil et al., 1997) or ER^{T2}-Cre-ER^{T2} (Matsuda and Cepko, 2007). This technique uses two transgene cassettes: in the first cassette, a tamoxifen-dependent Cre recombinase is expressed under control of an activity-dependent promoter, and in the second cassette, a "STOP signal", which is flanked by recombination sequences [such as single loxP or double loxP (such as DIO or FLEX)], is placed between the reporter gene of interest and a

constitutive promoter. Upon tamoxifen administration within a sharp time window when the drug-sensitive Cre recombinases are expressed in activated neurons, these recombinases excise the "STOP" signal from the second cassette and the reporters will then be expressed constitutively. One group developed several knock-in mice, called targeted recombination in active population (TRAP), which express CreER^{T2} in the endogenous c-*fos* and *Arc* locus (Guenthner et al., 2013). Independently, we developed a combinatorial AAV-based system which expresses ER^{T2}-Cre-ER^{T2} downstream of the synthetic E-SARE promoter (Kawashima et al., 2013).

Chronic labeling of once-activated neuronal ensembles using activity-dependent promoters holds huge promises in neuroscience. For example, persistent expression of fluorescent tracers which was induced by E-SARE-driven ER^{T2}-Cre-ER^{T2} successfully labeled and allowed live imaging of long-distance (>3 mm) axons projecting from eye-specific neurons in the lateral geniculate nucleus (LGN) to the layer 4 of the visual cortex (Kawashima et al., 2013). This validates the usefulness of activity-dependent promoters even in functional connectomics studies, where long-distance axons from mixed, but functionally segregated neurons, could be traced to multiple independent target regions. We anticipate that these new toolkits for chronic labeling of active ensembles will provide a much awaited experimental basis to interrogate various aspects of neuronal circuits underlying long-term plastic changes of the brain, such as during nervous system development, during establishment of long-lasting remote memory over months, or in association with age-related neuronal changes over several years.

FUTURE PERSPECTIVES

While vastly improved over the past, the current repertoire of activity-dependent promoters can still be significantly improved. For example, controlling the activity-dependent promoters through drug-controlled transcriptional silencers (Freundlieb et al., 1999) or light-controlled transcription repressors/activators (Wang et al., 2012; Konermann et al., 2013) will enable a much more precise temporal restriction of the neuronal activity that triggers activity-driven expression of the reporter protein. Also, further enhancement of expression levels or dynamic ranges of activity-regulated promoters might be possible through large-scale unbiased mutational screenings (Melnikov et al., 2012). As the developments of a comprehensive genetic toolkit based on activity-dependent promoters progresses, the range of applications for imaging, manipulating and chronically labeling an active ensemble will undoubtedly continue to expand at a fast pace, while also creating massive opportunities to shed new lights on complex animal behaviors that are driven by mixed ensembles of active neurons in heterologous neuronal circuits in multiple brain areas.

ACKNOWLEDGMENTS

We thank Dr. Paul Worley (Johns Hopkins University), Dr. Kenichi Ohki (Kyushu University), Drs. Masanobu Kano and Kazuo Kitamura (University of Tokyo), and Dr. Itaru Imayoshi (Kyoto University) for continuous collaboration and encouragement. We also thank Drs. Sayaka Takemoto-Kimura, Mio Nonaka, Nan Yagishita-Kyo, Satoshi Kamijo, Aki Adachi-Morishima, and all the members of the Bito laboratory for discussion and support of the research. We apologize to many authors whose work could not be discussed in this article because of space limitations. This work was supported in part by grants-in-aid from the Japanese Ministry of Education, Culture, Sports, Science, and Technology (MEXT) and Japan Society for the Promotion of Science (JSPS; to Hiroyuki Okuno and Haruhiko Bito), grants from CREST–Japan Science and Technology Agency (JST; to Haruhiko Bito), the Strategic International Research Cooperative Program Japan–Mexico (SICPME-JST, to Haruhiko Bito), and the Mitsubishi, Takeda and Uehara Foundation (to Haruhiko Bito). Takashi Kawashima was supported by JSPS fellowships.

REFERENCES

Abel, T., Nguyen, P. V., Barad, M., Deuel, T. A., Kandel, E. R., and Bourtchouladze, R. (1997). Genetic demonstration of a role for PKA in the late phase of LTP and in hippocampus-based long-term memory. *Cell* 88, 615–626. doi: 10.1016/S0092-8674(00)81904-2

Alexander, G. M., Rogan, S. C., Abbas, A. I., Armbruster, B. N., Pei, Y., Allen, J., et al. (2009). Remote control of neuronal activity in transgenic mice expressing evolved G protein-coupled receptors. *Neuron* 63, 27–39. doi: 10.1016/j.neuron.2009.06.014

Barth, A. L. (2007). Visualizing circuits and systems using transgenic reporters of neural activity. *Curr. Opin. Neurobiol.* 17, 567–571. doi: 10.1016/j.conb.2007.10.003

Barth, A. L., Gerkin, R. C., and Dean, K. L. (2004). Alteration of neuronal firing properties after in vivo experience in a FosGFP transgenic mouse. *J. Neurosci.* 24, 6466–6475. doi: 10.1523/JNEUROSCI.4737-03.2004

Bito, H., Deisseroth, K., and Tsien, R. W. (1996). CREB Phosphorylation and Dephosphorylation: a Ca^{2+} - and Stimulus Duration – Dependent Switch for Hippocampal Gene Expression. *Cell* 87, 1203–1214. doi: 10.1016/S0092-8674(00)81816-4

Bito, H., Deisseroth, K., and Tsien, R. W. (1997). Ca^{2+}-dependent regulation in neuronal gene expression. *Curr. Opin. Neurobiol.* 7, 419–429. doi: 10.1016/S0959-4388(97)80072-4

Böer, U., Alejel, T., Beimesche, S., Cierny, I., Krause, D., Knepel, W., et al. (2007). CRE/CREB-driven up-regulation of gene expression by chronic social stress in CRE-luciferase transgenic mice: reversal by antidepressant treatment. *PLoS ONE* 2:e431. doi: 10.1371/journal.pone.0000431

Bourtchuladze, R., Frenguelli, B., Blendy, J., Cioffi, D., Schutz, G., and Silva, A. J. (1994). Deficient long-term memory in mice with a targeted mutation of the cAMP-responsive element-binding protein. *Cell* 79, 59–68. doi: 10.1016/0092-8674(94)90400-6

Boyden, E. S., Zhang, F., Bamberg, E., Nagel, G., and Deisseroth, K. (2005). Millisecond-timescale, genetically targeted optical control of neural activity. *Nat. Neurosci.* 8, 1263–1268. doi: 10.1038/nn1525

Chaudhuri, A., Matsubara, J. A., and Cynader, M. S. (1995). Neuronal activity in primate visual cortex assessed by immunostaining for the transcription factor Zif268. *Vis. Neurosci.* 12, 35–50. doi: 10.1017/S095252380000729X

Cifani, C., Koya, E., Navarre, B. M., Calu, D. J., Baumann, M. H., Marchant, N. J., et al. (2012). Medial prefrontal cortex neuronal activation and synaptic alterations after stress-induced reinstatement of palatable food seeking: a study using c-fos-GFP transgenic female rats. *J. Neurosci.* 32, 8480–8490. doi: 10.1523/JNEUROSCI.5895-11.2012

Curran, T., and Morgan, J. I. (1985). Superinduction of c-fos by nerve growth factor in the presence of peripherally active benzodiazepines. *Science* 229, 1265–1268. doi: 10.1126/science.4035354

Deisseroth, K., Bito, H., and Tsien, R. W. (1996). Signaling from synapse to nucleus: postsynaptic CREB phosphorylation during multiple forms of hippocampal synaptic plasticity. *Neuron* 16, 89–101. doi: 10.1016/S0896-6273(00)80026-4

Descalzi, G., Li, X.-Y., Chen, T., Mercaldo, V., Koga, K., and Zhuo, M. (2012). Rapid synaptic potentiation within the anterior cingulate cortex mediates trace fear learning. *Mol. Brain* 5, 6. doi: 10.1186/1756-6606-5-6

Dolmetsch, R. E., Pajvani, U., Fife, K., Spotts, J. M., and Greenberg, M. E. (2001). Signaling to the nucleus by an L-type calcium channel-calmodulin complex through the MAP kinase pathway. *Science* 294, 333–339. doi: 10.1126/science.1063395

Eguchi, M., and Yamaguchi, S. (2009). In vivo and in vitro visualization of gene expression dynamics over extensive areas of the brain. *Neuroimage* 44, 1274–1283. doi: 10.1016/j.neuroimage.2008.10.046

Feil, R., Wagner, J., Metzger, D., and Chambon, P. (1997). Regulation of Cre recombinase activity by mutated estrogen receptor ligand-binding domains. *Biochem. Biophys. Res. Commun.* 237, 752–757. doi: 10.1006/bbrc.1997.7124

Filipkowski, R. K. (2000). Tactile experience induces c-fos expression in rat barrel cortex. *Learn. Mem.* 7, 116–122. doi: 10.1101/lm.7.2.116

Flavell, S. W., and Greenberg, M. E. (2008). Signaling mechanisms linking neuronal activity to gene expression and plasticity of the nervous system. *Annu. Rev. Neurosci.* 31, 563–590. doi: 10.1146/annurev.neuro.31.060407.125631

Freundlieb, S., Schirra-Mu, C., and Bujard, H. (1999). A tetracycline controlled activation / repression system with increased potential for gene transfer into mammalian cells. *J. Gene. Med.* 1, 4–12. doi: 10.1002/(SICI)1521-2254(199901/02)1:1<4::AID-JGM4>3.0.CO;2-Y

Fujii, H., Inoue, M., Okuno, H., Sano, Y., Takemoto-Kimura, S., Kitamura, K., et al. (2013). Nonlinear decoding and asymmetric representation of neuronal input information by CaMKIIα and calcineurin. *Cell Rep.* 3, 978–987. doi: 10.1016/j.celrep.2013.03.033

Garner, A. R., Rowland, D. C., Hwang, S. Y., Baumgaertel, K., Roth, B. L., Kentros, C., et al. (2012). Generation of a synthetic memory trace. *Science* 335, 1513–1516. doi: 10.1126/science.1214985

Geusz, M. E., Fletcher, C., Block, G. D., Straume, M., Copeland, N. G., Jenkins, N., et al. (1997). Long-term monitoring of circadian rhythms in c-fos gene expression from suprachiasmatic nucleus cultures. *Curr. Biol.* 7, 758–766. doi: 10.1016/S0960-9822(06)00334-4

Ginty, D. D., Kornhauser, J. M., Thompson, M. A., Bading, H., Mayo, K. E., Takahashi, J. S., et al. (1993). Regulation of CREB phosphorylation in the suprachiasmatic nucleus by light and a circadian clock. *Science* 260, 238–241. doi: 10.1126/science.8097062

Gossen, M., and Bujard, H. (1992). Tight control of gene expression in mammalian cells by tetracycline-responsive promoters. *Proc. Natl. Acad. Sci. U.S.A.* 89, 5547–5551. doi: 10.1073/pnas.89.12.5547

Greenberg, M. E., and Ziff, E. B. (1984). Stimulation of 3T3 cells induces transcription of the c-fos proto-oncogene. *Nature* 311, 433–438. doi: 10.1038/311433a0

Grinevich, V., Kolleker, A., Eliava, M., Takada, N., Takuma, H., Fukazawa, Y., et al. (2009). Fluorescent Arc/Arg3.1 indicator mice: a versatile tool to study brain activity changes in vitro and in vivo. *J. Neurosci. Methods* 184, 25–36. doi: 10.1016/j.jneumeth.2009.07.015

Guenthner, C. J., Miyamichi, K., Yang, H. H., Heller, H. C., and Luo, L. (2013). Permanent genetic access to transiently active neurons via TRAP: targeted recombination in active populations. *Neuron* 78, 773–784. doi: 10.1016/j.neuron.2013.03.025

Guzowski, J. F., McNaughton, B. L., Barnes, C. A., and Worley, P. F. (1999). Environment-specific expression of the immediate-early gene Arc in hippocampal neuronal ensembles. *Nat. Neurosci.* 2, 1120–1124. doi: 10.1038/16046

Hartzell, A. L., Burke, S. N., Hoang, L. T., Lister, J. P., Rodriguez, C. N., and Barnes, C. A. (2013). Transcription of the immediate-early gene Arc in CA1 of the hippocampus reveals activity differences along the proximodistal axis that are attenuated by advanced age. *J. Neurosci.* 33, 3424–3433. doi: 10.1523/JNEUROSCI.4727-12.2013

Impey, S., Mark, M., Villacres, E. C., Poser, S., Chavkin, C., and Storm, D. R. (1996). Induction of CRE-mediated gene expression by stimuli that generate long-lasting LTP in area CA1 of the hippocampus. *Neuron* 16, 973–982. doi: 10.1016/S0896-6273(00)80120-8

Inoue, M., Yagishita-Kyo, N., Nonaka, M., Kawashima, T., Okuno, H., and Bito, H. (2010). Synaptic activity-responsive element (SARE): a unique genomic structure with an unusual sensitivity to neuronal activity. *Commun. Integr. Biol.* 3, 443–446. doi: 10.4161/cib.3.5.12287

Izumi, H., Ishimoto, T., Yamamoto, H., Nishijo, H., and Mori, H. (2011). Bioluminescence imaging of Arc expression enables detection of activity-dependent and plastic changes in the visual cortex of adult mice. *Brain Struct. Funct.* 216, 91–104. doi: 10.1007/s00429-010-0297-2

Kang, H., Sun, L. D., Atkins, C. M., Soderling, T. R., Wilson, M. A., and Tonegawa, S. (2001). An important role of neural activity-dependent CaMKIV signaling in the consolidation of long-term memory. *Cell* 106, 771–783. doi: 10.1016/S0092-8674(01)00497-4

Kasof, G. M., Mandelzys, A., Maika, S. D., Hammer, R. E., Curran, T., and Morgan, J. I. (1995). Kainic acid-induced neuronal death is associated with DNA damage and a unique immediate-early gene response in c-fos-lacZ transgenic rats. *J. Neurosci.* 15, 4238–4249.

Kawashima, T., Kitamura, K., Suzuki, K., Nonaka, M., Kamijo, S., Takemoto-Kimura, S., et al. (2013). Functional labeling of neurons and their projections using the synthetic activity-dependent promoter E-SARE. *Nat. Methods* 10, 889–895. doi: 10.1038/nmeth.2559

Kawashima, T., Okuno, H., Nonaka, M., Adachi-Morishima, A., Kyo, N., Okamura, M., et al. (2009). Synaptic activity-responsive element in the Arc/Arg3.1 promoter essential for synapse-to-nucleus signaling in activated neurons. *Proc. Natl. Acad. Sci. U.S.A.* 106, 316–321. doi: 10.1073/pnas.0806518106

Kida, S., Josselyn, S. A., Peña de Ortiz, S., Kogan, J. H., Chevere, I., Masushige, S., et al. (2002). CREB required for the stability of new and reactivated fear memories. *Nat. Neurosci.* 5, 348–355. doi: 10.1038/nn819

Knapska, E., Macias, M., Mikosz, M., Nowak, A., Owczarek, D., Wawrzyniak, M., et al. (2012). Functional anatomy of neural circuits regulating fear and extinction. *Proc. Natl. Acad. Sci. U.S.A.* 109, 17093–17098. doi: 10.1073/pnas.1202087109

Konermann, S., Brigham, M. D., Trevino, A. E., Hsu, P. D., Heidenreich, M., Cong, L., et al. (2013). Optical control of mammalian endogenous transcription and epigenetic states. *Nature* 500, 472–476. doi: 10.1038/nature12466

Koya, E., Cruz, F. C., Ator, R., Golden, S. A., Hoffman, A. F., Lupica, C. R., et al. (2012). Silent synapses in selectively activated nucleus accumbens neurons following cocaine sensitization. *Nat. Neurosci.* 15, 1556–1562. doi: 10.1038/nn.3232

Koya, E., Golden, S. A., Harvey, B. K., Guez-Barber, D. H., Berkow, A., Simmons, D. E., et al. (2009). Targeted disruption of cocaine-activated nucleus accumbens neurons prevents context-specific sensitization. *Nat. Neurosci.* 12, 1069–1073. doi: 10.1038/nn.2364

Link, W., Konietzko, U., Kauselmann, G., Krug, M., Schwanke, B., Frey, U., et al. (1995). Somatodendritic expression of an immediate early gene is regulated by synaptic activity. *Proc. Natl. Acad. Sci. U.S.A.* 92, 5734–5738. doi: 10.1073/pnas.92.12.5734

Liu, X., Ramirez, S., Pang, P. T., Puryear, C. B., Govindarajan, A., Deisseroth, K., et al. (2012). Optogenetic stimulation of a hippocampal engram activates fear memory recall. *Nature* 484, 381–385. doi: 10.1038/nature11028

Lyford, G. L., Yamagata, K., Kaufmann, W. E., Barnes, C. A., Sanders, L. K., Copeland, N. G., et al. (1995). Arc, a growth factor and activity-regulated gene, encodes a novel cytoskeleton-associated protein that is enriched in neuronal dendrites. *Neuron* 14, 433–445. doi: 10.1016/0896-6273(95)90299-6

Man, P.-S., Wells, T., and Carter, D. A. (2007). Egr-1-d2EGFP transgenic rats identify transient populations of neurons and glial cells during postnatal brain development. *Gene Expr. Patterns* 7, 872–883. doi: 10.1016/j.modgep.2007.06.006

Mao, Z., Bonni, A., Xia, F., Nadal-Vicens, M., and Greenberg, M. E. (1999). Neuronal activity-dependent cell survival mediated by transcription factor MEF2. *Science* 286, 785–790. doi: 10.1126/science.286.5440.785

Matsuda, T., and Cepko, C. L. (2007). Controlled expression of transgenes introduced by in vivo electroporation. *Proc. Natl. Acad. Sci. U.S.A.* 104, 1027–1032. doi: 10.1073/pnas.0610155104

Matsuo, N., Reijmers, L., and Mayford, M. (2008). Spine-type-specific recruitment of newly synthesized AMPA receptors with learning. *Science* 319, 1104–1107. doi: 10.1126/science.1149967

Melnikov, A., Murugan, A., Zhang, X., Tesileanu, T., Wang, L., Rogov, P., et al. (2012). Systematic dissection and optimization of inducible enhancers in human cells using a massively parallel reporter assay. *Nat. Biotechnol.* 30, 271–277. doi: 10.1038/nbt.2137

Mikuni, T., Uesaka, N., Okuno, H., Hirai, H., Deisseroth, K., Bito, H., et al. (2013). Arc/Arg3.1 is a postsynaptic mediator of activity-dependent synapse elimination in the developing cerebellum. *Neuron* 78, 1024–1035. doi: 10.1016/j.neuron.2013.04.036

Moratalla, R., Vickers, E., Robertson, H., Cochran, B., and Graybiell, A. (1993). Coordinate expression striatum by cocaine of c-fos and jun B is induced in the rat striatum by cocaine. *J. Neurosci.* 13, 423–433.

Morgan, J. I., Cohen, D. R., Hempstead, J. L., and Curran, T. (1987). Mapping patterns of c-fos expression in the central nervous system after seizure. *Science* 237, 192–197. doi: 10.1126/science.3037702

Müller, R., Bravo, R., Burckhardt, J., and Curran, T. (1984). Induction of c-fos gene and protein by growth factors precedes activation of c-myc. *Nature* 312, 716–720. doi: 10.1038/312716a0

Norman, C., Runswick, M., Pollock, R., and Treisman, R. (1988). Isolation and properties of cDNA clones encoding SRF, a transcription factor that binds to the c-fos serum response element. *Cell* 55, 989–1003. doi: 10.1016/0092-8674(88)90244-9

Ogawa, S., Lee, T. M., Kay, A. R., and Tank, D. W. (1990). Brain magnetic resonance imaging with contrast dependent on blood oxygenation. *Proc. Natl. Acad. Sci. U.S.A.* 87, 9868–9872. doi: 10.1073/pnas.87.24.9868

Ohki, K., Chung, S., Ch'ng, Y. H., Kara, P., and Reid, R. C. (2005). Functional imaging with cellular resolution reveals precise micro-architecture in visual cortex. *Nature* 433, 597–603. doi: 10.1038/nature03274

Okuno, H. (2011). Regulation and function of immediate-early genes in the brain: beyond neuronal activity markers. *Neurosci. Res.* 69, 175–186. doi: 10.1016/j.neures.2010.12.007

Okuno, H., Akashi, K., Ishii, Y., Yagishita-Kyo, N., Suzuki, K., Nonaka, M., et al. (2012). Inverse synaptic tagging of inactive synapses via dynamic interaction of Arc/Arg3.1 with CaMKIIβ. *Cell* 149, 886–898. doi: 10.1016/j.cell.2012.02.062

Osten, P., and Margrie, T. W. (2013). Mapping brain circuitry with a light microscope. *Nat. Methods* 10, 515–523. doi: 10.1038/nmeth.2477

Pham, T. A., Impey, S., Storm, D. R., and Stryker, M. P. (1999). CRE-mediated gene transcription in neocortical neuronal plasticity during the developmental critical period. *Neuron* 22, 63–72. doi: 10.1016/S0896-6273(00)80679-0

Pintchovski, S. A., Peebles, C. L., Kim, H. J., Verdin, E., and Finkbeiner, S. (2009). The serum response factor and a putative novel transcription factor regulate expression of the immediate-early gene Arc/Arg3.1 in neurons. *J. Neurosci.* 29, 1525–1537. doi: 10.1523/JNEUROSCI.5575-08.2009

Ragan, T., Kadiri, L. R., Venkataraju, K. U., Bahlmann, K., Sutin, J., Taranda, J., et al. (2012). Serial two-photon tomography for automated ex vivo mouse brain imaging. *Nat. Methods* 9, 255–258. doi: 10.1038/nmeth.1854

Ramirez, S., Liu, X., Lin, P.-A., Suh, J., Pignatelli, M., Redondo, R. L., et al. (2013). Creating a false memory in the hippocampus. *Science* 341, 387–391. doi: 10.1126/science.1239073

Ramírez-Amaya, V., Vazdarjanova, A., Mikhael, D., Rosi, S., Worley, P. F., and Barnes, C. A. (2005). Spatial exploration-induced Arc mRNA and protein expression: evidence for selective, network-specific reactivation. *J. Neurosci.* 25, 1761–1768. doi: 10.1523/JNEUROSCI.4342-04.2005

Reijmers, L. G., Perkins, B. L., Matsuo, N., and Mayford, M. (2007). Localization of a stable neural correlate of associative memory. *Science* 317, 1230–1233. doi: 10.1126/science.1143839

Robertson, L. M., Kerppola, T. K., Vendrell, M., Luk, D., Smeyne, R. J., Bocchiaro, C., et al. (1995). Regulation of c-fos expression in transgenic mice requires multiple interdependent transcription control elements. *Neuron* 14, 241–252. doi: 10.1016/0896-6273(95)90282-1

Saffen, D. W., Cole, A. J., Worley, P. F., Christy, B. A., Ryder, K., and Baraban, J. M. (1988). Convulsant-induced increase in transcription factor messenger RNAs in rat brain. *Proc. Natl. Acad. Sci. U.S.A.* 85, 7795–7799. doi: 10.1073/pnas.85.20.7795

Sagar, S. M., Sharp, F. R., and Curran, T. (1988). Expression of c-fos protein in brain: metabolic mapping at the cellular level. *Science* 240, 1328–1331. doi: 10.1126/science.3131879

Sanders, J., Cowansage, K., Baumgärtel, K., and Mayford, M. (2012). Elimination of dendritic spines with long-term memory is specific to active circuits. *J. Neurosci.* 32, 12570–12578. doi: 10.1523/JNEUROSCI.1131-12.2012

Schilling, K., Luk, D., Morgan, J. I., and Curran, T. (1991). Regulation of a fos-lacZ fusion gene: a paradigm for quantitative analysis of stimulus-transcription coupling. *Proc. Natl. Acad. Sci. U.S.A.* 88, 5665–5669. doi: 10.1073/pnas.88.13.5665

Small, S. A., Chawla, M. K., Buonocore, M., Rapp, P. R., and Barnes, C. A. (2004). Imaging correlates of brain function in monkeys and rats isolates a hippocampal subregion differentially vulnerable to aging. *Proc. Natl. Acad. Sci. U.S.A.* 101, 7181–7186. doi: 10.1073/pnas.0400285101

Smeyne, R. J., Schilling, K., Robertson, L., Luk, D., Oberdick, J., Curran, T., et al. (1992). fos-lacZ transgenic mice: mapping sites of gene induction in the central nervous system. *Neuron* 8, 13–23. doi: 10.1016/0896-6273(92)90105-M

Smith-Hicks, C., Xiao, B., Deng, R., Ji, Y., Zhao, X., Shepherd, J. D., et al. (2010). SRF binding to SRE 6.9 in the Arc promoter is essential for LTD in cultured Purkinje cells. *Nat. Neurosci.* 13, 1082–1089. doi: 10.1038/nn.2611

Sokoloff, L., Reivich, M., Kennedy, C., Des Rosiers, M. H., Patlak, C. S., Pettigrew, K. D., et al. (1977). The [14C]deoxyglucose method for the measurement of local cerebral glucose utilization: theory, procedure, and normal values in the conscious and anesthetized albino rat. *J. Neurochem.* 28, 897–916. doi: 10.1111/j.1471-4159.1977.tb10649.x

Staiger, J. F., Masanneck, C., Bisler, S., Schleicher, A., Zuschratter, W., and Zilles, K. (2002). Excitatory and inhibitory neurons express c-Fos in barrel-related columns after exploration of a novel environment. *Neuroscience* 109, 687–699. doi: 10.1016/S0306-4522(01)00501-2

Steiner, H., and Gerfen, C. R. (1994). Tactile sensory input regulates basal and apomorphine-induced immediate-early gene expression in rat barrel cortex. *J. Comp. Neurol.* 344, 297–304. doi: 10.1002/cne.903440210

Steward, O., Wallace, C. S., Lyford, G. L., and Worley, P. F. (1998). Synaptic activation causes the mRNA for the IEG Arc to localize selectively near activated postsynaptic sites on dendrites. *Neuron* 21, 741–751. doi: 10.1016/S0896-6273(00)80591-7

Tian, J. B., and Bishop, G. A. (2002). Stimulus-dependent activation of c-Fos in neurons and glia in the rat cerebellum. *J. Chem. Neuroanat.* 23, 157–170. doi: 10.1016/S0891-0618(01)00153-3

Tsai, J. C., Liu, L., Cooley, B. C., DiChiara, M. R., Topper, J. N., and Aird, W. C. (2000). The Egr-1 promoter contains information for constitutive and inducible expression in transgenic mice. *FASEB J.* 14, 1870–1872. doi: 10.1096/fj.99-1072fje

Vazdarjanova, A., Ramirez-amaya, V., Insel, N., Plummer, T. K., Rosi, S., Chowdhury, S., et al. (2006). Spatial exploration induces ARC, a only in calcium / calmodulin-dependent protein kinase II-positive principal excitatory and inhibitory neurons of the rat forebrain. *J. Comp. Neurol.* 498, 317–329. doi: 10.1002/cne.21003

Vousden, D. A., Epp, J., Okuno, H., Nieman, B. J., van Eede, M., Dazai, J. et al. (in press). Whole-brain mapping of behaviorally-induced neural activation in mice. *Brain Struc. Func.*

Wada, M., Watanabe, S., Chung, U., Higo, N., Taniguchi, T., and Kitazawa, S. (2010). Noninvasive bioluminescence imaging of c-fos expression in the mouse barrel cortex. *Behav. Brain Res.* 208, 158–162. doi: 10.1016/j.bbr.2009.11.024

Waltereit, R., Wulff, P., Scafidi, J., Staubli, U., Kauselmann, G., Bundman, M., et al. (2001). Arg3. 1 / Arc mRNA induction by Ca^{2+} and cAMP requires protein kinase a and mitogen-activated protein kinase / extracellular regulated kinase activation. *J. Neurosci.* 21, 5484–5493.

Wang, K. H., Majewska, A., Schummers, J., Farley, B., Hu, C., Sur, M., et al. (2006). In vivo two-photon imaging reveals a role of arc in enhancing orientation specificity in visual cortex. *Cell* 126, 389–402. doi: 10.1016/j.cell.2006.06.038

Wang, X., Chen, X., and Yang, Y. (2012). Spatiotemporal control of gene expression by a light-switchable transgene system. *Nat. Methods* 9, 266–269. doi: 10.1038/nmeth.1892

West, A. E., Chen, W. G., Dalva, M. B., Dolmetsch, R. E., Kornhauser, J. M., Shaywitz, A. J., et al. (2001). Calcium regulation of neuronal gene expression. *Proc. Natl. Acad. Sci. U.S.A.* 98, 11024–11031. doi: 10.1073/pnas.191352298

Wilson, Y., Nag, N., Davern, P., Oldfield, B. J., McKinley, M. J., Greferath, U., et al. (2002). Visualization of functionally activated circuitry in the brain. *Proc. Natl. Acad. Sci. U.S.A.* 99, 3252–3257. doi: 10.1073/pnas.042701199

Yassin, L., Benedetti, B. L., Jouhanneau, J.-S., Wen, J. A., Poulet, J. F. A., and Barth, A. L. (2010). An embedded subnetwork of highly active neurons in the neocortex. *Neuron* 68, 1043–1050. doi: 10.1016/j.neuron.2010.11.029

Zhai, S., Ark, E. D., Parra-Bueno, P., and Yasuda, R. (2013). Long-distance integration of nuclear ERK signaling triggered by activation of a few dendritic spines. *Science* 342, 1107–1111. doi: 10.1126/science.1245622

Conflict of Interest Statement: The authors declare that the research was conducted in the absence of any commercial or financial relationships that could be construed as a potential conflict of interest.

Received: 15 February 2014; paper pending published: 06 March 2014; accepted: 01 April 2014; published online: 23 April 2014.

*Citation: Kawashima T, Okuno H, and Bito H (2014) A new era for functional labeling of neurons: activity-dependent promoters have come of age. Front. Neural Circuits **8**:37. doi: 10.3389/fncir.2014.00037*

This article was submitted to the journal Frontiers in Neural Circuits.

frontiers in
NEURAL CIRCUITS

MINI REVIEW ARTICLE
published: 17 October 2014
doi: 10.3389/fncir.2014.00124

Dissecting inhibitory brain circuits with genetically-targeted technologies

Dona K. Murphey[1]*, Alexander M. Herman[2] and Benjamin R. Arenkiel[2,3,4,5]

[1] *Department of Neurology, Baylor College of Medicine, Houston, TX, USA*
[2] *Program in Developmental Biology, Baylor College of Medicine, Houston, TX, USA*
[3] *Department of Molecular and Human Genetics, Baylor College of Medicine, Houston, TX, USA*
[4] *Department of Neuroscience, Baylor College of Medicine, Houston, TX, USA*
[5] *Jan and Dan Duncan Neurological Research Institute at Texas Children's Hospital, Houston, TX, USA*

Edited by:
Mariano Soiza-Reilly, Institut National de la Santé et de la Recherche Médicale, France

Reviewed by:
Michael M. Halassa, Massachusetts Institute of Technology, USA
Stephen Shea, Cold Spring Harbor Laboratory, USA

****Correspondence:***
Dona K. Murphey, Department of Neurology, Baylor College of Medicine, One Baylor Plaza, Houston, TX 77030, USA
e-mail: dk140085@bcm.edu

The evolution of genetically targeted tools has begun to allow us to dissect anatomically and functionally heterogeneous interneurons, and to probe circuit function from synapses to behavior. Over the last decade, these tools have been used widely to visualize neurons in a cell type-specific manner, and engage them to activate and inactivate with exquisite precision. In this process, we have expanded our understanding of interneuron diversity, their functional connectivity, and how selective inhibitory circuits contribute to behavior. Here we discuss the relative assets of genetically encoded fluorescent proteins (FPs), viral tracing methods, optogenetics, chemical genetics, and biosensors in the study of inhibitory interneurons and their respective circuits.

Keywords: interneurons, optogenetics, chemical genetics, viral tracing, channelrhodopsin, interneuron diversity

INTRODUCTION

Interneurons subserve sensory processing (Lee et al., 2012, 2013; Hamilton et al., 2013; Pfeffer et al., 2013; Fu et al., 2014), movement (Brown et al., 2014), learning (Kravitz et al., 2012), reward (Witten et al., 2010; van Zessen et al., 2012), and disease (Gradinaru et al., 2009; Kravitz et al., 2010; Krook-Magnuson et al., 2013; Peng et al., 2013; Brown et al., 2014; Cho and Sohal, 2014; Ledri et al., 2014), and genetic technologies allow for their targeted study (Taniguchi et al., 2011; Kepecs and Fishell, 2014). Various molecular, morphological, and electrophysiological properties (Ascoli et al., 2008) delimit interneuron diversity. Molecular features can be used to investigate whether cell shape or passive and active membrane properties of neurons in circuits of interest represent(s) a homogeneous class (Taniguchi et al., 2013), and morphological and electrophysiological properties of the neurons that express a characteristic marker can further elaborate within class diversity of molecularly defined populations. Additional strategies can then be used to iteratively refine molecular heterogeneity (Ma et al., 2006; Runyan et al., 2010; Chittajallu et al., 2013; Povysheva et al., 2013; Sohn et al., 2014).

Many molecular features arise from post-mitotic cell-type specification by changes in receptor expression, cell-intrinsic activity, and the activity of connected partners to modify a handful of mutually exclusive cardinal classes. Genetically targeted tools for marking and manipulating neuronal activity differentially exploit molecular expression to delimit interneuronal subtypes. In particular, the widespread application of conditionally-expressed fluorescent proteins (FPs) (Hadjantonakis et al., 2003; Livet et al., 2007), virally mediated anatomical tracers (Wickersham et al., 2007; Beier et al., 2011), optogenetic reporters (Zhang et al., 2006; Berndt et al., 2014), designer receptors exclusively activated by designer drugs (DREADD receptors) (Wess et al., 2013), and genetically-encoded subcellular biosensors (Hodgson et al., 2008; Tantama et al., 2012; Glykys et al., 2014), has allowed us dissect the contributions of specific interneurons and even their subcellular compartments to circuit function, behavior, and disease in genetically tractable mice. We discuss the benefits and challenges of these methods first with an eye to how we target the interneurons of interest for investigation.

STRATEGIES FOR GENOMIC TARGETING OF INTERNEURONS

Recapitulating endogenous gene expression is key to cell type-specific study (Luo et al., 2008) and can be achieved by standard, bacterial artificial chromosome (BAC) (Heintz, 2001; Ting and Feng, 2014), and site-directed transgenic methods. Standard and BAC transgenic methods both rely on random integration, which may help to study interneuron subpopulations that express the same *cis*-regulatory elements. However, site-directed integration, made possible through integrases or gene targeted knockins, more faithfully recapitulates endogenous gene expression and is therefore often preferred. Binary expression systems and/or conditional mutagenesis based on site-directed DNA recombination confer even greater experimental reliability and flexibility (Garcia-Otin and Guillou, 2006; Miyoshi et al., 2010).

It is important to note that the cell type-specificity of genetic targeting relies on accurate endogenous promoter expression.

To aid in this effort there is a rapidly evolving set of comprehensive gene expression data for the mouse brain during development, and across different areas in adult brain tissue (Allen Brain Atlas, www.brain-map.org, and GENSAT, www.gensat.org). Established Cre driver lines (Kimura et al., 1996; Qiu et al., 1997; Schurmans et al., 1997; Schwaller et al., 1999; Kerr et al., 2000; Gyurko et al., 2002; Misgeld et al., 2002; Qian et al., 2002; Robledo et al., 2002; Kusakabe et al., 2006; Chattopadhyaya et al., 2007; Liodis et al., 2007; Taniguchi et al., 2011; Wang et al., 2014) (**Table 1**) have to date provided the greatest genetic traction on neocortical interneurons (Taniguchi, 2014) and local and long-range inhibitory neurons of the striatum (Brown et al., 2014; Nelson et al., 2014) and hippocampus (Melzer et al., 2012; Kepecs and Fishell, 2014). It is of note, however, that lineage-specific patterns of gene expression can carry into unanticipated cell types in other parts of the brain or body through early recombination events. Because only static patterns of cortical and hippocampal expression have been extensively characterized (Taniguchi et al., 2011), expression validation is critical. But, importantly, lineage effects can be co-opted by temporally restricted inducible transgenes (Rothermel et al., 2013) in order to study the developmental expression (Dymecki and Kim, 2007; Kumar et al., 2013) of cell-type-specific promoters. Complementary virus-mediated transgene expression in adult brain tissue might avoid lineage-associated issues by only targeting cell types that express a given marker at the time of viral delivery.

VIRAL DELIVERY OF GENETICALLY ENCODED TOOLS IN INTERNEURONS

Restriction of a reporter to a subset of neurons in a given brain area or developmental time point can be achieved by viral delivery of genetic constructs driven by cell type-specific promoters. Viral delivery of transgenes driven by short promoters (Nathanson et al., 2009) has not effectively captured a genetically homogeneous subpopulation of neurons, but conditional Cre-dependent [e.g., Flip Excision (Flex) (Schnutgen et al., 2003) or Lox-Stop-Lox] transgenes driven by strong ubiquitous promoters segregate neurons spatially and temporally in a way not possible through genomic strategies. Viral injections are constrained by their physical properties, however. Viral genome size limits the size of the genetic constructs viruses can carry, and efficiency of uptake and direction of infectivity (Rothermel et al., 2013) depend on viral capsid serotype, genetic construct (Betley and Sternson, 2011), and the targeted brain region (Taymans et al., 2007). Controls should ensure that successful viral infection does not alter cell function. Acknowledging these caveats, gene targeting through both conventional strategies, and virus-mediated transgene delivery, offer an increasingly powerful reserve of anatomical and functional tools we highlight below.

GENETICALLY ENCODED ANATOMICAL DISSECTION OF INTERNEURONS

Interneurons assume diverse somatic shapes and patterns of dendritic/axonal arborization in cortical (Markram et al., 2004; Ascoli

Table 1 | Useful mouse lines for commonly studied interneurons.

Gene name	Cre/Cre-ER/Tet	Knockout	Fluorescent/Functional reporter	References
Agrp	Cre^{Jax}, Cre-ER	Germline	N/A	Qian et al., 2002; Wang et al., 2013
Avp	Cre^{Jax}	$Conditional^{IMSR}$	GFP^{MMRRC}	
Calb2	Cre^{Jax}, $Cre\text{-}ER^{Jax}$	Germline	GFP^{MMRRC}	Schurmans et al., 1997
Cck	Cre^{Jax}, $Cre\text{-}ER^{Jax}$	$Germline^{Jax}$	GFP^{MMRRC}	
Chat	Cre^{Jax}, $Cre\text{-}ER^{Jax}$	Germline, $Conditional^{Jax}$	GFP^{Jax}, $Chat\text{-}Chr2::eYFP^{Jax}$	Misgeld et al., 2002
Crh	Cre^{Jax}	$Germline^{Jax}$	GFP^{MMRRC}	
Dlx1	Cre^{MMRRC}, $Cre\text{-}ER^{Jax}$	Germline	$tdTomato^{MMRRC}$	Qiu et al., 1997
Dlx5/6	Cre^{Jax}, $Cre\text{-}ER^{Jax}$	Germline	GFP^{Jax}	Robledo et al., 2002
Gad1 (Gad67)	Cre	$Germline^{Jax}$, Conditional	GFP^{Jax}	Chattopadhyaya et al., 2007; Taniguchi et al., 2011
Gad2 (Gad65)	Cre^{Jax}, $Cre\text{-}ER^{Jax}$	$Germline^{Jax}$	GFP^{MMRRC}, $mCherry^{Jax}$	
Gal (Galanin)	Cre^{MMRRC}	Germline	GFP^{MMRRC}	Kerr et al., 2000
Lhx6	$Cre\text{-}ER^{Jax}$	Germline	GFP^{MMRRC}	Liodis et al., 2007
Nos1	Cre^{Jax}, $Cre\text{-}ER^{Jax}$	$Germline^{Jax}$, Conditional	GFP^{MMRRC}	Gyurko et al., 2002
Nkx2.1	Cre^{Jax}, $Cre\text{-}ER^{Jax}$	Germline, Conditional	GFP^{MMRRC}	Kimura et al., 1996; Kusakabe et al., 2006
Pvalb	Cre^{Jax}, $Cre\text{-}ER^{Jax}$, $Tet\text{-}Off^{Jax}$	Germline	GFP^{MMRRC}, $Pvalb\text{-}Chr2::eYFP^{Jax}$	Schwaller et al., 1999
Slc32a1 (Vgat)	Cre^{Jax}, $Cre\text{-}ER^{Jax}$	$Germline^{Jax}$, $Conditional^{Jax}$	GFP^{MMRRC}, $Vgat\text{-}Chr2::eYFP^{Jax}$	
Sst	Cre^{Jax}, $Cre\text{-}ER^{Jax}$, $Tet\text{-}Off^{Jax}$	$Germline^{Jax}$	N/A	
Npy	Cre^{MMRRC}, $Tet\text{-}Off^{Jax}$	$Germline^{Jax}$	GFP^{Jax}	
Vip	Cre^{Jax}	$Germline^{Jax}$	GFP^{MMRRC}	

Availability index: Jax, Jackson Laboratory; MMRRC, Mutant Mouse Regional Resource Center; IMSR, International Mouse Strain Resource.

et al., 2008) and subcortical structures (Petryszyn et al., 2014). Certain morphologies tend to elaborate certain electrophysiological properties, but there is both variability and overlap of form and function. While some fundamental features are conserved within classes (Rudy et al., 2011; Pfeffer et al., 2013), we still find notable heterogeneity among even well-described groups (Ma et al., 2006; Runyan et al., 2010; Chittajallu et al., 2013; Povysheva et al., 2013; Sohn et al., 2014). Dissecting this heterogeneity has become tractable with genetically-encoded FPs (Hadjantonakis et al., 2003; Livet et al., 2007; Kremers et al., 2011) whose cell-fill and membrane-directed expression has allowed for real-time visualization of interneurons in intact functional preparations such as juxtacellular recording or calcium imaging (Tukker et al., 2007; Kato et al., 2013; Chiovini et al., 2014; Lee et al., 2014) as well as more precise surveys of circuit connectivity. FPs have also been useful for certain neuropeptidergic subclasses of interneurons such as SST and VIP, in which the extensive processing of propeptides and the extra-somatic localization of their products have made these cell types difficult to visualize using conventional immunohistochemistry (Nassel, 1993). It is important to recognize that FPs exhibit variable stability (turnover, photo/pH/temperature stability) subject to differential regulation in each cell type. To better characterize cell shape and connectivity, however, genetically targeted FP expression offers a good promontory. The use of neurotropic viruses further reveals circuit connectivity of specific cell types.

Neurotropic viruses selectively infect neurons. Polysynaptic, monosynaptic, anterograde, and retrograde transport of viral vectors for cell labeling are now possible (Kuypers and Ugolini, 1990; Zemanick et al., 1991; Enquist and Card, 2003). One of the first viral tracing vectors to be implemented was modified herpes simplex virus (HSV), which shows both anterograde and retrograde transport and has recently been engineered to be cre-dependent for greater cell type-specificity (Lo and Anderson, 2011). HSV can be used to establish the polysynaptic connectivity of a circuit, but this viral tracing approach has been limited by cytotoxicity. Emergent methods for genetically-encoded monosynaptic viral tracing (Wickersham et al., 2007; Beier et al., 2011) now offer more sophisticated alternatives toward dissecting neuronal circuits. Using genetically engineered rabies virus (RV), alongside pseudotyping and cell type specific targeting approaches (Wall et al., 2010; Weible et al., 2010), we can now safely query monosynaptic inputs onto cells. Moreover, RV can encode dual fluorescent and functional reporters, such that monosynaptic pairs can be visualized and manipulated dynamically (Osakada et al., 2011).

As powerful as the new viral vectors are toward revealing brain connectivity, interpreting genetically targeted monosynaptic tracing studies in interneuronal circuits can be vexing. Interneurons, more so than principal excitatory neurons, promiscuously synapse onto other inhibitory cells in order to exert disinhibitory control in development (Kuhlman et al., 2013) and in the adult brain (Lee et al., 2013; Pfeffer et al., 2013; Pi et al., 2013; Xu et al., 2013). Reciprocal intraclass chemical synapses and/or electrical gap junctions coordinate activity across large populations of neurons (Tamas et al., 1998, 2000; Chiu et al., 2013; Hioki et al., 2013) and over considerable distances (Buzsaki et al., 2004; Caputi et al., 2013), confounding the identification of presynaptic-postsynaptic partners. Polysynaptic tracers and functional tools can be further implemented to clarify connectivity.

GENETICALLY ENCODED FUNCTIONAL DISSECTION OF INHIBITORY CIRCUITS

Recently, the light-activated non-specific cation channel channelrhodopsin-2 (ChR2) and its variants (Mattis et al., 2012) have been extremely valuable toward unraveling fundamentals of functional connectivity both *ex vivo* and *in vivo* (Huang et al., 2013; Jennings et al., 2013; Stamatakis et al., 2013; Halassa et al., 2014; Roux et al., 2014; Siegle and Wilson, 2014; Sparta et al., 2014). However, the interpretation of optogenetic manipulations in inhibitory neurons must be approached with some caution given the diversity of cell type-specific responses to photic stimulation. For example, using varying light stimulation parameters to activate different ChR2-expressing cell types, we learned that cortical somatostatin-positive interneurons exhibit heterogeneous firing properties, and that all regular-spiking interneuron subtypes evaluated including somatostatin, corticotropin-releasing hormone (CRH), and cholinergic interneurons could be functionally silenced, rather than activated, when photically stimulated with prolonged light pulses (Herman et al., 2014). An appropriate strategy would be to first identify the effect of stimulation on the cell type of interest using intracellular recordings or imaging techniques in order to avoid confounding interpretations at the level of post-synaptic electrophysiological probes and/or behavioral readouts. Any differential responses to optogenetic activation may then help to further subclassify interneurons.

As an alternative, or in parallel with optogenetic activation by ChR2, inhibition through light-activated chloride pumps (halorhodopsins) (Gradinaru et al., 2008; Tye et al., 2011) or proton pumps (archaerhodopsins) (Madisen et al., 2012; Beppu et al., 2014) allows us to query the direct circuit effect of temporally precise neuronal silencing. Whereas the light-gated activators have been relatively robust to engineering, the inhibitors have required ongoing reengineering to address issues such as intracellular accumulation/aggregation (halorhodopsins) and limited hyperpolarization due to proton pump kinetics (archaerhodopsins). Recently, two different groups developed an appealing alternative to inhibitory pumps by site-directed mutagenesis of channelrhodopsin, transforming it into a chloride-conducting channel. Notably, inhibitory channels have proven to be more efficient than ion pumps due to independence from photon-gated movement of individual ions, and preservation of normal electrochemical gradients (Berndt et al., 2014; Wietek et al., 2014). Reversibly silencing inhibitory interneurons can be quite useful with our growing knowledge of the behavioral contingencies that determine interclass activity differences (Letzkus et al., 2011; Lapray et al., 2012; Pi et al., 2013), as well as their differential role in network oscillations (Roux et al., 2014). This genetically targeted manipulation can also be used in the study of diseases with an evolving dysfunction of specific interneuronal cell types (Gernert et al., 2000, 2002; Kalanithi et al., 2005; Kataoka et al., 2010; Gittis et al., 2011; Kim et al., 2014), particularly to examine trial-by-trial, or time-locked variability in electrophysiology and behavior in the disease state.

Table 2 | Common genetically-targeted technologies in neuroscience research.

			Strengths	Challenges	References
Anatomical	Genetically-encoded fluorescent proteins	GFP, RFP, BFP, etc.	Can visualize soma or projections, can be tagged with functional reporters or overexpression constructs, real time visualization, many variants	Stability (turnover, photo/pH/temperature stability), fluorescent tags may affect tagged protein's function	Hadjantonakis et al., 2003; Livet et al., 2007; Kremers et al., 2011
	Genetically-encoded viral tracing	Rabies	Neurotropic, retrograde propagation, may be pseudotyped for infection selectivity, can reveal polysynaptic or monosynaptic connectivity, can be combined with functional reporters, high expression	Cytotoxicity (limits experimental time frame), nascent anterograde tracing strategies, can be used in concert with functional reporters, polysynaptic tracing cannot distinguish first-order connectivity	Wickersham et al., 2007; Wall et al., 2010; Weible et al., 2010; Beier et al., 2011; Osakada et al., 2011
		HSV	Cre-dependent variants available for specificity, polysynatpic tracing, retrograde and anterograde varieties available	Very high cytotoxicity (limits experimental time frame) limiting its use with functional reporters, polysynaptic tracing cannot distinguish first-order connectivity	Kuypers and Ugolini, 1990; Zemanick et al., 1991; Enquist and Card, 2003; Lo and Anderson, 2011
Functional	Genetically-encoded optogenetics	Excitatory Channelrhodopsin	Precise temporal control, can be used to directly assess functional connectivity, can be used *in vitro*/*ex vivo*/*in vivo*/awake, many variants with differential photo-kinetics	Potential for channel desensitization or depolarization block, not always sufficient for *in vivo* chronic activation experiments, physiologically relevant for excitable cell types more than for non-excitable cell types	Zhang et al., 2006; Mattis et al., 2012; Hochbaum et al., 2014
		Inhibitory Channelrhodopsin	Precise temporal inhibition, independent of photon-gated ion movement, more physiologic	Dependence on external pH	Berndt et al., 2014; Wietek et al., 2014
		Halorhodopsin	Precise temporal inhibition	Subcellular trafficking issues in older variants	Gradinaru et al., 2010; Tye et al., 2011
		Archaerhodopsin	Same as for halorhodopsins but new variants hyperpolarize more, can be used to manipulate pH, can be used as an actuator as well as an indicator	Limited by proton pump kinetics often requiring continuous photostimulation, older variants dim with long time constants and photocurrents	Madisen et al., 2012; Beppu et al., 2014; Hochbaum et al., 2014
	Genetically-encoded chemical genetics	nAchR, TRPV1	Endogenous receptor expression and ligand application to most faithfully recapitulate neuronal activation, timescale of activation within seconds	Unpredictable interactions with the native ligand-receptor pair, baseline depolarization in the absence of ligand	Drenan et al., 2008; Kim et al., 2012
		Interspecies channel proteins or GPCRs	Ligand-receptor selectivity	G-protein-coupled receptor off-target effects, ligand usually does not cross blood-brain barrier and thus must be applied locally using invasive procedures	Lechner et al., 2002; Slimko et al., 2002
		GABAA	Single modified endogenous GABAA receptor can be agonized and antagonized by different ligands (zolpidem, DMCM, respectively)	Requires a genetically-engineered zolpidem-insensitive background	Wulff et al., 2007

(Continued)

Table 2 | Continued

		Strengths	Challenges	References
	PSEM	Ligand-receptor selectivity, are not GPCR-based and thus minimize G-protein-coupled off-target effects, non-invasive ligand administration	May not be adequate for sustained activation/inhibition over prolonged periods compared to other methods (e.g., DREADDs).	Magnus et al., 2011; Sternson and Roth, 2014
	DREADD	Minute-hour activation/inhibition, manipulates excitable and non-excitable cells, recapitulates dysfunction in disease, non-invasive ligand administration	G-protein-coupled receptor off-target effects, requires different receptors for activation versus inhibition	Ferguson et al., 2011; Krashes et al., 2011; Ray et al., 2011; Wulff and Arenkiel, 2012; Wess et al., 2013
Genetically-encoded molecular imaging	GCAMP	*In vivo* imaging of neuronal activity, continually re-engineered for improved signal to noise	Limited dynamic range, indirect measure of action potentials, cannot parse resting from tonic activity, trade-off between Ca^{2+}-binding affinity and response	Tian et al., 2009
	Twitch (FRET-based)	More stable long-term *in vivo* imaging, brighter, subcellular visualization, differentiates resting state Ca^{2+} from tonic firing, large dynamic range, linear responses	Indirect measure of action potentials, trade-off between high calcium binding affinity and response kinetics.	Thestrup et al., 2014
	Clomeleon (FRET-based)	Can be used to study developmental neuronal changes in Cl^- as well as network effects of GABA activity	Lower affinity (~ 30 mM) compared to the intracellular Cl^- concentration (~10 mM); pH sensitive, photobleach at different rates, interfering with FRET signal	Kuner and Augustine, 2000; Glykys et al., 2014
	SynaptopHluorin	Measures the release of neurotransmitters	Diffusional loss of the reporter	Granseth et al., 2006

Given the timescale at which optogenetic reporters function, they are appropriate for manipulating rapid, time-sensitive circuit properties that influence behaviors. However, for behaviors or disease states that require changes in activity to persist over longer intervals, chronic photic activation or inhibition of neurons can be technically cumbersome and even deleterious to the cells under investigation. If the scientific question requires persistent activity manipulation in a population of neurons to influence behaviors occurring over larger timescales, pharmacologically-activated designer receptors offer an alternative approach (Wulff and Arenkiel, 2012). Transgenic overexpression of an endogenous ionic receptor can be modulated by application of its ligand to produce membrane depolarization (Drenan et al., 2008; Kim et al., 2012), but interactions with the native ligand-receptor pair might unpredictably influence experimental outcomes. Chemically and genetically engineered ligand gated ion channels (Wulff et al., 2007) insensitive to endogenous ligands (Wulff et al., 2007; Magnus et al., 2011; Sternson and Roth, 2014), or mammalian expression of channel proteins or excitatory or inhibitory G protein-coupled receptors (GPCRs) from invertebrates (Lechner et al., 2002; Slimko et al., 2002) strategically attempt to avoid this confound, but engineered GPCRs offer perhaps the most elegant alternative (Armbruster et al., 2007). A recent incarnation of these is the DREADDs (designer receptors exclusively activated by designer drugs) (Armbruster et al., 2007), which employ an engineered receptor-synthetic ligand pair that is completely orthogonal to its endogenous equivalent, exhibits little or no baseline activity, and allows for genetically targeted activation or inhibition (Ferguson et al., 2011; Krashes et al., 2011; Ray et al., 2011). GPCRs mediate intracellular signaling cascades activated by various monoaminergic neurotransmitters and neuropeptides, more faithfully recapitulating the postsynaptic changes that may ensue with activation or inhibition of interneuronal cell types. As many neuropsychiatric disorders are the result of dysfunction or loss of these interneurons, designer GPCRs may also generate conditions that most resemble disease states. Furthermore, they offer the unique advantage of functionally dissecting intact deep subcortical circuits in a way that is more difficult or not possible with optogenetic and imaging methods used readily at the cortical surface. In order to study the complex compensatory changes that may occur with chronic, irreversible cell type-specific loss, we can employ genetically targeted lesions (Buch et al., 2005). Both reversible ligand-mediated methods and genetic lesions offer the advantage of being minimally invasive, and require only viral delivery of a receptor and peripheral application of its cognate ligand. These techniques can also be used concurrently with electrophysiological recordings without introducing overt artifacts, though a

remarkable new alternative enables cross-talk free all-optogenetic actuation and indication using genetically modified channelrhodopsins and archaerhodopsins (Hochbaum et al., 2014) as well.

Genetically encoded molecular indicators augment the information that is available through traditional electrophysiological and behavioral assays of circuit function. These biosensors come in many varieties; briefly discussed here are fluorescent indicators for calcium, chloride, and neurotransmitter vesicular release. Calcium biosensors come in two forms—single wavelength sensors and ratiometric sensors that rely on fluorescence energy resonance transfer (FRET). GCaMP, an example of the former, is a fusion of GFP with calmodulin, an intracellular protein that binds calcium. In the presence of calcium, calmodulin undergoes a conformational change, which renders the GFP brighter than at baseline (Tian et al., 2009), thus allowing the detection of increased neuronal activity that occurs with calcium entry. This tool fundamentally relies on measurements of relative fluorescence. FRET allows for more stable and high resolution long term imaging, which can be used to study the neuromodulatory role of interneurons in fluctuating brain states as well as subcellular localization of GPCR signaling (protein kinase A) by neuromodulators (Chen et al., 2014). Interneurons tend to have characteristic projections onto the soma, dendrites, and axons of postsynaptic target cells, subcellular compartments that can be resolved by this technique. Ratiometric measurements can also differentiate resting state Ca^{2+} from Ca^{2+} influx of tonically firing neurons, a property that also segregates differentially between and within interneuronal classes. While calcium indicators have been especially useful to study neuronal activity (Thestrup et al., 2014), this reflects only the spiking behavior of the interneurons rather than their network level inhibitory outputs. A complementary approach to study inhibition takes advantage of the genetically encoded fluorescent chloride indicator, clomeleon (Kuner and Augustine, 2000). Clomeleon can be used to study network effects of GABA activity, and uniquely, developmental neuronal changes in Cl^- to report neuronal inhibition. Finally, synaptopHluorin is a genetically encoded neurotransmitter indicator engineered as a fusion between synapsin, a presynaptic vesicular fusion protein, and a pH sensitive GFP. In an acidic environment of synaptic vesicles prior to release, the GFP does not fluoresce. Alkalinization of the vesicles upon release into the extracellular space with neuronal activity results in bright fluorescence. Together, each of these neuroimaging tools allows for insight into the circuit connectivity of interneurons.

CONCLUSIONS AND DIRECTIONS FOR FUTURE RESEARCH

Interneurons exhibit heterogeneous origins, morphologies, and functions that render their detailed characterization challenging. We advocate for an intersectional dissection of this heterogeneity. Starting with genetic and molecular tools (**Table 2**), we can characterize cardinal groups of interneurons that we further parse with powerful new techniques such as single cell gene expression analyses (Kamme et al., 2003) to elaborate iteratively what molecules better define classes. Though we did not expand on functionally characterizing interneurons with an eye to their role in specific behaviors (Kvitsiani et al., 2013; Courtin et al., 2014) and their dysfunction/attrition in disease (Verret et al., 2012; Benarroch, 2013; Del Pino et al., 2013), this may also help to constrain their undeniably vast genetic and molecular diversity. As interneuron classes are delimited operationally, and dynamically refined using genetically targeted methods, answers emerge about the shared molecular features of specific neuronal subsets that can then be exploited to generate targeted genetic approaches to their further study.

ACKNOWLEDGMENTS

We would like to thank Kathleen Quast for her input on the manuscript. This was supported by T32NS043124 to Dona K. Murphey and NS078294 to Benjamin R. Arenkiel.

REFERENCES

Armbruster, B. N., Li, X., Pausch, M. H., Herlitze, S., and Roth, B. L. (2007). Evolving the lock to fit the key to create a family of G protein-coupled receptors potently activated by an inert ligand. *Proc. Natl. Acad. Sci. U.S.A.* 104, 5163–5168. doi: 10.1073/pnas.0700293104

Ascoli, G. A., Alonso-Nanclares, L., Anderson, S. A., Barrionuevo, G., Benavides-Piccione, R., Burkhalter, A., et al. (2008). Petilla terminology: nomenclature of features of GABAergic interneurons of the cerebral cortex. *Nat. Rev. Neurosci.* 9, 557–568. doi: 10.1038/nrn2402

Beier, K. T., Saunders, A., Oldenburg, I. A., Miyamichi, K., Akhtar, N., Luo, L., et al. (2011). Anterograde or retrograde transsynaptic labeling of CNS neurons with vesicular stomatitis virus vectors. *Proc. Natl. Acad. Sci. U.S.A.* 108, 15414–15419. doi: 10.1073/pnas.1110854108

Benarroch, E. E. (2013). Neocortical interneurons: functional diversity and clinical correlations. *Neurology* 81, 273–280. doi: 10.1212/WNL.0b013e31829c002f

Beppu, K., Sasaki, T., Tanaka, K. F., Yamanaka, A., Fukazawa, Y., Shigemoto, R., et al. (2014). Optogenetic countering of glial acidosis suppresses glial glutamate release and ischemic brain damage. *Neuron* 81, 314–320. doi: 10.1016/j.neuron.2013.11.011

Berndt, A., Lee, S. Y., Ramakrishnan, C., and Deisseroth, K. (2014). Structure-guided transformation of channelrhodopsin into a light-activated chloride channel. *Science* 344, 420–424. doi: 10.1126/science.1252367

Betley, J. N., and Sternson, S. M. (2011). Adeno-associated viral vectors for mapping, monitoring, and manipulating neural circuits. *Hum. Gene Ther.* 22, 669–677. doi: 10.1089/hum.2010.204

Brown, J., Pan, W. X., and Dudman, J. T. (2014). The inhibitory microcircuit of the substantia nigra provides feedback gain control of the basal ganglia output. *eLife* 3:e02397. doi: 10.7554/eLife.02397

Buch, T., Heppner, F. L., Tertilt, C., Heinen, T. J., Kremer, M., Wunderlich, F. T., et al. (2005). A Cre-inducible diphtheria toxin receptor mediates cell lineage ablation after toxin administration. *Nat. Methods* 2, 419–426. doi: 10.1038/nmeth762

Buzsaki, G., Geisler, C., Henze, D. A., and Wang, X. J. (2004). Interneuron Diversity series: circuit complexity and axon wiring economy of cortical interneurons. *Trends Neurosci.* 27, 186–193. doi: 10.1016/j.tins.2004.02.007

Caputi, A., Melzer, S., Michael, M., and Monyer, H. (2013). The long and short of GABAergic neurons. *Curr. Opin. Neurobiol.* 23, 179–186. doi: 10.1016/j.conb.2013.01.021

Chattopadhyaya, B., Di Cristo, G., Wu, C. Z., Knott, G., Kuhlman, S., Fu, Y., et al. (2007). GAD67-mediated GABA synthesis and signaling regulate inhibitory synaptic innervation in the visual cortex. *Neuron* 54, 889–903. doi: 10.1016/j.neuron.2007.05.015

Chen, Y., Saulnier, J. L., Yellen, G., and Sabatini, B. L. (2014). A PKA activity sensor for quantitative analysis of endogenous GPCR signaling via 2-photon FRET-FLIM imaging. *Front. Pharmacol.* 5:56. doi: 10.3389/fphar.2014.00056

Chiovini, B., Turi, G. F., Katona, G., Kaszás, A., Pálfi, D., Maák, P., et al. (2014). Dendritic spikes induce ripples in parvalbumin interneurons during hippocampal sharp waves. *Neuron* 82, 908–924. doi: 10.1016/j.neuron.2014.04.004

Chittajallu, R., Craig, M. T., McFarland, A., Yuan, X., Gerfen, S., Tricoire, L., et al. (2013). Dual origins of functionally distinct O-LM interneurons revealed by differential 5-HT(3A)R expression. *Nat. Neurosci.* 16, 1598–1607. doi: 10.1038/nn.3538

Chiu, C. Q., Lur, G., Morse, T. M., Carnevale, N. T., Ellis-Davies, G. C., and Higley, M. J. (2013). Compartmentalization of GABAergic inhibition by dendritic spines. *Science* 340, 759–762. doi: 10.1126/science.1234274

Cho, K., and Sohal, V. S. (2014). Optogenetic approaches for investigating neural pathways implicated in schizophrenia and related disorders. *Hum. Mol. Genet.* 23, R64–R68. doi: 10.1093/hmg/ddu225

Courtin, J., Chaudun, F., Rozeske, R. R., Karalis, N., Gonzalez-Campo, C., Wurtz, H., et al. (2014). Prefrontal parvalbumin interneurons shape neuronal activity to drive fear expression. *Nature* 505, 92–96. doi: 10.1038/nature12755

Del Pino, I., Garcia-Frigola, C., Dehorter, N., Brotons-Mas, J. R., Alvarez-Salvado, E., de Lagrán, M. M., et al. (2013). Erbb4 deletion from fast-spiking interneurons causes schizophrenia-like phenotypes. *Neuron* 79, 1152–1168. doi: 10.1016/j.neuron.2013.07.010

Drenan, R. M., Grady, S. R., Whiteaker, P., McClure-Begley, T., McKinney, S., Miwa, J. M., et al. (2008). *In vivo* activation of midbrain dopamine neurons via sensitized, high-affinity alpha 6 nicotinic acetylcholine receptors. *Neuron* 60, 123–136. doi: 10.1016/j.neuron.2008.09.009

Dymecki, S. M., and Kim, J. C. (2007). Molecular neuroanatomy's "Three Gs": a primer. *Neuron* 54, 17–34. doi: 10.1016/j.neuron.2007.03.009

Enquist, L. W., and Card, J. P. (2003). Recent advances in the use of neurotropic viruses for circuit analysis. *Curr. Opin. Neurobiol.* 13, 603–606. doi: 10.1016/j.conb.2003.08.001

Ferguson, S. M., Eskenazi, D., Ishikawa, M., Wanat, M. J., Phillips, P. E., Dong, Y., et al. (2011). Transient neuronal inhibition reveals opposing roles of indirect and direct pathways in sensitization. *Nat. Neurosci.* 14, 22–24. doi: 10.1038/nn.2703

Fu, Y., Tucciarone, J. M., Espinosa, J. S., Sheng, N., Darcy, D. P., Nicoll, R. A., et al. (2014). A cortical circuit for gain control by behavioral state. *Cell* 156, 1139–1152. doi: 10.1016/j.cell.2014.01.050

Garcia-Otin, A. L., and Guillou, F. (2006). Mammalian genome targeting using site-specific recombinases. *Front. Biosci.* 11, 1108–1136. doi: 10.2741/1867

Gernert, M., Bennay, M., Fedrowitz, M., Rehders, J. H., and Richter, A. (2002). Altered discharge pattern of basal ganglia output neurons in an animal model of idiopathic dystonia. *J. Neurosci.* 22, 7244–7253.

Gernert, M., Hamann, M., Bennay, M., Löscher, W., and Richter, A. (2000). Deficit of striatal parvalbumin-reactive GABAergic interneurons and decreased basal ganglia output in a genetic rodent model of idiopathic paroxysmal dystonia. *J. Neurosci.* 20, 7052–7058.

Gittis, A. H., Leventhal, D. K., Fensterheim, B. A., Pettibone, J. R., Berke, J. D., and Kreitzer, A. C. (2011). Selective inhibition of striatal fast-spiking interneurons causes dyskinesias. *J. Neurosci.* 31, 15727–15731. doi: 10.1523/JNEUROSCI.3875-11.2011

Glykys, J., Dzhala, V., Egawa, K., Balena, T., Saponjian, Y., Kuchibhotla, K. V., et al. (2014). Local impermeant anions establish the neuronal chloride concentration. *Science* 343, 670–675. doi: 10.1126/science.1245423

Gradinaru, V., Mogri, M., Thompson, K. R., Henderson, J. M., and Deisseroth, K. (2009). Optical deconstruction of parkinsonian neural circuitry. *Science* 324, 354–359. doi: 10.1126/science.1167093

Gradinaru, V., Thompson, K. R., and Deisseroth, K. (2008). eNpHR: a Natronomonas halorhodopsin enhanced for optogenetic applications. *Brain Cell Biol.* 36, 129–139. doi: 10.1007/s11068-008-9027-6

Gradinaru, V., Zhang, F., Ramakrishnan, C., Mattis, J., Prakash, R., Diester, I., et al. (2010). Molecular and cellular approaches for diversifying and extending optogenetics. *Cell* 141, 154–165. doi: 10.1016/j.cell.2010.02.037

Granseth, B., Odermatt, B., Royle, S. J., and Lagnado, L. (2006). Clathrin-mediated endocytosis is the dominant mechanism of vesicle retrieval at hippocampal synapses. *Neuron* 51, 773–786. doi: 10.1016/j.neuron.2006.08.029

Gyurko, R., Leupen, S., and Huang, P. L. (2002). Deletion of exon 6 of the neuronal nitric oxide synthase gene in mice results in hypogonadism and infertility. *Endocrinology* 143, 2767–2774. doi: 10.1210/endo.143.7.8921

Hadjantonakis, A. K., Dickinson, M. E., Fraser, S. E., and Papaioannou, V. E. (2003). Technicolour transgenics: imaging tools for functional genomics in the mouse. *Nat. Rev. Genetics* 4, 613–625. doi: 10.1038/nrg1126

Halassa, M. M., Chen, Z., Wimmer, R. D., Brunetti, P. M., Zhao, S., Zikopoulos, B., et al. (2014). State-dependent architecture of thalamic reticular subnetworks. *Cell* 158, 808–821. doi: 10.1016/j.cell.2014.06.025

Hamilton, L. S., Sohl-Dickstein, J., Huth, A. G., Carels, V. M., Deisseroth, K., and Bao, S. (2013). Optogenetic activation of an inhibitory network enhances feedforward functional connectivity in auditory cortex. *Neuron* 80, 1066–1076. doi: 10.1016/j.neuron.2013.08.017

Heintz, N. (2001). BAC to the future: the use of bac transgenic mice for neuroscience research. *Nat. Rev. Neurosci.* 2, 861–870. doi: 10.1038/35104049

Herman, A. M., Huang, L., Murphey, D. K., Garcia, I., and Arenkiel, B. R. (2014). Cell type-specific and time-dependent light exposure contribute to silencing in neurons expressing Channelrhodopsin-2. *eLife* 3:e01481. doi: 10.7554/eLife.01481

Hioki, H., Okamoto, S., Konno, M., Kameda, H., Sohn, J., Kuramoto, E., et al. (2013). Cell type-specific inhibitory inputs to dendritic and somatic compartments of parvalbumin-expressing neocortical interneuron. *J. Neurosci.* 33, 544–555. doi: 10.1523/JNEUROSCI.2255-12.2013

Hochbaum, D. R., Zhao, Y., Farhi, S. L., Klapoetke, N., Werley, C. A., Kapoor, V., et al. (2014). All-optical electrophysiology in mammalian neurons using engineered microbial rhodopsins. *Nat. Methods* 11, 825–833. doi: 10.1038/nmeth.3000

Hodgson, L., Pertz, O., and Hahn, K. M. (2008). Design and optimization of genetically encoded fluorescent biosensors: GTPase biosensors. *Methods Cell Biol.* 85, 63–81. doi: 10.1016/S0091-679X(08)85004-2

Huang, L., Garcia, I., Jen, H. I., and Arenkiel, B. R. (2013). Reciprocal connectivity between mitral cells and external plexiform layer interneurons in the mouse olfactory bulb. *Front. Neural Circuits* 7:32. doi: 10.3389/fncir.2013.00032

Jennings, J. H., Rizzi, G., Stamatakis, A. M., Ung, R. L., and Stuber, G. D. (2013). The inhibitory circuit architecture of the lateral hypothalamus orchestrates feeding. *Science* 341, 1517–1521. doi: 10.1126/science.1241812

Kalanithi, P. S., Zheng, W., Kataoka, Y., DiFiglia, M., Grantz, H., Saper, C. B., et al. (2005). Altered parvalbumin-positive neuron distribution in basal ganglia of individuals with Tourette syndrome. *Proc. Natl. Acad. Sci. U.S.A.* 102, 13307–13312. doi: 10.1073/pnas.0502624102

Kamme, F., Salunga, R., Yu, J., Tran, D. T., Zhu, J., Luo, L., et al. (2003). Single-cell microarray analysis in hippocampus CA1: demonstration and validation of cellular heterogeneity. *J. Neurosci.* 23, 3607–3615.

Kataoka, Y., Kalanithi, P. S., Grantz, H., Schwartz, M. L., Saper, C., Leckman, J. F., et al. (2010). Decreased number of parvalbumin and cholinergic interneurons in the striatum of individuals with Tourette syndrome. *J. Comp. Neurol.* 518, 277–291. doi: 10.1002/cne.22206

Kato, H. K., Gillet, S. N., Peters, A. J., Isaacson, J. S., and Komiyama, T. (2013). Parvalbumin-expressing interneurons linearly control olfactory bulb output. *Neuron* 80, 1218–1231. doi: 10.1016/j.neuron.2013.08.036

Kepecs, A., and Fishell, G. (2014). Interneuron cell types are fit to function. *Nature* 505, 318–326. doi: 10.1038/nature12983

Kerr, B. J., Cafferty, W. B., Gupta, Y. K., Bacon, A., Wynick, D., McMahon, S. B., et al. (2000). Galanin knockout mice reveal nociceptive deficits following peripheral nerve injury. *Eur. J. Neurosci.* 12, 793–802. doi: 10.1046/j.1460-9568.2000.00967.x

Kim, E. H., Thu, D. C., Tippett, L. J., Oorschot, D. E., Hogg, V. M., Roxburgh, R., et al. (2014). Cortical interneuron loss and symptom heterogeneity in Huntington disease. *Ann. Neurol.* 75, 717–727. doi: 10.1002/ana.24162

Kim, Y. H., Back, S. K., Davies, A. J., Jeong, H., Jo, H. J., Chung, G., et al. (2012). TRPV1 in GABAergic interneurons mediates neuropathic mechanical allodynia and disinhibition of the nociceptive circuitry in the spinal cord. *Neuron* 74, 640–647. doi: 10.1016/j.neuron.2012.02.039

Kimura, S., Hara, Y., Pineau, T., Fernandez-Salguero, P., Fox, C. H., Ward, J. M., et al. (1996). The T/ebp null mouse: thyroid-specific enhancer-binding protein is essential for the organogenesis of the thyroid, lung, ventral forebrain, and pituitary. *Genes Dev.* 10, 60–69. doi: 10.1101/gad.10.1.60

Krashes, M. J., Koda, S., Ye, C., Rogan, S. C., Adams, A. C., Cusher, D. S., et al. (2011). Rapid, reversible activation of AgRP neurons drives feeding behavior in mice. *J. Clin. Invest.* 121, 1424–1428. doi: 10.1172/JCI46229

Kravitz, A. V., Freeze, B. S., Parker, P. R. L., Kay, K., Thwin, M. T., Deisseroth, K., et al. (2010). Regulation of parkinsonian motor behaviours by optogenetic control of basal ganglia circuitry. *Nature* 466, 622–626. doi: 10.1038/nature09159

Kravitz, A. V., Tye, L. D., and, and Kreitzer, A. C. (2012). Distinct roles for direct and indirect pathway striatal neurons in reinforcement. *Nat. Neurosci.* 15, 816–818. doi: 10.1038/nn.3100

Kremers, G. J., Gilbert, S. G., Cranfill, P. J., Davidson, M. W., and Piston, D. W. (2011). Fluorescent proteins at a glance. *J. Cell Sci.* 124(Pt 2), 157–160. doi: 10.1242/jcs.072744

Krook-Magnuson, E., Armstrong, C., Oijala, M., and Soltesz, I. (2013). On-demand optogenetic control of spontaneous seizures in temporal lobe epilepsy. *Nat. Commun.* 4:1376. doi: 10.1038/ncomms2376

Kuhlman, S. J., Olivas, N. D., Tring, E., Ikrar, T., Xu, X., and Trachtenberg, J. T. (2013). A disinhibitory microcircuit initiates critical-period plasticity in the visual cortex. *Nature* 501, 543–546. doi: 10.1038/nature12485

Kumar, A., Vlachos, I., Aertsen, A., and Boucsein, C. (2013). Challenges of understanding brain function by selective modulation of neuronal subpopulations. *Trends Neurosci.* 36, 579–586. doi: 10.1016/j.tins.2013.06.005

Kuner, T., and Augustine, G. J. (2000). A genetically encoded ratiometric indicator for chloride: capturing chloride transients in cultured hippocampal neurons. *Neuron* 27, 447–459. doi: 10.1016/S0896-6273(00)00056-8

Kusakabe, T., Kawaguchi, A., Hoshi, N., Kawaguchi, R., Hoshi, S., and Kimura, S. (2006). Thyroid-specific enhancer-binding protein/NKX2.1 is required for the maintenance of ordered architecture and function of the differentiated thyroid. *Mol. Endocrinol.* 20, 1796–1809. doi: 10.1210/me.2005-0327

Kuypers, H. G., and Ugolini, G. (1990). Viruses as transneuronal tracers. *Trends Neurosci.* 13, 71–75. doi: 10.1016/0166-2236(90)90071-H

Kvitsiani, D., Ranade, S., Hangya, B., Taniguchi, H., Huang, J. Z., and Kepecs, A. (2013). Distinct behavioural and network correlates of two interneuron types in prefrontal cortex. *Nature* 498, 363–366. doi: 10.1038/nature12176

Lapray, D., Lasztoczi, B., Lagler, M., Viney, T. J., Katona, L., Valenti, O., et al. (2012). Behavior-dependent specialization of identified hippocampal interneurons. *Nat. Neurosci.* 15, 1265–1271. doi: 10.1038/nn.3176

Lechner, H. A., Lein, E. S., and Callaway, E. M. (2002). A genetic method for selective and quickly reversible silencing of Mammalian neurons. *J. Neurosci.* 22, 5287–5290.

Ledri, M., Madsen, M. G., Nikitidou, L., Kirik, D., and Kokaia, M. (2014). Global optogenetic activation of inhibitory interneurons during epileptiform activity. *J. Neurosci.* 34, 3364–3377. doi: 10.1523/JNEUROSCI.2734-13.2014

Lee, S. H., Kwan, A. C., and Dan, Y. (2014). Interneuron subtypes and orientation tuning. *Nature* 508, E1–E2. doi: 10.1038/nature13128

Lee, S. H., Kwan, A. C., Zhang, S., Phoumthipphavong, V., Flannery, J. G., Masmanidis, S. C., et al. (2012). Activation of specific interneurons improves V1 feature selectivity and visual perception. *Nature* 488, 379–383. doi: 10.1038/nature11312

Lee, S., Kruglikov, I., Huang, Z. J., Fishell, G., and Rudy, B. (2013). A disinhibitory circuit mediates motor integration in the somatosensory cortex. *Nat. Neurosci.* 16, 1662–1670. doi: 10.1038/nn.3544

Letzkus, J. J., Wolff, S. B., Meyer, E. M., Tovote, P., Courtin, J., Herry, C., et al. (2011). A disinhibitory microcircuit for associative fear learning in the auditory cortex. *Nature* 480, 331–335. doi: 10.1038/nature10674

Liodis, P., Denaxa, M., Grigoriou, M., Akufo-Addo, C., Yanagawa, Y., and Pachnis, V. (2007). Lhx6 activity is required for the normal migration and specification of cortical interneuron subtypes. *J. Neurosci.* 27, 3078–3089. doi: 10.1523/JNEUROSCI.3055-06.2007

Livet, J., Weissman, T. A., Kang, H., Draft, R. W., Lu, J., Bennis, R. A., et al. (2007). Transgenic strategies for combinatorial expression of fluorescent proteins in the nervous system. *Nature* 450, 56–62. doi: 10.1038/nature06293

Lo, L., and Anderson, D. J. (2011). A Cre-dependent, anterograde transsynaptic viral tracer for mapping output pathways of genetically marked neurons. *Neuron* 72, 938–950. doi: 10.1016/j.neuron.2011.12.002

Luo, L., Callaway, E. M., and Svoboda, K. (2008). Genetic dissection of neural circuits. *Neuron* 57, 634–660. doi: 10.1016/j.neuron.2008.01.002

Ma, Y., Hu, H., Berrebi, A. S., Mathers, P. H., and Agmon, A. (2006). Distinct subtypes of somatostatin-containing neocortical interneurons revealed in transgenic mice. *J. Neurosci.* 26, 5069–5082. doi: 10.1523/JNEUROSCI.0661-06.2006

Madisen, L., Mao, T., Koch, H., Zhuo, J. M., Berenyi, A., Fujisawa, S., et al. (2012). A toolbox of Cre-dependent optogenetic transgenic mice for light-induced activation and silencing. *Nat. Neurosci.* 15, 793–802. doi: 10.1038/nn.3078

Magnus, C. J., Lee, P. H., Atasoy, D., Su, H. H., Looger, L. L., and Sternson, S. M. (2011). Chemical and genetic engineering of selective ion channel-ligand interactions. *Science* 333, 1292–1296. doi: 10.1126/science.1206606

Markram, H., Toledo-Rodriguez, M., Wang, Y., Gupta, A., Silberberg, G., and Wu, C. (2004). Interneurons of the neocortical inhibitory system. *Nat. Rev. Neurosci.* 5, 793–807. doi: 10.1038/nrn1519

Mattis, J., Tye, K. M., Ferenczi, E. A., Ramakrishnan, C., O'Shea, D. J., Prakash, R., et al. (2012). Principles for applying optogenetic tools derived from direct comparative analysis of microbial opsins. *Nat. Methods* 9, 159–172. doi: 10.1038/nmeth.1808

Melzer, S., Michael, M., Caputi, A., Eliava, M., Fuchs, E. C., Whittington, M. A., et al. (2012). Long-range-projecting GABAergic neurons modulate inhibition in hippocampus and entorhinal cortex. *Science* 335, 1506–1510. doi: 10.1126/science.1217139

Misgeld, T., Burgess, R. W., Lewis, R. M., Cunningham, J. M., Lichtman, J. W., and Sanes, J. R. (2002). Roles of neurotransmitter in synapse formation: development of neuromuscular junctions lacking choline acetyltransferase. *Neuron* 36, 635–648. doi: 10.1016/S0896-6273(02)01020-6

Miyoshi, G., Hjerling-Leffler, J., Karayannis, T., Sousa, V. H., Butt, S. J. B., Battiste, J., et al. (2010). Genetic fate mapping reveals that the caudal ganglionic eminence produces a large and diverse population of superficial cortical interneurons. *J. Neurosci.* 30, 1582–1594. doi: 10.1523/JNEUROSCI.4515-09.2010

Nassel, D. R. (1993). Neuropeptides in the insect brain: a review. *Cell Tissue Res.* 273, 1–29. doi: 10.1007/BF00304608

Nathanson, J. L., Jappelli, R., Scheeff, E. D., Manning, G., Obata, K., Brenner, S., et al. (2009). Short promoters in viral vectors drive selective expression in mammalian inhibitory neurons, but do not restrict activity to specific inhibitory cell-types. *Front. Neural Circuits* 3:19. doi: 10.3389/neuro.04.019.2009

Nelson, A. B., Hammack, N., Yang, C. F., Shah, N. M., Seal, R. P., Kreitzer, A. C., et al. (2014). Striatal cholinergic interneurons Drive GABA release from dopamine terminals. *Neuron* 82, 63–70. doi: 10.1016/j.neuron.2014.01.023

Osakada, F., Mori, T., Cetin, A. H., Marshel, J. H., Virgen, B., and Callaway, E. M. (2011). New rabies virus variants for monitoring and manipulating activity and gene expression in defined neural circuits. *Neuron* 71, 617–631. doi: 10.1016/j.neuron.2011.07.005

Peng, Z., Zhang, N., Wei, W., Huang, C. S., Cetina, Y., Otis, T. S., et al. (2013). A reorganized GABAergic circuit in a model of epilepsy: evidence from optogenetic labeling and stimulation of somatostatin interneurons. *J. Neurosci.* 33, 14392–14405. doi: 10.1523/JNEUROSCI.2045-13.2013

Petryszyn, S., Beaulieu, J. M., Parent, A., and Parent, M. (2014). Distribution and morphological characteristics of striatal interneurons expressing calretinin in mice: a comparison with human and nonhuman primates. *J. Chem. Neuroanat.* 59–60, 51–61. doi: 10.1016/j.jchemneu.2014.06.002

Pfeffer, C. K., Xue, M., He, M., Huang, Z. J., and Scanziani, M. (2013). Inhibition of inhibition in visual cortex: the logic of connections between molecularly distinct interneurons. *Nat. Neurosci.* 16, 1068–1076. doi: 10.1038/nn.3446

Pi, H. J., Hangya, B., Kvitsiani, D., Sanders, J. I., Huang, Z. J., and Kepecs, A. (2013). Cortical interneurons that specialize in disinhibitory control. *Nature* 503, 521–524. doi: 10.1038/nature12676

Povysheva, N. V., Zaitsev, A. V., Gonzalez-Burgos, G., and Lewis, D. A. (2013). Electrophysiological heterogeneity of fast-spiking interneurons: chandelier versus basket cells. *PLoS ONE* 8:e70553. doi: 10.1371/journal.pone.0070553

Qian, S., Chen, H., Weingarth, D., Trumbauer, M. E., Novi, D. E., Guan, X., et al. (2002). Neither agouti-related protein nor neuropeptide Y is critically required for the regulation of energy homeostasis in mice. *Mol. Cell. Biol.* 22, 5027–5035. doi: 10.1128/MCB.22.14.5027-5035.2002

Qiu, M., Bulfone, A., Ghattasa, I., Menesesb, J. J., Christensenc, L., Sharpe, P. T., et al. (1997). Role of the Dlx homeobox genes in proximodistal patterning of the branchial arches: mutations of Dlx-1, Dlx-2, and Dlx-1 and -2 alter morphogenesis of proximal skeletal and soft tissue structures derived from the first and second arches. *Dev. Biol.* 185, 165–184. doi: 10.1006/dbio.1997.8556

Ray, R. S., Corcoran, A. E., Brust, R. D., Kim, J. C., Richerson, G. B., Nattie, E., et al. (2011). Impaired respiratory and body temperature control upon acute serotonergic neuron inhibition. *Science* 333, 637–642. doi: 10.1126/science.1205295

Robledo, R. F., Rajan, L., Li, X., and Lufkin, T. (2002). The Dlx5 and Dlx6 homeobox genes are essential for craniofacial, axial, and appendicular skeletal development. *Genes Dev.* 16, 1089–1101. doi: 10.1101/gad.988402

Rothermel, M., Brunert, D., Zabawa, C., Díaz-Quesada, M., and Wachowiak, M. (2013). Transgene expression in target-defined neuron populations mediated by retrograde infection with adeno-associated viral vectors. *J. Neurosci.* 33, 15195–15206. doi: 10.1523/JNEUROSCI.1618-13.2013

Roux, L., Stark, E., Sjulson, L., and Buzsáki, G. (2014). *In vivo* optogenetic identification and manipulation of GABAergic interneuron subtypes. *Curr. Opin. Neurobiol.* 26C, 88–95. doi: 10.1016/j.conb.2013.12.013

Rudy, B., Fishell, G., Lee, S., and Hjerling-Leffler, J. (2011). Three groups of interneurons account for nearly 100% of neocortical GABAergic neurons. *Dev. Neurobiol.* 71, 45–61. doi: 10.1002/dneu.20853

Runyan, C. A., Schummers, J., Van Wart, A., Kuhlman, S. J., Wilson, N. R., Huang, Z. J., et al. (2010). Response features of parvalbumin-expressing interneurons

suggest precise roles for subtypes of inhibition in visual cortex. *Neuron* 67, 847–857. doi: 10.1016/j.neuron.2010.08.006

Schnutgen, F., Doerflinger, N., Calléja, C., Wendling, O., Chambon, P., and Ghyselinck, N. B. (2003). A directional strategy for monitoring Cre-mediated recombination at the cellular level in the mouse. *Nat. Biotechnol.* 21, 562–565. doi: 10.1038/nbt811

Schurmans, S., Schiffmann, S. N., Gurden, H., Lemaire, M., Lipp, H. P., Schwam, V., et al. (1997). Impaired long-term potentiation induction in dentate gyrus of calretinin-deficient mice. *Proc. Natl. Acad. Sci. U.S.A.* 94, 10415–10420. doi: 10.1073/pnas.94.19.10415

Schwaller, B., Dick, J., Dhoot, G., Carroll, S., Vrbova, G., Nicotera, P., et al. (1999). Prolonged contraction-relaxation cycle of fast-twitch muscles in parvalbumin knockout mice. *Am. J. Physiol.* 276(2 Pt 1), C395–C403.

Siegle, J. H., and Wilson, M. A. (2014). Enhancement of encoding and retrieval functions through theta phase-specific manipulation of hippocampus. *eLife* 3:e03061. doi: 10.7554/eLife.03061

Slimko, E. M., McKinney, S., Anderson, D. J., Davidson, N., and Lester, H. A. (2002). Selective electrical silencing of mammalian neurons *in vitro* by the use of invertebrate ligand-gated chloride channels. *J. Neurosci.* 22, 7373–7379.

Sohn, J., Hioki, H., Okamoto, S., and Kaneko, T. (2014). Preprodynorphin-expressing neurons constitute a large subgroup of somatostatin-expressing GABAergic interneurons in the mouse neocortex. *J. Comp. Neurol.* 522, 1506–1526. doi: 10.1002/cne.23477

Sparta, D. R., Hovelso, N., Mason, A. O., Kantak, P. A., Ung, R. L., Decot, H. K., et al. (2014). Activation of prefrontal cortical parvalbumin interneurons facilitates extinction of reward-seeking behavior. *J. Neurosci.* 34, 3699–3705. doi: 10.1523/JNEUROSCI.0235-13.2014

Stamatakis, A. M., Jennings, J. H., Ung, R. L., Blair, G. A., Weinberg, R. J., Neve, R. L., et al. (2013). A unique population of ventral tegmental area neurons inhibits the lateral habenula to promote reward. *Neuron* 80, 1039–1053. doi: 10.1016/j.neuron.2013.08.023

Sternson, S. M., and Roth, B. L. (2014). Chemogenetic tools to interrogate brain functions. *Annu. Rev. Neurosci.* 37, 387–407. doi: 10.1146/annurev-neuro-071013-014048

Tamas, G., Buhl, E. H., Lörincz, A., and Somogyi, P. (2000). Proximally targeted GABAergic synapses and gap junctions synchronize cortical interneurons. *Nat. Neurosci.* 3, 366–371. doi: 10.1038/73936

Tamas, G., Somogyi, P., and Buhl, E. H. (1998). Differentially interconnected networks of GABAergic interneurons in the visual cortex of the cat. *J. Neurosci.* 18, 4255–4270.

Taniguchi, H. (2014). Genetic dissection of GABAergic neural circuits in mouse neocortex. *Front. Cell. Neurosci.* 8:8. doi: 10.3389/fncel.2014.00008

Taniguchi, H., He, M., Wu, P., Kim, S., Paik, R., Sugino, K., et al. (2011). A resource of Cre driver lines for genetic targeting of GABAergic neurons in cerebral cortex. *Neuron* 71, 995–1013. doi: 10.1016/j.neuron.2011.07.026

Taniguchi, H., Lu, J., and Huang, Z. J. (2013). The spatial and temporal origin of chandelier cells in mouse neocortex. *Science* 339, 70–74. doi: 10.1126/science.1227622

Tantama, M., Hung, Y. P., and Yellen, G. (2012). Optogenetic reporters: fluorescent protein-based genetically encoded indicators of signaling and metabolism in the brain. *Prog. Brain Res.* 196, 235–263. doi: 10.1016/B978-0-444-59426-6.00012-4

Taymans, J. M., Vandenberghe, L. H., Haute, C. V., Thiry, I., Deroose, C. M., Mortelmans, L., et al. (2007). Comparative analysis of adeno-associated viral vector serotypes 1, 2, 5, 7, and 8 in mouse brain. *Hum. Gene Ther.* 18, 195–206. doi: 10.1089/hum.2006.178

Thestrup, T., Litzlbauer, J., Bartholomäus, I., Mues, M., Russo, L., Dana, H., et al. (2014). Optimized ratiometric calcium sensors for functional *in vivo* imaging of neurons and T lymphocytes. *Nat. Methods* 11, 175–182. doi: 10.1038/nmeth.2773

Tian, L., Hires, S. A., Mao, T., Huber, D., Chiappe, M. E., Chalasani, S. H., et al. (2009). Imaging neural activity in worms, flies and mice with improved GCaMP calcium indicators. *Nat. Methods* 6, 875–881. doi: 10.1038/nmeth.1398

Ting, J. T., and Feng, G. (2014). Recombineering strategies for developing next generation BAC transgenic tools for optogenetics and beyond. *Front. Behav. Neurosci.* 8:111. doi: 10.3389/fnbeh.2014.00111

Tukker, J. J., Fuentealba, P., Hartwich, K., Somogyi, P., and Klausberger, T. (2007). Cell type-specific tuning of hippocampal interneuron firing during gamma oscillations *in vivo*. *J. Neurosci.* 27, 8184–8189. doi: 10.1523/JNEUROSCI.1685-07.2007

Tye, K. M., Prakash, R., Kim, S.-Y., Fenno, L. E., Grosenick, L., Zarabi, H., et al. (2011). Amygdala circuitry mediating reversible and bidirectional control of anxiety. *Nature* 471, 358–362. doi: 10.1038/nature09820

van Zessen, R., Phillips, J. L., Budygin, E. A., and Stuber, G. D. (2012). Activation of VTA GABA neurons disrupts reward consumption. *Neuron* 73, 1184–1194. doi: 10.1016/j.neuron.2012.02.016

Verret, L., Mann, E. O., Hang, G. B., Barth, A. M., Cobos, I., Ho, K., et al. (2012). Inhibitory interneuron deficit links altered network activity and cognitive dysfunction in Alzheimer model. *Cell* 149, 708–721. doi: 10.1016/j.cell.2012.02.046

Wall, N. R., Wickersham, I. R., Cetin, A., De La Parra, M., and Callaway, E. M. (2010). Monosynaptic circuit tracing *in vivo* through Cre-dependent targeting and complementation of modified rabies virus. *Proc. Natl. Acad. Sci. U.S.A.* 107, 21848–21853. doi: 10.1073/pnas.1011756107

Wang, H. X., Waterhouse, B. D., and Gao, W. J. (2013). Selective suppression of excitatory synapses on GABAergic interneurons by norepinephrine in juvenile rat prefrontal cortical microcircuitry. *Neuroscience* 246, 312–328. doi: 10.1016/j.neuroscience.2013.05.009

Wang, Q., Liu, C., Uchida, A., Chuang, J. C., Walker, A., Liu, T., et al. (2014). Arcuate AgRP neurons mediate orexigenic and glucoregulatory actions of ghrelin. *Mol. Metab.* 3, 64–72. doi: 10.1016/j.molmet.2013.10.001

Weible, A. P., Schwarcz, L., Wickersham, I. R., DeBlander, L., Wu, H., Callaway, E. M., et al. (2010). Transgenic targeting of recombinant rabies virus reveals monosynaptic connectivity of specific neurons. *J. Neurosci.* 30, 16509–16513. doi: 10.1523/JNEUROSCI.2442-10.2010

Wess, J., Nakajima, K., and Jain, S. (2013). Novel designer receptors to probe GPCR signaling and physiology. *Trends Pharmacol. Sci.* 34, 385–392. doi: 10.1016/j.tips.2013.04.006

Wickersham, I. R., Lyon, D. C., Barnard, R. J., Mori, T., Finke, S., Conzelmann, K. K., et al. (2007). Monosynaptic restriction of transsynaptic tracing from single, genetically targeted neurons. *Neuron* 53, 639–647. doi: 10.1016/j.neuron.2007.01.033

Wietek, J., Wiegert, J. S., Adeishvili, N., Schneider, F., Watanabe, H., Tsunoda, S. P., et al. (2014). Conversion of channelrhodopsin into a light-gated chloride channel. *Science* 344, 409–412. doi: 10.1126/science.1249375

Witten, I. B., Lin, S. C., Brodsky, M., Prakash, R., Diester, I., Anikeeva, P., et al. (2010). Cholinergic interneurons control local circuit activity and cocaine conditioning. *Science* 330, 1677–1681. doi: 10.1126/science.1193771

Wulff, P., and Arenkiel, B. R. (2012). Chemical genetics: receptor-ligand pairs for rapid manipulation of neuronal activity. *Curr. Opin. Neurobiol.* 22, 54–60. doi: 10.1016/j.conb.2011.10.008

Wulff, P., Goetz, T., Leppä E., Linden, A. M., Renzi, M., Swinny, J. D., et al. (2007). From synapse to behavior: rapid modulation of defined neuronal types with engineered GABAA receptors. *Nat. Neurosci.* 10, 923–929. doi: 10.1038/nn1927

Xu, H., Jeong, H. Y., Tremblay, R., and Rudy, B. (2013). Neocortical somatostatin-expressing GABAergic interneurons disinhibit the thalamorecipient layer 4. *Neuron* 77, 155–167. doi: 10.1016/j.neuron.2012.11.004

Zemanick, M. C., Strick, P. L., and Dix, R. D. (1991). Direction of transneuronal transport of herpes simplex virus 1 in the primate motor system is strain-dependent. *Proc. Natl. Acad. Sci. U.S.A.* 88, 8048–8051. doi: 10.1073/pnas.88.18.8048

Zhang, F., Wang, L. P., Boyden, E. S., and Deisseroth, K. (2006). Channelrhodopsin-2 and optical control of excitable cells. *Nat. Methods* 3, 785–792. doi: 10.1038/nmeth936

Conflict of Interest Statement: The authors declare that the research was conducted in the absence of any commercial or financial relationships that could be construed as a potential conflict of interest.

Received: 15 August 2014; accepted: 22 September 2014; published online: 17 October 2014.

*Citation: Murphey DK, Herman AM and Arenkiel BR (2014) Dissecting inhibitory brain circuits with genetically-targeted technologies. Front. Neural Circuits **8**:124. doi: 10.3389/fncir.2014.00124*

This article was submitted to the journal Frontiers in Neural Circuits.

frontiers in
NEURAL CIRCUITS

METHODS ARTICLE
published: 06 August 2014
doi: 10.3389/fncir.2014.00092

Robust quantification of orientation selectivity and direction selectivity

Mark Mazurek[1], Marisa Kager[2,3†] and Stephen D. Van Hooser[3]*

[1] Department of Biology, Metropolitan State University of Denver, Denver, CO, USA
[2] InSPIRE Program, Concord Academy, Concord, MA, USA
[3] Department of Biology, Brandeis University, Waltham, MA, USA

Edited by:
Benjamin R. Arenkiel, Baylor College of Medicine, USA

Reviewed by:
James Schummers, Max Planck Florida Institute, USA
David J. Margolis, Rutgers University, USA

***Correspondence:**
Stephen D. Van Hooser, Department of Biology, Brandeis University, 415 South St. MS008, Waltham, MA, USA
e-mail: vanhoosr@brandeis.edu

†Present address:
Marisa Kager, Harvey Mudd College, Claremont, USA

Neurons in the visual cortex of all examined mammals exhibit orientation or direction tuning. New imaging techniques are allowing the circuit mechanisms underlying orientation and direction selectivity to be studied with clarity that was not possible a decade ago. However, these new techniques bring new challenges: robust quantitative measurements are needed to evaluate the findings from these studies, which can involve thousands of cells of varying response strength. Here we show that traditional measures of selectivity such as the orientation index (*OI*) and direction index (*DI*) are poorly suited for quantitative evaluation of orientation and direction tuning. We explore several alternative methods for quantifying tuning and for addressing a variety of questions that arise in studies on orientation- and direction-tuned cells and cell populations. We provide recommendations for which methods are best suited to which applications and we offer tips for avoiding potential pitfalls in applying these methods. Our goal is to supply a solid quantitative foundation for studies involving orientation and direction tuning.

Keywords: Monte Carlo, sampling, neural data analysis

INTRODUCTION

In the visual cortex of all examined mammalian species (Hubel and Wiesel, 1959, 1962), many neurons respond strongly to bars or edges at a particular preferred orientation. In some mammals such as carnivores, primates, and tree shrews, these orientation-selective cells are organized into functional columns (Hubel and Wiesel, 1962, 1968; Humphrey and Norton, 1980), and in other animals such as rodents there are no maps of orientation selectivity yet individual cells exhibit strong orientation selectivity (Girman et al., 1999; Ohki et al., 2005; Van Hooser et al., 2005; Mrsic-Flogel et al., 2007). Further, a substantial subset of orientation-selective cells also exhibit direction selectivity (Hubel and Wiesel, 1962; Weliky et al., 1996). That is, they respond more strongly to a properly oriented bar moving in a preferred direction as compared to any other direction. The functional organization and development of orientation- and direction-selective cells are the focus of intense current research.

A number of measures have been devised to assess the strength and significance of orientation and direction selectivity for a given cell (Henry et al., 1974; De Valois et al., 1982; Swindale, 1998; Ringach et al., 2002; Grabska-Barwinska et al., 2012). Traditionally, these techniques were applied to spike responses obtained from cells recorded extracellularly with microelectrodes. These cells were often identified as candidates for recording precisely because they exhibited some substantial selectivity to an oriented test stimulus that was employed while the investigator moved the electrode, hunting for cells.

New challenges—the advent of unbiased optical recording techniques such as 2-photon calcium imaging that sample all cells regardless of selectivity (Stosiek et al., 2003; Kerr et al., 2005; Garaschuk et al., 2006) and the need to characterize cells in developing animals with poor, emerging selectivity—have introduced new difficulties for assessing orientation and direction selectivity. Some of the traditional measures of selectivity can give noisy or spuriously high values when applied to cells that don't exhibit at least moderate selectivity. Further, exciting new molecular and circuit techniques are permitting the testing of very precise circuit hypotheses about the mechanisms underlying orientation and direction selectivity. Knowledge about statistical power—the number of cells or repetitions of a stimulus that are needed in order to observe a change in selectivity of a particular size—is critical for these studies.

Here we characterize the robustness of several measures of orientation and direction selectivity on simulated responses. We provide a recommendation for analysis methods for the principle questions that investigators usually ask: (1) How much orientation or direction selectivity does a cell exhibit? (2) Does a cell exhibit significant orientation or direction selectivity? (3) Has a manipulation introduced a significant change in the amount of orientation or direction selectivity at the population level? Further, we provide tables for statistical power, to estimate the amount of data that would be required to accurately answer these questions. These methods could in principle be extended to other sensory response properties or other modalities; however, their performance depends on the form of the underlying response function, so they may perform less reliably in domains aside from orientation and direction selectivity.

MATERIALS AND METHODS

COORDINATE SYSTEMS

There is no standard coordinate system for indicating orientation or direction space. In this paper, we use "compass" coordinates, in which a horizontal bar moving upward is considered to be moving at 0°, and angles increase in a clockwise manner. Another common coordinate system is the Cartesian system, where 0° indicates a vertical bar moving to the right, and angles increase in a counterclockwise direction. One can transform between these two systems using the following equations:

$$\theta_{cartesian} = 90° - \theta_{compass}$$

$$\theta_{compass} = 90° - \theta_{cartesian}$$

Because there is no standard coordinate system for orientation and direction, and because some readers may be unfamiliar with orientation and direction, it is helpful to use pictures to indicate stimulus orientation and direction in slides and in published figures, as we do here.

ANGULAR ADDITION

In several equations, we express angles in terms of the sum of angles. For example, for a direction tuning curve we define the positive orthogonal orientation as follows: $\theta_{orth+} = \theta_{pref} + 90°$. Note that these angles are summed modulo 360° in direction space and modulo 180° in orientation space. For example, in direction space, $359° + 2° = 361°$ modulo $360° = 1°$.

RELATIONSHIP OF *OI* AND *DI* TO OTHER COMMONLY USED MEASURES OF ORIENTATION AND DIRECTION SELECTIVITY

In this paper, we use *OI* and *DI* as the normalized measures of "peak to trough" orientation selectivity and direction selectivity (see "Results"): $OI = (R_{pref\_ori} - R_{orth})/R_{pref\_ori}$ and $DI = (R_{pref} - R_{null})/R_{pref}$. Many papers use a slightly modified version of these measures that we will call the OSI and DSI: $OSI = (R_{pref\_ori} - R_{orth})/(R_{pref\_ori} + R_{orth})$ and $DSI = (R_{pref} - R_{null})/(R_{pref} + R_{null})$. Still other papers use the "orthogonal to peak" ratio to quantify orientation selectivity: $O/P = R_{orth}/R_{pref\_ori} = 1 - OI$. In making quantitative comparisons across papers, the reader should note carefully which is being used.

The response at the preferred orientation R_{pref_ori} and the response at the preferred direction R_{pref} can be determined in different ways. In some measures, these are taken to be the best response to one of the stimulus orientations or directions that was explicitly measured; that is, if we measure responses at stimulus directions $\theta_1, \theta_2, \ldots, \theta_n$, then we choose the response at the best θ_i. In other measures, we perform a fit to the tuning curve, and choose the maximum value of the fit as R_{pref_ori} or R_{pref}.

MONTE CARLO SIMULATIONS

In Monte Carlo simulations of orientation and direction tuning curves, the "true" preferred angle and tuning widths were varied randomly so that a variety of tuning curve shapes were analyzed. Ranges were selected to correspond to typical values observed in V1 neurons. Each underlying "true" curve was a double Gaussian. The underlying angle preferences were chosen according to a uniform distribution between 0° and 360°. Tuning widths were chosen randomly according to a Gamma distribution with shape 3 and scale 6: $\sigma = (Gamma(3, 6) + 10°)/1.18$.

In many of the figures, we examined curves with 21 values of underlying *OI* or *DI*. These were produced in the double Gaussian equation (see **Results**) by setting the baseline rate $C = 10 - (i - 1)/2$, $R_p = (i - 1)/2$, $R_n = (i - 1)/4$, for i from 1 to 21. In other figures we examined 21 values of underlying *DI*: $C = 0$, $R_p = 10$, $R_n = 10 - (i - 1)/2$. Note that all of these curves with varying direction selectivity exhibit high orientation selectivity (that is, orientation selectivity and direction selectivity levels were not co-varied).

To calculate statistical power for simulated 2-condition experiments, we simulated underlying orientation or direction curves with exactly the *OI* or *DI* specified, and randomly varied the preferred angle and tuning width as described above. We simulated 100 populations of increasing sizes, and calculated the minimum size when X% of these simulations produced significant differences by applying a t-test with confidence X%, for $X = 95$, 99, and 99.9.

NOISE MODELS

In each set of simulations, the simulated noise parameter is described. We used two types of noise. The most common type of noise, intended to capture the statistics of spikes recorded with an extracellular electrode, was a constant Gaussian noise value that was added to responses of all orientations on all trials. This constant value is often expressed as a percentage of the maximum response, which was usually 10 Hz. So, 20% noise means 2 Hz noise was added to individual trial measurements.

A more recent technique for recording neural responses is 2-photon imaging with Oregon Green BAPTA-1 AM (OGB-1AM) (Stosiek et al., 2003; Ohki et al., 2005; Garaschuk et al., 2006). This method involves bulk loading of neural tissue with a calcium indicator bound to an AM-ester, leading to the uptake of the calcium indicator by all neurons within the loading region. This technique produces noise characteristics that differ from extracellular spike recordings. Specifically, because 2-photon calcium imaging records intracellular calcium concentration rather than membrane voltage, it tends to show a lower signal-to-noise ratio and a constant background signal. By examining the responses in previous experiments (Li et al., 2008), we modeled this noise as Gaussian noise with magnitude equal to a constant factor plus a component that depended on the response at each direction, such that noise = 20% + 10% * response magnitude.

RESULTS

Orientation selectivity has been observed in the visual cortex of every mammal that has been examined, including carnivores (Hubel and Wiesel, 1962), primates (Hubel and Wiesel, 1968), rodents, including murid (Girman et al., 1999; Niell and Stryker, 2008), and sciurid rodents (Heimel et al., 2005; Van Hooser et al., 2005), and marsupials (Rocha-Miranda et al., 1976; Ibbotson and Mark, 2003).

Orientation selectivity is traditionally assessed by sweeping a bar or by drifting sinusoidal gratings across the cell's receptive field in different directions (Hubel and Wiesel, 1962; Movshon

et al., 1978, pp.101–120), although it can also be assessed by flashing static bars at different orientations (Palmer and Davis, 1981). The example cell in **Figure 1A** exhibits a substantial response to bars that are rotated at a 45° angle from horizontal. The stimulus in **Figure 1A** moves in two opposite directions. The response to upward and rightward motion (45°) is stronger than the response to downward and leftward motion (225°), indicating that the cell is sensitive not only to the orientation of the stimulus but also its direction of motion. Note that every cell that is direction-selective by this criterion is also orientation-selective, but an orientation-selective cell is not necessarily direction-selective, because a cell could exhibit equal responses to the two opposite directions.

The responses of this example cell are shown on a graph in **Figure 1B**. Each response is presented as a firing rate: the number of spikes evoked by each stimulus has been divided by the duration of the stimulus in seconds. We imagine that the experimenter has collected some responses to "blank" stimuli, where the screen remains blank for the same time duration as for each bar stimulus, and has subtracted these "blank" or "background" responses from each measurement so that we are examining the contribution of the oriented stimulus to the cell's firing rate and not ongoing background activity. This collection of responses to a set of different orientations or directions is called an "orientation tuning curve" or a "direction tuning curve," respectively. The major descriptive features of orientation and direction tuning curves are illustrated. The stimulus angle that evokes the maximum response R_{pref} is called the preferred direction (θ_{pref}), while the opposite direction is called the null direction ($\theta_{pref} + 180°$).

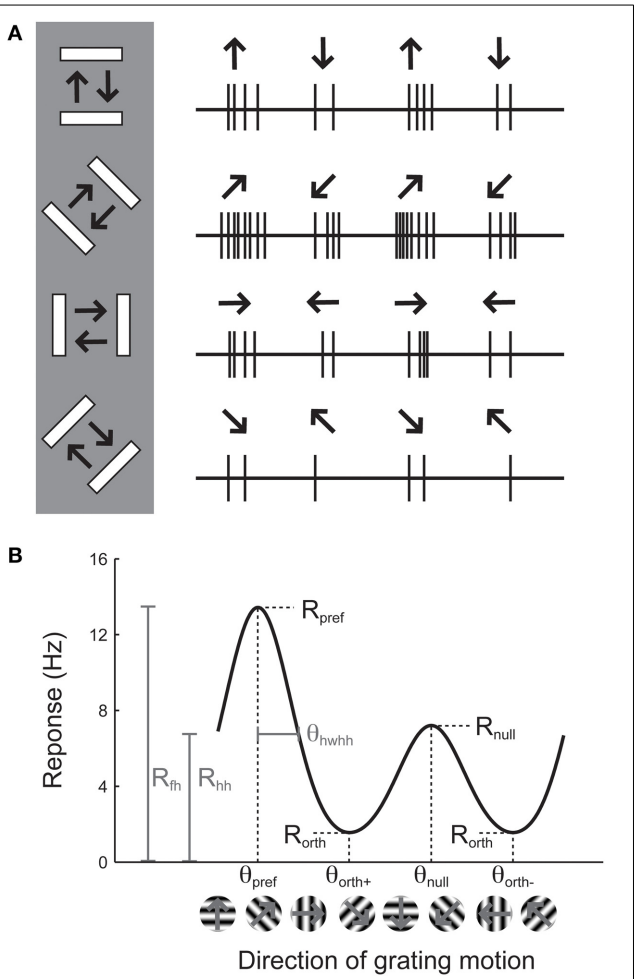

FIGURE 1 | Illustration of the assessment of orientation and direction selectivity. (A) Left: Depiction of a bar stimulus moving at different orientations across the receptive field of an example cell. The cell's responses to each orientation are indicated at the right. The preferred orientation is 45°. During each presentation of the bar stimulus, the stimulus moves back and forth in two opposite directions. This cell responds more strongly to movement of the bar toward 45° than it does to the opposite direction (225°). **(B)** A graph of responses to the same cell to sinusoidal gratings drifting in several directions. The cell gives the largest response (R_{pref}) to 45° (θ_{pref}), and a weaker response (R_{null}) to the opposite direction 225° (θ_{null}). The cell responds less strongly to stimulation at either of the two orthogonal orientations (θ_{orth+} and θ_{orth+}). The cell's response decreases as the direction of the stimulus deviates from θ_{pref}; the difference between θ_{pref} and the angle that causes the response to drop to half (R_{hh}) its maximum value is called the half width at half height (θ_{hwhh}).

QUANTIFYING THE DEGREE OF ORIENTATION AND DIRECTION SELECTIVITY

From the graphical tuning curve in **Figure 1B**, it is easy to imagine two major notions of orientation selectivity. One is a comparison of the cell's response to the preferred orientations ($R_{pref} + R_{null}$) compared to the responses (R_{orth+} and R_{orth-}) at the orientations that are orthogonal ($\theta_{orth+} = \theta_{pref} + 90°$, $\theta_{orth-} = \theta_{pref} - 90°$) to the preferred orientation. This method has been employed in numerous studies, and we refer to it here as the *orientation index* (OI):

$$OI = (R_{pref} + R_{null} - (R_{orth+} + R_{orth-}))/(R_{pref} + R_{null})$$

Note that it is not necessary to stimulate with directional stimuli in order to obtain a measure of orientation selectivity. Indeed, in many studies, the bars are drifted back and forth and the responses to each pair of opposite directions are averaged together. In this "orientation space," the angle of stimulation ranges from 0° to 180°. We can calculate the orientation selectivity index in this case by using the preferred response (R_{pref_ori}) and the response R_{orth} at the orthogonal orientation ($\theta_{orth} = \theta_{pref} + 90°$)

$$OI = (R_{pref\_ori} - R_{orth})/R_{pref\_ori}.$$

The OI can nominally vary from 0 (no selectivity) to 1 (perfect selectivity), although it can exceed 1 if the response to the orthogonal orientation drops below the background firing rate, that is, when R_{orth} is negative.

In direction space, a *direction index* can be defined similarly:

$$DI = (R_{pref} - R_{null})/R_{pref}.$$

Another major notion of orientation or direction selectivity is the sensitivity of the response to the preferred angle. One can imagine measuring the amount one needs to change the orientation (or direction) angle from the preferred for the response to drop by some amount, such as by half (R_{hh}, the response at half-height). The angle difference θ_{hwhh} indicates how far in orientation space

one must adjust the angle from the optimal to obtain half of the response height. This type of selectivity has been referred to as a cell's *orientation tuning width*. Measuring the orientation tuning width requires either substantial sampling of responses to different angles, or performing a tuning curve fit, which we will turn to later.

Owing to the mathematical simplicity of the *OI*, most studies over the years have employed the *OI* to assess orientation selectivity. By ear, it is easy to assess whether or not a cell exhibits perfect orientation selectivity with the *OI* (that is, when there are no responses to the orthogonal angle), and the *OI* is very easy to compute numerically even when one is measuring spikes or firing rates. When applied to cells with substantial selectivity, it provides a simple and valid measure of orientation selectivity. **Figure 2** shows simulated responses from a model neuron (**i**) with a theoretical or "true" *OI* of 0.77; we have simulated 10 repeated trials of each direction; 5 Hz of random noise was added to each simulated trial, and the means are plotted. The empirical *OI*, measured by taking the average of the responses at the preferred orientation subtracting the responses at the orthogonal orientation, and normalizing, we obtain a value (0.83) very close to the "true" *OI* value of 0.77.

However, the case of a model cell (**ii**) with no orientation selectivity is also shown in **Figure 2**. Again, we have simulated 10 trials with 5 Hz of added noise. If we blindly report the empirical measure of *OI*, we obtain a value 0.58, a value much larger than the "true" value of 0. The reason is that we always choose the angle of the empirical maximum response to be "preferred," and, in this case, that angle was just the angle that had the largest response due to noise only (there was no orientation signal). By random chance in this example, the responses at the angles that correspond to the orthogonal orientations (represented by the squares) are both less than the responses to the preferred orientation (represented by the triangles), so the *OI* is large.

In single unit recording studies in adult animals, one often ignores cells with weak responses, but if one is conducting an imaging study of 100's of neurons, or developmental research in animals with weakly responsive cells, it is highly likely that some neurons will exhibit weak orientation selectivity. If the *OI* is applied blindly, it is likely that many of these weakly selective neurons will have empirical *OI* values that are high, only due to noise.

VECTOR SPACES FOR ORIENTATION AND DIRECTION

We can improve the situation by plotting the responses to individual stimuli in a vector space. In **Figure 3**, we have replotted the responses of model cells (**i**,**ii**) and a new model cell (**iii**) in polar plots. **Figure 3A** shows the responses plotted in orientation space, where values for responses to the two opposite directions have been averaged, and angles vary from 0° and 180°. **Figure 3B** shows the responses plotted in direction space, where angles vary from 0° to 360°. The graphs also show, in gray, the vector that is the sum of all of the mean responses in vector space. In these examples, the length of the vector sum is more related to the amount of orientation selectivity as compared to the *OI* index.

The normalized length of this vector in orientation space is computed as follows:

$$L_{ori} = \left| \frac{\sum_k R(\theta_k) \exp(2i\theta_k)}{\sum_k R(\theta_k)} \right|,$$

where $R(\theta_k)$ is the response to angle θ_k. In direction space this length is the following:

$$L_{dir} = \left| \frac{\sum_k R(\theta_k) \exp(i\theta_k)}{\sum_k R(\theta_k)} \right|.$$

The normalized vector length is related to a classic quantity in circular statistics called the *circular variance* (Batschelet, 1981;

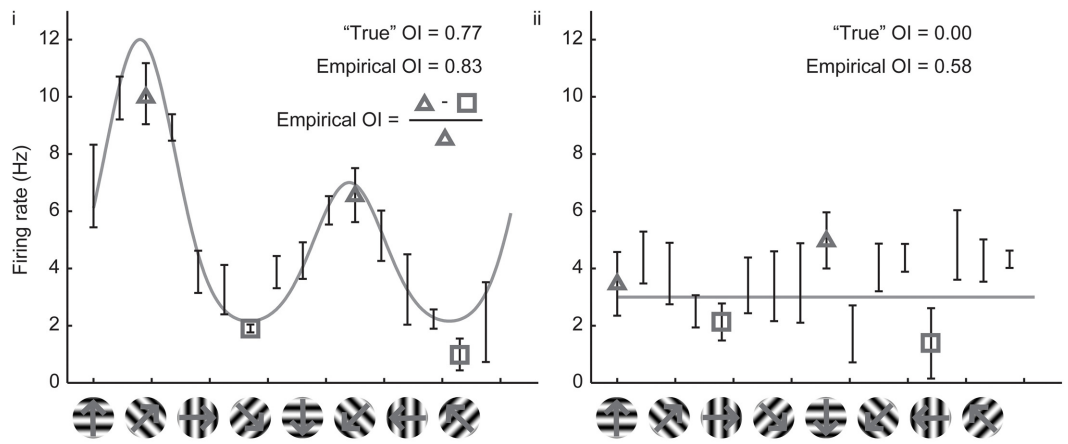

FIGURE 2 | Calculation of the empirical orientation selectivity index (*OI*). **(i)** Simulated responses (10 trials, 5 Hz per trial noise) to a model cell with an underlying direction tuning curve indicated in gray. Error bars indicate standard error around the mean of the simulated responses. To calculate *OI*, responses from the preferred orientation angle are averaged together (triangles) and the responses to the orthogonal angles (squares) are subtracted. This quantity is normalized by the response to the preferred orientation angle (triangles). There is good qualitative agreement between the empirical *OI* and the "true" *OI*. **(ii)** Same, for a model cell that is not orientation selective. The empirical *OI* is still very large due to the noise in the simulated responses, and is not qualitatively similar to the "true" underlying *OI*.

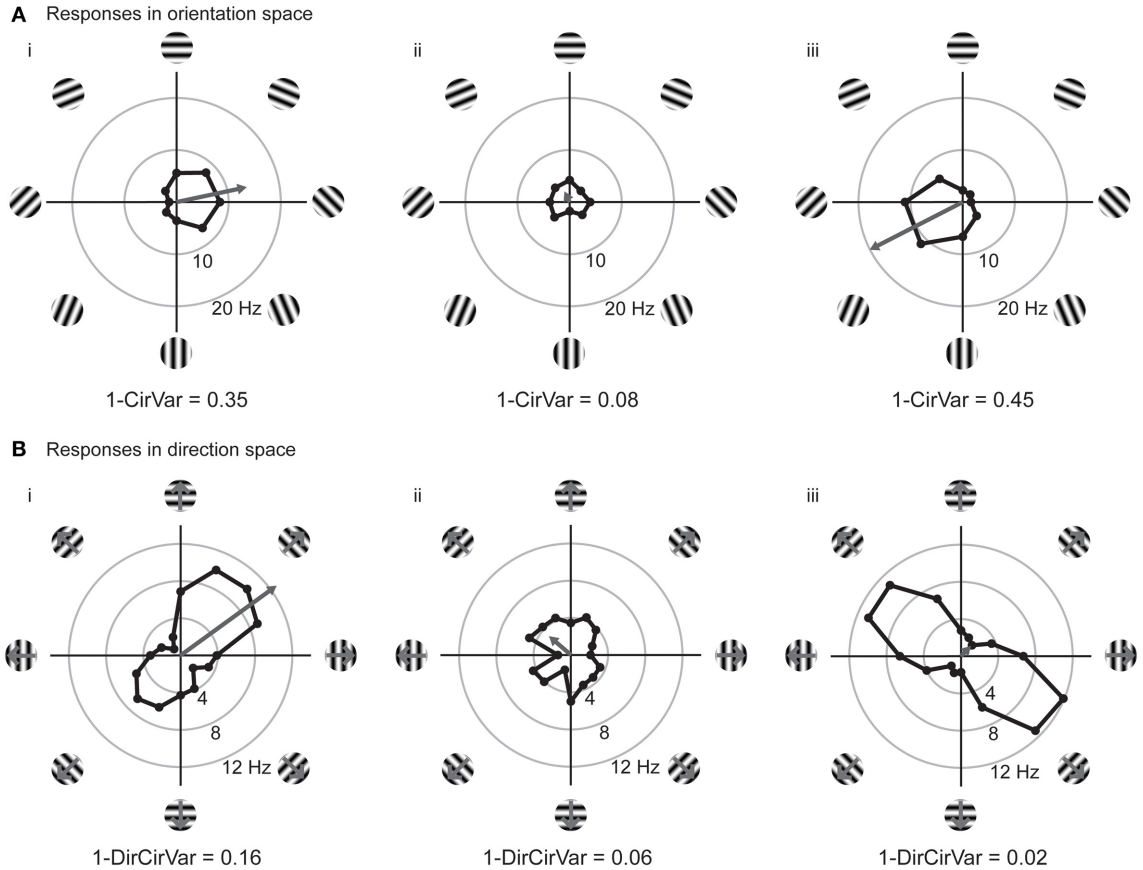

FIGURE 3 | Responses of model cells in polar coordinates on the complex plane. (A) Responses of model cells in orientation space. Response (in spikes per second) at each angle is indicated by the distance from the origin. Orientation angles vary from 0 (horizontal) to 90° (vertical) and back to 0°/180° (horizontal). Gray arrow indicates the vector mean of the responses to individual orientations. The normalized length of the mean response vector is the quantity L_{ori}, which is 1 minus the circular variance (1-*CirVar*). Model cells **i** and **ii** are the same as in **Figure 2**. **(B)** Responses of the same cells plotted in direction space. Direction of motion is indicated, response at each angle is indicated by the distance from the origin. Note that 0° and 180° both correspond to horizontal stimulus orientations, but moving in upward and downward directions, respectively. Gray arrow indicates the vector mean of responses to individual directions. Note that cell **iii** is highly orientation selective for oblique bars but is poorly selective for stimulus direction.

Ringach et al., 2002):

$$1 - CirVar = L_{ori}$$

We use the abbreviation *CirVar* to differentiate the circular variance from the classic statistical quantity called "coefficient of variation," which is often abbreviated as CV. We similarly define a quantity called 1-*DirCirVar*:

$$1 - DirCirVar = L_{dir}$$

This definition differs (by a factor of 2) from the classic definition of circular variance in direction space (Batschelet, 1981), but we leave off the factor of 2 here so that a cell with maximal selectivity has a 1-*DirCirVar* of 1 (rather than 2).

The vector lengths in orientation space (1-*CirVar*) and in direction space (1-*DirCirVar*) for the model cells **i–iii** are shown in **Figure 3**. There are two important things to notice in comparison to the *OI*. First, model cell **ii** has a high (spurious) empirical *OI* value (**Figure 2ii**) but has a small 1-*CirVar* value, indicating that 1-*CirVar* is closer to the true selectivity of the cell, which is 0. Second, a cell can only have a 1-*CirVar* value of 1 when it exhibits a response to 1 orientation and no other orientations. Cells with high selectivity that would have *OI* values near 1, such as model cells **i** and **iii**, generally have lower 1-*CirVar* values, since cells typically respond to more than a single orientation; that is, the response tuning generally has some width. Thus, circular variance depends on both selectivity and tuning width.

COMPARING *OI* AND CIRCULAR VARIANCE (AND *DI* AND DIRECTION CIRCULAR VARIANCE)

When one records a neuron experimentally, one can only obtain a limited number of samples of the neuron's responses. One would like to use these sampled responses to make the best guess about the neuron's "true" properties, which cannot be examined directly but can only be inferred from experimental observations. Here we used Monte Carlo simulations to consider which index, *OI* or

circular variance, allows one to make the best guess about the true orientation selectivity.

We created 21 model orientation tuning curves that ranged in "true" selectivity from 0 to 1 (**Figure 4A**). From each model, we simulated 100 tuning curves with 10 experimental trials each by adding 50% single trial noise; the exact angle preference and tuning width was chosen randomly (see Materials and Methods). We then calculated the *OI* and 1-*CirVar* for each simulation (**Figure 4**).

The percentile distribution of empirical *OI* values for each "true" *OI* value is shown in **Figure 4B**. There is a wide range of empirical *OI* values; for example, when the "true" *OI* is 0,

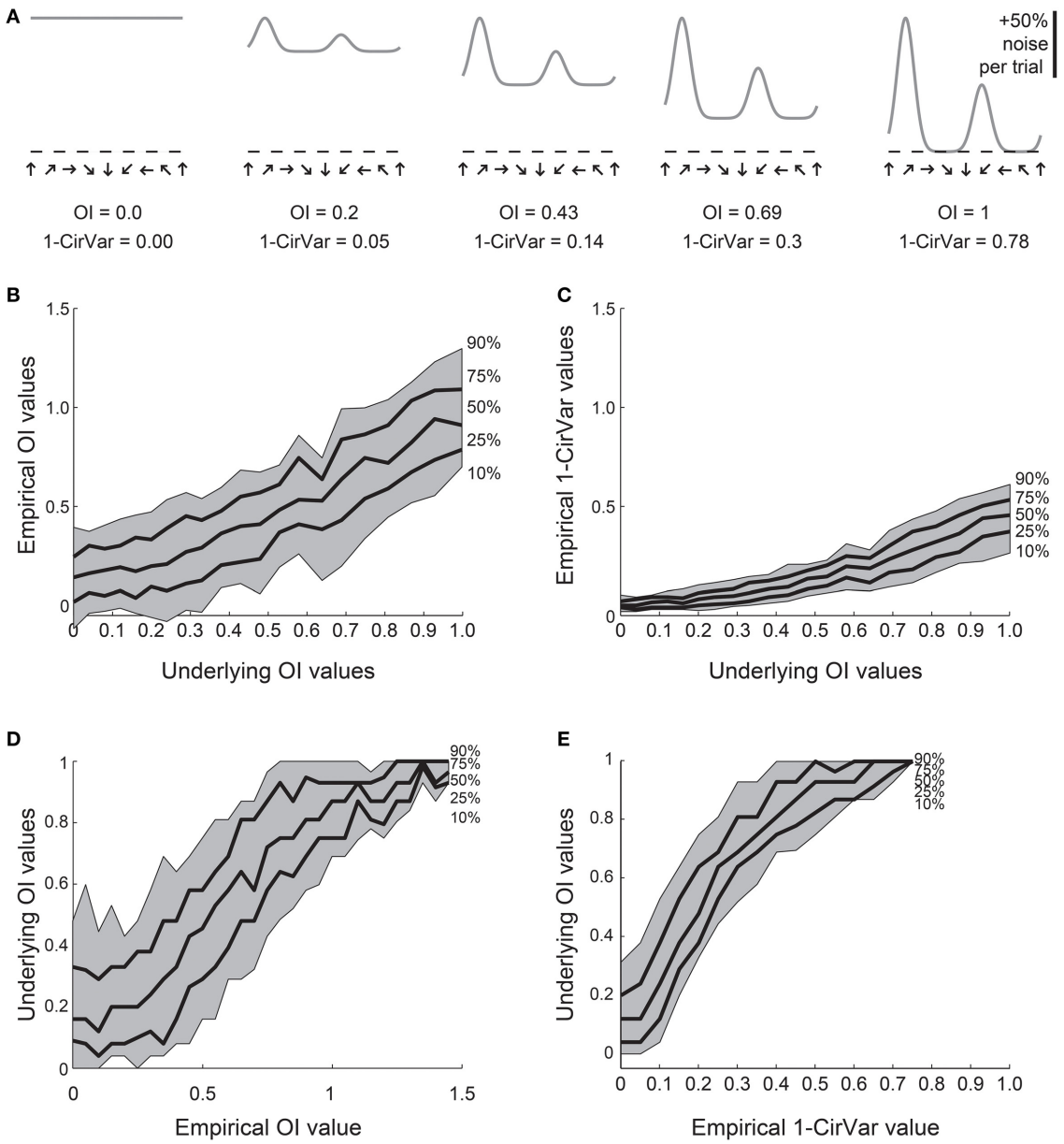

FIGURE 4 | Comparison of *OI* and circular variance measures for simulated data. We created 100 simulations of tuning curves for each of 21 underlying "true" tuning curves, ranging from $OI = 0$ to $OI = 1$, some shown in **(A)**. Each trial had 50% noise added. **(B)** Percentiles of the empirically determined *OI* for the 100 simulations at each underlying "true" *OI* value. Note that for cells with 0 true selectivity, the empirical *OI* values range from slightly negative to almost 0.5. **(C)** Percentiles of the empirically determined 1-*CirVar* index for each of the underlying "true" *OI* values. Note that when "true" *OI* is low, the 1-*CirVar* is always low. The index 1-*CirVar* increases as "true" *OI* increases but the range of values remains narrower than the corresponding range of empirical *OI* values in **(B)**. **(D)** The inverse of **(B)**; given we observed an empirical *OI* value of x, what is the range of possible "true" *OI* values that produced x in our simulations? An empirical *OI* of 0 could have arisen from cells with "true" *OI* values ranging from 0 to 0.5, and an empirical *OI* of 0.5 could have arisen from cells with a "true" *OI* ranging from about 0.1 to about 0.8. **(E)** The inverse of **(C)**. A 1-*CirVar* of 0 could have arisen from a "true" *OI* ranging from 0 to about 0.3, and 1-*CirVar* of 0.25 could have arisen from a "true" *OI* ranging from about 0.4 to 0.8. The range of possible underlying "true" *OI* values is much narrower when 1-*CirVar* is used as a readout as compared to *OI*.

empirical *OI* values ranged from slightly negative to about 0.5. By contrast (**Figure 4C**), the distribution of circular variance values is much tighter; when "true" *OI* is 0, the 1-*CirVar* value is always nearly 0.

While the results in **Figures 4B,C** show the range of empirical *OI* and 1-*CirVar* values that one might expect for a given "true" *OI*, the most relevant relationship for experimentalists is the inverse relationship: given that one observes an empirical *OI* value of *X* or a 1-*CirVar* value of *Y*, what are the likely "true" *OI* values that could underlie these empirical values? As shown in **Figure 4D**, knowing the empirical *OI* value tells one very little about the "true" *OI* value: for example, if the empirical *OI* is 0, the "true" *OI* could be as high as 0.5. On the other hand (**Figure 4E**), the circular variance gives more information about the "true" *OI*: if we obtain an empirical 1-*CirVar* of 0, the "true" *OI* is likely to be less than 0.3; if we obtain an empirical 1-*CirVar* of 0.25, the "true" *OI* is likely to be between 0.4 and 0.7.

We performed similar simulations for direction selectivity, comparing the empirical *DI* with the empirical 1-*DirCirVar* (**Figure 5**). The difference in uncertainty about the "true" *DI* between the *DI* and 1-*DirCirVar* is less pronounced than the difference in uncertainty between the *OI* and 1-*CirVar*, but nevertheless the empirical 1-*DirCirVar* provides more information about the "true" *DI* than the empirical *DI*.

The Monte Carlo simulation results presented in **Figures 4**, **5** provide strong evidence that circular variance is a more robust and reliable indicator of the amount of orientation or direction selectivity than the *OI* or *DI*. The circular variance works well when selectivity is strong or weak. We recommend the use of circular variance whenever quantification of the amount of orientation or direction selectivity is necessary.

Experimentalists are also interested in knowing how many stimulus trials and stimulus angle steps should be presented to the animal in order to provide a quality estimate of the neuron's true orientation or direction selectivity. We performed Monte Carlo simulations where we systematically varied the single trial noise, number of stimulus trials, and the number of stimulus angles in order to understand how these factors influenced error in uncovering the "true" *OI* or *DI* (**Figure 6**). As expected, more trials and more angles were always better, but 45° angle steps and eight trials (or 22.5° steps with four trials) appear to be the minimum required for a quality assessment of direction selectivity. Naturally, this result depends on the reliability of the neuron being studied; neurons with lower responsiveness or higher noise will require more trials and/or stimulus angles.

SIGNIFICANCE OF ORIENTATION AND DIRECTION TUNING

When one suspects a cell is selective for stimulus orientation and/or direction, it is often important to verify this selectivity statistically. We need tools that allow us to answer the question "is a cell's selectivity for orientation/direction statistically significant?" In principle, one could simply measure a selectivity coefficient on each trial and perform statistics on this distribution of coefficients. However, the flaw in this analysis is in determining the null hypothesis with selectivity coefficients, and the flaw applies whether one uses *OI*/*DI* or 1-*CirVar*/1-*DirCirVar*. Specifically, for all these coefficients, the expected value in the absence of selectivity is greater than zero because any variance across stimulus angles, whether stimulus-driven or random, always produces coefficient values greater than zero. Thus, one could not use this method to prove that a particular measured coefficient was not simply produced by noise.

We have found that the best way to detect selectivity is to measure the magnitude of orientation or direction vectors (**Figure 7**). For this test, we organize data into "trials," where a trial is one response at each stimulus orientation or direction. The orientation or direction vector is calculated on each trial as the vector sum of responses on that trial measured in orientation or direction space, respectively. The magnitude of the vector correlates with the degree of selectivity, and the expected magnitude is zero for zero selectivity. Hence we can perform statistics on the distribution of vector magnitudes against the null hypothesis H0: that the magnitude equals zero.

For detecting orientation selectivity we use Hotelling's T^2-test, which is a multivariate generalization of Student's *T*-test, to ask whether the 2-dimensional mean of orientation vectors is significantly different from [0,0] (**Figure 7C**). **Figure 8** shows that this test reliably detects orientation selectivity. In this figure, a model cell is simulated at different levels of underlying *OI* and different numbers of trials. The figure shows the number of trials that would be needed to detect different *OI* levels vs. $OI = 0$ at three levels of sensitivity (95, 99, and 99.9%). The test is specific for orientation selectivity, with *p*-values distributed uniformly when $OI = 0$.

For detecting direction selectivity, it is possible in principle to apply Hotelling's T^2-test to direction vectors. However, we have found that this method of testing for direction selectivity is quite insensitive because direction space is generally sampled too crudely to provide a reliable distribution of direction vectors. To address this problem, we developed a new test which we call the "direction dot product test." This test uses both orientation vectors and direction vectors to assess the direction selectivity of a cell (**Figure 7F**).

In the direction dot product test, the first step is to obtain the orientation axis of the cell by calculating the angle of the average orientation vector. Next, we calculate the magnitude of the projection of each direction vector onto the orientation axis (this is what we call the "direction dot product" for each direction vector). This gives us a 1-dimensional distribution of direction dot product values, one value for each direction vector. Finally, Student's *T*-test is performed on the distribution of direction dot products with H0: mean = 0. The test yields a *p*-value for whether the average magnitude of a distribution of direction vectors is significantly greater than zero.

The direction dot product reliably detects direction selectivity. **Figure 9** shows the direction dot product test applied to direction vectors from a simulated cell's response. The cell is simulated at different levels of underlying *DI* and different numbers of trials. The figure shows the number of trials that would be needed to detect different *DI* levels vs. $DI = 0$ at three levels of sensitivity (95, 99, and 99.9%). The test is specific for direction selectivity, with *p*-values distributed uniformly when $DI = 0$.

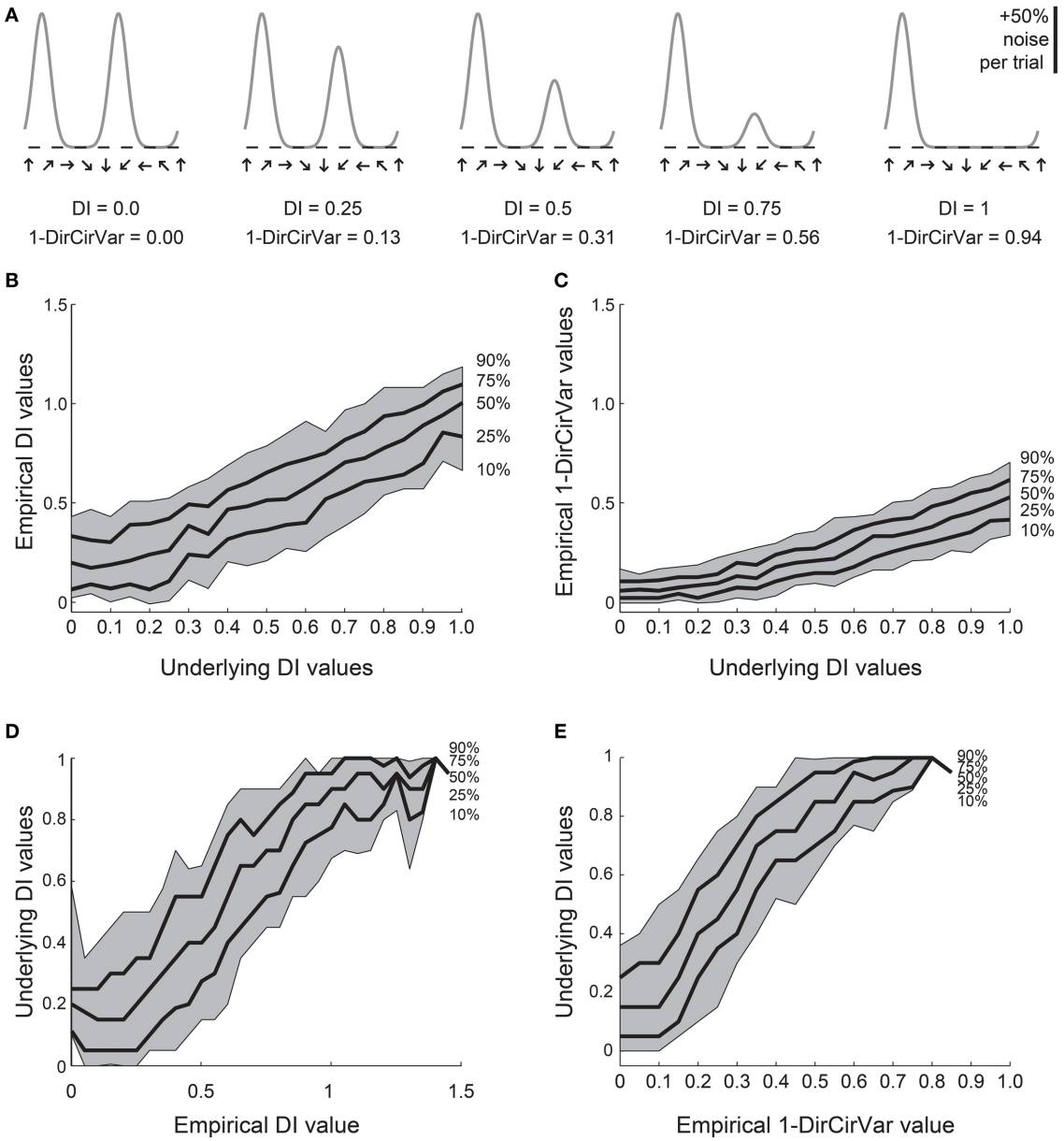

FIGURE 5 | Comparison of *DI* and direction circular variance measures for simulated data. We created 100 simulations of tuning curves for each of 21 underlying "true" tuning curves, ranging from $DI = 0$ to $DI = 1$, some curves shown in **(A)**. Each trial had 50% noise added. **(B)** Percentiles of the empirically determined *DI* for the 100 simulations at each underlying "true" *DI* value. Note that for cells with 0 true selectivity, the empirical *DI* values range from about 0 to about 0.5. **(C)** Percentiles of the empirically determined 1-*DirCirVar* index for each of the underlying "true" *DI* values. Note that when "true" *DI* is low, the 1-*DirCirVar* is always low. The index 1-*DirCirVar* increases as "true" *OI* increases but the range of values remains narrower than the corresponding range of empirical *DI* values in **(B)**. **(D)** The inverse of **(B)**; given we observed an empirical *DI* value of x, what is the range of possible "true" *DI* values that produced x in our simulations? An empirical *DI* of 0 could have arisen from cells with "true" *DI* values ranging from about 0 to 0.5, and an empirical *DI* of 0.5 could have arisen from cells with a "true" *DI* ranging from about 0.1 to 0.7. **(E)** The inverse of **(C)**. A 1-*DirCirVar* of 0 could have arisen from a "true" *DI* ranging from 0 to about 0.4, and 1-*DirCirVar* of 0.25 could have arisen from a "true" *DI* ranging from about 0.1 to 0.7. The range of possible underlying "true" *DI* values is narrower when 1-*DirCirVar* is used as a readout as compared to *DI*.

QUANTIFYING UNCERTAINTY AND DIFFERENCES IN ORIENTATION AND DIRECTION PREFERENCES

Another objective that arises when one has a cell with selectivity for orientation/direction is to estimate the uncertainty of the measured selectivity parameters. Above we described tools for asking whether selectivity was significantly greater than zero. However, one might also like to obtain a measure of dispersion (e.g., standard deviation) or a confidence interval (e.g., standard error) for selectivity parameters. In principle, one could simply obtain this from the distribution of *OI*/*DI*/1-*OriCirVar*/1-*DirCirVar* values measured on repeated trials. However, these measures behave inconsistently as response properties vary, especially as selectivity approaches zero, so estimating the distribution of parameters or confidence intervals from them is

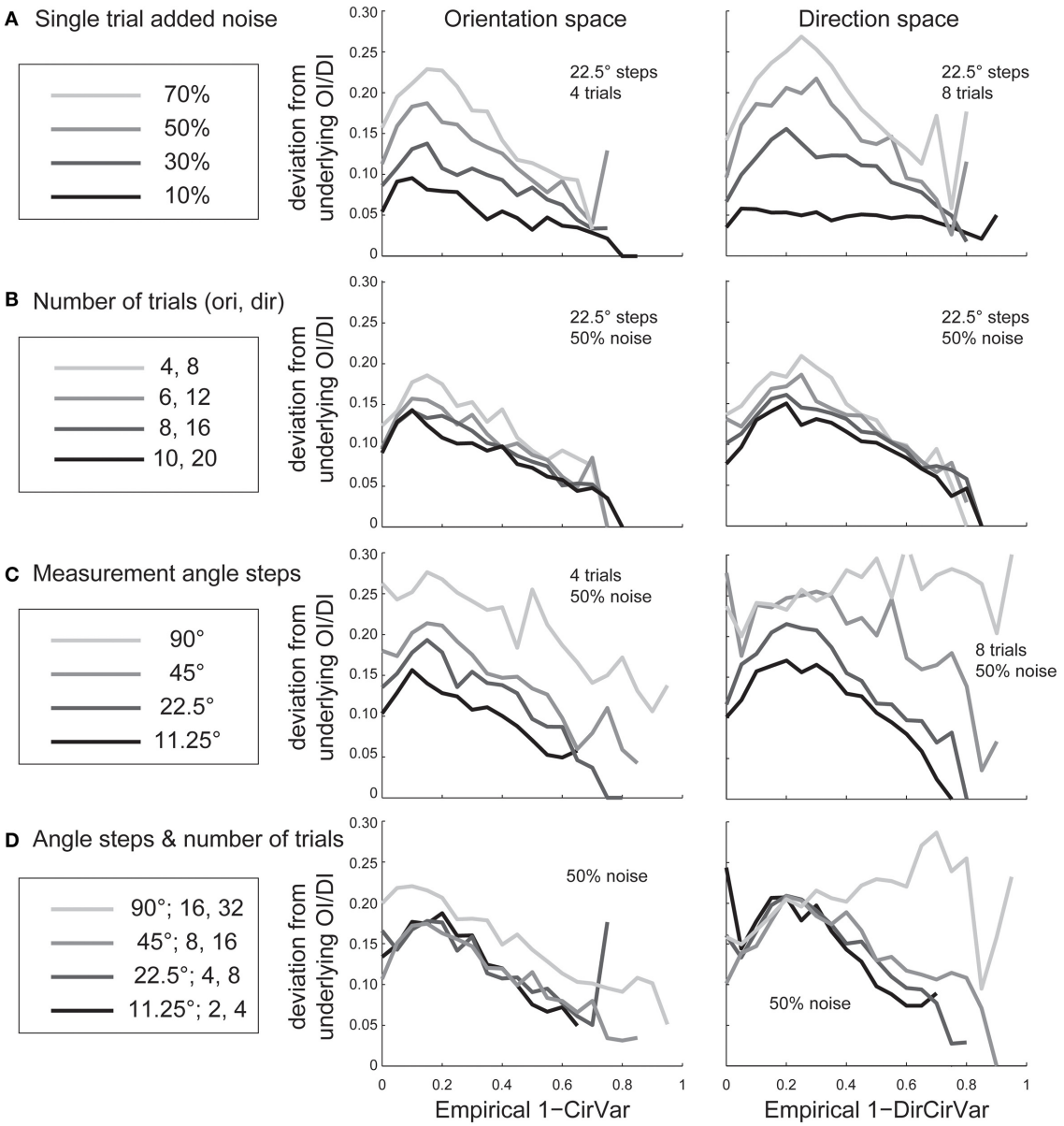

FIGURE 6 | The dependence of error in identifying the true *OI* on neural noise and stimulus sampling. On the Y axis of all plots is the average deviation between the "true" *OI* (or *DI*) and the "best guess" of *OI* (or *DI*) based on the empirical 1-*CirVar* (or 1-*DirCirVar*). **(A)** Dependence of error on single trial noise as a percentage of the maximum response rate to the preferred direction. **(B)** Dependence of error on the number of trials. More trials offer modest improvements in average accuracy. **(C)** Dependence of error on number of angle steps. Additional angle steps offer a big improvement in estimating the amount of orientation or direction selectivity present. **(D)** Dependence of error for assorted numbers of trials and angle steps.

not very meaningful. Fortunately, selectivity measures can be successfully employed to ask more specific statistical questions.

One common question, especially in the era of 2-photon imaging where many cells are recorded simultaneously, is to ask whether one population of cells has different average selectivity than another population (or, equivalently, whether a population recorded at one point in time has different average selectivity than the same population recorded at another point in time). The approach is simple: Measure selectivity coefficients from each cell in the two populations, and perform a 2-sample *T*-test to measure whether selectivity differs between them. The test can be performed using *OI*/*DI* or 1-*OriCirVar*/1-*DirCirVar* values. **Table 1** shows results from simulations asking how many cells would be required to detect differences in underlying *OI* or *DI* at different levels of confidence. The table shows that, as seen above, circular variance performs better than *OI*/*DI*.

As an aside, one might wonder whether statistics on raw vectors could be used to answer this question. Since vector magnitudes correlate with selectivity, why not compare the vectors between the populations to see if selectivity has changed?

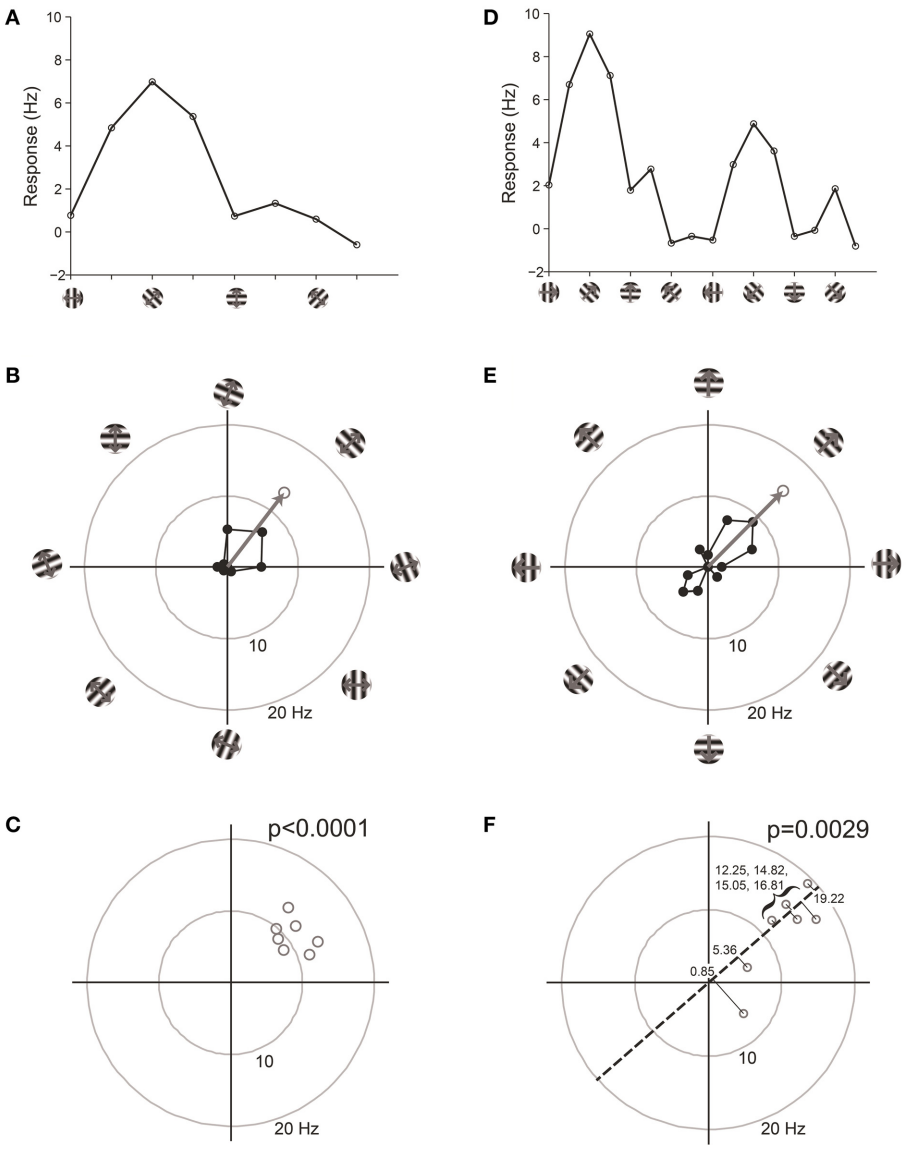

FIGURE 7 | Vector-based statistical tests with orientation (A–C) and direction (D–F) responses. This figure uses data from a model cell with strong tuning: Underlying $OI = 0.9$, $DI = 0.5$, noise = 20%. 16 directions (22.5° steps) were tested. For the orientation analysis, opposite directions at the same orientation were averaged together. **(A)** One trial from the model cell plotted in orientation response. Note that a "trial" is defined here as one measurement at each stimulus orientation. **(B)** The response from the trial shown in **(A)**, plotted in polar coordinates. *Black:* The response obtained at individual orientations. *Gray:* The vector sum of the responses at individual orientations. This is the "orientation vector" on this trial. **(C)** Orientation vectors from seven trials from the model cell. *Gray circles* show the orientation vectors from the seven trials. The *p*-value above the graph gives the result of Hotelling's T^2-test, which tests for whether the 2-dimensional mean of this distribution of orientation vectors is different from [0, 0]. **(D)** One trial from the model cell plotted in direction space. Here a "trial" is defined as one measurement at each stimulus direction. **(E)** The response from the trial shown in **(D)**, plotted in polar coordinates. *Gray:* The vector sum of the responses at individual directions. This is the "direction vector" on this trial. **(F)** Direction vectors from seven trials from the model cell. *Gray circles* show the direction vectors from the seven trials. The *dashed line* is orientation axis from this cell, obtained by measuring the angle of the average orientation vector. *Black lines* show the projection of the direction vectors onto the orientation axis (the "direction dot products"). *Numbers* give the magnitude of the direction dot product for each direction vector. The *p*-value above the graph gives the result of Student's *T*-test applied to the direction dot product values against H0: Mean = 0.

The answer is that vector magnitudes, while they do correlate with selectivity, also correlate with tuning width and response magnitude (see **Figure 3**). If two populations differ in any of these response parameters, they will produce different vectors. Hence a test that looks for differences in vectors can give a positive result even if the populations are equally selective. Note that this effect isn't a problem when testing for the presence of selectivity, as we do in **Figure 7**, because here the null hypothesis is zero magnitude, which can only occur when selectivity is zero. Thus, statistics on raw vectors are suitable for detecting

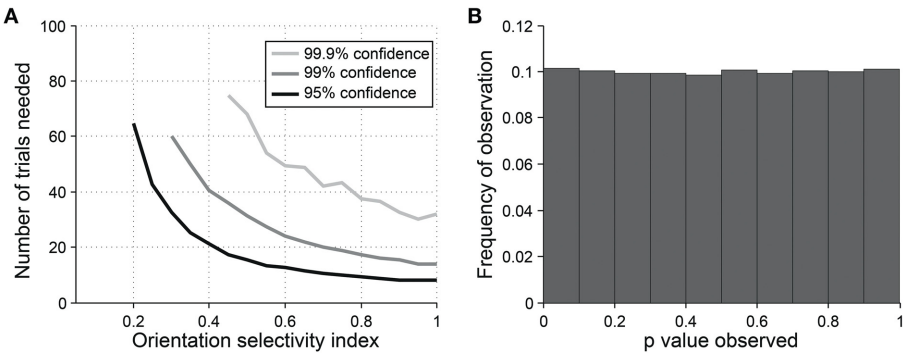

FIGURE 8 | Sensitivity and specificity of Hotelling's T-squared test for detecting orientation selectivity. (A) Repeated simulations were performed with a single cell at different levels of underlying *OI* and different numbers of trials. 16 angles (22.5° steps) were used; noise = 40% at all conditions. Sensitivity of Hotelling's T-squared test was measured at three levels of significance: 95, 99, and 99.9%. For example, the black line shows the number of trials needed such that one would detect an *OI* difference of X with 95% confidence. **(B)** A cell was simulated with seven trials at underlying $OI = 0$. The simulation was repeated 200,000 times and each time a *p*-value was measured against H0: $OI = 0$. The frequency of observed *p*-values was uniform between 0 and 1, which is what would be expected for an unbiased test by repeated sampling of an unoriented cell.

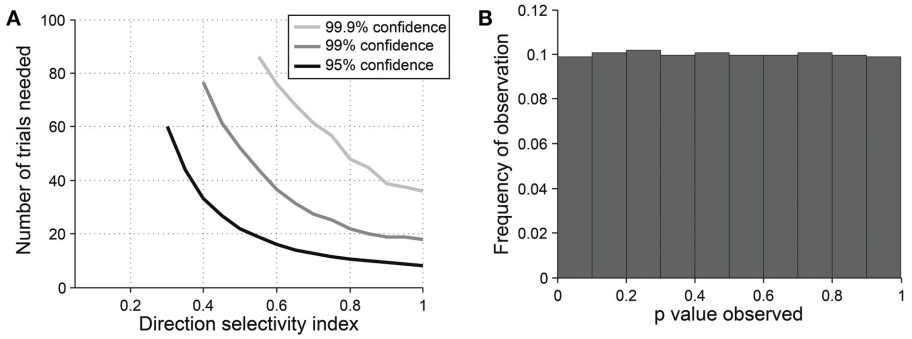

FIGURE 9 | Sensitivity and specificity of the direction dot product test for detecting direction selectivity. (A) Repeated simulations were performed with a single cell at different levels of underlying *DI* and different numbers of trials; $OI = 1$ for all simulations. 16 angles (22.5° steps) were used; noise = 4 Hz at all conditions. Sensitivity of the direction dot product test was measured at three levels of significance: 95, 99, and 99.9%. **(B)** A cell was simulated with 7 trials at underlying $DI = 0$, $OI = 1$. The simulation was repeated 200,000 times and each time a *p*-value was measured against H0: $DI = 0$. The frequency of observed *p*-values was uniform between 0 and 1, which is what would be expected for an unbiased test by repeated sampling of cells that are indifferent to direction.

the presence of selectivity, but not for detecting differences in selectivity.

Another common question is whether some specific response parameter differs between two cell populations. For example, one might wish to look for differences in preferred orientation between two populations. In this case, a vector-based test can be useful. Orientation vectors are affected by preferred orientation, so differences in preferred orientation lead to different distributions of vectors from the cells. Hotelling's T^2-test (specifically the 2-sample version of the test, analogous to the 2-sample Student's T-test) can be used to detect such a difference. **Figure 10** shows the sensitivity of the 2-sample Hotelling's T^2-test in detecting differences in preferred orientation between two populations of cells.

However, this test must be used with caution. Vectors are affected by all response parameters including preferred orientation, tuning width, and response magnitude, so a positive result simply means that one or more of these parameters differs between the two populations; it cannot prove that the difference is in preferred orientation or any other single parameter. The test may be useful as a broad screen to detect generalized differences in response parameters. But if a difference in a specific response parameter is sought, the best method is to perform statistics with iterative fitting, as described below.

EXTRACTING PARAMETERS OF ORIENTATION AND DIRECTION TUNING CURVES WITH FITS

In order to address the question of how well a given population of neurons encodes the orientation or direction of a stimulus, it is often important to know the precise parameters of a cell's tuning function such as its tuning angle or tuning width. Previous work using Monte Carlo simulations (Swindale, 1998) found that the best method for estimating tuning parameters from orientation or direction responses is to fit these responses with a Gaussian curve. In orientation space, we can fit the responses using a single Gaussian:

Table 1 | Minimum number of cells per condition that are needed to distinguish underlying orientation or direction selectivity index differences for two noise models.

***OI* base + Δ**	**If readout is *OI***			**If readout is 1-*CirVar***		
	0.95	**0.99**	**0.999**	**0.95**	**0.99**	**0.999**
0.5 + 0.1	16/100	37/190	201/365	9/43	16/85	26/130
0.5 + 0.2	6/20	13/40	40/80	5/6	7/15	12/28
0.5 + 0.3	5/6	8/15	19/21	5/4	5/6	8/9
***DI* base + Δ**	**If readout is *DI***			**If readout is 1-*DirCirVar***		
	0.95	**0.99**	**0.999**	**0.95**	**0.99**	**0.999**
0.15 + 0.1	103/1k	183/2k	313/3k	38/181	69/324	117/519
0.15 + 0.2	26/145	48/265	74/410	10/40	18/64	29/112
0.15 + 0.3	11/45	21/80	34/145	5/12	9/23	15/40
0.3 + 0.1	84/291	152/521	233/950	30/80	56/147	92/250
0.3 + 0.2	20/58	39/109	64/170	9/20	15/36	24/61
0.3 + 0.3	10/22	18/41	31/75	5/10	8/14	13/21
0.5 + 0.1	76/131	141/241	218/384	26/43	43/76	82/140
0.5 + 0.2	20/30	37/50	59/110	8/10	13/20	22/31
0.5 + 0.3	10/11	17/20	27/35	5/5	7/10	12/14

*The top three rows assume that the control group has an underlying OI that is 0.5, and the experimental group has the increment indicated in each row. The bottom rows assume that the control group has an underlying DI that is 0.15, 0.3, or 0.5 as specified, and the experimental group has the increment indicated in each row. The middle and right columns show the minimum cells that are needed to distinguish the control and experimental groups with a T-test at several confidence levels (0.95, 0.99, 0.999) if the experimenter is calculating OI (or DI) values as a readout (middle columns), or if the experimenter is calculating 1-CirVar (or 1-DirCirVar) values (right columns). The number of cells indicated is the number of cells required per condition (control or experimental), so twice this number would be required for a total experiment. Two noise models were used. In the data points to the left of the slash, 40% noise was added to the responses. In the data points to the right of the slash, "2-photon OGB-1AM" noise was used; that is, noise = 20% + 10 * response. Angle step size was 22.5°. Note that many fewer cells are needed to evaluate changes in orientation and direction selectivity if 1-CirVar or 1-DirCirVar is used as a readout as compared to OI or DI.*

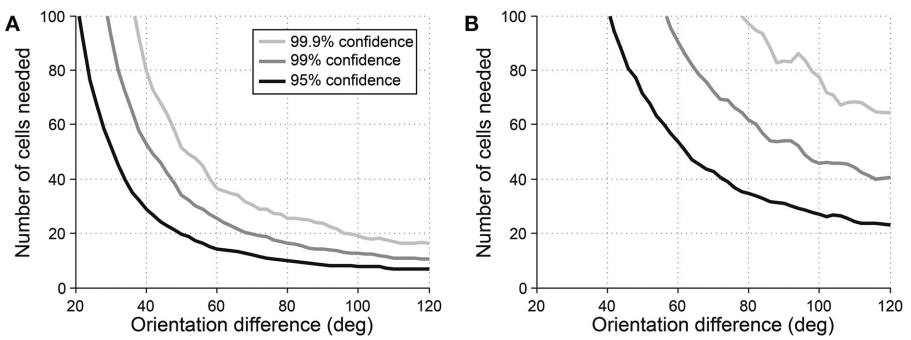

FIGURE 10 | Sensitivity of the 2-sample version of Hotelling's T-squared test for detecting differences preferred orientation between different cell populations. Cells were simulated with seven trials each. We systematically varied the size of the cell populations and the size of the difference in preferred orientation. We measured the sensitivity for detecting the difference at three levels of confidence: 95, 99, and 99.9%. **(A)** Simulations performed using single-trial noise of 40% in all conditions. **(B)** Simulations performed using "2-photon OGB-1AM noise": noise = 20 % + (10% × expected response).

$$R(\theta) = C + R_p e^{-\frac{ang_{ori}(\theta-\theta_{pref})^2}{2\sigma^2}},$$

where C is a constant offset, θ_{pref} is the preferred orientation, R_p is the above-offset response to the preferred orientation, $\text{ang}_{\text{ori}}(x) = \min(x, x - 180, x + 180)$, wraps angular difference values onto the interval 0° to 90°, and σ is a tuning width parameter. If we wish to only analyze the portion of the response above the offset, then the tuning width (half-width at half-height) is equal to $\sqrt{\log 4}\sigma$ (half-width at half height) (Carandini and Ferster, 2000).

In direction space, we can use a double Gaussian with the following equation:

$$R(\theta) = C + R_p e^{-\frac{ang_{dir}(\theta-\theta_{pref})^2}{2\sigma^2}} + R_n e^{-\frac{ang_{dir}(\theta+180-\theta_{pref})^2}{2\sigma^2}},$$

where C and θ_{pref} are defined as before, R_p is the above-offset response to the preferred direction, R_n is the above-offset response to the null direction, and $\text{ang}_{\text{dir}}(x) = \min(x, x - 360, x + 360)$, wraps angular difference values onto the interval 0° to 180°, and σ is a tuning width parameter. Again, if we wish to only analyze the portion of the response above the offset, then the tuning width (half-width at half-height) is equal to $\sqrt{\log 4}\sigma$ (half-width at half height) (Carandini and Ferster, 2000; Moore et al., 2005).

Although Gaussian fits are the best method for determining response parameters (Swindale, 1998), in practice there are several pitfalls to avoid. Several data analysis packages, such as Matlab (MathWorks) offer the ability to fit functions to data, but blindly applying a least squares fit to the data using the above functions often leads to poor fits. Common errors are described in **Figure 11A**. This problem is intractable in neural data because one never knows the "true" underlying response function, so it's impossible to say for certain that one fit is better than another. Hence, here we simulate responses with a known underlying response function, allowing us to evaluate the quality of our fits objectively.

To prevent poor fitting, we use 2 *ad-hoc* procedures. First, we provide several constraints on the fit parameters. We constrain the width parameter σ to be at least as large as $\alpha/2$, where α is the angle step used for stimulation; we force C to lie in the interval [-M,M], where M is the largest response to any stimulus; and R_p and R_n are constrained to lie in the interval [0, 3 M]. Second, we start the search using initial conditions that we expect will result in a good fit: $\theta_{pref} = \theta_M$ where $M = R(\theta_M)$, $R_p = R_n = M$, $C = 0$, and we explore several initial values for $\sigma \equiv \{\alpha/2, \alpha, 40°, 60°, 90°\}$. We take the fit with the lowest least square error for all these initial values of σ as the best fit of the data.

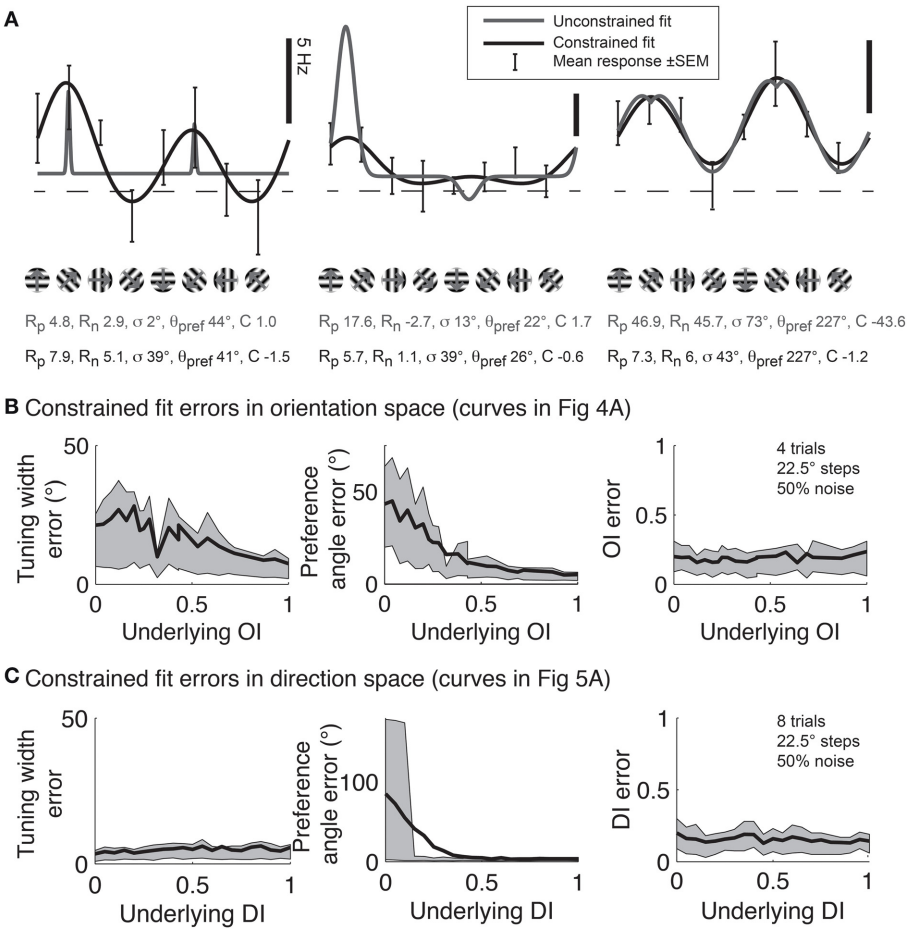

FIGURE 11 | Gaussian fits for assessing orientation and direction selectivity. (A) Common errors with unconstrained fits (gray lines). Left: the unconstrained fit has gotten stuck in a local squared error minimum, using a tiny tuning width to fit 2 points very accurately. Middle: The unconstrained fit has used a peak response R_p that is much larger than any point actually present in the data, and a physiologically implausible negative weight for the null direction. Right: The unconstrained fit has found a reasonable fit, but the parameters do not make physical sense. The unconstrained fit posits a constant offset that is highly negative, with large responses to the preferred and null directions. All of these fitting error can be solved by constraining the fit parameters to values that make physical sense (solid lines, see text). **(B)** Mean errors in tuning width, preferred angle, and *OI* for Monte Carlo simulations of cells with the underlying *OI*s in **Figure 4**. Gray patch indicates 25–75% interval **(C)** Mean errors in tuning width, preferred angle, and *OI* for Monte Carlo simulations of cells with the underlying *DI*s in **Figure 5**. Gray patch indicates 25–75% interval.

Using this *ad-hoc* fitting method, we can explore how well we can identify the tuning width and preferred angle for the same model cells we explored in **Figure 4**. The performance of the fit improves as the underlying *OI* increases (**Figure 11B**), although the error in angle preference is relatively large when *OI* is small. Because this error in angle preference is large when *OI* is small, we use another *ad-hoc* rule: we never report tuning widths or angle preferences from fits unless the data exhibits significant orientation selectivity by the Hotelling T^2-test. The simulations of the model cells of varying direction selectivity in **Figure 5** are fit with double Gaussian functions in **Figure 11C**. All of the tuning curves in **Figures 5**, **11B,C** exhibit significant orientation selectivity, so the fit of tuning width and *DI* is excellent. As expected, when the underlying *DI* is smaller than about 0.25, the noise in the empirical responses obscures which of the two opposite directions along the preferred orientation axis is the "true" preferred direction.

The relationships between fit quality and noise and number of stimulus trials and stimulus angles are plotted in **Figure 12**. As with the circular variance index values, more angle steps are always better, but 22.5° step sizes provide relatively high quality fits when used with 6–8 trials.

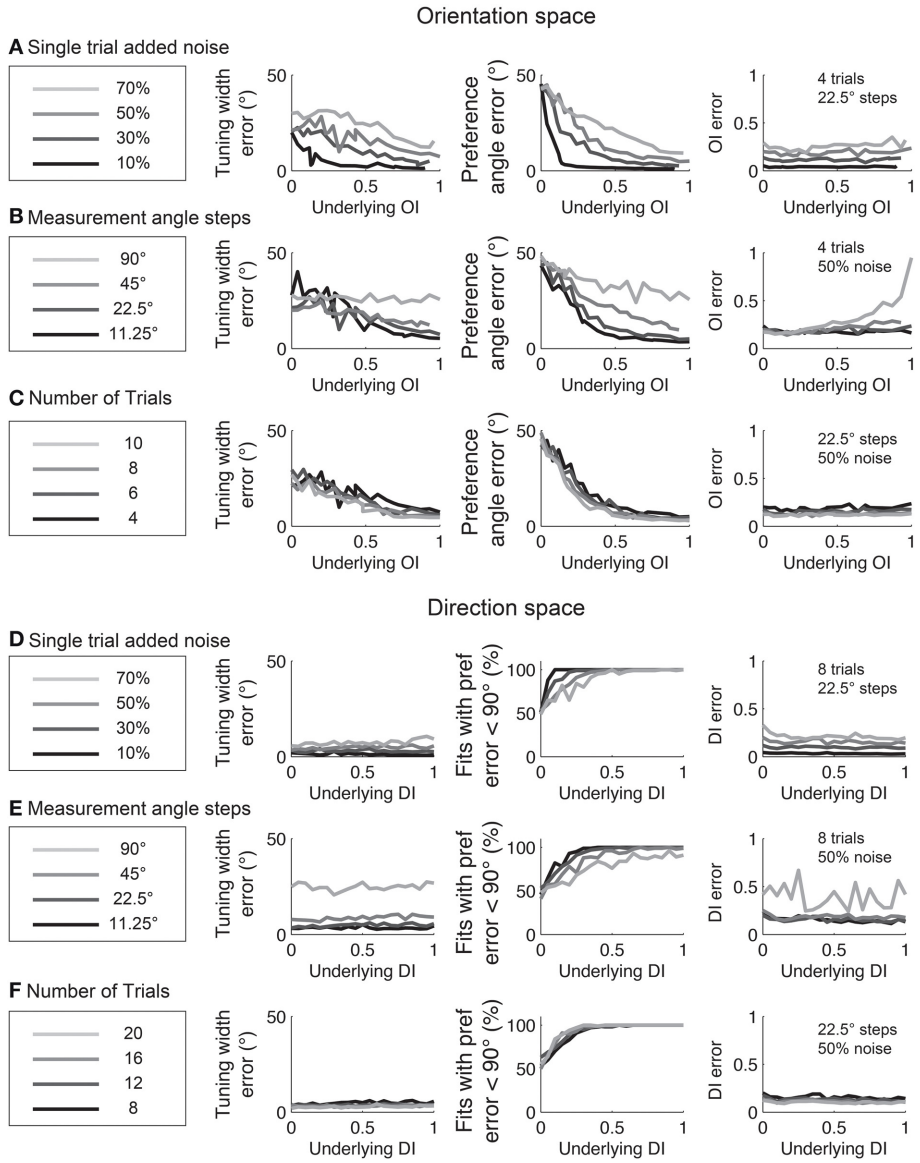

FIGURE 12 | The dependence of errors in identifying tuning width, preference angle, and *OI*/*DI* on neural noise and stimulus sampling. On the Y axis of all plots is the median error between the "true" underlying quantity and the value provided by the fit. **(A–C)** are in orientation space, and **(D–F)** are in direction space. **(A,D)** Dependence of error on single trial noise as a percentage of the maximum response rate to the preferred direction. **(B,E)** Dependence of error on number of angle steps. Additional angle steps offer a modest improvement in estimating the fit parameters. **(C,F)** Dependence of error on the number of trials. More trials offer modest improvements in average accuracy.

QUANTIFYING UNCERTAINTY IN FIT PARAMETERS USING ITERATIVE FITS

Finally, one useful outcome of iterative fitting is that it can be used to estimate uncertainty in fit parameters and to do statistics on these parameters. The simplest method for doing this uses the Hessian matrix, which measures the steepness of the error function near the local minimum where the fit algorithm settles. The matrix is obtained by sampling the error function near the local minimum and measuring the partial second derivative of this function for each parameter; standard Matlab optimization tools produce the Hessian matrix as an output parameter. Once obtained, the Hessian matrix can be transformed to obtain standard errors of fit parameters, and these can then be used to perform statistics (Press et al., 1992).

Unfortunately, the Hessian method does not work for fitting orientation and direction curves. Since the Hessian matrix represents the second partial derivatives of the error function, it can only be obtained when the error function is reasonably smooth. As described above, achieving adequate fits of orientation and direction data requires strict constraints on the fitting procedure. Because of these constraints, the error function is not smooth and thus a meaningful Hessian matrix generally cannot be obtained when fitting orientation and direction curves.

Another method for using iterative fitting to quantify uncertainty in parameters is the bootstrap method. In this method, samples of data are repeatedly selected at random, with replacement, and fits are performed to each sample. The distribution of parameters obtained in these fits provides a reasonable estimate of the parameter distribution in the underlying population (Press et al., 1992), and hence this distribution can be used to calculate standard errors and to do statistics.

In a previous study we employed the bootstrap method to estimate the distribution of preferred direction in individual cells from 2-photon recordings before and after extended exposure to a motion stimulus (**Figure 13**, modified from Li et al.). To obtain a distribution of preferred direction, we used the N trials obtained from a cell and created a "simulated" cell by randomly resampling these trials N times with replacement. The simulated data was then fit with a double Gaussian as described above. This procedure was repeated 100 times and the preferred direction was obtained for each simulation, yielding a distribution of preferred direction values from this cell.

One way we used this distribution was to detect significant direction selectivity. We quantified the "uncertainty" in direction preference, which is the percentage of simulations whose preferred direction differed from the mean preferred direction by more than 90°. This uncertainty can vary between 0 and 50%, so we interpret (*uncertainty* × 2) as a p-value for significant direction selectivity. We found that the sensitivity and specificity of this method for detecting direction selectivity is similar to what we obtain with the dot product direction test described above.

There are several drawbacks to the bootstrap method. First, the method is very computationally intensive, with a standard test requiring several days of computer time. More importantly, results obtained from the bootstrap method depend on a variety of factors that are not related to the data. Specifically, the outcome of the test depends on the fitting algorithm employed, the initial value used in the fit, and the constraints placed on the fit. Researchers using the bootstrap method must take care to record and publicize details about their technique so that others may reproduce their findings.

An alternative approach that generates confidence intervals is a Bayesian approach, such as that described in Cronin et al. (2010). The authors develop methods for estimating the entire probability distribution of each parameter value.

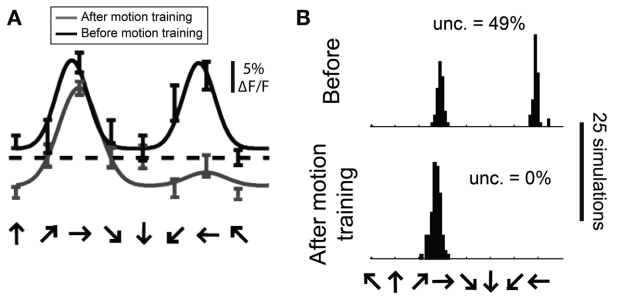

FIGURE 13 | Estimating the distribution of preferred direction using bootstrap methods. (A) Data from a cell recorded with 2-photon calcium imaging using OGB-1AM before and after extended exposure to a motion stimulus ("motion training"). Bars show ±1 standard error of the response. Solid lines show best fits with double Gaussian functions. The dashed line indicates mean response to a gray screen. **(B)** Distribution of preferred directions in bootstrap simulations of the cell shown in **(A)**. The data from this cell was randomly resampled with replacement, creating a "simulated" cell, and this simulated data set was fit with double Gaussian functions. This procedure was repeated 100 times in each training condition, yielding the observed distributions of preferred direction. "Unc." lists the preference uncertainty, meaning the percentage of simulations whose preferred direction differed from the mean direction by more than 90°.

DISCUSSION

Orientation and direction tuning are probably the most intensively studied response properties in the cortex. Historically, these studies have focused on cells with strong selectivity as determined by simple comparisons between preferred and non-preferred responses; cells without such obvious selectivity were often declared, simply, "unselective." However, the advent of advanced techniques for recording and manipulating neurons requires us to investigate subtle differences between cells and to extend our analysis to cells with low selectivity. We need statistical tools that are suitable for addressing these subtle questions.

Traditional measures for quantifying orientation and direction selectivity rely on assigning the stimulus evoking the strongest response as the "preferred" stimulus for the cell and assign the opposite stimulus as "non-preferred." The most commonly-used measures, *OI* and *DI*, compare the strongest stimulus to orthogonal stimuli (for *OI*) or opposite-direction stimuli (for *DI*). Our analysis shows that these measures are generally unreliable, especially for cells that have low selectivity or high noise (**Figures 2**, **4**). The key flaw with *OI*/*DI* and related measures is that preferred and non-preferred stimuli are always taken from sampled values of orientation/direction; if the true preferred stimulus lies between sampled values (which is likely to be the case), it will be missed.

Table 2 | Recommended methods for answering several common scientific questions involving orientation and direction selectivity.

Question	Recommended method
Quantifying the degree of orientation selectivity	1-*OriCirVar*
Quantifying the degree of direction selectivity	1-*DirCirVar*
Testing for significance of orientation selectivity	Hotelling's T^2-test on orientation vectors
Testing for significance of direction selectivity	Direction dot product test on direction vectors
Comparing orientation selectivity between two populations	2-sample Student's *T*-test on 1-*OriCirVar* values
Comparing direction selectivity between two populations	2-sample Student's *T*-test on 1-*DirCirVar* values
Screening for any difference in response parameters (e.g., preferred orientation, tuning width, peak height) between two populations	2-sample Hotelling's T^2-test on orientation vectors
Extracting response parameters such as tuning angle or tuning width	Fit data with Gaussian (for orientation data) or double Gaussian (for direction data)
Quantifying the confidence/uncertainty of response parameters such as tuning angle or tuning width	Bootstrap method: Resample data with replacement, then fit resampled data with Gaussian (for orientation data) or double Gaussian (for direction data)

To obtain an accurate estimate of preferred and non-preferred stimuli, one must extrapolate between measured values. Vector-based methods effectively extrapolate measured responses by calculating the vector average of responses on each trial. Specifically, for quantifying selectivity, we recommend 1-*OriCirVar* (for orientation) and 1-*DirCirVar* (for direction). These measures demonstrate greater reliability than *OI*/*DI* (**Figures 4**, **5**) and they are more sensitive than *OI*/*DI* for detecting differences in selectivity between two populations (**Table 1**).

Vectors can also be used to assess whether a cell's selectivity is statistically significant. In this approach, we ask whether the 2-dimensional mean of orientation or direction vectors is significantly from zero. Specifically, Hotelling's T^2-test on orientation vectors is reliable for detecting orientation selectivity (**Figure 8**) and the direction dot product test is reliable for detecting direction selectivity (**Figure 9**).

In some cases, we need to probe beyond selectivity to ask about specific response parameters such as tuning angle or tuning width. Vectors can be used to detect differences in these parameters between two populations (**Figure 10**); however, vector-based methods cannot identify which particular parameter or parameters are responsible for the difference. To answer such precise questions, we recommend another method of extrapolation: fitting data with Gaussian curves (for orientation) or double Gaussian (for direction). Swindale (1998) showed that least squared fitting with these functions provided the best method for extracting response parameters from orientation and direction data. This method provides accurate estimates of response parameters for cells with significant selectivity, provided that the fitting routine is appropriately constrained to avoid erroneous local minima (**Figures 11**, **12**).

Fitting also offers a tool for estimating the uncertainty of response parameters via the bootstrap method, where the data is randomly resampled multiple times with replacement and fits are performed to the resampled data. This method generates a distribution of values for each parameter which serves as an accurate estimate of the true distribution (**Figure 12**). Hence this method allows precise statistical questions to be asked about each response parameter underlying a cell's response. Note that alternative methods for fitting data and estimating parameters have been used (e.g., Cronin et al., 2010); we have not compared these methods to those described here.

Table 2 summarizes our recommendations for which method is best suited to a variety of quantitative questions regarding cells with orientation and direction tuning. Our goal is to provide tools for researchers to ask more refined statistical questions than have been possible using traditional measures such as *OI*/*DI*. As research advances into the precise mechanisms underlying orientation and direction tuning, robust quantitative methods will be required to distinguish competing theories. We hope the tools presented here will help accomplish this goal.

AUTHOR CONTRIBUTIONS

Mark Mazurek, Marisa Kager, and Stephen D. Van Hooser performed analysis, Mark Mazurek and Stephen D. Van Hooser wrote the paper with comments from Marisa Kager.

REFERENCES

Batschelet, E. (1981). *Circular Statistics in Biology*. New York, NY: Academic Press.

Carandini, M., and Ferster, D. (2000). Membrane potential and firing rate in cat primary visual cortex. *J. Neurosci.* 20, 470–484.

Cronin, B., Stevenson, I. H., Sur, M., and Kording, K. P. (2010). Hierarchical Bayesian modeling and Markov chain Monte Carlo sampling for tuning-curve analysis. *J. Neurophysiol.* 103, 591–602. doi: 10.1152/jn.00379.2009

De Valois, R. L., Yund, E. W., and Helper, N. (1982). The orientation and direction selectivity of cells in macaque visual cortex. *Vision Res.* 22, 531–544. doi: 10.1016/0042-6989(82)90112-2

Garaschuk, O., Milos, R. I., Grienberger, C., Marandi, N., Adelsberger, H., and Konnerth, A. (2006). Optical monitoring of brain function *in vivo*: from neurons to networks. *Pflugers Arch.* 453, 385–396. doi: 10.1007/s00424-006-0150-x

Girman, S. V., Sauve, Y., and Lund, R. D. (1999). Receptive field properties of single neurons in rat primary visual cortex. *J. Neurophysiol.* 82, 301–311.

Grabska-Barwinska, A., Ng, B. S., and Jancke, D. (2012). Orientation selective or not? - Measuring significance of tuning to a circular parameter. *J. Neurosci. Methods* 203, 1–9. doi: 10.1016/j.jneumeth.2011.08.026

Heimel, J. A., Van Hooser, S. D., and Nelson, S. B. (2005). Laminar organization of response properties in primary visual cortex of the gray squirrel (*Sciurus carolinensis*). *J. Neurophysiol.* 94, 3538–3554. doi: 10.1152/jn.00106.2005

Henry, G. H., Dreher, B., and Bishop, P. O. (1974). Orientation specificity of cells in cat striate cortex. *J. Neurophysiol.* 37, 1394–1409.

Hubel, D. H., and Wiesel, T. N. (1959). Receptive fields of single neurones in the cat's striate cortex. *J. Physiol.* 148, 574–591.

Hubel, D. H., and Wiesel, T. N. (1962). Receptive fields, binocular interaction and functional architecture in the cat's visual cortex. *J. Physiol.* 160, 106–154.

Hubel, D. H., and Wiesel, T. N. (1968). Receptive fields and functional architecture of monkey striate cortex. *J. Physiol.* 195, 215–243.

Humphrey, A. L., and Norton, T. T. (1980). Topographic organization of the orientation column system in the striate cortex of the tree shrew (*Tupaia glis*). I. Microelectrode recording. *J. Comp. Neurol.* 192, 531–547.

Ibbotson, M. R., and Mark, R. F. (2003). Orientation and spatiotemporal tuning of cells in the primary visual cortex of an Australian marsupial, the wallaby *Macropus eugenii*. *J. Comp. Physiol. A Neuroethol. Sens. Neural Behav. Physiol.* 189, 115–123. doi: 10.1007/s00359-002-0379-6

Kerr, J. N., Greenberg, D., and Helmchen, F. (2005). Imaging input and output of neocortical networks *in vivo*. *Proc. Natl. Acad. Sci. U.S.A.* 102, 14063–14068. doi: 10.1073/pnas.0506029102

Li, Y., Van Hooser, S. D., Mazurek, M., White, L. E., and Fitzpatrick, D. (2008). Experience with moving visual stimuli drives the early development of cortical direction selectivity. *Nature* 456, 952–956. doi: 10.1038/nature 07417

Moore, B. D., Alitto, H. J., and Usrey, W. M. (2005). Orientation tuning, but not direction selectivity, is invariant to temporal frequency in primary visual cortex. *J. Neurophysiol.* 94, 1336–1345. doi: 10.1152/jn.01224.2004

Movshon, J. A., Thompson, I. D., and Tolhurst, D. J. (1978). Spatial summation in the receptive fields of simple cells in the cat's striate cortex. *J. Physiol.* 283, 53–77.

Mrsic-Flogel, T. D., Hofer, S. B., Ohki, K., Reid, R. C., Bonhoeffer, T., and Hübener, M. (2007). Homeostatic regulation of eye-specific responses in visual cortex during ocular dominance plasticity. *Neuron* 54, 961–972. doi: 10.1016/j.neuron.2007.05.028

Niell, C. M., and Stryker, M. P. (2008). Highly selective receptive fields in mouse visual cortex. *J. Neurosci.* 28, 7520–7536. doi: 10.1523/JNEUROSCI.0623-08.2008

Ohki, K., Chung, S., Ch'ng, Y. H., Kara, P., and Reid, R. C. (2005). Functional imaging with cellular resolution reveals precise micro-architecture in visual cortex. *Nature* 433, 597–603. doi: 10.1038/nature03274

Palmer, L. A., and Davis, T. L. (1981). Comparison of responses to moving and stationary stimuli in cat striate cortex. *J. Neurophysiol.* 46, 277–295.

Press, W. H., Teukolsky, S. A., Vetterling, W. T., and Flannery, B. P. (1992). *Numerical Recipes in C*. Cambridge: Cambridge University Press.

Ringach, D. L., Shapley, R. M., and Hawken, M. J. (2002). Orientation selectivity in macaque V1: diversity and laminar dependence. *J. Neurosci.* 22, 5639–5651.

Rocha-Miranda, C. E., Linden, R., Volchan, E., Lent, R., and Bombar-Dieri, R. A. Jr. (1976). Receptive field properties of single units in the opossum striate cortex. *Brain Res.* 104, 197–219.

Stosiek, C., Garaschuk, O., Holthoff, K., and Konnerth, A. (2003). *In vivo* two-photon calcium imaging of neuronal networks. *Proc. Natl. Acad. Sci. U.S.A.* 100, 7319–7324. doi: 10.1073/pnas.1232232100

Swindale, N. V. (1998). Orientation tuning curves: empirical description and estimation of parameters. *Biol. Cybern.* 78, 45–56.

Van Hooser, S. D., Heimel, J. A., Chung, S., Nelson, S. B., and Toth, L. J. (2005). Orientation selectivity without orientation maps in visual cortex of a highly visual mammal. *J. Neurosci.* 25, 19–28. doi: 10.1523/JNEUROSCI.4042-04.2005

Weliky, M., Bosking, W. H., and Fitzpatrick, D. (1996). A systematic map of direction preference in primary visual cortex. *Nature* 379, 725–728.

Conflict of Interest Statement: The authors declare that the research was conducted in the absence of any commercial or financial relationships that could be construed as a potential conflict of interest.

Received: 04 April 2014; accepted: 17 July 2014; published online: 06 August 2014.
Citation: Mazurek M, Kager M and Van Hooser SD (2014) Robust quantification of orientation selectivity and direction selectivity. Front. Neural Circuits ***8****:92. doi: 10.3389/fncir.2014.00092*
This article was submitted to the journal Frontiers in Neural Circuits.

frontiers in
NEURAL CIRCUITS

METHODS ARTICLE
published: 27 June 2014
doi: 10.3389/fncir.2014.00068

Imaging ATUM ultrathin section libraries with WaferMapper: a multi-scale approach to EM reconstruction of neural circuits

Kenneth J. Hayworth[1]*, Josh L. Morgan[2]*, Richard Schalek[2], Daniel R. Berger[2], David G. C. Hildebrand[2] and Jeff W. Lichtman[2]

[1] *Howard Hughes Medical Institute, Ashburn, VA, USA*
[2] *Department of Molecular and Cell Biology, Harvard University, Cambridge, MA, USA*

Edited by:
Benjamin R. Arenkiel, Baylor College of Medicine, USA

Reviewed by:
Julian Budd, University of Sussex, UK
Richard J. Weinberg, University of North Carolina, USA

****Correspondence:***
Kenneth J. Hayworth, Howard Hughes Medical Institute, Janelia Farm Research Campus, 19700 Helix Dr., Ashburn, VA 20147, USA
e-mail: hayworthk@janelia.hhmi.org;
Josh L. Morgan, Department of Molecular and Cell Biology, Harvard University, 52 Oxford St., Cambridge, MA 02138, USA
e-mail: joshmorgan@fas.harvard.edu

The automated tape-collecting ultramicrotome (ATUM) makes it possible to collect large numbers of ultrathin sections quickly—the equivalent of a petabyte of high resolution images each day. However, even high throughput image acquisition strategies generate images far more slowly (at present ~1 terabyte per day). We therefore developed WaferMapper, a software package that takes a multi-resolution approach to mapping and imaging select regions within a library of ultrathin sections. This automated method selects and directs imaging of corresponding regions within each section of an ultrathin section library (UTSL) that may contain many thousands of sections. Using WaferMapper, it is possible to map thousands of tissue sections at low resolution and target multiple points of interest for high resolution imaging based on anatomical landmarks. The program can also be used to expand previously imaged regions, acquire data under different imaging conditions, or re-image after additional tissue treatments.

Keywords: connectomics, ATUM, volume EM, scanning electron microscopy, ultramicrotome, imaging software, tape collection, serial-section electron microscopy

INTRODUCTION

The three dimensional (3D) structure of biological tissues can be ascertained at high resolution by cutting plastic-embedded tissue into a series of ultrathin sections, imaging those sections with an electron microscope, and reconstructing the objects contained therein *(volume EM)*. Obtaining such volumetric reconstructions is especially useful for analysis of nervous system samples because nerve cells distribute their processes over extended volumes and only with the resolution of electron microscopy (EM) is it possible to identify the network of synaptic connections between all the neurons. This dense synaptic connectivity data is critical to understanding how nervous systems process information (Morgan and Lichtman, 2013).

Until recently, volume EM required manually collecting a series of ultrathin sections onto the nanometers thin plastic film of a transmission electron microscope (TEM) grid. Because of the thin substrate, the process of making serial sections can be painstaking and is subject to tissue loss that poses a serious challenge for very large volume reconstructions (Gay and Anderson, 1954; Harris et al., 2006). With the introduction of high-performance field emission scanning electron microscopy (SEM) (Joy, 1991; Bogner et al., 2007), high quality images can be acquired from the surface of ultrathin sections thereby removing the need to mount sections on an electron-transmissive substrate. Several new imaging strategies have emerged to take advantage of EM surface imaging to facilitate the production of large EM image volumes.

One strategy that is based on SEM surface imaging is to image the surface of a plastic-embedded block of brain tissue that is mounted directly inside the SEM. Tens of nanometers of the block's top surface are then removed by either a microtome in the serial blockface EM (SBEM) approach or a focused ion beam (FIB) in the FIB-SEM approach to expose a new surface for imaging. This procedure can be repeated many thousands of times to produce a volume EM image set (Denk and Horstmann, 2004; Knott et al., 2008).

A second strategy, which we adopt in this paper, takes advantage of the surface imaging capabilities of SEM by mounting ultrathin sections on a much more stable substrate than can be used in TEM. In the recently invented Automatic Tape-collecting UltraMicrotome SEM (ATUM-SEM) process (Schalek et al., 2011), the ultrathin sections cut by a commercial ultramicrotome are immediately and automatically collected from the knife's water boat onto the surface of a partially submerged conveyor belt made of sturdy plastic tape (**Figure 1**). SEM imaging of the series of sections collected on the tape produces a dataset of micrographs which renders individual planes through a 3D tissue volume. This tape collection allows thousands of ultrathin sections to be collected in an automatic way. Because of the uninterrupted flow of tissue onto the relatively wide conveyor belt, the sections obtained can be thinner, larger in area (several square

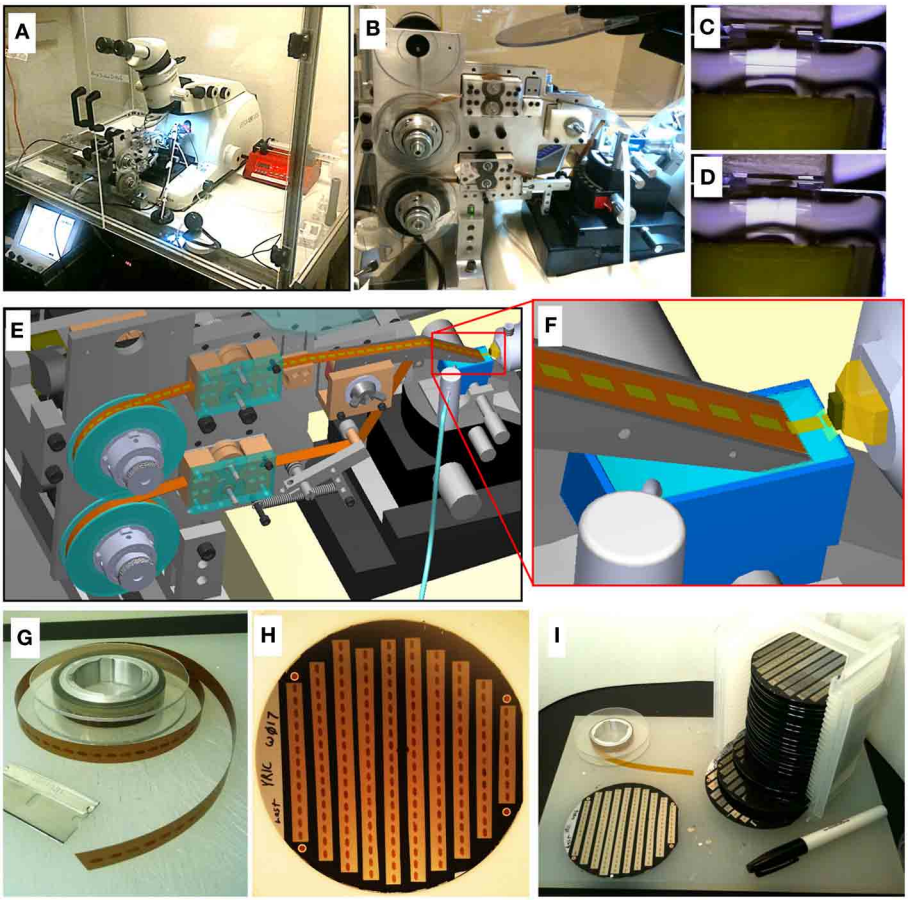

FIGURE 1 | ATUM-SEM process. (A) Picture of ATUM tape collection device installed on a commercial ultramicrotome housed in an environmental control chamber. **(B)** Side view of ATUM. **(C,D)** Sequential video images of section collection. **(E)** CAD rendering of ATUM showing path collected sections take from the knife boat to the final take-up reel. **(F)** CAD zoom in on knife boat showing collection process. **(G)** Picture of unraveled tissue-tape on take-up reel containing a series of ultrathin sections. Each dark rectangle is a section. **(H)** Picture of a 100 mm diameter silicon wafer with 10 tissue-tape strips adhered to it. There are a total of 162 ultrathin sections on this one wafer. **(I)** Picture of 20 wafers all filled with tape strips from a single ATUM run consisting of over 15 m of tissue tape. This collection of 20 wafers is a single UltraThin Section Library (UTSL) containing over 3000 ultrathin sections, representing a total tissue volume of over 0.2 mm^3.

millimeters each), and of higher quality (without tears, etc.) than are obtained by manual collection for TEM.

A major challenge of the ATUM-SEM approach is setting up many thousands of targeted image acquisitions from tissue sections spread across meters of ATUM collection tape. To convert these sections into an image volume, the ATUM's tape must be mounted in the SEM and a region of interest on a section must be positioned beneath the electron beam for imaging. The corresponding region of interest must be found again and again on all subsequent sections. Each section's target region must be positioned, rotated, and focused beneath the electron beam to obtain a high resolution image series. Here we describe a semi-automatic microscope control software package named WaferMapper that can orchestrate all of these steps to produce volume EM image sets from an ATUM tape.

With the proper software solution for handling the additional imaging complexity, the ATUM-SEM process has several potential advantages over alternative techniques. The most obvious advantage over block-face techniques is that the ATUM-SEM technique does not destroy the tissue as it is being imaged. Low resolution images of the entire tissue volume can, therefore, be taken relatively quickly. This overview image volume can be used to plan efficient, targeted high resolution imaging volumes encompassing only those regions crucial to the biological study at hand. Additional high resolution imaging forays on the same sectioned material can be conducted at multiple later times if desired.

The importance of this ability becomes apparent when one considers the time and storage requirements involved in imaging 3D volumes at nanometer resolutions. For example, consider a $0.5 \times 2.5 \times 3$ mm block of mouse brain trimmed to encompass regions of the lateral geniculate nucleus (LGN) and primary visual cortex (V1) along with intact axonal projections connecting the two (MacLean et al., 2006). On the ATUM, such a "visual thalamocortical slice" block could potentially be reduced to a tape of $17,000 \times 30$ nm thick sections collected

with just a few days of sectioning. If imaged in total, with a typical 5 nm in-plane resolution, this volume would require storage of 5 petabytes of image data (17,000 sections each montage imaged with $500,000 \times 600,000$ pixels). Worse still, if imaged at a standard rate of about 10 megapixels per second, a single microscope would require over 15 years to image the volume, seemingly putting such a study out of reach today. However, the actual connected regions of the LGN and V1 represent only a tiny fraction of the full slice volume which they span. If one could direct high-resolution imaging mainly to those regions which are actually connected then the total imaging time could potentially be reduced by a factor of 10× or more. One way to efficiently direct such high-resolution imaging would be to utilize an iterative process of first making a low resolution image set of the entire volume and then use several passes of directed, medium and high-resolution imaging to narrow in on and eventually high-resolution image only those parts containing an intact thalamocortical circuit. An additional advantage afforded by non-destructive ultrathin section collection is that imaging time can be further reduced by dividing up the ATUM tape so that it can be simultaneously imaged in parallel across multiple SEMs.

This type of parallel, multi-scale, directed-access volume EM imaging—which is not possible in blockface approaches and extremely difficult when handling individual TEM grids—is possible given the large tissue volumes and the robustness to re-imaging and tissue handling of the ATUM-SEM technique. In this paper we use the term "UltraThin Section Library" (UTSL) to describe a collection of many thousand ATUM-collected ultrathin sections which have been securely mounted on wafers for SEM imaging and which have undergone all of the coordinate mapping steps and low resolution overview imaging necessary to allow quick and easy random-access imaging of any point in the volume. These mapping steps are performed through our custom SEM-automation software–WaferMapper.

Our vision is that a researcher using such an UTSL and WaferMapper should be able to quickly browse through the entire tissue volume at low resolution, identify salient anatomical features, and then graphically specify a subvolume for automated imaging. The WaferMapper software then instructs which wafers to load into the SEM leaving the software to automate all subsequent imaging operations.

In order to take full advantage of a large tissue library, the mapping and imaging software must meet the following criteria:

- **Automated imaging**—The first goal of an automated image acquisition software package is to allow a user to image the corresponding region of tissue on all of the sections in a tissue library without having to manually direct the microscope to each section. Ideally, the user should be able to pick a target region within the software, load a wafer, and leave the microscope while the imaging takes place automatically.
- **High throughput**—To reconstruct large regions of tissue at high resolution, images must be acquired quickly. Scan speeds within a single image currently range from about 0.5 to 20 million pixels per second (MPS) using the commercially available SEMs and detectors described in this paper. This large range of imaging speeds reflects the wide range of staining techniques used in connectomics studies as well as differences in the efficiency and bandwidth of different types of detectors used under various imaging conditions. Ideally the acquisition overhead (time spent between image scanning) should be less than the actual image acquisition time. Eliminating human involvement in the image acquisition procedure is an important part of reducing overhead. In addition, however, automated steps such as stage movements, focusing, and image retakes also need to be accomplished quickly so as not to slow down the throughput. (We provide a table breaking down actual data acquisition times for key WaferMapper steps in the Example data section below).
- **Robustness**—The software must allow for variations in tissue properties, as well as staining, cutting, and imaging conditions. In particular, the software must be able to find and image the corresponding region in serial sections that may appear different due to staining artifacts, damage during cutting, or biological changes in the tissue. If changes in the tissue or the microscope result in failures to target the correct tissue region or acquire high quality images, these failures should be detected and corrected without the requirement of human intervention.

WaferMapper has been designed to meet these three goals. Its central strategy is to first map the dataset using low resolution imaging so that the time consuming process of high resolution imaging can be intelligently targeted and automatically executed. In addition, WaferMapper checks its own work -making sure that it has successfully navigated to the correct position in the tissue and that the images are of acceptable quality. Using this software, we have been able to collect image volumes from a wide range of ATUM-collected tissue libraries (including a mouse cortex UTSL, a mouse cerebellum UTSL, a mouse thalamus UTSL, and a larval zebrafish UTSL). These 3D image volumes ranged in size from about 1 to 100 terabytes of image data and required the imaging of many thousands of ultrathin sections.

SAMPLE PREPARATION

TISSUE PROCESSING

All experiments were performed according to the guidelines of the Harvard Animal Care and Use Committee. The tissue samples for ATUM are standard EM blocks preserved using aldehydes, stained with osmium tetroxide, and embedded in a hard resin (Hayat, 2000). For large volumes to be imaged quickly, good contrast is essential. We often use a combination of the (R)OTO technique for enhancing osmium staining *en bloc* and lead citrate post section staining (Tapia et al., 2012). It is important to note, that by thickening and darkening membranes, this technique can make synapses more difficult to identify in single sections. A great deal of this ambiguity is resolved when a synapse is reconstructed in its 3D context. There are also a number of staining techniques that can be used to enhance synaptic labeling. Regrettably, most EM protocols were not developed to penetrate volumes that extend for 100 s of microns in depth. The lack of uniformity in staining, in general, can be a significant problem. More uniform staining can be achieved by decreasing stain concentration and increasing incubation time. However, with any particular sample there

is a significant risk that the stain will not be acceptable all the way through the volume. One of the benefits of generating the low resolution image series with WaferMapper is that the thousands of sections can be evaluated for tissue quality before the more time-consuming high resolution imaging is begun. Once high resolution imaging is completed, WaferMapper can also be used to reimage ambiguous structures under different imaging conditions or after further post section staining.

SECTIONING AND SAMPLE PREPARATION

ATUM uses a reel-to-reel conveyor belt to collect sections from the water boat of standard ultramicrotome diamond knives. Once sections are cut and float into the water boat, they come in contact with the inclined surface of the moving collection tape that juts out of the water (**Figure 1**). Depending on the size of the tissue block, 1000–10,000 sections can be collected over a 24 h period with no human interaction. Once the ATUM sectioning and collection process is started, the operator typically leaves the room and can check in on cutting remotely via video. Knife water level is maintained automatically by a video feedback mechanism controlling a digital syringe pump. After sectioning about 100 μm of tissue, the microtome reaches the end of its useful range and has to be manually reset. At this time, the sample can also be moved to a fresh position on the diamond knife so that knife sharpness does not become a problem. In this way, large volumes can be sectioned with only a single interruption every several thousand sections. For some samples, it is possible to collect thousands of sections without tissue loss. However, many factors such as heterogenetity in the tissue, and knife dullness can result in sections breaking or folding as they are being cut. For most connectomics applications we are able to tolerate one or two damaged sections per hundred as long as damage is not occurring in sequential sections.

The tape containing the sections is next cut into strips and mounted on 100 mm diameter silicon wafers which are flat, conductive (doped) and vacuum safe. To adhere the tape to the wafer, the surface of the wafer is covered with double sided conductive tape. Each section needs a path to ground or it will become electrically charged during SEM imaging. This grounding can be accomplished by thin-film depositing a carbon coating over the entire surface of the wafer with tape strips attached (typically works well with backscattered electron detection). If the tissue will be imaged using voltages that cannot penetrate a carbon coating (see section: Imaging Hardware), use of a collection tape that is pre-coated with a conductive layer is required. The top surface of the conductive tape can then be connected to ground by using conductive tape or paint along its edges. Because this approach also works with backscattered electron detection, we are able to first use backscattered imaging to acquire large field of view overview images with minimal field distortion (because of high electron voltages) and then switch to secondary electron imaging if it is optimal for the smaller field of view high resolution imaging step.

Once the tape segments are mounted onto silicon wafers, we affix fiducial markers (Copper Reference Finder TEM grids style H6 from Ted Pella work well) to the double sided carbon tape at the corners of the wafers. This is critical for the wafer mapping process, described in detail below. A standard wafer box (**Figure 1**) can hold 25 silicon wafers containing hundreds of sections each, resulting in a 10,000-section UTSL that can be stored in a desk drawer.

IMAGING HARDWARE

There are several SEM imaging systems commercially available that could be used for imaging ultrathin section libraries generated by ATUM sectioning. The software presented here was developed to drive off-the-shelf Sigma and Merlin SEMs (Carl Zeiss Microscopy LLC, Oberkochen, Germany) fitted with Fibics scan generators (Fibics Inc., Ottawa Ca.). All results presented here were imaged with one of these microscopes. The Fibics scan generator allowed for images to be acquired with pixel dimensions up to 32 by 32 k. Both of these microscopes have multiple detectors that include an outside-the-lens secondary electron detector, a below the lens backscatter detector, and an in-lens secondary electron detector. We use the in-lens secondary electron detector for high speed imaging because this detector's response speed was sufficient to keep up with high scan rates (10 MPS in the case of the Sigma and 20 MPS in the case of the Merlin). When imaged with this detector, our samples yielded the best signal using 1.7–3.5 keV and therefore required collection on an ATUM tape having conductive coating rather than thin-film carbon coating the sections after collection. We also found that the "depth of field" mode with extended depth of focus available with the Merlin is helpful for acquiring large fields of view of potentially uneven surfaces. Both microscope types were also fitted with an Evactron plasma generator (XEI Scientific, Redwood City, CA) to clean and etch surface material before imaging tape affixed to wafers.

IMAGING STRATEGY AND WORKFLOW

A consequence of automated sectioning is that far more tissue can be cut than can currently be imaged at the highest EM resolution. Because this tissue is mounted on silicon wafers and imaged with an SEM, it is relatively easy to image, store, and reimage the tissue. It is possible, therefore, to treat ATUM cut samples as an UTSL to be sampled on demand. For some experiments, large target areas might be imaged once at high resolution. Other experiments might involve various small high resolution volumes being fit onto a low resolution map of the total tissue volume. The experimental flexibility gained by the UTSL depends critically on developing the means to allow easy navigation within the digital volume. This section (Imaging strategy and workflow) contains an outline of the intent of the low and high resolution imaging steps. The following section (Implementation: WaferMapper) contains a detailed description of the WaferMapper implementation. Graphical depictions of some of the key concepts (UTSL, wafer, fiducial, section overview image, aligned stack of overview images, target point) can be found in **Figure 2A**.

LOW RESOLUTION MAPPING

The first step in generating a UTSL is mapping the positions of each of the sections on all the silicon wafers. The low resolution mapping step can be accomplished using either an optical image or an EM image montage of the entire silicon wafer. Sections are identified automatically and then any instances of unlabeled sections or debris labeled as sections are corrected manually. This

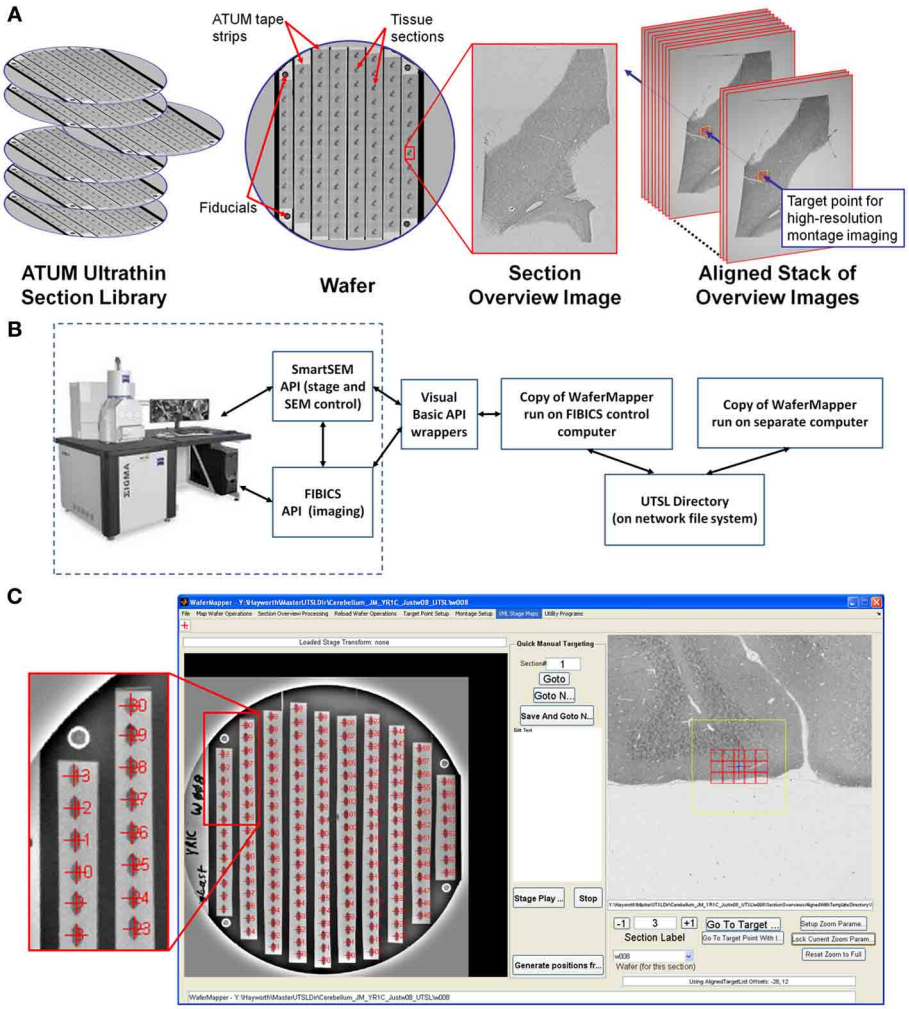

FIGURE 2 | Overview of WaferMapper terminology, SEM system integration, and Graphical User Interface (GUI). (A) Graphical depiction of some of the key terms described in the text. **(B)** Block diagram showing how one copy of the WaferMapper program is used to automate SEM imaging while a separate copy is used to handle offline tasks such a browsing the aligned section overviews stack and graphically planning montage imaging volumes. A central UTSL Directory structure organizes all metadata and images related to the library. **(C)** The WaferMapper GUI is organized around a wafer-level overview display (left) and a section overview display (right). Each tissue section on the wafer-level overview display is marked by a red cross along with its section number. In the section overview display, a red cross designates the target point for high-resolution imaging. In this case the red cross is overlaid by a smaller blue cross designating where autofocuses should occur (which, in general, can be offset from the target point). The yellow box in the section overview display denotes the field-of-view used for local target point alignment (see section: Target point setup). The red boxes in the section overview display are the high resolution montage tile positions defined in the montage parameters (see section: Montage parameters).

procedure marks the position of each section. For the microscope to consistently find the mapped section positions, reference points (fiducials) are imaged on each wafer (**Figure 2A**). Any time a mapped wafer is loaded into the SEM, the fiducial points are re-imaged and compared to the original fiducial images to determine the correction factor required to translate the wafer map coordinate system onto the new wafer position.

The second step in creating a UTSL requires obtaining a more detailed low resolution image of each section (but not the whole wafer). For this imaging phase, the microscope automatically uses the map of section positions obtained for each wafer (see above) to drive the microscope stage to each section on a wafer and obtain a "section overview" image (see **Figure 2A**). The overview image generally includes all of the tissue in the section (typically several square millimeters) while using a pixel size just small enough to identify features relevant to the future targeting of image volumes within the section (commonly 1 μm pixel size). After acquiring the overview images they are digitally registered to each other to remove effects of inter-section rotation and translation. The resultant "aligned stack of overview images" (see **Figure 2A**) constitutes a 3D coordinate map of tissue locations used for all subsequent navigation of the UTSL.

HIGH RESOLUTION IMAGE ACQUISITION

With the low resolution UTSL overview map it becomes possible to select one or more target regions for higher resolution

imaging throughout the volume. A center position "target point" (see **Figure 2A**) for a targeted region is recorded and in some cases a second higher resolution local registration (setting translation parameters only) is performed now with the target position at its focus. At high resolution, a target region may require imaging a mosaic of multiple overlapping images arranged in rows and columns. Imaging the target region therefore requires defining "montage parameters" (i.e., size of the imaging mosaic, resolution, and other imaging parameters). Once these parameters are set, each wafer can be loaded onto the microscope stage and imaged automatically.

High resolution data collection begins with loading a wafer and imaging the fiducials to adjust the wafer's section overview map to register it to the new position of the wafer on the microscope stage. These adjustments are typically in the range of 100 s of microns. With the montage parameters loaded, the microscope now has sufficient information to acquire a series at high resolution for each loaded wafer. Once the high resolution imaging step is initiated, the microscope automatically moves the stage to the first section and then moves to the target position. The scan rotation based on the stored parameters is initiated so that all the sections are acquired in the same orientation. The microscope then automatically adjusts focus and stigmation at the target region.

Correct focus and stigmation are critical for SEM imaging of tissue sections spread across ATUM tape strips and adhered to silicon wafers. The depth-of-field in typical SEM imaging is small relative to typical wafer and tape mounting variability. The beam focus must therefore be adjusted to match the z-position of the tissue as the stage moves across millimeters of tissue and centimeters of silicon wafer. Generating a high resolution beam spot also depends on stigmators compensating for any aberrations in the focusing of the electron beam. Our experience is that the optimal stigmation changes during an imaging period as the focus depth and microscope conditions change. Acquiring a dataset with consistent image quality therefore requires periodic automated focusing and stigmation.

We find that, when we apply the focus algorithms currently available on the Zeiss Sigma and Merlin, our focus quality is unacceptable about 5% of the time. Therefore, high resolution images undergo an automatic quality check which can trigger a corrective focus and stigmation followed by re-imaging. Because focus and stigmation can take as long as imaging time and failure rates can vary with tissue and imaging conditions, a variety of focusing strategies are made available (described below). When the high resolution imaging of a section is completed, the digital data is automatically moved from a local data buffer to long-term network storage.

If high resolution imaging is interrupted at any point, no data is lost. The wafer can be removed from the microscope for storage and then reloaded when convenient. Because this procedure exposes the wafer to air and can affect the microscope chamber and column conditions, there may be a delay of an hour or so before imaging conditions are ideal. We have been able to return to a wafer after years of bench-top storage for reimaging. However, it is likely that storing a UTSL for many years without degradation will require placing tissue sections in a desiccation or vacuum chamber. Tissue contrast can be altered by the initial imaging process (particularly at focus points), however this change is usually not destructive as long as surface contamination of the wafer is minimal.

IMPLEMENTATION: WaferMapper

The software that oversees the steps outlined above is a MATLAB®-based program called WaferMapper. The MATLAB® script allows researchers with limited programing background to readily customize the code according to their particular needs. The WaferMapper source code is freely accessible through a Google code SVN server (https://wafermapper.googlecode.com, See user guide for Matlab toolbox dependencies.) and we encourage any interested parties to participate in the further development of WaferMapper. A detailed, step-by-step user's manual is also available at this site.

In addition to the MATLAB® code, we provide two C wrappers for interacting with the Zeiss SmartSEM API (to control the microscope) and the Fibics scan generator API (for acquiring high pixel density images). Although WaferMapper was written to drive the Zeiss/Fibics SEM system, it can be adapted to other imaging systems with the addition of appropriate command wrappers. For those who wish to build their own imaging software, the following description of our implementation should still be helpful as a practical guide to managing and imaging a UTSL.

OVERVIEW

Figure 2B is a block diagram showing how WaferMapper interfaces with SEM hardware. WaferMapper can be run as a standalone application for steps which do not require SEM control. A UTSL directory structure, stored on a network file system, organizes all metadata and images related to a particular library. **Figure 2C** shows the WaferMapper graphical user interface (GUI). The GUI is organized around a wafer-level overview display and a section overview display. The red crosses designate the position of mapped sections. When WaferMapper is connected to the SEM and the currently loaded wafer is displayed, the user can quickly move the SEM stage position to any point on the wafer by clicking on the wafer image or to any point in a section by clicking on and zooming in on the section overview display. When WaferMapper is run on a computer not connected to the SEM, the user can browse through all wafer images and through the entire stack of aligned section overviews to graphically define a target region for high resolution montage imaging.

Figure 3 is a flowchart showing all key steps in the creation and imaging of a UTSL using the WaferMapper software. Conceptually, the process is broken into three key phases. The first is an "SEM Wafer Mapping Phase" in which the software is used to map out the locations of all sections across all wafers in the library, and in which low resolution overview images of all sections are acquired by automation of SEM stage movements and imaging. The second is a "Target and Montage Definition Phase" in which WaferMapper (usually being run on a non-acquisition computer) is used to align all section overviews and is used to graphically define a subregion for high resolution montage imaging. The final phase is the "High Resolution Montage Imaging Phase" in which WaferMapper automates the SEM operations necessary to acquire

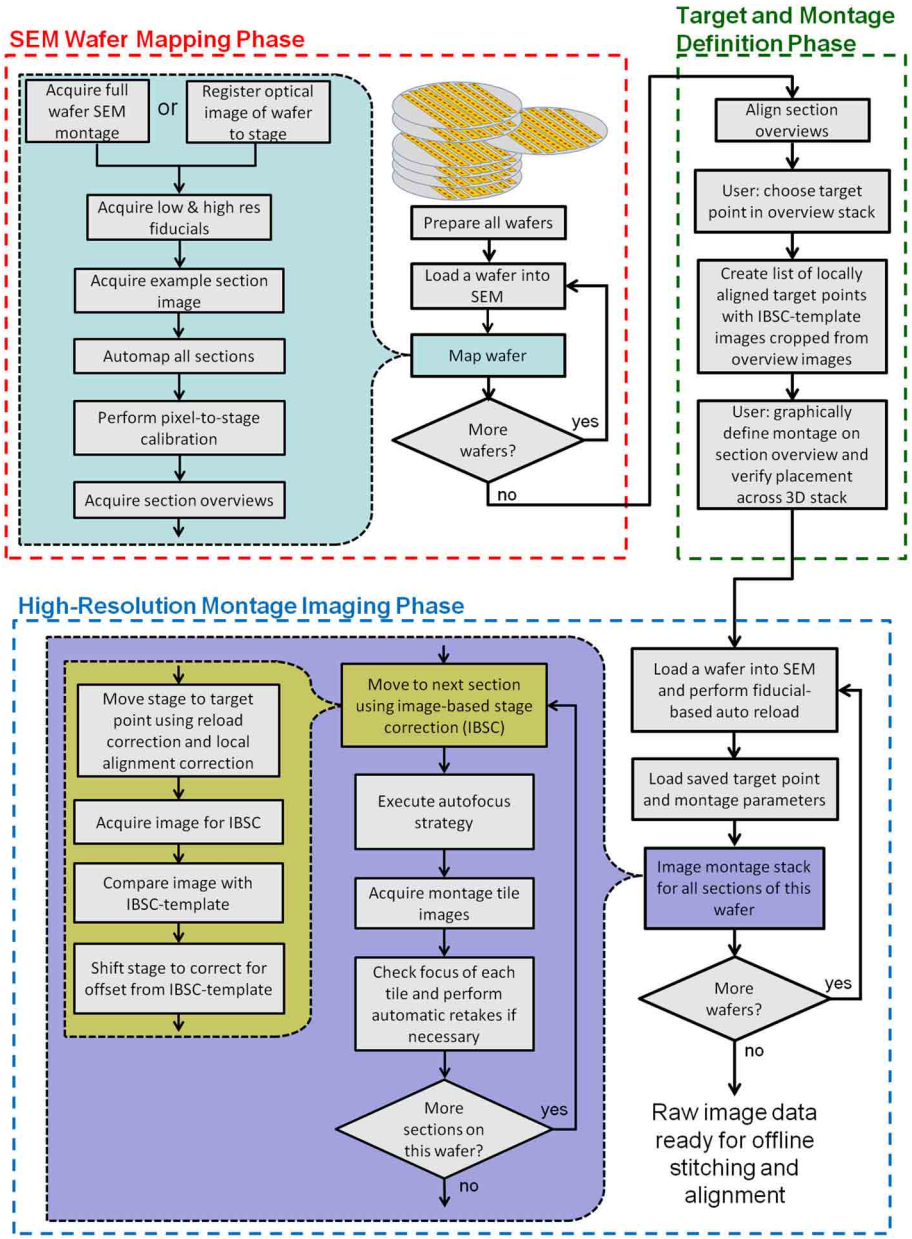

FIGURE 3 | Flow chart showing all key steps in the creation and imaging of a UTSL using WaferMapper. The process is broken into three phases: an "SEM Wafer Mapping Phase," a "Target and Montage Definition Phase," and a "High-Resolution Montage Imaging Phase." IBSC, Imaged Based Stage Correction (see section: Starting high resolution image acquisition).

the defined high resolution volume data. Each of these phases is described in detail below.

SEM WAFER MAPPING PHASE

The goal of the "SEM Wafer Mapping Phase" is to produce a set of images and metadata covering all wafers and all sections in a UTSL. This collection of images and metadata (e.g., stage coordinates of all section overview images and fiducial images, pixel-to-stage calibration scaling factor, pixel size, dwell time, etc.) allows reloading of wafers and automatic movements of the stage to preselected target points within each section. Because a UTSL may consist of tens or hundreds of wafers and many thousands of sections, we have tried to automate the majority of the steps in this process.

Acquiring a full wafer image

An image of the entire surface of the wafer is acquired before mapping of sections begins. This image can be generated optically or using an electron microscope. The benefit of generating the image in the electron microscope is that contrast will be based on electron scattering, i.e., metalized tissue will stand out from the background. However, full wafer imaging is time-consuming

(∼20 min on the Merlin and 60 min on the Sigma) given that the limited field of view of an electron microscope necessitates acquiring many individual montage tiles. We have often found, however, that even images of the wafer rapidly taken with an optical camera while the wafer is being lit indirectly via a diffuse white background are of sufficient quality to serve as a full wafer image so long as all of the ultrathin sections and fiducials are visible in the image (**Figure 4A**). The regularity and resolution of the full wafer image will determine how accurately the next stage of mapping, overview image acquisition, can be targeted. We typically acquire overview images with a field of view approximately a millimeter larger than the tissue section which corresponds to about a half millimeter of fault tolerance in the full wafer image.

If WaferMapper already has access to an optical image of a loaded wafer, the user can navigate to "Map Wafer Operations" > "Acquire Full Wafer Montage" and select the option to load that camera-acquired full wafer image. The full wafer image must then be mapped into the microscope's stage space by selecting three or four fiducial points on the wafer's image and manually driving the stage to the corresponding locations. To create a new wafer image within the SEM, the user can first select "Map Wafer Operations" > "Wafer Parameters" to define the image resolution and dwell time of the full wafer image. The user then navigates to "Map Wafer Operations" > "Acquire Full Wafer Montage," defines the edges of the wafer image and begins montaged acquisition.

Once a full wafer image has been mapped onto stage space or acquired within the SEM, the wafer image can be used for navigation. The user can select "Map Wafer Operations" > "Free View" and then click on any point in the wafer image to drive the stage to the corresponding location.

Acquire images of wafer fiducial marks

At the core of a mapped UTSL is a set of related coordinate systems which allows every point in the aligned stack of section overview images to be mapped back to a particular position of the SEM stage. Since there is typically a significant offset introduced when reloading a wafer into the SEM, we also acquire a set of images of fiducial marks that are permanently placed on the corners of the wafer. The stage positions of these fiducial points are used as a reference frame for all other stage positions. The first step of acquiring overview images is, therefore, to image the fiducial points on the wafer first at low resolution (3 μm per pixel), then at high resolution (0.25 μm per pixel). By selecting "Map Wafer Operations" > "Acquire Low Res. Fiducials," the user can use the full wafer image to navigate to fiducial points on the wafer and acquire images of these points. These images can then be used any time the wafer is reloaded to map section overview space back onto microscope stage space.

Automap all sections

Once the fiducials have been imaged, the next step is to automatically determine the positions of all sections on the wafer. The user selects "Map Wafer Operations" > "Acquire Example Section Image" and either is directed to cut out an example image of a section from the full wafer image (if a full wafer optical image is being used) or is able to acquire a new example image of a section by SEM (if a full wafer SEM montage is being used). This example section image is then used as a template which is scanned across the full wafer image at a range of image rotations to pick out the positions of the other sections with sufficient precision to drive section overview imaging. This process is displayed in **Figure 4** for an example wafer whose whole wafer image was obtained by a full wafer SEM montage (left), and for an example wafer whose whole wafer image was obtained by an optical camera while the wafer was lit indirectly via a diffuse white background (right).

The "Map Wafer Operations" > "Threshold image" command calls up a new GUI (see **Figure 4B**) which is used to set upper and lower gray scale thresholds to convert both the full wafer image and the example section image into binary masks. Next the user selects "Map Wafer Operations" > "Auto Map All Sections" to open up the automap GUI (see **Figure 4C**). Within this GUI, the example section binary mask is used as a convolution kernel and convolved at multiple rotations across the full wafer binary mask. The result is a heat map image whose "brightest" points correspond to high correlations between the wafer image and the example section image. Bright points in the heat map image correspond to locations on the wafer image that resemble the example section. The user selects a threshold for heat map image and the centroids of image patches that pass threshold constitute the section locations (see **Figure 4D**). With mouse clicks and zoom operations, the user can add or remove section positions to correct any mistakes made by the automatic section finding. On most wafers there will be a few additions and subtractions to the section list. Once all of the sections are marked, the sections are automatically assigned number labels according to their position on the collection tape. Typically this automap process will find and correctly label >95% of sections on a wafer. Sections that are not identified automatically, usually because they lay close to a high contrast edge or because two sections are too close together, can be identified manually and added by the user with a few mouse clicks.

Pixel-to-stage calibration

To use overview images of sections to direct stage positioning, the relationship between pixel size and stage travel must be precisely defined. Slight inaccuracies, arising from imperfect calibration of the microscope, can result in noticeable errors in WaferMapper's ability to target the correct region of tissue. To compensate for potential discrepancies between pixel size and stage travel, we perform a pixel-to-stage calibration immediately before the acquisition of the section overview images. This process produces a pixel-to-stage conversion factor which is specific to the particular set of imaging conditions used for the overview images. The pixel to stage conversion factor is determined by selecting "Map Wafer Operations" > "Perform Pixel to Stage Calibration." The user is then prompted to select an image target. The microscope takes an image of the target region using the same settings that will be used to acquire the section overview images, moves the stage a defined distance and then takes a new image. By comparing the displacement in the images, a pixel-to-stage conversion factor is

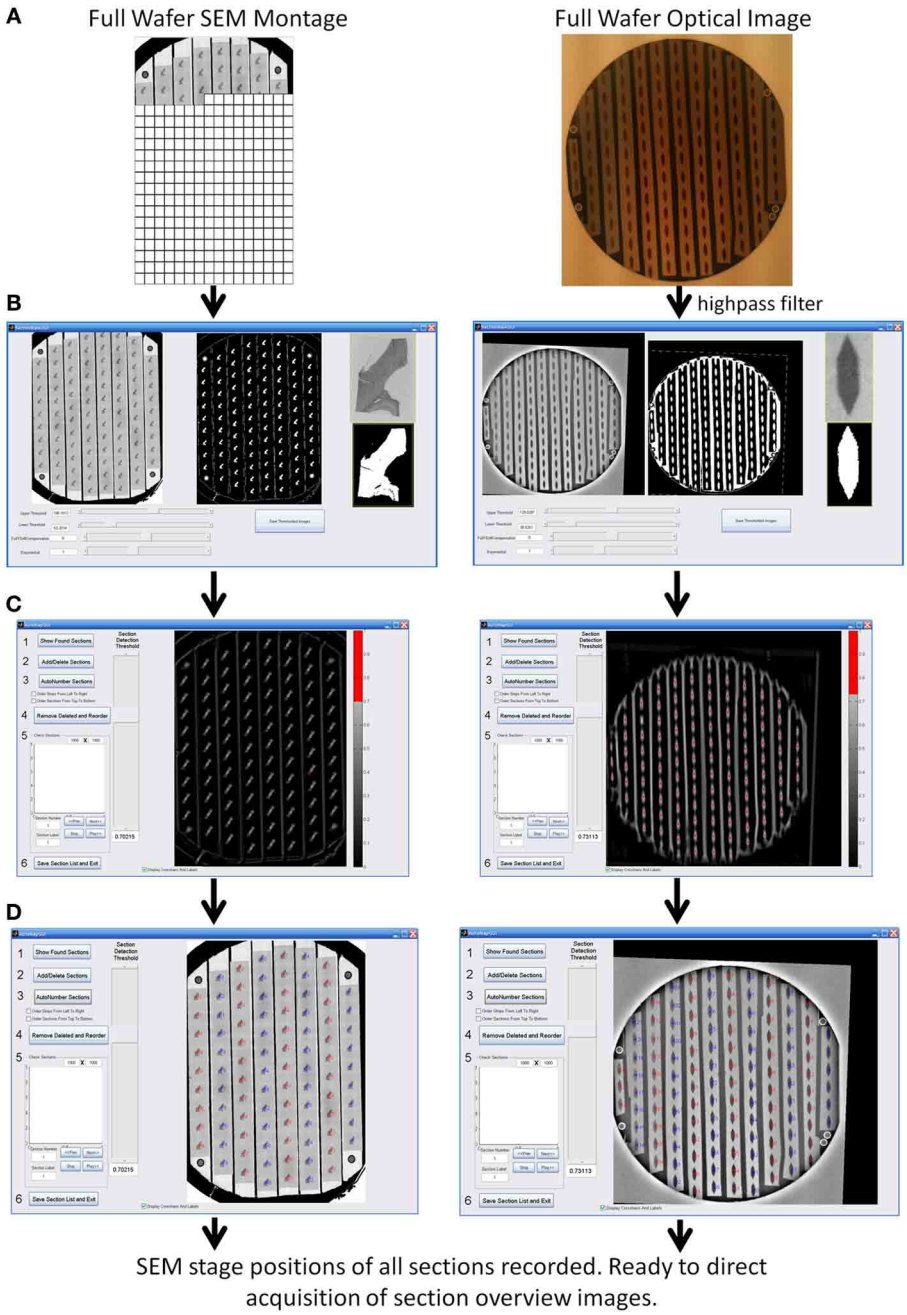

FIGURE 4 | WaferMapper process steps for automatically finding the positions of all sections on a wafer. (A) Acquisition and registration of a full wafer image to the SEM stage using either a full wafer SEM montage (left) or a full wafer unprocessed optical image (right). **(B)** Thresholding of full wafer image and example section image creating binary masks. **(C)** Convolution of the example section mask over the full wafer image creates a heat map whose hottest points correspond to likely section locations. **(D)** After the user selects a suitable threshold for the heat map, the program marks the locations of all centroids as individual sections and numbers the sections in strips according to the order the tape strips were collected on the ATUM machine.

obtained and recorded as part of the metadata associated with this wafer.

Acquire section overviews

With fiducials mapped, sections identified, and the stage calibrated, WaferMapper has all the information it requires to begin acquiring an overview image of every section on the wafer. When the user selects "Map Wafer Operations" > "Acquire Section Overview Images," WaferMapper drives the stage to the first section and begins acquiring images using the user-defined settings for this UTSL. The default setting is to acquire 3 mm-wide images with pixel sizes slightly smaller than 1 μm. These settings can be

changed according to the size of the target sample, the accuracy of the section targeting and the desired precision of the 3D map of the UTSL. Depending on the number of sections and the imaging parameters, the process of acquiring section overviews typically takes 30 min–3 h per wafer depending on the number of sections and the desired overview image quality.

Repeat for all wafers

This mapping procedure is repeated for every wafer in the UTSL. **Figure 5** shows an example of a fully mapped UTSL consisting of 2637 sections of mouse cerebellum tissue spanning 16 wafers. The mapping procedure for this UTSL was based on optical camera images of each wafer. **Figure 6** shows an example of a fully mapped UTSL consisting of 1025 sections of mouse cortex tissue spanning 11 wafers. The mapping procedure for this UTSL was based on full wafer SEM montage images of each wafer.

OFFLINE TARGET AND MONTAGE DEFINITION PHASE

With the mapping data acquired, the section overview images can now be assembled into a 3D map of the tissue volume in which high resolution imaging targets can be selected.

Align section overviews

Each section overview image must be aligned to its neighbors across all wafers in order for the stack of images to be treated as an image volume. Here we describe the cross-correlation based alignment strategy that we have used to acquire all data sets to date. For this method, we find the y translation, x translation and rotation that produces the highest cross-correlation value between two images.

Typically, the section overviews for a particular wafer are aligned on a non-acquisition computer with access to the UTSL directory while other wafers are being imaged. To align images, the user first selects a template image either from the current wafer (if this is the first wafer mapped in the UTSL) or from the previous wafer which has already undergone section overview alignment. By aligning each wafer to a section in the previous wafer, a single aligned stack is created spanning all wafers in the UTSL.

At this stage in alignment, each section on the wafer is aligned to the selected template image. The section-to-section registration produced by this alignment is not as good as an alignment procedure that compares neighboring sections, but the template matching has the advantage of not accumulating drift and being robust to single "problem" sections in the stack. The automated alignment of each wafer usually takes 10–30 min using 3.2 GHz processors on a standard desktop computer.

Any mistakes in the alignment can be corrected using "Section Overview Processing" > "Check and Correct Alignment GUI," which calls up an easy to use GUI in which alignments can be quickly reviewed and corrected by simple mouse drags. It is not necessary, at this point, that the resulting alignment is perfect. The alignment only needs to be good enough that, when an imaging target point is chosen on one section overview, a second stage of target point alignment (described below) can access the appropriate region of each section overview.

By following the above procedure, a small UTSL can be mapped in several hours. A larger dataset, consisting of ∼10,000 sections might take closer to 1 weeks (working 8 h per day). The end product of the mapping process is a set of full wafer images that can be used to navigate around each wafer and a low resolution 3D image volume of the tissue sections that can be used to direct high resolution image capture.

Target point setup

The first step of defining a target point for high resolution imaging is to choose an XY position from within a section overview image. This XY position, the "target point," will be used as the reference point for targeting high resolution imaging and will serve as the center of a second stage of more precise local alignment of the section overviews. The user selects a target point by loading a UTSL and wafer into WaferMapper and selecting "Target Point Setup" > "Choose Target Point in Aligned Section Overview." The user is then prompted to click on a point within the displayed section overview image and can save the target point for later use. Unlike the previous steps in the wafer mapping process, in which it is expected that a single map is generated for a given UTSL, the selection of target points is a branch point where many target points can be defined, one for each high resolution subvolume to be imaged.

Once a target point is selected, a new targeted alignment is executed by selecting "Target Point Setup" > "Generate and Save List of Aligned Target Points." For this alignment, a relatively small window is extracted from each section overview image. Each subregion of the section overview images is aligned to a running average of previously aligned subregions. This process takes about 10 min per wafer. The goal of this second stage of alignment is to produce a better local section to section registration than can be generated from an alignment of the entire section overview images themselves. Once this alignment is completed, any mistakes can be corrected using the "Target Point Setup" > "Check and Correct Target Point Alignment" GUI.

The results of each target point alignment are stored in a new Aligned Target List subdirectory in the UTSL containing all of the aligned subregion images for use in image-based stage correction (IBSC), described below, and a new datafile called "AlignedTargetList.mat." "AlignedTargetList.mat" contains the pixel offsets needed to align each of these cropped subregions. These pixel offsets (when combined with the pixel-to-stage calibration factor determined during the mapping phase) will be used in the high resolution imaging phase to quickly position the SEM stage for imaging each section.

Montage parameters

The position, dimensions and imaging conditions of each high resolution dataset are defined within "Montage Setup" > "Set Montage Parameters." The central position of each image montage is set relative to the aligned target point by defining an X offset, Y offset and North Angle. The dimensions of the montage are set by defining the field of view of each tile ("Tile FOV") and the number of rows and columns of tiles in each montage. Additionally, the overlap between tiles is defined here. For our systems, four micrometers of overlap was sufficient to consistently acquire images without gaps between tiles. WaferMapper provides a graphical overlay of the montage tile positions on top

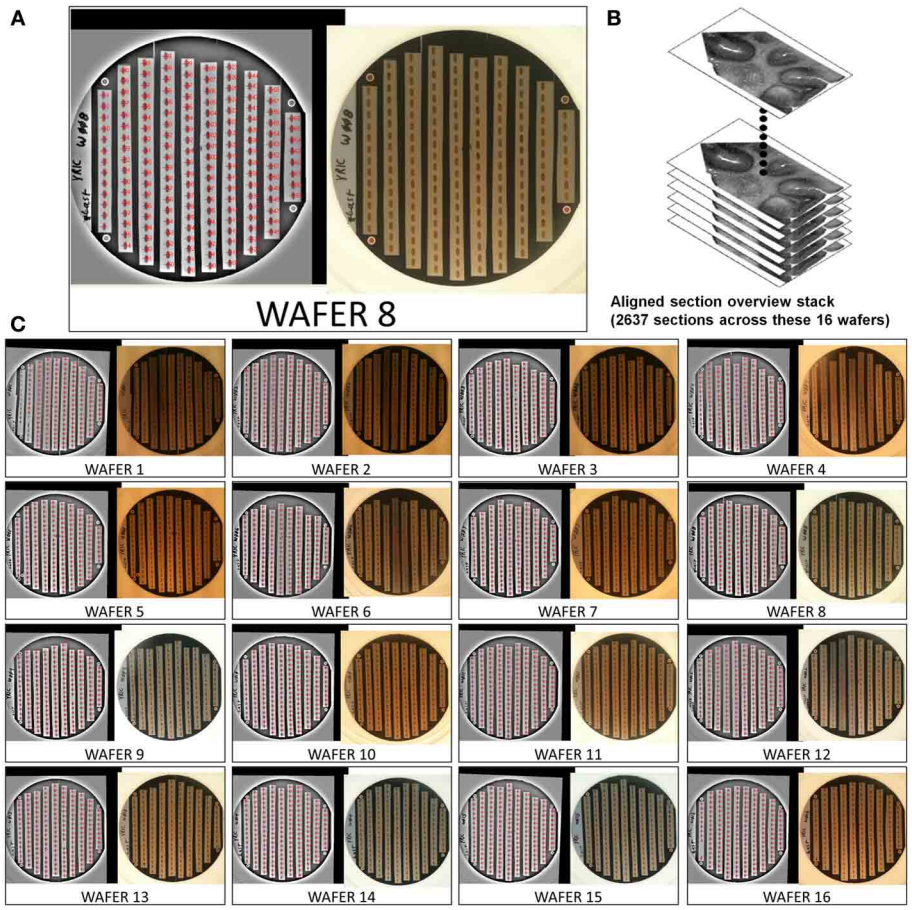

FIGURE 5 | Example of a 2637 section UTSL of mouse cerebellum tissue spanning 16 wafers. An optical image of each wafer was taken and used as the basis of automapping all sections. **(A)** Optical image of wafer 8 (right), filtered optical image with automapped positions of all sections labeled (left). **(B)** Graphical depiction representing the stack of 2637 overview section images acquired during the mapping phase. **(C)** All 16 automapped wafers in this UTSL.

of its section overview display (**Figure 7**), allowing the user to scroll through the entire stack of section overviews and graphically check placement of the montage tiles across all sections prior to the start of a long imaging run.

The pixel size ("Tile FOV"/"Tile width") and pixel dwell time must be set to achieve the necessary balance between image scanning time and image quality. Using high contrast staining and the in-lens secondary electron detector we were able to obtain images with acceptable noise levels using the maximum scan speed of our microscopes (50–100 ns), however these results depend heavily on the tissue preparation and imaging configuration. The Fibics scan generator allows image sizes up to 32×32 k pixels, which means 100 μm-wide images can be acquired at 4 nm per pixel resolution. Being able to scan large field-of-view images at high resolution reduces the impact of tile to tile overhead on image acquisition time and generally increases the efficiency of managing large datasets.

WaferMapper includes the option to take an overview image of the targeted imaging region before the high resolution imaging begins. Being able to take advantage of this option requires that the microscope setup that is used to acquire high resolution images is also amenable to large field of view imaging.

HIGH RESOLUTION MONTAGE IMAGING PHASE

Reload

Once the section overviews have been acquired, the wafer can be removed from the microscope and stored. When the wafer is placed in a new SEM or returned to the same one, the position of the wafer on the stage will not be exactly the same as when the wafer was mapped. To bring the wafer map into register with the new position on the stage, the user can follow the steps listed under the "Reload Wafer Operations" menu. The first step is to manually set the coarse offset of the stage. The microscope drives to the first fiducial point on the wafer and the user manually rotates and translates the stage to correct for any gross change in position. "Free view with Offset" can then be used to confirm that the new wafer position is roughly correct. Once the stage rotation and translation have been adjusted within approximately a millimeter of the mapped position, the user can then run "Do all steps for Stage Correction." The microscope will then automatically drive to the fiducial positions, take new images and compare

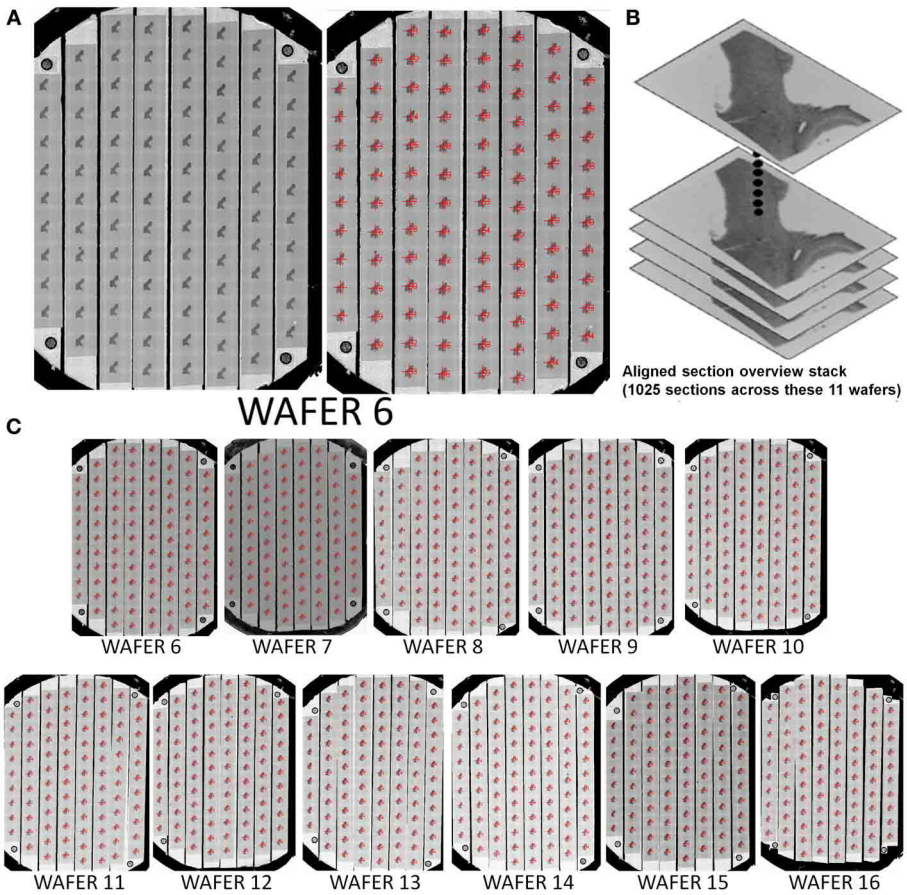

FIGURE 6 | Example of a 1025 section UTSL of mouse cortex tissue spanning 11 wafers. A full wafer SEM montage image of each wafer was taken and used as the basis of automapping all sections. **(A)** Full wafer SEM montage of wafer 6 (right), same image with automapped positions of all sections labeled (left). **(B)** Graphical depiction representing the stack of 1025 overview section images acquired during the mapping phase. **(C)** All 11 automapped wafers in this UTSL.

these images with the original images of the fiducials. This comparison is used to find a coordinate transformation that will be used to translate between stage space and wafer map space for the remainder of the imaging session. This ability to automatically register a reloaded wafer is also crucial when it is necessary to retake images, when imaging a new region, and when sharing a UTSL between different laboratories. Once reloaded, a wafer's metadata, in principle, contains all the information necessary for another lab with the same SEM setup to replicate an imaging run.

Quality check

The ability to acquire a high quality large-scale SEM dataset depends heavily on imaging with the correct focus and stigmation settings. The depth of field of the SEM is typically around ∼0.5–10 μm, depending on the imaging modality, so that multiple focus points might be required to image a large montage. Depending on the sample, imaging conditions and stability of the microscope, periodic refocusing and restigmating might be required regardless of the sample flatness. To acquire images for days without human intervention, WaferMapper uses a variety of strategies to minimize blurry images.

WaferMapper includes an algorithm that evaluates the quality of SEM images. We designed this algorithm to be able to quickly judge the quality of very large images and then to base its evaluation not on the average quality of the image, but on the quality of the best regions of the image. By only paying attention to areas with the most high frequency contrast, quality values are less sensitive to changes in tissue statistics that might come from blood vessels or section edges. For the quality check to read and analyze images without adding to the tile-to-tile overhead time, the quality check samples only a small fraction of the available pixels. Quality check reads in a grid, usually 200 × 200, of 3 × 3 pixel image kernels from a newly acquired image (**Figure 8A**). These samples are then fit into a 200 × 200 by 9 image volume.

To find a quality value for each grid point, we find the relative contrast of different patterns within the 3 × 3 pixel kernel. One set of patterns finds the difference in the average intensities of adjacent lines of pixels (two horizontal comparisons and two vertical comparisons). The other set of patterns compares the difference in the average intensities between groups of interleaved pixels (**Figure 8B**). A well-focused SEM image of cell membranes will tend to produce relatively more contrast in the adjacent lines

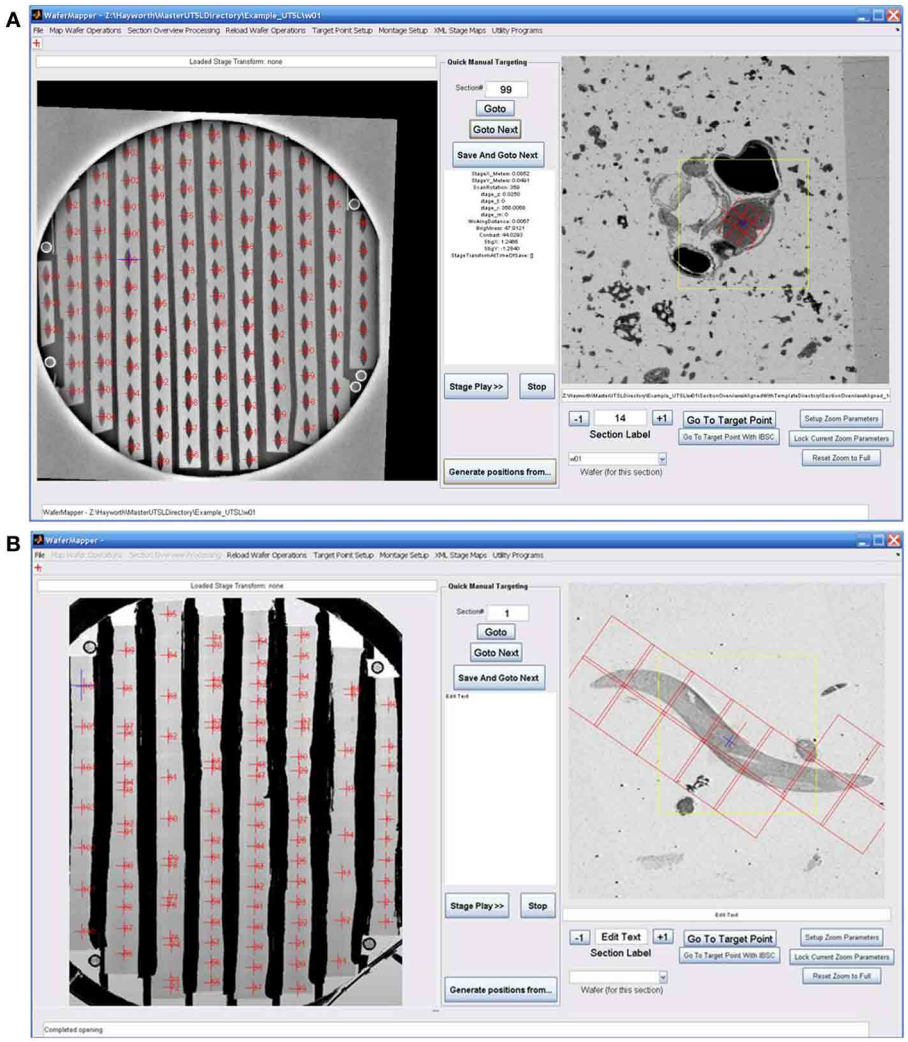

FIGURE 7 | Examples of graphically defining an imaging target and montage. (A) Image shows the WaferMapper GUI being used to graphically define a 3 × 3-tile montage (red boxes) covering just the brain region in a larval zebrafish UTSL. **(B)** Image shows WaferMapper used to graphically define a 3 × 7-tile montage (red boxes) covering a single worm in a *C. elegans* UTSL. Note the ability to selectively designate a subset of montage tiles for imaging. Of crucial importance is the software's ability allowing the user to scroll through the entire stack of section overviews to graphically check placement of the imaging montage across all sections prior to the start of any long imaging run. The yellow box in the section overview display denotes the field-of-view used for local target point alignment (see section: Target point setup). The small blue cross denotes the autofocus position to be used, which in this case is deliberately offset from the center of the montage.

pixel patterns than in the interleaved pixel patterns. Once a quality value is obtained for each grid point, a quality value for the entire image is obtained by averaging a small percentage of the best grid points. In this way, changes in tissue statistics have a relatively small effect on the quality rating. This method can also be used to identify poor quality regions of the tissue or of the imaging field.

Within WaferMapper's "Montage Parameters" setup menu, the user can choose to have the quality check performed at several points in the image acquisition process. First, a quality check can be performed after each autofocus to determine if the correct working distance has been obtained. After each autofocus, WaferMapper can take a quick image and perform a quality check. If the quality value exceeds the user-defined threshold, high resolution imaging begins. Otherwise, the image is refocused. Second, the user can choose to have a quality check performed after each tile is acquired. If the image quality fails to pass a user defined threshold, the image is refocused and retaken. Finally, the quality values of each tile are displayed on the down-sampled stage-stitched image of the montage (**Figure 8C**). Stage stitched images, with the quality values displayed on top, provide an easy way for the user to monitor the imaging process and to review the performance of the microscope.

Focusing strategies

The best possible image quality will usually be achieved by autofocusing, then autostigmating and then autofocusing again (focus-stig-focus) before each tile is acquired. However, this

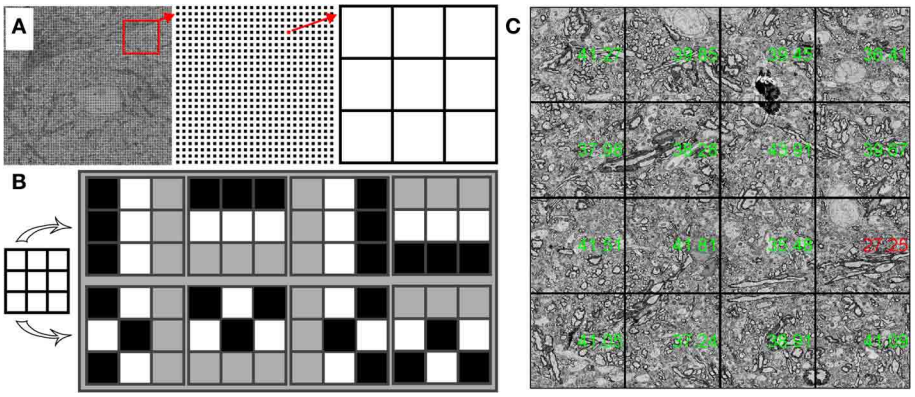

FIGURE 8 | Structure of quality check procedure. (A) A 200 × 200 array of 3 × 3 pixel kernels is extracted from an SEM image. **(B)** Structured (top) and unstructured (bottom) contrast patterns are compared to obtain a quality value for each 3 × 3 pixel kernel. **(C)** Stage stitched montage of images displayed with quality values in green (passing) and red (below threshold).

procedure can take significantly longer than the acquisition of a single tile. Therefore, a variety of strategies are offered in WaferMapper for increasing the efficiency of high throughput data collection. In many cases a single autofocus before each montage will be sufficient to produce acceptable image quality. For large montages a three-by-three grid of focus points can be acquired and then fit to a plane that predicts the optimal focus point for each tile of the large montage. Alternatively, tiles can be pooled and a central focus point acquired before a two-by-two box of tiles is acquired.

In a typical example we might choose to focus-stig-focus once per section as long as image quality stays above threshold. When the microscope starts a new section it will first drive to a predefined central focus point within the montage. The microscope then takes a quick image approximately the size of an image tile and drives to the region within the image with the highest contrast. In this way, WaferMapper avoids autofocusing on regions, such as the interior of blood vessels, which provide no useful information to the focus algorithm. The microscope then performs a focus-stig-focus and begins imaging the first section. The order in which the tiles are imaged is determined by the proximity of the focus point so that, if refocusing is required, best advantage is taken of each focus point. Once an image is acquired, the quality is evaluated. If the tile passes, the microscope moves onto the next tile. If the tile fails, the microscope refocuses and takes the image again. At any point in the imaging process a user can review either the images or the quality values being produced by the microscope and assign sections to be retaken. This strategy of only focusing once if the quality values stay above threshold works well when image acquisition time is small relative to the time it takes to autofocus and when the majority of tiles can be imaged using a single focus point.

Starting high resolution image acquisition

With the aligned target points loaded and the montage parameters set, WaferMapper is ready to acquire images. The user selects "Montage Setup" > "Acquire Montage Stack Main" and is prompted to select a target directory. This target directory can be anywhere; however, image writing and quality check work best if the data is saved on a local solid state drive. This data can then be managed and transferred through a network connection to a large data server. In addition to writing the images in this directory, a log file is written that records all stage movements, image qualities and image conditions.

When starting image acquisition, the user will also be asked whether or not WaferMapper should use IBSC. The accuracy of targeting we were able to achieve using wafer fiducials only was usually limited to about ±15 μm. We found that we could significantly improve this accuracy using IBSC. When this option is selected, WaferMaper acquires a quick image every time it drives to a new section. This image is processed using a difference of Gaussians filter to enhance features on the scale of cell bodies. This section's aligned subregion target image (cutout of the section overview image after local alignment during the Target Point Setup step, see section: Target point setup) is likewise filtered and compared with the newly acquired image using cross correlation. If the stage movement was completely accurate, then the two images should match exactly. If they do not, then WaferMapper uses the offset obtained from the cross-correlation to adjust the stage position and then checks its work with a second image. The accuracy with which this second image matches the section overview target is also recorded within the log file.

EXAMPLE DATA

Data sets have been acquired using WaferMapper that range in size from 1 to 100 terabytes. **Figures 9**, **10** show some example images from WaferMapper runs of a mouse cerebellum UTSL and a mouse cortex UTSL. These figures illustrate the range of scales which must be spanned by the mapping software in order to precisely target automated imaging of a small montage volume within the much larger volume of the full UTSL. Below we describe the mapping, imaging and data set acquired from one test of WaferMapper on the mouse cerebellum UTSL shown in **Figure 5**. **Table 1** provides actual average data acquisition times and rates for the various steps in the mapping and imaging process. These times were recorded during a separate, multi-month imaging project using the WaferMapper software.

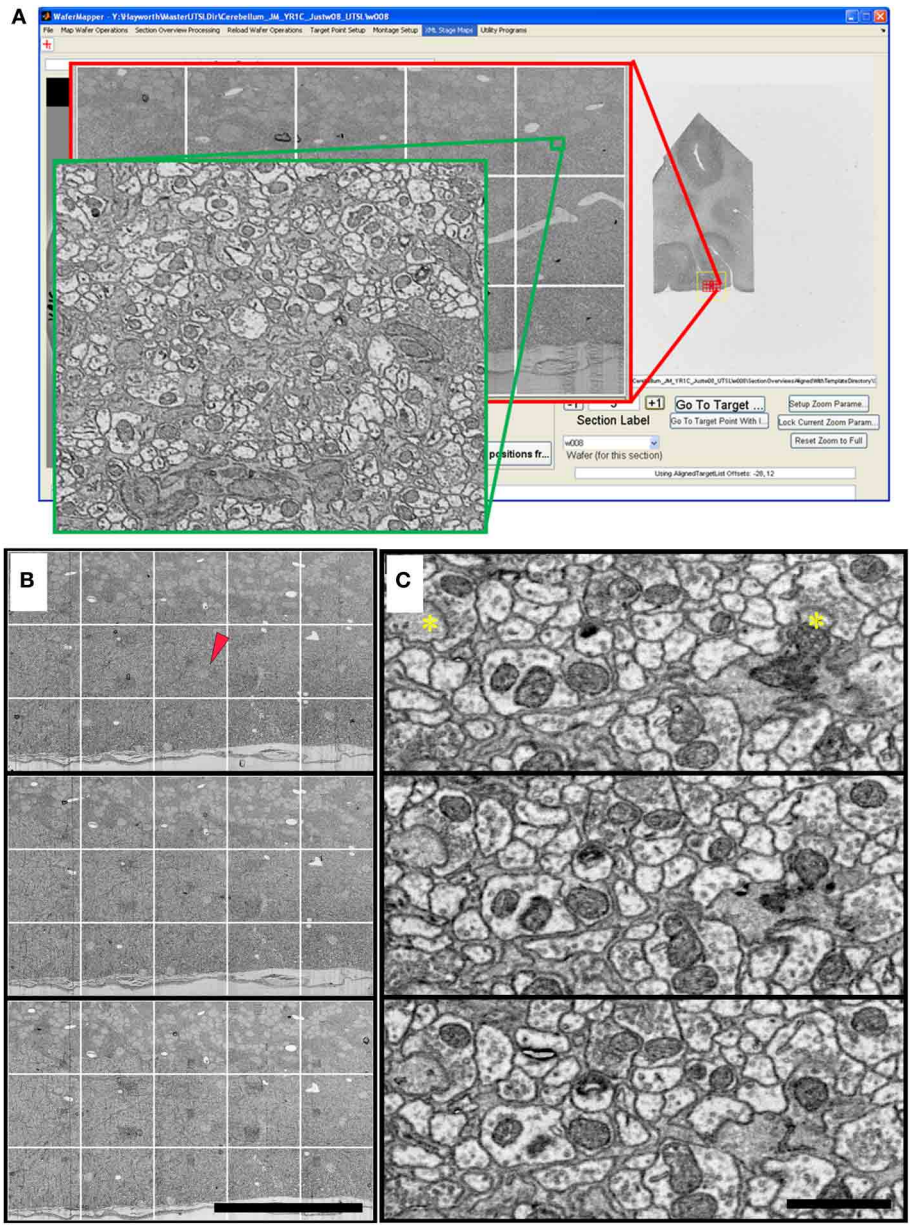

FIGURE 9 | Cerebellum UTSL example data. (A) Image of WaferMapper GUI showing a graphically-defined 3 × 5-tile montage targeted near the surface of a cerebellar folium. Zoom overlays show high resolution images of that region. **(B)** Montage images of three successive ultrathin sections in this cerebellum UTSL acquired automatically by WaferMapper (scale bar = 100 μm). Red arrow shows location of corresponding high resolution images shown in **(C)**. **(C)** Cut outs of high resolution data imaged at 10 MPS and aligned in FIJI (scale bar = 1 μm). Asterisks mark position of two synapses.

CEREBELLUM

The cerebellum of an adult mouse was cut into several 300 μm-thick vibratome sections and stained with osmium tetroxide and uranyl acetate. The tissue was embedded in Embed 812 (Electron Microscopy Sciences). A block containing one of these vibratome sections was trimmed to include a 1 × 3 mm wide region of cerebellum. The blockface was trimmed so that the leading and trailing edges of each section come to a point. This shape helps minimize cutting disruptions caused by the contact of the block face with the diamond knife and the removal of the section from the edge of the diamond knife. Eight thousand ultrathin sections were cut at a thickness of 30 nm and collected on carbon coated Kapton tape. A subset of this ATUM run's tape containing 2637 sections was cut into strips and mounted on 16 wafers as shown in **Figure 5**.

Mapping

The WaferMapper software was used to map these 16 wafers and acquire overview images of each section to generate a low resolution 3D map of the tissue. Viewing the aligned overview stack in

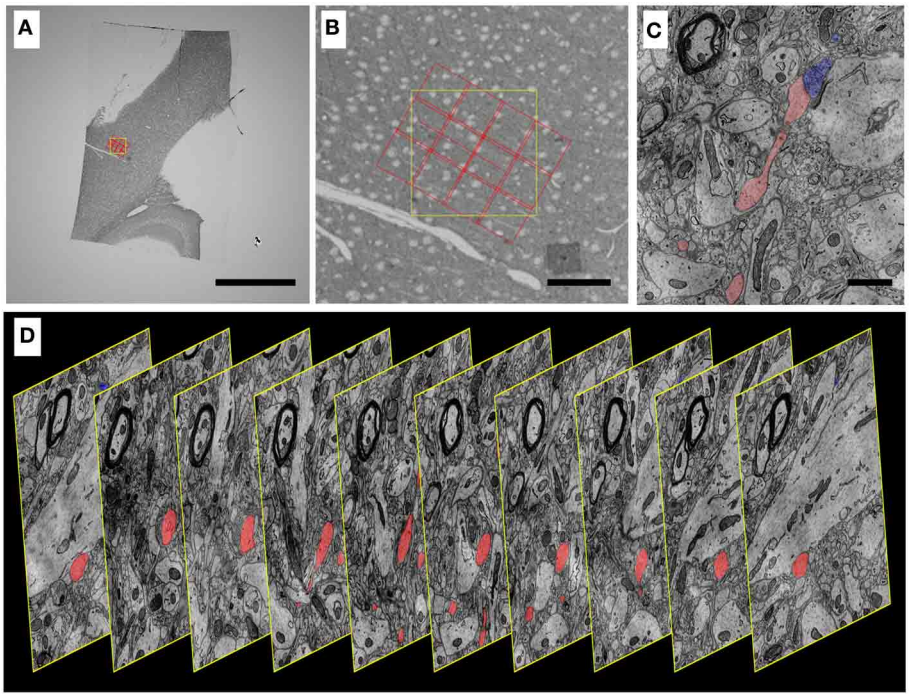

FIGURE 10 | Progressively higher resolution images through a mouse cortex UTSL mapped and imaged by the WaferMapper software. (A) Single section of the 1025 section mouse cortex UTSL whose wafers are displayed in full in **Figure 6**. This image is from a screen capture of the WaferMapper program showing the location of a 3 × 4-tile montage overlaying a target region. (scale bar = 1 mm). **(B)** Zooming in on the section overview display in WaferMapper allows the graphical display of the montage to be finely positioned relative to blood vessel and cell body landmarks visible at the resolution of the section overview images. (scale bar = 100 μm). **(C)** Zooming in again, this time to a small region of one image from a larger stack of images automatically acquired by WaferMapper of this same UTSL. The outlines of two neuronal processes sharing a synapse are shown highlighted in color. (scale bar = 1 μ). **(D)** Graphic displaying every 10th image from this same aligned dataset acquired by WaferMapper. ATUM sections were cut at 30 nm thickness, thus these images are displayed here at 300 nm intervals through the tissue.

WaferMapper, an imaging target point was selected from a region of the molecular layer of the cerebellum where the arbors of the Purkinje cells were parallel to the plane of microtome sectioning. By selecting "Target Point Setup" > "Generate and Save List of Aligned Target Points," the software was used to generate a second, local alignment, suitable for directing the high resolution imaging.

Imaging

Using WaferMapper's GUI display of the aligned overview stack, we graphically defined a high resolution imaging montage that encompassed the arbors of several Purkinje cells (**Figure 9A**). The montage consisted of three rows and five columns of tiles. Each title consisted of 12, 800 × 12, 800 pixels resulting in a total 4 nm resolution montage that covered about 250 × 150 μm of cerebellum. High resolution images were collected from 498 sections spanning three wafers and ∼15 μm of cerebellum (**Figures 9B,C**). The acquisition of the high resolution data required ∼100 h of microscope time on a Zeiss Sigma. Approximately one third of this acquisition time was consumed by scanning voxels at 10 MPS. The remaining acquisition time was spent primarily on autofocusing. We found that this imaging time could be significantly reduced on a Zeiss Merlin due to its faster scan speed and larger depth-of-field.

FUTURE DIRECTIONS

SOFTWARE DEVELOPMENT

We wrote WaferMapper in MATLAB® so that researchers who are not primarily programmers could readily add to the code according to the needs of their experiments. To date, each large dataset acquired with WaferMapper has involved modifications of the code. While the core version of WaferMapper we have released should be able to acquire most types of data, we see collaborative development of the code as critical to WaferMapper's usefulness as new technologies and new uses for ultrathin section libraries evolve.

WaferMapper meets our initial simple goal of producing a data acquisition pipeline in which more time is spent acquiring image montages than is spent finding the right place to image. However, even during the production of this software, there have been significant improvements in SEM scan speed and more improvements are on the way. The future development of WaferMapper will hopefully produce streamlined versions of the code as well as a version with fewer Matlab toolbox dependencies. At the time of the submission of this publication, the most pressing areas for further code development are finding faster and more reliable methods of both focusing the microscope, judging image quality, and aligning section overviews and target points (**Table 1**). A branch of the code being developed, primarily by

Table 1 | Breakdown of the time required for each step of data acquisition using ATUM-SEM and WaferMapper.

Sample preparation	**Time (varies with tissue size and staining method)**
Tissue processing	1–2 weeks
Sectioning	8–30 s/section
Constructing wafers	∼30 min/wafer (100–500 sections per wafer)
Wafer mapping	**Time per wafer**
Full wafer image (optical)	3 min/wafer
Wafer loading into chamber	5 or ∼45 min/wafer (with or without load lock)
Full wafer image (EM alternative to optical)	20, 60 min/wafer (Merlin, Sigma)
Section mapping	∼10 min/wafer
Section overview image acquisition	30–120 min/wafer (depending on desired image quality)
Offline wafer mapping*	**Time per wafer (using 2 Intel Xeon x5672 3.2 GHz 4 core processors)**
Section overview alignment (automatic)*	10–30 min/wafer
Manual correction of overview alignment	0–20 min/wafer
Target point alignment*	10–30 min/wafer
Manual correction of target point alignment	0–20 min/wafer
High resolution imaging	**Time per wafer**
Wafer load into microscope	5 or ∼45 min/wafer (with or without load lock)
WaferMapper reload procedure	∼10 min/wafer
Montage setup	∼5 min/wafer
Montage time	
Movement to section	∼10 s
Image based stage correction	∼1 min
Focus-stigmation-focus*	∼2 min
Pixel dwell time	50–3000 ns (depending on tissue signal and detector)
Time between tiles (with quality check)	8 s
Estimated project breakdown	**High speed imaging of 10,000 sections using 100,000 × 100,000 pixel montages**
Raw pixel scan time (minimum)	57 days
Montage acquisition time (with overhead)	104 days
Total data acquisition time (start to finish)	130 days

Asterisks indicate steps that could significantly benefit from further software development.

Forrest Coleman, aligns SURF points over a large number of sections as an alternative to cross correlation to improve the targeting of high resolution imaging within UTSLs. We find that this solution is often more robust than the current implementation of cross correlation. This branch of the code and others will be made available through the Google Code SVN server. We encourage other users of the WaferMapper software to test code and to add to the repository as new solutions are developed.

STITCHING AND ALIGNMENT

Small EM volumes (<1 terabyte) can be aligned on a powerful desktop computer using publicly available alignment software such as the registration plugins for Fiji (Schindelin et al., 2012). However, the stitching and alignment of high resolution images becomes increasingly difficult as data sets become larger. The computational power required to manipulate and process terabytes of images requires hardware that is not standard in most labs and, while most steps in alignment are amenable to parallelization, running these steps in parallel often requires changes in code and expertise in managing clusters. Because of these problems, aligning multi-terabyte datasets is currently being done by only a few groups. However, the recent production of many multi-terabyte EM volumes has spurred efforts to scale up alignment tools to make it easier for the broader research community to turn hundreds of terabytes of EM images into usable 3D tissue maps.

THE PROMISE OF ULTRATHIN SECTION LIBRARIES FOR COLLABORATIVE CONNECTOMICS

A major goal of the integration of automated tape collection and automated imaging of sections is to make volume EM easy enough to be a standard technique that many labs can use to study biological samples that are tens or hundreds of micrometers wide. However, we also wish to stress the potential of UTSLs to allow a new type of collaborative neuroscience. As discussed above, the ATUM in a few days of cutting can potentially produce so many ultrathin sections that it might take decades to image them in total at high resolution. A typical research publication using ATUM-SEM and WaferMapper might end up acquiring high resolution images from only 1% of the total volume of a collected UTSL. For example, in the visual thalamocortical slice case outlined in the introduction one researcher may end up imaging and sparsely tracing only a finely targeted $300 \times 300 \times 300\,\mu m$ volume in cortical layer IV -mapping out the local connectivity of thalamic afferents and interneurons in that area. Once this research is published, other labs may wish to build upon this connectomics data by performing additional imaging and tracing in neighboring regions of the same brain, literally starting their tracing work from the very same neurons in this already published study. In this way, a collaboration of multiple research labs could muster the time and resources necessary to elaborate the connectomes of larger inter-regional circuits than any one lab could by working alone.

In this paradigm, some research labs might specialize in producing UTSLs with the highest quality ultrastructure preservation and staining, encompassing brain regions that are of interest to many labs (for example, a visual thalamocortical slice UTSL, a barrel cortex UTSL, a hippocampal slice UTSL, etc.). Some of these UTSLs may even be designed to include prior functional

imaging to augment expected connectomics studies. This design of UTSLs tailored for wider research interest would be similar to the way some labs today specialize in the creation of transgenic animals designed specifically for wider research use. Other labs would then specialize in curating and EM imaging these UTSLs, providing (perhaps for a fee) the highest quality 3D volume data on request of research groups. This strategy would be similar to the way some groups in the astronomical community specialize in the design and construction of the highest quality telescopes whose specifications far outstrip the funds and resources of any single astronomical research group. We would like to argue that, for truly large-scale cellular connectomics, the neuroscience community has reached a similar need for pooling of resources, and a similar need to create dedicated "Connectome Observatories" whose high-quality, large volume EM imaging abilities are designed to be shared by the entire neuroscience community.

CONCLUSION

There are many challenges to imaging ultrathin sections that are absent from technologies that image intact tissue (such as confocal imaging, SBEM, or FIB-SEM). However, these challenges can be overcome and even turned into advantages if software is available to map a tissue library prior to high resolution imaging. With WaferMapper, we were able to target the acquisition of large volumes of high resolution images from tissue libraries consisting of many thousands of ultrathin sections. We are hopeful that this software will continue to develop within an open source community as it is adapted to new experiments and imaging systems. More generally, we believe a multi-scale mapping and imaging approach is key to taking advantage of the large number of ultrathin sections that can now be generated using ATUM.

ACKNOWLEDGMENTS

We would like to thank Juan Carlos Tapia and Dan Bumbarger for providing some of the tissue used in the example images. This work was supported by NIH/NINDS (High Resolution Connectomics of Mammalian Neural Circuits, TR01 1R01NS076467-01) and NIH (Imprinting a connectome: developmental circuit approach to mental illness, Conte 1P50MH094271-01, NIH 5T32MH20017, NIH 5T32HL007901). The content is solely the responsibility of the authors and does not necessarily represent the official views of the National Institutes of Health.

REFERENCES

Bogner, A., Jouneau, P. H., Thollet, G., Basset, D., and Gauthier, C. (2007). A history of scanning electron microscopy developments: towards "wet-STEM" imaging. *Micron* 38, 390–401. doi: 10.1016/j.micron.2006.06.008

Denk, W., and Horstmann, H. (2004). Serial block-face scanning electron microscopy to reconstruct three-dimensional tissue nanostructure. *PLoS Biol.* 2:e329. doi: 10.1371/journal.pbio.0020329

Gay, H., and Anderson, T. F. (1954). Serial sections for electron microscopy. *Science* 120, 1071–1073. doi: 10.1126/science.120.3130.1071

Harris, K., Perry, E., Bourne, J., Feinberg, M., Ostroff, L., and Hurlburt, J. (2006). Uniform serial sectioning for transmission electron microscopy. *J. Neurosci.* 26, 12101–12103. doi: 10.1523/JNEUROSCI.3994-06.2006

Hayat, M. A. (2000). *Principles and Techniques of Electron Microscopy: Biological Applications*. Cambridge; New York: Cambridge University Press.

Joy, D. C. (1991). The theory and practice of high-resolution scanning electron microscopy. *Ultramicroscopy* 37, 216–233. doi: 10.1016/0304-3991(91)90020-7

Knott, G., Marchman, H., Wall, D., and Lich, B. (2008). Serial section scanning electron microscopy of adult brain tissue using focused ion beam milling. *J. Neurosci.* 28, 2959–2964. doi: 10.1523/JNEUROSCI.3189-07.2008

MacLean, J. N., Fenstermaker, V., Watson, B. O., and Yuste, R. (2006). A visual thalamocortical slice. *Nat. Methods* 3, 129–134. doi: 10.1038/nmeth849

Morgan, J. L., and Lichtman, J. W. (2013). Why not connectomics? *Nat. Methods* 10, 494–500. doi: 10.1038/nmeth.2480

Schalek, R., Kasthuri, N., Hayworth, K., Berger, D., Tapia, J., Morgan, J., et al. (2011). Development of high-throughput, high-resolution 3D reconstruction of large-volume biological tissue using automated tape collection ultramicrotomy and scanning electron microscopy. *Microsc. Microanal.* 17, 966–967. doi: 10.1017/S1431927611005708

Schindelin, J., Arganda-Carreras, I., Frise, E., Kaynig, V., Longair, M., Pietzsch, T., et al. and Cardona A. (2012). Fiji: an open-source platform for biological-image analysis. *Nat. Methods* 9, 676–682. doi: 10.1038/nmeth.2019

Tapia, J. C., Kasthuri, N., Hayworth, K. J., Schalek, R., Lichtman, J. W., Smith, S. J., and Buchanan, J. (2012). High-contrast en bloc staining of neuronal tissue for field emission scanning electron microscopy. *Nat. Protoc.* 7, 193–206. doi: 10.1038/nprot.2011.439

Conflict of Interest Statement: Harvard University has applied for patents covering some aspects of the ATUM-SEM process. The authors declare that the research was conducted in the absence of any commercial or financial relationships that could be construed as a potential conflict of interest.

Received: 10 April 2014; accepted: 05 June 2014; published online: 27 June 2014.
Citation: Hayworth KJ, Morgan JL, Schalek R, Berger DR, Hildebrand DGC and Lichtman JW (2014) Imaging ATUM ultrathin section libraries with WaferMapper: a multi-scale approach to EM reconstruction of neural circuits. Front. Neural Circuits ***8****:68. doi: 10.3389/fncir.2014.00068*
This article was submitted to the journal Frontiers in Neural Circuits.

frontiers in
NEURAL CIRCUITS

METHODS ARTICLE
published: 24 December 2013
doi: 10.3389/fncir.2013.00201

Inference of neuronal network spike dynamics and topology from calcium imaging data

Henry Lütcke[1†], Felipe Gerhard[2†], Friedemann Zenke[2], Wulfram Gerstner[2] and Fritjof Helmchen[1,3]*

[1] Laboratory of Neural Circuit Dynamics, Brain Research Institute, University of Zurich, Zurich, Switzerland
[2] School of Computer and Communication Sciences and School of Life Sciences, Brain-Mind Institute, Ecole Polytechnique Fédérale de Lausanne, Lausanne, Switzerland
[3] Neuroscience Center Zurich, University of Zurich and ETH Zurich, Zurich, Switzerland

Edited by:
Peter Saggau, Baylor College of Medicine, USA

Reviewed by:
Kresimir Josic, University of Houston, USA
Eftychios A. Pnevmatikakis, Columbia University, USA
Keith A. Cordiner, Baylor College of Medicine, USA
Keith Kelleher, Salk Institute for Biological Studies, USA

***Correspondence:**
Fritjof Helmchen, Brain Research Institute, University of Zurich, Winterthurerstrasse 190, CH-8057 Zurich, Switzerland
e-mail: helmchen@hifo.uzh.ch

† These authors have contributed equally to this work.

Two-photon calcium imaging enables functional analysis of neuronal circuits by inferring action potential (AP) occurrence ("spike trains") from cellular fluorescence signals. It remains unclear how experimental parameters such as signal-to-noise ratio (SNR) and acquisition rate affect spike inference and whether additional information about network structure can be extracted. Here we present a simulation framework for quantitatively assessing how well spike dynamics and network topology can be inferred from noisy calcium imaging data. For simulated AP-evoked calcium transients in neocortical pyramidal cells, we analyzed the quality of spike inference as a function of SNR and data acquisition rate using a recently introduced peeling algorithm. Given experimentally attainable values of SNR and acquisition rate, neural spike trains could be reconstructed accurately and with up to millisecond precision. We then applied statistical neuronal network models to explore how remaining uncertainties in spike inference affect estimates of network connectivity and topological features of network organization. We define the experimental conditions suitable for inferring whether the network has a scale-free structure and determine how well hub neurons can be identified. Our findings provide a benchmark for future calcium imaging studies that aim to reliably infer neuronal network properties.

Keywords: calcium, action potential, reconstruction, connectivity, scale-free, hub neurons

INTRODUCTION

Information processing in the nervous system is mediated by distributed spatiotemporal spiking activity patterns in networks of neurons. Experimentally, neuronal network dynamics have been difficult to investigate, especially under the relevant *in vivo* conditions for studying the neural underpinnings of sensory, motor, and cognitive phenomena. While multi-electrode arrays or silicon-based multi-electrode probes allow for simultaneous electrophysiological recording of spike trains from tens to hundreds of neurons with high temporal precision (Buzsaki, 2004), these techniques also suffer from a number of limitations. Assigning the recorded signal to multiple neurons in the proximity of the recording electrode remains challenging ("spike-sorting problem") (Einevoll et al., 2011) and, most importantly, multi-electrodes sample neural tissue non-homogeneously, with highly active neurons in the vicinity of the recording electrodes being overrepresented (Olshausen and Field, 2005). This sampling bias can lead to spurious results in effective connectivity studies (Gerhard et al., 2011). Finally, extracellular multi-unit recordings commonly provide little information about cell type identity and spatial distribution of the recorded neurons.

Two-photon calcium imaging in the living brain has emerged as a powerful alternative technique, using either synthetic small-molecule or genetically-encoded calcium indicators (reviewed in Garaschuk et al., 2006; Grienberger and Konnerth, 2012; Knopfel, 2012; Looger and Griesbeck, 2012). Calcium signals imaged with high-affinity indicators can serve as proxy of spike dynamics because each action potential (AP) is associated with a rather stereotypical somatic calcium influx causing a characteristic elementary calcium transient. Calcium imaging addresses several of the limitations inherent in multi-electrode recordings. Most importantly, it enables comprehensive sampling of the activity of many, if not all, neurons within a local population, currently up to about 500 neurons with cell number trading off against temporal resolution (1 Hz to 1 kHz) and signal-to-noise ratio (SNR) (Grewe and Helmchen, 2009; Lütcke and Helmchen, 2011). Moreover, calcium signals can be assigned unequivocally to individual neurons, permitting the analysis of the spatial distribution of neuronal activity patterns (Dombeck et al., 2009; Kampa et al., 2011) and long-term repeated functional probing of the exact same neuronal populations (Margolis et al., 2012; Lütcke et al., 2013). Finally, calcium imaging may be combined with genetic tools or *post hoc* labeling approaches to identify specific subtypes of neurons (Kerlin et al., 2010; Hofer et al., 2011; Langer and Helmchen, 2012), or with retrograde tracers to reveal long-range projection patterns of the imaged neurons (Chen et al., 2013a).

Because two-photon imaging conventionally is based on relatively slow frame rates (1–15 Hz), the majority of calcium imaging studies to date have focused on static neuronal properties such as sensory tuning curves (Ohki et al., 2005, 2006; Rothschild et al., 2010). In recent years, however, advanced laser scanning methods have been developed that enable high-speed population imaging (25 Hz and higher, up to 1 kHz) (Nikolenko et al., 2008;

Otsu et al., 2008; Grewe et al., 2010; Ranganathan and Koester, 2010; Bonin et al., 2011; Katona et al., 2012). In some cases spike times could be inferred with near-millisecond temporal precision (Grewe et al., 2010; Ranganathan and Koester, 2010; Fernández-Alfonso et al., 2013). In combination with dedicated analysis routines, high-speed two-photon calcium imaging should thus be capable, in principle, to report dynamic AP patterns in local neuronal populations. Besides providing unique opportunities to measure network activity *in vivo*, such experiments could even make it possible to extract structural information about network connectivity and topology, given sufficient accuracy of spike inference in the network.

A plethora of different algorithms have been developed to infer the spike train underlying a particular observed calcium indicator fluorescence trace. They can be broadly classified into deconvolution-based approaches to estimate changes in neuronal activity without attempting to reconstruct the occurrence of individual spikes (Yaksi and Friedrich, 2006; Vogelstein et al., 2009, 2010), template-matching techniques that infer spike times based on knowledge of the prototypical waveform of the single-AP evoked calcium transient (Kerr et al., 2007; Greenberg et al., 2008; Grewe et al., 2010; Onativia et al., 2013) and machine-learning algorithms, which require training on data sets with known "ground truth" (Sasaki et al., 2008). Little attention has been given, however, to a systematic study of how spike inference is influenced by different experimental parameters, such as SNR or signal acquisition rate. Experimentally, this is difficult to address because it would require a whole set of experiments with simultaneous *in vivo* calcium imaging and electrophysiological recordings from many neurons under various conditions. At present, only selective calibration experiments are feasible, testing the sensitivity of calcium indicators by simultaneous imaging and recording of single neurons (Kerr et al., 2005). Nonetheless, a thorough investigation of the effect of experimental parameters on spike inference would be an invaluable resource for experimentalists in order to plan experiments as well as interpret results, especially in view of the recent developments in imaging technology and indicator design. Only a few studies, employing mostly theoretical analysis or numerical simulations, have started to more systematically analyze the prospects and limits of spike inference from optical recordings (Sjulson and Miesenbock, 2007; Wilt et al., 2013) as well as of extracting network information from inferred population spike dynamics (Vogelstein et al., 2010; Mishchenko et al., 2011; Stetter et al., 2012).

Here, we present a quantitative simulation framework to generate two-photon calcium imaging signals from the spiking activity of neocortical neurons, simulated either for individual cells or for subsets of neurons within a large-scale network. Using simulated single-neuron fluorescence signals we first characterize the influence of relevant parameters of the reconstruction algorithm on spike inference, exemplified here for the recently introduced "peeling" algorithm that iteratively removes detected single-AP evoked calcium transients from the observed fluorescence signal (Grewe et al., 2010). To guide experimentalists, we provide a systematic and quantitative analysis of the impact of several parameters related either to imaging data acquisition, indicator properties, or inference routine. We evaluate how these parameters—within value ranges relevant for real experiments—influence the fractions of correctly inferred and falsely discovered APs as well as the temporal precision of spike inference. We also extend the peeling algorithm to consider calcium indicator saturation at high spike rates.

Using a large-scale neuronal network simulation, we subsequently show that structural connectivity between neurons can be partially inferred even from limited amounts of imaging data, from a sparse subset of the population, and under fluctuating, unobserved, common input. We show that parametric statistical models can extract substantially more information than pairwise cross-correlational analysis. Based on our spike inference analysis we then examine to what extent the inference of network properties is expected to deteriorate for realistic calcium imaging conditions. Finally, we investigate whether statistical network properties, such as scale-free topologies (Barabasi and Albert, 1999) and hub neurons (Feldt et al., 2011) can be recovered from the estimated connectivity matrices. Our results suggest that the current state-of-the-art in calcium imaging technology not only comes very close to the criteria required for reliable and accurate spike inference in neuronal networks but also enables at least in part to gain additional information about network connectivity and topological features.

RESULTS

A FRAMEWORK FOR SIMULATIONS OF NEURAL NETWORK CALCIUM IMAGING DATA

Our first aim was to create a simulation environment for mimicking actually recorded calcium indicator fluorescence traces (both in single neurons and in a network of spiking neurons), which then can be treated in exactly the same way as real experimental data. The advantages of exploring simulated fluorescence transients are: (1) the reconstructed spike trains can always be compared to the ground truth of original spike trains; (2) many artificial spike trains can be easily generated; and (3) spike trains in networks with known connectivity can be utilized to explore the possibility of extracting information about network structure from calcium imaging data. As a result, different parameters related either to the network itself, the experimental conditions or the analysis routines can be systematically varied to evaluate their relative influences (**Figure 1A**).

To generate artificial AP-evoked fluorescence signals, we simulated spike trains either in single neurons (Poisson process with time-independent mean firing rate r) or in a simulated network of leaky integrate-and-fire neurons (see Materials and Methods). Spike trains were converted to fluorescence signals, taking into account their relationship to changes in intracellular free calcium concentration ($[Ca^{2+}]_i$). As commonly done for experimental data, we expressed calcium signals as relative percentage fluorescence changes ($\Delta F/F$). We first presumed a linear relationship between $[Ca^{2+}]_i$ changes and $\Delta F/F$, which is justified for relatively isolated brief transients as they occur for sparse spiking (for treatment of non-linear indicator saturation at high firing rates see below). This is self-explanatory. In the linear case, $\Delta F/F$ traces were generated by convolving spike trains with a kernel with a fast exponential rise (time constant τ_{on}) and a slower exponential decay (time constant τ_{off}), mimicking the stereotyped

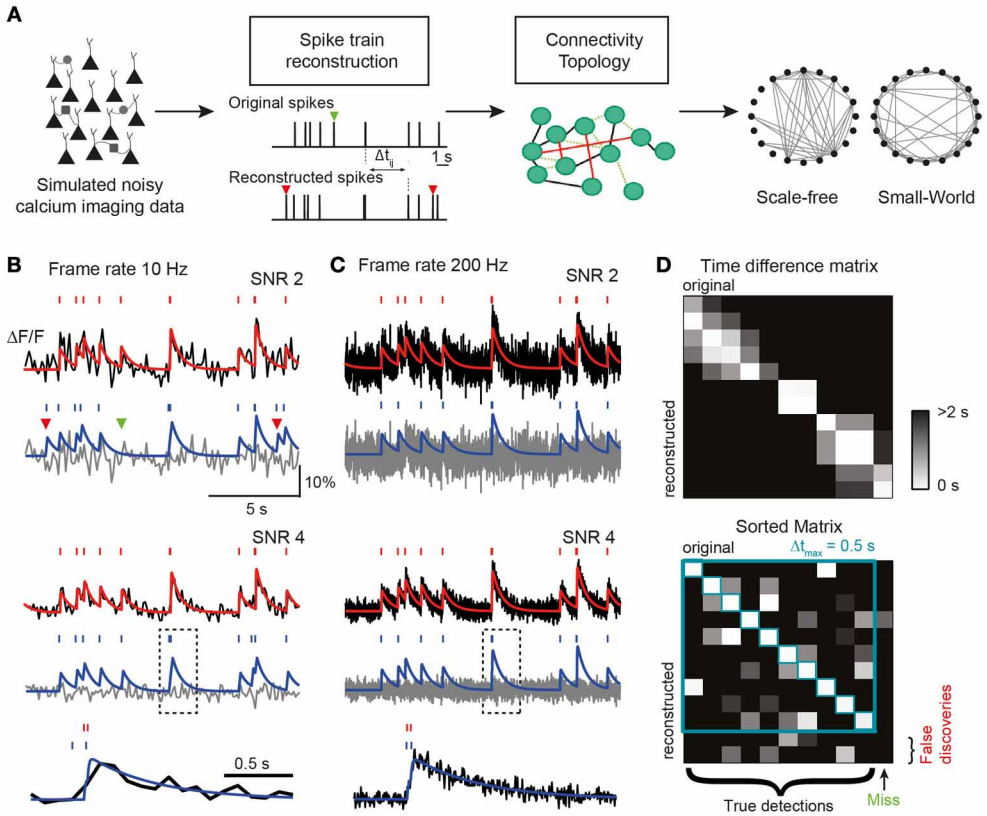

FIGURE 1 | (A) Conceptual link between neuronal network dynamics and structure in our study. Network dynamics measurable with calcium imaging techniques is simulated to investigate how well spike trains can be reconstructed for a broad value range of the most important experimental parameters. Reconstruction performance is condensed in three key parameters (TPR, true positive rate; FDR, false discovery rate; and $\sigma_{\Delta t}$, temporal precision), which are used to analyze how well structural network properties such as topological characteristics (right) can be revealed depending on the attainable accuracy of spike train reconstruction. Missed (green) and falsely detected (red) spikes indicated by arrowheads. **(B–D)** Simulation of calcium traces from spike trains and subsequent reconstruction of firing pattern. **(B)** Top: simulated noise-free (red) and noisy (black) calcium traces for the example Poisson spike train ($SNR = 2$; $f = 10$ Hz). Bottom: reconstruction of spike train from simulated noisy calcium trace using the peeling algorithm. Reconstructed spike train and model calcium trace in blue. Gray: residual calcium trace. Note the missed (green) and two false spikes (red). Middle: same traces but with a better SNR of 4. Bottom: expanded view of example calcium transient in gray box on faster time scale. Note the timing imprecision of reconstructed spike timing due to the low frame rate. **(C)** Same data as in **(B)** but with a higher frame rate. Note the improved reconstruction, especially at the faster time scale (bottom). **(D)** Illustration of simulated original spike train and reconstructed spike train ($SNR = 2$; $f = 10$ Hz). Spikes are matched based on the Δt matrix of all spike-pair-intervals Δt_{ij} between original and reconstructed trains. After sorting the matrix according to the rank of Δt and applying a threshold Δt_{max}, spikes are either matched or remain as "misses" or "false discoveries." Unmatched spikes i with $\Delta t_{ij} > \Delta t_{max}$ for all j are undetected original spikes (misses) and unmatched spikes j with $\Delta t_{ij} > \Delta t_{max}$ for all i are spurious reconstructed spikes (false discoveries).

single AP-evoked calcium transient typically observed in neocortical pyramidal neurons with the synthetic indicator Oregon Green BAPTA-1 (OGB-1) (Kerr et al., 2005; Grewe et al., 2010). Realistic Gaussian noise was added to the simulated calcium signals to yield different SNRs (see Materials and Methods). SNR was defined as the ratio of the peak amplitude of the elementary calcium transient divided by the standard deviation of baseline activity. Finally, noisy calcium traces were subsampled from the original temporal resolution (2 kHz) to a given target frame rate, f, by selecting the center data point of each time interval ($1/f$). This procedure resembles the laser scanning approach used in most two-photon microscopes. **Figures 1B,C** show examples of simulated $\Delta F/F$ traces for two different frame rates (10 and 200 Hz) and noise levels (SNR 2 and 4).

In the following, we address three major questions with this simulation framework. First, how good is the reconstruction of spike trains in individual neurons under systematically varied conditions? Second, in how far can one extract information about physiological connectivity from the more or less accurate inferred spike times in the network? Finally, what level of reconstruction performance is necessary to infer statistical features of the underlying network topology, such as the identification of hub neurons or scale-free properties?

ANALYSIS OF SPIKE INFERENCE FROM SIMULATED CALCIUM SIGNALS IN INDIVIDUAL NEURONS

Our simulation framework provides a convenient strategy for the comprehensive evaluation of various algorithms that have been

devised for inferring spike trains from noisy calcium recordings (Greenberg et al., 2008; Sasaki et al., 2008; Grewe et al., 2010; Vogelstein et al., 2010). However, a comparison of different algorithms was not the goal of this study. Rather, we exemplify how the performance of one particular spike reconstruction approach, the peeling algorithm introduced in (Grewe et al., 2010), depends on different experimental parameters. In principle the same systematic approach can be followed for other reconstruction algorithms using the MATLAB code provided (Supplementary Materials).

The peeling algorithm is based on iterative subtraction of a template elementary calcium transient at event onset times detected by a Schmitt trigger routine, thus "peeling" away calcium transients until a residual noise trace remains (**Figures 1B–D**). Besides the parameters describing the template calcium transient, the main parameters of the peeling algorithm are two thresholds (an initial high-passing and a second low-passing one) and the minimum duration between the two threshold crossings that has to pass by in order to count as an event (see Materials and Methods). The peeling algorithm returns a list of spike times in continuous time (independent of acquisition rate). Examples of spike trains reconstructed from simulated calcium traces using the peeling algorithm are shown in **Figures 1B,C**. An advantage of the peeling algorithm is that it can be extended to conditions, under which indicator saturation becomes relevant (see below).

The reconstructed spike train may contain false negatives (missed spikes) and false positives (falsely discovered spikes). To quantify the performance of the inference algorithm, we compared the original and reconstructed spike train as follows. We first calculated a matrix of spike time differences (Δt) for all pairs of original and reconstructed spikes (**Figure 1D**). We then assigned the first spike pair based on the smallest time difference, repeated this best-matching approach for the remaining spikes, and iterated until no further pair was found to meet a tolerance time window criterion (by default $\Delta t_{max} = 0.5$ s). The remaining "lonely" spikes constituted missed and falsely discovered spikes, respectively (**Figure 1D**). The outcome of this comparative approach was condensed in two main parameters: the true positive rate TPR_{AP} (number of correctly detected spikes divided by the original number of spikes; also called "sensitivity" or "recall") and the false discovery rate FDR_{AP} (number of falsely discovered spikes divided by the number of reconstructed spikes, with (1-FDR_{AP}) also referred to as "precision"). We preferred to use the FDR rather than the false positive rate (FPR, number of time bins with falsely reconstructed spikes divided by the total number of time bins without original spike) because FPR depends on time binning and becomes arbitrarily small for high acquisition rate and sparse spiking. TPR_{AP} and FDR_{AP} on the other hand provide an intuitive quantification of the fractions of accurately and inaccurately detected spikes (see also Materials and Methods). We furthermore quantified the temporal precision of correctly retrieved spikes as the mean and standard deviation (mean$\Delta t \pm \sigma_{\Delta t}$) of the difference between matched reconstructed and original spike times.

We first investigated how SNR and acquisition rate influence spike inference under conditions commonly observed for cortical pyramidal neurons (assuming OGB-1 labeling: single-AP peak $\Delta F/F$ amplitude 7%; decay time constant 1 s; low average firing rate of 0.2 Hz). **Figure 2A** summarizes the reconstruction accuracy in terms of TPR_{AP} and FDR_{AP} for different SNR levels and frame rates. As expected, lower noise levels and faster frame rates were associated with better reconstruction performance. Near-perfect reconstruction accuracy was achieved at surprisingly low frame rates, with little improvement above 30 Hz (**Figure 2A**), in agreement with the experimentally verified performance of the peeling algorithm $TPR_{AP} = 95.5\%$ and $FDR_{AP} = 1.5\%$ for 181–490 Hz acquisition rate and SNR levels between 2 and 5 (Grewe et al., 2010). Even at very high noise levels (SNR 1–1.5) of simulated traces, very good reconstruction performance was attained at higher sampling rates ($\geq$100 Hz). Note that choosing a shorter temporal window for declaring correct AP detections ($\Delta t_{max} = 0.1$ s instead of 0.5 s) impaired reconstruction accuracy at lower frame rates ($\leq$10 Hz) whereas accuracy at high frame rates remained largely unaffected (**Figure 2B**). We next asked how spike inference might be influenced by additional noise factors, such as variability in the main parameters describing the single AP-evoked calcium transient (A_{Peak} and τ_{off}). To address this question, we selected variable values of A_{Peak} and τ_{off} for the calcium transient model of each AP, based on a normal distribution with mean $A_{Peak} = 7\%$ and mean $\tau_{off} = 1$ s and $SD = 10\%$ of the mean value (i.e., 0.7% for A_{Peak} and 0.1 s for τ_{off}). Results of this simulation (**Figure 2C**) revealed only minor decreases in reconstruction performance, compared to the noiseless parameter scenario (**Figure 2A**), demonstrating that spike inference with the peeling algorithm is relatively robust against small, random fluctuations in critical parameters.

Spike reconstruction performance is not only determined by imaging parameters, such as SNR or acquisition rate, but also by properties of the detection algorithm itself, notably the settings for different thresholds (see Materials and Methods). To evaluate the effects of different decision criteria (thresholds) on signal detection, we investigated the trade-off between falsely discovered spikes (1 − FDR_{AP}; "precision") and correctly detected spikes (TPR_{AP}; "recall") [so-called "precision-recall" (PR) curve; **Figures 2D,E**]. Using error rate α_{AP} (see Materials and Methods) as performance metric, we confirmed that sensitive spike detection is achievable at relatively low SNR, provided that frame rates are high enough (e.g., >100 Hz; **Figure 2F**).

INFLUENCE OF INDICATOR PROPERTIES AND PARAMETER CHOICES

We next investigated how properties of the calcium indicator itself might affect spike reconstruction performance. Calcium indicators are Ca^{2+}-binding molecules with characteristic binding kinetics and affinity, and they can be applied in different concentrations. These parameters affect the shape of recorded fluorescence transients, in particular the onset time, the peak fluorescence (and thus SNR), and the decay time course (Göbel and Helmchen, 2007). For the majority of commonly used calcium indicators these properties have been measured and they are usually reported for new indicators (see for example Hendel et al., 2008). We asked how

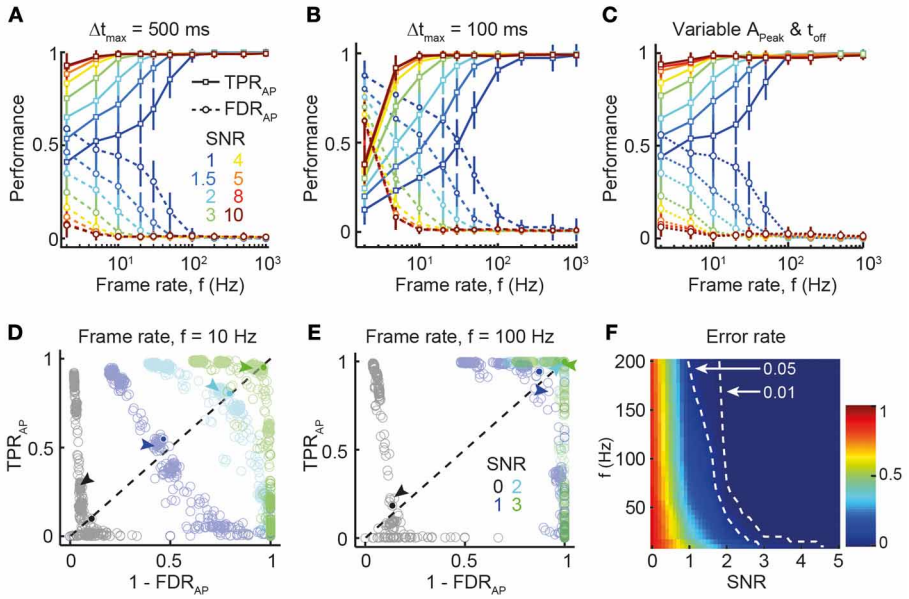

FIGURE 2 | Dependence of spike reconstruction performance on SNR and frame rate. (A) TPR_{AP} (solid lines) and FDR_{AP} (dotted lines) as function of frame rate (x-axis) and SNR (different colors). Temporal window for declaring correct AP detection: 500 ms. Mean ± SD. **(B)** Same analysis as **(A)** but with narrower temporal window for declaring correct AP detection (100 ms). **(C)** Similar simulation as in **(A,B)**, but with variable calcium transient parameters A_{Peak} and τ_{off}. For each AP, corresponding values for A_{Peak} and τ_{off} were selected from a normal distribution with mean $A_{Peak} = 7\%$ and mean $\tau_{off} = 1$ s and $SD = 10\%$ of the mean value. Temporal window for declaring correct AP detection: 500 ms. **(D)** PR-curve showing the trade-off between TPR_{AP} and FDR_{AP} for different SNR at $f = 10$ Hz (see SNR legend in **E**). Data points indicate different combinations of Schmitt-trigger thresholds for the spike reconstruction algorithm (see Materials and Methods). Arrows mark the data points corresponding to thresholds employed for reconstruction in this study. Solid circles indicate the break-even point used for quantifying overall reconstruction performance. The error rate is the normalized distance of the break-even point from the top-right corner (perfect reconstruction accuracy). **(E)** Same analysis as **(D)** at $f = 100$ Hz frame rate. Marked data points for SNR 2 and 3 are superimposed in top-right corner, indicating near-perfect reconstruction accuracy. **(F)** Error rate for all combinations of SNR and frame rate (linear interpolation between simulated parameter combinations). Dashed lines indicated thresholds for 0.01 and 0.05 error rates.

variation in one of the most important parameters governed by indicator properties, the decay time constant τ_{off}, affects reconstruction performance given different experimental constraints (notably frame rate and SNR). For common synthetic indicators such as OGB-1, τ_{off} is about 0.5–1 s for typical indicator concentrations, while other recently developed highly sensitive genetically encoded calcium indicators (GECIs) can display slower decays (e.g., $\tau_{off} = 2$–4 s for YC-Nano15) (Horikawa et al., 2010). Our simulations clearly show that longer decay times do not preclude accurate detection of APs, at least for sparse firing regimes (**Figure 3A**). Contrarily, we observed a rapid deterioration of reconstruction performance for faster decay times ($\tau_{off} < 0.5$ s), most notably at lower acquisition rates and SNRs (**Figure 3B**). Intuitively, this can be explained by a too low sampling density resulting in frequent misses of the brief initial peak of calcium transients. These results suggest that the use of new calcium indicators with faster fluorescence decay times (Chen et al., 2013b) would only be beneficial in combination with imaging at sufficiently high speed.

Algorithms for spike inference from fluorescence signals typically rely on the use of a standard single-AP calcium transient (see above). Although the shape of this elementary calcium transient is rather stereotyped (as long as saturation can be neglected; see below) and often well-characterized for a certain cell type, variations among individual cells do exist and uncertainties remain about the values to choose for the parameters of the reconstruction algorithm. We therefore explored to what extent reconstruction performance depends on the accurate choice of parameters for the elementary calcium transient. We simulated AP-evoked $\Delta F/F$ traces with a fixed decay time constant $\tau_{off,\ Sim}$ of 1 s but for spike train reconstruction we systematically varied the presumed decay time constant $\tau_{off,\ Recon}$ between 0.1 and 2 s (**Figure 3C**). Reconstruction with shorter $\tau_{off,\ Recon}$ dramatically increased the fraction of falsely detected APs while TPR_{AP} remained unaltered. Choosing too long decay times for reconstruction led to a smaller decline of TPR_{AP} while FDR_{AP} remained low. Overall spike reconstruction accuracy decreased by 35% for a 50% decrease in assumed $\tau_{off,\ Recon}$ ($\tau_{off,\ Recon} = 0.5$ s) while a corresponding doubling ($\tau_{off,\ Recon} = 2$ s) reduced accuracy by only 10% (**Figure 3C**). Another parameter that may be partly unknown under experimental conditions is the peak fluorescence A_{Peak} for a single AP. We found that under-estimation of A_{Peak} led to a dramatic increase in FDR_{AP} while over-estimation again caused a more graceful degradation in TPR_{AP} (**Figure 3D**). Given that the true values for A_{Peak} and τ_{off} are frequently unknown under experimental conditions, our analysis suggests that over-estimating these parameter may be a good strategy to optimize spike reconstruction accuracy (**Figures 3C,D**).

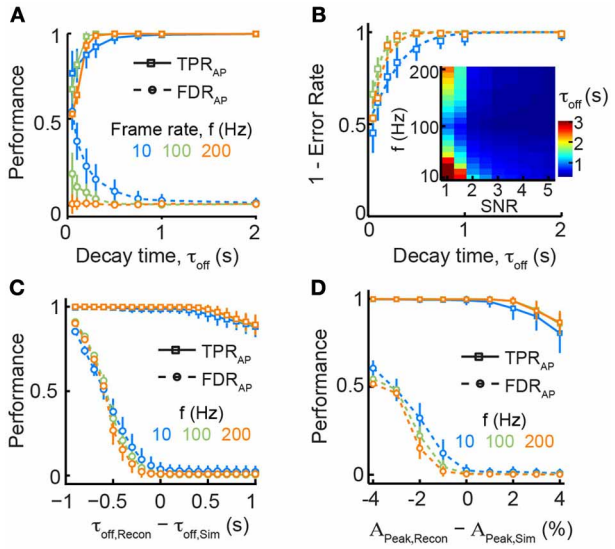

FIGURE 3 | Dependence of spike train reconstruction on assumed calcium transient parameters. (A) TPR_{AP} (solid lines) and FDR_{AP} (dotted lines) as function of decay time τ_{Off} and frame rate f for fixed $SNR = 3$. Note that faster decay times lead to markedly reduced reconstruction performance especially at slow sampling rates. **(B)** Overall performance accuracy ($1 - \alpha_{AP}$) increases for longer decay times. Dashed lines are logistic fits to the data points. The fits were used to compute the minimal decay time that would be necessary to reach an error rate $\alpha_{AP} = 0.05$ (inset). **(C)** Robustness of reconstruction performance against deviations from model parameters: decay time, τ_{Off}. Data were simulated with $\tau_{Off,Sim} = 1$ s and reconstruction was performed assuming different values for $\tau_{Off,Recon}$. Note that reconstruction with faster decay times leads to a strong increase in FDR_{AP} whereas slower decay times lead to a more graceful deterioration of TPR_{AP} ($SNR = 3$). **(D)** Robustness of reconstruction performance against deviations from model parameters: peak calcium amplitude, A_{Peak}. Data were simulated with $A_{Peak,Sim} = 7\%$ $\Delta F/F$ and reconstruction was performed assuming different values for $A_{Peak,Recon}$. Reconstruction with smaller A_{Peak} results in many more falsely detected APs whereas over-estimation of A_{Peak} leads to a more graceful deterioration of TPR_{AP} ($SNR = 3$).

SPIKE INFERENCE UNDER CONDITIONS OF INDICATOR SATURATION

So far, we have assumed sparse spiking conditions (low firing rate), for which $\Delta F/F$ can be presumed to relate linearly to $[Ca^{2+}]_i$. However, episodes of AP bursts with higher firing rates, e.g., during optimal sensory stimulation (Decharms et al., 1998) or under awake conditions (Greenberg et al., 2008), will cause larger $[Ca^{2+}]_i$ elevations and increasingly drive high-affinity indicators into saturation. We therefore also incorporated saturation effects in our simulation framework and extended the peeling algorithm to account for saturating fluorescence transients during burst episodes of APs (see Materials and Methods). To evaluate the performance of the reconstruction algorithm for higher firing rates, we simulated saturating fluorescence traces in response to 5–10 s long episodes of AP firing rate at 1–30 Hz. At high firing rates fluorescence traces reached $\Delta F/F$ values greater than 60% (**Figure 4A**), corresponding to saturation levels around 0.7. Due to saturation, the amplitude of individual AP-evoked $\Delta F/F$ transients decreases at elevated $[Ca^{2+}]_i$ levels (**Figure 4B**). However, taking this saturation effect into account in an improved version of the peeling algorithm (see Materials and Methods) we could still recover the majority of spikes, even at high firing rates, as exemplified for $SNR = 3$ in **Figure 4C**. When the mean saturation level during the spiking episode increased at higher firing rates, we observed very little, if any, decrease in the overall reconstruction performance. Note, however that this result depended critically on saturation being implemented in the reconstruction step. When we simulated saturating $[Ca^{2+}]_i$ traces but attempted to reconstruct them without taking saturation into account (using the linear approximation), error rates increased dramatically (**Figure 4D**). In summary, the results of the previous sections demonstrate that the peeling algorithm enables robust and highly accurate spike inference over a large range of imaging, indicator and experimental parameters.

TEMPORAL PRECISION OF SPIKE INFERENCE

Given that accurate spike reconstruction can be achieved with our reconstruction algorithm for a wide range of parameter combinations, we next wanted to explore the temporal precision of accurate reconstructions (returning to low average firing rate of 0.2 Hz). **Figure 5A** shows example distributions of spike time differences at three different sampling rates (mean $\Delta t \pm \sigma_{\Delta t}$ for 10 Hz: -9 ± 35 ms; 100 Hz: -4 ± 5 ms; 1000 Hz: 0 ± 1 ms). Again, these results are in line with the experimentally determined spike time reconstruction precision of the peeling algorithm (SNR 2–5; Grewe et al., 2010). At very high sampling rates and good SNR, spike train reconstruction approached sub-millisecond accuracy, as quantified by the standard deviation (SD) of the Δt distribution (**Figures 5B,C**; $\tau_{off} = 1$ s, $\tau_{on} = 10$ ms). For example, at a rate of 1 kHz, $\sigma_{\Delta t}$ was 0.67 and 0.56 ms for SNR 8 and 10, respectively (**Figure 5C**, inset), which is close to the limit set by the sampling interval. Of note, temporal precision was little influenced by τ_{off} (data not shown) and only slightly reduced by slower onset times (at $\tau_{on} = 20$ ms, $\sigma_{\Delta t}$ was 0.95 and 0.76 ms for SNR 8 and 10, respectively; at $\tau_{on} = 50$ ms, $\sigma_{\Delta t}$ was 2.90 and 3.12 ms for SNR 8 and 10, respectively). These results demonstrate that recently developed high-speed imaging approaches should be adequate for accurate spike reconstruction with high temporal precision. Our analysis furthermore suggests that the recent development of high-SNR GECIs (Horikawa et al., 2010; Chen et al., 2013b), even if these exhibit slightly slower onsets, may soon allow for accurate spike reconstruction from calcium imaging data with millisecond precision.

The two variables α_{AP} and $\sigma_{\Delta t}$ (ignoring mean Δt which will cancel out in a network reconstruction analysis based on relative differences of spike times of multiple neurons) describe in condensed form the overall performance of spike reconstruction in terms of accuracy and temporal precision. In the second part of our study, our goal was to apply this framework to simulated large-scale networks of spiking neurons with known connectivity and investigate how the attainable levels of spike reconstruction accuracy and temporal precision affect the extraction of synaptic coupling structure between neurons in order to estimate structural network connections within local neuronal populations.

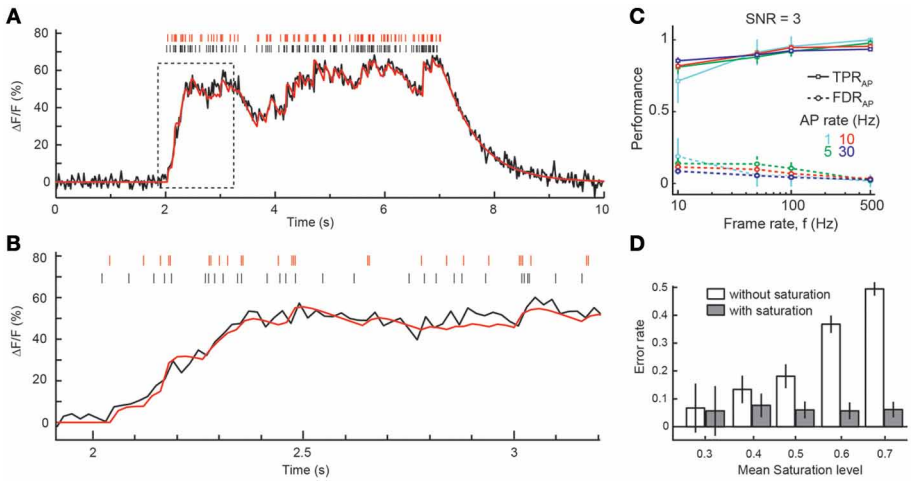

FIGURE 4 | Spike inference from episodes with high firing rates. (A) Example simulation of an episode of 30 Hz firing for 5 s. The fluorescence trace was simulated with a frame rate of 50 Hz and $SNR = 3$ using the model of calcium dynamics including indicator saturation. Black: simulated APs and $\Delta F/F$ trace. Red: reconstructed APs and result of peeling algorithm with saturation model. **(B)** Zoom of initial part of the episode (boxed region in **A**). Note the decreasing amplitude of single-AP transients at high $\Delta F/F$ due to saturation. **(C)** TPR_{AP} (solid lines) and FDR_{AP} (dotted lines) as function of frame rate (x-axis) and firing rate (different colors). $SNR = 3$. Temporal window for declaring correct AP detection: 100 ms. **(D)** Dependence of error rate on mean saturation level during burst episodes with (gray) and without (white) taking saturation into account in the spike reconstruction with the peeling algorithm. Note the large increase in error rate at high saturation levels when a non-saturating, linear superposition of $\Delta F/F$ transients is wrongly presumed. Analysis in **(D)** is based on simulations with frame rate $\geq$50 Hz and $SNR = 3$ and 10. All simulated $\Delta F/F$ traces were generated using the model of calcium dynamics including indicator saturation. All panels show mean $\pm$ SD.

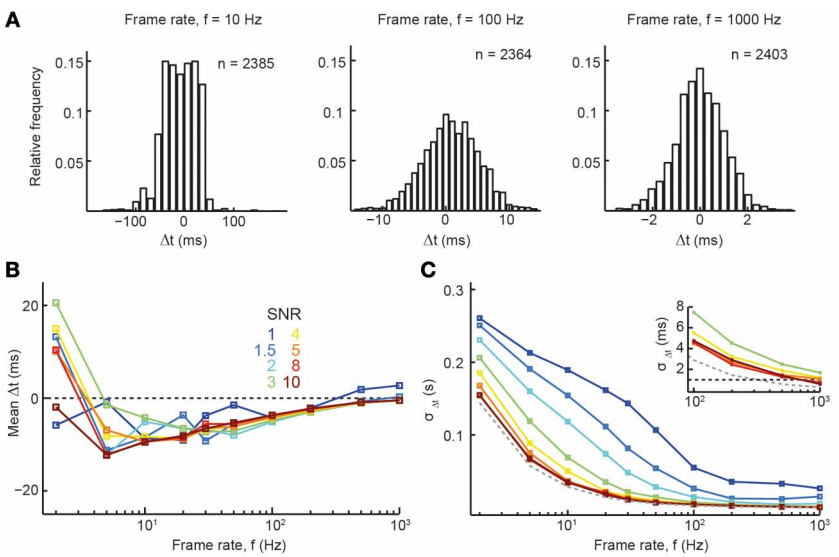

FIGURE 5 | Precision of spike time inference. (A) Histogram of the spike time differences between original and reconstructed spike trains for 3 different frame rates ($SNR = 5$). **(B,C)** Summary parameters for the distribution of spike time differences between original and reconstructed spikes. **(B)** Mean spike time difference, Δt. **(C)** Standard deviation of the distribution of spike time differences, $\sigma_{\Delta t}$. Dashed gray line: theoretical limit set by frame rate. Dashed black line (inset) indicates 1 ms precision. Relevant simulation parameters: firing rate = 0.2 Hz, A = 7%, $\tau_{On} = 10$ ms, $\tau_{Off} = 1$ s.

SIMULATION OF LARGE-SCALE NETWORK DYNAMICS OF SPIKING NEURONS

To investigate how the different experimental parameters impact the analysis of the network dynamics, we extended our simulation framework to generate realistic dynamics of cortical networks under *in vivo* recording conditions. We performed large-scale neural network simulations of 25,000 neurons with sparse, random connectivity of 10% and balanced excitatory and inhibitory subpopulations (**Figures 6A,B**) in line with classical models of cortical networks (Brunel, 2000; Vogels et al., 2005). Neuronal

dynamics were modeled with leaky-integrate-and-fire (LIF) models and conductance-based synapses with individual dynamics for GABA, AMPA, and NMDA conductances (see Materials and Methods). Despite their phenomenological nature, LIF models have shown good to excellent correspondence with the complex response properties of single neurons (Badel et al., 2008; Mensi et al., 2012). In addition to the synaptic input from within the simulated population, each neuron received additional correlated Poisson spike trains whose rates were temporally modulated on all possible time scales to mimic shared input from other cortical layers and areas.

The resulting network state was balanced with irregular, asynchronous activity with sparse average firing rates of around 0.2 Hz and global rate fluctuations (see raster plot in **Figure 6A**). The explicit modeling of slow NMDA conductances (time scale $\tau^{\mathrm{NMDA}} = 100$ ms) led to a more decorrelated activity than in standard neural network simulations (not shown). Because of the size of the simulated network, individual synaptic couplings were relatively weak and single presynaptic APs elicited small postsynaptic potentials and did typically not trigger postsynaptic APs (**Figure 6B**).

How much can we learn about the structure and topology of the network by observing its activity and dynamics through functional signals as provided by calcium imaging experiments? Incomplete and finite observations as well as intrinsic noise sources fundamentally limit the ability to infer structural connectivity from functional signals. Experimentally, only a small fraction of all interacting circuit elements can be recorded for a limited amount of time. We respected this limitation in our simulation framework by randomly picking 50 (excitatory) neurons from the whole population and extracting their coupling structure despite the fact that there were 24,950 unobserved neurons in addition to correlated, fluctuating, external noise sources (**Figures 6A,B**). Furthermore, we did not allow arbitrarily long recording sessions, but limited ourselves to what could be observed with less than 3 h of simulated, sparse activity. These numbers were chosen to be in the realm of currently achievable experimental conditions for current high-speed calcium imaging set-ups.

INFERENCE OF STRUCTURAL CONNECTIVITY FROM NETWORK ACTIVITY: ESTABLISHING AN UPPER LIMIT

With the aforementioned limitations, we do not expect to unambiguously recover the network connectivity from observing network activity *even if* we had access to the unperturbed spiking activity with full temporal resolution. We therefore proceeded by first establishing an estimate of the upper bound of how well the network structure could be reconstructed in the case of infinitely precise spike time measurements. Subsequently, we analyzed how the SNR and sampling rate of calcium imaging experiments influence the reconstruction performance relative to this reference value.

To extract the coupling structure from the spike sequence of the subset of 50 neurons we used non-linear point process models (Generalized Linear Models, GLM; see Materials and Methods), which recently have been applied on electrophysiological data (Pillow et al., 2008; Vidne et al., 2012). Briefly, a probabilistic model is fit for each neuron that explains the observed spike times using the neuron's previous activity and a constant baseline rate. Causal couplings between neurons are introduced through parameterized kernels that describe how spikes of putatively presynaptic neurons modulate the spiking probability of the modeled neuron. The model is considerably simpler than the neuron models used in the simulation, e.g., the model is unaware of the true simulation parameters and timescales and does not explicitly model the shared input from the external Poisson processes, making connectivity extraction a non-trivial task. Features of the estimated coupling filters, such as their size or statistical significance, can be used to assign a single coupling strength for each possible directed connection (Gerhard et al., 2011, 2013). After applying a threshold, we obtain an estimate of the binary connectivity structure of the network. For a given threshold, the performance of the reconstruction algorithm can be summarized in the fraction of correctly identified couplings, $\mathrm{TPR}_{\mathrm{links}}$, and the fraction of erroneously inferred connections among all detected links, $\mathrm{FDR}_{\mathrm{links}}$ (**Figure 6C**). Analogous to the quantification of spike train reconstruction performance, the trade-off between the two quantities is given by the choice of threshold as visualized in a PR-curve (**Figure 6D**). In the following, we summarize the threshold-independent performance of a network reconstruction using the same measure (as in the first part on spike train inference) by the achieved error rate α_{links}.

As a result, we found that with a simulated recording time of less than 3 h (or ∼2000 observed spikes per neuron), we were able to achieve an error rate between 0.5 and 0.6 (**Figure 6D**). This provides an optimal lower bound on the achievable error rate under conditions of a noiseless spike detector. We note that a naive analysis based on pairwise spike train cross-correlations resulted in significantly fewer correct links and more false positives (error rates close to 0.7, **Figure 6D**), indicating the necessity of using modern statistical models to infer network structure from functional imaging.

CONNECTIVITY INFERENCE AFTER IMPERFECT SPIKE TRAIN RECONSTRUCTION

An advantage of the systematic approach followed for the spike train reconstruction from noisy calcium signals is that once the key parameters α_{AP} and $\sigma_{\Delta t}$ have been determined, we can apply a surrogate transformation to the simulated spike trains of the network simulation and investigate to what degree the quality of spike train reconstruction impacts our ability to draw conclusions about the network connectivity relative to the upper bound established above. We repeated the connectivity reconstruction procedure as described above for perturbed spike trains (see Materials and Methods) and evaluated how the different performance metrics affect the connectivity inference.

First, we looked at the impact of the two parameters independently (**Figure 6E**). As expected, the measured error rate in the link reconstruction increased with increasing error rate in the AP reconstruction (**Figure 6E**, left). Given the broad range of frame rates and SNR in calcium imaging for which low error rates α_{AP} were achieved (**Figure 2**), error rates α_{links} close to the best value

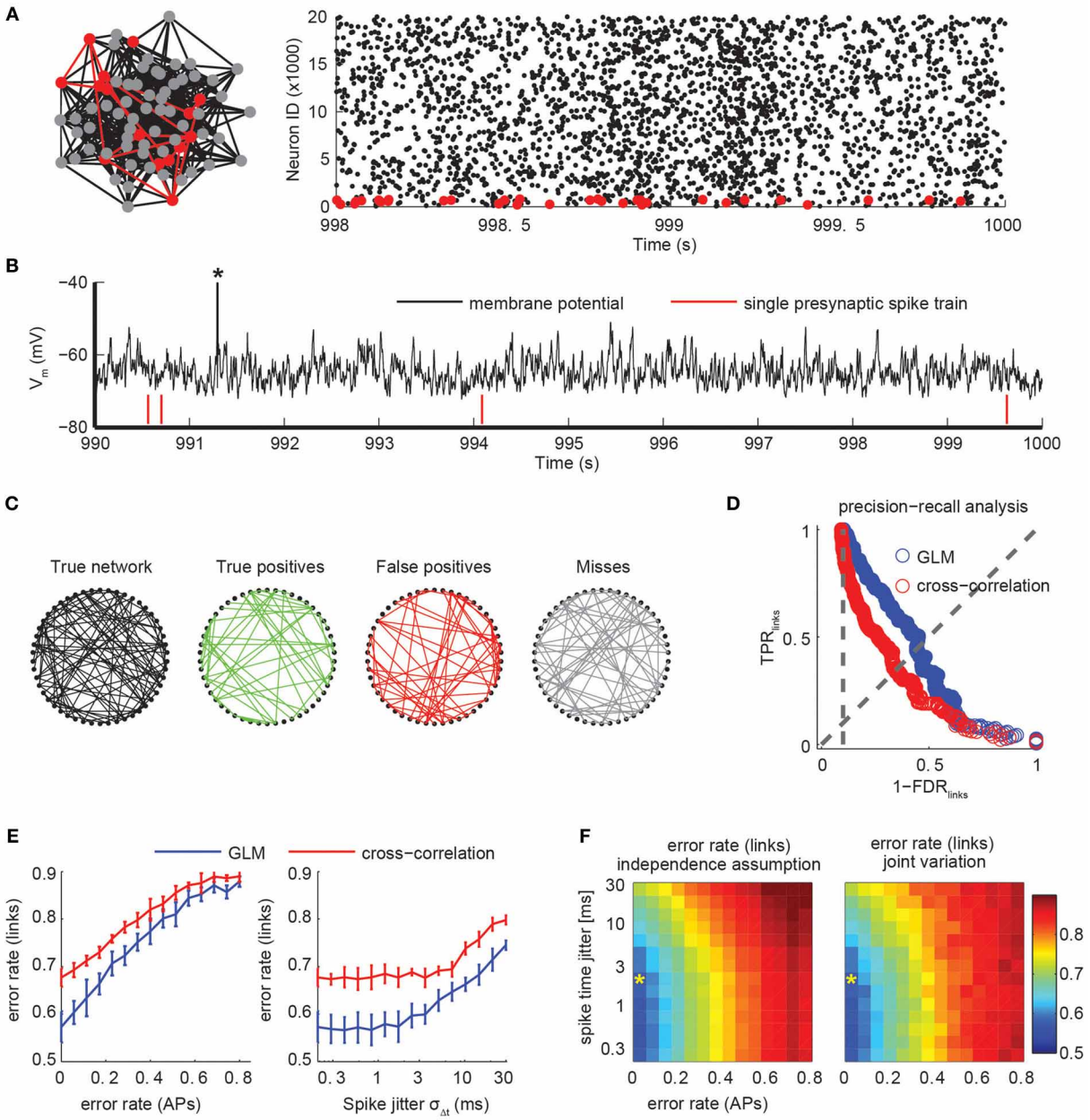

FIGURE 6 | Connectivity extraction using imperfect spike trains. (A) A population of 25,000 excitatory and inhibitory neurons with sparse, random connectivity was simulated using integrate-and-fire models with conductance-based synapses. Firing activity was sparse and irregular. Subsets of 50 neurons (red) were randomly selected and only those spike trains were used to infer their mutual synaptic connectivity (left). Raster plot of the activity of the excitatory subpopulation for 2 s (right). Only every third spike is shown. **(B)** Membrane potential of a randomly selected neuron. The average neuron fired sparsely (note truncated AP marked by asterisk). Synaptic couplings were weak so that single presynaptic APs (red ticks) did not elicit APs by itself. **(C)** True network connectivity and connectivity estimated using GLMs for a randomly selected subset of 50 neurons (links divided into correctly identified links in green, false positive links in red and missed links in gray). Error rate was 0.5. **(D)** Trade-off in network reconstruction performance between TPR_{links} and FDR_{links}. Performance for unperturbed spike trains using a GLM-based reconstruction (blue) or pairwise cross-correlation analysis (red). Error rate is defined as the intersection with the diagonal and is lower for the GLM than for the cross-correlation for all settings of the threshold. Chance level is indicated with the vertical, dotted line. **(E)** Error rates of the link reconstruction after spike perturbations for variations of the error rate in AP detection only (left, assuming no temporal jitter) and for variation of temporal precision of spike times by introducing a Gaussian jitter with width $\sigma_{\Delta t}$ (right; assuming zero error rate in AP reconstruction). Chance level for link reconstruction is 0.9 error rate. Error bars indicate SD over repetitions using random subsets of the network. **(F)** Error rate of link reconstruction as a joint function of error rate (APs) and spike jitter, assuming both effects act independently on the error rate (left) or when jointly varied (right). The similarity indicates that effects of AP detection and its temporal precision act multiplicatively on the expected error rate for link reconstruction. Asterisk indicates the performance level that is realistically achievable with state-of-the-art high speed two-photon calcium imaging (Grewe et al., 2010; Ranganathan and Koester, 2010).

(∼0.55) should be reachable for many experimental conditions. With spike trains perturbed by introducing a temporal jitter $\sigma_{\Delta t}$, error rates in the link reconstruction increase in a more graceful manner, reaching chance level only for $\sigma_{\Delta t} > 30$ ms (**Figure 6E**, right). At experimentally attainable temporal precision ($\sigma_{\Delta t} =$ 1–3 ms; see above), error rates are indistinguishable from the perfect recovery case. For comparison, we also indicated the performance reachable using a standard pairwise cross-correlational analysis, which produced substantially higher error rates than the point process models for all relevant parameter regimes (**Figure 6E**).

We then jointly varied α_{AP} and $\sigma_{\Delta t}$ and found that the error rate in the link reconstruction can be well-predicted by the assumption that contributions from the two factors act independently and in a multiplicative way on α_{links} (**Figure 6F**).

In summary, our analysis indicates that GLMs allow at least partial extraction of effective network connectivity from imperfectly reconstructed spike trains of moderate length from spontaneous, asynchronous network activity. Importantly, we show that a temporal precision of spike reconstruction in the millisecond-range is the major determinant for accurate estimation of neuronal couplings, given that near-perfect reconstruction accuracy can be achieved under a wide range of imaging conditions ($\alpha_{AP} \sim 0$, see above). This finding further highlights the importance of recently developed high-speed imaging approaches.

IDENTIFICATION OF GRAPH TOPOLOGY

Through our simulation framework, we estimate that noisy calcium signals from a set of neurons immersed in a larger cortical neural population contain significant information about the underlying network structure that goes beyond what can be trivially extracted using cross-correlational analysis. Absolute reconstruction performance is, however, currently limited by several factors, some of which are at least partially under the control of the experimentalist. We therefore asked what level of reconstruction will be sufficient for inferring high-level features and statistical properties of the network structure. We addressed this question with a sensitivity analysis for two different applications that are inspired by recent experimental and theoretical studies: the quantification of scale-free properties of the network and the identification of hub neurons with imperfect network reconstruction.

First, we considered the class of *scale-free networks* (Barabasi and Albert, 1999): Scale-free networks are characterized through a degree distribution that follows a power law $p(x) \sim x^{-\mu}$, where the probability that a neuron of the network has x synaptic connections scales like a power law with characteristic exponent μ. We generated prototypical examples of scale-free networks of size $N = 1000$ neurons and exponent $\mu = 3$ and analyzed the impact of expected network reconstruction performance with varying error rates α_{links} and assuming that the identification of a link between any two neurons is statistically independent of any other connection (**Figure 7**). Thus, we obtained simulated reconstructed networks that differed in their statistical properties from the original scale-free network. We fitted power-law distributions to the reconstructed degree distributions and assessed goodness-of-fit with a semi-parametric bootstrapping method (**Figures 7A,B**). Although link over- and under-sampling does in general not result in a pure power-law (Han et al., 2005; Stumpf et al., 2005), many of the resulting networks were still compatible with the scale-free assumption for the tail of their degree distributions ($p_{gof} > 0.05$). However, the estimated exponent could be considerably different from the original one. In general, we found a stronger decay of the degree distribution (more negative power law exponent) upon imperfect network reconstruction (**Figures 7C,D**), regardless of the underlying network density (varied between 2 and 10%), i.e., the number of links present in the network. Only if reconstruction errors get moderately high (e.g., $\alpha_{links} > 0.75$ for networks with 2% link density), the power-law distribution was not evident anymore. The difference between the fitted and original scaling exponent varied with the network density. For denser networks, the sensitivity to imperfections of the detection of the scale-free property based on the data sample is increased. For example, an error

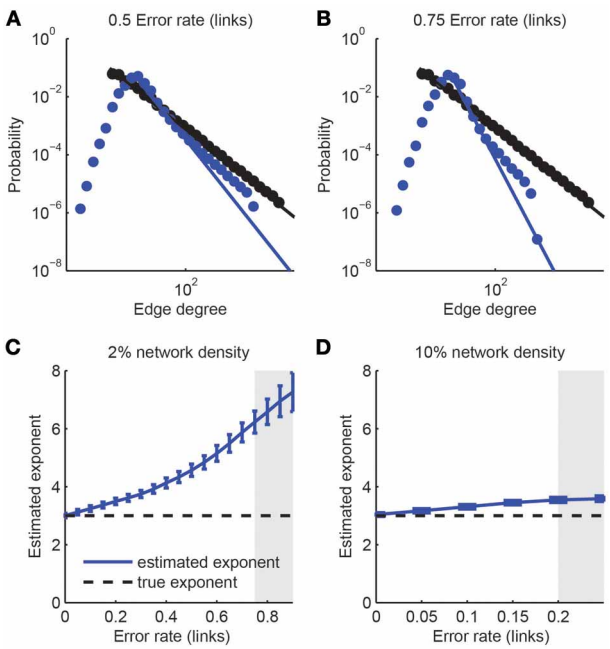

FIGURE 7 | Detection of scale-free graphs upon imperfect connectivity reconstruction. (A,B) Degree distributions of networks after simulated reconstructions. The degree distribution of the original network (1000 neurons, 4% link density) follows a power law $p(x) \sim x^{-3}$ above a minimal degree (black dots and line). Reconstructed networks (blue dots) were obtained with varying error rate in the link reconstruction, ranging from 0.50 (left) to 0.75 (right). In all cases the best-fitting power law to the tail of the degree distribution is indicated (blue line). **(C,D)** Estimated power-law coefficients, obtained from power-law fits to the tails of estimated degree distribution, as a function of error rate in link reconstruction for different network densities. Error bars: standard deviation over 1000 simulations. The coefficient of the original network is indicated by the horizontal dashed line. A goodness-of-fit test was applied to each fit. If more than 50% of the *p*-values were below 0.05, the region is grayed out, indicating that the resulting degree distributions were generally inconsistent with the power-law assumption.

rate of up to 0.75 was tolerated for sparsely connected networks (density 2%) while an error rate of 0.2 (which is not realistically achievable under experimental conditions) was sufficient to make the degree distribution distinct from a power-law for denser networks (10% connectivity; **Figure 7D**). A detailed analysis of the contributions separate from missed links and false positive links indicated that the consistent over-estimation of the power-law exponent was mostly due to the introduction of false positive links (results not shown) while it remained almost unaffected by non-perfect TPR_{links}. This suggests that when considering the trade-off between TPR_{links} and FDR_{links}, emphasis should be put to minimize the number of false positive links on the expense of the link detection power.

Hub neurons are another concept relevant for graph theory (Feldt et al., 2011): Hub neurons are those neurons with a comparatively high degree, i.e., large numbers of incoming or outgoing connections in the network. As before, we started with networks of size $N = 1000$ neurons and a scale-free topology. We classified individual neurons as hub neurons when their degree was in the upper-most decile of the degree distribution (**Figure 8A**). Imperfect network reconstruction, for example due to non-perfect link reconstruction or the insertion of false positive links, generally scattered the degree distribution and therefore the identity of hub neurons. Consequently, not all original hub neurons remained within the top decile of the estimated degree distribution (**Figures 8B,C**). We quantified the robustness with regard to reconstruction errors with the "hit rate," i.e., the fraction of hub neurons of the original network that were correctly classified as hub neurons in the reconstructed network. As expected, the hit rate decreased steadily with increasing error rate in the link reconstruction (**Figures 8D,E**), with only slight dependence on the original network density. Surprisingly, however, hub classification could still be robustly achieved (75% hit rate) for relatively high error rates (0.6–0.75). We conclude that hubs can be detected in a relatively robust manner even in the presence of large link reconstruction errors.

DISCUSSION

In this study we analyzed inference of spike dynamics in neuronal networks, as well as inference of underlying structural properties, based on population fluorescence data as they are typically acquired during *in vivo* two-photon calcium imaging experiments. We established a simulation framework that—unlike experiments—allows comprehensive exploration of parameter spaces. Systematic parameter variation helps to explore the limits of what is currently achievable, identify critical parameters, motivate further methods improvements, and guide the experimenter in the optimization of their imaging conditions. Our results indicate that with state-of-the-art methods, especially high-speed two-photon calcium imaging, it is now feasible to reconstruct spike trains in populations of several tens of neurons with high precision. Remaining uncertainties in exact spike times lower, but do not preclude, retrieval of partial information about network connectivity and topological features. *In vivo* calcium imaging combined with the analysis tools described here thus promises to become a powerful method to analyze the functional organization of neuronal networks in the brain.

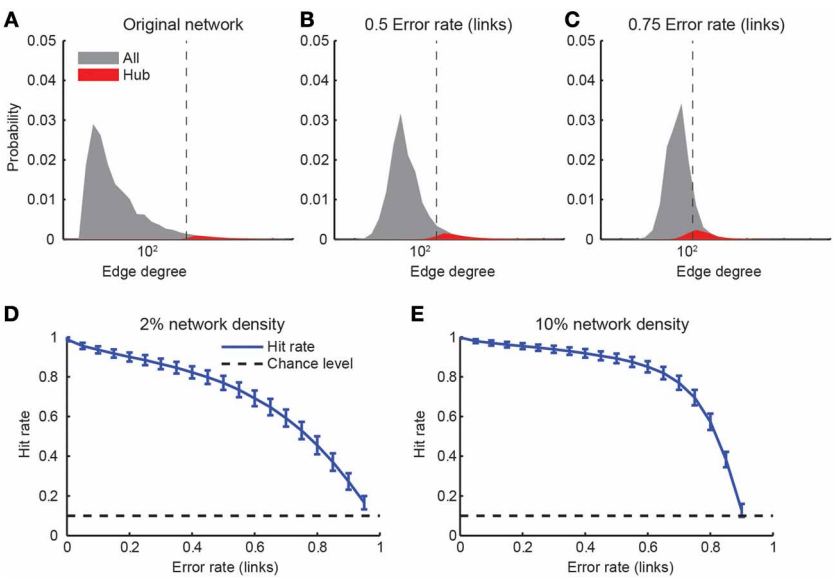

FIGURE 8 | Detection of hub neurons upon imperfect connectivity reconstruction. (A–C) Degree distributions of networks after simulated reconstructions. The degree distribution of the original network **(A)** followed a power law $p(x) \sim x^{-3}$ above a minimal degree of 20. Hub neurons were defined as the 10% of neurons with the highest degree (red areas). Imperfectly reconstructed networks were obtained by assuming varying error rates **(B,C)**. Vertical dashed lines indicate the beginning of the upper-most decile of the estimated distribution. **(D,E)** Hit rate of hub neuron identification as a function of varying degree of link reconstruction error for two different network densities. Error bars: standard deviation over 1000 simulations. Chance level indicated by dashed lines.

POTENTIAL AND LIMITS OF SPIKE INFERENCE

In the first part of this study, we highlighted the utility of our simulation framework to reveal non-trivial relations among the key imaging parameters and the accuracy of spike inference. Our systematic analysis of spike train reconstruction (here exemplified for the peeling algorithm) provides a resource for experimentalists, from which the expected reconstruction performance for a given set of experimental conditions can be obtained (**Figures 2–5**). Similar analyses can easily be implemented for alternative spike reconstruction algorithms (Yaksi and Friedrich, 2006; Vogelstein et al., 2009, 2010) and other experimental conditions. Our analysis reveals a number of novel insights. First, we show that near-optimal spike train reconstruction (i.e., detecting nearly all spikes with negligible numbers of false positives) may be achieved at experimentally tractable noise levels ($SNR \geq 2$) with surprisingly low sampling rates (20–30 Hz). Frame scanning with conventional mirror-based laser scanners typically is limited to 10–20 Hz for 50–100 lines, as the standard galvanometer can be driven at about 1 kHz at maximum. Nonetheless, faster acquisition rates (even >100 Hz) are possible with standard scanners using free line-scans on preselected neuronal subsets (Göbel and Helmchen, 2007; Nikolenko et al., 2007; Lillis et al., 2008; Rothschild et al., 2010), albeit usually at the expense of total dwell time per cell (and thus SNR). Alternatively, full-frame scanning up to 100 Hz has been achieved by fast scanning along one axis with a resonant galvanometer (4–12 kHz resonance frequencies) (Rochefort et al., 2009; Bonin et al., 2011). All these methods with the capability of scanning neuronal populations at greater than video rate (25 Hz) should enable high-quality spike inference.

Two trade-offs, however, need to be considered. Gaining speed in the range of 10–100 Hz will only help to improve spike inference if a sufficient SNR is maintained (**Figure 2A**). In addition, effective sampling rate usually relates inversely to the number of recorded cells for a given SNR, so that a compromise between speed and population size is required. For a fair comparison of imaging approaches and spike reconstruction accuracies one should thus rely on populations of similar size. Fundamentally, these trade-offs arise from the fact that SNR is ultimately limited by photon statistics (Wilt et al., 2013). Of course, the SNR will be lower at higher frame rates given the same excitation power. However, high-speed scanning at low excitation rate can have the additional benefit of reduced phototoxicity and thus prolonged experiment time (Chen et al., 2012). In addition, detection of fluorescence photons should be maximized, for example by using a low-magnification, high numerical aperture objective for detection (Oheim et al., 2001) or by employing supplementary detection schemes (Engelbrecht et al., 2009).

A second insight is that ultra-fast imaging (sampling rates >500 Hz) in combination with high SNR levels permits spike reconstruction with millisecond or even sub-millisecond precision. Such high acquisition rates for neuronal populations, e.g., 0.5 kHz for about 50 neurons, are possible with random-access scanning using acousto-optical deflectors (Reddy and Saggau, 2005; Grewe et al., 2010; Ranganathan and Koester, 2010). To fully exploit the potential of highest-speed calcium imaging it will be essential, however, to reduce additional noise sources such as baseline fluctuations, bleaching effects, or motion artifacts to a minimum.

Our analysis furthermore suggests that the combination of ultra-fast imaging and high SNR may be achievable with the next generation of highly sensitive GECIs (Horikawa et al., 2010; Chen et al., 2013b). Our results reveal that faster decay kinetics of the indicator does not necessarily lead to better spike reconstruction. Intuitively, if the decay time of the calcium indicator dye is faster than the frame duration, peaks will occasionally be missed, thereby reducing detection accuracy. Thus, emerging faster calcium indicators, especially new GECIs, might be of limited use unless combined with new microscopy techniques that allow for faster image acquisition. In addition, because slow onset kinetics slightly reduces the achievable temporal precision, GECIs with fast onset characteristics are desirable if uncertainty of spike times needs to be minimized, for example to extract network structural properties.

INFERRING NETWORK STRUCTURE FROM CALCIUM IMAGING DATA

Our simulation framework summarizes the effects of noise, calcium indicator dynamics, and imperfect reconstruction with two key quantities: the error rate (a combination of the fraction of correctly identified spikes and the rate of erroneously detected spikes) and the precision of reconstructed spike times. Based on these parameters, we could estimate how well we are likely to be able to estimate network connectivity. The goodness of connectivity estimation may again be summarized by the same key metric: the error rate in the network link reconstruction. This parameter has an influence on the estimation of graph properties, as we have exemplified for scale-free topology and the identification of hub neurons. Similarly, our framework should allow analysis of the robustness of other graph statistics such as small-world properties or the distribution of higher-order network motifs.

The modular structure of our framework enabled us to predict the effect of experimental parameters on the global estimation of statistical graph properties by simply following its effect through the different stages. For the benefit of experimenters, we can illustrate the utility of our simulation framework with a practical example, assuming state-of-the-art technology. Using the high-affinity calcium indicator OGB-1 in combination with AOD-based random-access sampling at ≈500 Hz, neuronal calcium signals have been measured in mouse neocortex with SNR up to 5 (Grewe et al., 2010). These parameters will allow spike reconstruction with near-perfect accuracy (**Figure 3A**, $TPR_{AP} > 0.95$, $FDR_{AP} < 0.05$, therefore, $\alpha_{AP} < 0.05$) as well as 2–3 ms temporal precision (**Figure 5C**, inset). In this parameter range, spike detection is sufficiently accurate so that no information loss is expected to occur with respect to the reconstruction of synaptic connections (**Figure 6E**, left). The imperfect temporal precision, however, leads to a slightly increased error rate in the link reconstruction compared to sub-millisecond temporal precision (**Figure 6E**, right). The approximate error rate can be also directly read from **Figure 6F**. Under otherwise optimal conditions, we would obtain an error rate $\alpha_{links} \approx 0.60$, therefore we expect to recover around 40% of the synaptic connections ($TPR_{links} = 0.4$) with $FDR_{links} = 0.6$. According to this estimate, robust identification of hub neurons should still be feasible (**Figures 8D,E**) and

scale-free properties might be just identifiable (but heavily biased) depending on the underlying connection density (**Figures 7C,D**).

The absolute numbers in the example above should be regarded as ballpark estimates rather than precise predictions of reconstruction performance because inference is based purely on simulated data and our particular choice of algorithms. Real reconstruction performance could be weaker than predicted due to effects such as unobserved neuromodulation, weak synaptic strengths, or oscillatory background activity. In addition, connectivity reconstruction could potentially be improved by using more complex point process models that explicitly model global state fluctuations (Smith and Brown, 2003) by attempting to infer the dynamics of unobserved neurons (Vidne et al., 2012) or by employing Bayesian methods (see below).

Few other studies explored the possibility of reconstructing network connectivity from calcium imaging data. Mishchenko and colleagues presented a sensitivity analysis using a Bayesian approach combined with MCMC (Markov Chain Monte Carlo) techniques (Mishchenko et al., 2011). The combined estimation of spike times and connectivity make their approach computationally very expensive. Our modular approach offers the advantage that we can identify the crucial experimental parameters and propagate their effect through the spike time estimation to the network level. Mishchenko et al. did not consider the effect of imperfect link reconstruction for the inference of higher-level topological features of the network. Our results suggest that the optimal choice of experimental parameters can strongly depend on which feature of the network one wants to estimate most reliably. Finally, we note that their recommendation to use frame rates of at least 30 Hz "to achieve meaningful reconstruction results" (Mishchenko et al., 2011) is in alignment with our findings, although both methodology and details of the simulation vary considerably between approaches.

Another study proposed a method based on information-theoretic measures to infer effective connectivity from calcium imaging experiments and evaluate it on simulated data (Stetter et al., 2012). Our approach extends their analysis in a number of different aspects. First, their approach is only suitable for recordings with low sampling frequencies. The information-theoretic measure (transfer entropy) they use to infer couplings does not easily scale up to high-speed recordings because of the need to estimate high-dimensional probability distributions. Activity levels were coarsely discretized, which will have a negative impact on the performance especially for low SNRs. Second, their measure of coupling strength cannot distinguish between excitatory and inhibitory couplings, is pairwise only (i.e., it does not take into account the activity of other recorded cells) and is limited in how temporal aspects of couplings between cells can be modeled. All of these limitations can be overcome by the use of non-linear point process models based on the estimated spike trains, as proposed in this study. Last, (Stetter et al., 2012) did not study the impact of different experimental conditions and can therefore give only limited guidance on how to design experimental set-ups.

We note that we use the peeling algorithm coupled with point process models as an example of a combination of methods to extract connectivity. We favored a two-step procedure of first reconstructing spike trains and then inferring connectivity based on estimated spike times over directly modeling couplings between fluorescence traces (Stetter et al., 2012; Turaga et al., in press). Given that spikes are triggering neurotransmitter release at synapses (at least for most cortical cell types) we expect our approach to be closer to the biological mechanism of how neural signals are coupled, and therefore to be superior in estimating connectivity. A formal comparison would though require the evaluation of both methods on the same simulated data sets.

Due to our modular analysis, the last part of our study (how high-level network properties can be recovered given an expected link reconstruction performance) is independent of the underlying methods to infer connectivity once the performance of any such reconstruction method is quantified in terms of expected link detection power and false discovery rates. Thus, a similar sensitivity analysis could be performed for additional network measures (such as small-world properties or network motifs), and our conclusions readily apply to connectivity estimates obtained from electrophysiology, e.g., from multi-electrode arrays or other imaging modalities.

FUTURE DIRECTIONS

Two-photon calcium imaging has conventionally been calibrated by simultaneous imaging and electrophysiological recording of single neurons (Kerr et al., 2005). Based on the ground truth provided by the electrical recording, the performance of spike inference from calcium imaging data can be verified, albeit the extent of such analysis (e.g., to test various experimental conditions) is limited due to the technical difficulties. Similarly, connectivity inference and extraction of topological network properties will eventually require experimental verification against ground truth data. A first attempt has been made by Gerhard et al. (2013) who showed that the effective connectivity derived from spiking activity using a point process model similar to the one used here matches the physiological connectivity in a very small, but well-defined neural circuit. While it remains a difficult task to test these methods on larger populations, novel approaches have recently emerged that at least partially may allow such verification, including large-scale anatomical circuit reconstructions using electron microscopy (Bock et al., 2011; Briggman et al., 2011) and automated light-microscope techniques in combination with expression of cell type–specific markers and trans-synaptic tracers (Osten and Margrie, 2013). In addition, connectivity mapping can be performed following *in vivo* calcium imaging and re-identification of the recorded neuronal populations in extracted tissue using various physiological techniques, such as multi-cell electrophysiological recordings in acute brain slices (Hofer et al., 2011; Ko et al., 2011) or two-photon photo-stimulation with single-cell resolution using caged compounds or specially tailored opsins (Prakash et al., 2012). At present, these methods are, however, limited to specific individual neurons or small groups of neurons at most.

Our study may be extended in several directions. In particular, the heterogeneity of neuronal cell types could be taken into account. All above considerations straightforwardly apply to superficial neocortical pyramidal neurons, which produce large single-AP evoked calcium transients and display relatively low

spontaneous firing rates. Our extension of the peeling algorithm to account for indicator saturation should also allow reconstruction of brief AP bursts and episodes of higher firing rates, which is especially relevant for awake studies (Greenberg et al., 2008; Wolfe et al., 2010) and for deep-layer cortical pyramidal neurons that generally display higher AP rates (De Kock and Sakmann, 2008). Inhibitory interneurons, especially fast-spiking parvalbumin-expressing cells, have much smaller single-AP evoked calcium transients as well as higher firing rates (Hofer et al., 2011), suggesting that accurate spike inference may not be feasible for these neurons (*SNR* presumably below 0.5). On the other hand, recent *in vitro* electrophysiological work indicated that inhibitory neurons form a relatively unspecific and densely connected network in neocortical circuits (Fino and Yuste, 2011; Packer and Yuste, 2011). Another promising direction of future calcium imaging studies is to resolve the precise functional and structural topology of highly specific local networks of pyramidal neurons (Song et al., 2005). Our findings indicate that the technical requirements to achieve this goal may be just in reach.

MATERIALS AND METHODS

SIMULATION OF SINGLE-NEURON SPIKE TRAINS, CALCIUM DYNAMICS, AND INDICATOR FLUORESCENCE SIGNALS

Simulation of single-neuron spike trains and calcium indicator fluorescence signals and all analysis were performed in Matlab (The Mathworks, Natick, MA, USA). We generated spike trains by a Poisson process assuming a low mean firing rate (0.2 Hz) similar to what has been reported for spontaneous activity of pyramidal cells in both anesthetized and awake rodent sensory cortex (Wolfe et al., 2010). In addition, to examine the effect of calcium indicator saturation we explored episodes of higher firing rates between 1 and 30 Hz as they occur in pyramidal neurons, e.g., upon sensory stimulation (Greenberg et al., 2008).

A general description of AP-evoked fluorescence signals needs to consider the transformation of changes in intracellular free calcium concentration $[Ca^{2+}]_i$ to the particular type of fluorescence readout. Here, we use the widely adopted $\Delta F/F$ approach, expressing calcium signals as relative percentage fluorescence changes after background subtraction. In this case the transformation between $[Ca^{2+}]_i$ and fluorescence signal is given by (Helmchen, 2012):

$$[Ca^{2+}]_i = \frac{[Ca^{2+}]_{rest} + K_d \frac{\Delta F/F}{\Delta F/F_{max}}}{\left(1 - \frac{\Delta F/F}{\Delta F/F_{max}}\right)} \quad (1)$$

or reversely expressed by:

$$\Delta F/F = \Delta F/F_{max} \frac{[Ca^{2+}]_i - [Ca^{2+}]_{rest}}{[Ca^{2+}]_i + K_d} \quad (2)$$

Here, $[Ca^{2+}]_{rest}$ denotes the resting calcium concentration, K_d the dissociation constant of the calcium indicator, and $\Delta F/F_{max}$ the maximal $\Delta F/F$ reached upon saturation. Note that this transformation is a non-linear relationship. For fluorescence transients far from saturation ($[Ca^{2+}]_i \ll K_d$) Equation 2 can be linearized to:

$$\Delta F/F = \frac{\Delta F/F_{max}}{K_d}([Ca^{2+}]_i - [Ca^{2+}]_{rest}) = \frac{\Delta F/F_{max}}{K_d}\Delta[Ca^{2+}]_i \quad (3)$$

This linear description is a good approximation for AP-evoked fluorescence signals in the low firing regime measured for example with a high-affinity indicator such as OGB-1 (Grewe et al., 2010) (**Figures 9A,B**). In this case each AP evokes a stereotype, elementary somatic calcium transient, which can be approximated with a rapidly rising and exponentially decaying function:

$$\Delta F/F = A\left(1 - e^{-(t-t_0)/\tau_{on}}\right) e^{-(t-t_0)/\tau_{off}} \text{ for } t \geq t_0 \quad (4)$$

Here, t_0 denotes the time point of spike occurrence, τ_{on} the onset rise time, τ_{off} the decay time, and A an amplitude scale parameter. The peak amplitude A_{Peak} of the single-AP evoked calcium transient is given by:

$$A_{peak} = A\tau_{off}\left(\frac{\tau_{on}}{\tau_{on} + \tau_{off}}\right)^{\frac{\tau_{on}}{\tau_{off}}}(\tau_{on} + \tau_{off})^{-1} \quad (5)$$

For the calcium indicator OGB-1, typical values of these parameters for neocortical pyramidal neurons are $\tau_{on} = 10$ ms, $A_{peak} = 7\%\ \Delta F/F$, $\tau_{off} = 0.5$–1 s (Grewe et al., 2010). For the low firing regime we used the canonical elementary $\Delta F/F$ transient (Equation 4) as impulse response function. Other more complex shapes of the elementary transient, for example a double-exponential decay (Grewe et al., 2010), could be easily incorporated into the simulation framework. Because of the linear approximation, we obtained the fluorescence traces for the entire duration of the simulations by convolving the simulated spike trains with this elementary $\Delta F/F$ transient.

At higher AP firing rates, $[Ca^{2+}]_i$ may reach levels sufficiently high to cause substantial saturation of the calcium indicator. We therefore incorporated the possibility to account for indicator saturation in our simulation framework. Assuming a non-cooperative calcium binding characteristics, the saturation level S (ranging from 0 to 1) is given by:

$$S = \frac{[CaB]}{[B]_T} = \frac{[Ca^{2+}]_i}{[Ca^{2+}]_i + K_d} = \frac{[Ca^{2+}]_{rest} + K_d \frac{\Delta F/F}{\Delta F/F_{max}}}{[Ca^{2+}]_{rest} + K_d} \quad (6)$$

Here, $[B]_T$ denotes the indicator concentration in the cell and the equation's right side was obtained by insertion of equation 1. Importantly, indicator saturation not only leads to a non-linear transformation between $[Ca^{2+}]_i$ and $\Delta F/F$ but also directly affects buffered $[Ca^{2+}]_i$ dynamics, an aspect that has been neglected in previous attempts to incorporate indicator saturation in spike inference algorithms (Vogelstein et al., 2009; Stetter et al., 2012). Differentiation of Equation 6 with respect to $[Ca^{2+}]_i$ yields the so-called Ca^{2+}-binding ratio κ_B (or "buffering capacity") of the indicator, which decreases with increasing $[Ca^{2+}]_i$ levels near saturation:

$$\kappa_B = [B]_T \frac{\partial S}{\partial [Ca^{2+}]_i} = \frac{\partial [CaB]}{\partial [Ca^{2+}]_i} = \frac{[B]_T K_d}{([Ca^{2+}]_i + K_d)^2} \quad (7)$$

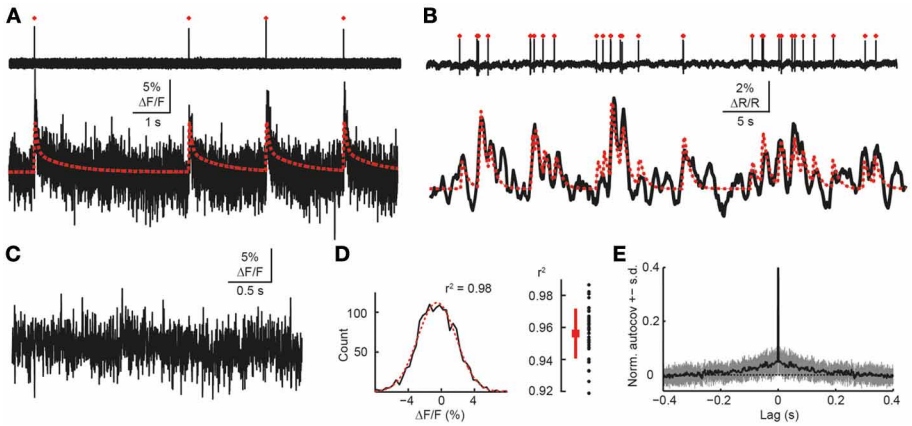

FIGURE 9 | Validation of simulation framework with experimental data. (A) Simultaneous cell-attached recording and high-speed two-photon calcium imaging in mouse neocortex *in vivo*. Top trace: cell-attached recording, APs marked by red dots. Bottom trace: measured cellular $\Delta F/F$ calcium signal (black) as well as simulated $\Delta F/F$ traces (red) for the recorded spike train. Imaging data were acquired with OGB-1 at 490 Hz sampling rate (Grewe et al., 2010). Note that a non-saturating model with double-exponential decay was used in this case to generate the simulated trace. **(B)** Simultaneous cell-attached recording and two-photon calcium imaging using the genetically-encoded calcium indicator YC3.60 (Lütcke et al., 2010). Top trace: cell-attached recording, APs marked by red dots. Bottom trace: measured cellular calcium signal (black) as well as simulated $\Delta F/F$ traces (red) for the recorded spike train (sampling rate: 7.81 Hz; expressed as relative percentage change $\Delta R/R$ of the YFP/CFP fluorescence ratio). A non-saturating model with single-exponential decay was used to generate the simulated trace. **(C)** Noise $\Delta F/F$ trace during episode without AP, as confirmed by simultaneous cell-attached recording (data not shown). Sampling rate: 490 Hz. **(D)** Left: distribution of signal intensities for data shown in **(C)**. Gaussian fit in red ($r^2 = 0.98$). Right: distribution of goodness-of-fit of Gaussian fits (r^2) for pooled data set (96 s total recording time). **(E)** Mean normalized autocovariance (±SD) for pooled noise data set. Peak at 0 s lag clipped.

Note that the Ca^{2+}-binding ratio critically depends on the indicator's Ca^{2+}-binding affinity and its total concentration. The effect of adding an exogenous Ca^{2+}-buffer such as the indicator on AP-evoked somatic calcium signals is well-understood for neocortical pyramidal neurons and is typically approximated by a single-compartment model, which assumes chemical equilibrium and neglects diffusion (Helmchen and Tank, 2011). The model additionally considers an endogenous Ca^{2+}-binding ratio κ_S, which we assumed to be constant [$\kappa_S = 100$; (Helmchen et al., 1996)], and the Ca^{2+} extrusion rate γ ($800\,s^{-1}$) (Helmchen and Tank, 2011). $[Ca^{2+}]_{rest}$ was assumed 50 nM. The relaxation of $[Ca^{2+}]_i$ from an elevated level back to resting level is then described by the following non-linear differential equation:

$$\frac{d[Ca^{2+}]_i}{dt} = \frac{-\gamma\,\Delta[Ca^{2+}]_i}{(1+\kappa_S+\kappa_B)} = -\gamma\left(1+\kappa_S+\frac{[B]_T K_d}{([Ca^{2+}]_i+K_d)^2}\right)^{-1}([Ca^{2+}]_i-[Ca^{2+}]_{rest}) \quad (8)$$

To calculate the model $[Ca^{2+}]_i$ traces for a given spike train, we numerically solved Equation 8 for each spike-to-spike interval starting from the $[Ca^{2+}]_i$ level reached after each AP. This level was calculated by incrementing the pre-AP $[Ca^{2+}]_i$ level at the moment of the next spike's occurrence t_{spike} by

$$\Delta[Ca^{2+}]_i(t_{spike}) = \frac{\Delta[Ca^{2+}]_T}{(1+\kappa_S+\kappa_B)} = \left(1+\kappa_S+\frac{[B]_T K_d}{([Ca^{2+}]_i(t_{spike})+K_d)^2}\right)^{-1}\Delta[Ca^{2+}]_T \quad (9)$$

Here, $\Delta[Ca^{2+}]_T$ denotes the total intracellular calcium concentration change caused by an AP, which was assumed 7.6 μM. The reduction of κ_B at elevated $[Ca^{2+}]_i$ levels due to indicator saturation thus leads to an increase of $\Delta[Ca^{2+}]_i$ per AP. The sharp increments of $[Ca^{2+}]_i$ for each spike were smoothed with an exponential rising onset function ($\tau_{on} = 20$ ms) similar to Equation 4. Finally, we transformed the $[Ca^{2+}]_i$ trace to a $\Delta F/F$ trace using equation 1, presuming the following reasonable parameter values for OGB-1: $K_d = 250$ nM, $[B]_T = 50$ μM, $\Delta F/F_{max} = 93\%$. With these parameter settings, a single-AP evoked $\Delta F/F$ transient from resting $[Ca^{2+}]_i$ level was similar to the stereotype $\Delta F/F$ transient described by Equation 4. Note that despite the increased $\Delta[Ca^{2+}]_i$ at elevated $[Ca^{2+}]_i$ levels the non-linear transformation between $[Ca^{2+}]_i$ and $\Delta F/F$ (Equation 1) has the effect that the $\Delta F/F$-increment per AP becomes small closer to saturation (see **Figure 4B**).

For both the linear (low firing rate) and non-linear (higher firing rates) case, we added Gaussian white noise with standard deviation SD_{noise} to the simulated $\Delta F/F$ traces. We assumed a realistic range of signal-to-noise ratios (SNR) for AP-evoked calcium transients, where we defined SNR as:

$$SNR = \frac{A_{peak}}{SD_{noise}} \quad (10)$$

We verified the assumption of Gaussian noise by empirically determining the noise distribution from random-access calcium imaging data (OGB-1; 490 Hz scan rate) (Grewe et al., 2010) when no spike had occurred (as verified by simultaneous electrophysiology). Without exception, noise distributions could be well-approximated by fitting a Gaussian curve ($r^2 = 0.96 \pm 0.02$),

suggesting that residual noise in two-photon calcium imaging indeed can be assumed normally distributed (**Figures 9C,D**) and contains little, if any, auto-correlation at lags >0.1 s (**Figure 9E**). Gaussian noise is a reasonable assumption because the number of detected photons is likely to be much greater than 100 under two-photon imaging conditions (Ranganathan and Koester, 2010). We note that for extremely low light conditions this assumption may not be valid. As the last step in our generation of simulated $\Delta F/F$ traces, we subsampled the resulting noisy $\Delta F/F$ trace from the original temporal resolution of 2 kHz to a given target frame rate, f, by selecting the center data point for each time interval Δt, where $\Delta t = 1/f$.

In summary, our analysis indicates that the presented simulation framework provides a valid model for AP-evoked calcium signals measured *in vivo* using two-photon microscopy. While experimental data may be characterized by additional noise sources not captured in our model (for example slow drifts or motion artifacts), these are generally easy to identify and remove prior to further data analysis. Whereas the linear description is appropriate for many cases and has been widely adopted (Yaksi and Friedrich, 2006; Vogelstein et al., 2010; Mishchenko et al., 2011), we have here also generalized our approach to the non-linear regime by considering indicator saturation. Extension to include further non-linearities—such as for example saturation of endogenous buffers, cooperative indicator Ca^{2+}-binding, e.g., for GECIs (Pologruto et al., 2004; Horikawa et al., 2010; Chen et al., 2013b), or diffusional equilibration—will be straight forward. Likewise, other non-linear relationships between $[Ca^{2+}]_i$ and fluorescence readouts different from $\Delta F/F$, for example using ratiometric measurements, could also be considered.

RECONSTRUCTION OF SPIKE TRAINS FROM CALCIUM INDICATOR SIGNALS

Action potentials were recovered from simulated $\Delta F/F$ traces using the peeling algorithm that we have introduced previously (Grewe et al., 2010). Briefly, AP-evoked fluorescence signal events were detected using Schmitt-trigger thresholding (high threshold: +1.75 SD, low threshold: −1 SD, minimal duration: 0.3 s) with additional integral check (at least 50% of theoretical noise-free integral). In the original peeling algorithm we assumed a linear relationship between $[Ca^{2+}]_i$ and $\Delta F/F$, which we also applied here for the low firing regime. Specifically, a stereotype single-AP evoked $\Delta F/F$ transient waveform (with the same parameters as used for the simulation of $[Ca^{2+}]_i$ transients, unless noted otherwise) was iteratively subtracted ("peeled off") as long as the integral of the residual trace remained positive and threshold-passing occurred.

An advantage of the model-based nature of the peeling algorithm is that a non-linearity like indicator saturation can be easily incorporated. Here, we extended the peeling algorithm to take saturation into account, in order to enable spike reconstruction from saturating $\Delta F/F$ traces at high AP firing rates (up to 30 Hz). To this end, the single-AP evoked $\Delta F/F$ transient was recalculated for each AP taking the respective pre-AP $[Ca^{2+}]_i$ level into account (again presuming parameter values for OGB-1; see above). More specific, the $[Ca^{2+}]_i$-level dependent $\Delta F/F$ transient was calculated by taking the difference between the $\Delta F/F$ relaxation traces from post-AP and pre-AP levels (both computed by transforming the respective $[Ca^{2+}]_i$ decays, obtained by solving the differential Equation 8). For comparison of error rates we applied either the simple linear or the saturating peeling algorithm to $[Ca^{2+}]_i$ traces generated with a saturating indicator.

For both the linear and saturating peeling approach, the temporal precision of detected spikes was further improved by optimization of spike times (±1 s around the spike time determined with the peeling algorithm; ±0.1 s for high AP rates). Optimization was performed by minimizing the squared sum of the residual trace using a pattern search algorithm (implemented in the Matlab Optimization toolbox).

To examine spike detection performance independent of the particular Schmitt-trigger thresholds, we performed "precision-recall" (PR) analysis (see **Table 1**) by selecting combinations of Schmitt-trigger thresholds over wide ranges (high threshold: −2 to +5 SD; low threshold: −5 to +2 SD; minimal duration: 0–1 s) (**Figures 2D,E**). Within the framework of PR analysis (Davis and Goadrich, 2006), we defined the break-even point as the data point closest to the unity line. Error rate α_{AP} was defined as max(FDR, 1-TPR) at this point (range 0–1). Intuitively, α_{AP} describes the distance of the break-even point from the upper-right corner of the PR-curve, which represents optimal performance (Davis and Goadrich, 2006).

COMPARISON OF ORIGINAL AND RECONSTRUCTED SPIKE TRAINS

Spike time comparison was performed by successively matching spikes in the original and reconstructed spike train based on ascending spike time difference (up to a maximal difference of 0.5 s, see **Figure 1D**). Remaining spikes in the original spike train reduce the true positive rate (calculated as fraction of total spikes in the original spike train) while spikes remaining in the reconstructed train contribute to the false discovery rate (calculated as a fraction of total spikes in the reconstructed spike

Table 1 | Overview of spike metrics to quantify spike reconstruction accuracy.

		Simulated spike train		
		Spike occurred	**No spike occurred**	**Total**
Reconstructed spike train	**Spike detected**	True positive, TP	False discovery, FD	TP + FD
	No spike detected	Missed spike, MS	Correct reject, CR	
	Total	TP + MS		

Simulated spikes may be either detected (true positive, TP) or missed (MS) by the reconstruction algorithm. We call the ratio of true discoveries to the total number of simulated spikes the True Positive Rate, TPR = TP/(TP + MS) or "recall." On the other hand, spikes detected by the reconstruction algorithm may be matched by a simulated spike (true positive, TP) or represent false detections (false discovery, FD). We call the ratio of false discoveries to the total number of detected spikes the False Discovery Rate, FDR = FD/(TP + FD). In information retrieval theory (Davis and Goadrich, 2006), (1 − FDR) is also known as "precision." Both TPR and FDR are defined as 0 for the special case of no simulated or reconstructed spikes, respectively.

train). We quantify reconstruction performance by the following parameters (**Table 1**):

1. True positive rate (TPR): fraction of correctly detected spikes (out of total spikes in original spike train); $TPR \in [0, 1]$,
2. False discovery rate (FDR): fraction of false discoveries (out of total spikes in reconstructed spike train); $FDR \in [0, 1]$,
3. Temporal precision: mean and standard deviation of spike time differences between original and reconstructed spike trains, meanΔ_t and $\sigma_{\Delta t}$, respectively (only for correct detections).

LARGE-SCALE NETWORK SIMULATION AND DETAILED NEURON MODEL

We simulated a network of 25,000 leaky integrate-and-fire neurons with conductance-based synapses (Zenke et al., 2013). 80% of the neurons were modeled as excitatory and 20% as inhibitory. Connectivity was chosen randomly with a density of 10%. In addition, each neuron received common excitatory input from a pool of 2000 independent Poisson processes that were connected randomly to all neurons with 10% probability. The rate of the external input was modeled as a pink noise stochastic process with a mean firing rate of 2 Hz per process and exhibiting fluctuations on all time scales ($1/f$ power spectrum) to mimick complex temporal dynamics of common-input in cortical networks. The network was tuned to the balanced state with asynchronous and irregular firing activity with a mean spiking activity of ∼0.2 Hz.

Specifically, the membrane voltage U_i of a single cell i evolved according to:

$$\tau^m \frac{dU_i}{dt} = \left(U^{\text{rest}} - U_i\right) + g_i^{\text{exc}}(t)\left(U^{\text{exc}} - U_i\right) + g_i^{\text{inh}}(t)\left(U^{\text{inh}} - U_i\right) \tag{11}$$

with membrane time constants $\tau^m = 20$ ms for excitatory neurons and $\tau^m = 10$ ms for inhibitory neurons, resting potential $U^{\text{rest}} = -70$ mV, reversal potentials $U^{\text{exc}} = 0$ mV and $U^{\text{inh}} = -80$ mV and conductances $g_i^{\text{exc}}(t)$ and $g_i^{\text{inh}}(t)$ specified below. A spike was triggered when U_i crossed the spiking threshold ϑ_i. After each spike, U_i was reset to the resting value U^{rest} and the threshold ϑ_i set to $\vartheta^{\text{spike}} = 50$ mV to implement a refractoriness mechanism. Following a reset, the threshold exponentially decayed to its resting value $\vartheta^{\text{rest}} = -50$ mV according to

$$\tau^{\text{thr}} \frac{d\vartheta_i}{dt} = \left(\vartheta^{\text{rest}} - \vartheta_i\right) \tag{12}$$

with time constant $\tau^{\text{thr}} = 5$ ms. The spike train $S_j(t)$ emitted by neuron j is given as $S_j(t) = \sum_k \delta(t - t_j^k)$, where the sum runs over all k corresponding spike times t_j^k. Inhibitory synaptic conductances of the downstream neurons were affected by presynaptic spikes as:

$$\tau^{\text{GABA}} \frac{dg_i^{\text{inh}}}{dt} = -g_i^{\text{inh}} + \sum_{j \in \text{inh}} w_{ij} S_j(t) \tag{13}$$

with $\tau^{\text{GABA}} = 10$ ms. Excitatory synapses were modeled containing a fast AMPA component with exponential decay ($\tau^{\text{AMPA}} =$ 5 ms) and a slow NMDA component ($\tau^{\text{NMDA}} = 100$ ms):

$$\tau^{\text{AMPA}} \frac{dg_i^{\text{AMPA}}}{dt} = -g_i^{\text{AMPA}} + \sum_{j \in \text{exc}} w_{ij} S_j(t) \tag{14}$$

$$\tau^{\text{NMDA}} \frac{dg_i^{\text{NMDA}}}{dt} = -g_i^{\text{NMDA}} + g_i^{\text{AMPA}} \tag{15}$$

The complete excitatory postsynaptic potential (EPSP) was obtained by a weighted sum of the AMPA and NMDA conductances:

$$g_i^{\text{exc}}(t) = 0.5 g_i^{\text{AMPA}}(t) + 0.5 g_i^{\text{NMDA}}(t) \tag{16}$$

The weight values w_{ij} of the synapse connecting neuron j with i ($w_{ij} = 0$ if the connection does not exist) are given as follows: $w(E \to E) = w(E \to I) = 0.2$ and $w(I \to E) = w(I \to I) = 0.9$. The external Poisson inputs were connected with a constant weight $w(\text{ext} \to E, I) = 0.22$. For computational efficiency, the voltage dependence of NMDA channels was omitted. All differential equations were integrated numerically using a forward Euler scheme with 0.1 ms time step using custom-written C/C++ code. Spike trains were generated for a total duration of $T =$ 10,000 s.

CONNECTIVITY RECONSTRUCTION BASED ON COUPLED POINT PROCESS MODELS

We selected subsets of $N = 50$ excitatory neurons from the population that had an average firing rate of 0.6 Hz or higher and reconstructed the connectivity between neurons of this subpopulation based on their spike trains of length $T = 10{,}000$ s. To extract the coupling, we fitted coupled GLMs to the spike trains. Full details on the methodology can be found in (Gerhard et al., 2011). Briefly, spike trains are discretized into a sequence of binary values which represent spiking activity within time windows of length 1 ms. The instantaneous firing probability for each time bin is modeled as a non-linear transformation of the sum of covariates. These include effects from past spiking of the neuron itself as well as spikes from other neurons. All coupling filters are parameterized using a set of spline basis functions and parameters are estimated using standard maximum-likelihood techniques. Note that the strength of the stochastic common-input to each neuron is unobserved and therefore not explicitly modeled. The coefficients corresponding to the cross-coupling filters are used to define the effective coupling structure: The integral of each interaction filter represents its strength (Gerhard et al., 2013). A binary decision about the presence of a directed link can be enforced by thresholding the matrix of coupling strengths. The pair of $\text{TPR}_{\text{links}}$ (fraction of correctly identified connections) and $\text{FDR}_{\text{links}}$ (false discovery rate) defines the error rate for the link reconstruction as the smallest α_{links} that guarantees $\text{FDR}_{\text{links}} \leq \alpha_{\text{links}}$ and $\text{TPR}_{\text{links}} \geq 1 - \alpha_{\text{links}}$. Results generally show the averaged performance derived from the analysis of several random subpopulations of the full network. To derive the expected error rate in the link reconstruction under the assumption that the effect of the absolute detection power (α_{AP}) and spike time jitter ($\sigma_{\Delta t}$) act independently (**Figure 6F**), we use the intuition that detection powers $\sim 1 - \alpha$ would combine multiplicatively, so that,

approximately:

$$\alpha_{\text{links, independent}} \approx 1 - \frac{\left(1 - \alpha_{\text{links, due to } \alpha_{AP}}\right)\left(1 - \alpha_{\text{links, due to } \sigma_{\Delta t}}\right)}{1 - \alpha^*_{\text{links}}} \tag{17}$$

where α^*_{links} is the best achievable error rate (in case of perfect spike reconstruction).

CROSS-CORRELATION ANALYSIS

For comparison, we also implemented a connectivity extraction algorithm based on spike count correlations. We binned the spike trains into bins of size Δt_{cc} and calculated the pairwise Pearson's cross-correlation coefficient of the resulting time series for each pair of neurons in the selected subpopulation. The negative logarithm of the significance value, i.e., the surprise, served as coupling strength. Note that this yielded symmetric (i.e., bidirectional) couplings. We swept through a wide range of values for Δt_{cc} (0.5–500 ms) and chose the one with best performance, resulting in $\Delta t_{cc} = 5$ ms.

SURROGATE MODEL OF SPIKE TRAIN RECONSTRUCTION

We perturbed the spike trains using surrogate transformations to simulate the effect of the errors introduced by imperfect spike reconstruction from noisy calcium imaging data. Specifically, we used the two key parameters that were used to describe the performance of the single-neuron spike reconstruction (error rate α_{AP} and spike jitter $\sigma_{\Delta t}$). For any error rate $\alpha_{AP} > 0$, spikes were randomly removed from the simulated spike trains to match the desired TPR_{AP}. Simultaneously, spikes were added at random times up to the prescribed level of FDR_{AP}. The temporal imprecision $\sigma_{\Delta t}$ was introduced by an additional jitter to all spike times given by a Gaussian distribution around zero with standard deviation $\sigma_{\Delta t}$. We repeated the connectivity estimation based on the perturbed spike trains and measured the performance using the error rate α_{links} whose value should be compared to the reference value achievable in the case of unperturbed original spike trains (assuming perfect spike time reconstruction).

IDENTIFICATION OF GRAPH TOPOLOGY

Scale-free networks

We generated scale-free networks of size 1000 neurons by constructing unweighted, undirected graphs whose degree distributions follow a power law $p(x) \sim x^{-\mu}$ above a minimal degree $k = 20$ with exponent $\mu = 3$, using the standard configuration model (Molloy and Reed, 1995). k was chosen as to produce an average link density of 4%, unless otherwise noted. We simulated the joint effect of calcium dynamics, spike train reconstruction and connectivity extraction by assuming that links are reconstructed with an error rate α_{links}. This surrogate keeps the overall link density approximately constant. We then obtained the degree distribution of the reconstructed network and fitted a power law on its tail where the minimal degree and exponent were obtained using maximum-likelihood methods (Clauset et al., 2009). We constrained the exponent μ to be between 1 and 9 which covers all empirically observed scale-free networks. A goodness-of-fit test was applied to each fit using a Monte Carlo version of the Kolmogorov–Smirnov test (Clauset et al., 2009). We repeated the process of generation, imperfect reconstruction and re-fitting 1000 times and reported the median of the estimated power-law coefficient together with its standard deviation. We concluded that an estimated degree distribution was inconsistent with a power-law shape whenever the median p-value of the fit was below 0.05, i.e., a p-value < 0.05 occurred in more than half of the cases. Histograms of degree distributions were obtained with logarithmically spaced bins and by pooling distributions across all simulations.

Hub neurons

We generated scale-free networks of size 1000 neurons and power-law exponent $\mu = 3$ as described above. We classified hub neurons in these networks as the 100 neurons with the highest degrees. We then simulated an imperfect network reconstruction as before and estimated how well neurons can be classified to be hub neurons as follows: The hit rate specifies the fraction of original hub neurons that belong to the 100 neurons with highest degree in the reconstructed network. A random assignment would lead to a hit rate of 10% (chance level). All estimates are based on 1000 simulations of independent networks.

ACKNOWLEDGMENTS

This work was supported by a grant from the Forschungskredit of the University of Zurich to Henry Lütcke; two grants from the Swiss National Science Foundation (SNSF) to Felipe Gerhard and Wulfram Gerstner (200020-117975 and 200020-132871); an SNSF grant to Fritjof Helmchen (3100A0-114624); the EU-FP7 program (BRAIN-I-NETS project 243914 and BrainScaleS project 269921 to Felipe Gerhard, Friedemann Zenke, Fritjof Helmchen, and Wulfram Gerstner) and a grant from the Swiss SystemsX.ch initiative (project 2008/2011-Neurochoice) to Fritjof Helmchen. We thank B. Grewe for collecting the data shown in **Figures 9A,C**.

SUPPLEMENTARY MATERIAL

The Supplementary Material for this article can be found online at: http://www.frontiersin.org/journal/10.3389/fncir.2013.00201/abstract

REFERENCES

Badel, L., Lefort, S., Brette, R., Petersen, C. C., Gerstner, W., and Richardson, M. J. (2008). Dynamic I-V curves are reliable predictors of naturalistic pyramidal-neuron voltage traces. *J. Neurophysiol.* 99, 656–666. doi: 10.1152/jn.01107.2007

Barabasi, A. L., and Albert, R. (1999). Emergence of scaling in random networks. *Science* 286, 509–512. doi: 10.1126/science.286.5439.509

Bock, D. D., Lee, W. C., Kerlin, A. M., Andermann, M. L., Hood, G., Wetzel, A. W., et al. (2011). Network anatomy and *in vivo* physiology of visual cortical neurons. *Nature* 471, 177–182. doi: 10.1038/nature09802

Bonin, V., Histed, M. H., Yurgenson, S., and Reid, R. C. (2011). Local diversity and fine-scale organization of receptive fields in mouse visual cortex. *J. Neurosci.* 31, 18506–18521. doi: 10.1523/JNEUROSCI.2974-11.2011

Briggman, K. L., Helmstaedter, M., and Denk, W. (2011). Wiring specificity in the direction-selectivity circuit of the retina. *Nature* 471, 183–188. doi: 10.1038/nature09818

Brunel, N. (2000). Dynamics of sparsely connected networks of excitatory and inhibitory spiking neurons. *J. Comput. Neurosci.* 8, 183–208. doi: 10.1023/A:1008925309027

Buzsaki, G. (2004). Large-scale recording of neuronal ensembles. *Nat. Neurosci.* 7, 446–451. doi: 10.1038/nn1233

Chen, J. L., Carta, S., Soldado-Magraner, J., Schneider, B. L., and Helmchen, F. (2013a). Behavior-dependent recruitment of long-range projection neurons in somatosensory cortex. *Nature* 499, 336–340. doi: 10.1038/nature12236

Chen, T. W., Wardill, T. J., Sun, Y., Pulver, S. R., Renninger, S. L., Baohan, A., et al. (2013b). Ultrasensitive fluorescent proteins for imaging neuronal activity. *Nature* 499, 295–300. doi: 10.1038/nature12354

Chen, X., Leischner, U., Varga, Z., Jia, H., Deca, D., Rochefort, N. L., et al. (2012). LOTOS-based two-photon calcium imaging of dendritic spines *in vivo*. *Nat. Protoc.* 7, 1818–1829. doi: 10.1038/nprot.2012.106

Clauset, A., Shalizi, C. R., and Newman, M. E. J. (2009). Power-law distributions in empirical data. *Siam Rev.* 51, 661–703. doi: 10.1137/070710111

Davis, J., and Goadrich, M. (2006). "The relationship between Precision-Recall and ROC curves," in *Proceedings of the 23rd International Conference on Machine Learning*. (Pittsburgh, PA: ACM).

Decharms, R. C., Blake, D. T., and Merzenich, M. M. (1998). Optimizing sound features for cortical neurons. *Science* 280, 1439–1443. doi: 10.1126/science.280.5368.1439

De Kock, C. P., and Sakmann, B. (2008). High frequency action potential bursts (>or= 100 Hz) in L2/3 and L5B thick tufted neurons in anaesthetized and awake rat primary somatosensory cortex. *J. Physiol.* 586, 3353–3364. doi: 10.1113/jphysiol.2008.155580

Dombeck, D. A., Graziano, M. S., and Tank, D. W. (2009). Functional clustering of neurons in motor cortex determined by cellular resolution imaging in awake behaving mice. *J. Neurosci.* 29, 13751–13760. doi: 10.1523/JNEUROSCI.2985-09.2009

Einevoll, G. T., Franke, F., Hagen, E., Pouzat, C., and Harris, K. D. (2011). Towards reliable spike-train recordings from thousands of neurons with multielectrodes. *Curr. Opin. Neurobiol.* 22, 11–17. doi: 10.1016/j.conb.2011.10.001

Engelbrecht, C. J., Gobel, W., and Helmchen, F. (2009). Enhanced fluorescence signal in nonlinear microscopy through supplementary fiber-optic light collection. *Opt. Express* 17, 6421–6435. doi: 10.1364/OE.17.006421

Feldt, S., Bonifazi, P., and Cossart, R. (2011). Dissecting functional connectivity of neuronal microcircuits: experimental and theoretical insights. *Trends Neurosci.* 34, 225–236. doi: 10.1016/j.tins.2011.02.007

Fernández-Alfonso, T., Nadella, K. M., Iacaruso, M. F., Pichler, B., Roš, H., Kirkby, P. A., et al. (2013). Monitoring synaptic and neuronal activity in 3D with synthetic and genetic indicators using a compact acousto-optic lens two-photon microscope. *J. Neurosci. Methods* 222C, 69–81. doi: 10.1016/j.jneumeth.2013.10.021

Fino, E., and Yuste, R. (2011). Dense inhibitory connectivity in neocortex. *Neuron* 69, 1188–1203. doi: 10.1016/j.neuron.2011.02.025

Garaschuk, O., Milos, R. I., Grienberger, C., Marandi, N., Adelsberger, H., and Konnerth, A. (2006). Optical monitoring of brain function *in vivo*: from neurons to networks. *Pflugers Arch.* 453, 385–396. doi: 10.1007/s00424-006-0150-x

Gerhard, F., Kispersky, T., Gutierrez, G. J., Marder, E., Kramer, M., and Eden, U. (2013). Successful reconstruction of a physiological circuit with known connectivity from spiking activity alone. *PLoS Comput. Biol.* 9:e1003138. doi: 10.1371/journal.pcbi.1003138

Gerhard, F., Pipa, G., Lima, B., Neuenschwander, S., and Gerstner, W. (2011). Extraction of network topology from multi-electrode recordings: is there a small-world effect? *Front. Comput. Neurosci.* 5:4. doi: 10.3389/fncom.2011.00004

Göbel, W., and Helmchen, F. (2007). *In vivo* calcium imaging of neural network function. *Physiology (Bethesda)* 22, 358–365. doi: 10.1152/physiol.00032.2007

Greenberg, D. S., Houweling, A. R., and Kerr, J. N. (2008). Population imaging of ongoing neuronal activity in the visual cortex of awake rats. *Nat. Neurosci.* 11, 749–751. doi: 10.1038/nn.2140

Grewe, B. F., and Helmchen, F. (2009). Optical probing of neuronal ensemble activity. *Curr. Opin. Neurobiol.* 19, 520–529. doi: 10.1016/j.conb.2009.09.003

Grewe, B. F., Langer, D., Kasper, H., Kampa, B. M., and Helmchen, F. (2010). High-speed *in vivo* calcium imaging reveals neuronal network activity with near-millisecond precision. *Nat. Methods* 7, 399–405. doi: 10.1038/nmeth.1453

Grienberger, C., and Konnerth, A. (2012). Imaging calcium in neurons. *Neuron* 73, 862–885. doi: 10.1016/j.neuron.2012.02.011

Han, J. D., Dupuy, D., Bertin, N., Cusick, M. E., and Vidal, M. (2005). Effect of sampling on topology predictions of protein-protein interaction networks. *Nat. Biotechnol.* 23, 839–844. doi: 10.1038/nbt1116

Helmchen, F. (2012). "Calcium imaging," in *Handbook of Neural Activity Measurement,* eds R. Brette and A. Destexhe (Cambridge: Cambridge University Press).

Helmchen, F., Imoto, K., and Sakmann, B. (1996). Ca2+ buffering and action potential-evoked Ca^{2+} signaling in dendrites of pyramidal neurons. *Biophys. J.* 70, 1069–1081. doi: 10.1016/S0006-3495(96)79653-4

Helmchen, F., and Tank, D. W. (2011). "A single compartment model of calcium dynamics in dendrites and nerve terminals," in *Imaging in Neuroscience: A Laboratory Manual,* eds F. Helmchen and A. Konnerth (New York, NY: Cold Spring Harbor Laboratory Press).

Hendel, T., Mank, M., Schnell, B., Griesbeck, O., Borst, A., and Reiff, D. F. (2008). Fluorescence changes of genetic calcium indicators and OGB-1 correlated with neural activity and calcium *in vivo* and *in vitro*. *J. Neurosci.* 28, 7399–7411. doi: 10.1523/JNEUROSCI.1038-08.2008

Hofer, S. B., Ko, H., Pichler, B., Vogelstein, J., Ros, H., Zeng, H., et al. (2011). Differential connectivity and response dynamics of excitatory and inhibitory neurons in visual cortex. *Nat. Neurosci.* 14, 1045–1052. doi: 10.1038/nn.2876

Horikawa, K., Yamada, Y., Matsuda, T., Kobayashi, K., Hashimoto, M., Matsu-Ura, T., et al. (2010). Spontaneous network activity visualized by ultrasensitive Ca(2+) indicators, yellow Cameleon-Nano. *Nat. Methods* 7, 729–732. doi: 10.1038/nmeth.1488

Kampa, B. M., Gobel, W., and Helmchen, F. (2011). Measuring neuronal population activity using 3D laser scanning. *Cold Spring Harb. Protoc.* 2011, 1340–1349. doi: 10.1101/pdb.prot066597

Katona, G., Szalay, G., Maak, P., Kaszas, A., Veress, M., Hillier, D., et al. (2012). Fast two-photon *in vivo* imaging with three-dimensional random-access scanning in large tissue volumes. *Nat. Methods* 9, 201–208. doi: 10.1038/nmeth.1851

Kerlin, A. M., Andermann, M. L., Berezovskii, V. K., and Reid, R. C. (2010). Broadly tuned response properties of diverse inhibitory neuron subtypes in mouse visual cortex. *Neuron* 67, 858–871. doi: 10.1016/j.neuron.2010.08.002

Kerr, J. N., De Kock, C. P., Greenberg, D. S., Bruno, R. M., Sakmann, B., and Helmchen, F. (2007). Spatial organization of neuronal population responses in layer 2/3 of rat barrel cortex. *J. Neurosci.* 27, 13316–13328. doi: 10.1523/JNEUROSCI.2210-07.2007

Kerr, J. N., Greenberg, D., and Helmchen, F. (2005). Imaging input and output of neocortical networks *in vivo*. *Proc. Natl. Acad. Sci. U.S.A.* 102, 14063–14068. doi: 10.1073/pnas.0506029102

Knopfel, T. (2012). Genetically encoded optical indicators for the analysis of neuronal circuits. *Nat. Rev. Neurosci.* 13, 687–700. doi: 10.1038/nrn3293

Ko, H., Hofer, S. B., Pichler, B., Buchanan, K. A., Sjostrom, P. J., and Mrsic-Flogel, T. D. (2011). Functional specificity of local synaptic connections in neocortical networks. *Nature* 473, 87–91. doi: 10.1038/nature09880

Langer, D., and Helmchen, F. (2012). *Post hoc* immunostaining of GABAergic neuronal subtypes following *in vivo* two-photon calcium imaging in mouse neocortex. *Pflugers Arch.* 463, 339–354. doi: 10.1007/s00424-011-1048-9

Lillis, K. P., Eng, A., White, J. A., and Mertz, J. (2008). Two-photon imaging of spatially extended neuronal network dynamics with high temporal resolution. *J. Neurosci. Methods* 172, 178–184. doi: 10.1016/j.jneumeth.2008.04.024

Looger, L. L., and Griesbeck, O. (2012). Genetically encoded neural activity indicators. *Curr. Opin. Neurobiol.* 22, 18–23. doi: 10.1016/j.conb.2011.10.024

Lütcke, H., and Helmchen, F. (2011). Two-photon imaging and analysis of neural network dynamics. *Rep. Prog. Phys.* 74. doi: 10.1088/0034-4885/74/8/086602

Lütcke, H., Margolis, D. J., and Helmchen, F. (2013). Steady or changing? Long-term monitoring of neuronal population activity. *Trends Neurosci.* 36, 375–384. doi: 10.1016/j.tins.2013.03.008

Lütcke, H., Murayama, M., Hahn, T., Margolis, D. J., Astori, S., Zum Alten Borgloh, S. M., et al. (2010). Optical recording of neuronal activity with a genetically-encoded calcium indicator in anesthetized and freely moving mice. *Front. Neural Circuits* 4:9. doi: 10.3389/fncir.2010.00009

Margolis, D. J., Lütcke, H., Schulz, K., Haiss, F., Weber, B., Kügler, S., et al. (2012). Reorganization of cortical population activity imaged throughout long-term sensory deprivation. *Nat. Neurosci.* 15, 1539–1546. doi: 10.1038/nn.3240

Mensi, S., Naud, R., Pozzorini, C., Avermann, M., Petersen, C. C., and Gerstner, W. (2012). Parameter extraction and classification of three cortical neuron types reveals two distinct adaptation mechanisms. *J. Neurophysiol.* 107, 1756–1775. doi: 10.1152/jn.00408.2011

Mishchenko, Y., Vogelstein, J. T., and Paninski, L. (2011). A bayesian approach for inferring neuronal connectivity from calcium fluorescent imaging data. *Ann. Appl. Stat.* 5, 1229–1261. doi: 10.1214/09-AOAS303

Molloy, M., and Reed, B. (1995). A critical-point for random graphs with a given degree sequence. *Random Struct. Algor.* 6, 161–179. doi: 10.1002/rsa.3240060204

Nikolenko, V., Poskanzer, K. E., and Yuste, R. (2007). Two-photon photostimulation and imaging of neural circuits. *Nat. Methods* 4, 943–950. doi: 10.1038/nmeth1105

Nikolenko, V., Watson, B. O., Araya, R., Woodruff, A., Peterka, D. S., and Yuste, R. (2008). SLM microscopy: scanless two-photon imaging and photostimulation with spatial light modulators. *Front. Neural Circuits* 2:5. doi: 10.3389/neuro.04.005.2008

Oheim, M., Beaurepaire, E., Chaigneau, E., Mertz, J., and Charpak, S. (2001). Two-photon microscopy in brain tissue: parameters influencing the imaging depth. *J. Neurosci. Methods* 111, 29–37. doi: 10.1016/S0165-0270(01)00438-1

Ohki, K., Chung, S., Ch'ng, Y., Kara, P., and Reid, R. (2005). Functional imaging with cellular resolution reveals precise micro-architecture in visual cortex. *Nature* 433, 597–603. doi: 10.1038/nature03274

Ohki, K., Chung, S., Kara, P., Hubener, M., Bonhoeffer, T., and Reid, R. C. (2006). Highly ordered arrangement of single neurons in orientation pinwheels. *Nature* 442, 925–928. doi: 10.1038/nature05019

Olshausen, B. A., and Field, D. J. (2005). How close are we to understanding v1? *Neural Comput.* 17, 1665–1699. doi: 10.1162/0899766054026639

Onativia, J., Schultz, S. R., and Dragotti, P. L. (2013). A finite rate of innovation algorithm for fast and accurate spike detection from two-photon calcium imaging. *J. Neural Eng.* 10, 046017. doi: 10.1088/1741-2560/10/4/046017

Osten, P., and Margrie, T. W. (2013). Mapping brain circuitry with a light microscope. *Nat. Methods* 10, 515–523. doi: 10.1038/nmeth.2477

Otsu, Y., Bormuth, V., Wong, J., Mathieu, B., Dugue, G. P., Feltz, A., et al. (2008). Optical monitoring of neuronal activity at high frame rate with a digital random-access multiphoton (RAMP) microscope. *J. Neurosci. Methods* 173, 259–270. doi: 10.1016/j.jneumeth.2008.06.015

Packer, A. M., and Yuste, R. (2011). Dense, unspecific connectivity of neocortical parvalbumin-positive interneurons: a canonical microcircuit for inhibition? *J. Neurosci.* 31, 13260–13271. doi: 10.1523/JNEUROSCI.3131-11.2011

Pillow, J. W., Shlens, J., Paninski, L., Sher, A., Litke, A. M., Chichilnisky, E. J., et al. (2008). Spatio-temporal correlations and visual signalling in a complete neuronal population. *Nature* 454, 995–999. doi: 10.1038/nature07140

Pologruto, T. A., Yasuda, R., and Svoboda, K. (2004). Monitoring neural activity and [Ca2+] with genetically encoded Ca2+ indicators. *J. Neurosci.* 24, 9572–9579. doi: 10.1523/JNEUROSCI.2854-04.2004

Prakash, R., Yizhar, O., Grewe, B., Ramakrishnan, C., Wang, N., Goshen, I., et al. (2012). Two-photon optogenetic toolbox for fast inhibition, excitation and bistable modulation. *Nat. Methods* 9, 1171–1179. doi: 10.1038/nmeth.2215

Ranganathan, G. N., and Koester, H. J. (2010). Optical recording of neuronal spiking activity from unbiased populations of neurons with high spike detection efficiency and high temporal precision. *J. Neurophysiol.* 104, 1812–1824. doi: 10.1152/jn.00197.2010

Reddy, G. D., and Saggau, P. (2005). Fast three-dimensional laser scanning scheme using acousto-optic deflectors. *J. Biomed. Opt.* 10, 064038. doi: 10.1117/1.2141504

Rochefort, N. L., Garaschuk, O., Milos, R. I., Narushima, M., Marandi, N., Pichler, B., et al. (2009). Sparsification of neuronal activity in the visual cortex at eye-opening. *Proc. Natl. Acad. Sci. U.S.A.* 106, 15049–15054. doi: 10.1073/pnas.0907660106

Rothschild, G., Nelken, I., and Mizrahi, A. (2010). Functional organization and population dynamics in the mouse primary auditory cortex. *Nat. Neurosci.* 13, 353–360. doi: 10.1038/nn.2484

Sasaki, T., Takahashi, N., Matsuki, N., and Ikegaya, Y. (2008). Fast and accurate detection of action potentials from somatic calcium fluctuations. *J. Neurophysiol.* 100, 1668–1676. doi: 10.1152/jn.00084.2008

Sjulson, L., and Miesenbock, G. (2007). Optical recording of action potentials and other discrete physiological events: a perspective from signal detection theory. *Physiology* 22, 47–55. doi: 10.1152/physiol.00036.2006

Smith, A. C., and Brown, E. N. (2003). Estimating a state-space model from point process observations. *Neural Comput.* 15, 965–991. doi: 10.1162/089976603765202622

Song, S., Sjostrom, P. J., Reigl, M., Nelson, S., and Chklovskii, D. B. (2005). Highly nonrandom features of synaptic connectivity in local cortical circuits. *PLoS Biol.* 3:e68. doi: 10.1371/journal.pbio.0030068

Stetter, O., Battaglia, D., Soriano, J., and Geisel, T. (2012). Model-free reconstruction of excitatory neuronal connectivity from calcium imaging signals. *PLoS Comput. Biol.* 8:e1002653. doi: 10.1371/journal.pcbi.1002653

Stumpf, M. P., Wiuf, C., and May, R. M. (2005). Subnets of scale-free networks are not scale-free: sampling properties of networks. *Proc. Natl. Acad. Sci. U.S.A.* 102, 4221–4224. doi: 10.1073/pnas.0501179102

Turaga, S. C., Buesing, L., Packer, A. M., Dalgleish, M., Petit, N., Hausser, M., et al. (in press). Inferring neural population dynamics from multiple partial recordings of the same neural circuit. *Adv. Neural Inf. Process. Syst.*

Vidne, M., Ahmadian, Y., Shlens, J., Pillow, J. W., Kulkarni, J., Litke, A. M., et al. (2012). Modeling the impact of common noise inputs on the network activity of retinal ganglion cells. *J. Comput. Neurosci.* 33, 97–121. doi: 10.1007/s10827-011-0376-2

Vogels, T. P., Rajan, K., and Abbott, L. F. (2005). Neural network dynamics. *Annu. Rev. Neurosci.* 28, 357–376. doi: 10.1146/annurev.neuro.28.061604.135637

Vogelstein, J. T., Packer, A. M., Machado, T. A., Sippy, T., Babadi, B., Yuste, R., et al. (2010). Fast nonnegative deconvolution for spike train inference from population calcium imaging. *J. Neurophysiol.* 104, 3691–3704. doi: 10.1152/jn.01073.2009

Vogelstein, J. T., Watson, B. O., Packer, A. M., Yuste, R., Jedynak, B., and Paninski, L. (2009). Spike inference from calcium imaging using sequential Monte Carlo methods. *Biophys. J.* 97, 636–655. doi: 10.1016/j.bpj.2008.08.005

Wilt, B. A., Fitzgerald, J. E., and Schnitzer, M. J. (2013). Photon shot noise limits on optical detection of neuronal spikes and estimation of spike timing. *Biophys. J.* 104, 51–62. doi: 10.1016/j.bpj.2012.07.058

Wolfe, J., Houweling, A. R., and Brecht, M. (2010). Sparse and powerful cortical spikes. *Curr. Opin. Neurobiol.* 20, 306–312. doi: 10.1016/j.conb.2010.03.006

Yaksi, E., and Friedrich, R. W. (2006). Reconstruction of firing rate changes across neuronal populations by temporally deconvolved Ca2+ imaging. *Nat. Methods* 3, 377–383. doi: 10.1038/nmeth874

Zenke, F., Hennequin, G., and Gerstner, W. (2013). Synaptic plasticity in neural networks needs homeostasis with a fast rate detector. *PLoS Comput. Biol.* 9:e1003330. doi: 10.1371/journal.pcbi.1003330

Conflict of Interest Statement: The authors declare that the research was conducted in the absence of any commercial or financial relationships that could be construed as a potential conflict of interest.

Received: 15 July 2013; accepted: 04 December 2013; published online: 24 December 2013.

Citation: Lütcke H, Gerhard F, Zenke F, Gerstner W and Helmchen F (2013) Inference of neuronal network spike dynamics and topology from calcium imaging data. Front. Neural Circuits 7:201. doi: 10.3389/fncir.2013.00201

This article was submitted to the journal Frontiers in Neural Circuits.